

AGARD CONFERENCE  
PROCEEDINGS NO. 3



# **Propagation Factors in Space Communications**

THE ADVISORY GROUP  
FOR AEROSPACE RESEARCH AND DEVELOPMENT  
OF  
THE NORTH ATLANTIC TREATY ORGANIZATION



Editor  
W. T. BLACKBAND  
ROYAL AIRCRAFT ESTABLISHMENT  
FARNBOROUGH  
ENGLAND





Published by



TECHNIVISION  
MAIDENHEAD, ENGLAND

COPYRIGHT



1967

ADVISORY GROUP FOR  
AEROSPACE RESEARCH AND DEVELOPMENT  
NORTH ATLANTIC TREATY ORGANIZATION

LIBRARY OF CONGRESS CARD NO. 66-28578

Set in Baskerville 10 on 11 pt

Printed and Bound

by



W. and J. MACKAY and CO LTD  
LONDON and CHATHAM, ENGLAND

vii

---

# CONTENTS

<i>Chapter</i>	<i>Page</i>
PREFACE	xi
INTRODUCTION	xiii
PART I	
GENERAL SURVEY OF PROPAGATION FACTORS	
1-1 A survey of tropospheric, ionospheric and extra-terrestrial effects on radio propagation between the earth and space vehicles <span style="float: right;"><i>G. H. Millman</i></span>	3
PART 2	
PROPAGATION IN THE INTERPLANETARY SPACE	
2-1 The effect of the interplanetary medium on S-band telecommunications <span style="float: right;"><i>M. Easterling and R. Goldstein</i></span>	59
2-2 Atmospheric and interplanetary refraction effects on high precision planetary radar measurements <span style="float: right;"><i>D. O. Muhleman and P. Reichley</i></span>	73
2-3 A summary of preliminary results of the <i>Mariner IV</i> radio-occultation experiment <span style="float: right;"><i>A. J. Kliore, D. L. Cain, G. S. Levy, V. R. Eshleman, G. Fjeldbo and F. D. Drake</i></span>	75
PART 3	
IONOSPHERIC EFFECTS	
3-1 Ionospheric refraction of H.F. radio waves propagating between the earth and orbiting satellites <span style="float: right;"><i>R. G. Maliphant</i></span>	85
3-2 Etude de l'amplitude du champ radioélectrique d'un satellite a l'horizon de la station <span style="float: right;"><i>J. F. Aurejac et J. Papet-Lepine</i></span>	105
3-3 Ionospheric resonance phenomena at V.H.F. and H.F. and their effects on space telecommunications <span style="float: right;"><i>Irvine Paghis</i></span>	133
3-4 Irregularities and plasma resonances observed by the fixed frequency topside sounder satellite <span style="float: right;"><i>W. Calvert and T. E. Van Zandt</i></span>	161
3-5 Electron content measurements with a stationary satellite <span style="float: right;"><i>E. Harnischmacher</i></span>	163
3-6 Using ionospheric prediction charts to tentatively forecast V.L.F. signal intensity in satellite communications <span style="float: right;"><i>H. J. Albrecht</i></span>	175
3-7 Large-scale irregularities and horizontal gradient of the ionosphere from active satellite transmission measurements <span style="float: right;"><i>M. Anastassiades and D. Matsoukas</i></span>	181
3-8 Diffraction of random waves in a homogeneous anisotropic medium <span style="float: right;"><i>K. C. Yeh</i></span>	195
3-9 Topside spread-F and satellite radio scintillations <span style="float: right;"><i>J. L. Jespersen</i></span>	203
3-10 Polarization variations of satellite-emitted radio signals <span style="float: right;"><i>H. Soicher, G. Vogt, P. R. Arendt, W. H. Fischer and J. Grau</i></span>	209

# CONTENTS

<i>Chapter</i>		<i>Page</i>
3-11	Effects of ionospheric irregularities on space data acquisition in the auroral zone <i>E. J. Fremouw</i>	225
3-12	Auroral zone radio star scintillation measurements and interpretations <i>J. M. Lansinger</i>	241
3-13	Effects of non-inverse-frequency-squared absorption events <i>S. M. Bennett and G. F. Rourke</i>	261

## PART 4

### RE-ENTRY PLASMA SHEATH EFFECTS

4-1	Ionospheric effects of solar X-ray enhancements <i>Tudor B. Jones</i>	275
4-2	Radio-wave propagation through re-entry plasma sheaths <i>M. P. Bachynski</i>	287
4-3	Electro-magnetic wave propagation through an ionized gas layer as an optimal process <i>M. Z. v. Krzywoblocki</i>	309
4-4	Methods of improving radio-wave propagation through the plasma sheath <i>R. Rawhouser</i>	327
4-5	Surface wave propagation along a dielectric rod immersed in an unmagnetized plasma and its application to measuring electron density <i>P. N. Robson and R. D. Stewart</i>	337
4-6	Effects of the plasma sheath on antenna performance <i>C. T. Swift and H. Hodara</i>	351
4-7	Noise produced by terrestrial sources in the near-earth space <i>K. Rawer</i>	383

## PART 5

### TROPOSPHERIC EFFECTS

5-1	Absorption of radio waves in the troposphere <i>D. T. Gjessing</i>	411
5-2	Tropospheric refraction and its influence on the coverage of long range radars <i>D. T. Gjessing</i>	423
5-3	Étude expérimentale de la baisse de gain d'antenne dans les liaisons transhorizon <i>L. Boithias and J. Battesti</i>	431
5-4	The influence of wave-front coherence on the radiation parameters of large-size antennas <i>C. Colavito</i>	433
5-5	Laser wave propagation through the atmosphere <i>H. Hodara</i>	445
5-6	Propagation factors at 3.2 millimetres <i>L. A. Hoffman</i>	475
5-7	Space communications propagation studies at Lincoln Laboratory <i>L. J. Ricardi</i>	523
5-8	A review of refraction effects on the apparent angle of arrival of radio signals <i>B. R. Bean and R. E. McGavin</i>	529
	CLOSING REMARKS <i>M. Anastassiades</i>	547

### SUPPLEMENT—TRANSLATIONS

3-2	Study of the amplitude of the radio electric field of a satellite at the horizon of a receiving station <i>J. F. Aurejac and J. Papet-Lepine</i>	551
-----	---	-----

Subject Index

Names Index

Places and Institutions Index

## PREFACE

The Ionospheric Research Committee of the Avionics Panel of AGARD/NATO held its tenth annual symposium meeting in Rome 21–25 September 1965. The subject chosen for discussion was "Propagation factors in space communications". This volume presents the full text of those papers which have not been printed elsewhere and also an account of the informal discussions which followed the presentation of the papers.

## INTRODUCTION

The chapters of this book deal with the broad problems of space communications and not just those of commercial space communications such as arise in the use of a satellite-borne microwave relay in a telephone or television link. Thus on one hand in Chapter 2.2 the propagation effects on high-precision planetary radar measurements are discussed, and Chapters 4-2 to 4-6 cover various aspects of the problem of transmitting through the plasma sheath surrounding a space vehicle during its re-entry into the atmosphere.

If the signals in the lower frequency bands are to be used in space communication the effects of the ionosphere upon their propagation must be predicted. Many papers discuss the effects upon propagation of irregularities in the electron distribution in the ionosphere. These papers fall into two groups, those that are based upon ground observation of satellite-borne transmitters, and those which recount the use of a topside sounder carried in a satellite. The use of the topside sounder has shown that the irregularities in the ionosphere visible from below extend up above the  $F_2$  maximum to at least 800 or 1000 km in altitude. They are thus rather like inverted icebergs with their greatest extent floating above the  $F_2$  maximum and only a relatively small part visible from below. Members of the Ionospheric Research Committee have been studying these irregularities for several years by observation of the Faraday rotation of the plane of polarization of the signals from satellite transmitters. Several chapters are devoted to accounts of this work. The correlation of these ground-based observations with those made using the topside sounder will not be easy but much knowledge must emerge in the process.

The possibility of using ionospheric prediction charts in order to forecast VLF signal intensity in satellite communications is discussed in Chapter 3-6. In that frequency band we are solely concerned with ionospheric effects; however, at the other end of the radio spectrum the millimetric wave propagation is limited by tropospheric turbulence. Chapter 5-6 discusses experimental work in this field at a wavelength of 3.2 mm.

A number of papers in Part 5 dealing with tropospheric propagation effects discuss the limit to the gain of large aerials which results from tropospheric turbulence.

The effects of the troposphere extend in frequency beyond the radio spectrum and Chapter 5-5 gives an account of laser beam propagation and the effects of turbulence upon it.

At the meeting of the Ionospheric Research Committee held in Athens in 1960 there was some discussion of whether or not the study of the ionospheres of planets other than the Earth should come within the terms of reference of the Committee. It seemed at that time to be a somewhat academic subject for discussion, but so fast have the boundaries of knowledge been pushed back that in Chapter 2-3 we have a summary of the preliminary results of the

## INTRODUCTION

*Mariner IV* radio occultation experiment, and this includes an ionization-versus-height profile for the ionosphere of Mars. With progress at this rate what will the editor of the IRC 1970 Proceedings find before him?

W. T. Blackband

CP-2

PART I

GENERAL SURVEY OF PROPAGATION FACTORS

---





## CHAPTER I-I

# A SURVEY OF TROPOSPHERIC, IONOSPHERIC, AND EXTRA-TERRESTRIAL EFFECTS ON RADIO PROPAGATION BETWEEN THE EARTH AND SPACE VEHICLES

GEORGE H. MILLMAN

General Electric Company, Syracuse, New York, U.S.A.

### SUMMARY

Radio waves, when propagating through the troposphere and ionosphere, undergo various types of signal degradation and perturbation due to the nonisotropic and turbulent characteristics of the media. Some of the propagation anomalies which prevail are angular bending, group time delay, phase instability, Doppler frequency shift, attenuation, rotation of the plane of polarization, dispersion effects, and scintillations. In addition, the presence of celestial bodies such as the sun and radio stars introduces noise interference. These natural occurring phenomena are discussed in terms of their influence on earth-space radio transmissions at frequencies in the VHF range and above.

### INTRODUCTION

With the advent of the space age, there have arisen stringent requirements on electronic systems which are essential for the guidance, tracking and control of space vehicles and for communication within the earth-space vehicle complex.

In analyzing and evaluating the capabilities and performance of various electronic system concepts, it is necessary to consider the degradation in the signal information brought about by the propagating medium. In general, the troposphere and the ionosphere are the regions surrounding the earth which affect the propagation of electromagnetic waves.

Signal deterioration results from the fact that there exist in the earth's atmosphere spatial inhomogeneities which are continuously varying as a function of time. The spatial variations, for the most part, yield statistical-bias errors, while the time-varying component results in fluctuating inaccuracies.

Some of the propagational anomalies which prevail when electromagnetic waves traverse the atmosphere are *refractive bending*, *time delays*, Doppler effects, attenuation, scintillations in phase, amplitude and angle-of-arrival, and ionospheric polarization and dispersion effects.

In addition, the presence of celestial radio noise sources such as the sun and radio stars are capable of reducing the overall system sensitivity.

In this paper, these phenomena are described, and estimates are made of the magnitude of the effects as a function of both frequency (above VHF) and spatial geometric coordinates.

## REFRACTION EFFECTS

When radio waves are propagated through the troposphere and the ionosphere they experience a change in direction or refractive bending. This phenomenon, which results from the nonisotropic characteristics of the media, introduces an error in the measurement of the angular position of a space vehicle.

A typical ray path trajectory in the vertical plane is shown in Fig. 1. The elevation angle error due to refraction,  $\Delta E$ , is the angle between the apparent path direction and the direct line-of-sight path.

The index of refraction in the troposphere is greater than unity, and decreases monotonically with altitude. At approximately 30 km this value can be taken as unity for most purposes. In the case of the ionosphere, which commences at about 70 km altitude, the index of refraction is less than unity and is a minimum at the level of maximum ionization density. The region of unity refractive index between the troposphere and ionosphere can be considered to be free space.

In the calculation of the average bias refraction errors (and also the time-delay effects), the basic assumption employed was that the deviating media can be considered to be stratified into spherical layers of constant refractive index. The computational procedure has already been published (1) and therefore will not be discussed in this paper.

The accuracy of this method, which is dependent upon the number of stratified layers within each medium, can be greatly improved by merely increasing the number of layers, i.e. decreasing the thickness of each individual layer element (2).

**Tropospheric refraction** – The index of refraction in the troposphere is a function of such meteorological variables as temperature, pressure, and water vapor, and can be represented by:

$$(n - 1) \times 10^6 = \frac{a}{T} \left( p + \frac{b\epsilon}{T} \right) \quad (1)$$

where  $T$  is the air temperature in degrees Kelvin,  $p$  is the total pressure in millibars, and  $\epsilon$  is the partial pressure of water vapor in millibars.

The values of the constants  $a$  and  $b$  are generally accepted to be 77.6°K/mb and 4810°K respectively, as suggested by Smith and Weintraub (3).

The first term in Eq. 1,  $ap/T$ , applies to both optical and radio frequencies, while the second term,  $ab\epsilon/T^2$ , is the water-vapor relationship required only at radio frequencies.

It should be noted that the above expression for the refractivity of air is independent of frequency in the range of 100 to 10 000 Mc/s.

The standard atmospheric models used in this analysis were formulated by Campen and Cole (4). The refractivity of a completely wet standard atmosphere (100 per cent relative humidity at all levels) is approximated by the function:

$$N_w = 338 - 50.9Z + 4.39Z^2 - 0.245Z^3 + 0.0071Z^4 - 0.00006Z^4 \quad (2)$$

where:

$$N_w = (n_w - 1) \times 10^6 \quad (3)$$

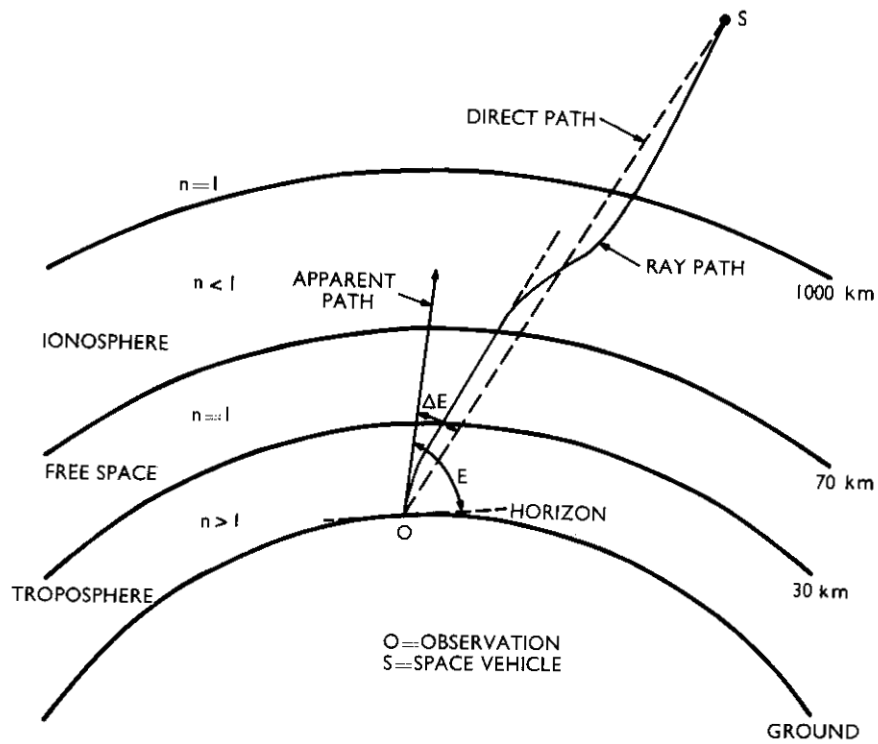


FIG. 1 Typical ray-path trajectory

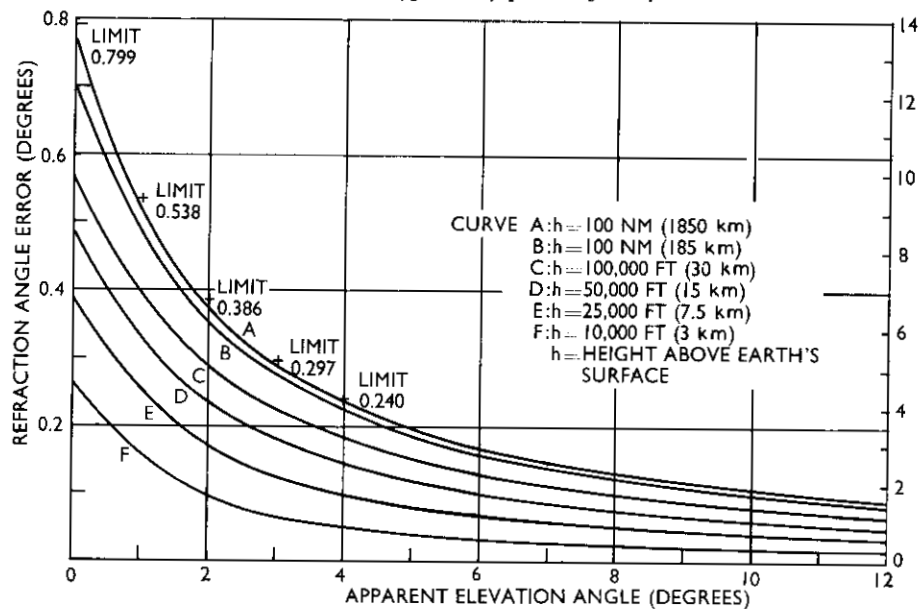


FIG. 2 Tropospheric refraction errors for a standard atmosphere with 100 per cent relative humidity

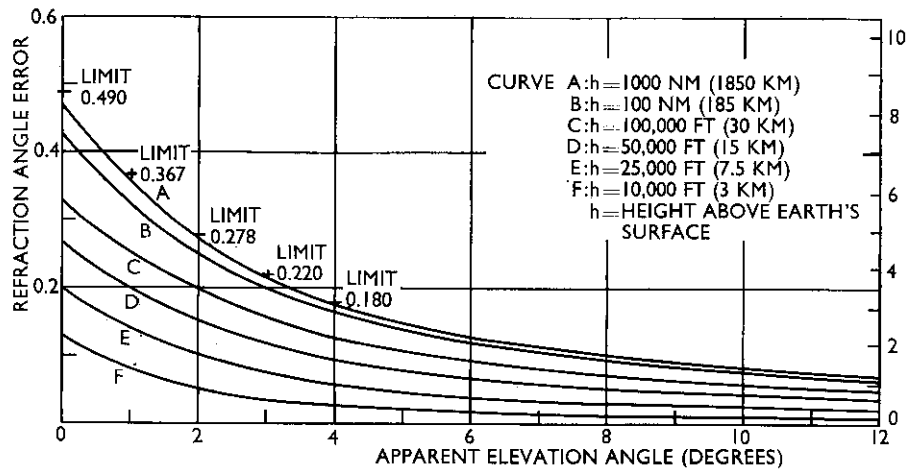


FIG. 3 Tropospheric refraction errors for a standard atmosphere with 0 per cent relative humidity

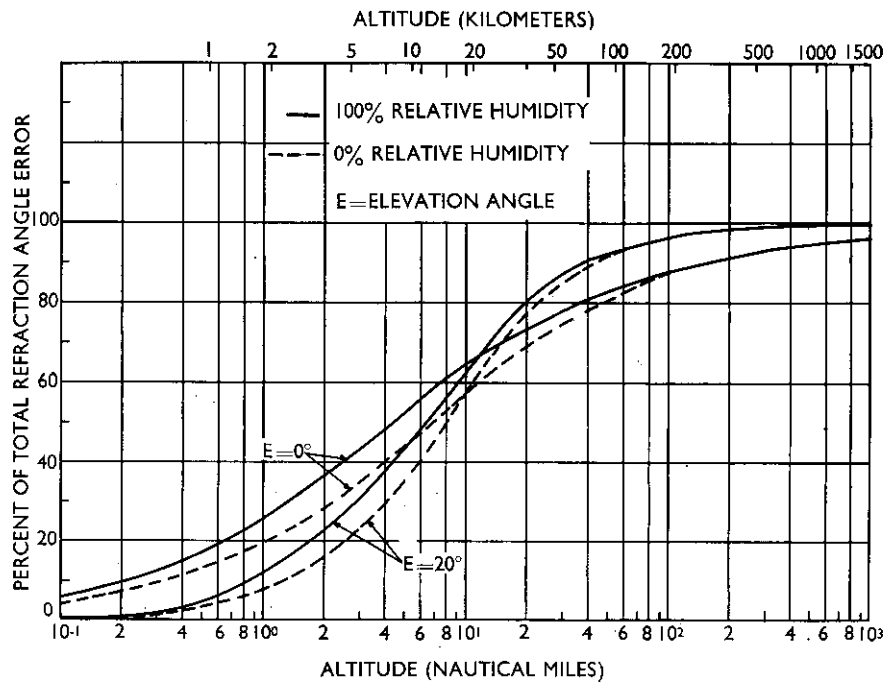


FIG. 4 Percentage of total tropospheric refraction error as a function of altitude for a standard atmosphere

For the case of a completely dry standard atmosphere (0 per cent relative humidity at all levels), the profile of refractivity is defined by:

$$N_d = 262 - 25.1Z + 0.92Z^2 - 0.016Z^3 + 0.0001Z^4 \quad (4)$$

Equations 2 and 4 are valid for  $0 \leq Z \leq 10$  km. Above this altitude, the refractivity is assumed to decay exponentially as:

$$N_{w,d} = N_{ow,od} e^{-h/25} \quad (5)$$

where  $h$  is the altitude in thousands of feet and  $N_{ow}$  and  $N_{od}$  are the values of  $N_w$  and  $N_d$ , respectively, at the earth's surface.

Figures 2 and 3 are plots of the refraction-angle error for the two atmospheric models. It is seen that maximum refraction occurs at  $0^\circ$  elevation angle and at heights beyond the deviating region. The refraction error resulting from the wet atmospheric model is greater than that from the dry model.

Bean and Cahoon (5) and Bean (6) have shown that the elevation-angle error is correlated with the surface-refractive index.

The percentage of the total tropospheric refraction as a function of altitude is shown in Fig. 4. It is of interest to note that, for both models, approximately 60 per cent of the total bending takes place at an altitude of 20 km.

With regard to azimuthal angular refraction, this effect arises whenever there are horizontal gradients of refractive index. Meteorological observations have shown, however, that such horizontal variations are small compared with the vertical variation of the indices of refraction. An analysis (unpublished) of refractometer data taken by the General Electric Company indicates an average value of 0.1 milliradian on cloudy days and 0.03 milliradian on clear days.

The general topic of tropospheric refraction is reviewed in great detail in a recent publication by Bean (7).

**Ionospheric refraction** – The index of refraction in the ionosphere is defined by:

$$n = \left[ 1 - \frac{4\pi N_e e^2}{m\omega^2} \right]^{1/2} \quad (6)$$

where  $N_e$  is the electron density in electrons/cm<sup>3</sup>,  $e$  is the electron charge ( $4.8 \times 10^{-10}$  esu),  $m$  is the electron mass ( $9.1 \times 10^{-28}$  gm), and  $\omega$  is the angular frequency of the incident wave in radians/sec. This relationship is valid when the earth's magnetic field and the electron-collision frequency are neglected.

It is evident that, for the ionosphere, the refractive index is inversely proportional to the frequency squared.

The distribution of electron density with height under consideration in this analysis was assumed to follow the Chapman model of the form:

$$N_e = N_m e^{1/2[1 - (h - h_m)/H_s - e^{-(h - h_m)/H_s}]} \quad (7)$$

where  $N_m$  is the electron density at the level of maximum ionization,  $h_m$ , and  $H_s$  is the scale height of the neutral particles. The Chapman layer is formed under highly ionized conditions; namely, the atmosphere is isothermal, the

ionizing radiation from the sun is monochromatic, and the recombination coefficient, or ion decay, is constant with height.

The daytime and nighttime values of the parameters defining the electron density profiles used in the calculations are presented in Table 1.

TABLE 1

## ELECTRON DENSITY MODELS

Time of day	Layer	$H_s$ (km)	$h_m$ (km)	$N_m$ (electrons/cm <sup>3</sup> )
Daytime	E	10	100	$1.5 \times 10^5$
	F <sub>1</sub>	40	200	$3.0 \times 10^5$
	F <sub>2</sub>	50	300	$1.25 \times 10^6$
Nighttime	E	10	120	$0.8 \times 10^4$
	F	45	250	$4.0 \times 10^5$

The ionospheric refraction error at a frequency of 100 Mc/s is shown in Fig. 5 as a function of the apparent angle of elevation at the earth's surface. An interesting feature of this plot is that at a constant altitude the error increases with elevation angle, attaining a maximum value between approximately 3° and 5°. At the very low angles, the error remains somewhat the same for all altitudes greater than 370 km. As the elevation angle is increased, however, it becomes apparent that the error maximizes at about 555 km. Minimum error is attained at astronomical distances.

The tropospheric and ionospheric refraction errors computed at an altitude of 555 km are given in Fig. 6. It is seen that the tropospheric error is predominant for propagation near the horizon and that the ionospheric contribution takes over as the elevation angle is increased. The angle at which the ionospheric error is greater than the tropospheric error is dependent upon the transmission frequency and the characteristics of the media. For the particular refractive index models under investigation, the crossover point is at 2° elevation angle.

It is of interest to note that similar results have been reported by Weisbrod and Colin (8).

Figure 6 also discloses that the ionospheric refraction error is inversely proportional to the square of frequency and is a minimum during the nighttime. The angular error for the 200 Mc/s nighttime case is less than the tropospheric estimates.

The data shown in Fig. 7 reveal that, for 0° elevation angle, the error increases monotonically with height. The monotonic function implies that the angular bending due to the curvature of the earth is more effective than the ionospheric contribution. It is evident, however, that at an elevation angle of 5° the error due to the ionosphere is greater than that resulting from the sphericity of the earth.

**Experimental measurements** – Experimental measurements of the total deviation of solar radiation in the entire atmosphere have been performed by McCready *et al* (9) and by Marner and Ringoen (10), whose results are presented in Fig. 8.

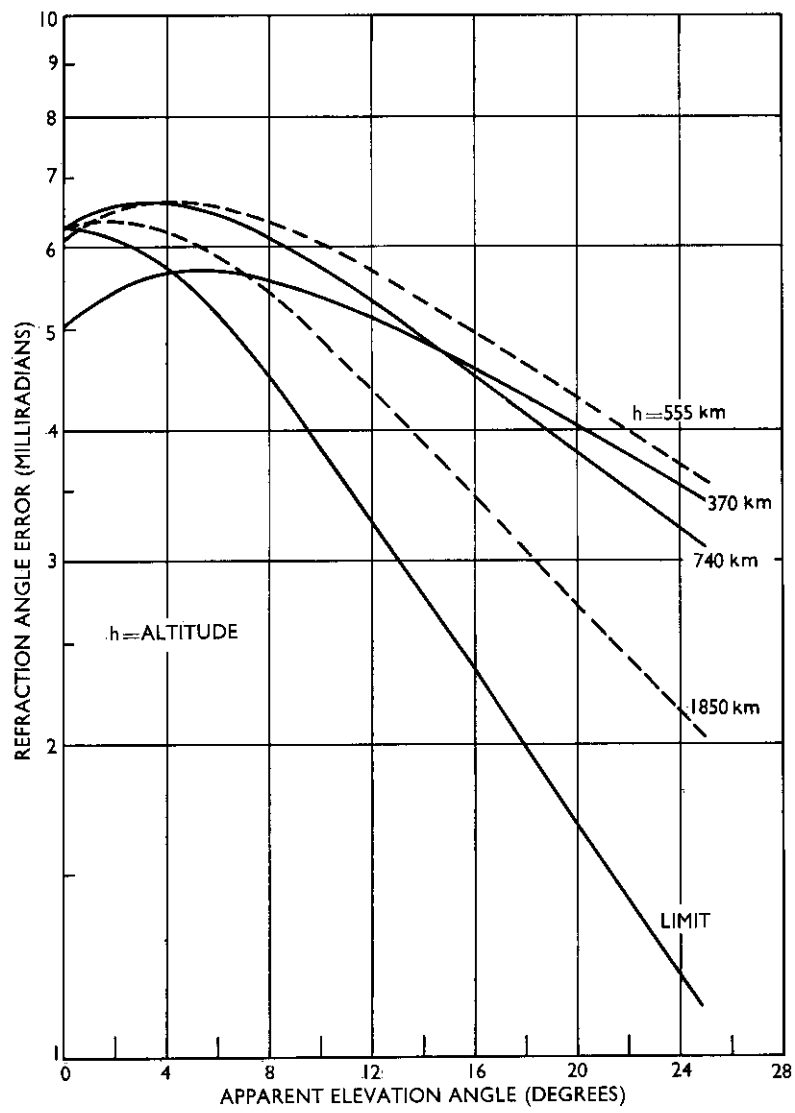


FIG. 5 Ionospheric refraction errors at 100 Mc/s

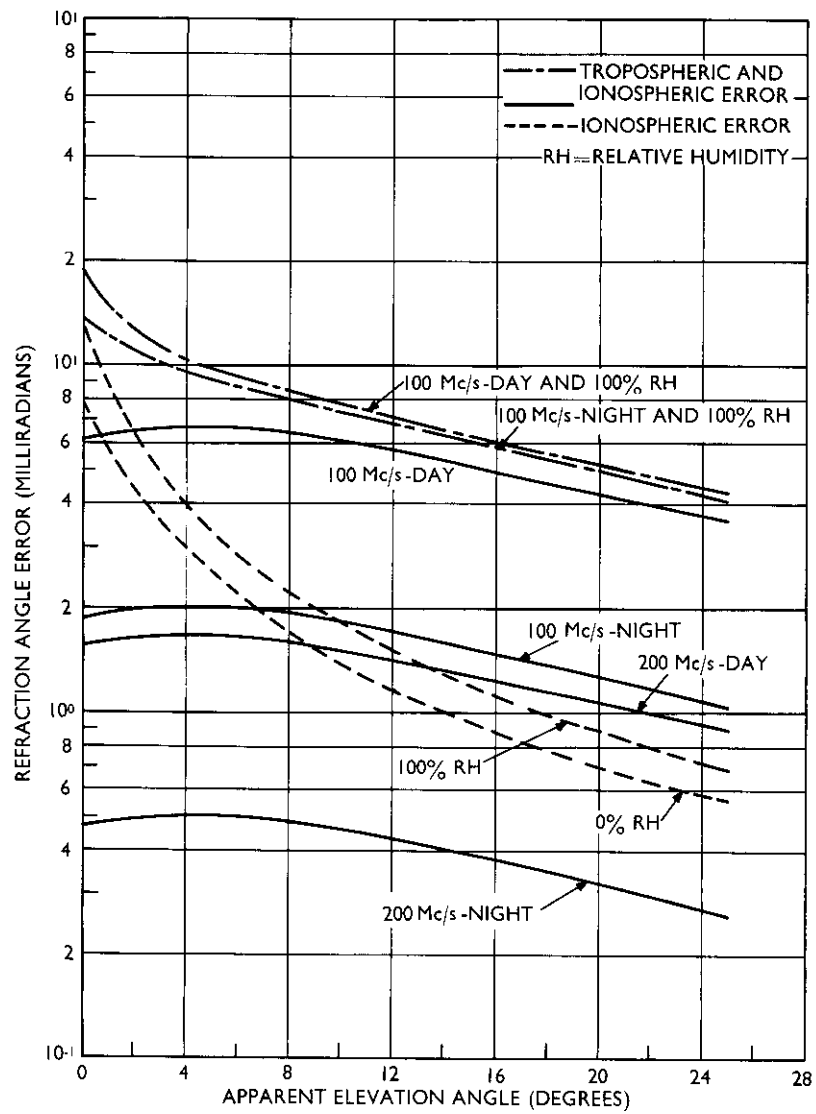


FIG. 6 Tropospheric and ionospheric refraction errors at 555 km altitude



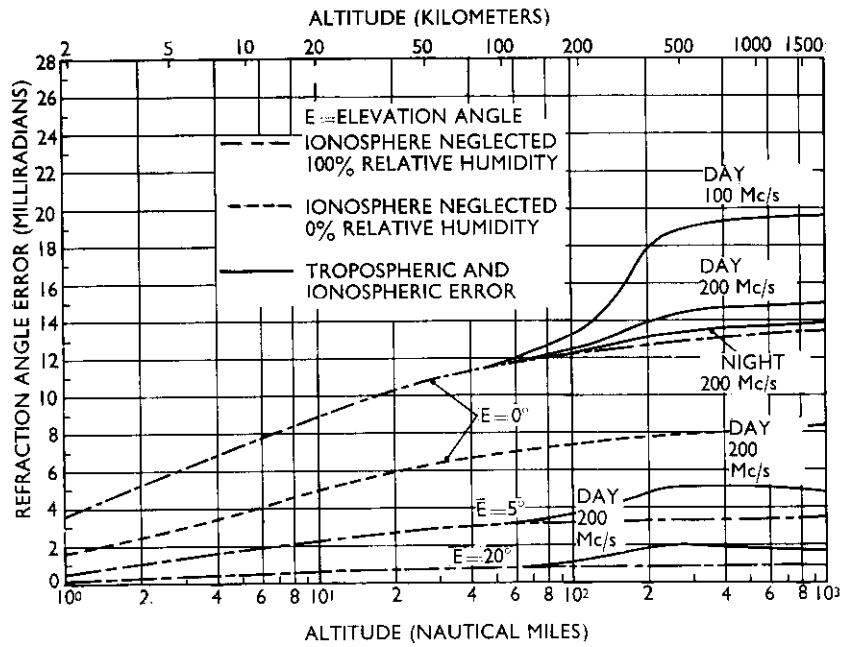


FIG. 7 Total atmospheric refraction errors at 100 and 200 Mc/s

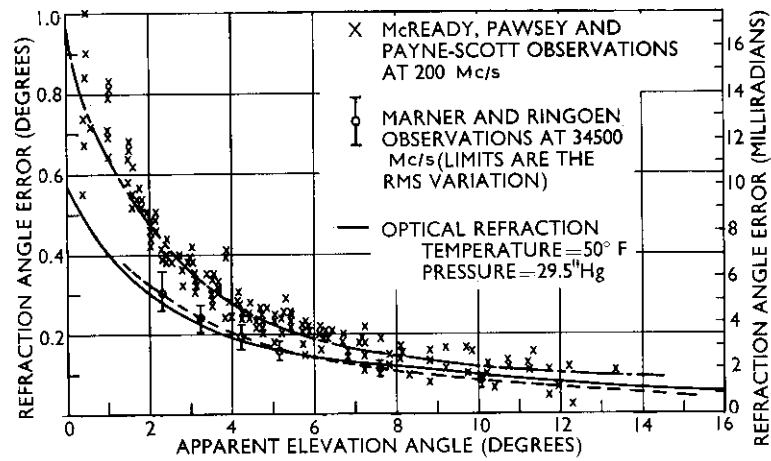


FIG. 8 Average atmospheric refraction for propagation of solar radiation through the atmosphere

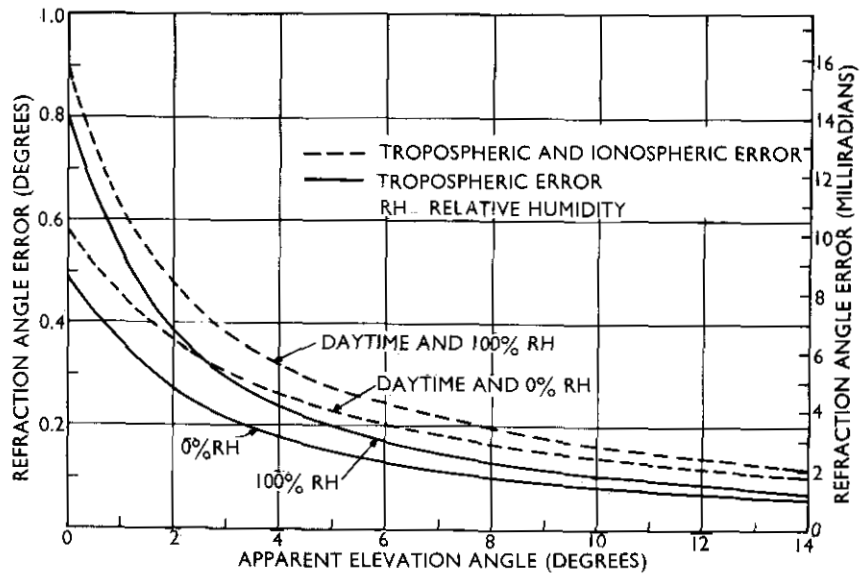


FIG. 9 Limit of tropospheric and ionospheric refraction errors at 200 Mc/s

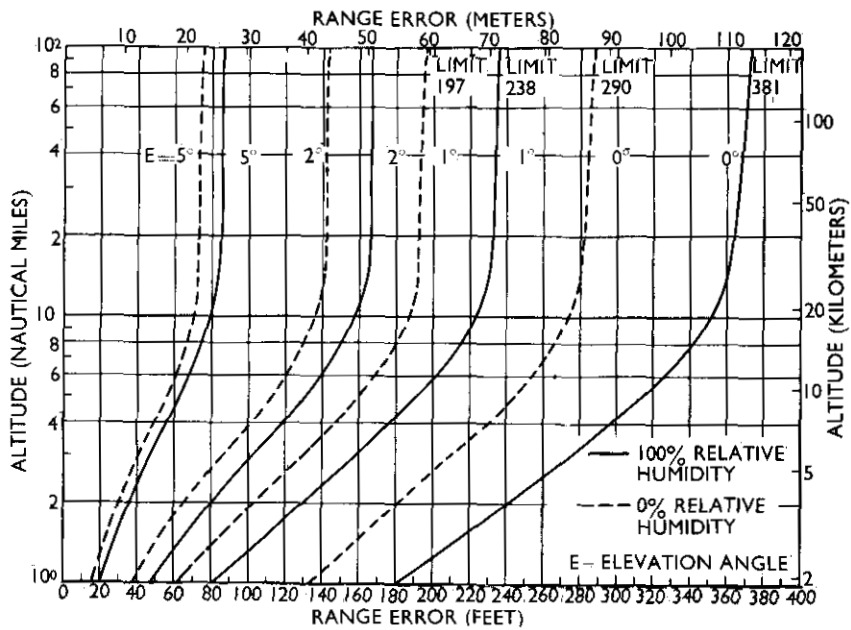


FIG. 10 Tropospheric range errors, one-way transmission path

Marner's and Ringoen's measurements were made at 34 500 Mc/s with a radio sextant. The r.m.s. variation in the radio refraction is indicated by the vertical bars, while the dashed line through the data represents the average refraction. Since ionospheric ray-bending effects are minute at a frequency of 34 500 Mc/s, it can be concluded that the refractive deviations were caused entirely by the tropospheric medium.

The curve through the 200 Mc/s result was computed by McCready *et al* (10) on the basis of an assumed linear variation of refractive index with height.

It would appear that the difference between the 200 Mc/s and 34 500 Mc/s data can be attributed to the ionosphere.

On comparing Fig. 8 with the calculations depicted in Fig. 9, it is seen that both sets of experimental data fall within the bounds set up by the limits of refraction error theoretically postulated.

Aarons *et al* (11) measured the refraction of 218 Mc/s solar radiation. The refraction error at sunrise at 0° elevation angle ranged between 45' and 1° 35' with an average of 1° 0.5'.

The total refraction of 53 Mc/s radiation from Cygnus-A measured at 15° elevation angle by Lawrence *et al* (12) was observed to be 0.5°.

#### TIME DELAY EFFECTS

Time delays or range errors are always inherent in the measurement of range by pulse techniques, mainly because the velocity of electromagnetic propagation in the atmosphere is slightly less than the free-space velocity. An additional source of error is the increase in path length brought about by the refractive bending of the propagated ray. In the computations (by the stratified layer method) of the data to be presented, both factors are taken into account.

According to Bean (7), the geometric range error, which is the difference in length between the ray path and direct path, as defined in Fig. 1, does not represent a significant portion of the total range error in the troposphere except at very small elevation angles between 0° and about 3°.

**Tropospheric time delay** – As shown in Fig. 10, the magnitude of the range error is a direct function of the elevation angle and path length and is also a function of the amount of humidity in the air. The maximum range error, for a one-way transmission path, is of the order of 116 m (381 ft).

Figure 11 shows that, irrespective of the refractive index model, approximately 90 to 95 per cent of the retardation occurs below the 20 km altitude. For horizon transmission, 50 per cent of the delay is accomplished within an altitude of about 2 km, while, at 20° elevation angle, the altitude corresponding to the 50 per cent delay has increased to about 5.5 km.

**Ionospheric time delay** – The ionospheric range errors, at a frequency of 200 Mc/s for a one-way transmission path, are plotted in Fig. 12. It is seen that the error is greatest during the daytime, attaining a maximum value of about 915 m (3000 ft).

According to Fig. 13, 50 per cent of the error takes place within the 280 km level for the nighttime model and irrespective of the angle of elevation, while for the daytime case it occurs at 325 km altitude.

It should be noted that the presence of the ionosphere introduces an increase in the effective group path length relative to free space and that, for frequencies in the VHF range and above, the one-way range increase (in centimeters) can be expressed, as a first approximation, by the function:

$$\Delta R_g = \frac{40 \times 10^6}{f^2} \int_0^s N_e ds \quad (8)$$

where the frequency,  $f$ , is in c/s and the integrated electron density is in electrons/cm<sup>2</sup>.

In Fig. 14, the limit of the tropospheric and ionospheric range errors is plotted as a function of elevation angle. It is seen that the ionospheric error is relatively independent of elevation angle below approximately 5° and that the error, during the daytime and at 200 Mc/s, is of the order of eight times larger than the corresponding error introduced by the troposphere.

It follows, from the inverse square of frequency dependency, as illustrated by Eq. 8, that at a frequency of about 575 Mc/s the tropospheric and ionospheric contributions to the propagation time delays at 0° elevation angle are of the same order of magnitude. Above 575 Mc/s, the tropospheric error becomes the more predominant one. At 30° elevation angle, however, the ionospheric error remains the larger for frequencies below 800 Mc/s.

#### DOPPLER EFFECTS

The frequency of a radio signal emitted from a space vehicle and received on the earth experiences an apparent shift owing to the Doppler effect. This phenomenon occurs because of the relative motion between the source of transmission and the stationary receiver terminal.

Inaccuracies in the measurement of the Doppler frequency shift and the radial velocity of a moving vehicle are brought about by the refractive characteristics of the troposphere and ionosphere. The errors are basically due to the fact that the direction of the refracted ray at an object in space is different from the unrefracted direct line-of-sight path.

It can be shown (1) that the error in the Doppler frequency shift of a satellite transmission can be described, to a first approximation, by:

$$\Delta f_a = -\frac{f}{c} \Delta E_T V \sin \psi \quad (9)$$

where  $\Delta f_a$  is the error in the difference between the received frequency and the transmitted frequency  $f$ ,  $V$  is the velocity of the moving object, and  $c$  is the free-space velocity. The term  $V \sin \psi$ , according to Fig. 15, is the velocity component perpendicular to the direct line-of-sight path.

The angle  $\Delta E_T$  is given by the relationship:

$$\Delta E_T = \cos^{-1} \left[ \frac{r_o}{r_o + h} \cos (E - \Delta E) \right] - \cos^{-1} \left[ \frac{n_G r_o}{n_T (r_o + h)} \cos E \right] \quad (10)$$

where  $n_G$  and  $n_T$  are the refractive indices at the ground and space vehicle, respectively,  $r_o$  is the radius of the earth, and  $\Delta E$  is the refraction-angle error corresponding to the elevation angle,  $E$ , and height,  $h$ .

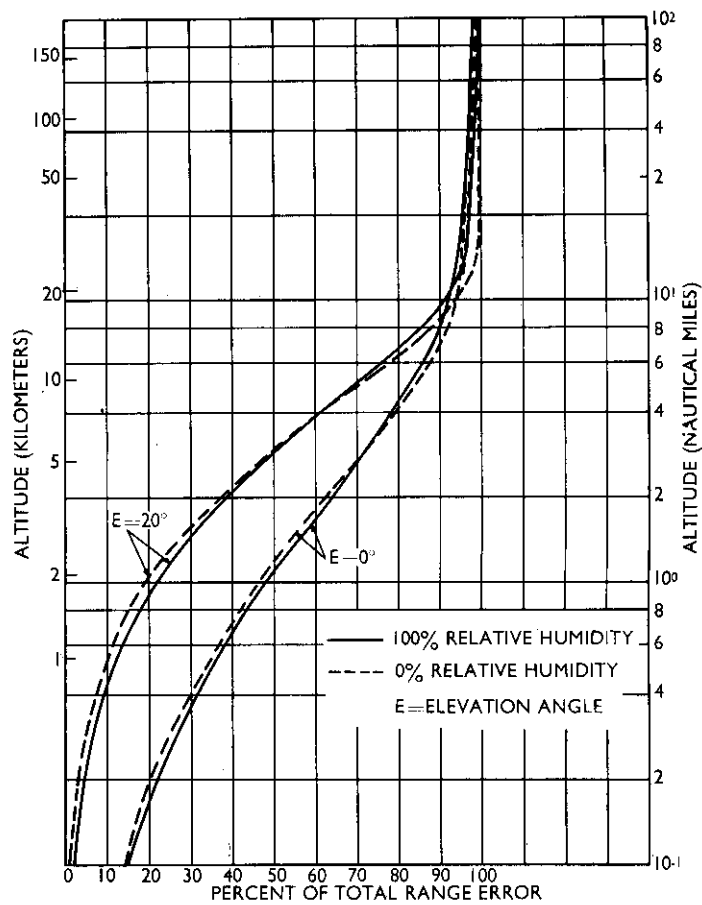


FIG. 11 Percentage of total tropospheric range error as a function of altitude

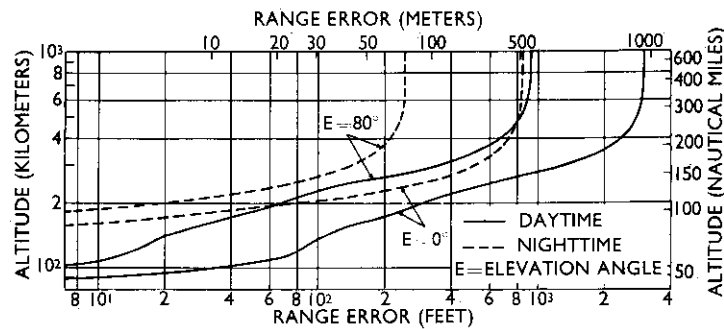


FIG. 12 Ionospheric range errors at 200 Mc/s, one-way transmission path

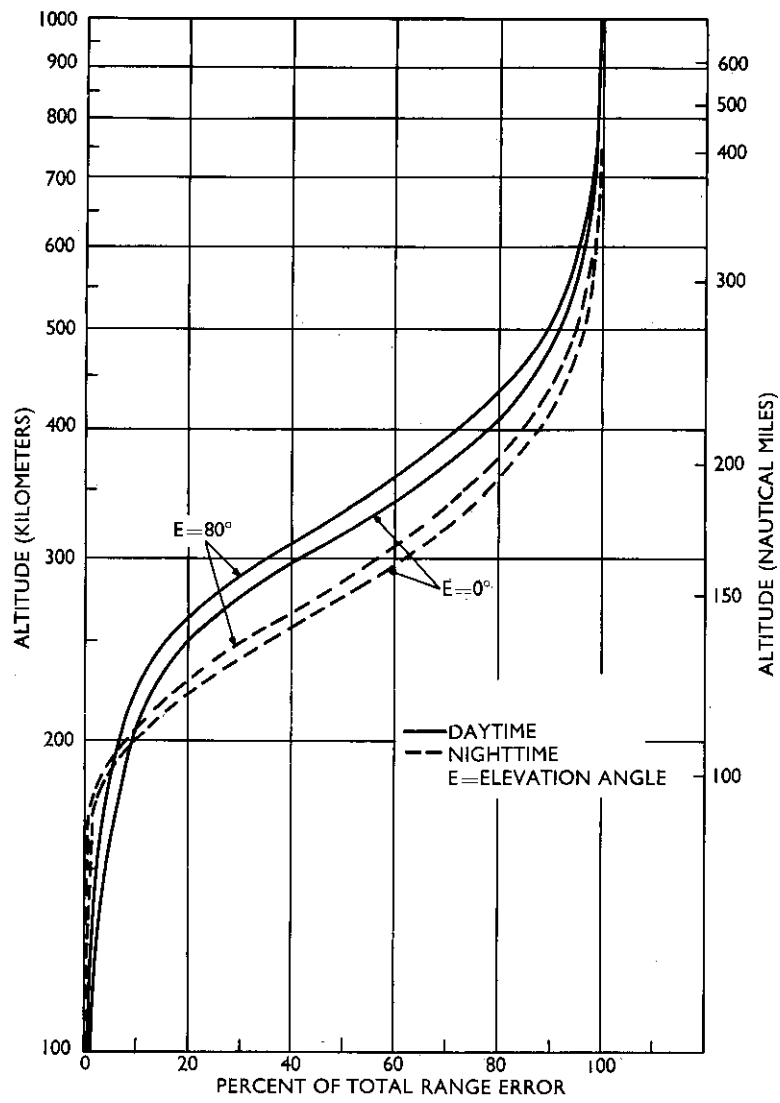


FIG. 13 Percentage of total ionospheric range error as a function of altitude

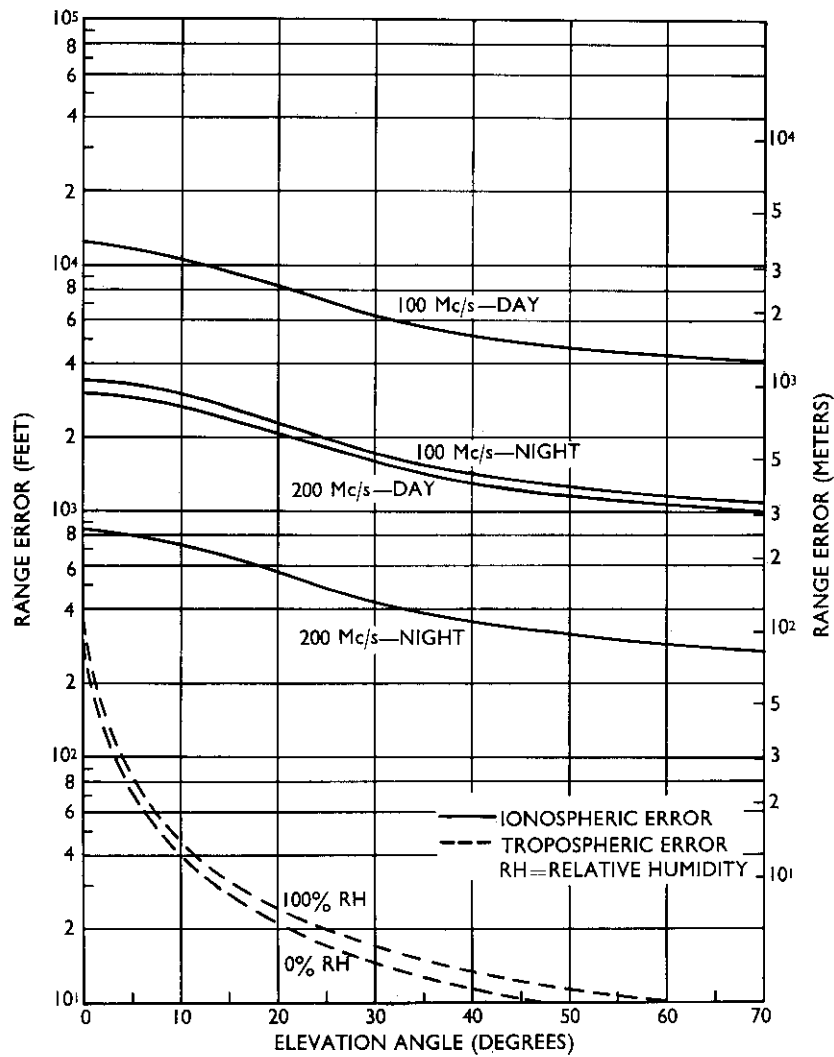


FIG. 14 Limit of tropospheric and ionospheric range errors, one-way transmission path

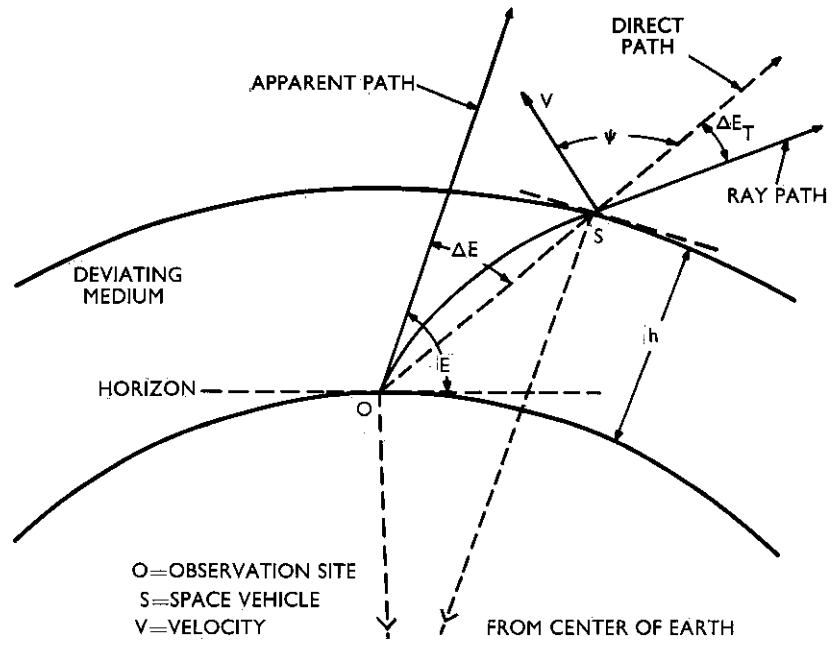


FIG. 15 Deviation of ray path at space-vehicle position

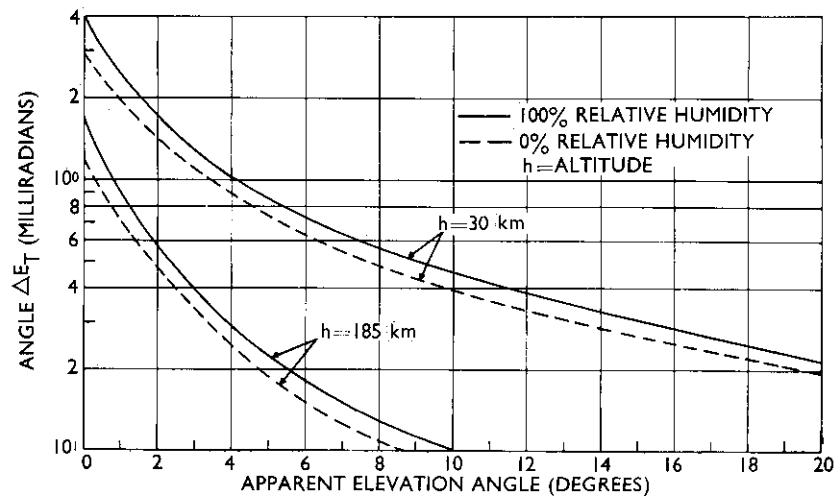


FIG. 16 Angle  $\Delta E_T$  for the troposphere



It is evident from the above expressions that the Doppler shift error, and thus the velocity error in the radial direction, is a maximum when the vehicle movement is directed along a path perpendicular to the unrefracted line-of-sight path.

Another source of error on a Doppler frequency measurement, which is not considered in this analysis, is that due to imperfect knowledge of the index of refraction at the space vehicle. This is only important when the vehicle is embodied either in the troposphere or the ionosphere. For vehicles at altitudes greater than 1000 km and transmission frequencies above 100 Mc/s, the effect of the uncertainty in electron density of the ionosphere on  $n_T$  can be neglected.

It should be noted that, unlike the refraction and range errors, the Doppler frequency shift errors are not cumulative. In other words, the total Doppler error, for a target traversing the ionosphere, is only the localized error at the specific point in the medium. The troposphere merely acts as a refractive medium.

**Tropospheric effect** – The function  $\Delta E_T$  for the troposphere is plotted in Fig. 16 as a function of the apparent angle of elevation. For both the 30 and 185 km calculations, the refractive index of the medium at the two altitudes was assumed to be unity.

It is seen that, for a given altitude,  $\Delta E_T$  decreases monotonically with elevation angle and is, to a great extent, altitude dependent. It is of interest to note that the region of maximum  $\Delta E_T$ , at  $0^\circ$  elevation angle, centers in the vicinity of 9 and 12 km for the 100 and 0 per cent relative humidity model, respectively (13).

Figure 17 illustrates the Doppler frequency error for the two tropospheric models based on an assumed vehicle velocity of 10 km/s and altitude of 30 km. It is evident that the greatest error is present for the standard atmosphere with the highest humidity. The error is directly proportional to the transmission frequency; at 100 Mc/s and horizon propagation, the maximum error is approximately 13 c/s.

**Ionospheric effect** – Fig. 18 depicts the variation of  $\Delta E_T$  at a frequency of 200 Mc/s for an assumed target height of 300 km for the daytime electron-density model and 250 km for the nighttime model.

A comparison of Fig. 18 with Fig. 16 reveals that the tropospheric  $\Delta E_T$  decreases with elevation angle at a greater rate than the ionospheric  $\Delta E_T$ .

As illustrated in Fig. 19,  $\Delta E_T$  for the ionosphere is inversely proportional to the square of the transmission frequency, while for the troposphere it is independent of frequency.

From the results presented in Fig. 20, it is seen that the ionospheric Doppler frequency error is a maximum during the daytime and at low elevation angles. For an assumed vehicle speed of 10 km/s, the error at 100 Mc/s and at a ground elevation angle of  $0^\circ$  is of the order of 41 c/s. For the nighttime, under similar conditions, the error reduces to about 15 c/s.

It should be noted that the Doppler frequency error caused by the ionosphere is inversely proportional to frequency, while for the troposphere the error is directly proportional to frequency.

The presence of the ionosphere, in addition to imposing an error in the Doppler frequency shift by virtue of the refractive bending of the ray path, introduces a perturbation in the observed frequency. Since the frequency of a wave is related to the time derivative of the phase or phase path length, it can be readily shown that the ionospheric frequency shift (in c/s) can be written as:

$$\Delta f = - \frac{40 \times 10^6}{cf} \frac{d}{dt} \int_0^s N_e ds \quad (11)$$

where  $f$  is in c/s and the integral is the integrated electron density along the ray path in electrons/cm<sup>2</sup>.

#### SCINTILLATION EFFECTS

The existence of small-scale variations in the index of refraction in the troposphere has been observed by microwave refractometer techniques. It is generally accepted that these fluctuations are responsible for the optical twinkling of radio stars.

The radiation emitted from discrete radio stars is relatively constant; however, at times the extra-terrestrial signals impinging on the earth's surface are found to fluctuate in a random manner. Irregular fluctuations in the apparent angular position of the sources have also been detected. The fluctuations or scintillations both in amplitude and position have been experimentally verified to be induced by irregularities in the electron density distribution in the ionosphere through which the radiation passes.

In this section, estimates are made of the magnitude of the effects of the inhomogeneities in the troposphere and ionosphere on the measurement of the angle-of-arrival, phase, range and amplitude of radio-wave signals propagated in an earth-space vehicle environment.

#### Angle-of-arrival scintillation

**The Troposphere** – Random variations in the angle-of-arrival are produced by gradients in the index of refraction at right-angles to the ray path.

Using a ray-theory approach, Muchmore and Wheelon (14) have developed an expression for the mean-square deviation in the angle-of-arrival for a turbulent troposphere, given by:

$$\overline{\theta^2} = \frac{2 \times 10^{-12} \sqrt{\pi} L \overline{\Delta N^2}}{l_0} \quad (12)$$

where  $\overline{\theta^2}$  is in radians,  $L$  is the path length through the turbulence,  $l_0$  is the scale length of the turbulent eddy, and  $\overline{\Delta N^2}$  is the mean-square fluctuation in the refractivity,  $N$ . It should be noted that this relationship, which was derived on the assumption of a gaussian correlation function for the scale of turbulence, is independent of frequency.

Figure 21 is a plot of the root-mean-square angular deviation in the troposphere as a function of the various parameters. Assuming  $l_0 = 65$  m (200 ft),  $\overline{\Delta N^2} = 0.25$ , and a path length of 100 km, the r.m.s. angular deviation evaluates to approximately 0.035 milliradian. The r.m.s. deviation becomes smaller for larger sizes of the turbulent eddies.

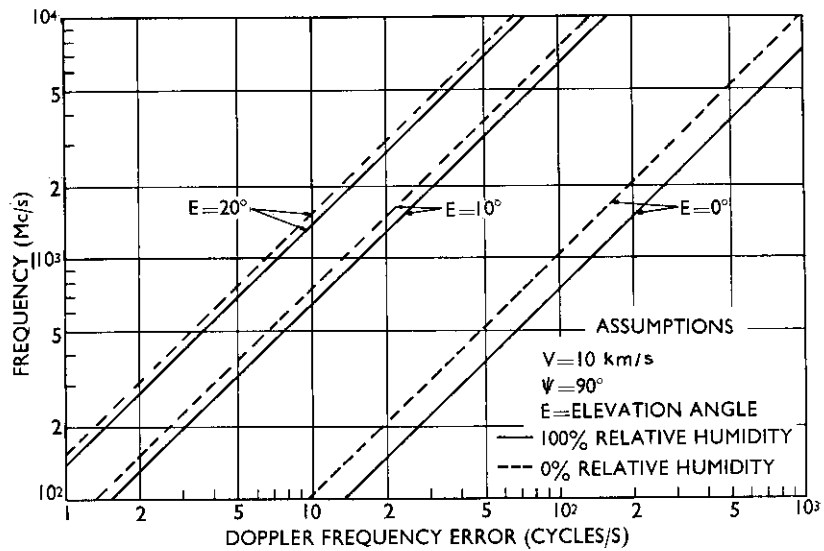


FIG. 17 Doppler frequency error for the troposphere for a space vehicle at 30 km altitude, one-way transmission path

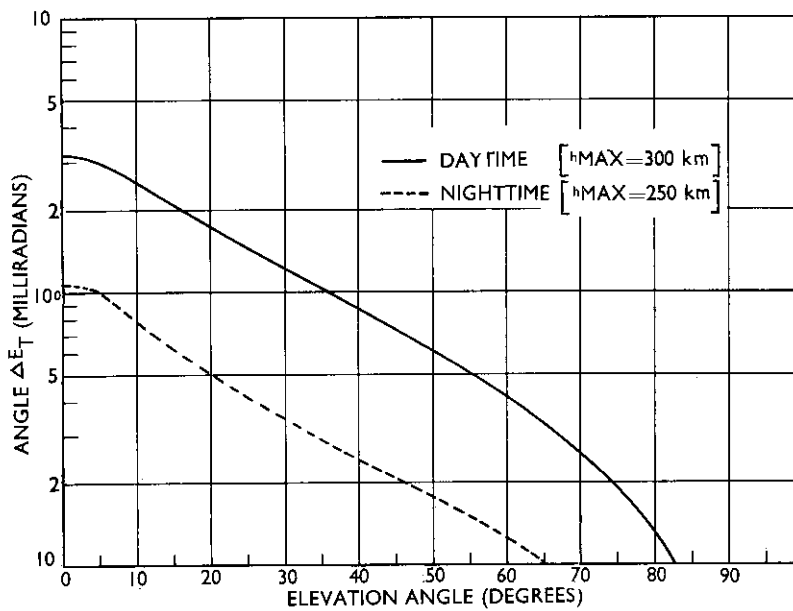


FIG. 18 Angle  $\Delta E_T$  at 200 Mc/s as a function of elevation angle for space vehicle located at maximum electron density altitude

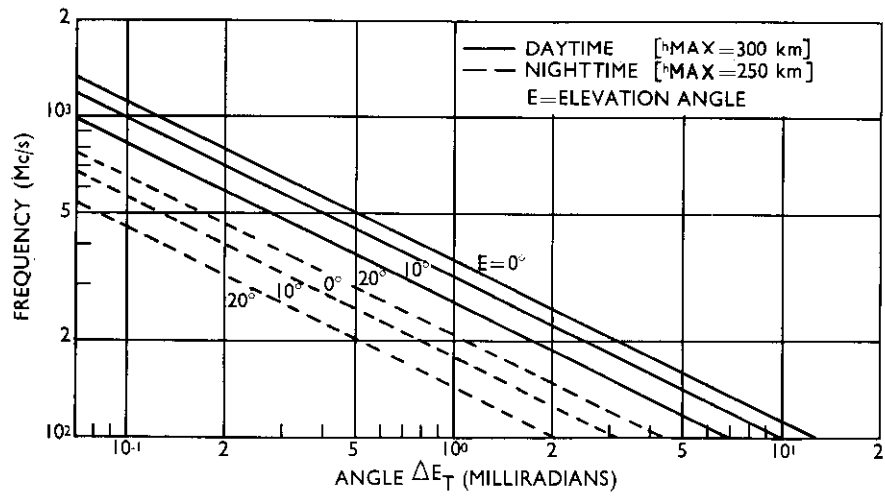


FIG. 19 Angle  $\Delta E_T$  for the ionosphere as a function of frequency for space vehicle located at maximum electron density altitude

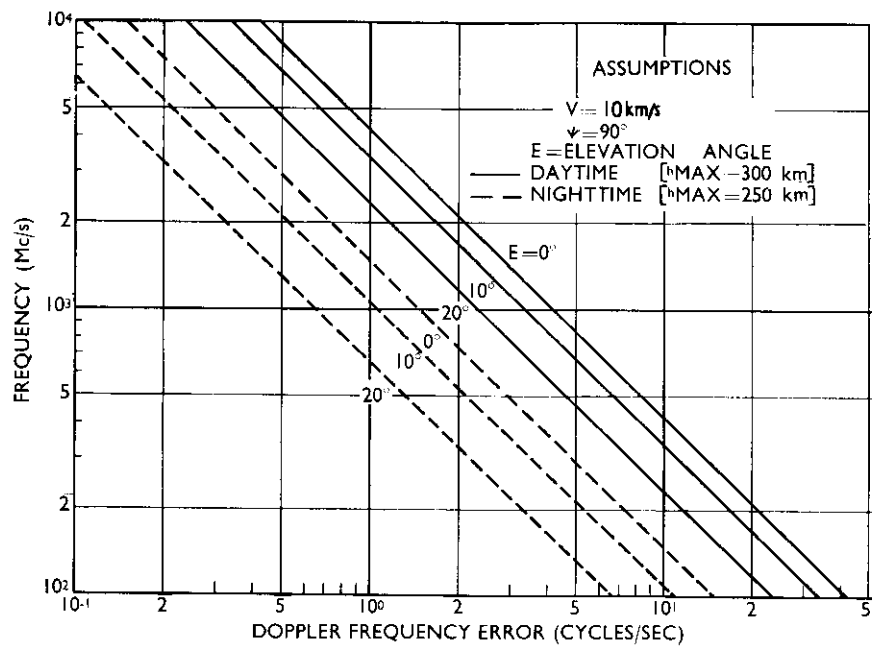


FIG. 20 Doppler frequency error for the ionosphere for a space vehicle at maximum electron density altitude, one-way transmission path

**The Ionosphere** – The mean-square deviation in the angle-of-arrival in the ionosphere, according to Booker's (15) theory on the scintillation of radio stars, can be expressed by:

$$\overline{\theta^2} = \frac{L \omega_N^4}{2l_o \omega^4} \left( \frac{\Delta N_e}{N_e} \right)^2 \quad (13)$$

where  $\omega_N$  is the angular plasma frequency,  $\omega$  is the angular frequency of the transmitted radio wave,  $(\Delta N_e/N_e)^2$  is the mean-square fractional deviation of the electron density from the average, and  $L$  and  $l_o$  are defined in the same manner as in Eq. 12.

It should be mentioned that, in order to be consistent with the nomenclature of Muchmore and Wheelon (14), the parameters  $L$  and  $l_o$  in Eq. 12 are used in place of  $D$  and  $L$ , respectively, given in Booker's (15) paper.

It is interesting to note that Muchmore and Wheelon's results for the troposphere, Eq. 12, are also directly applicable to the ionosphere. Since the ionospheric refractive index is frequency dependent, it is convenient to express the refractivity fluctuations in terms of the fluctuations in the electron density. It can be readily shown from Eq. 3 and 6 that:

$$\Delta N^2 = \frac{10^{12} \omega_N^4}{4\omega^4} \left( \frac{\Delta N_e}{N_e} \right)^2 \quad (14)$$

Substituting Eq. 14 in Eq. 12 results in an expression which is a factor of 1.33 times larger than Booker's Eq. 13.

The ratios of  $(\omega_N/\omega) = 10^{-1}$  and  $5 \times 10^{-2}$ , described in the calculations of Fig. 22, imply plasma frequencies of 10 and 5 Mc/s, respectively, for a transmission frequency of 100 Mc/s. Assuming  $l_o = 1$  km,  $(\omega_N/\omega) = 10^{-1}$ ,  $(\Delta N_e/N_e)^2 = 10^{-7}$ , and a turbulent path length of 100 km, the r.m.s. angular deviation for an undisturbed ionosphere becomes 0.022 milliradian.

Because of the inverse frequency-squared dependency, the r.m.s. angular deviation at 200 Mc/s for the same conditions reduces to approximately 0.006 milliradian.

Since the angular scintillation is dependent on the mean-square fractional deviation in the electron density, it can be expected that the scintillation would increase during an ionospheric disturbance or in the auroral ionosphere.

Radio-star noise observations by Hewish (16) at 40 Mc/s disclosed a typical angular flicker of two or three minutes of arc (0.58 to 0.87 milliradian). During highly disturbed conditions, the flicker increased to as much as one-half a degree (8.7 milliradians).

Extrapolating Hewish's data by the inverse frequency square law to 200 Mc/s results in a typical average scintillation of 0.029 milliradian, which is slightly higher than the theoretical estimate based on Fig. 22.

Lawrence *et al* (17) have detected, utilizing radio-star measurement techniques, an r.m.s. angular scintillation of approximately 2.1 milliradians at 53 Mc/s and 0.5 milliradian at 108 Mc/s.

Little *et al* (18) reported that, for the radio-star observations made at 223 Mc/s at Alaska, scintillations greater than about one minute of arc (0.29 milliradian) were observed 10 per cent of the time, 0.5 minute of arc

(0.15 milliradian) 28 per cent of the time and 0.2 minute of arc (0.06 milliradian) 65 per cent of the time.

### Phase scintillation

**The Troposphere** – The small-scale irregularities in the troposphere also introduce fluctuations in the phase of radio-wave signals. According to Muchmore and Wheelon (14), the mean-square phase shift in a single ray, assuming an exponential space correlation for the scale of turbulence, is approximated by the function:

$$\overline{\phi^2} = \frac{8 \times 10^{12} \pi^2 l_o L \overline{\Delta N^2}}{\lambda^2} \quad (15)$$

This relationship is applicable for a point antenna. The phase shift for a finite antenna aperture is given by:

$$\overline{\alpha^2} = \overline{\phi^2} \left(1 - \frac{R^2}{l_o^2} + \dots\right) \quad (16)$$

where  $R$  is the radius of the antenna.

Equation 15 shows that the r.m.s. phase fluctuations in the troposphere are directly proportional to the frequency.

Assuming  $l_o = 65$  m,  $\overline{\Delta N^2} = 0.25$ , and a path length of 100 km, the r.m.s. phase jitter at 1000 Mc/s, as given in Fig. 23, would therefore be slightly over  $2^\circ$ .

Radio-phase measurements taken simultaneously over the same 6 km path by Herbstreit and Thompson (19) on 1040 Mc/s and Deam and Fannin (20) on 9350 Mc/s yielded r.m.s. phase variations of  $1.09^\circ$  and  $12.6^\circ$ , respectively. The ratio of the phase variations was of the same order of magnitude as the ratio of the frequencies as predicted by theory.

**The Ionosphere** – The mean-square phase fluctuation in the ionosphere, as derived by Booker (15), is given by the relationship:

$$\overline{\Delta\phi^2} = \frac{l_o L \omega_N^4}{4c^2 \omega^2} \left(\frac{\overline{\Delta N_e}}{N_e}\right)^2 \quad (17)$$

Substituting Eq. 14 in Muchmore and Wheelon's (15) Eq. 15, there results an expression which is  $\sqrt{2}$  times larger than that of Eq. 17.

It should be noted that the r.m.s. phase fluctuation for the ionosphere is inversely proportional to frequency, while for the troposphere it is directly related.

According to Fig. 24, the r.m.s. phase fluctuation at 100 Mc/s for  $(\omega_N/\omega) = 10^{-1}$ ,  $l_o (\overline{\Delta N_e}/N_e)^2 = 10^{-7}$  km and  $L = 100$  km is  $1.9^\circ$ . It follows that, at 1000 Mc/s, the phase deviation reduces to  $0.2^\circ$ , which is an order of magnitude less than the corresponding tropospheric estimate.

### Range scintillation

**The Troposphere** – The mean-square range scintillation for the troposphere

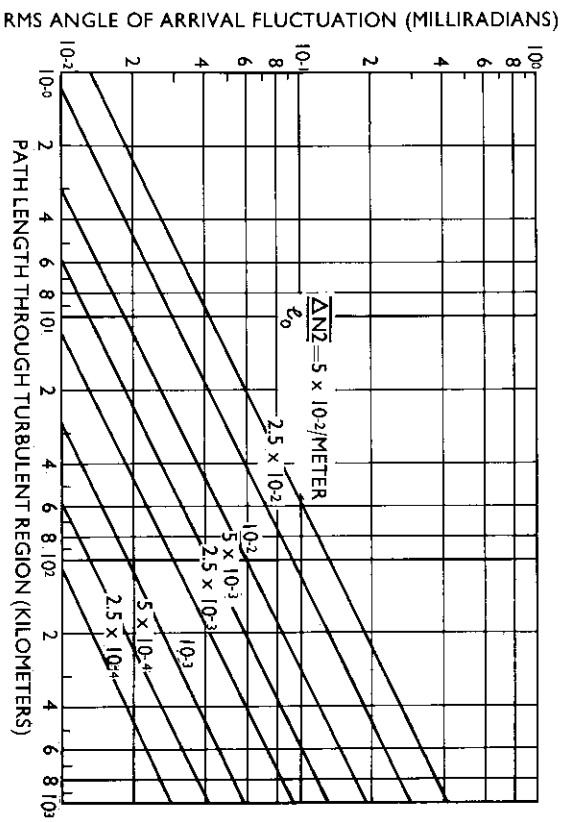


FIG. 21 R.M.S. deviation in the angle-of-arrival for propagation through the troposphere

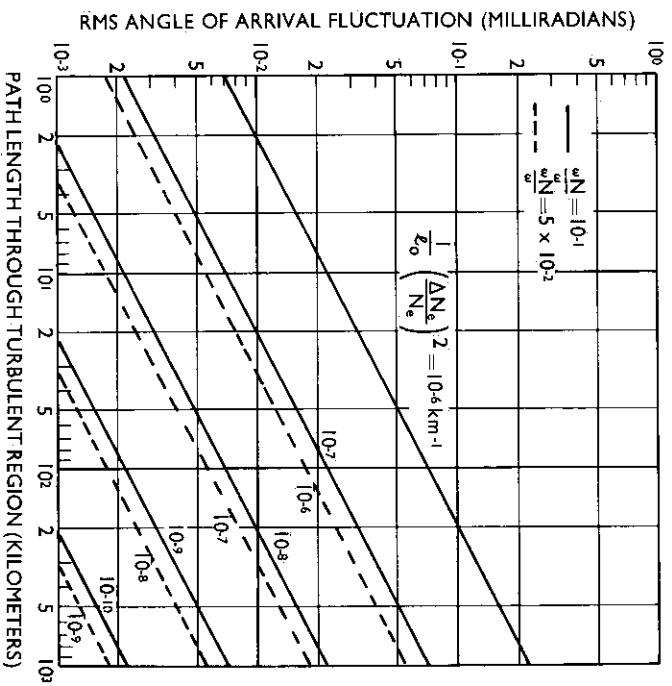


FIG. 22 R.M.S. deviation in the angle-of-arrival for propagation through the ionosphere

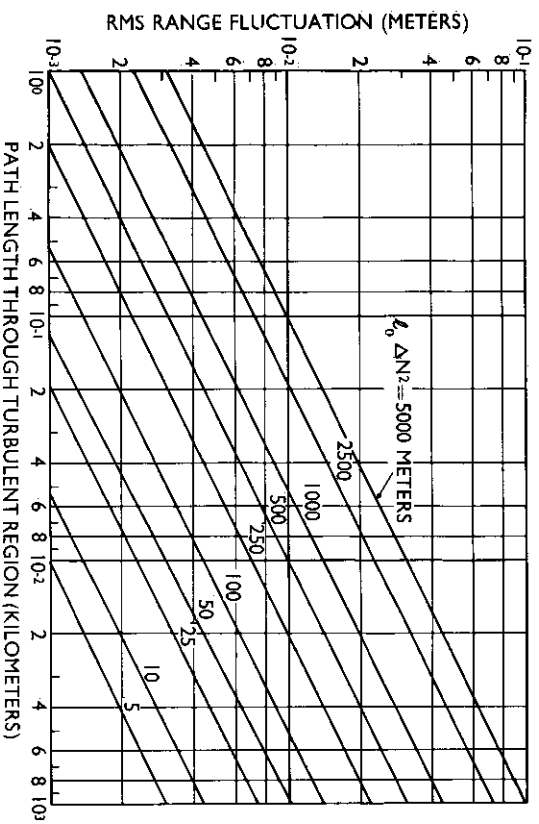


FIG. 23 R.M.S. phase fluctuation at 1000 Mc/s for propagation through the troposphere, one-way transmission path

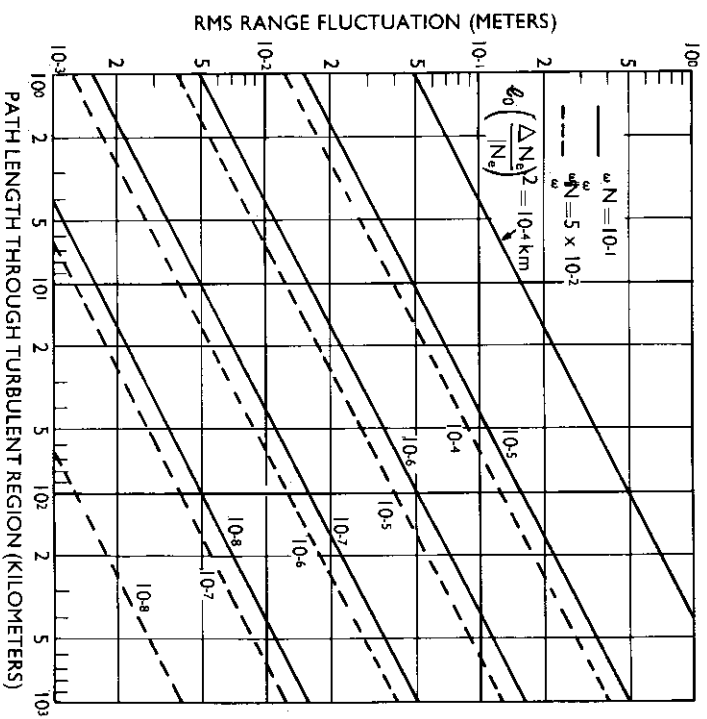


FIG. 24 R.M.S. phase fluctuation at 100 Mc/s for propagation through the ionosphere, one-way transmission path



can be obtained directly from Eq. 15. It is evident that this parameter is given by:

$$\overline{R^2} = 2 \times 10^{-12} l_o L \overline{\Delta N^2} \quad (18)$$

In other words, tropospheric range fluctuations are independent of frequency.

Using the values of  $l_o$ ,  $L$  and  $\overline{\Delta N^2}$  for the troposphere considered previously, it follows, from Fig. 25, that r.m.s. range fluctuation could be of the order of 0.18 cm.

**The Ionosphere** – Using Booker's expression for the ionospheric phase fluctuations, Eq. 17, it follows that the mean-square range deviation becomes:

$$\overline{R^2} = \frac{l_o L \omega_N^4}{4 \omega^4} \left( \frac{\overline{\Delta N_e}}{N_e} \right)^2 \quad (19)$$

The parametric plots of this equation, shown in Fig. 26, indicate that at 100 Mc/s, for  $(\omega_N/\omega) = 10^{-1}$ ,  $l_o (\overline{\Delta N_e}/N_e)^2 = 10^{-7}$  km, and  $L = 100$  km,  $\sigma_R = 1.6$  cm.

### Amplitude scintillation

**The Ionosphere** – Booker (15) and Lawrence *et al* (12) have shown that the mean-square fractional deviation of the amplitude of a signal from a source at infinite distance is related to the phase fluctuation or the mean-square fractional deviation of the electron density by:

$$\left( \frac{\overline{\Delta A}}{A} \right)^2 = \frac{\pi^2 z^2 L \omega_N^4}{l_o^3 \omega^4} \left( \frac{\overline{\Delta N_e}}{N_e} \right)^2 \quad (20)$$

where  $z$  is the distance from the scatterers in the ionosphere to the ground,  $\Delta A$  is a measure of the amplitude deviations in the resultant signal and  $A$  is the mean amplitude.

The derivation of this expression is based on Hewish's (21) theory of the diffraction of radio waves which are passing through a phase-varying screen in the ionosphere. The basic assumption is that the distance of the diffraction screen, or irregularities, from the ground is small compared to the Fresnel-zone distance (i.e. the distance at which an irregularity subtends one Fresnel zone).

It is seen that the r.m.s. amplitude fluctuation is inversely proportional to the square of the frequency.

Assuming  $z = 400$  km,  $L = 100$  km,  $l_o = 1$  km,  $(\overline{\Delta N_e}/N_e)^2 = 10^{-7}$ , and  $(\omega_N/\omega) = 10^{-1}$ , which is applicable for a frequency of 100 Mc/s, the r.m.s. amplitude scintillation, as shown in Fig. 27, is about 0.04.

According to the analysis of 108 Mc/s radiation from a radio star (17), this value of  $(\overline{\Delta A}/A)^2$  would imply that for this particular set of conditions the scintillations would not be detectable.

Ionospheric scintillations of radio stars have been observed at a frequency of 425 Mc/s at Trinidad by the General Electric Company (unpublished data) only during a severe magnetic disturbance.

Little and Maxwell (22) have found that during aurorae, the amplitude

scintillations were about four times more rapid than during normal conditions which, at 81 Mc/s, were about one to three fluctuations per minute. The scintillation rate and the velocity of ionospheric irregularities were approximately proportional to the planetary magnetic index.

Lawrence *et al* (12) have modified Eq. 20 to take into account radiating sources of varying distances from the irregularities. The mean-square scintillation amplitude, for the general case, becomes:

$$\left(\frac{\Delta A}{A}\right)^2 = \left(\frac{z'}{z + z'}\right)^2 \frac{\pi^2 z^2 L \omega_N^4}{l_o^3 \omega^4} \left(\frac{\Delta N_e}{N_e}\right)^2 \quad (21)$$

where  $z'$  is the distance of the source from the irregularities in the ionosphere. This equation would apply in the case of a satellite orbiting the earth.

The fraction  $z'/(z + z')$  is plotted in Fig. 28 as a function of the distance ratio  $z'/z$ .

#### ATTENUATION OF RADIO WAVES

**Tropospheric attenuation** – The absorption of radio waves in the troposphere is the result of the presence of both free molecules and suspended particles such as water drops condensed in fog and rain. In a non-condensed atmosphere the absorption is basically due to the interaction of the signal with the electric moment of the water-vapor molecule and with the magnetic moment of the oxygen molecule.

The theoretical calculations by Van Vleck (23) of the anticipated absorption of electromagnetic waves by oxygen and uncondensed water vapor are shown in Fig. 29. The water-vapor curve was determined on the basis of a water-vapor density of 7.5 gm/m<sup>3</sup> at sea-level at 20°C, which is typical of temperate latitudes in the summer.

It is evident that below 13000 Mc/s the attenuation by oxygen is predominant. The peaks in the absorption curve of both gases are the result of resonance effects. For oxygen, resonance occurs at wavelengths in the vicinity of 0.5 cm (60 Gc/s) and 0.25 cm (120 Gc/s). At the former wavelength the decay constant is approximately 14 dB/km. For water vapor, at the resonance wavelength of 1.35 cm (22.235 Gc/s), the absorption is 0.020 dB/km per gm/m<sup>3</sup>.

It should be noted that the decay constant of oxygen and water vapor decreases with altitude; for example, at an altitude of 7.6 km, the oxygen absorption at 3000 Mc/s has decreased to approximately 22 per cent of its value at the ground (24). For a frequency of 10000 Mc/s, both the oxygen and water-vapor value at the 7.6 km level is about 17 per cent of that at the ground (24).

The one-way attenuation due to oxygen, as predicted by Van Vleck (23), is presented in Fig. 30. The data were derived on the assumption that the oxygen content is effective to an altitude of 7.6 km (25000 ft). It is seen that, at an elevation angle of 3°, 0.8 dB one-way absorption can occur at 3000 Mc/s. At vertical incidence, the one-way path attenuation due to oxygen should not exceed 0.05 dB. The absorption of water vapor at a frequency of 3000 Mc/s is quite insignificant.

The experimental measurements (11) of the oxygen decay constant at 9350 Mc/s indicate a value of the order of 0.00585 dB/km. These data, which

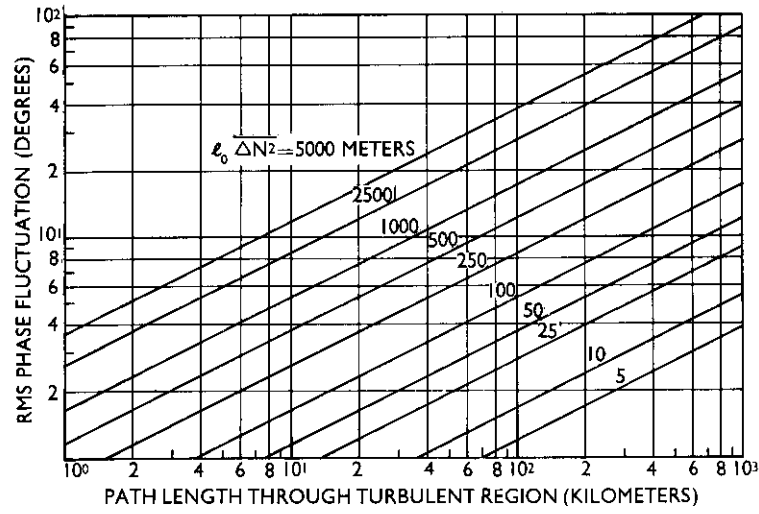


FIG. 25 R.M.S. range fluctuation for propagation through the troposphere, one-way transmission path

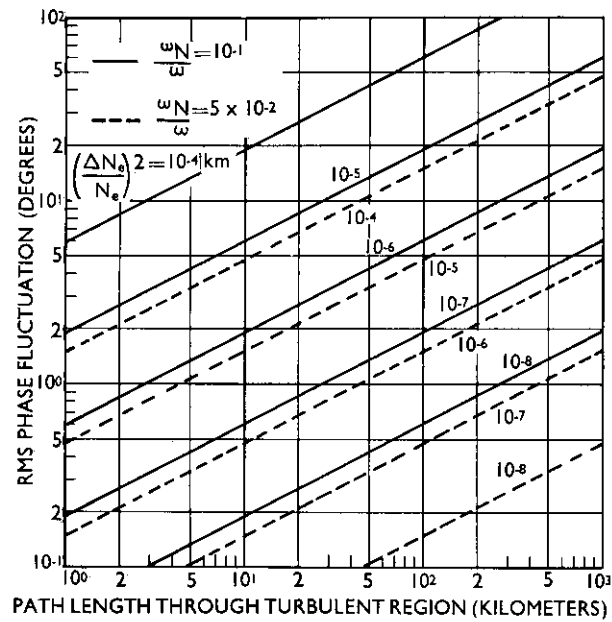


FIG. 26 R.M.S. range fluctuation for propagation through the ionosphere, one-way transmission path

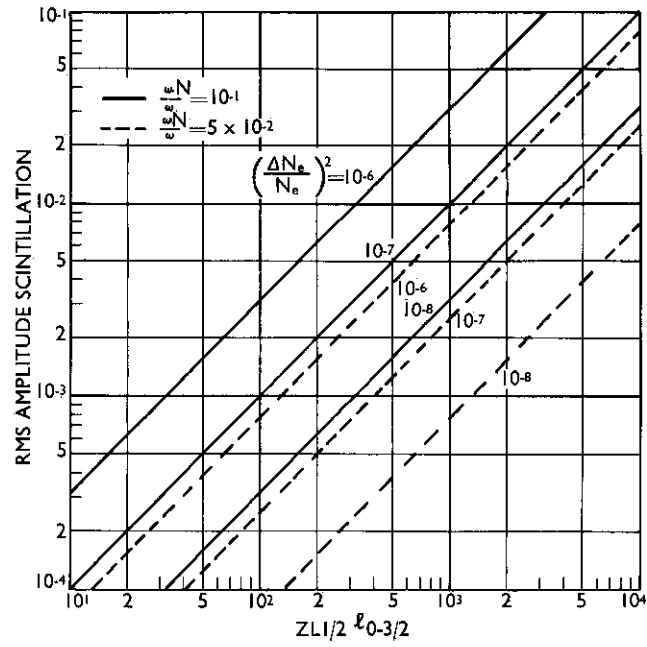


FIG. 27 R.M.S. fractional deviation of amplitude scintillation for propagation through the ionosphere from a radiating source at infinite distance

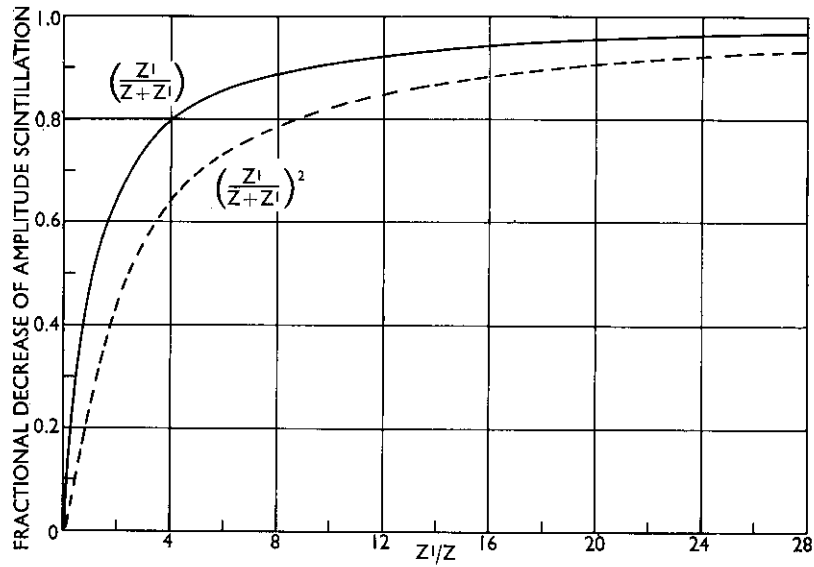


FIG. 28 Fractional decrease of amplitude scintillation as a function of the distance of radiating source from ionospheric irregularities (after Lawrence, Little and Chivers)

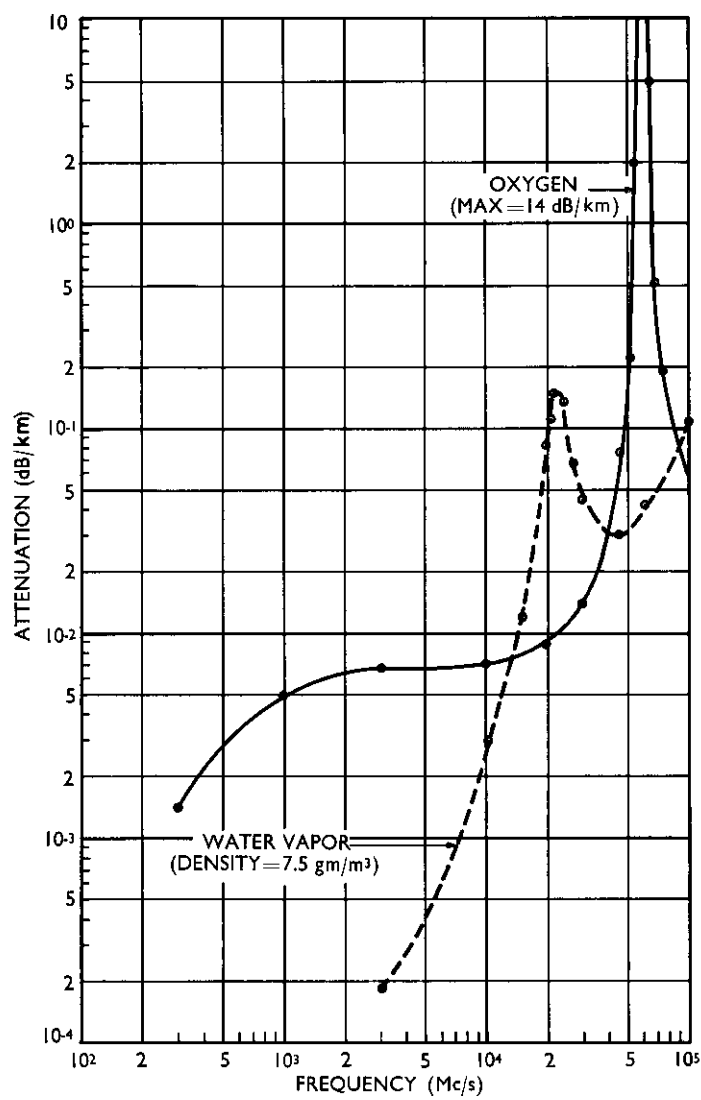


FIG. 29 Tropospheric attenuation of oxygen and uncondensed water vapor at sea-level for a temperature of 20°C (after Van Vleck)

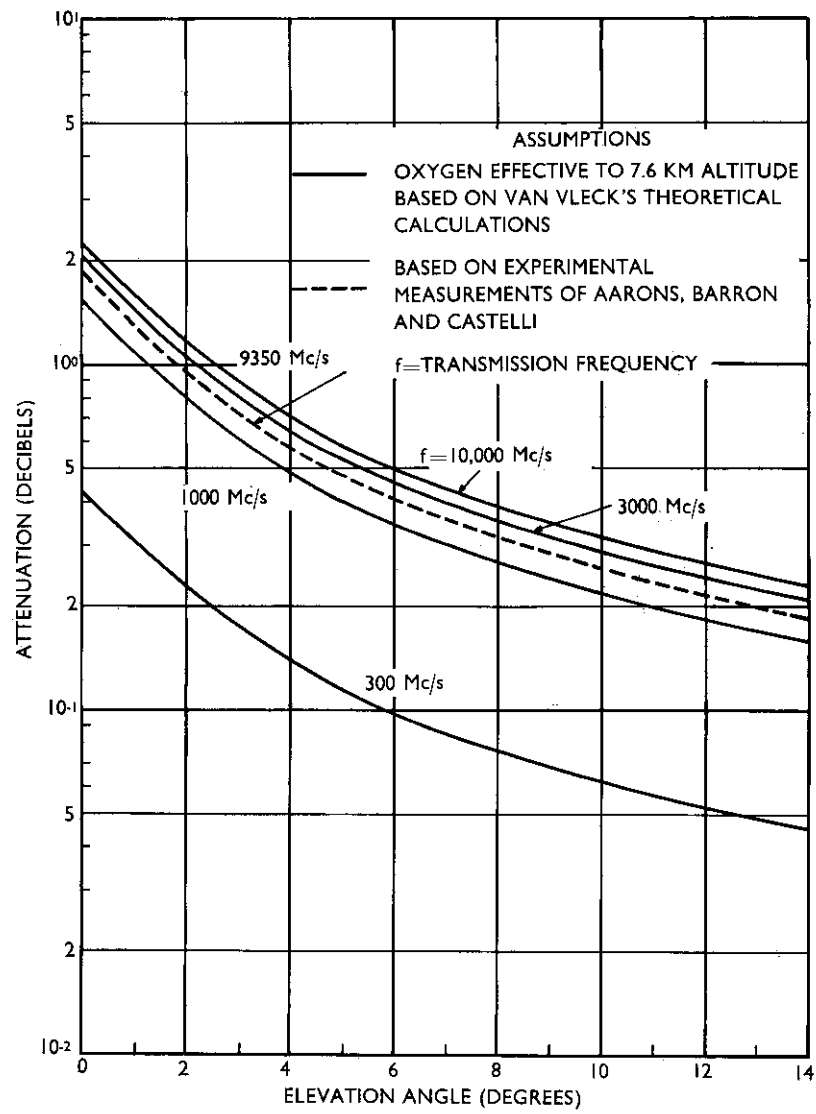


FIG. 30 Attenuation in the troposphere due to oxygen, one-way transmission path

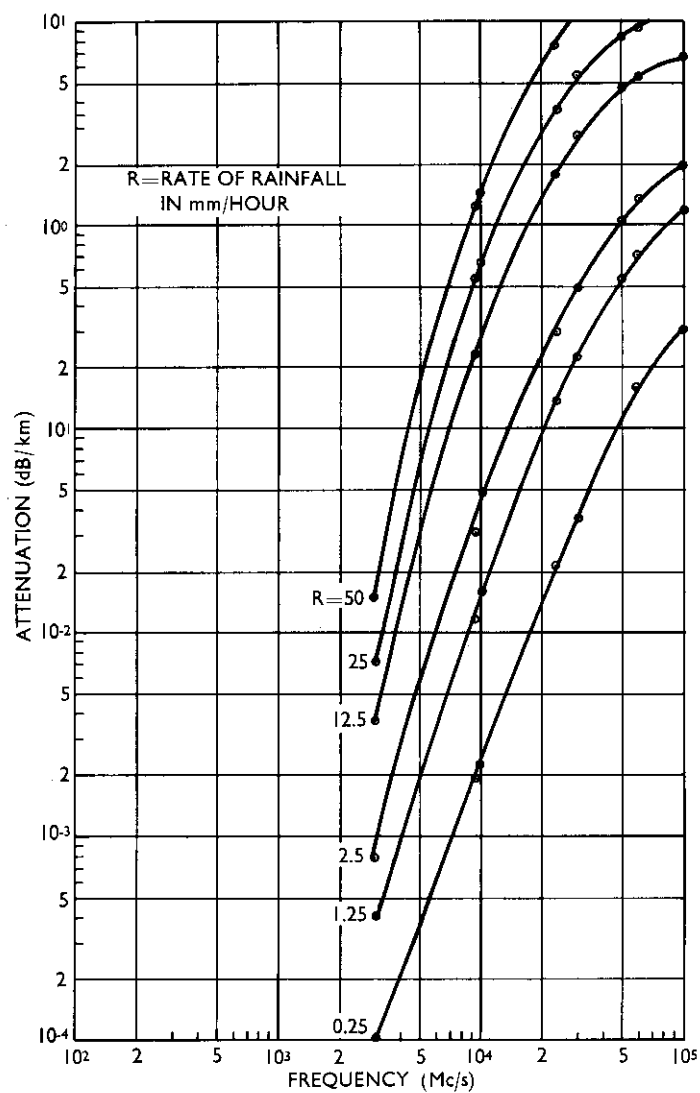


FIG. 31 Attenuation as a function of frequency for rainfalls of various intensities, temperature  $18^{\circ}\text{C}$ , one-way transmission path (from Kerr, after Ryde and Ryde)

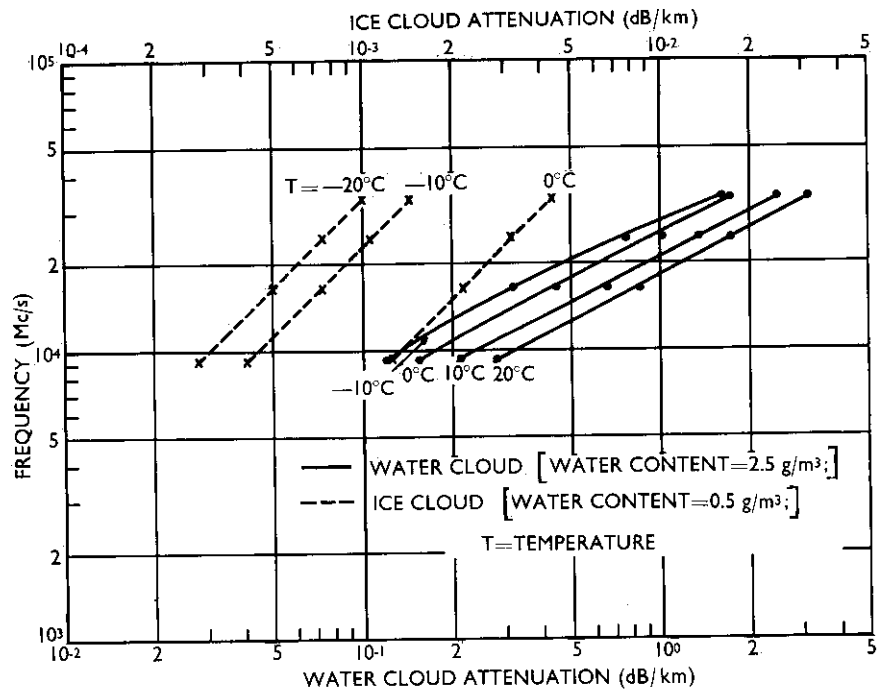


FIG. 32 Attenuation by water and ice clouds, one-way transmission path (from Bean, after Gunn and East)

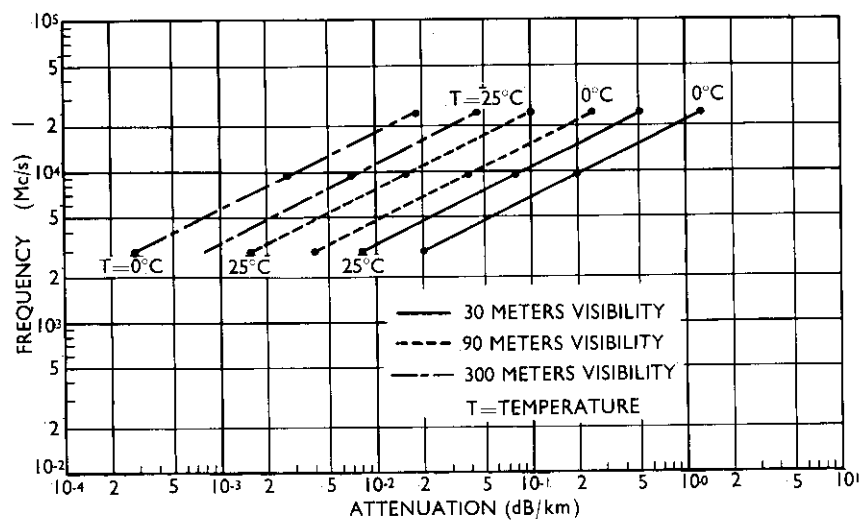


FIG. 33 Attenuation by fog, one-way transmission path (from Bean, after Saxton and Hopkins)



are also plotted in Fig. 30, are slightly less than the theoretical estimates of Van Vleck (23).

Scattering and absorption are the two mechanisms which cause the attenuation of radio waves when passing through a medium containing water droplets or precipitation.

For fog and clouds where the particle radii are small ( $\approx 0.01$  cm), the attenuation basically results from absorption at all frequencies up to at least 60 Gc/s (25). In the case of rain, where the particle radii may vary from 0.05 to 0.7 cm, the absorption mechanism is still predominant up to frequencies in the microwave range.

The one-way attenuation (25) as a function of frequency for rainfalls of various intensities at a temperature of 18°C is depicted in Fig. 31. The precipitation rate of 0.25 mm/h is classified as a drizzle, 1 mm/h as a light rain, 4 mm/h as a moderate rain, 16 mm/h as a heavy rain, and 30 mm/h as an extremely heavy rain.

The attenuation decay constants of Fig. 31 are temperature dependent (25). As an example, at a frequency of 3000 Mc/s the attenuation is increased by a factor of 2 for all precipitation rates at 0°C. When the temperature is 40°C, the decay constant reduces to about 59 per cent of the 18°C value.

Assuming that a rain cloud or thunderhead attains an altitude of 7.6 km, it follows from Fig. 31 that, for a precipitation rate of 12 mm/h, the one-way attenuation for a 10000 Mc/s frequency propagated at vertical incidence could be as great as 2.2 dB.

Figure 32 is a plot of the attenuation by water and ice clouds (24). It is seen that the attenuation is directly proportional to frequency and is also temperature dependent. The losses encountered by transmission through an ice cloud are about two orders of magnitude smaller than the losses through an equivalent cloud of water particles (24).

Fog is caused by water droplets suspended in the air in sufficient concentration to reduce the visibility at the ground below 1000 m (26). Figure 33 is a plot of the attenuation by fog for various grades of visibility (24). The data indicate that the attenuation at 25°C is about a factor of 2.5 smaller than that at 0°C. For a fog extending 500 m vertically with a visibility of 30 m, the one-way attenuation, at 10000 Mc/s and 0°C temperature is simply 0.11 dB.

Under severe hailstorm conditions (27) (particle diameter size of 2 cm and melting rates of 100 mm/h), approximately 1.7 dB/km attenuation could exist at X-band frequencies and 0.036 dB/km at 3000 Mc/s (27). For ice spheres of 0.25 cm diameter, the attenuation decreases by about factors of 46 and 16, respectively.

Signal loss in snow is the result of scattering and absorption. Based on the analysis of Atlas *et al* (28), snow exhibits very small attenuation at X-band and lower frequencies even for excessive rates of snowfall of 125 mm/h.

**Ionospheric attenuation** – Attenuation in the ionosphere is due to electron collision processes. This is brought about when a radio wave traversing an ionized medium sets up a periodic force on the electrons which causes them to vibrate. The absorption of signal energy takes place when the electrons colliding with other particles (such as the neutral particles and heavy ions)

in the medium are forced to give up some of their energy to these particles.

It can be shown that, for frequencies in the VHF and UHF range, the ionospheric attenuation (in dB) for a one-way transmission path can be expressed by the integral:

$$A = \frac{1.17 \times 10^{-2}}{f^2} \int_0^s N_e \nu ds \quad (22)$$

where  $f$  is the frequency in c/s,  $N_e$  is the electron density in electrons/cm<sup>3</sup>,  $ds$  is the path differential in centimeters, and  $\nu$  is the electron collision frequency in collisions per second.

This relationship is based on the assumptions that the earth's magnetic field can be neglected, the operating frequency is much greater than the electron collision frequency, and non-deviative type of absorption is applicable, or in other words, the refractive index is approximately unity.

In estimating the magnitude of the ionospheric absorption it was assumed, as a first approximation, that the collision frequency of the electrons obeyed the exponential law:

$$\nu = \nu^! e^{-(h^! - h)/H_s} \quad (23)$$

where  $\nu^!$  is the collision frequency at altitude  $h^!$ , and  $H_s$  is the scale height in the region. This expression implies that the atmosphere is considered to be chemically homogeneous and isothermal.

The parameters which describe the electron collision frequency model utilized in this paper are presented in Table 2.

TABLE 2

COLLISION FREQUENCY PARAMETERS

Layer	$H_s$ (km)	$h^!$ (km)	$\nu^!$ (sec <sup>-1</sup> )
E	10	100	$3 \times 10^5$
F	45	134	$10^4$

Figure 34 is a plot of the total ionospheric attenuation as a function of frequency. It is seen that the attenuation is inversely proportional to the square of the operating frequency with the daytime absorption being about thirty times greater than the nighttime effect. These calculations were based on a Chapman distribution of electron density, defined by Eq. 7 with parameters specified in Table 1.

The attenuation at 100 Mc/s, as a function of the ground elevation angle, as shown in Fig. 35, gives evidence of the effect of the sphericity of the earth on the elevation angle in the ionosphere. For a ray tangential to the earth's surface, the minimum departure angle of the ray with respect to the tangent plane in the ionosphere is between 8° and 10° depending upon the altitude of ray emergence; thus the ionospheric attenuation (and also refraction and time-of-day effects) is a slowly varying function for low angles of elevation, as seen in Fig. 35.

It is interesting to note that, for the daytime model of electron density at

0° and 90° elevation angle, 90 per cent of the total attenuation is attained at altitudes of 100 and 116 km, respectively, and 99 per cent at approximately 250 and 270 km, respectively.

The D-layer of the ionosphere, located at about 70 km altitude, is believed to account for the large variations in attenuation of radio waves between summer and winter and day and night. A sudden ionospheric disturbance (or S.I.D.), which is caused by intense ultraviolet and X-ray radiation and protons penetrating into the earth's atmosphere and increasing the ionization in the lower ionospheric regions and which occurs almost simultaneously with observed solar flares during the daylight hours, results in increased absorption for frequencies of short and medium wavelengths.

The possible existence of F-layer absorption has been postulated by Lusignan (29) and Steiger and Warwick (30) based on cosmic noise observations at frequencies of 27.5 and 18 Mc/s, respectively.

During severe auroral disturbances the absorption of 30.5 Mc/s cosmic noise has been found by Little and Leinbach (31) to be in excess of 4 dB.

Little (32) has reported that 65 Mc/s cosmic radio waves have also undergone absorption during aurorae. He found the frequency of occurrence of absorption in excess of 10 per cent to be more prevalent at midday and least frequent during the evening. The absorption was correlated with polar black-out conditions and geomagnetic K indices.

The observations of 81.5 Mc/s extra-terrestrial signals from discrete noise sources by Little and Maxwell (22) displayed a decrease in signal amplitude of about 10 per cent during an aurora.

#### IONOSPHERIC POLARIZATION ROTATION

When a linearly polarized radio wave traverses the ionosphere it separates into two independent components, both in the general case, elliptically polarized with opposite senses of rotation. For frequencies in the VHF range and above, the waves are circularly polarized. Since the two waves progress inside the ionized medium with different velocities of propagation, their phase relationships are continuously being altered. On emerging from the ionosphere the waves recombine to form a linearly polarized wave whose plane of polarization has been rotated with respect to that of the incident wave. This phenomenon, which is commonly referred to as the Faraday effect, is brought about by the interaction of the electromagnetic wave with the electrons in the presence of the earth's magnetic field.

The amount of angular rotation,  $\phi$  (in radians), experienced by a linearly polarized wave traversing a one-way path in the ionosphere can be represented by the function (1):

$$\phi = \frac{2.362 \times 10^4}{f^2} \int_0^h f(h) H \cos \theta N_e dh \quad (24)$$

where  $H$  is the magnetic field intensity in gauss,  $f(h)$  is the secant of the angle between the ray path and the zenith,  $dh$  is the height differential in cm, and  $\theta$  is the propagation angle (i.e. the angle between the direction of the earth's magnetic lines of force and the direction of electromagnetic propagation). The terms  $f$  and  $N_e$  have previously been defined.

Equation 24 is representative of the quasi-longitudinal mode of propagation. For frequencies in the 400 Mc/s range, this relationship is valid for  $0 \leq \theta \leq 89^\circ$ . At 100 Mc/s this propagation mode would also apply for angle  $\theta$  greater than  $5^\circ$  off perpendicularity (33).

It is seen that the rotation is inversely proportional to the square of frequency and directly proportional to the integrated product of the electron density and the component of the earth's magnetic field along the propagation path.

The term  $f(h) H \cos \theta$ , defined as the geometric factor  $M$  by Yeh and Gonzalez (33), is to a great extent dependent upon the location of the observation site on the earth's surface. The function, as viewed from Trinidad, varies over quite a wide range of values when oriented at low elevation angles, toward the north and south (34). As the elevation angle is increased there is a noticeable reduction in the spread of its value with height.

In the case of quasi-transverse propagation, the one-way polarization rotation evaluates to:

$$\phi = \frac{3.304 \times 10^{10}}{f^3} \int_0^h f(h) H^2 \sin^2 \theta N_e dh \quad (25)$$

It is evident that, for this mode of propagation, the polarization rotation is inversely proportional to the cube of frequency and directly proportional to the integrated product of the electron density and the square of the component of the earth's magnetic field perpendicular to the path of propagation.

The polarization rotation for the two modes of propagation, depicted in Fig. 36, reveals that the rotation for the longitudinal case, is slightly more than 100 times greater than that for the transverse condition. The calculations are based on the daytime and nighttime electron density distributions defined in Table 1 and a magnetic field intensity of 0.62 gauss which is applicable to the polar regions.

Faraday measurements conducted at 425 Mc/s at Trinidad by means of radar pulses reflected off the surface of the spherical satellite Echo I disclosed a maximum angular rotation along a one-way path of about  $500^\circ$  (35), (36). Since the magnetic field intensity in the equatorial ionosphere is of the order of 0.31 gauss (i.e. one-half the value of the intensity in the arctic region), it becomes evident that the Trinidad results are somewhat higher than the estimates given in Fig. 36. This discrepancy can most likely be attributed to the fact that the integrated electron density profile (i.e. electron content) at Trinidad was larger than that used in the calculations.

Figure 37 is a plot of the maximum attainable angular rotation at 100 Mc/s. It is seen that, for a given angle of elevation, the daytime shift is of the order of 3.8 times greater than the nighttime effect; in addition, assuming identical propagation conditions, the maximum polarization shift for transmissions along the horizon is approximately 3.5 times greater than that at the zenith.

According to Fig. 38, 90 per cent of the total rotation takes place between 475 and 510 km for the daytime conditions and all elevation angles, while for the nighttime distribution it reduces to the 400 to 410 km region. It is of interest to note that very little rotation exists above 1000 km; in other words, the contribution of the integrated electron density to the angular rotation is

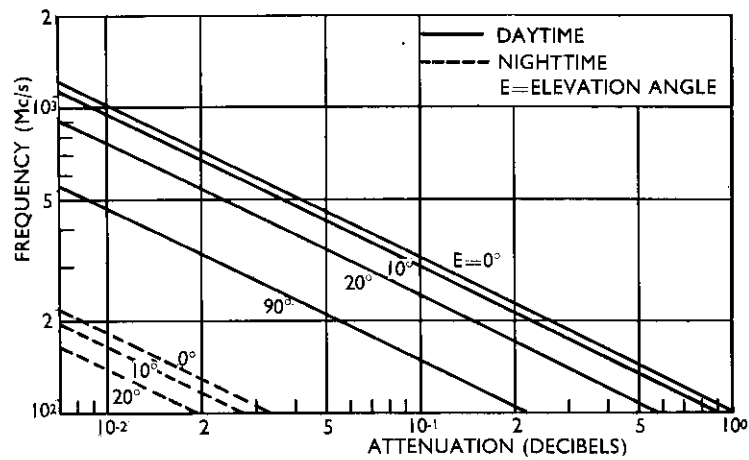


FIG. 34 Ionospheric attenuation as a function of frequency, one-way transmission path

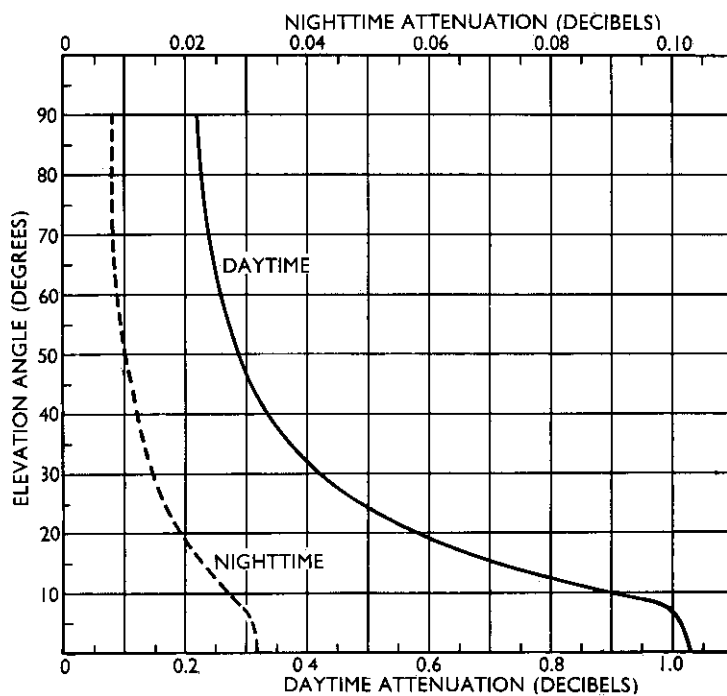


FIG. 35 Ionospheric attenuation at 100 Mc/s as a function of elevation angle, one-way transmission path

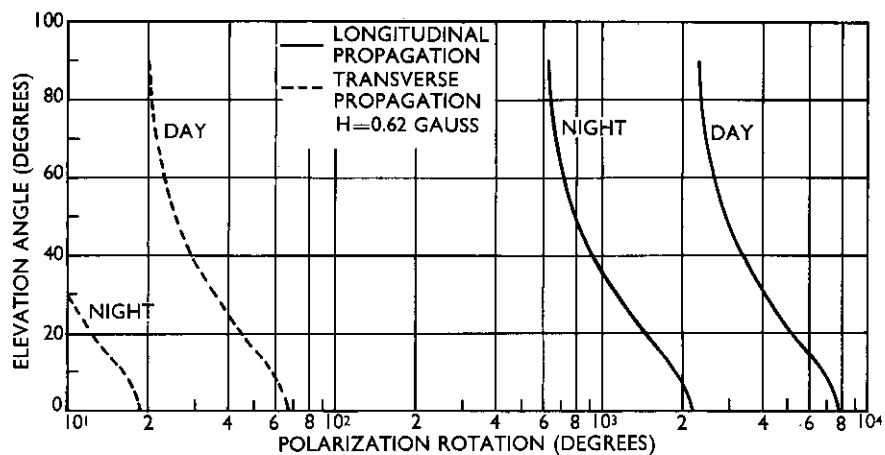


FIG. 36 Limit of polarization rotation as a function of frequency for propagation along the horizon and one-way transmission path

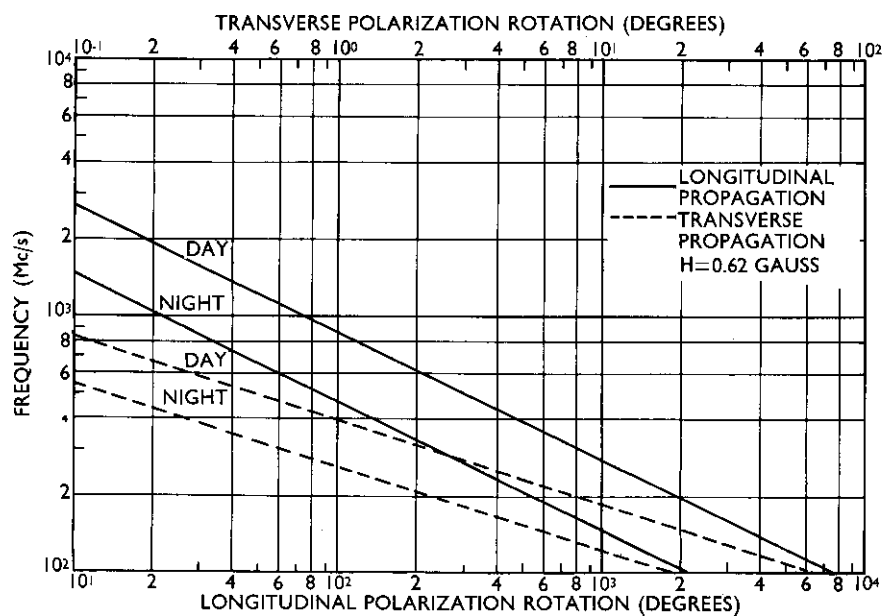


FIG. 37 Limit of polarization rotation at 100 Mc/s for one-way transmission path

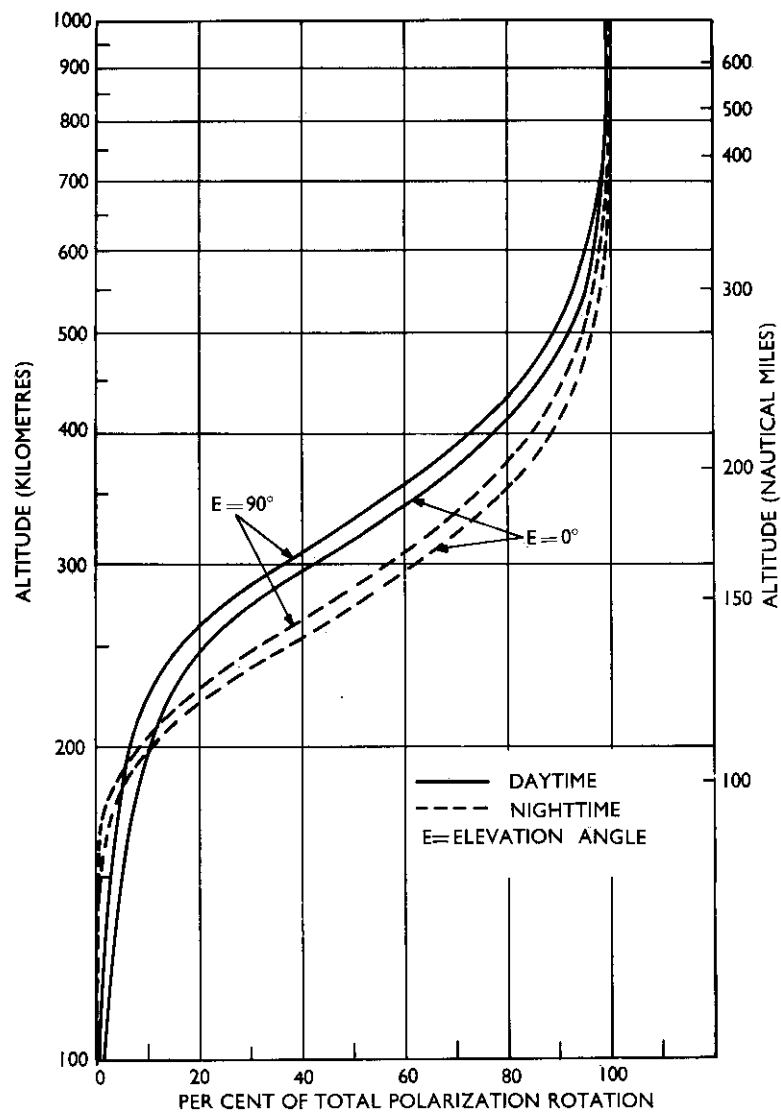


FIG. 38 Percentage of total polarization rotation as a function of altitude

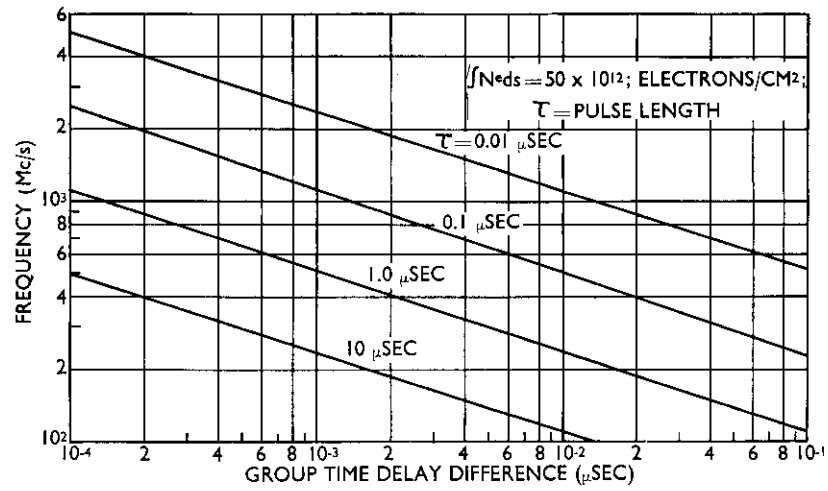


FIG. 39 Difference in the time delay between the lower and upper frequencies of the spectrum of a pulse transmitted through the ionosphere, one-way transmission path

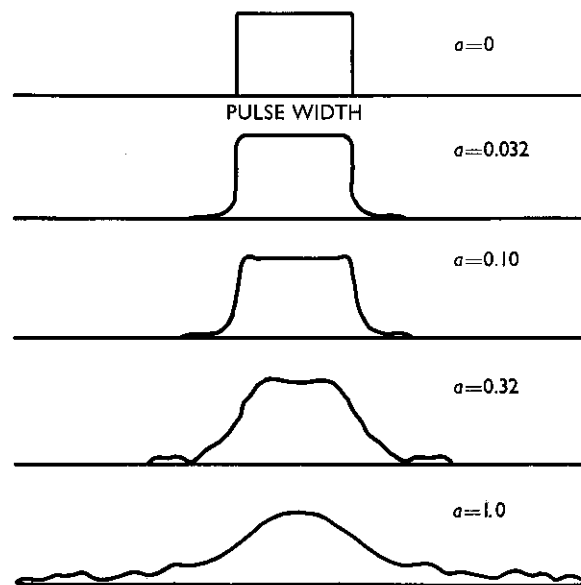


FIG. 40 Pulse shape distortion due to dispersion in a waveguide (after Elliott)



negligible above this level. This characteristic of the ionosphere has been discussed by Evans (37) and Millman (36), (38).

Bowhill (39) has shown that, for a given direction of satellite motion, the rate of polarization rotation of satellite transmissions should be a constant as observed at any receiving installation. His analysis was based on the assumptions that (a) the earth is flat, (b) the satellite is moving in a horizontal direction with a uniform velocity, and (c) the ionosphere is horizontally stratified.

The Trinidad radar-satellite reflection observations at 425 Mc/s tend to confirm Bowhill's prediction (35), (38). It was found that, in general, the Faraday rotation rate was approximately constant during a major portion of the satellite orbit, the deviations occurring during the beginning and end of the track when the satellite was at a low elevation angle. The rate of polarization rotation at 425 Mc/s, for a two-way transmission path, varied between  $0.11^\circ/\text{s}$  and  $1.11^\circ/\text{s}$ , depending upon the time of day and the geometric coordinates of the orbital trajectory.

It should be noted that radar and communications systems employing circular polarization both on transmission and reception will not be affected by the Faraday rotation phenomenon.

#### IONOSPHERIC DISPERSION EFFECTS

Because of the dispersive characteristics of the ionosphere (i.e. its refractive index is a function of frequency), the envelope of a pulse travels at a velocity less than that of the waves within the pulse. As the radiation travels through the ionosphere, the frequency components in the signal pulse spectrum undergo different phase shifts. This phenomenon could cause pulse distortion, depending upon the bandwidth of the spectrum and the carrier frequency.

Ionospheric dispersion effects could limit the range resolution capabilities of a radar system and also could distort wide-band high-information-rate data link systems.

It can be shown (13) that, for a one-way transmission path, the difference in the time delay between the two frequencies at opposite ends of the spectrum of a pulse is given by:

$$\Delta t = \frac{80 \times 10^6 \Delta f}{c f^3} \int_0^s N_e ds \quad (26)$$

where  $f$  is the transmitted frequency in c/s,  $\Delta f$  is the bandwidth associated with the pulse length  $\tau$  ( $\Delta f = 1/\tau$ ),  $N_e$  is the electron density in electrons/cm<sup>3</sup>, and  $c$  is the free-space velocity in cm/s.

It is seen that time difference is inversely proportional to the cube of the carrier frequency and the pulse length, and directly proportional to the integrated electron density along the path traversed by the wave.

An estimate of the difference in the group time delay between the lower and upper frequencies of the spectrum of a pulse transmitted through the ionosphere is illustrated in Fig. 39. Assuming an integrated electron density of  $50 \times 10^{12}$  electrons/cm<sup>2</sup> (this magnitude is comparable to the average daytime electron content in a one-square-centimeter vertical column through the ionosphere as deduced from radar-lunar (40) and radar-satellite observations (36) at Trinidad), the time-delay difference encountered by a pulse

width of  $0.1 \mu\text{s}$  (10 Mc/s bandwidth) at a carrier frequency of 1000 Mc/s is about  $1.33 \times 10^{-3} \mu\text{s}$ . If the signal spectral bandwidth is increased to 100 Mc/s (pulse width of  $0.01 \mu\text{s}$ ), the difference in the time delay becomes  $1.33 \times 10^{-2} \mu\text{s}$ , which is slightly greater than the duration of the pulse. It should be noted that when the group time-delay difference is of the order of the pulse length, the shape of the transmitted signal can be expected to be distorted after passage through the ionosphere.

Counter and Reidel (41) have applied to the ionosphere the analysis of Elliot (46) pertaining to the effects of the dispersive characteristics of a waveguide on pulse shape degradation. They have described the degree of pulse degradation,  $a$ , in terms of ionospheric parameters by the function:

$$a = \frac{2}{\tau f^{3/2}} \left[ \frac{1.6 \times 10^8}{\pi c} \int_0^s N_e ds \right]^{1/2} \quad (27)$$

According to Fig. 40, there is no distortion when  $a = 0$ , while the distortion in the waveform is serious for  $a = 1$ .

As shown in Fig. 41, for a frequency of 100 Mc/s and an electron content of  $50 \times 10^{12}$  electrons/cm<sup>2</sup>, the degradation in the shape of a pulse of  $1.0 \mu\text{s}$  width is appreciable ( $a = 0.58$ ), while at 1000 Mc/s under the same conditions, the distortion is insignificant ( $a = 0.018$ ).

For c.w. transmissions, the waves of different frequencies will experience different phase shifts on their passage through the ionosphere. It can be shown that the difference in the relative phase shift,  $\Delta\phi$  (in cycles), due to the ionosphere, for a one-way transmission path is expressed by:

$$\Delta\phi = \frac{40 \times 10^6 f_s}{cf^2} \int_0^s N_e ds \quad (28)$$

where  $f_s$  is the frequency separation and  $f$ , in this case, is the average of the two transmitted frequencies.

Figure 42 is a plot of the estimated difference in the phase between two frequencies transmitted during the daytime, at vertical incidence, from a location in the low latitudes. It is found that, for  $f = 100$  Mc/s and  $f_s = 1$  Mc/s, the phase difference is 6.7 cycles.

For low elevation angles, the integrated electron density along the transmission path would increase by approximately a factor of 3.5, which in turn would result in an increase in the difference in phase to about 23.4 cycles.

#### COSMIC NOISE

The sun, the Milky Way, the center of the galaxy, and discrete radio stars are astronomical sources which emit electromagnetic waves in the radio-frequency spectrum. When this cosmic radiation is intercepted by an antenna and enters a receiver, it affects the system sensitivity in the same manner as does thermal receiver noise. The effective receiver noise temperature depends on the actual receiver temperature, the background noise intercepted by the antenna, and the lossiness of the networks connecting the receiver to the antenna. Since extra-terrestrial radio noise contributes to this temperature

and hence may tend to reduce the system sensitivity, it must be taken into account in the analysis of earth-space radio propagation systems.

The sun radiates high-intensity electromagnetic wave noise greatly in excess of the black body intensity of 6000°K deduced from optical and thermal data. If the radio noise from the sun is observed continuously, it is found that, during sunspot activity, irregular increases of radio noise can occur lasting for periods of several days at a time. The radio noise is enhanced by the order of 10 to 20 dB greater than the base level of the quiet sun. As reported by Shapley and Davis (42), a noise burst recorded at 480 Mc/s, which accompanied a major solar flare, was 1000 times the normal output of the entire sun.

In addition to the increase in the general level of radio noise when sunspots are visible and active, sudden bursts of a few seconds' duration and rapid fluctuations of the flux density are a common characteristic of a solar disturbance.

Experimental measurements (43) of the apparent temperature of the quiet sun over a wide range of frequencies are shown in Fig. 43. The solid line through the observational data is the assumed average linear function.

R.F. noise distributed over a band of frequencies is radiated from a number of regions in the galaxy. Figure 43 also shows the results of observations of the intensity and distribution of radio frequency radiation from the galaxy at frequencies (44) from 9.5 to 1000 Mc/s.

Pawsey (45) has compiled a fairly complete catalog of the positions and intensities of discrete radio stars. Figure 44 is a plot of the flux densities of the major discrete sources which can be detected in both the northern and southern hemispheres. The flux density of the quiet sun, which is also presented in Fig. 44, was deduced from the solar data given in Fig. 43.

An increase in system noise temperature, in essence, alters the maximum range capability of a communication and radar system. According to the standard free-space inverse-square-law equation, the maximum communication range is specified by:

$$R_{\max} \propto \left( \frac{P_t}{S_{\min}} \right)^{1/2} \propto \left( \frac{1}{T_s} \right)^{1/2} \quad (29)$$

where  $P_t$  is the transmitted peak power,  $S_{\min}$  is the minimum detectable signal, and  $T_s$  is the effective system noise temperature.

The effective system noise temperature can be calculated from the expression:

$$T_s = \frac{T_a}{L_r} + \left( 1 - \frac{1}{L_r} \right) T_L + (F_o - 1) T_o \quad (30)$$

where  $L_r$  is the line loss factor from antenna to receiver (can be assumed to be approximately 2 dB),  $T_L$  is the temperature of the receive transmission line components (usually 290°K),  $T_o$  is the reference noise temperature (290°K), and  $F_o$  is the noise figure of the receiver referred to  $T_o$ .

The apparent noise temperature of the antenna,  $T_a$ , is usually composed of contributions from many external sources such as the sky background radiation, the radiation from a warm earth scattered by particles into the main lobe of an antenna, the leakage from a warm earth into the minor lobe

pattern of an antenna, and the reradiation from an absorbing medium. In this analysis it is assumed that, as a first approximation, the extra-terrestrial noise sources solely determine the apparent antenna temperature, the other contributions mentioned above being neglected.

If the celestial noise radiator has an angular area larger than the angular dimensions of the antenna beam, then, neglecting the other sources, the temperature of this source determines the antenna temperature. If the angular size of the source is small compared to the antenna angular beam size, then the apparent antenna temperature is directly proportional to the effective area of the receiving antenna and the flux density of the noise source.

Table 3 shows the apparent antenna temperatures at 100 and 1000 Mc/s and the reduction in range for a one-way path caused by the quiet sun, the major radio stars, and distributed galactic noise regions. The calculations are based on an effective antenna aperture of 309 m<sup>2</sup> (25.6 m or 84-ft-diameter parabolic antenna with an antenna efficiency factor of 0.6) and a receiver noise figure of 1.5 dB.

TABLE 3  
REDUCTION IN RANGE FOR A ONE-WAY  
PATH DUE TO THE PRESENCE OF COSMIC NOISE SOURCES

Radio source	Apparent antenna temperature (degrees Kelvin)		Percent reduction in range	
	100 Mc/s	1000 Mc/s	100 Mc/s	1000 Mc/s
Sun (quiet)	6710	39,200	77.4	90.5
Cassiopeia	2070	319	61.5	27.2
Cygnus-A	1340	201	54.0	20.0
Taurus	201	103	19.8	12.1
Centaurus	196	38	19.6	4.9
Virgo	134	24	14.7	3.1
Center of galaxy	6600	25	77.3	3.4
Milky Way	1050	<10	49.5	<1.3

It is obvious that, for this example, the sun is the major source of interference at the higher frequency, while Cassiopeia, Cygnus-A and Taurus are somewhat less significant. The appearance of the other radio stars, the galactic center, and the Milky Way in the antenna beam does not introduce any appreciable system deterioration. The interference from all cosmic radio noise sources, except the sun, is reduced as the transmission frequency is increased.

#### CONCLUSIONS

The propagation errors such as refraction, time delays and Doppler effects discussed in this survey are illustrative of normal atmospheric conditions. In order to compensate for these errors it is necessary that the variation of the index of refraction be known throughout the whole atmosphere. Since refractive index measurements made in the troposphere and ionosphere do not

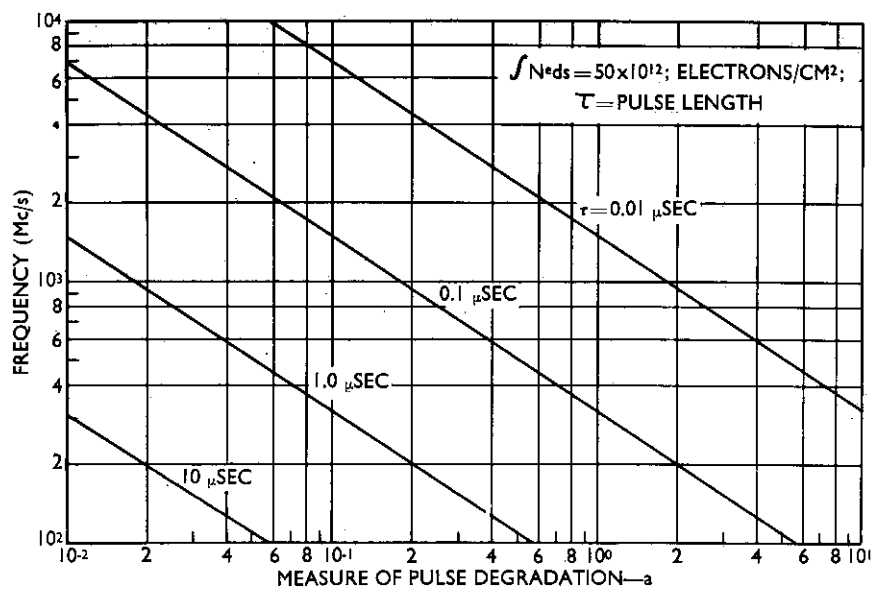


FIG. 41 Pulse shape distortion for propagation through the ionosphere, one-way transmission path

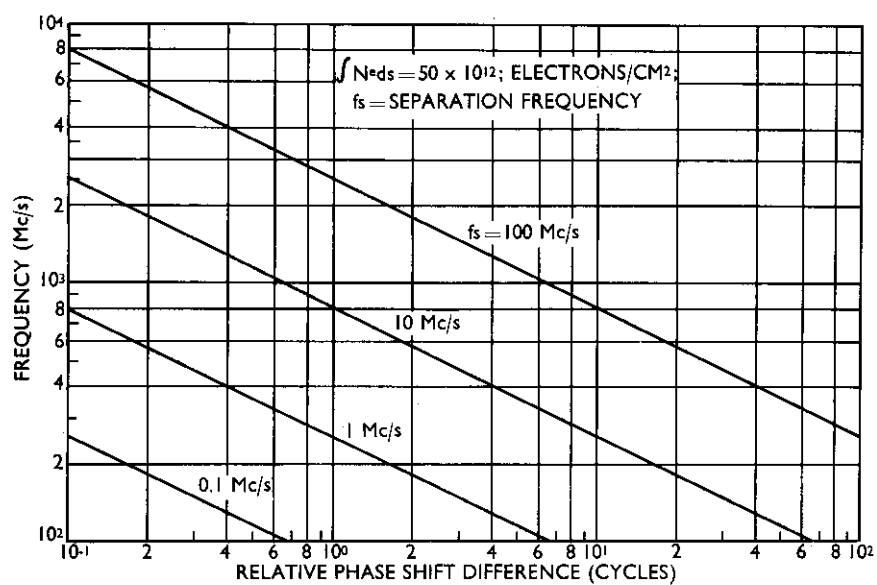


FIG. 42 Difference in relative phase shift between two frequencies transmitted through the ionosphere, one-way transmission path

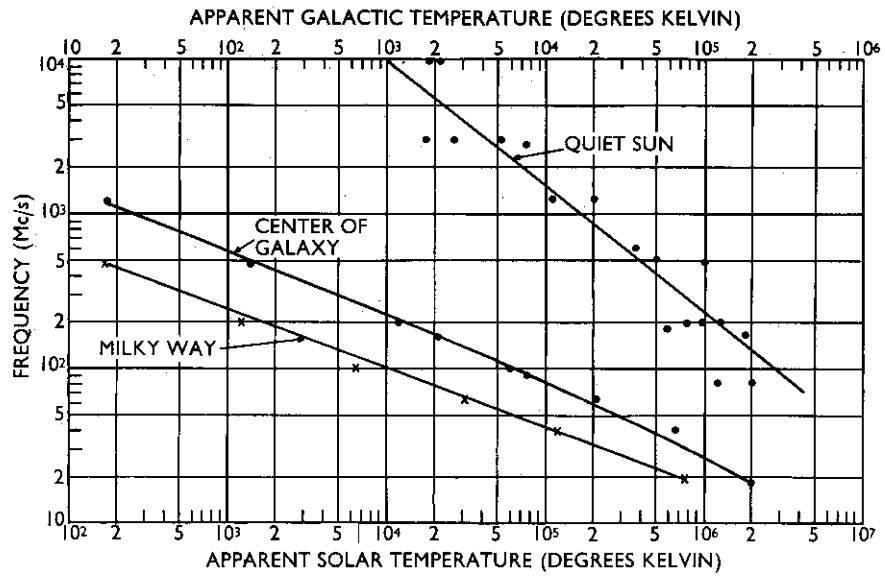


FIG. 43 Apparent temperature of the quiet sun (after Pawsey and Smerd) and galactic radiation (after Piddington)

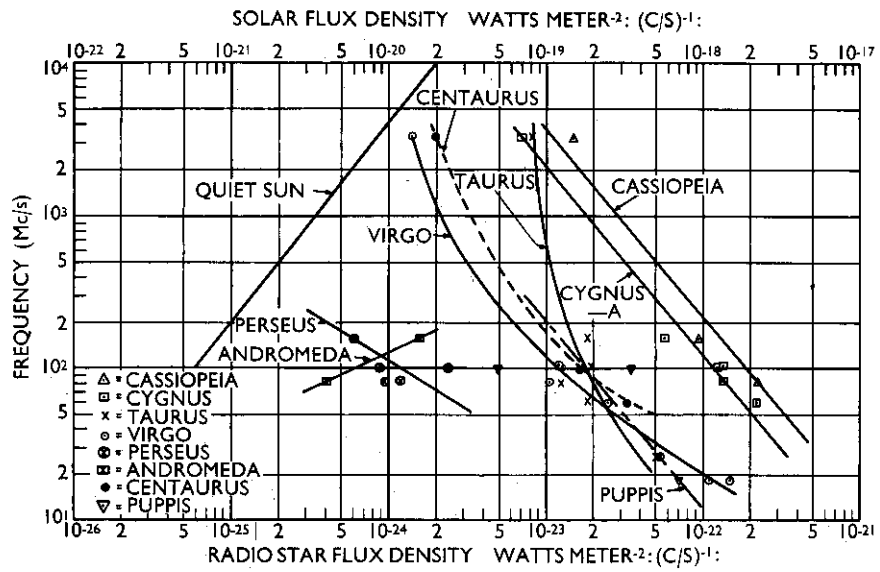


FIG. 44 Flux density of discrete radio sources (after Pawsey) and the quiet sun

generally describe the true atmospheric conditions along the actual paths traversed by the radio waves, the theoretically calculated bias errors, which would normally be used for correction purposes, could be in error by as much as  $\pm 10$  to 20 per cent. The residual bias errors (after compensation) and the fluctuations about the bias may contribute to the ultimate accuracy of tracking and guidance systems.

For frequencies below 100 to 200 Mc/s, ionospheric refraction is larger than the tropospheric effect except at very low angles of elevation. In the case of time delay effects, however, the ionospheric contribution is predominant up to frequencies in the range of 600 to 800 Mc/s.

Doppler errors in the troposphere are directly proportional to frequency, while in the ionosphere they are inversely related. Doppler effects can be compensated for, to some extent, when the angular bending and space vehicle velocity are known.

Fluctuations in the angle-of-arrival, phase, range and amplitude are imposed by the dynamic properties of the atmosphere (i.e. the temporal and spatial variations of the inhomogenities). The frequency dependence of the root-mean-square scintillations in the troposphere and ionosphere is summarized in the following table.

Scintillation effect	Troposphere	Ionosphere
Angle of arrival	Independent of $f$	$f^{-2}$
Phase	$f$	$f^{-1}$
Range	Independent of $f$	$f^{-2}$
Amplitude	—	$f^{-2}$

The influence of the ionosphere on the various scintillation effects can be considered to be negligible, under normal ionospheric conditions, at frequencies of the order of 500 Mc/s and above.

The attenuation due to the various processes and constituents in the troposphere and ionosphere is a minimum in the frequency range of approximately 500 to 1000 Mc/s. Ionospheric attenuation is inversely proportional to the square of frequency and is the more effective one in the VHF range. Above 1000 Mc/s, tropospheric attenuations become predominant, increasing directly with frequency.

The rotation of the plane of polarization due to the ionospheric Faraday effect is negligible for frequencies above about 2000 to 3000 Mc/s. The effect of this phenomenon on lower radio frequencies can be minimized by utilizing circular polarization on transmission and reception.

The dispersive characteristics of the ionosphere can distort the pulse shape of signals transmitted in the medium. For spectral bandwidths greater than about one per cent of the carrier frequency, the dispersive effects could become severe, depending upon the electron content along the path of propagation.

The extra-terrestrial radio noise sources, such as the sun, radio stars, galactic center and the Milky Way, can degrade the sensitivity of earth-space transmission systems by raising the background noise level. Except for the sun, the interference of the cosmic noise sources is reduced for frequencies above 1000 Mc/s.

## DISCUSSION

W. DIEMINGER – It was mentioned by the author that there are very few or no direct measurements of the frequency-dependent refraction of satellite signals in the atmosphere. We were able to observe by pure accident the refraction directly when recording Faraday rotation of a satellite transmitting on two frequencies, 130.00 and 130.03 Mc/s. We had a typical beating effect which was displaced in time by approximately 2 seconds. This is shown in Fig. A. Apparently the beating was caused by an aeroplane crossing the path from the satellite to the observing site. Because the path is not identical for both frequencies the interference occurs at different times as shown in Fig. B. Unfortunately it was impossible to obtain the flight data of the aeroplane and so we were not able to evaluate the observation numerically. As a matter of fact, the time delay corresponds to a horizontal distance between both paths of the order of 200 m if a speed of 1 000 km/h is assumed for the aeroplane. This value is compatible with the theory of refraction assuming reasonable electron densities in the ionosphere.

M. ANASTASSIADES – The differential refraction of signals emitted simultaneously on two frequencies (20 and 40 Mc/s) is frequently observed as a result of ionospheric irregularities. In Greece we have such data recorded at Athens, Crete and Alexandropolis.

P. G. L. SIMON – Considering the systematic refraction errors due to both troposphere and ionosphere you said that we must consider the correction as a rough estimate. In the case of an earth-to-space precise-tracking system aiming at a  $1\mu$  radian accuracy at 1 000 Mc/s, to what extent can we expect to correct angle measurements for bending? What is the order of magnitude of residual errors?

G. H. MILLMAN – The residual would be about 10 per cent of the correction. This could be reduced by measurements of radiorefractivity at the ground and by radio sonde measurements. At 1 000 Mc/s there would not be any ionospheric refraction, but at lower frequencies ionospheric soundings would be needed to reduce the residual.

W. T. BLACKBAND – It is interesting to compare the curve of refraction angle versus elevation based on measurements at 8 350 Mc/s by Nichols\* with those quoted by the author in Fig. 8. It will be noted that Nichols' curve lies between those previously observed at 200 and 34 500 Mc/s. These curves together with that for optical frequencies are plotted in Fig. C. It should be borne in mind that while these average curves show a progression with rising frequency, the scatter of individual measurements of refraction is great enough to obscure this frequency dependence.

\* NICHOLS, D. E. T. Determination of the total refraction of 3.6 cm wavelength radiation passing through the ionosphere. Royal Aircraft Establishment Report 66193, 1966.



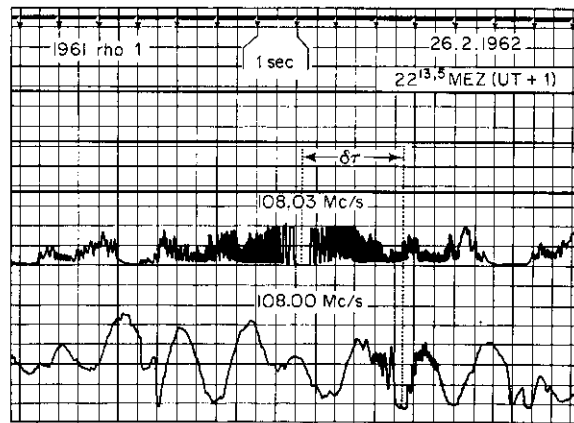


FIG. A Refraction effect in Faraday rotation record

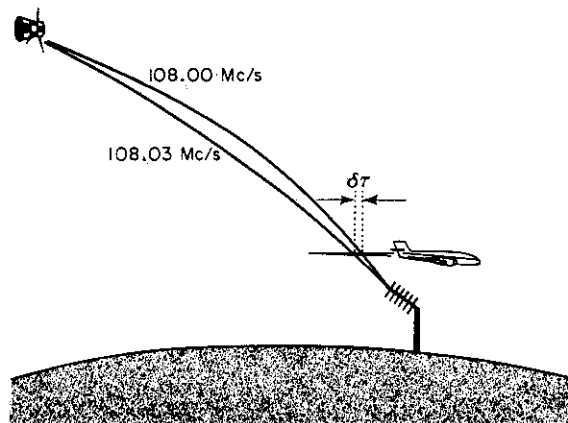


FIG. B Geometry of the refraction effect

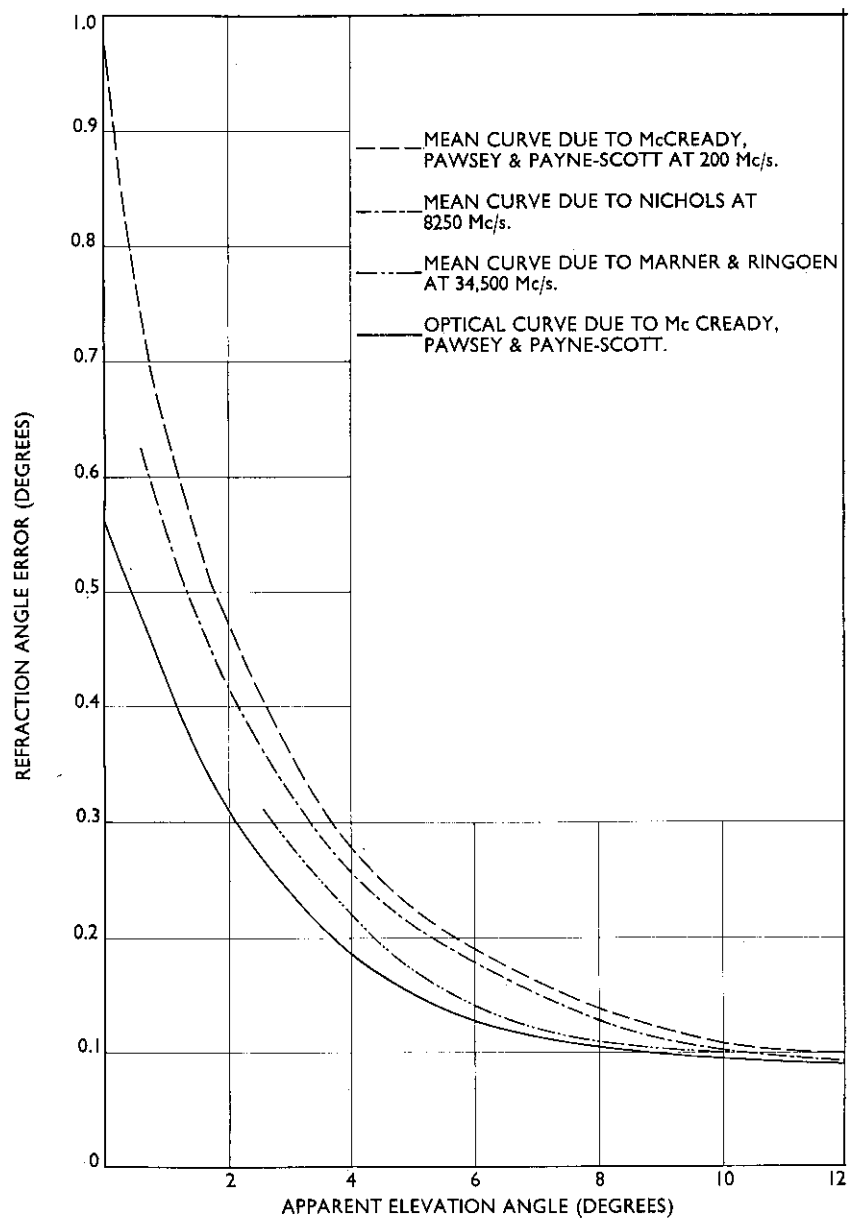


FIG. C Refraction effect at different frequencies  
(after Nichols)

## REFERENCES

1. MILLMAN, G. H., "Atmospheric Effects on VHF and UHF Propagation". *Proc. IRE* 46, 1492-1501, 1958.
2. MILLMAN, G. H. "Tropospheric Effects on Radar Target Measurements". *Proceedings of the Seventh Weather Radar Conference*, American Meteorological Society, 1958.
3. SMITH, E. K., and WEINTRAUB, S., "The Constants in the Equation for Atmospheric Refractive Index at Radio Frequencies". *Proc. IRE* 41, 1035-7, 1953.
4. CAMPEN, C. F., and COLE, A. E., "Tropospheric Variations of Refractive Index at Microwave Frequencies". *Geophysical Research Directorate, Air Force Surveys in Geophysics* 79, 1955.
5. BEAN, B. R., and CAHOON, B. A., "The Use of Surface Weather Observations to Predict the Total Atmospheric Bending of Radio Waves at Small Elevation Angles". *Proc. IRE* 45, 1545-6, 1957.
6. BEAN, B. R., "Comparison of Observed Tropospheric Refraction with Values Computed from the Surface Refractivity". *Trans IRE AP-9*, 415-16, 1961.
7. BEAN, B. R., "Tropospheric Refraction". *Advances in Radio Research*, 53-120, Academic Press, 1964.
8. WEISBROD, S., and COLIN, L., "Refraction of VHF signals at Ionospheric Heights". *Trans IRE AP-8*, 107-9, 1960.
9. MCCREADY, L. L., PAWSEY, J. L., and PAYNE-SCOTT, R., "Solar Radiation at Radio Frequencies and its Relation to Sunspots". *Proc. Roy. Soc. A* 190, 357, 1947.
10. MARNER, G. R., and RINGOEN, R. M., "Atmospheric Refraction of 8.7 mm Radiation". *Collins Radio Co., Report CTR-162*, 1956.
11. AARONS, J., BARRON, W. R., and CASTELLI, J. P., "Radio Astronomy Measurements at VHF and Microwaves". *Proc. IRE* 46, 325-33, 1958.
12. LAWRENCE, R. S., LITTLE, C. G., and CHIVERS, H. J. A., "A Survey of Ionospheric Effects Upon Earth-Space Radio Propagation". *Proc. IRE* 52, 4-27, 1964.
13. MILLMAN, G. H., "Atmospheric and Extraterrestrial Effects on Radio Wave Propagation", *General Electrical Tech. Inf. Ser. Rep. R61EMH29*, 1961.
14. MUCHMORE, R. B., and WHEELON, A. D., "Line-of-Sight Propagation Phenomena-I Ray Treatment", *Proc. IRE* 43, 1437-49, 1955.
15. BOOKER, H. G., "The Use of Radio Stars to Study Irregular Refraction of Radio Waves in the Ionosphere", *Proc. IRE* 46, 298-314, 1958.
16. HEWISH, A., "The Diffraction of Galactic Radio Waves as a Method of Investigating the Irregular Structure of the Ionosphere", *Proc. Roy. Soc.* 214, 494-514, 1952.
17. LAWRENCE, R. S., JESPERSEN, J. L., and LAMB, R. C., "Amplitude and Angular Scintillations of the Radio Source Cygnus-A Observed at Boulder, Colorado", *J. Res. Nat. Bur. Stand.* 65D, 333-50, 1961.
18. LITTLE, C. G., REID, G. C., STILTNER, E., and MERRITT, R. P., "An Experimental Investigation of the Scintillation of Radio Stars Observed

- at Frequencies of 223 and 456 Mc/s from a Location Close to the Auroral Zone", *J. Geophys. Res.* 67, 1763-84, 1962.
19. HERBSTREIT, J. W., and THOMPSON, M. C., "Measurements of the Phase of Radio Waves Received over Transmission Paths with Electrical Lengths Varying as a Result of Atmospheric Turbulence", *Proc. IRE* 43, 1391-1401, 1955.
  20. DEAM, A. P., and FANNIN, B. M., "Phase-Difference Variations in 9350-Megacycle Radio Signals Arriving at Spaced Antennas", *Proc. IRE* 43, 1402-4, 1955.
  21. HEWISH, A., "The Diffraction of Radio Waves in Passing through a Phase-Changing Ionosphere", *Proc. Roy. Soc. A* 209, 81-96, 1951.
  22. LITTLE, C. G., and MAXWELL, A., "Scintillation of Radio Stars during Aurorae and Magnetic Storms", *J. Atmos. Terr. Phys.* 2, 356, 1952.
  23. VAN VLECK, J. H., "Propagation of Short Radio Waves". Radiation Laboratory Series 13, 641-64, McGraw-Hill, 1951.
  24. BEAN, B. R., "Attenuation of Radio Waves in the Troposphere". *Advances in Radio Research*, 121-56, Academic Press, 1964.
  25. KERR, D. E., "Propagation of Short Radio Waves", Radiation Laboratory Series, 13, 671-92, McGraw-Hill, 1951.
  26. BERRY, F. A., BOLLAY, E., and BEERS, N. R., "Handbook of Meteorology", 727-36, McGraw-Hill, 1945.
  27. RYDE, J. W., "The Attenuation and Radar Echoes Produced at Centimetre Wave-Lengths by Various Meteorological Phenomena". *Meteorological Factors in Radio-Wave Propagation*, 169-88, Phys. Soc. (London), 1946.
  28. ATLAS, D., PLANK, V. G., PAULSEN, W. H., CHMELA, A. C., MARSHALL, J. S., EAST, T. W. R., and GUNN, K. L. S., "Weather Effect on Radar". *Geophys. Res. Direct., Air Force Surveys in Geophysics*, 23, 1952.
  29. LUSIGNAN, B., "Cosmic Noise Absorption Measurements at Stanford, California and Pullman, Washington", *J. Geophys. Res.* 65, 3895-902, 1960.
  30. STEIGER, W. R., and WARWICK, J. W., "Observations of Cosmic Radio Noise at 18 Mc/sec in Hawaii", *J. Geophys. Res.* 66, 57-66, 1961.
  31. LITTLE, C. G., and LEINBACH, H., "Some Measurements of High Latitude Ionospheric Absorption Using Extraterrestrial Radio Waves". *Proc. IRE* 46, 334-55, 1958.
  32. LITTLE, C. G., "High Latitude Ionospheric Observations Using Extraterrestrial Radio Waves". *Proc. IRE* 42, 1700-1, 1954.
  33. YEH, K. C., and GONZALEZ, V. H., "Note on the Geometry of the Earth's Magnetic Field Useful to Faraday Effect Experiments". *J. Geophys. Res.* 65, 3209-14, 1960.
  34. MILLMAN, G. H., PINEO, V. C., and HYNEK, D. P., "Ionospheric Investigations by the Faraday Rotation of Incoherent Backscatter", *J. Geophys. Res.* 69, 4051-65, 1964.
  35. MILLMAN, G. H., and SANDERS, A. E., "An Analysis of Ionospheric Characteristics from Echo I Radar Measurements". General Electric Tech. Inf. Ser. Rep. R61EMH49, 1961.
  36. MILLMAN, G. H., "Electron Content of the Ionosphere Deduced from Radar Satellite Reflections". *Electron Density Distributions in*

- Ionosphere and Exosphere, 256-65, North-Holland Publishing Co., 1964.
37. EVANS, J. V., "The Measurement of the Electron Content of the Ionosphere by the Lunar Radio Echo Method". Proc. Phys. Soc. B 69, 953-5, 1956.
  38. MILLMAN, G. H., "Ionospheric Investigations by Radar Reflections from Echo I". Radio Astronomical and Satellite Studies of the Atmosphere, 150-62, North-Holland Publishing Co., 1963.
  39. BOWHILL, S. A., "The Faraday-Rotation Rate of a Satellite Radio Signal". J. Atmos. Terr. Phys. 13, 175-6, 1958.
  40. MILLMAN, G. H., "Radar Lunar Measurements of the Electron Content of the Ionosphere". J. Geophys. Res. 69, 429-40, 1964.
  41. COUNTER, V. A., and RIEDEL, E. P., "Calculations of Ground-Space Propagation Effects". Lockheed Aircraft Corporation, Rep. LMSD-2461, 1958.
  42. SHAPLEY, A. H., and DAVIS, R. M., "Solar Eruption of May 10, 1949". Science 110, 159, 1949.
  43. PAWSEY, J. L., and SMERD, S. F., "Solar Radio Emission". The Sun, 466-531, Univ. Chicago Press, 1953.
  44. PIDDINGTON, J. H., "The Origin of Galactic Radio Frequency Radiation". Monthly Notices Roy. Astro. Soc. III, 46, 1951.
  45. PAWSEY, J. L., "A Catalog of Reliably Known Discrete Sources of Cosmic Radio Waves", Astrophys. J. 121, 1-5, 1955.
  46. ELLIOTT, R. S., "Pulse Waveform Degradation Due to Dispersion in Waveguide" Trans. IRE MTT-5, 254-7, 1957.

## ACKNOWLEDGEMENTS

NICHOLS, D. E. T. R.A.E. Report, 1965.



CP-3

PART 2

PROPAGATION IN THE INTERPLANETARY SPACE

---





THE EFFECT OF THE INTERPLANETARY MEDIUM  
ON S-BAND TELECOMMUNICATIONS

M. EASTERLING and R. GOLDSTEIN

Jet Propulsion Laboratory, Pasadena, Calif., U.S.A.

## SUMMARY

The space within our solar system, which is normally thought of as being empty, we know in reality is not, although its content is extremely tenuous. Consideration of the accumulated effects on microwave signals traveling through many millions of miles of space becomes important. Mechanisms have been postulated for the generation of multipath, rotation of polarization, deflection, attenuation and other telecommunication problems in space. There is no *a priori* way of assessing the magnitude of the effects of the interplanetary medium on telecommunications. However, since the advent of radar astronomy, we have a method of measuring these influences under the actual conditions of interest. The medium has been tested by sending waves through it, then analyzing the echoes reflected from the planets. The techniques used and the results obtained at S-band over a considerable area of the plane of the ecliptic are described in this paper.

## INTRODUCTION

The telecommunication system used with a deep-space craft serves two major functions. One is the transmission of information to and from the spacecraft. The other is making measurements from which the position and velocity of the spacecraft can be determined, not only to provide location tags for the scientific data collected but also, as a means for guiding the spacecraft to its desired destination.

The propagation properties of interplanetary space, which is not a void, have profound effects on both of these functions. Mechanisms have been postulated for the generation of multipath, change of sense of polarization, deflection, attenuation and other telecommunications problems in space. There is no *a priori* way of assessing the magnitude of space-medium effects, but it was obviously of first importance to determine such effects before launching spacecraft to the planets. Accordingly, a number of planetary radar experiments have been conducted at various times since 1961; one of the purposes was to determine the propagation properties of the interplanetary medium at S-band near the frequencies to be used for spacecraft telecommunications. This report describes the measurements made, the conclusions to be drawn from the data, and gives tracking data from the *Mariner II* and *Mariner IV* spacecraft that confirm some of the conclusions.

HISTORY OF RADAR EXPERIMENTS AND *MARINER* FLIGHTS

The first JPL planetary radar experiments were in 1961 with Venus as the target; they were conducted near the time of that planet's closest approach to Earth. Equipment used was the bistatic radar that had been used for *Project Echo*, two 85 ft antennas, a 10 kW transmitter, and a receiver with a maser amplifier. The frequency selected was 2388 Mc/s, which was near the operating frequency planned for future spacecraft. This experiment demonstrated the feasibility of using microwaves for interplanetary tracking and communications.

The first successful interplanetary spacecraft, which was launched August 27, 1962, flew past Venus on December 14 of that year. The frequencies used were 890 Mc/s on the up-link and 960 Mc/s on the down-link. Originally, these frequencies had been chosen for the *Ranger* spacecraft, because the S-band components were not sufficiently developed. Even so, the *Mariner II* verified the results of the planetary radar experiment by maintaining communications with the Earth until the attitude stabilization system expended its gas, 20 days after the Venus encounter.

During 1962, near the time of closest approach of the planet, a second Venus radar experiment was conducted; this one was during the *Mariner II* tracking. The radar was a monostatic version of the 1961 radar with some improvements, particularly in system temperature. The results confirmed the findings of the 1961 experiment.

Early in 1963 the first experiment was conducted with Mars as a target. This was made possible by the addition of a 100 kW transmitter to the radar used on Venus in 1962. In May of 1963 a second experiment was conducted with Mercury as a target.

During the latter part of 1963 extensive rebuilding of the radar resulted in a considerable improvement (a decrease from 65°K to 30°K) in system temperature and in advanced signal-processing methods. The following experiment was a lengthy one, lasting over five months; the long duration was possible because of the greatly improved radar performance.

The latest experiment was conducted during February, March and April of 1965 with Mars as a target; this activity took place during the flight of *Mariner IV*, which was launched on November 28, 1964, and flew past Mars on July 14, 1965. Duration of the aforementioned experiments and of the *Mariner* tracking are shown in Fig. 1.

As a result of the combined radar experiments and *Mariner* tracking, a significant portion of the plane of the ecliptic has been probed. Figure 2 shows the region probed by the several radar experiments, all at 2388 Mc/s. Figure 3 shows the region probed by the *Mariner* tracking. The *Mariner II* tracking was done at L-band using 890 Mc/s on the up-link and 960 Mc/s on the down-link. The *Mariner IV* used S-band 2115 Mc/s on the up-link and 2295 Mc/s on the down-link. Together, the radar and spacecraft tracking have covered the region between the orbits of Venus and Mars fairly well.

## ATTENUATION

The inverse square law is usually assumed in the design of deep-space communications. But the question arises as to whether this law remains valid over distances of millions of kilometers. Perhaps there is an absorption effect

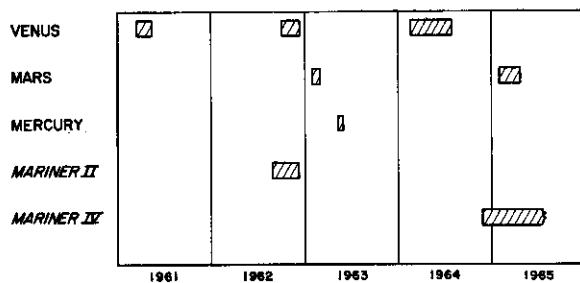


FIG. 1 JPL radar and tracking experience

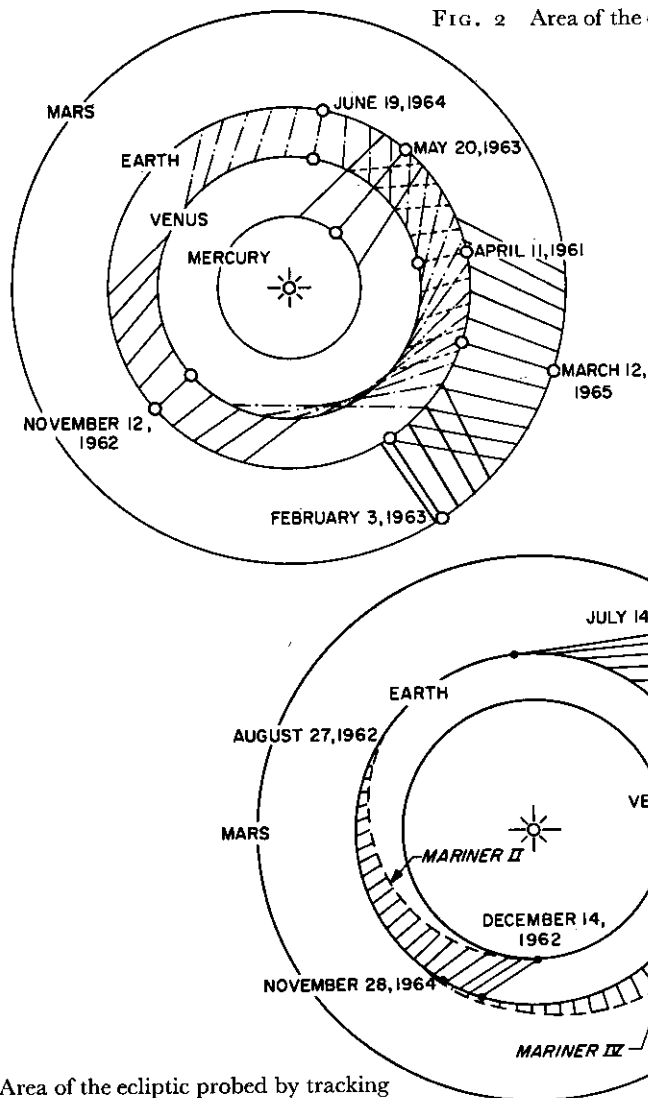


FIG. 2 Area of the ecliptic probed by radar

FIG. 3 Area of the ecliptic probed by tracking

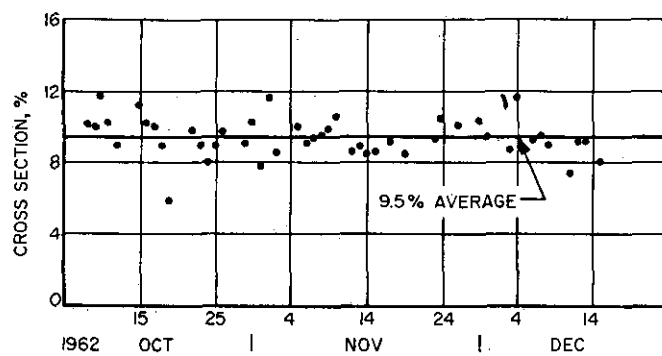


FIG. 4 Radar cross-section of Venus, 1962

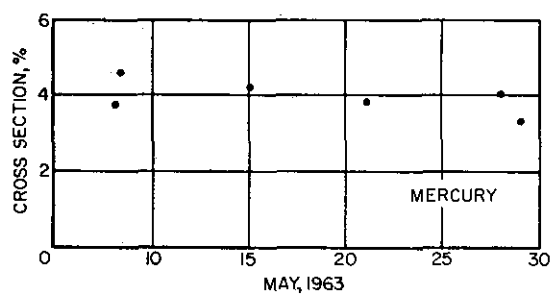


FIG. 5 Radar cross-section of Mercury, 1963

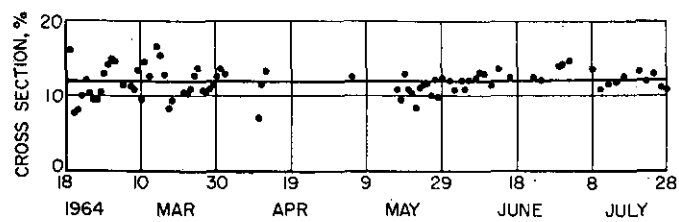


FIG. 6 Radar cross-section of Venus, 1964

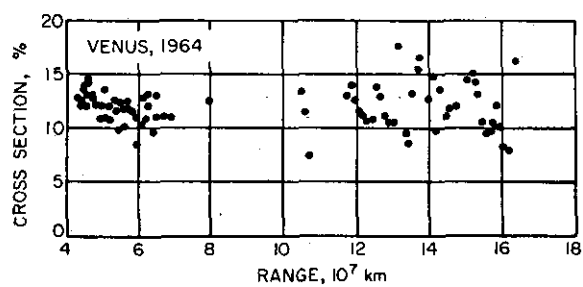


FIG. 7 Radar cross-section as a function of range

that must be accounted for in such a design. In so far as S-band is concerned, the planetary radar experiments have answered these questions for a considerable area of the ecliptic plane. For these experiments, the radar was configured as a radiometer and the total power of the echo was measured. Such measurements were made of Venus (over several conjunctions), Mercury and Mars. The results are expressed in terms of the radar cross-section of the target plane. Radar cross-section is a function of the object and is, thus, independent of transmitter power, receiver sensitivity and distance (the latter only if the inverse square law is valid). Figures 4, 5 and 6 are plots of the measured radar cross-sections of Venus, Mercury and of Venus  $1\frac{1}{2}$  years later.

If space had no attenuation effect, the radar cross-sections would be constant. Of course, some fluctuations must be expected because of the extremely minute amount of power contained in a planetary echo, which is immersed in relatively strong random noise. Additional fluctuations are caused by rotation of the target planet, bringing into view surfaces of possibly different reflection characteristics. However, if an unexpected space loss exists, the cross-section would diminish with distance. The radar is a sensitive instrument for this measurement, as the wave must propagate through the medium twice. Figure 7 shows the radar cross-section of Venus replotted, with distance as the abscissa.

In all of these figures, it can be seen that there was no measurable space loss – even to distances greater than  $160 \times 10^6$  km.

The *Mariner* spacecraft tracking experiences confirm the results of the radar experiments concerning the attenuation of the interplanetary medium at microwave frequencies. The *Mariner II* spacecraft used L-band frequencies, but the results are consistent with the radar results. Figure 8 shows the down-link received signal strength for typical tracking intervals during the flight. The nominal signal levels were computed from measurements taken in the spacecraft before launch and based on the assumption that propagation was through free space. The discrepancy between the nominal and the measured signal level is due partly to changes in the spacecraft equipment caused by launch and exposure to the space environment and partly to drifts in the ground equipment and difficulties in calibration. Since experience with spacecraft equipment under test indicates that it is quite stable and the transmitted power is monitored and telemetered back to the Earth, most of the discrepancy must be attributed to the ground station and the great difficulty in making accurate calibrations at these signal levels. However, even though there is a discrepancy between the measured signal level and the expected signal level, there is no significant trend to the data which can be attributed to the presence of a lossy medium in interplanetary space.

Typical tracking data from the *Mariner IV* are shown in Fig. 9. The frequency range here, 2115 Mc/s on the up-link and 2295 on the down-link, is much closer to the radar frequency (2388 Mc/s). The data for the first segment were taken when the spacecraft was transmitting on its low-gain antenna, so the signal level is lower than the others which were taken when the spacecraft was transmitting on its high-gain antenna. The irregularities in the nominal signal level are due to the antenna pattern.

In the cases of both spacecraft, the data are offset from the nominal data

by several dB, but a good fit could be obtained merely by displacing the nominal value. In the case of *Mariner IV* the skew of such a fit would certainly be less than 1 dB. From these data it can be inferred that the loss due to the medium itself, as distinct from the loss due to the geometry, is less than 1 dB over 200 million kilometers – truly a lossless medium!

#### POLARIZATION

A subtle, but potentially disastrous, type of interaction between radio waves and the interplanetary medium has been proposed by Lusignea (1). According to this mechanism, protons driven from the Sun at relativistic speeds can change the sense of polarization of a radio wave from, say, right-hand circular polarization to left-hand. The implied hazard is serious. An antenna that is set to receive an expected type of polarization would not be able to receive a signal at all were the polarization to become reversed during transit across space.

A method of utilizing the planetary radar for determining the magnitude of this effect was devised, as follows. A spectrally pure, right-hand, circularly polarized wave was beamed at Venus. Echoes were observed in both right and left circular polarization, and spectrograms of these echoes were produced. Analysis was complicated by the fact that Venus, itself, as well as the space medium under investigation, causes changes in the polarization of the echo. Most of the signal will be left-hand circularly polarized (having been reflected only once), but some will be in the right-hand sense (double, or other even-order reflections).

However, it is possible to separate the Venus-induced depolarization from that induced by the medium, because the spectra of the two polarizations of a Venus echo have quite different shapes. Most of the single reflections occur near the sub-Earth point, where there is little Doppler broadening of the spectrum. Consequently, this spectrum shows a tall central peak. On the other hand, double reflections occur more uniformly over the surface; the resultant spectrum is much wider, and the central peak is completely lacking.

Figure 10 is a pair of spectrograms (one normal polarization, one reversed) taken of Venus near the conjunction of 1964. The total echo power in the reversed case is less by a factor of 18, so that spectrum has been drawn to a magnified scale (times 30). The two peaks in that spectrogram are the result of topographic features on the planet Venus. They were seen to move slowly across the spectrograms, from the high-frequency side to the low, carried by Venus's rotation. Notice that the central peak is completely missing in this mode. The error flag represents  $\pm 3$  times the standard deviation imputable to random fluctuations.

Any mechanism of the medium that changes the sense of polarization would cause some fraction of the spectrum with the high central peak to be superposed on the other spectrum. No such peak can be seen in the spectrum of Fig. 10, nor were there any observed in any of the measurements taken during the two months about the 1964 Venus conjunction.

We may, therefore, place a severe upper limit on the magnitude of any such depolarizing effect. Reasoning that if a peak of  $3\sigma$  magnitude were present, it would be observed, we can establish the limit of the effect as  $< \frac{1}{1250}$  parts. That is, the amount of power coupled from one mode of

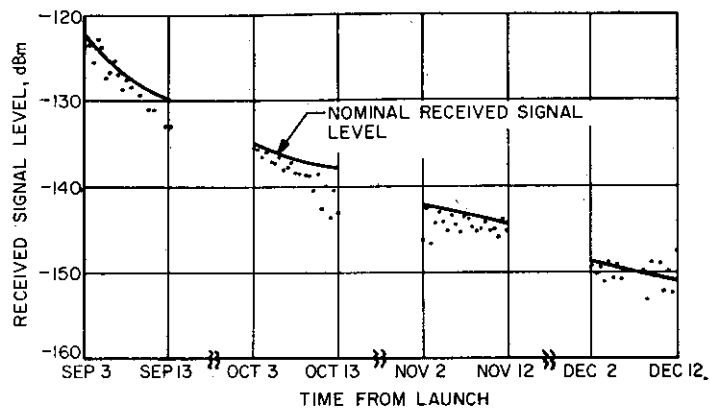


FIG. 8 Mariner II tracking data

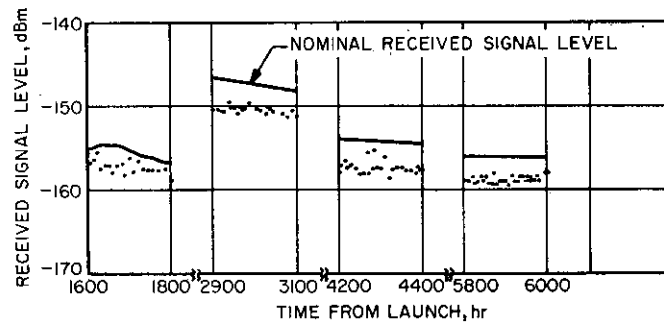


FIG. 9 Mariner IV tracking data

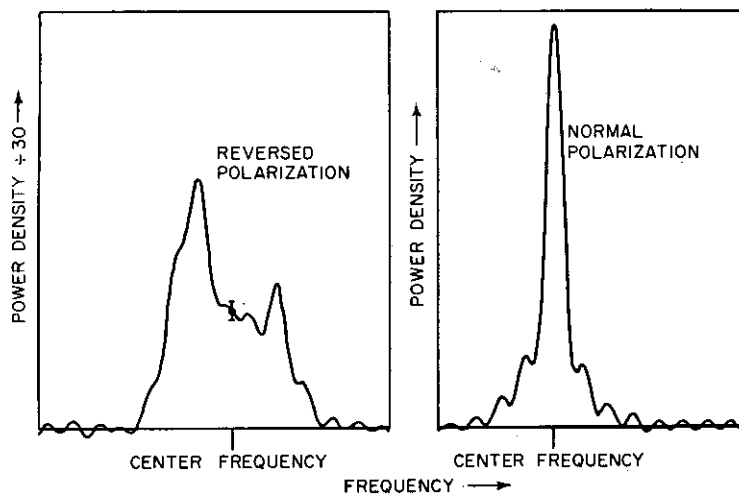


FIG. 10 Venus spectrograms, normal and reversed polarization

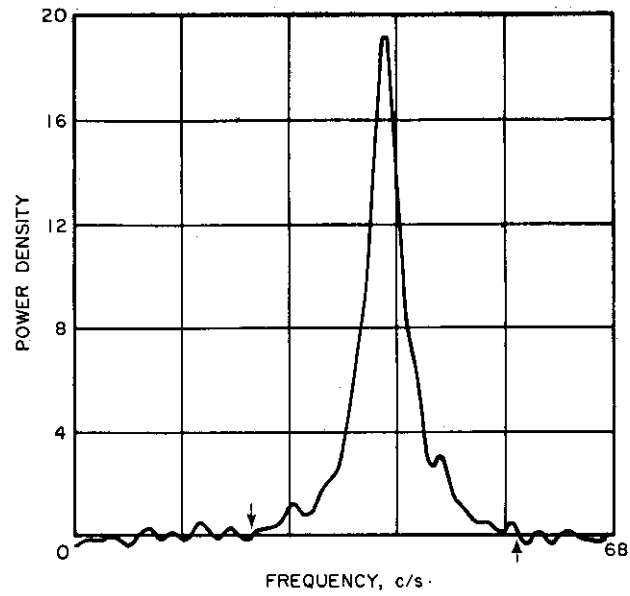


FIG. 11 Venus spectrogram averaged over 31 minutes, November 10, 1962

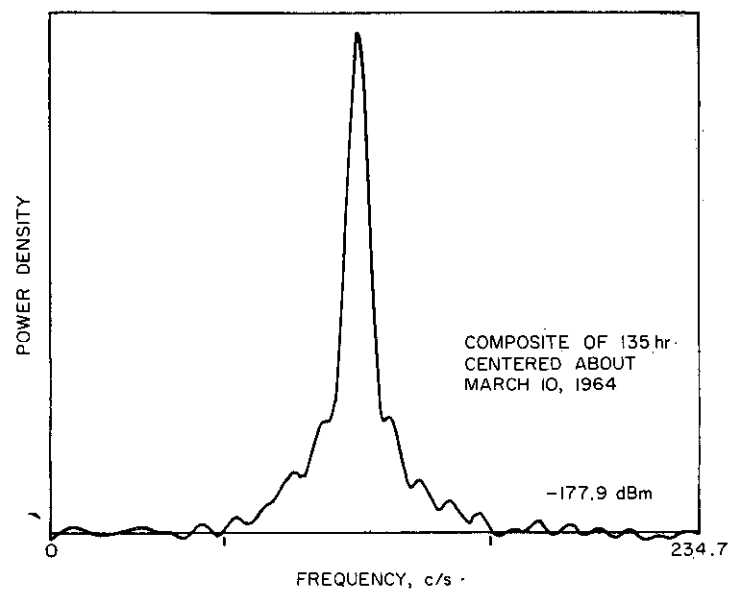


FIG. 12 Venus spectrogram averaged over 135 hours



polarization to the other during the entire round trip flight to Venus and back was less than  $-31$  dB.

#### PATH LENGTH

One of the two major uses of a spacecraft telecommunications system is to gather data from which the trajectory of the spacecraft can be computed. The trajectory is used to provide location tags for the scientific data collected and, projected into the future, as a basis for guiding the spacecraft to its desired destination. This use of ground-based radio guidance rather than, for example, on-board navigational equipment, results in considerable simplification of the spacecraft. However, it would not be feasible were the tracking data from the telecommunications system inadequate. The data that can be obtained are of three kinds: angle, Doppler and range. Angle data are useful only during the very first part of a mission because of lack of resolution. The Doppler data are very powerful and quite adequate in cases in which the model on which the celestial mechanics is based is well determined. In cases in which the model is not so well determined (for example, the lunar or planetary mass and motion accuracy required for precise orbiting), range measurements are also needed. It was determined that, if the propagation path of the microwaves were, in fact, along the geometrical path, it would be possible to measure the Doppler and range with sufficient accuracy to guide a spacecraft. Therefore, one of the purposes of the planetary radar experiments has been to examine the path length of microwave signals in interplanetary space.

The technique that has been used to examine the path length is to assume that the microwaves follow a geometrical path as though they were traversing truly free space and to look for discrepancies in the measurements. Three kinds of variations in path length that might have been expected to occur are: a short-term variation in path length, a long-term variation in path length, and a systematic variation in path length with distance.

The power spectrum of the radar return from Venus provides direct evidence concerning both the short-term and long-term variation of path length. In measuring the power spectrum the local oscillator is continuously tuned according to an ephemeris so that the signal presented to the spectrum analyzer is centered at some fixed frequency. The purpose of the ephemeris-controlled local oscillator is, of course, to remove the Doppler shift due to the relative motions of the radar and the target planet. The important point is that the ephemeris is computed with the assumption that the microwaves are traveling in free space. Figure 11 shows a typical power spectrum taken of Venus over an observation time of 31 min. We are fortunate in the shape of the Venus spectrum. The central peak is very sensitive to changes in the path length (or to imperfections in the measuring equipment or ephemeris, for that matter). The width of the peak is only about 5 c/s. From this, we may infer that the change in path length relative to that predicted is less than 5 wavelengths/s. Since a wavelength is 12.5 cm and the path length was twice the  $42 \times 10^6$  km distance from Earth to Venus at that time, the variation in path length was less than 1.5 parts in  $10^{12}$ /s.

The spectrum of Venus shown in Fig. 12 is even more startling. It is a composite of 135 hours of observation over the period of February 19 through

March 30, 1964. The many spectrograms averaged together were averaged by computer, with no corrections made to their center frequencies. The center peak is nearly 11 c/s wide, but the effect is due mostly to the broadening of the entire spectrum. The width of the entire spectrum is determined by the rotation of Venus about its axis and the width varies with the aspect from which the planet is viewed. The total width of the second spectrum is approximately 100 c/s, while the width of the first is only 35 c/s. Thus, the width of the peak in the spectrum is relatively narrower than that in the first.

Tracking data were used as the basis for guiding the spacecraft to their destinations in both the *Mariner II* flight to Venus in 1962 and the *Mariner IV* flight to Mars in 1965. Not only did the guidance perform satisfactorily, but the tracking data provided confirmation of the radar results. In particular, the Doppler data from tracking the spacecraft provide an even more sensitive indicator of path-length change than does the radar power spectrum because, except for the Doppler shift, the signal returned from the spacecraft is monochromatic and coherent with the signal being transmitted from the ground. The measured Doppler shift is then an accurate measure of the rate of change of path length, and the measured Doppler may be compared precisely with that computed, using the assumption among others, that the path is in free space. Many such comparisons were made. A typical figure for *Mariner II* is that the measured radial velocity agreed with the computed radial velocity within 3 cm/s at a distance of  $50 \times 10^6$  km over periods of a minute. This implies that the actual path length is changing relative to the geometrical path length by no more than 1.6 parts in  $10^{13}$ /s.

A typical set of Doppler residuals from a *Mariner IV* tracking pass is shown in Fig. 13. Each day an orbit is fitted to the tracking data and the residuals plotted out, hour by hour, by the computer. The residuals show the variations of the Doppler relative to that predicted by the orbit. The fitting process removes any average offset between the Doppler shift predicted from geometrical considerations, but does not remove the short-term variations. Because the Doppler is counted for a minute, the resolution is to a fraction of a cycle. The largest variation is less than 0.030 c/s or 0.36 cm/s. This is somewhat less than 1 part in  $10^{13}$ /s.

The Doppler measurements provide a means for determining the rate at which the actual path may vary relative to the geometrical path; range measurements provide a means for determining the amount. The several Venus radar experiments have all included ranging experiments. A complete discussion of the ranging technique would be out of place here. Suffice it to say that the transmitted signal is modulated by a binary pseudo-random waveform. By cross-correlation, the phase of the returned modulation is determined relative to the transmitted modulation. Since a very accurate clock is used to time the transmitted modulation, the time displacement between the two is accurately determined and therefore, the time of flight. With the assumption that the propagation velocity is constant, the actual path length can be compared with the geometrical path length.

The results of the 1961 Venus ranging experiments are shown in Fig. 14 and 15. The reference to open-loop ranging and closed-loop ranging pertains to two somewhat different techniques that were used for determining the time of flight, and the two ephemerides pertain to the Duncombe

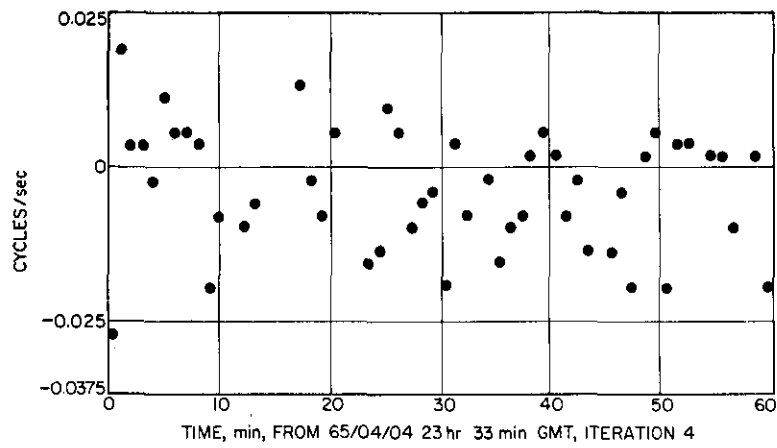


FIG. 13 Typical *Mariner IV* doppler residuals

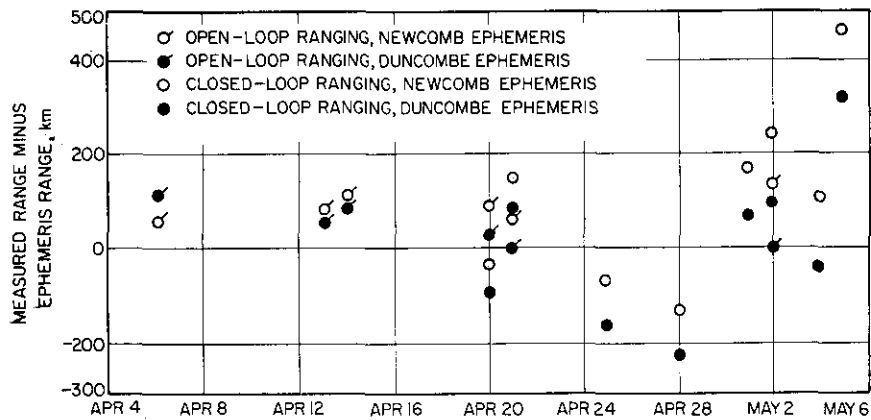


FIG. 14 1961 Venus range measurements vs time

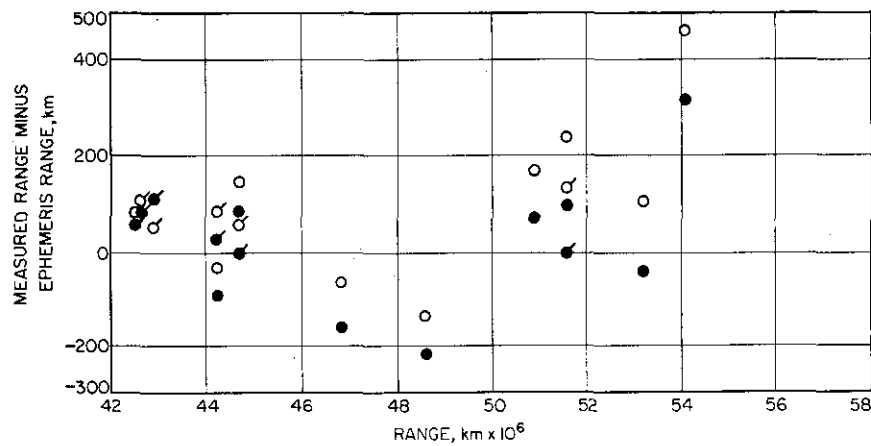


FIG. 15 1961 Venus range measurements vs distance

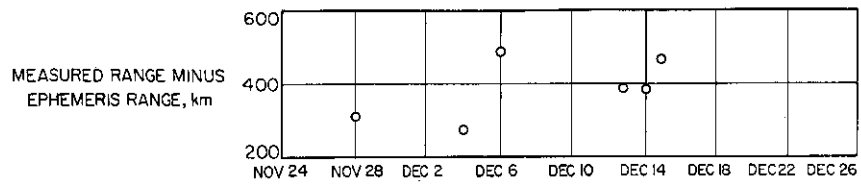


FIG. 16 Venus range measurements vs time

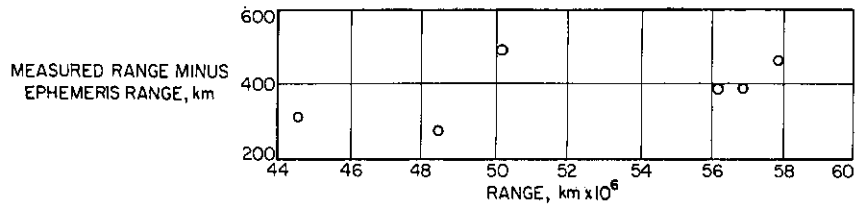


FIG. 17 1962 Venus range measurements vs distance

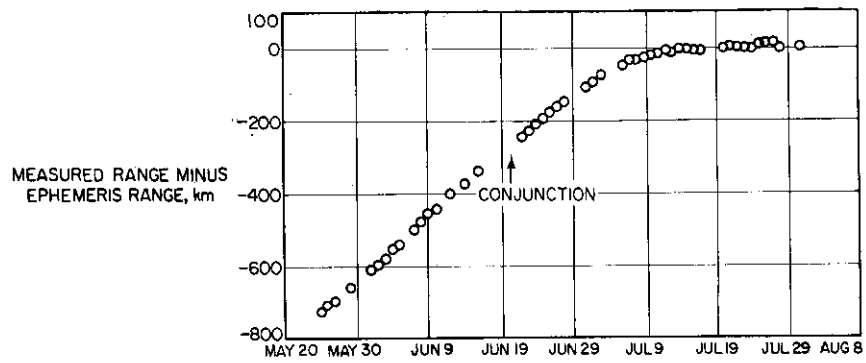


FIG. 18 1964 Venus range measurements vs time

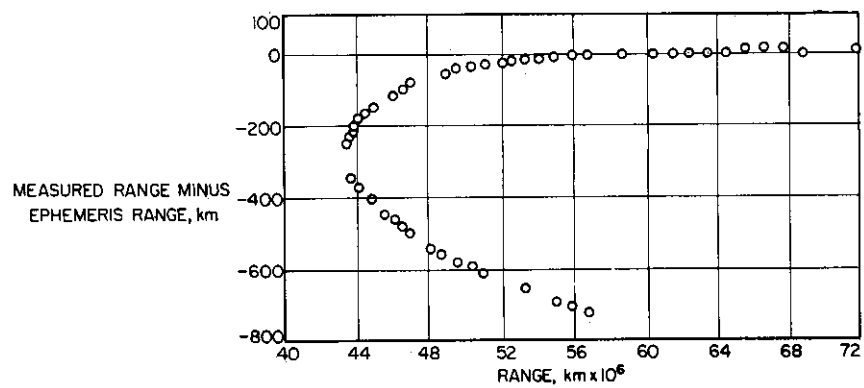


FIG. 19 1964 Venus range measurements vs distance

ephemeris and the Newcombe corrections to the Duncombe ephemeris (2), (3). At the time of this experiment there was considerable uncertainty about the value of the Astronomical Unit (AU) and about the accuracy of the ephemerides of the Earth and Venus, which is why the data were reduced in this particular way. The important point to be noted here is that any trend in the data is quite small. There is an average offset of some 100 km in the measured range relative to the geometrical range, but this is attributed to flaws in the ephemerides. The trend in these residuals would be something like 40 km over a time interval of 28 days or  $12 \times 10^6$  km of range. A best fit line could be passed through the data in order to make a more precise statement, but two difficulties are encountered. The one is that the data at the longer distances are considerably more noisy than those at the shorter distances, and no adequate statistical model exists for weighting the data. The other is that the shape of the line to be fitted is not known, since it depends on the particular flaws which exist in the ephemerides. Even so, it is reasonable to say that the long-term drift in actual path length relative to geometrical path length is less than 3.5 parts in  $10^{10}$ s or 1 part in  $10^6$ /unit distance. Furthermore, the average discrepancy between the actual path length and geometrical path length is less than 2 parts in  $10^6$ .

In one sense the ranging results from the 1962 Venus experiment (shown in Fig. 16 and 17) were disappointing because they showed a larger difference between measured distance and computed distance than did the 1961 experiment. This is not really a proper conclusion. Prior to the 1961 experiment, the accepted value of the AU was in error by several tens of thousands of kilometers. When the value was adjusted, as indicated by the radar results, the agreement shown in Fig. 14 and 15 was obtained. However, all of the error in the ephemerides was not in the value of the AU, and the other errors forced the 1962 results to be off. Here again, it is evident that there is no large-scale drift with time or with distance.

By the time of the 1964 Venus radar experiment, a new method of measuring range had been devised (4) which was capable of making much better measurements. The results of the 1964 Venus ranging experiment are shown in Fig. 18 and 19. From these figures it is evident that there is a definite trend to the data. Analysis shows that this trend is the kind of trend that would exist if there were an error in the orientation of the orbital ellipse of Venus, and much work is being done to attempt to refine the values of the orbital elements. If this premise is accepted, then the data can be compared with a best fit line to determine the maximum rate at which the actual path varies relative to the geometrical path. The r.m.s. variation of the data from a straight line over the first portion of the experiment is approximately 6 km at an average distance of  $50 \times 10^6$  km, and some of this variation may be due to surface relief on the planet. There is a strong temptation to continue on and draw conclusions about the actual variations in path length based on reasonable assumptions about the errors that must exist in the ephemerides. However, the only real conclusion is that the path length can be measured more accurately than it can be computed, possibly by as much as two orders of magnitude. From an engineering point of view this means that ground-based radio guidance of spacecraft is not limited at this time by any discrepancy which may exist between actual path length and geometrical path length.

## SUMMARY OF CONCLUSIONS

From the results of the several radar experiments, it may be inferred that the attenuation of the interplanetary medium to S-band between the orbits of the Earth and Venus is certainly less than 1 dB at distances up to  $170 \times 10^6$  km. The *Mariner II* gave similar results at L-band and the *Mariner IV* showed the attenuation of the interplanetary medium between the orbits of the Earth and Mars is less than 1 dB at distances over  $200 \times 10^6$  km.

In addition, radar experiments on Venus show that any mechanism which might reverse the sense of the polarization of circularly polarized signals at S-band is less than 0.1 per cent effective. The tracking of the *Mariner* spacecraft does not yield direct information on this matter, but the tracking data are consistent with these conclusions.

The path length of S-band signals in the region between the orbits of Venus and Earth has been shown by the radar experiments to be essentially the same as the geometrical path length. Specifically, the radar shows the path length varies relative to the geometrical path length by no more than 1.5 parts in  $10^{12}$ /s. The *Mariner* tracking improves this figure to less than 1 part in  $10^{13}$ /s. Range measurements on Venus show that the difference between the electrical and geometrical path lengths is less than 2 parts in  $10^6$  and that much of this uncertainty is probably due to flaws in the mathematical model used to compute the geometrical path length.

The general conclusion is that the interplanetary medium in the region between the orbits of Venus and Mars has no deleterious effects on communications with or tracking of spacecraft using S-band signals.

## REFERENCES

1. LUSIGNON, B. B., "Detection of solar particle streams by high frequency radio waves". J. Geophys. Res. 68, 20, 5617-32, 1963.
2. U.S. Nautical Almanac Office Astronomical Papers 14 and 15, Part IV.
3. U.S. Nautical Almanac Office Astronomical Papers 16, Part I.
4. TAUSWORTHE, R. C., "A precision planetary range-tracking radar". Trans. IEEE SET-II, 78-85, 1965.

## CHAPTER 2-2

ATMOSPHERIC AND INTERPLANETARY REFRACTION  
EFFECTS ON HIGH-PRECISION PLANETARY RADAR  
MEASUREMENTS

D. O. MUHLEMAN and P. REICHLEY

## SUMMARY

Extensive programs of radar observations of Venus, Mercury, Mars and the Moon have been carried out at L, S and X band frequencies. The most important data that have been obtained from these measurements form an extensive catalog of the range and range rate to the various planets relative to the Earth. These observations are being used to study the celestial mechanical motion of these bodies and the Earth. Because of the great precision of these measurements (1 part in  $10^7$  to  $10^8$ ) they contain considerable information on the refraction due to the Earth's atmosphere, ionosphere, interplanetary medium and in some cases, the solar corona. The orbital calculations demand that the effects be treated with precision for the determination of astronomical constants. Furthermore, these calculations yield significant information on the physical parameters of the medium.

In this paper we describe the mathematical details of the eight-figure computations of refraction corrections to range and range rate utilizing ray-tracing techniques. Future radar experiments using Venus or Mercury involving propagation (at S-band) through the solar corona are described. A discussion of the general relativistic effect on propagation very near the edge of the sun and experimental plans to detect the effect is included.

## DISCUSSION

V. R. ESHLEMAN - In the proposed relativity experiment considerable attention has been given to separating plasma and relativity effects on measurements to be made on a single radio frequency. I would suggest that emphasis be given to the possibility of making such measurements at several frequencies to aid in the separation of the effects.





## CHAPTER 2-3

A SUMMARY OF PRELIMINARY RESULTS OF THE  
*MARINER IV* RADIO-OCCULTATION EXPERIMENT

A. J. KLIORE, D. L. CAIN, G. S. LEVY

California Institute of Technology

V. R. ESHLEMAN, G. FJELDBO, Stanford University

F. D. DRAKE, Cornell University

The *Mariner IV* occultation experiment has provided very precise data relating to characteristics of the atmosphere and ionosphere of Mars. While this summary must be considered preliminary, since much analysis remains to be done, it seems clear that several rather surprising results have been established. These include:

- (a) The low values deduced for the molecular number density, mass density, pressure, scale height and temperature of the atmosphere near the surface of Mars;
- (b) the low values found for the scale height and temperature of the ionosphere, and the low height and low electron number density of the peak of the main ionospheric layer;
- (c) the conclusion that the predominant constituent of the atmosphere of Mars is carbon dioxide, based on considerations of the occultation results together with terrestrial spectroscopic measurements of the CO<sub>2</sub> abundance on Mars;
- (d) the preliminary conclusion that the altitude profile of atmospheric mass density does not cross over that of the earth, but remains several orders of magnitude lower, at least to an altitude of several hundred kilometers.

Plans for and descriptions of the *Mariner IV* occultation experiment have been published (1), (2), and more general considerations of radio-occultation experiments for the study of planetary atmospheres and ionospheres are also available (3), (4), (5), (6). Also, preliminary results of the *Mariner IV* measurements have been published (7). The present report is a brief summary and discussion of the principal conclusions that can be made at this time.

Figure 1 illustrates the extreme measurement and computational precision that was obtained. It shows phase-path changes due to the ionosphere (the approximate 10-cycle change maximizing at UT 02h 30m 12s on July 15) and atmosphere (the 30-cycle change maximizing at about 02h 31m 11s when the spacecraft disappeared behind Mars). The total phase change of the 2.2 Gc/s tracking signal during the period of time illustrated was about  $3 \times 10^{11}$  cycles. The lens-like action of the ionosphere and atmosphere of Mars

caused an apparent position change of the spacecraft of 75 cm toward the earth (ionosphere) and 2 m away from the earth (atmosphere). At about 02h 30m 22s a change of only about 4 cm was noted at each of the receiving stations (two in California and two in Australia), and it is believed that this represents a minor layer in the lower ionosphere of Mars.

Phase, frequency and amplitude measurements were made at each of the receiving sites. At extinction on immersion, the atmospheric effects were  $29 \pm 2$  cycles,  $5.5 \pm 0.5$  c/s, and 1.5 to 2.0 dB. Figure 2 illustrates how these measurements are related to the surface refractivity and scale height of the neutral atmosphere if it has an exponential refractivity profile. Since the measurements fit very well an assumed exponential profile, these extinction results are the basis for analysis of the atmosphere.

Table I summarizes atmospheric results for the two assumed models based on different amounts of CO<sub>2</sub>. For (a), 100 per cent CO<sub>2</sub> is assumed, while for (b) it is assumed that there is 80 to 100 per cent CO<sub>2</sub> by partial pressure with the remainder being N<sub>2</sub> or Ar in any ratio. Note that all of the results follow directly from the measured surface refractivity and scale height and the assumed constituent models. The preponderance of CO<sub>2</sub> in the models was chosen because the total surface pressure from the occultation experiment is approximately the same as the partial pressure of CO<sub>2</sub> detected in terrestrial spectroscopic observations of Mars (8), (9). The precision with which the spectroscopic observations can be used to define the CO<sub>2</sub> abundance exceeds the accuracy of total surface pressures derived from the same measurements. It is also important to note that the previously favored nitrogen-dominated atmosphere is precluded, since it would lead to a temperature (derived from the occultation scale height measurement) which is below the freezing-point of atmospheric CO<sub>2</sub>.

TABLE I  
ATMOSPHERE

1. Surface refractivity	$3.6 \pm 0.2$ N-units
2. Scale height	$9 \pm 1$ km
3. Surface number density	
(a) all CO <sub>2</sub>	$1.9 \pm 0.1 \times 10^{17}$ mol/cm <sup>3</sup>
(b) up to 20% N <sub>2</sub> and/or Ar	$2.1 \pm 0.2 \times 10^{17}$ mol/cm <sup>3</sup>
4. Surface mass density	
(a) all CO <sub>2</sub>	$1.43 \pm 0.10 \times 10^{-5}$ gm/cm <sup>3</sup>
(b) up to 20% N <sub>2</sub> and/or Ar	$1.50 \pm 0.15 \times 10^{-5}$ gm/cm <sup>3</sup>
5. Temperature	
(a) all CO <sub>2</sub>	$180 \pm 20^\circ\text{K}$
(b) up to 20% N <sub>2</sub> and/or Ar	$175 \pm 24^\circ\text{K}$
6. Surface pressure	
(a) all CO <sub>2</sub>	$4.9 \pm 0.8$ mb
(b) up to 20% N <sub>2</sub> and/or Ar	$5.1 \pm 1.1$ mb
7. Location	Immersion was between Electris and Mare Chronium at 55°S latitude, 117°E longitude, early afternoon, winter, solar zenith angle 70°.

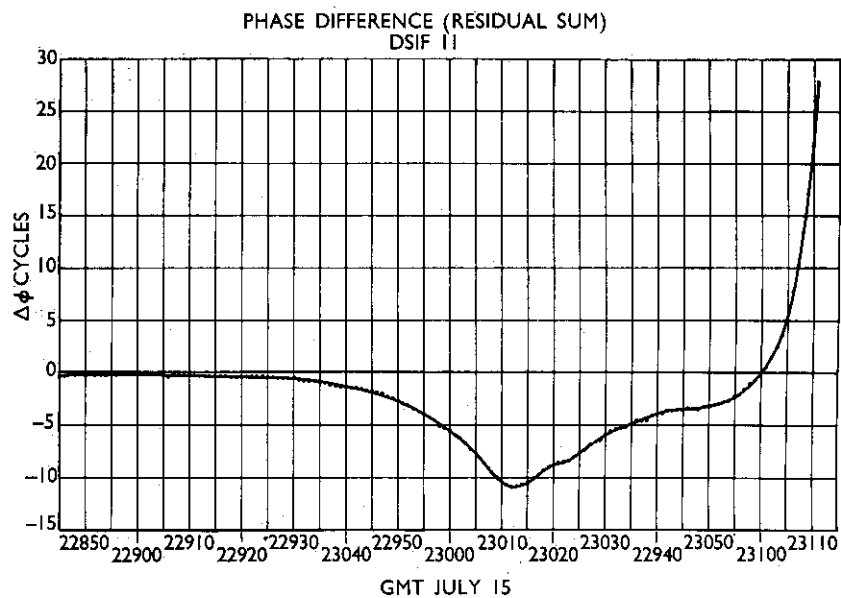


FIG. 1 Phase-path effects of the atmosphere and ionosphere of Mars during immersion of *Mariner IV*

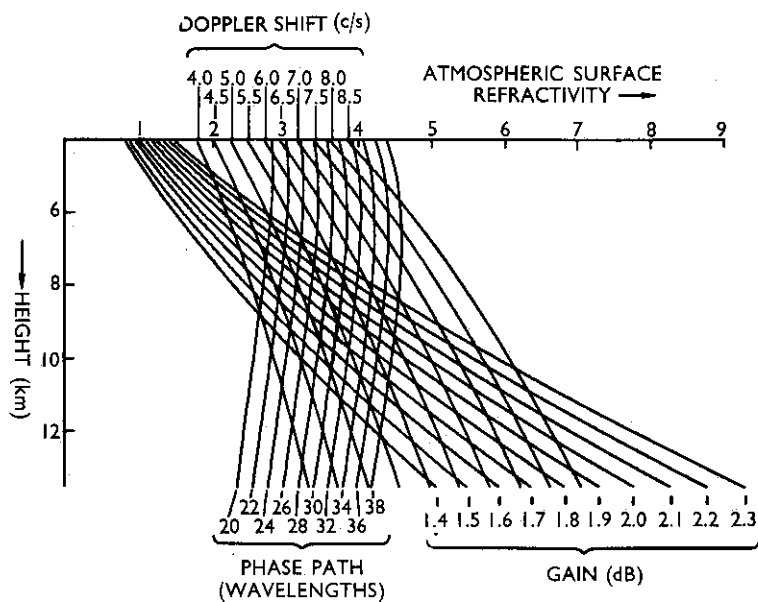


FIG. 2 Relationships between phase path, frequency and amplitude measurements at signal extinction and surface refractivity and scale height of the atmosphere of Mars

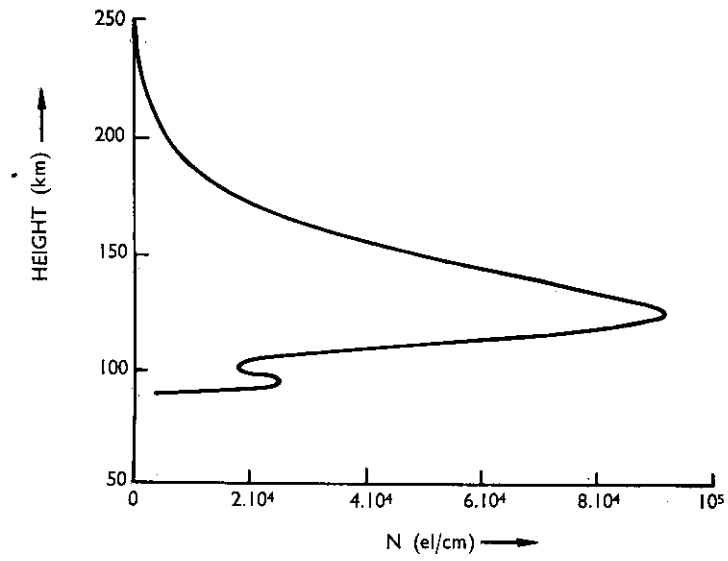


FIG. 3 Ionospheric density profile for the region over the Martian desert electris when the solar zenith angle was about  $70^\circ$

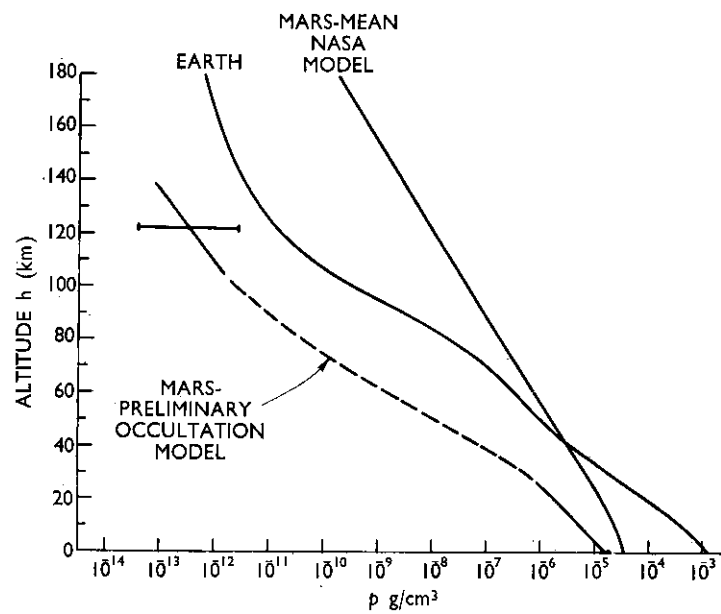


FIG. 4 A comparison of height profiles of atmospheric mass density for the Earth and Mars

The principal possible source of error in these results is the effect of occultation occurring over an elevated surface feature on the limb of Mars. All references to surface conditions in Table 1 are for the altitude of this feature, which is of course, unknown. The mean surface density and pressure would be about 1 per cent larger than the values given here for each 90 m of height of the occulting feature above the mean surface level. The emersion data are less accurate than those used to derive the immersion results of Table 1, but they give comparable numbers and indicate that it was not likely that an unusually high limb feature was involved on immersion.

From the measurements on immersion, the ionospheric profile of Fig. 3 has been derived. The main layer is well defined, while the lower layer at about 95 km ( $2.5 \times 10^4$  el/cm<sup>3</sup>) is less well established. These two layers may correspond to the E and F regions of the terrestrial ionosphere. On emersion, no ionosphere was detected. Measurement sensitivity was such that the ratio of nighttime to daytime electron number densities for the measured regions on Mars must be less than the average value for earth, but not necessarily less than for occasional conditions on earth. Table 2 summarizes the ionospheric results.

TABLE 2

## IONOSPHERE

**Immersion** (70° solar zenith angle, early afternoon)

- |   |   |
|---|---|
| 1. Maximum electron density                                       | $9.0 \pm 1.0 \times 10^4$ el/cm <sup>3</sup>                  |
| 2. Altitude of maximum  | $123 \pm 3$ km  |
| 3. Electron scale height above maximum                            | $24 \pm 3$ km   |
| 4. Atmospheric temperature above ionospheric maximum              |   |
| (a) 100% O  | $90 \pm 12^\circ\text{K}$                                     |
| (b) 100% CO   | $150 \pm 20^\circ\text{K}$                                    |
| 5. Preliminary estimate of the atmospheric mass density at 123 km | $2 \times 10^{-14}$ to $2 \times 10^{-12}$ gm/cm <sup>3</sup> |

**Emersion** (Over Mare Acidalium at 60°N latitude, 34°W longitude, night, summer, solar zenith angle 106°)

- |                             |                                      |
|-----------------------------|--------------------------------------|
| 1. Maximum electron density | $< 5 \times 10^3$ el/cm <sup>3</sup> |
|-----------------------------|--------------------------------------|

The surprisingly low ionospheric temperature also suggests that CO<sub>2</sub> is the main atmospheric constituent. This is because the dissociated CO<sub>2</sub> molecules (into CO and O) provide more efficient radiative cooling than would be the case for nitrogen.

Even with a very high preponderance of CO<sub>2</sub>, however, nitrogen could still play an important role in other ionospheric processes. The large uncertainty in the atmospheric mass density at ionospheric heights (Table 2-5) results from our uncertainty about ionospheric constituents, reactions and reaction rates. It had been suggested (10) that Mars would have four ionospheric

layers, the three lower ones like a Chapman layer, where there is a balance of production and recombination at the peak. The highest peak would then be a Bradbury layer, where the ionization peak is above the production peak due to the rapid decrease of the loss rate with increasing altitude. If the main Mars ionosphere is like a Bradbury layer, then the principal ion probably would be  $O^+$  and the mass density would be at the low end of the range given in the table. If it is like a Chapman layer, then the principal ion might be  $CO^+$  and the mass density would be higher. Nevertheless, as shown in Fig. 4, even with this large range the density must still be markedly lower than had been anticipated, and even lower than would be obtained by extrapolating the new near-surface values.

Because of the lower gravity on Mars, it was thought that the reduction of atmospheric mass density with altitude would proceed much more slowly on Mars than on the earth. Thus, almost regardless of conditions near the surface, it was suggested that at altitudes above 30 to 50 km the Mars atmospheric density would exceed that of the earth at the same altitude, becoming many orders of magnitude more dense at altitudes of 100 or 200 km. However, quite a different picture is evolving from analysis of the occultation measurements. It appears that the low temperatures of the atmosphere and particularly the ionosphere, together with the heavier molecules in the atmosphere of Mars, approximately compensate for the lower gravity in controlling density gradients. Thus the atmospheric mass density remains several orders of magnitude below that of the earth at least for heights up to about 200 km, where the mass density is approximately ten orders of magnitude below the surface values.

#### DISCUSSION

D. MUHLEMAN – You hypothesized the existence of oxygen at two points in your presentation, in one case ionized. Would not the  $O^+$  recombine in the night side? Would not this surmise be in conflict with the absence of any indication of oxygen in astronomical spectra of Mars?

V. R. ESHLEMAN – The neutral and ionized oxygen come from photo dissociation of carbon dioxide into CO and O and photo ionization of the oxygen. After recombinations we would have again  $CO_2$  – only minute traces of  $O_2$  could be formed.

K. DAVIES – Can Dr Eshleman tell us anything about the magnetic field of Mars and of its effect on radio propagation.

V. R. ESHLEMAN – The magnetometers did not detect any dipole field – that is the field was not one-tenth of 1 per cent of that of the earth. If there is no magnetic field the study of the ionosphere of Mars would be simple compared with that of the terrestrial one.

#### REFERENCES

1. KLIORÉ, A. J., CAIN, D. L., LEVY, G. S., ESHLEMAN, V. R., DRAKE, F. D., and FJELDBO, G., *Astronautics and Aeronautics* 7, 72, 1965.
2. KLIORÉ, A., CAIN, D. L., and HAMILTON, T. W., JPL Tech. Rpt. no. 32-674. Jet Propulsion Laboratory, Pasadena, California, 1964.

3. FJELDBO, G., Final Rpt. NSF G-21543, SU-SEL 64-025. Stanford Electronics Laboratories, Stanford, California, 1964.
4. ESHLEMAN, V. R., "Solar System Radio Astronomy", 14, 267. Plenum Press, New York, 1965.
5. FJELDBO, G., and ESHLEMAN, V. R., J. Geophys. Res. 70, 3217, 1965.
6. FJELDBO, G., ESHLEMAN, V. R., GARRIOTT, O. K., and SMITH, F. L., J. Geophys. Res. 70, 3701, 1965.
7. KLIORE, A. J., CAIN, D. L., LEVY, G. S., ESHLEMAN, V. R., FJELDBO, G., and DRAKE, F. D., Science 149, 1965.
8. KAPLAN, L. D., MUNCH, G., and SPINRAD, H., Astrophys. J. 139, 1, 1964.
9. KUIPER, G. P., Comm. of the Lunar and Planetary Lab. University of Arizona, Tucson, Arizona, 2, 1964.
10. CHAMBERLAIN, J. W., Astrophys. J. 136, 582, 1962.

## ACKNOWLEDGEMENTS

T. W. HAMILTON, J.P.L., contributions to the experiment.

MARINER PROJECT and DEEP SPACE NET PERSONNEL, J.P.L., preparation for the experiment and acquisition of data.

B. B. LUSIGNAN, Stanford University, contributions to the experiment.

NATIONAL AERONAUTICS AND SPACE ADMINISTRATION, research support under contracts NAS 7-100, Ns G-377 and NGR 05-020-065.





CP-3

PART 3  
IONOSPHERIC EFFECTS

---



## CHAPTER 3-1

# IONOSPHERIC REFRACTION OF HIGH-FREQUENCY RADIO WAVES PROPAGATING BETWEEN THE EARTH AND ORBITING SATELLITES

R. G. MALIPHANT

Government Communications Headquarters, Cheltenham, England

### SUMMARY

An equation is derived for the angular deviation of radio waves that penetrate through the earth's ionosphere. From this equation, a simple graphical method is produced for calculating the path of the ray emerging from the ionosphere. The method is used to determine the angle of arrival, at the earth's surface, of radio waves emanating from the *Topsi* satellite (S48), at the times of loss of the signal at a monitoring ground station. This condition occurs as the satellite recedes from the station, when the angle of elevation of the ray path approaches the limit for penetration of the ionosphere, and is a consequence of the rapid increase in deviative absorption of the radio waves. A comparison of the theoretical cut-off angles (neglecting absorption) and the experimental limits thus determined, shows the extent to which absorption limits the ground coverage of the satellite. It was found that when the local critical frequency of the ionosphere was fairly near the frequency of the satellite transmitter, the angle of elevation of the ray path as the signal became lost in the background noise came very near the theoretical limit, although the ray-path angle of elevation was often considerably above the line of sight path to the satellite.

### INTRODUCTION

In 1958, Chvojikova (1) showed that small angular deviations of radio waves penetrating the earth's ionosphere could be calculated from a measurement of the total electron content of the ionosphere in a vertical column of unit area, and that any variation due to the shape of the electron density profile was small enough to be ignored. This discovery allowed the deviation angle between the entering and emerging ray paths to be expressed in a simple form:

$$\alpha = \frac{1}{2} \left( \frac{f_c}{f} \right)^2 \frac{\tan \phi_m \sec^2 \phi_m}{\rho_m} \frac{n_T}{N_m} \quad (1)$$

where,

$\alpha$  = the deviation angle

$n_T$  = the total electron content in a vertical column of unit area

- $N_m$  = the maximum electron density and  $f_c$  is the corresponding critical frequency  
 $\rho_m$  = the height of maximum electron density measured from the centre of the earth  
 $\phi_m$  = the angle of elevation of the apparent ray path measured at that height.

(The apparent ray path is the rectilinear extension of the ray path formed below the ionosphere.)

A decrease in the wave frequency or a lowering of the elevation angle of the ray path causes the deviation angle to increase. Unfortunately, the simple formula Eq. 1 may be used only when the deviation angle is less than one degree. The distribution of electrons in the ionosphere must be considered when calculations are made of larger deviation angles. This problem is overcome in this paper by evaluating the functions that are sensitive to distribution changes in terms of a typical electron density distribution. The resulting functions are reasonably accurate for most conditions of the earth's ionosphere and are used in the derivation of a general equation which is similar in basic form to Eq. 1, but which may be used in the calculation of larger deviation angles. A nomogram is developed to assist in solving this equation for any desired values of the parameters and together with an additional nomogram forms the basis of a rapid graphical method for determining the path of a radio wave propagating between the earth and an orbiting satellite. The application of this method to data on signals received from the *Topsi* satellite will be described.

#### THE DEVIATION-ANGLE EQUATION

**Derivation of the equation** – The path of a ray penetrating the earth's ionosphere is illustrated in Fig. 1. The deviation angle between the entering and emerging rays is shown as  $\alpha_1$ . Chvojikova (1) indicated that this deviation angle is equal to the angles shown in the figure as  $\alpha_2$  and  $\alpha_3$  and a proof of this has been given by Maliphant (2). In this paper, the deviation angle will be determined from the angle  $\alpha_3$  and will be referred to simply as  $\alpha$ . From Fig. 1, it may be seen that:

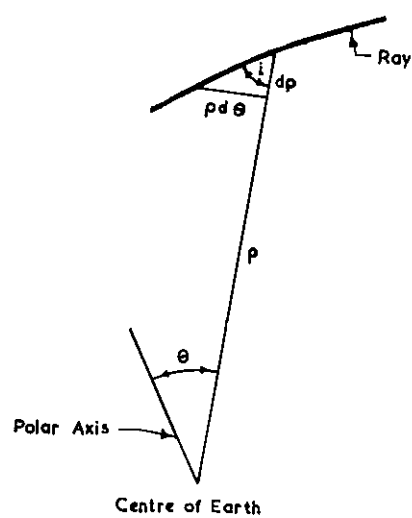
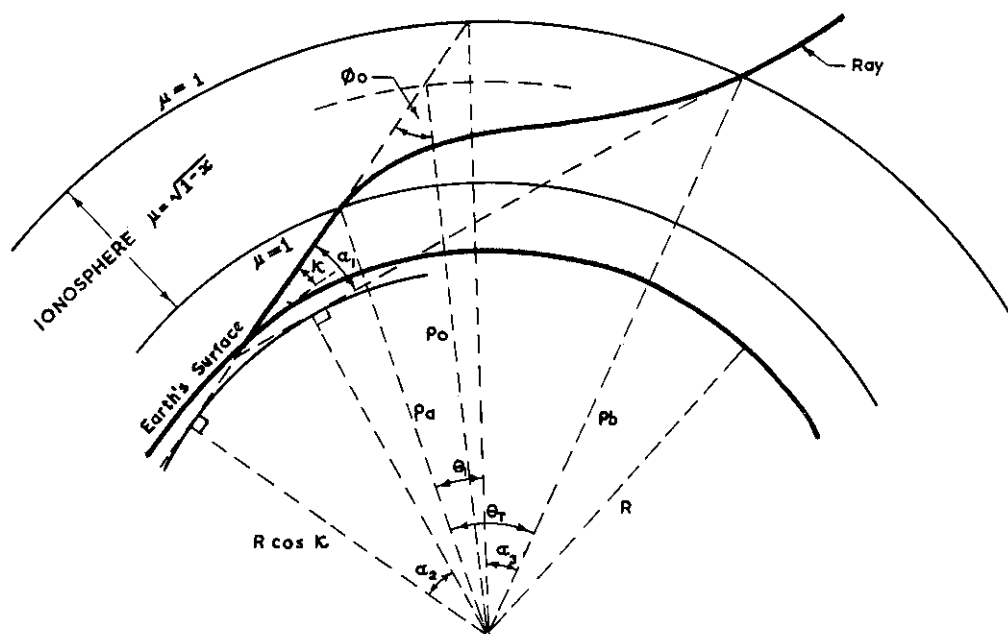
$$\alpha = \theta_T - \theta_1 \quad (2)$$

where  $\theta_T$  is the angle subtended at the centre of the earth by the limits of the true ray path in the ionosphere and  $\theta_1$  is the angle subtended by the apparent ray path over the same height limits. The application of Snell's law in spherical geometry yields:

$$\rho\mu \sin i = \rho \sin \phi = R \cos \kappa = \text{constant} \quad (3)$$

where  $i$  is the angle of incidence of the true ray path at height  $\rho$  at which the index of refraction is  $\mu$  and the angle of incidence of the apparent ray path is  $\phi$ ,  $R$  is the radius of the earth and  $\kappa$  is the angle of elevation of the ray path at the earth's surface.

The geometry of the ray section in Fig. 2 shows that the angle subtended at the centre of the earth may be deduced from the relation;



$$d\theta = \frac{\tan i}{\rho} d\rho \quad (4)$$

which, combined with Eq. 3, gives:

$$d\theta = \frac{\sin \phi}{\rho \sqrt{\mu^2 - \sin^2 \phi}} d\rho \quad (5)$$

If collision effects are neglected, the index of refraction is given by a simplification of the Appleton-Hartree formula and may be expressed by the equation:

$$\mu^2 = 1 - x \quad (6)$$

where  $x$  is a function of the local electron density, the wave frequency and parameters of the magnetic field.

The total angle subtended at the centre of the earth by the limits of the ray path in the ionosphere is then found by combining Eq. 5 and 6 to obtain:

$$\theta_T = \int_a^b \frac{\sin \phi}{\rho \sqrt{\cos^2 \phi - x}} d\rho \quad (7)$$

where  $a$  and  $b$  represent, respectively, the lower and upper height limits of the ionosphere.

If the index of refraction remains constant at unity, the ray path forms a straight line: the angle  $\theta_1$ , therefore, may be obtained from Eq. 7 by setting  $x$  equal to zero to obtain:

$$\theta_1 = \int_a^b \frac{\tan \phi}{\rho} d\rho \quad (8)$$

Thus, from Eq. 2, 7 and 8, the deviation angle is given by:

$$\alpha = \int_a^b \frac{\tan \phi}{\rho} [(1 - u)^{-\frac{1}{2}} - 1] d\rho \quad (9)$$

where:

$$u \equiv x \sec^2 \phi \quad (10)$$

The effect of the magnetic field on the deviation angle has been studied elsewhere (2). For most practical purposes, the deviation of the ordinary and extraordinary rays may be approximated by the intermediate value given by neglecting the magnetic field, in which case the quantity  $x$  becomes simply a function of electron density  $N$  or corresponding plasma frequency  $f_N$ , and the wave frequency  $f$ , given by:

$$x = \left(\frac{f_N}{f}\right)^2 = \left(\frac{f_c}{f}\right)^2 \cdot \frac{N}{N_m} \quad (11)$$

where  $N_m$  is the maximum electron density and  $f_c$  is the associated critical frequency.

It may be shown that the quantity  $u$  is equal to unity at the height of reflection of a ray. This is simply the well-known secant law as restated by

Maliphant (2) in a form applicable to the curved ionosphere:

$$f = f_v \sec \phi_r \quad (12)$$

where  $\phi_r$  is the angle of incidence of the apparent ray path at the true height of reflection of the ray and  $f_v$  is the equivalent vertical incidence frequency, that is the plasma frequency at the height of reflection.

For a ray that penetrates through the ionosphere,  $u$  is always less than unity and has a maximum value at a height only slightly below the height of maximum electron density. It is convenient, therefore, to refer to the square root of  $u$  measured at the height of maximum electron density, i.e.  $\frac{f_c}{f} \sec \phi_m$ , as the "deviation factor". The deviation increases as the deviation factor is increased towards unity, until at the boundary between penetration and reflection, the deviation angle becomes infinite.

Since  $u$  is always less than unity for penetrating rays, Eq. 9 may be expanded by the binomial theorem to give:

$$\begin{aligned} \alpha &= \frac{1}{2} \int_a^b \frac{\tan \phi}{\rho} \cdot u \left[ 1 + \frac{3}{4}u + \frac{5}{8}u^2 + \frac{35}{64}u^3 + \dots \right] d\rho \\ &= \frac{1}{2} \int_a^b x \frac{\tan \phi \sec^2 \phi}{\rho} \left[ 1 + \frac{3}{4}u + \frac{5}{8}u^2 + \frac{35}{64}u^3 + \dots \right] d\rho \end{aligned} \quad (13)$$

which, by application of the second law of the mean for integrals, may be written in the form:

$$\alpha = \frac{1}{2} \xi \int_a^b x \frac{\tan \phi \sec^2 \phi}{\rho} d\rho \quad (14)$$

where  $\xi$  is a number between the greatest and least values of the series over the interval  $(a, b)$ . The value of  $\xi$ , therefore, lies between unity and the value of the series at the height of maximum electron density.

Application of the same law of the mean to Eq. 14 yields the deviation angle:

$$\alpha = \frac{1}{2} \xi \frac{\tan \phi_0 \sec^2 \phi_0}{\rho_0} \int_a^b x d\rho \quad (15)$$

where  $\rho_0$  is some radius between the limits  $(a, b)$  and  $\phi_0$  is the value of  $\phi$  at this radius.

Finally, on substituting Eq. 11, and expressing the total electron content of the ionosphere in a vertical column of unit area as:

$$n_T \equiv \int_a^b N d\rho, \quad (16)$$

the deviation angle formula becomes:

$$\alpha = \frac{1}{2} \left( \frac{f_c}{f} \right)^2 \xi \frac{\tan \phi_0 \sec^2 \phi_0}{\rho_0} \cdot \frac{n_T}{N_m} \quad (17)$$

**Evaluation of the functions  $\xi$  and  $\rho_0$**  – To evaluate  $\xi$  and  $\rho_0$ , it is necessary to know the approximate distribution of electron density over the interval  $(a, b)$ . Measurements (3–7) have indicated that, in gross detail, the earth's ionosphere exhibits a fairly stable distribution which is approximately parabolic below the height of maximum electron density and merges into an exponential decline above this height, with roughly one-quarter of the total electron content distributed below the height of maximum electron density. The finer details of the electron density distribution will generally have little effect on the overall deviation angle of penetrating rays, and the functions  $\xi$  and  $\rho_0$  calculated for an average distribution will normally provide good approximations of the true functions for other distributions of electrons in the earth's ionosphere.

A typical distribution was obtained by averaging the results of Bowles (3) and Al'pert (4). This distribution, shown in Fig. 3, was used as the model for a digital computer ray-tracing program (8) to calculate the deviation angle  $\alpha$  for a range of frequencies and elevation angles. The functions  $\xi$  and  $\rho_0$  were determined from the results by the use of Eq. 17, the trial values of  $\rho_0$  being adjusted until the smallest spread was obtained in the values of  $\xi$  calculated for different frequencies at fixed values of the deviation factor. The calculated values of  $\xi^{-1}$  are shown in Fig. 4. It may be seen that a single function of the deviation factor, shown by the solid line, very closely approximates the calculated values. The figure also shows, by a broken line, the reciprocal of the series in Eq. 13 at the height of maximum electron density. It will be recalled that  $\xi$  must lie between unity and the value of the series at this height. The value of  $\rho_0$  was found to be 6800 km compared with a height of maximum electron density,  $\rho_m$ , for this profile of 6720 km. In order to determine the function relating this reference height to the height of maximum electron density, an approximate analytical calculation of  $\rho_0$  was made, with the model electron density profile represented by a parabolic and exponential distribution. It was found that the relationship between  $\rho_0$  and  $\rho_m$  calculated from the computer results can be expressed in the form:

$$\rho_0 = \rho_m \left[ 1 + 0.5333 \frac{y_m}{\rho_m} \right] \quad (18)$$

where  $y_m$  is the thickness of the parabolic layer below  $\rho_m$ . It has been shown by Appleton and Beynon (9) that the semi-thickness of an ionospheric layer generally increases with an increase in the height of maximum electron density in such a way that the relation  $\frac{y_m}{h_m}$  remains fairly constant. A more general expression for the reference height is obtained, therefore, when Eq. 18 is expressed in the form:

$$h_0 = h_m \left[ 1 + 0.5333 \frac{y_m}{h_m} \right] \quad (19)$$

where  $h_0$  and  $h_m$  are respectively, the reference height and the height of maximum electron density, measured from the earth's surface. The value of



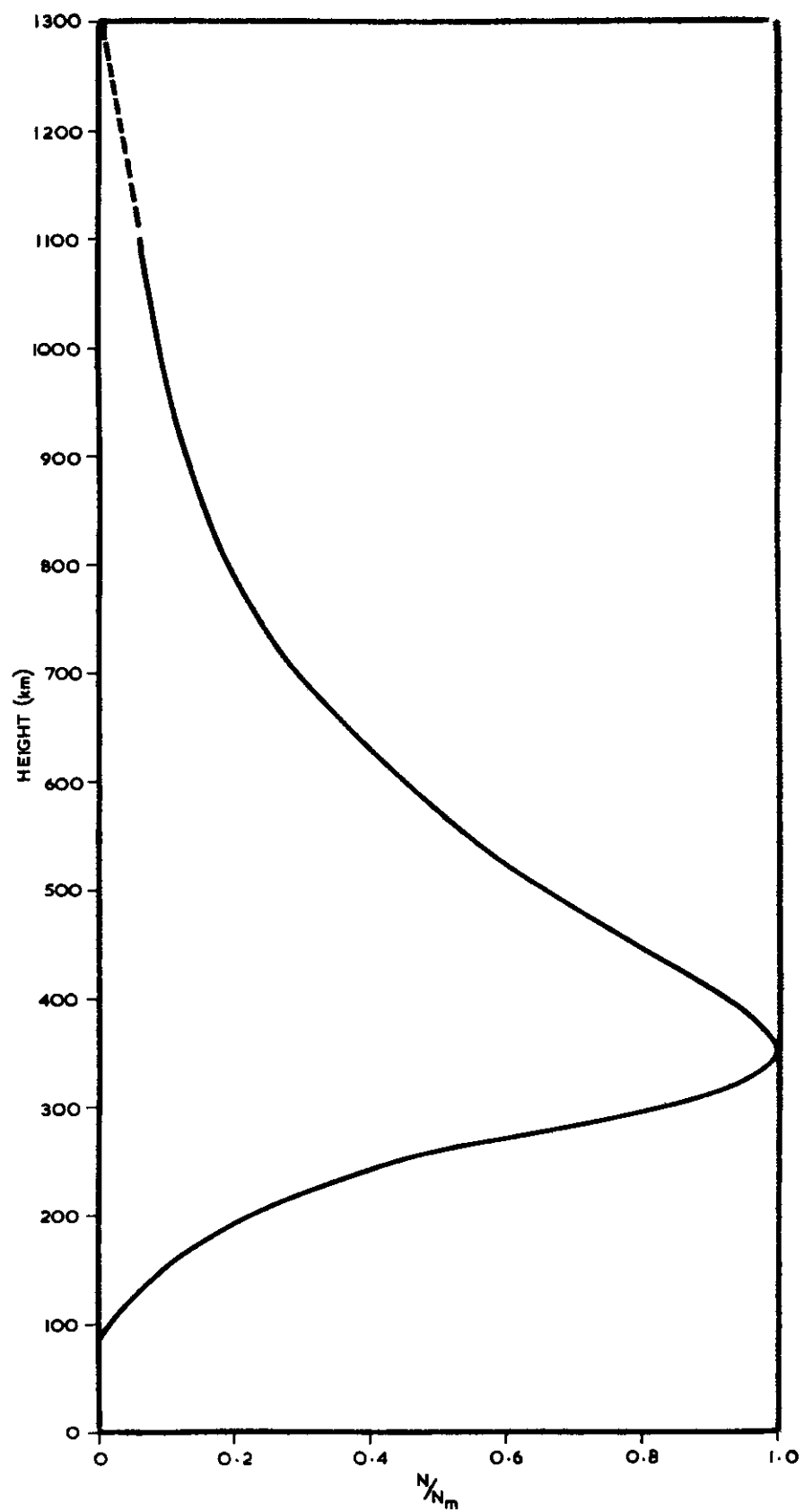


FIG. 3 Mean electron density distribution

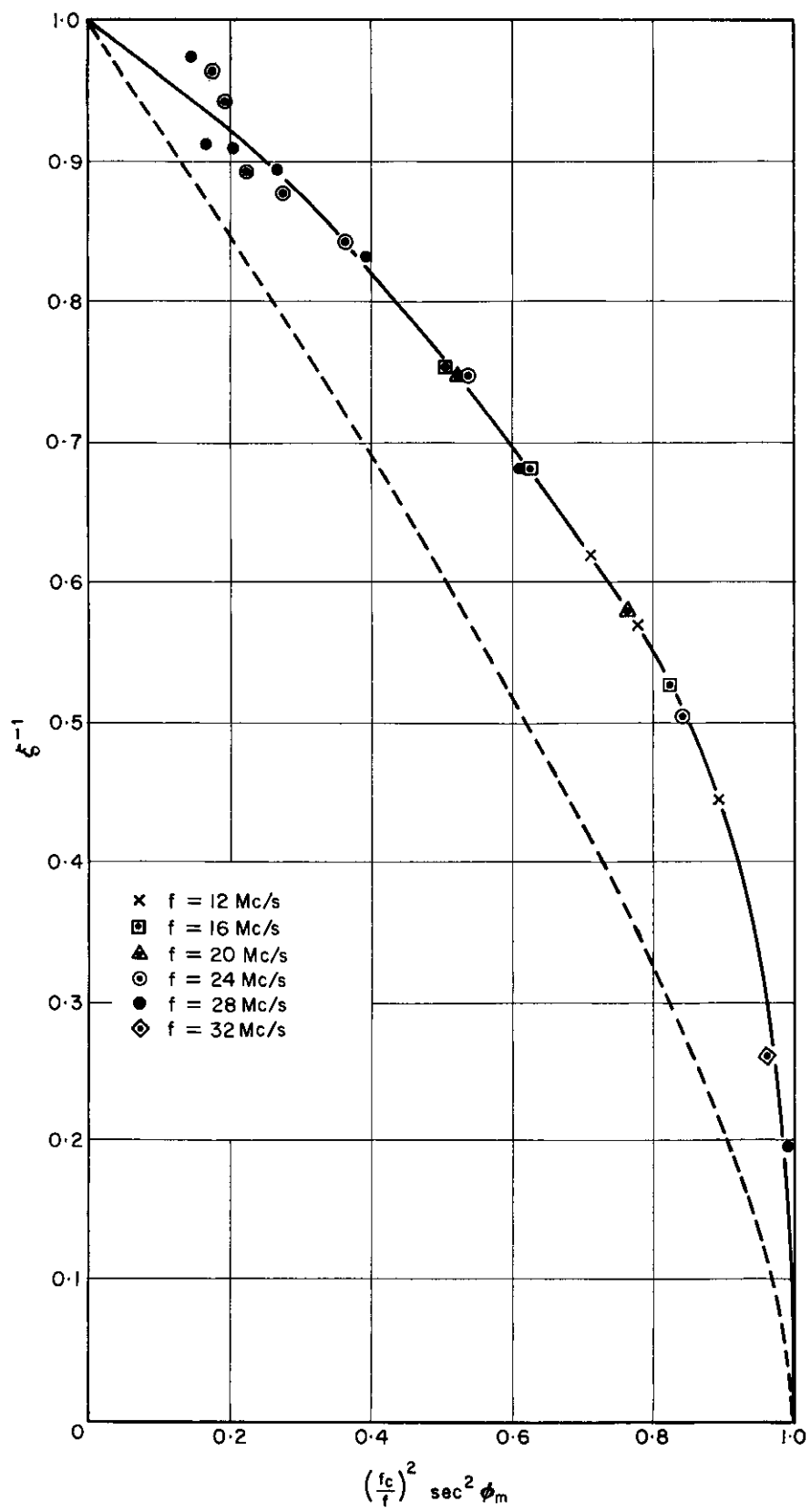


FIG. 4  $\xi^{-1}$  computed for mean profile (solid line) compared with the reciprocal of the series in Eq. 16 at  $h_m$  (broken line)

$\frac{y_m}{h_m}$  for the model distribution may then be considered a constant to give the simple relationship:

$$h_0 = 1.2286 h_m \quad (20)$$

This relationship was used in the construction of the nomogram to be described in the next section.

#### A NOMOGRAM FOR CALCULATING THE DEVIATION ANGLE ( $\alpha$ )

The nomogram shown in Fig. 5 has been constructed from Eqs. 17 and 20 together with the function of  $\frac{f_c}{f} \sec \phi_m$  shown for  $\xi$  by the solid curve in Fig. 4. The nomogram consists of two graphs whose axes form the branches of Z-type alignment charts with multiplication scales on the perpendicular axes so that the coordinates on one graph may be obtained from the known coordinates on the other graph. The ordinate of the upper graph is a function of  $\sec \phi_m$  and the abscissa is  $\left[ \frac{h_m}{\rho_0} \cdot \frac{\tan \phi_0}{2} \cdot \frac{\cos^2 \phi_m}{\cos^2 \phi_0} \right]$ . A point on these coordinates defines both the height of maximum electron density,  $h_m$ , and the angle of elevation of the ray path,  $\kappa$ ; the graph consists of curves of constant values of these quantities. The ordinate on the lower graph is a function of  $\left[ \frac{f_c}{f} \sec \phi_m \right]$  and the abscissa is  $\left[ \frac{1}{\rho_0} \cdot \frac{\tan \phi_0}{2} \cdot \frac{\cos^2 \phi_m}{\cos^2 \phi_0} \right] \cdot \frac{n_T}{N_m}$ . This graph consists of curves of constant values of the deviation angle,  $\alpha$ .

To use the nomogram, locate the intersection of  $h_m$  and  $\kappa$  on one of the grids of the upper graph and note the coordinates on the right hand and lower axes. Then extend straight lines from the ordinate, through the appropriate value of  $\frac{f}{f_c}$  and from the abscissa, through the value of  $\frac{n_T}{h_m N_m}$  to obtain the coordinates of the deviation angle  $\alpha$  on the corresponding axes of the lower graph. The scale of the ordinate for the lower graph was made linear in the fourth power of the deviation factor  $\left( \frac{f_c}{f} \sec \phi_m \right)$ , so that intermediate values of deviation angle could be obtained with good accuracy from the figure by linear interpolation between plotted values. The range of values on the ordinate extends from zero at the upper limit to unity at the lower limit. If the ordinate obtained from a combination of  $h_m$ ,  $\kappa$  and  $\frac{f}{f_c}$  falls below the lower limit, then the deviation factor is greater than unity and the ray is reflected. This is shown on the nomogram by arrows that indicate penetration above this limit and reflection below. The limiting case between reflection and penetration results in an infinite deviation angle.

The quantity  $h_m$  is introduced directly into the abscissa of the upper graph simply to make the required multiplication factor for the alignment chart equal to the function  $\frac{n_T}{h_m N_m}$ . This quantity is relatively stable around the value 1.1 which may be used as a guide when no value of  $n_T$  is available. The electron content of the parabolic approximation to the sub-peak

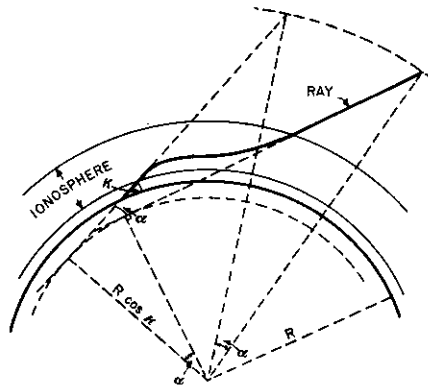
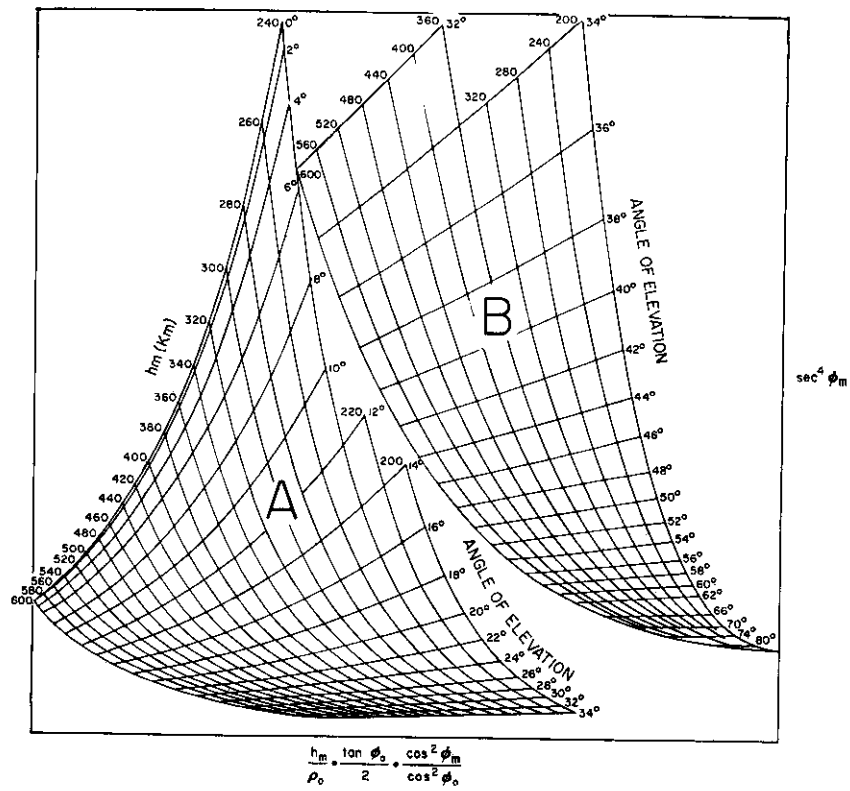


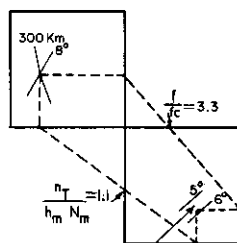
FIG. 5 Nomogram for calculating the deviation

# EXAMPLE

$$\begin{aligned} \kappa &= 8^\circ \\ h_m &= 300 \text{ km} \\ f_c &= 3.3 \\ \frac{n_T}{h_m N_m} &= 1.1 \end{aligned}$$

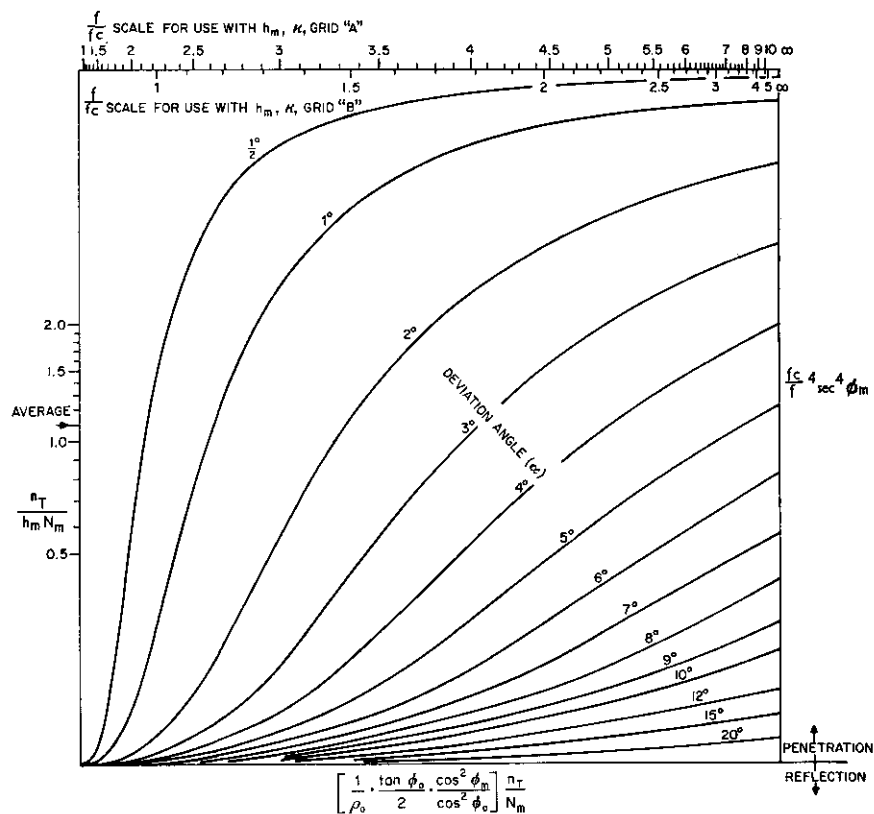
IF VALUE OF  $n_T$  IS NOT AVAILABLE,  
USE AVERAGE VALUE  $\frac{n_T}{h_m N_m} = 1.1$ ,

AS IN THIS EXAMPLE



READ  $\alpha = 5.7$  (USE LINEAR INTERPOLATION  
BETWEEN CURVES)

$\kappa$  = ANGLE OF ELEVATION  
 $h_m$  = HEIGHT OF MAXIMUM ELECTRON DENSITY  
 $f$  = WAVE FREQUENCY  
 $f_c$  = CRITICAL FREQUENCY OF F-LAYER  
 $N_m$  = MAXIMUM ELECTRON DENSITY  
 $n_T$  = TOTAL ELECTRON CONTENT OF IONOSPHERE ( $\int_0^\infty N dh$ )  
 $\alpha$  = DEVIATION OF RAY PENETRATING THE IONOSPHERE



angle ( $\alpha$ ) of a ray penetrating the ionosphere

distribution is given by  $2/3 y_m N_m$ , and since this is approximately a quarter of the total electron content, the quantity  $\frac{n_T}{h_m N_m}$  is approximately equal to  $\frac{8}{3} \cdot \frac{y_m}{h_m}$  which, as previously indicated, has been found to be a relatively constant parameter.

#### A NOMOGRAM FOR SATELLITE STUDIES

If the height of a satellite or other body in space is known and the deviation of the ray path between it and a ground station has been calculated, its position relative to the earth may easily be determined. Conversely, the true angle of elevation of the arriving radio wave may be determined when the position of the satellite is known together with the required ionospheric parameters.

The distance between the ground station and the location on the earth's surface directly below the satellite is given by:

$$D = R \theta \quad (21)$$

where:

$$\theta = \theta^1 + \alpha \quad (22)$$

and  $\theta^1$  is the angle subtended at the centre of the earth by the apparent ray path between the earth's surface and the height of the satellite. On substituting these height limits in Eq. 8, and carrying out the integration, one obtains:

$$\theta^1 = \arccos \left( \frac{R}{\rho_s} \cos \kappa \right) - \kappa \quad (23)$$

The nomogram shown in Fig. 6 has been constructed from the above equations and may be used to find  $\theta$  or  $D$ . The value of  $\theta^1$  is located on the abscissa, from the graph of angle of elevation plotted against height of the satellite. A straight line through this value and the value of  $\alpha$  on the parallel scale indicates the value of  $\theta$  or  $D$  on the remaining scale.

#### APPLICATION OF THE NOMOGRAMS TO SATELLITE MEASUREMENTS

Signals radiated on 5.47 Mc/s from a 45-watt transmitter in the *Topsi* satellite were monitored by the Radio Research Station, Slough, in the early morning and late afternoon or evening during August and September 1964. The locations of the satellite were obtained from tracking information, for the times at which the signal became lost in the background noise as the satellite receded from the monitoring ground station. The critical frequency of the F layer recorded at Slough at these times was used together with the information on the satellite's location, to determine the angle of elevation of the ray paths, using the nomograms of Fig. 5 and 6. A comparison of the lowest usable angles of elevation of the ray paths as determined by this technique and the theoretical minimum angles of elevation for penetration of the ionosphere is described below.

The *Topsi* satellite was launched on August 25, 1964, in a near circular orbit with perigee at 886 km and apogee at 1010 km. For the purpose of these calculations, it was assumed that the height of the satellite,  $h_s$ , was

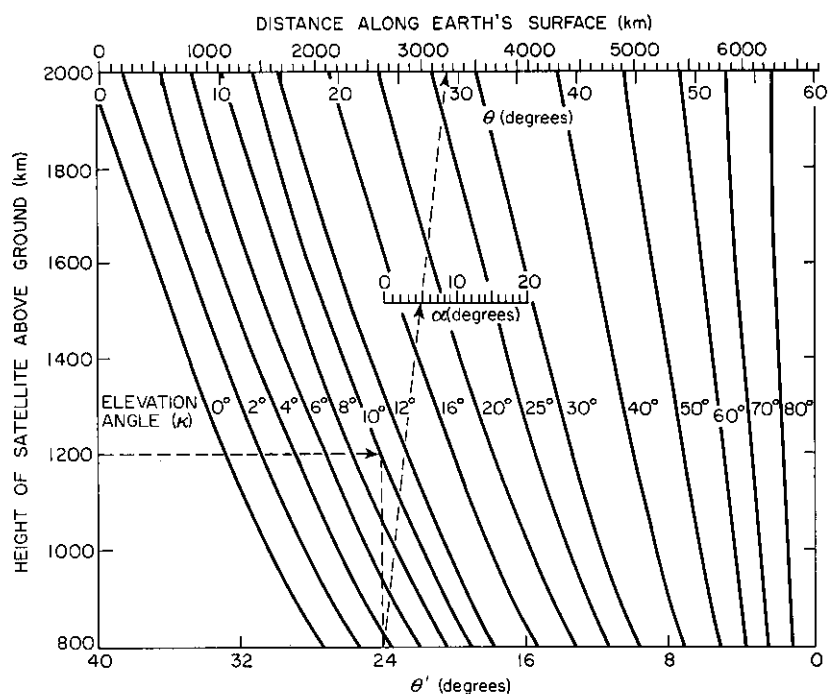


FIG. 6 Nomogram for calculating distance along earth's surface between ground-station and satellite

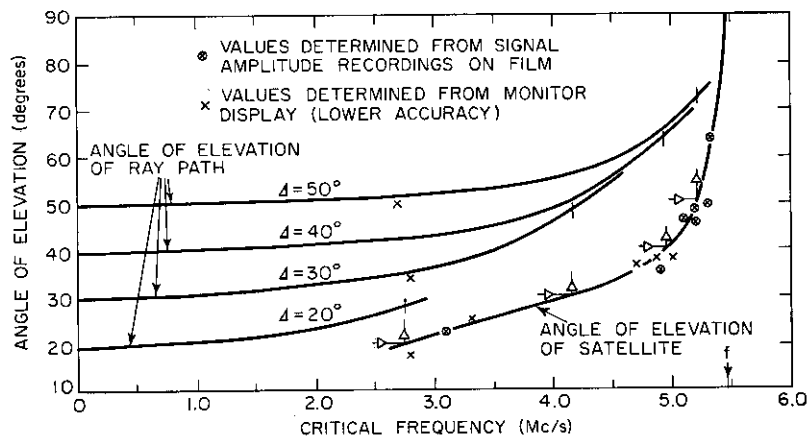


FIG. 7 Curves relating  $f_c$  with angle of elevation of ray path ( $\kappa$ ) for fixed values of  $\Delta$

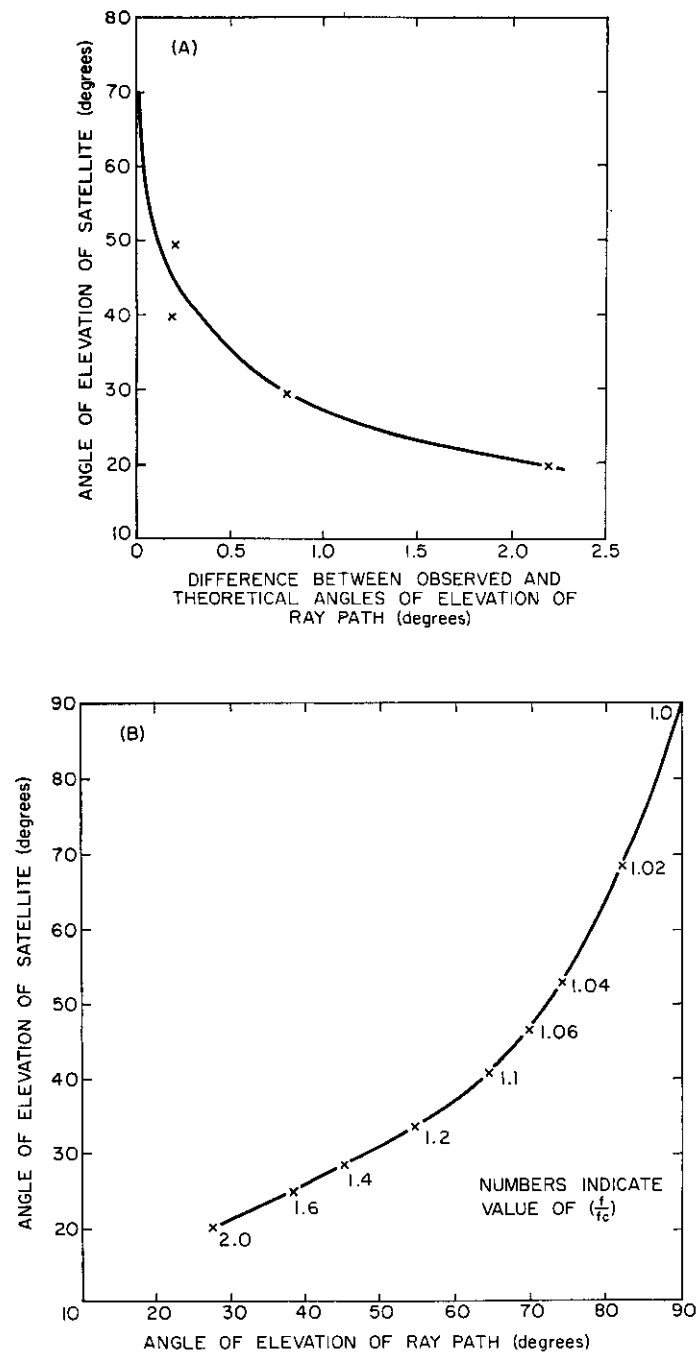


FIG. 8 Relationship between angle of elevation of satellite and minimum angle of elevation of ray path for communication with ground station



1 000 km and that the height of maximum electron density,  $h_m$ , was 250 km.

The approximately constant value of 1.1 was assumed for the quantity  $\frac{n_T}{h_m N_m}$ .

Since, at the height at which the satellite was orbiting the electron density had decreased to a very small value, the deviation of the ray from the satellite was assumed to be that of a ray traversing the full extent of the ionosphere and the results obtained from the nomograms were used directly.

The condition under study was near the limit between penetration and reflection, where the approximations used in the construction of the nomograms may produce significant errors. In particular, the limiting condition is assumed to occur when the deviation factor is unity. This approximation implies that, at the limit, reflection occurs at the height of maximum electron density, whereas it may be shown that the limiting condition of reflection actually is met at a height slightly below the height of maximum electron density: consequently, a radio wave propagated towards the earth from a satellite in space may penetrate slightly into the bottom side of the F layer and still be reflected back up again. This condition is described in the appendix and the equations derived for a parabolic profile near the region of maximum electron density have been used to calculate the theoretical limit for penetrating rays. However, the approximation is very good for most cases and the errors appear to be very small in the results described below, where the calculated angles of elevation have been obtained directly from the nomograms.

The nomogram of Fig. 6 was used to determine combinations of elevation angle  $\kappa$  and deviation angle  $\alpha$  that would satisfy the known height and distance of the satellite at the time of signal fade-out. The values of  $f/f_c$  required to give these particular combinations of  $\kappa$  and  $\alpha$  were then determined from the nomogram of Fig. 5, and the corresponding values of  $f_c$  calculated for a wave frequency of 5.47 Mc/s. Since the location of the satellite was known, its line of sight angle of elevation  $A$  could be determined. The observed relationship between the local critical frequency and the angle of elevation of the satellite at the times of signal fade-out has been plotted in Fig. 7 together with the relationship between  $f_c$  and the angle of elevation of the ray path as determined from the nomograms for particular angles of elevation of the satellite. The interpolation in  $f_c$  to obtain the angle of elevation of the ray path at the times of signal fade-out has been performed with the aid of Fig. 7 and the results are compared with the theoretical minimum angle of elevation in Table 1. For this initial study, the experimental results in Fig. 7 were approximated by a smooth curve, but a similar analysis of more individual measurements should indicate the extent of the daily variations in absorption, provided that the possible errors in the individual results can be estimated.

The theoretical minimum angles of elevation for penetration of the ionosphere were calculated from the formula:

$$\kappa = \arccos \frac{\rho_m}{R} \sqrt{1 - \left(\frac{f_c}{f}\right)^2} \left\{ \frac{3 + A}{4} \sqrt{1 + \frac{\left[\frac{1}{4} \cdot \frac{\rho_m}{\gamma_m} (1 - A)\right]^2}{(f/f_c)^2 - 1}} \right\} \quad (24)$$

where:

$$A = \sqrt{1 - 8 \left( \frac{y_m}{\rho_m} \right)^2 \left[ \left( \frac{f}{f_c} \right)^2 - 1 \right]} \quad (25)$$

This solution applies to a parabolic profile near  $h_m$  and follows from the requirement that  $\frac{d\rho}{d\theta}$  and  $\frac{d^2\rho}{d\theta^2}$  are both equal to zero. Its derivation is given in the appendix. It may be seen that the value of  $A$  is only slightly less than unity and when it is approximated with this value the quantity enclosed in the braces also becomes unity and Eq. 24 reduces to the condition that the deviation factor is unity. The error in  $\cos \kappa$ , caused by this approximation is usually less than 0.1 per cent.

It may be seen from Table 1 that the measured angles of elevation of the ray paths, as determined from the nomograms, are slightly above the theoretical limit for penetration of the ionosphere, with the angular difference increasing as the angle of elevation is reduced. This variation which is illustrated in Fig. 8, is thought to be due mainly to the absorption of the radio waves increasing at the lower angles of elevation: ray-path data obtained from the nomograms could be used with amplitude measurements to study further the effects of absorption on satellite communications. The difference between the angle of elevation of the ray path and the line-of-sight path to the satellite, as determined from Table 1, is indicated in Fig. 8. It is interesting to note that this difference exceeded  $20^\circ$  on a number of occasions.

TABLE 1  
RESULTS OF TOPSI SATELLITE MEASUREMENTS

$\Delta$ ( $^\circ$ )	$D$ (km)	$\alpha$ ( $^\circ$ )	$\kappa$ ( $^\circ$ )	$f/f_c$	$f_c$ (Mc/s)	Recorded $f_c$ (Mc/s)	Minimum $\kappa$ ( $^\circ$ )		
							Exp.	Theo.	Diff.
20	1744	0	20.0	$\infty$	0				
		2	24.7	2.51	2.18	2.74	28.2	26.0	2.2
		4	30.0	1.86	2.94				
30	1283	0	30.0	$\infty$	0				
		2	37.5	1.73	3.17	4.15	48.2	47.4	0.8
		4	45.0	1.39	3.95				
40	949	6	53.5	1.23	4.47				
		0	40	$\infty$	0				
		2	49	1.36	4.04	4.94	63.7	63.5	0.2
50	695	4	59	1.16	4.73				
		6	70	1.05	5.19				
		0	50	$\infty$	0				
		2	64	1.12	4.88	5.22	72.1	71.9	0.2
		4	75	1.03	5.31				

## CONCLUSIONS

Equations have been derived for calculating the refractive deviation of HF radio waves penetrating through the earth's ionosphere, and for determining the angle of elevation of the ray path from a satellite whose position is known. Nomograms have been constructed from these equations, to provide a rapid method for calculating the parameters of ray paths between satellites and the earth's surface. The method has been applied to data on the position of the *Topsi* satellite radiating on 5.47 Mc/s, to determine the angle of elevation of the ray path as the signals from its 45-watt transmitter became lost in noise at a monitoring ground station. These angles, which represent the lowest usable angles of elevation for transmission through the ionosphere, were found to be less than  $1^\circ$  above the theoretical limits (neglecting absorption) when the line-of-sight angle of elevation of the satellite was greater than  $28^\circ$ , although the difference between the angle of elevation of the ray path and the line-of-sight path to the satellite often exceeded  $20^\circ$ . The difference between the theoretical cut-off limit and the minimum usable angle of elevation determined from the nomograms was found to increase at the lower angles of elevation, probably as a consequence of the increased absorption and other losses. The nomograms described in this paper provide a rapid method for calculating the deviation of ray paths and could be used together with amplitude measurements to study further the effects of absorption on satellite communication.

## APPENDIX

**The Limiting Condition between Penetration and Reflection** – At the point at which a ray is reflected:

$$d\rho/d\theta = 0 \quad (\text{A1})$$

It has been shown (10) that at the limiting condition between penetration and reflection, the ray follows a path that remains parallel to the earth's surface. This condition is met when, in addition to Eq. A1 being satisfied:

$$d^2\rho/d\theta^2 = 0 \quad (\text{A2})$$

But

$$\frac{d^2\rho}{d\theta^2} = \frac{d\rho}{d\theta} \cdot \frac{d}{d\rho} \left( \frac{d\rho}{d\theta} \right) \quad (\text{A3})$$

and from Eq. 3, 4, 6 and 11,

$$\frac{d\rho}{d\theta} = \frac{\rho}{fR \cos \kappa} \sqrt{f^2 \rho^2 - f_N^2 \rho^2 - f^2 R^2 \cos^2 \kappa} \quad (\text{A4})$$

Hence, from Eqs. A3 and A4:

$$\begin{aligned} \frac{d^2\rho}{d\theta^2} = \frac{\rho}{f^2 R^2 \cos^2 \kappa} \left\{ 2 [f^2 \rho^2 - f_N^2 \rho^2 - f^2 R^2 \cos^2 \kappa] \right. \\ \left. + \left[ f^2 R^2 \cos^2 \kappa - \frac{df_N^2}{d\rho} \cdot \frac{\rho^3}{2} \right] \right\} \quad (\text{A5}) \end{aligned}$$

But, from Eqs. A1 and A4;

$$f^2 \rho^2 - f_N^2 \rho^2 - f^2 R^2 \cos^2 \kappa = 0 \quad (\text{A6})$$

and thus, from Eqs. A2, A5 and A6, at the point of inflection;

$$f^2 R^2 \cos^2 \kappa - \frac{df_N^2}{d\rho} \cdot \frac{\rho^3}{2} = 0 \quad (\text{A7})$$

Hence, from Eqs. A6 and A7, the limit condition is met when:

$$f^2 = \left[ f_N^2 + \frac{df_N^2}{d\rho} \cdot \frac{\rho}{2} \right] \rho = \rho_r \quad (\text{A8})$$

where  $\rho_r$  is the height of reflection, measured from the centre of the earth.

In the case of a parabolic layer:

$$f_N^2 = f_c^2 \left[ 1 - \left( \frac{\rho_m - \rho}{y_m} \right)^2 \right] \quad (\text{A9})$$

which, on substitution in Eq. A8, gives:

$$\rho_r^2 [2(f_c/y_m)^2] - \rho_r [3(f_c/y_m)^2 \rho_m] + \{f^2 + f_c^2 [(\rho_m/y_m)^2 - 1]\} = 0 \quad (\text{A10})$$

Hence:

$$\rho_r = \frac{\rho_m}{4} \left\{ 3 + \sqrt{1 - 8 (y_m/\rho_m)^2 [(f/f_c)^2 - 1]} \right\} \quad (\text{A11})$$

and from Eqs. 12, A9 and A11:

$$\kappa = \arccos \frac{\rho_m}{R} \sqrt{1 - (f_c/f)^2} \left\{ \frac{3 + A}{4} \sqrt{1 + \frac{\left[ \frac{1}{4} \cdot \frac{\rho_m}{y_m} (1 - A) \right]^2}{(f/f_c)^2 - 1}} \right\} \quad (\text{A12})$$

where:

$$A = \sqrt{1 - 8 (y_m/\rho_m)^2 [(f/f_c)^2 - 1]} \quad (\text{A13})$$

#### DISCUSSION

K. DAVIES - Has Mr Maliphant tried to use *Topsi* data and ray-tracing techniques to determine and hence map  $f_o F_2$ ?

R. G. MALIPHANT - We have not done so yet, but the possibility looks interesting and I hope to be able to look into it.

M. ANASTASSIADES - Did you ever try to apply your nomograms to other than *Topsi* frequencies? Do you think that your nomograms can have application to the frequencies of 20 and 40 Mc/s?

R. G. MALIPHANT - The nomograms were not originally developed for satellite studies, but were intended to assist in the design of the MIT Solar Radar at El Campo, Texas. The study included a calculation of the effects of the earth's magnetic field to determine whether the angular separation of the ordinary and extraordinary waves could be resolved with the available antennas.

It is only recently that I have attempted to use the nomograms in connection with satellite studies, and only *Topsi* satellite signal measurements have been utilized. It would be especially interesting to use the nomograms with measurements on two frequencies in an attempt to determine the critical frequency at a distance.

## REFERENCES

1. CHVOJKOVA, E., "Propagation of radio waves from cosmical sources". *Nature* 181, 105, 1958.
2. MALIPHANT, R. G., "The refractive deviation of radio waves that penetrate the earth's ionosphere". DRTE Report 1090, September 1962.
3. BOWLES, K. Distribution at 40°N for 1135 CST, Private Communication Feb. 27 1959.
4. AL'PERT, YA. L., *Priroda* 6, 85-87, 1958 (translated by E. R. Hope, DRB Report T304R).
5. EVANS, J. V., "The electron content of the ionosphere". *J. Atmos. and Terr. Phys.* 11, 259-71, 1957.
6. THOMAS, J. O., "The distribution of electrons in the ionosphere". *Proc. IRE* 47, 162-75, 1959.
7. SHERIFF, R. M., "A study of the total electron content of the F-region of the ionosphere over Ahmedabad, India". *J. Atmos. and Terr. Phys.* 8, 91-97, 1956.
8. MULDREW, D. B., "An ionospheric ray-tracing technique and its application to a problem in long-distance radio propagation". *IRE Trans. AP-7*, 393-6, Oct. 1959.
9. APPLETON, E. V., and BEYNON, W. J. G., "The application of ionospheric data to radio communication problems". *Proc. Phys. Soc. Part II* 59, 58-76, 1947.
10. MULDREW, D. B., and MALIPHANT, R. G., "Long-distance one-hop ionospheric radio-wave propagation". *J. Geophys. Res.* 67, 1805-15, May 1962.

## ACKNOWLEDGEMENTS

The development of the nomograms described in this paper was undertaken while the author was on the staff of the DEFENCE RESEARCH BOARD, Ottawa, Canada, and has been described in detail in DRTE Report No. 1090, from which most of the diagrams have been obtained. The remainder of this paper is the result of research performed at GOVERNMENT COMMUNICATIONS HEADQUARTERS, Cheltenham, England. The measurements on signals from the *Topsi* satellite were made by members of the staff of the RADIO RESEARCH STATION, Slough, England, and communicated to the author by MR. P. A. BRADLEY of that establishment. The *Topsi* satellite was built by AIRBORNE INSTRUMENTS LABORATORY to CRPL specifications and launched by NASA.



## CHAPTER 3-2

# ETUDE DE L'AMPLITUDE DU CHAMP RADIOELECTRIQUE D'UN SATELLITE A L'HORIZON DE LA STATION

J. F. AUREJAC et J. PAPET-LEPINE

Laboratoire de Physique de l'Atmosphère, Faculté des Sciences, Paris

## SUMMARY

Scintillations are observed in the radio signals received from satellites in the 20-60 Mc/s frequency band because of ionospheric irregularities. A statistical survey is made of recorded scintillations. For this survey they are divided into four classes producing changes of periods greater or less than 1 c/s and amplitudes greater or less than 25 per cent of the received signal. It is shown that for any one station the scintillations were not uniformly distributed in azimuth and that the distributions for each class differed.

## SOMMAIRE

A l'aide d'une antenne à gain élevé sur 40 MHz, susceptible d'être pointée dans toutes directions azimutales, il est possible de recevoir à la Station du Val-Joyeux (Paris) les signaux du satellite *Explorer 22* pour toutes les révolutions allant de 330° à 206° de longitude W au passage à l'équateur; ce qui représente, dans les cas extrêmes, des distances satellite observateur atteignant quelques fois plus de 5.000 km.

Du fait d'un très grand parcours ionosphérique, il est possible de mettre en évidence un renforcement considérable des effets dus à la réfraction et à l'action des irrégularités dans la répartition de la densité électronique du milieu traversé. C'est ainsi que l'on constate une forte augmentation des scintillations lorsque les angles d'élévation sont de l'ordre de 20° et en dessous. Ce renforcement des scintillations est particulièrement visible vers le Nord, mais également vers le Sud. Dans ce dernier cas, nous avons constaté une certaine corrélation entre l'activité magnétique et les indices de scintillations. Une comparaison systématique avec les résultats obtenus par d'autres stations est ensuite faite pour délimiter les zones où ces scintillations prennent naissance.

## INTRODUCTION

Lorsque l'ionosphère présente des irrégularités dans la répartition spatiale de la densité électronique, l'indice de réfraction varie beaucoup d'un point à un autre de l'ionosphère, et l'antenne de réception capte de nombreux parcours d'onde dont la phase est déterminée par ces parcours. La distribution des phases étant liée à la valeur locale de l'indice de réfraction, on devra donc constater une augmentation ou une diminution du champ reçu selon la

zone de densité irrégulière, par l'onde incidente, ainsi qu'une modification locale affectant l'excursion de fréquence due à l'effet Doppler. L'étude des variations brusques de l'amplitude, qui résulte du phénomène de scintillation, doit fournir des informations sur la constitution des zones où les irrégularités prennent naissance. Ces variations du signal émis sont amplifiées lorsque les satellites arrivent à l'horizon des récepteurs. D'importants phénomènes se produisent sous l'effet d'un très grand parcours à travers l'ionosphère qui renforce singulièrement l'effet de la réfraction d'une part et d'autre part l'action d'hétérogénéités relativement faibles dans la densité électronique.

Les problèmes de la réfraction ont déjà été abordés, mais surtout par voie théorique, et il n'apparaît pas jusqu'ici que les observations entreprises avec un dipôle de réception puissent rendre compte des phénomènes prévus, le champ diminuant rapidement avec l'éloignement du satellite. Il en est de même pour les scintillations. Si l'on constate bien une augmentation des scintillations lorsque les angles d'élévation décroissent, on ignore la nature et la structure des scintillations produites sous des angles d'élévations inférieurs, ou très inférieurs, à  $30^\circ$ .

#### CHAÎNE DE RÉCEPTION

Dans le but d'étudier la réfraction et l'action des hétérogénéités ionosphériques lorsque le satellite est bas sur l'horizon, nous avons tout d'abord construit une antenne Yagi de 9 éléments sur 54 MHz pour l'étude des signaux du satellite *Transit IV A* (61 omicron 1), puis une antenne Yagi de 11 éléments sur 40 MHz pour l'étude des signaux des satellites *Explorer 22* et 27 (1964-64 A et 1965-32 A). L'antenne est placée sur un pivot entraîné par un moteur asservi en azimut. Elle est fixe en élévation et son axe est placé à  $20^\circ$  au dessus de l'horizon, son angle d'ouverture étant un peu plus grand que  $40^\circ$  à - 6 dB. Le dispositif mécanique de restitution de l'angle d'azimut est assez délicat du fait des problèmes d'aérodynamique que posent les grandes dimensions de cette antenne, des erreurs de pointage pouvant se produire du fait des erreurs d'azimut engendrées suivant la force des rafales de vent. Une réalisation soignée du dispositif de télécommande permet de connaître, avec précision, l'azimut exact quelles que soient les fluctuations auxquelles est soumise l'antenne.

La chaîne de réception se compose d'une premier changement de fréquence qui sert également de préamplificateur et d'un récepteur superhétérodyne. Les oscillateurs locaux sont pilotés par des quartz à haute stabilité ( $10^{-7}$  par heure). L'amplitude du signal est transmise à un enregistreur de faible réponse et déroulant à faible vitesse (60 mm par minute) pour obtenir l'allure générale des phénomènes. En parallèle, un enregistreur de 100 Hz de réponse et déroulant à 75 em par minute, permet une analyse fine des scintillations.

#### RÉSULTATS GÉNÉRAUX

A partir des enregistrements faits sur des dipôles, nous avons toujours obtenu des scintillations importantes vers le Nord. Cependant, lorsque le satellite est assez bas sur l'horizon, des scintillations aussi importantes peuvent apparaître vers le Sud, et d'une façon générale, lorsque les ondes émises traversent des couches épaisses d'ionosphère. Ces phénomènes sont particulièrement visibles sur les enregistrements du signal de 20 MHz du satellite





FIG. 1 Enregistrement du signal de 20 MHz du satellite italien *SAN MARCO* pendant sa 400e révolution le 11 janvier 1965

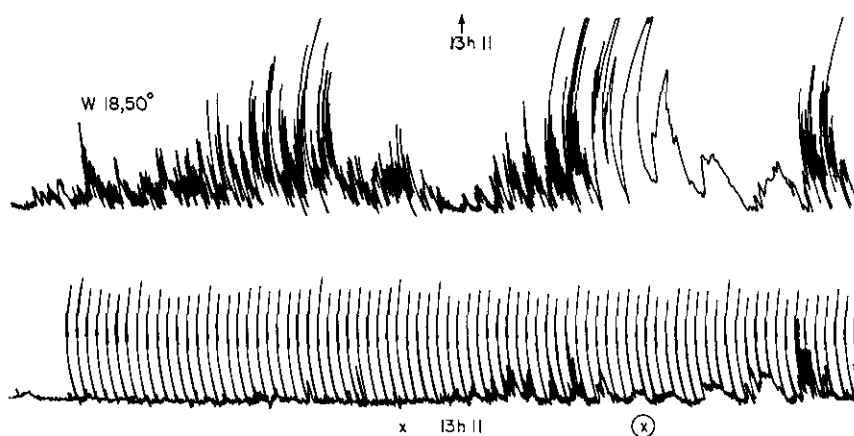


FIG. 2 Enregistrements du signal de 54 MHz du satellite américain *TRANSIT IV A*. Révolution 11724 du 22 octobre 1963. L'indice d'activité magnétique était à 13 h :  $K = 2$ . La piste du bas donne l'enregistrement effectué à partir d'une antenne Yagi. On peut voir sur ce dernier les fortes scintillations du type  $S = 2$  au début du passage, alors que les signaux parviennent à la station sous incidence presque rasante

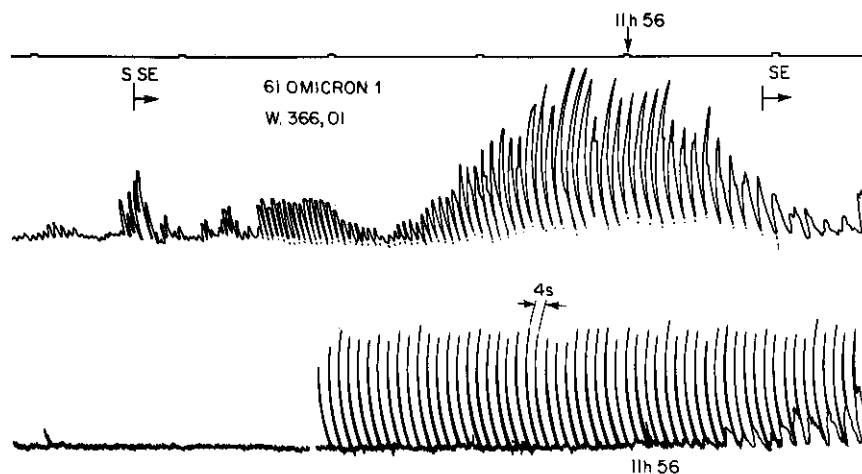


FIG. 3 Enregistrements du signal de 54 MHz du satellite américain *TRANSIT IV A*. Révolution 11751 du 20 octobre 1963. L'indice d'activité magnétique était à 12 h :  $K = 5$ . La piste du haut donne l'enregistrement effectué à partir d'une antenne Yagi. On peut remarquer l'absence de scintillations, ce qui permet de voir parfaitement les rotations Faraday particulièrement rapides dans la région intéressée

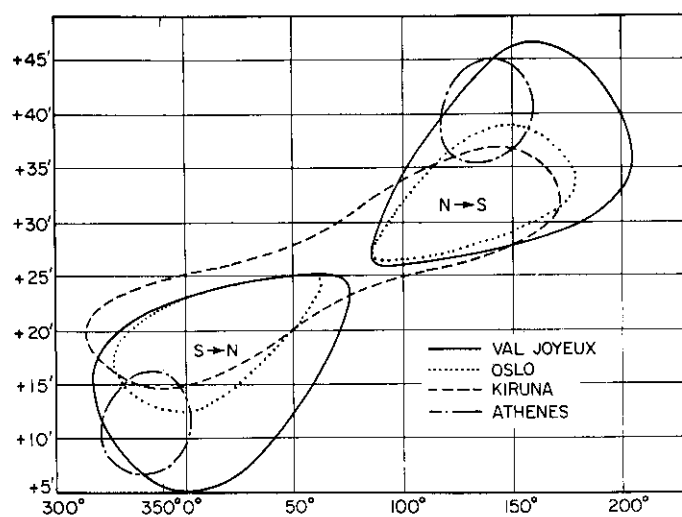


FIG. 4 Temps d'écoute probable de chaque station, à partir de l'heure de passage à l'équateur, en fonction de la longitude Ouest subsatellitique à l'équateur. Zones de chevauchement : Val-Joyeux : 3500 km de distance Loxochronique, Kjeller, Kiruna et Athenes : 2000 km

italien *San-Marco*, dont le point d'ascension maximale est à  $37^\circ$  de latitude Nord Fig. 1.

Bien que les fréquences utilisées soient différentes, ces dernières constations sont confirmées par les observations faites avec l'antenne à gain élevé. En effet, il est possible de recevoir les signaux du satellite *Explorer 22* par exemple, pour toutes les révolutions allant de  $315^\circ$  à  $210^\circ$  de longitude W au passage à l'équateur, ce qui représente des distances satellite - observateur de l'ordre de 5.000 km: la durée du passage étant ainsi augmentée de 5 à 6 minutes par rapport à la durée d'un passage normal reçu sur un dipole.

On constate ainsi une forte augmentation des scintillations lorsque les angles d'élévation de la direction de propagation sont inférieurs à  $20^\circ$ . Ce renforcement des scintillations est particulièrement visible vers le Nord, mais également vers le Sud. Dans ce dernier cas, et plus particulièrement dans le Sud-Est de la station, nous avons constaté que le renforcement n'avait pas toujours lieu et qu'il était lié à l'indice d'activité magnétique. En général, nous trouvons beaucoup de scintillations lorsque l'indice d'activité magnétique est faible. Ces scintillations de grande amplitude masquent complètement les rotations dues à l'effet Faraday. Tandis que pour une forte valeur de cet indice, les scintillations peu nombreuses et de faible amplitude se superposent aux rotations Faraday dont les zéros apparaissent alors nettement. Ceci est d'autant plus visible que dans cette direction, le produit du champ magnétique local par le cosinus de l'angle entre ce champ et la direction de propagation est important et que, de ce fait, la période des rotations Faraday est très courte dans cette direction (Fig. 2 et 3).

Cependant, un examen rapide montre que la structure des scintillations varie en fonction de l'angle d'azimut, en particulier les scintillations vues dans le Sud sont bien différentes de celles vues dans le Nord. Il semble même que cette différence de structure soit due à une nature différente. Les scintillations vues dans le Nord ne sont pas seulement dues aux couches épaisses d'ionosphère traversées, elles possèdent en plus un caractère que l'expérience qualitative permet de distinguer des autres.

Dans le but de rechercher ces différences de structure, il devenait intéressant de comparer systématiquement des résultats d'enregistrement de la Station du Val-Joyeux avec ceux obtenus par des stations européennes qui reçoivent le même signal sous des angles d'élévation plus élevés. Les zones intéressées se trouvant au Nord et au Sud-Est de la station, nous avons donc utilisé 223 enregistrements obtenus dans chacune des stations suivantes : Kíruna, Suède, ( $20^\circ 26'$  Long. E et  $67^\circ 50'$  Lat. N), Kjeller, Oslo, Norvège, ( $10^\circ 46'$  Long. E et  $60^\circ 13'$  Lat. N) et Athènes, Grèce, ( $23^\circ 43'$  Long. E et  $37^\circ 58'$  Lat. N) que recoupe la station du Val-Joyeux, Paris, France, ( $2^\circ 1'$  Long. E et  $48^\circ 49'$  Lat. N), (voir Fig. 4).

#### DEPOUILLEMENT DES DONNEES EXPERIMENTALES

En ce qui concerne l'étude de la réfraction à l'horizon, le dépouillement des données expérimentales s'effectue de la façon suivante. Pour chaque passage du satellite *Explorer 22*, on mesure le temps exact où se produit l'apparition du signal, puis la disparition du signal. Lorsque cette apparition, ou cette disparition, s'effectue lentement, on mesure le temps exact correspondant à une amplitude de 20 pour cent au-dessus du bruit de fond. Pour l'étude

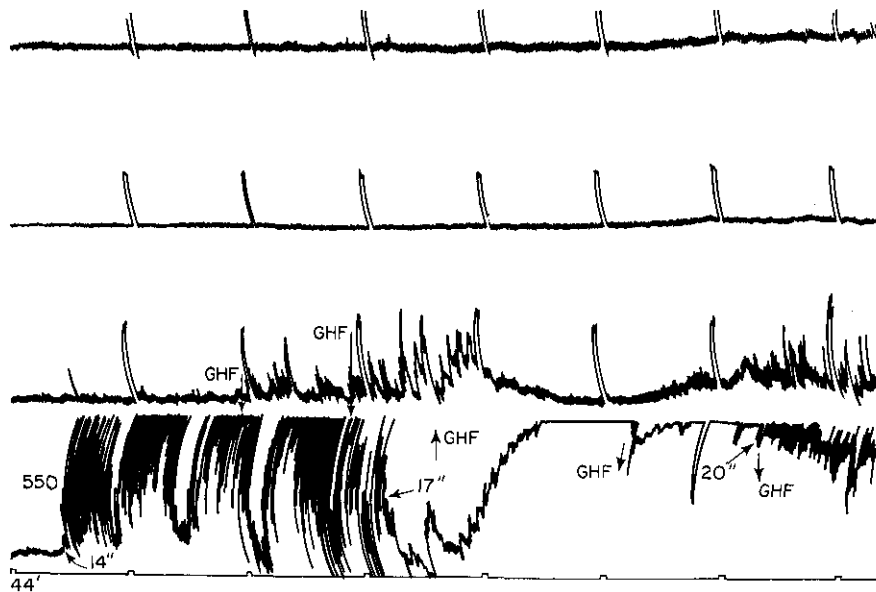


FIG. 5 Début de l'enregistrement du signal de 40 MHz du satellite américain EXPLORER 22 (Balise : S-66 B). Révolution 920 du 16 décembre 1964. Les deux pistes du haut sont réservées à l'enregistrement des signaux de 40 et 41 MHz recus sur un dipole. La troisième piste à partir du haut montre l'amplitude du signal de 20 MHz recu sur dipole. La piste du bas donne un exemple d'enregistrement du signal de 40 MHz recu sur une antenne Yagi. Le début de l'enregistrement montre des scintillations du type  $S = 2$  et la fin de la figure des scintillations du type  $S = 4$

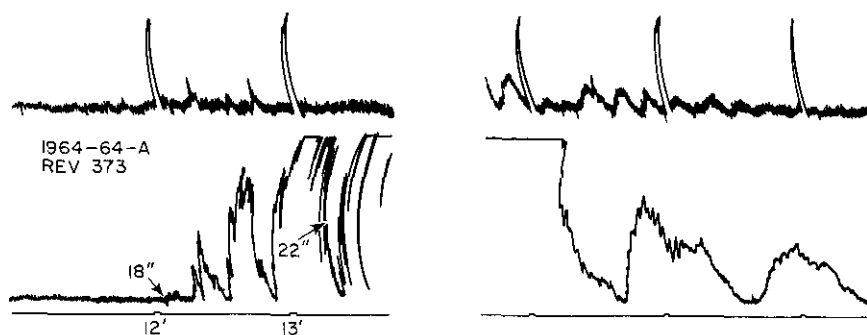


FIG. 6 Début et fin de l'enregistrement du signal de 40 MHz du satellite EXPLORER 22 recu sur une antenne Yagi. Le début montre des scintillations du type  $S = 3$  tandis que la fin montre des scintillations du type  $S = 5$

statistique de l'angle limite de réception, on distingue parfois entre les temps sûrs (variation nette du signal au-dessus du bruit de fond, variation généralement accompagnée de scintillations rapides pendant une durée de moins d'une minute) et les temps douteux donnés par une faible ondulation du bruit de fond (on note d'ailleurs que la différence entre ces temps varie généralement de 30 à 60 secondes). Enfin on mesure les temps correspondant à l'apparition et à la disparition des scintillations au début et à la fin du passage. L'antenne étant fixe en élévation, les résultats trouvés pour des angles d'élévation supérieurs à  $40^\circ$  sont entachés d'erreur du fait du diagramme de rayonnement de l'antenne.

Telles qu'on les voit sur les enregistrements les scintillations présentent une amplitude et une forme variée en fonction du temps. En pratique, il est donc nécessaire de faire une distinction entre les scintillations lentes et rapides, la limite étant fixée à 1 Hz. Cette distinction tient également compte du fait que les scintillations lentes sont beaucoup plus irrégulières, leur pseudo-période pouvant descendre jusqu'à 0,1 Hz. L'analyse fine montre que la fréquence des scintillations régulières est de l'ordre de 2 à 4 Hz ; quelquefois, on peut avoir, pendant plusieurs dizaines de secondes, des variations assez irrégulières ayant une pseudo-fréquence d'une vingtaine de hertz. Par ailleurs, on sépare ces deux types de scintillations en deux catégories, celles d'une amplitude de plus de 25 pour cent et celle d'une amplitude inférieure à 25 pour cent du niveau moyen du signal reçu. On distinguera donc pour chacune des stations 4 types de scintillations numérotés 2, 3, 4, 5 :

- type S = 2 :  $A > 25\%$ ,  $f_s > 1$  Hz
- S = 3 :  $A > 25\%$ ,  $f_s < 1$  Hz
- S = 4 :  $A < 25\%$ ,  $f_s > 1$  Hz
- S = 5 :  $A < 25\%$ ,  $f_s < 1$  Hz

Les Fig. 5 et 6 montrent des exemples d'enregistrements de l'amplitude du signal émis par le satellite *Explorer 22*. On peut y voir la différence entre l'enregistrement à partir d'une antenne à gain élevé et l'enregistrement sur un dipôle, ainsi que les différents types de scintillations rencontrés.

Les passages analysés de ce satellite se situent pendant la période du 25 décembre 1964 au 31 mars 1965. Sur 228 révolutions supposées favorables, il n'en a été retenu que 207 pour la station du Val-Joyeux, de telle façon qu'au moins une station étrangère ait pu enregistrer dans de bonnes conditions une de ces révolutions. Le Val-Joyeux possède donc 48 révolutions communes avec Athènes, 12 avec Kjeller et 66 avec Kiruna. On trouve également 60 révolutions communes à trois stations (Val-Joyeux, Athènes et Kiruna : 26; Val-Joyeux, Kiruna et Kjeller : 21 ; Val-Joyeux, Kjeller et Athènes : 13). Enfin, on trouve 21 révolutions communes aux quatre stations. L'ensemble de ces révolutions donne 1068 cas de scintillations.

#### DISTRIBUTION STATISTIQUE DES SCINTILLATIONS

Introduisons tout d'abord le degré de scintillations, que nous définirons comme étant le rapport du nombre de cas de scintillations observés au nombre de révolutions enregistrées dans une station. On trouve que le degré de scintillations est de 1,7 au Val-Joyeux, 1,9 à Athènes, 2,2 à Kjeller et 2,8 à Kiruna. On peut en déduire grossièrement que la probabilité de trouver des

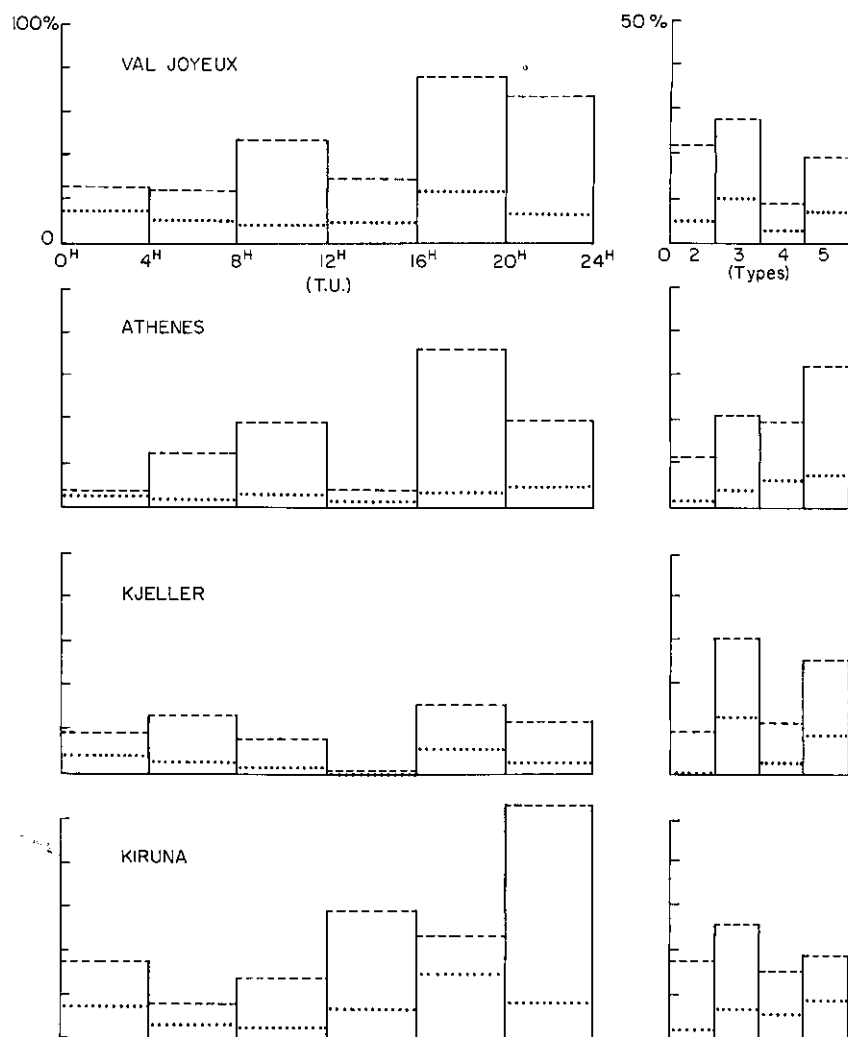


FIG. 7 Occurrence des scintillations en fonction de l'heure et du type pur un indice d'activité magnétique journalier. En pointillé pour  $K = 0$ , en trait hachuré pour  $K = 1$

scintillations est presque deux fois plus forte à la stations de Kiruna qu'à la station du Val-Joyeux.

Les tableaux 1, 2, 3 et 4 donnent les cas de scintillations pour chaque station, suivant la tranche horaire, le type de scintillations et la valeur de  $K$  (indice d'activité magnétique journalier). Des pourcentages (marqués sur le tableau pour cent TG) ont été calculés suivant le nombre de cas observés dans chacune des stations. Ces tableaux ont été fait à partir des seuls cas de propagation quasi longitudinale. Dans la bande des 40 MHz, l'angle  $\theta$  entre la direction du champ magnétique et la direction de propagation doit satisfaire les inégalités  $\theta > 91^\circ$  ou  $\theta < 89^\circ$ . Si :  $89^\circ < \theta < 91^\circ$ , nous sommes dans les cas de propagation transversale. Ces derniers, observés ici, sont assez rares; en pourcentage du total, on trouve : Val-Joyeux  $< 1$  pour cent, Kjeller  $< 2,7$  pour cent, Athènes  $< 0,5$  pour cent, Kiruna  $< 1,2$  pour cent.

Des tableaux précédents on tire une première série d'histogrammes donnant le nombre de cas de scintillations (échelle totale = 100 cas) en fonction de la tranche horaire pour  $K = 0$  et  $K = 1$  pour chaque station; un seconde série donnant la répartition des 4 types de scintillations considérées Fig. 7. On voit que l'on a successivement, dans l'ordre d'importance d'apparition, les cas suivants:

$$\left. \begin{array}{l} K = 1 \quad S = 3 \\ K = 1 \quad S = 5 \\ K = 1 \quad S = 2 \\ K = 1 \quad S = 4 \end{array} \right\} \begin{array}{l} f_s < 1 \text{ Hz} \\ f_s > 1 \text{ Hz} \end{array} \quad \begin{array}{l} K = 0 \quad S = 3 \text{ et } S = 5 \\ K = 0 \quad S = 4 \\ K = 0 \quad S = 2 \end{array}$$

Dans ces derniers on note que les types 3 et 5 sont prépondérants dans chacune des stations, ce qui tendrait à diminuer l'importance de l'amplitude des perturbations du signal radioélectrique. On constate d'autre part une inversion dans l'ordre d'importance pour  $S = 2$  et  $S = 4$  selon la valeur de l'indice d'activité magnétique. D'une façon générale, pour un indice d'activité magnétique journalier nul, il y a beaucoup moins de scintillations que pour  $K = 1$ .

L'examen de la Fig. 7, par tranche horaire, met en évidence le minimum observé pour la tranche horaire 12 — 16 h à Kjeller. Ceci est vérifié à Athènes sauf pour  $K = 0$  et  $S = 5$ , ainsi qu'au Val-Joyeux, qui se dédouble pour la tranche 20 — 24 h et pour  $K = 1$  et  $S = 3$  d'une part, et d'autre part pour  $K = 1$  et  $S = 4$ . En revanche, le minimum est déplacé dans la tranche horaire 4 — 8 h pour la station de Kiruna. Par ailleurs, le Val-Joyeux et Kiruna ont tendance à observer un seul maximum de scintillations (entre 16 et 24 h).

Par type de scintillation, on trouve la répartition suivante :  $S = 3$  : C'est le cas le plus fréquent pour le Val-Joyeux et Kiruna; avec un seul maximum très marqué entre 16 h et 20 h (Val-Joyeux) ou 20 h et 24 h (Kiruna pour  $K = 1$ ). On observe une plus grande répartition dans la journée pour Athènes et Kjeller avec le même maximum; mais atténué et, par contre, un minimum très marqué entre 12 h et 16 h.

$S = 5$  : C'est le cas le plus fréquent à Athènes et à Kjeller. On observe un maximum entre 16 h et 20 h, et un minimum entre 4 h et 8 h pour Le Val-Joyeux  $K = 0$  et Kiruna  $K = 1$ .

TABLEAU I

## VAL-JOYEUX

0-4	4-8	8-12	12-16	16-20	20-24	K	S	Total	% T.G.
1	—	1	2	5	6	0	2	15	4,3
6	3	—	4	14	5	0	3	32	9,2
2	1	3	1	1	—	0	4	8	2,3
5	6	4	2	4	2	0	5	23	6,6
14	10	8	9	24	13	<b>Total</b>		78	22,5
5	4	17	12	14	22	1	2	74	21,4
11	9	13	4	34	26	1	3	97	28,0
2	3	9	2	8	6	1	4	30	8,7
7	8	8	11	20	13	1	5	67	19,4
25	24	47	29	76	67	<b>Total</b>		268	77,4
39	34	55	38	100	80	<b>K = 0 &amp; 1</b>		346	100
						<b>Total</b>			
11,3	9,8	15,9	11,0	28,9	23,1	% T.G.			
<b>K = 0 &amp; 1</b>									
		<b>S</b>		<b>Total</b>		<b>% T.G.</b>	<b>Degré de scintillations</b>		
		2		89		25,7	0,4		
		3		129		37,3	0,6		
		4		38		11,0	0,2		
		5		90		26,0	0,5		



ETUDE DE L'AMPLITUDE DU CHAMP RADIOELECTRIQUE

TABLEAU 2

ATHENES

0-4	4-8	8-12	12-16	16-20	20-24	K	S	Total	% T.G.
1	—	—	—	1	—	0	2	2	1,0
2	—	1	—	2	2	0	3	7	3,4
—	3	3	1	2	2	0	4	11	5,4
2	1	1	2	2	5	0	5	13	6,4
5	4	5	3	7	9	Total		33	16,3
2	4	5	1	7	4	1	2	23	11,3
1	8	7	1	13	13	1	3	43	21,2
—	5	10	2	14	8	1	4	39	19,2
4	8	17	4	18	14	1	5	65	32,0
7	25	39	8	52	39	Total		170	83,7
12	29	44	11	59	48	K = 0 & 1		203	100
						Total			
5,9	14,2	21,7	5,4	29,1	23,6	% T.G.			

K = 0 & 1	S	Total	% T.G.	Degré de scintillations
	2	25	12,3	0,2
	3	50	24,6	0,5
	4	50	24,6	0,5
	5	78	38,4	0,7

TABLEAU 3

KJELLER

0-4	4-8	8-12	12-16	16-20	20-24	K	S	Total	% T.G.
—	—	—	—	—	—	0	2	0	0
4	3	3	—	5	3	0	3	18	12,1
1	—	—	—	—	2	0	4	3	2,0
3	2	—	—	6	1	0	5	12	8,0
8	5	3	0	11	6	<b>Total</b>		33	22,1
1	4	1	—	4	4	1	2	14	9,4
8	8	9	—	14	7	1	3	46	30,9
2	6	1	—	5	3	1	4	17	11,4
7	8	5	1	8	10	1	5	39	26,1
18	26	16	1	31	24	<b>Total</b>		116	77,8
26	31	19	1	42	30	<b>K = 0 &amp; 1</b>		149	100
						<b>Total</b>			
17,4	20,8	12,7	0,7	28,2	20,1	% T.G.			

K = 0 & 1	S	Total	% T.G.	Degré de scintillations
	2	14	9,4	0,2
	3	64	42,9	0,9
	4	20	13,4	0,3
	5	51	34,2	0,8

TABLEAU 4

KIRUNA

0-4	4-8	8-12	12-16	16-20	20-24	K	S	Total	% T.G.
1	0	1	1	3	2	0	2	8	2,2
3	0	1	4	8	7	0	3	23	6,2
4	2	3	4	6	1	0	4	20	5,4
6	4	0	4	12	6	0	5	32	8,6
14	6	5	13	29	16	<b>Total</b>		83	22,4
7	3	6	11	4	33	1	2	64	17,3
10	2	9	21	15	40	1	3	97	26,2
6	7	8	14	5	16	1	4	56	15,1
11	3	4	12	23	17	1	5	70	18,9
34	15	27	58	47	106	<b>Total</b>		287	77,6
48	21	32	71	76	122	<b>K = 0 &amp; 1</b>		370	100
						<b>Total</b>			
13,0	5,7	8,6	19,2	20,5	33,0	% T.G.			

<b>K = 0 &amp; 1</b>	<b>S</b>	<b>Total</b>	<b>% T.G.</b>	<b>Degré de scintillations</b>
	2	72	19,4	0,5
	3	120	32,4	0,9
	4	76	20,5	0,6
	5	102	27,6	0,8

$S = 2$  : On observe les mêmes tendances que pour  $S = 3$

$S = 4$  : On observe les mêmes tendances que pour  $S = 5$ ; sauf pour Kiruna où le maximum de 16 h — 20 h est remplacé par un minimum.

#### REPARTITION GEOGRAPHIQUE DES SCINTILLATIONS AUTOUR DE CHAQUE STATION

Le tableau 5, où l'on a indiqué dans chaque case le pourcentage de cas observés, donne cette répartition géographique.

La station d'Athènes observe toujours un maximum de scintillation vers le sud, sauf pour le type de scintillation  $S = 5$  où le maximum est au Nord.

Kiruna observe toujours un maximum vers le Nord (maximum très marqué pour  $S = 3$  et  $S = 2$ ) sauf pour le type de scintillation  $S = 5$  et  $S = 4$  où l'on trouve deux maximums pour  $K = 1$ , au Nord et au Sud: donc un comportement inverse de celui d'Athènes. Ajoutons que Kiruna présente toujours un maximum secondaire vers l'ouest.

Pour Kjeller, la répartition géographique des scintillations est assez uniforme avec cependant un minimum à l'est comme pour toutes les stations. On note également un maximum marqué au Nord pour  $S = 3$  et  $K = 0$ , ainsi que pour tous les types pour  $K = 1$ .

On note au Val-Joyeux une répartition relativement uniforme avec cependant un maximum vers le Nord et un maximum secondaire vers le Sud. Le maximum au Nord est plus accentué pour  $S = 3$  comme pour Kjeller et Kiruna.

TABLEAU 5

$K = 0$

	$S = 2$				$S = 3$				$S = 4$				$S = 5$			
	S	W	E	N	S	W	E	N	S	W	E	N	S	W	E	N
Val-Joyeux	47	0	18	35	14	0	30	56	0	0	70	30	8	0	36	56
Athènes	50	0	25	25	67	0	22	11	46	31	23	0	28	5	28	38
Kjeller	0	0	0	0	18	0	13	68	100	0	0	0	28	0	28	43
Kiruna	9	9	27	55	16	12	16	56	25	13	25	37	8	17	18	36

$K = 1$

	$S = 2$				$S = 3$				$S = 4$				$S = 5$			
	S	W	E	N	S	W	E	N	S	W	E	N	S	W	E	N
Val-Joyeux	27	0	35	38	9	1	41	49	11	0	50	39	17	0	44	39
Athènes	61	13	8	17	51	29	2	18	53	22	12	12	31	30	15	24
Kjeller	38	6	31	25	33	2	15	50	30	0	20	50	24	2	31	42
Kiruna	5	12	40	43	11	5	28	56	27	6	38	29	35	4	26	35

Plus généralement on peut noter la même tendance dans toutes les stations pour les cas  $S = 3$  et  $S = 5$  quelque soit  $K$ :

— tendance très nette à un maximum vers le Nord des stations pour  $S = 3$  sauf Athènes dont le maximum est vers le Sud

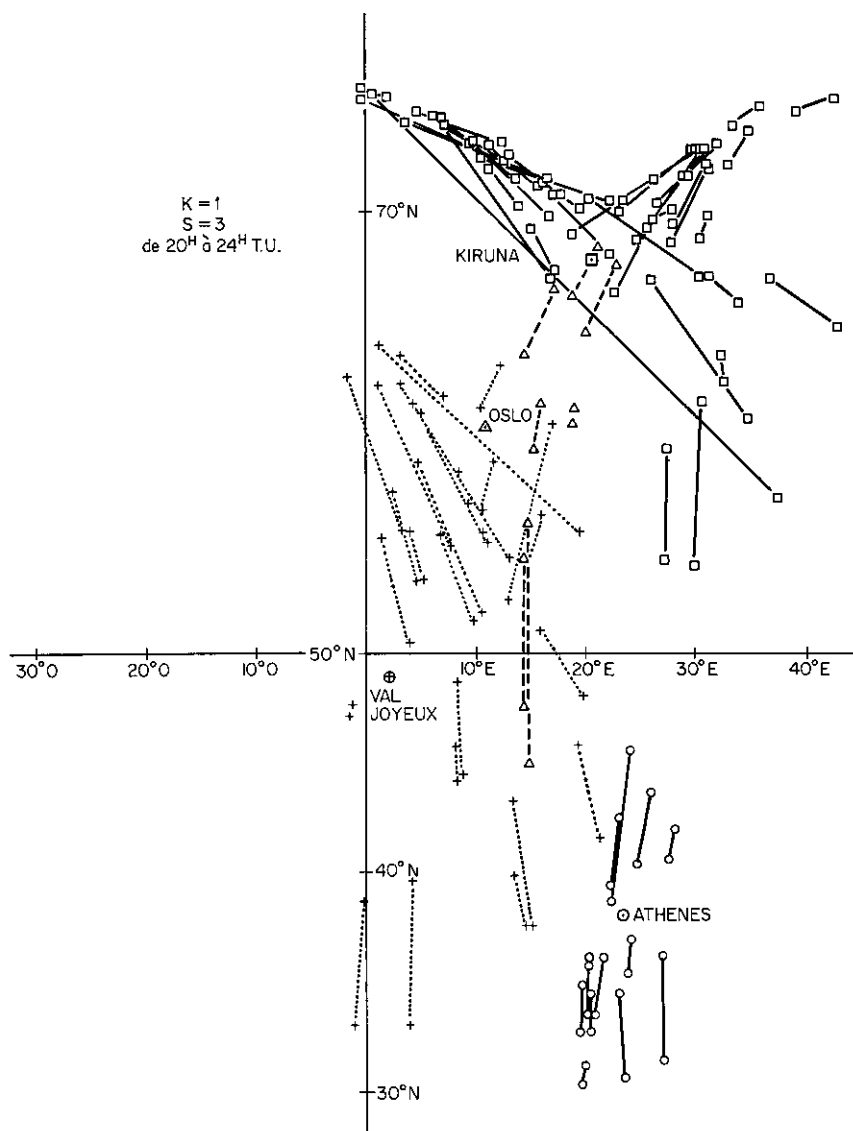


FIG. 8 Représentation géographique des zones de scintillations pour le type  $S = 3$

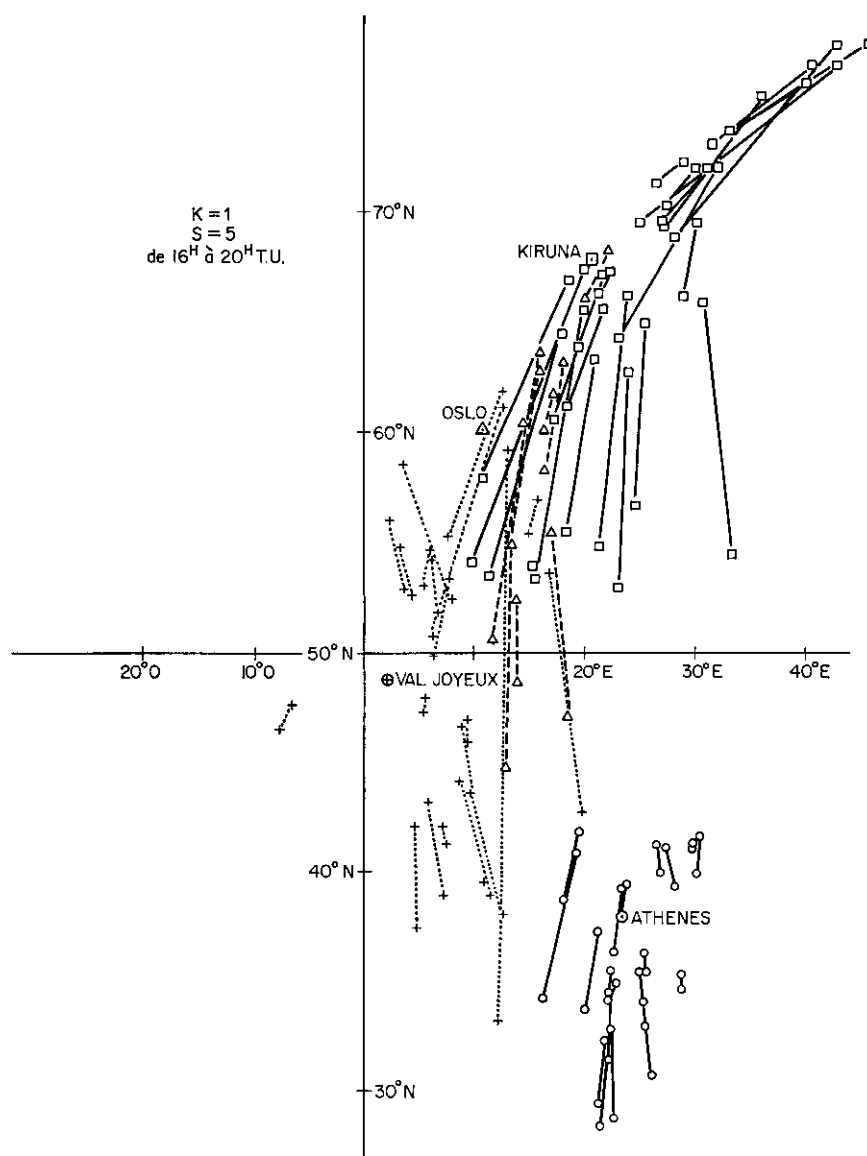


FIG. 9 Représentation géographique des zones de scintillations pour le type  $S = 5$

— tendance à une augmentation importante de la scintillation vers le Sud pour  $S = 5$  dans toutes les stations sauf pour Athènes qui présente alors un maximum vers le Nord pour  $K = 0$ .

Les types de scintillations  $S = 2$  et  $S = 4$  se présentent beaucoup moins souvent. On constate que pour le Val-Joyeux et Kjeller elles sont également réparties entre le Nord et le Sud de la station. Pour Athènes le maximum a lieu vers le Sud pour  $S = 2$  et  $S = 4$ . Pour Kiruna on a un maximum au Nord et un maximum secondaire vers l'Ouest.

#### REPRESENTATION GEOGRAPHIQUE DES ZONES DE SCINTILLATIONS

En portant la latitude en ordonnées et la longitude en abscisses, il est possible d'obtenir des graphiques montrant les limites temporelles des trajectoires subionosphériques dans lesquelles ont eu lieu des scintillations d'un type donné. On trace ensuite pour chaque type, autant de graphique qu'il y a de tranches horaires choisies et pour chaque valeur de l'indice d'activité magnétique journalier.

Nous donnons à titre l'exemple les diagrammes correspondant aux types de scintillations,  $S = 3$  et  $S = 5$  pour les tranches horaires respectives: 20 h — 24 h et 16 — 20 h Fig. 8 et 9. La figure 8 montre une représentation des zones de scintillations s'étendant de part et d'autre des trajectoires du satellite. Selon les passages montants ou descendants de ce satellite polaire on peut distinguer deux faisceaux partant ensemble du Sud et se terminant l'un au N-O l'autre au N-E de Kiruna. Dans le cas de la Fig. 9 il ne subsiste qu'un seul de ces faisceaux, celui qui converge vers le N-E de Kiruna. Il est à noter que cette convergence est le fait, à Kiruna, de révolutions de longitude Ouest à l'équateur de l'ordre de  $0^\circ$ , tandis que le Val-Joyeux tout en présentant également des révolutions venant de quelques  $150^\circ$ , contribue ainsi que les autres stations, à l'établissement de cette convergence.

On observe d'autre part que le type de scintillation  $S = 3$  a tendance à apparaître au Nord-Ouest des stations (sauf pour Athènes) les arcs de trajectoire scintillants tendant à s'orienter en forme de V dont la pointe prend la direction du Nord-Ouest de la station, dans une région pour laquelle l'angle  $\theta$  est voisin de  $90^\circ$ . Ce résultat montre que plus la scintillation observée est éloignée, plus le secteur angulaire dans lequel on le trouve en azimut est aigu, la direction de ce vecteur allant vers les valeurs de  $\theta$  qui approchent de  $90^\circ$ . Les scintillations du type  $S = 3$  apparaissent également dans l'Ouest et le Sud-Ouest des stations, mais cette apparition est alors fonction de l'heure. Les scintillations du type  $S = 5$  ont tendance à apparaître de 4 h à 12 h dans le Nord-Ouest des stations comme pour le type  $S = 3$ ; mais elles tendent à apparaître de 12 h à 24 h vers le Sud dans un secteur d'azimut allant du Sud au Sud-Ouest pour Kiruna et Kjeller; plus ouvert et allant du Sud-Est au Sud-Ouest pour le Val-Joyeux. Il faut cependant noter que l'intensité d'apparition des ces scintillations est fonction de l'heure. Par exemple : de 12 à 16 h le type  $S = 3$  est plus au nord que le type  $S = 5$ , de 16 à 20 h c'est le type  $S = 5$  qui est plus au Nord que le type  $S = 3$ , tandis que de 20 h à 24 h c'est à nouveau le type  $S = 3$  qui est plus au Nord que le type  $S = 5$ . On note également pour le Val-Joyeux quelques scintillations dans l'Ouest en fonction de l'heure.

On peut d'autre part relever des zones géographiques dans lesquelles se

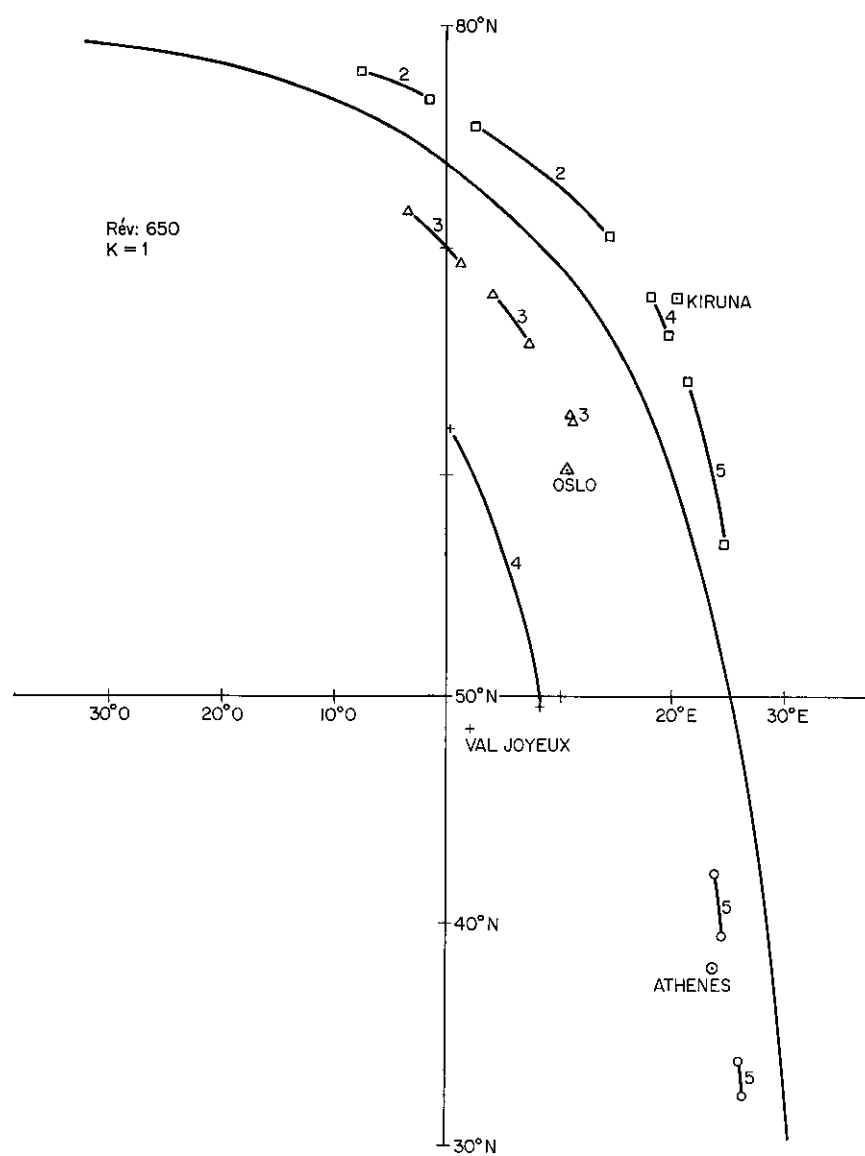


FIG. 10 Représentation géographique des zones de scintillations de la révolution n° 650. Les chiffres indiquent le type de scintillations



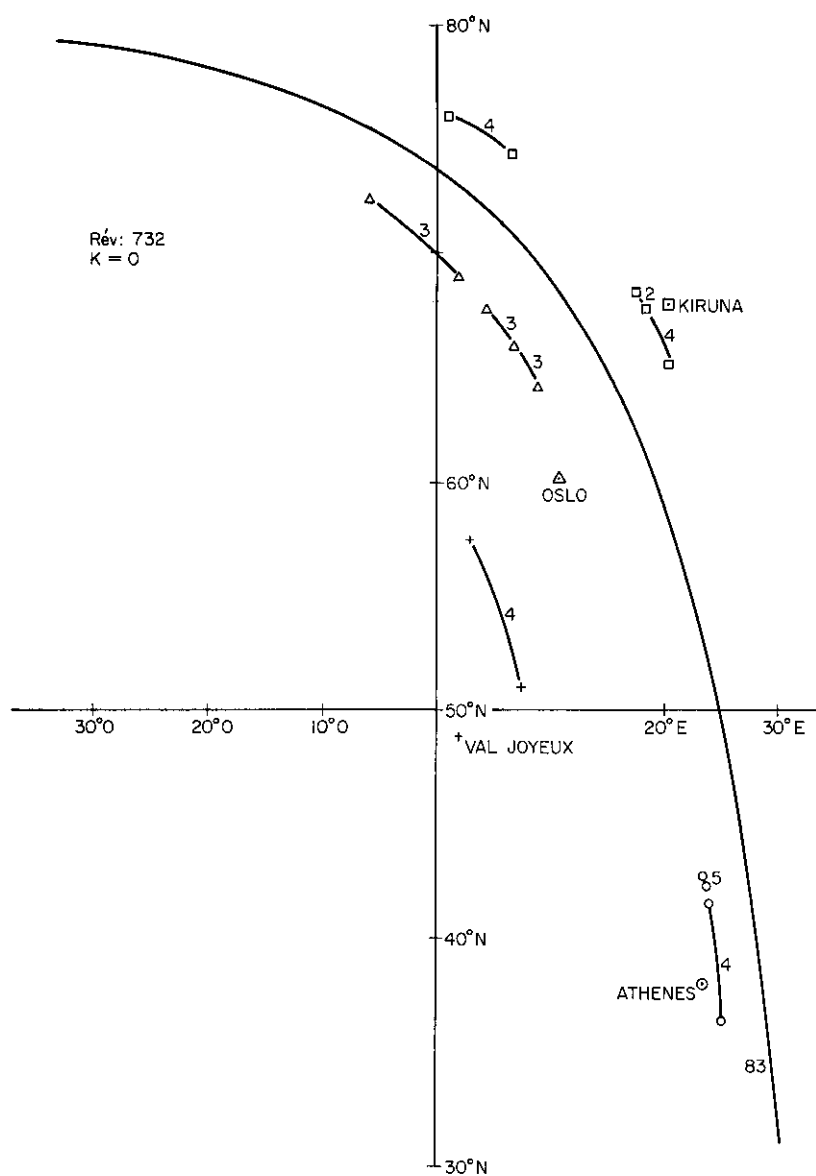


FIG. 11 Représentation géographique des zones de scintillations de la révolution n° 732. Les chiffres indiquent le type de scintillations

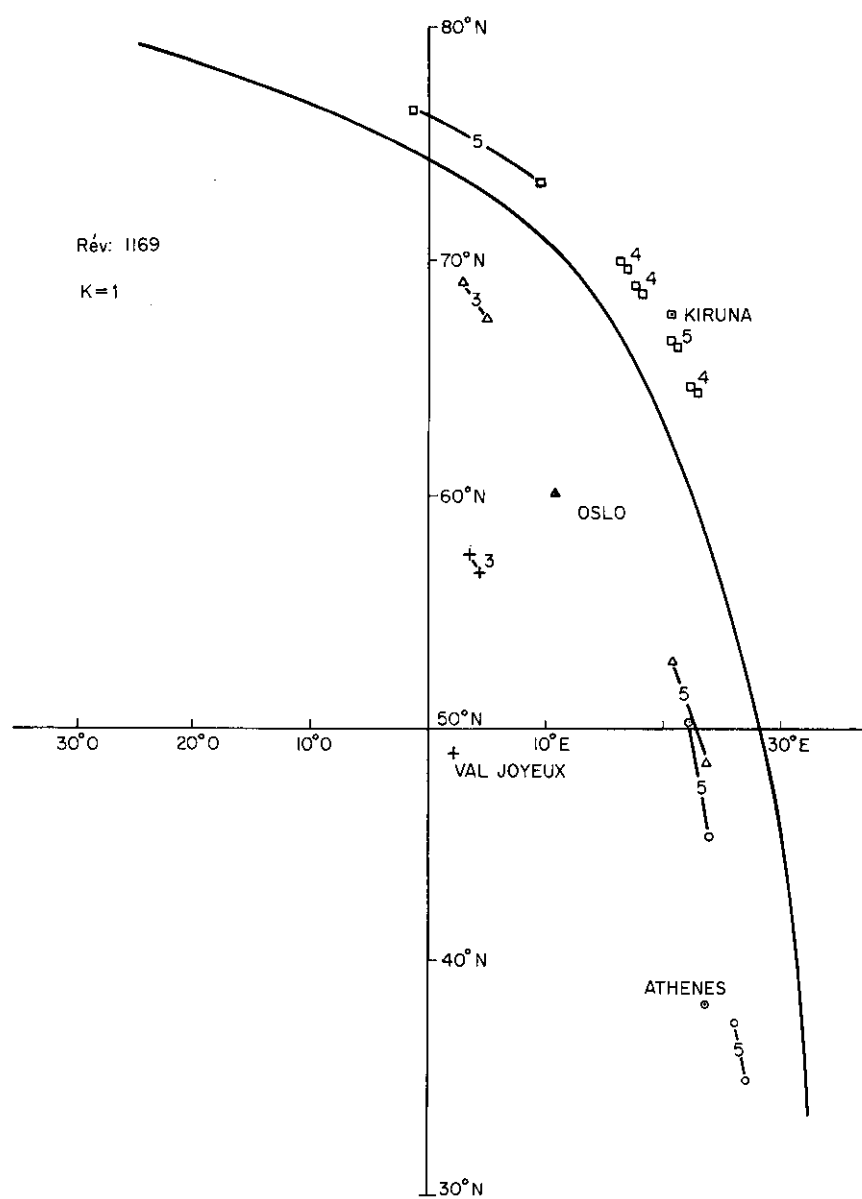


FIG. 12 Représentation géographique des zones de scintillations de la révolution n° 1169. Les chiffres indiquent le type de scintillations

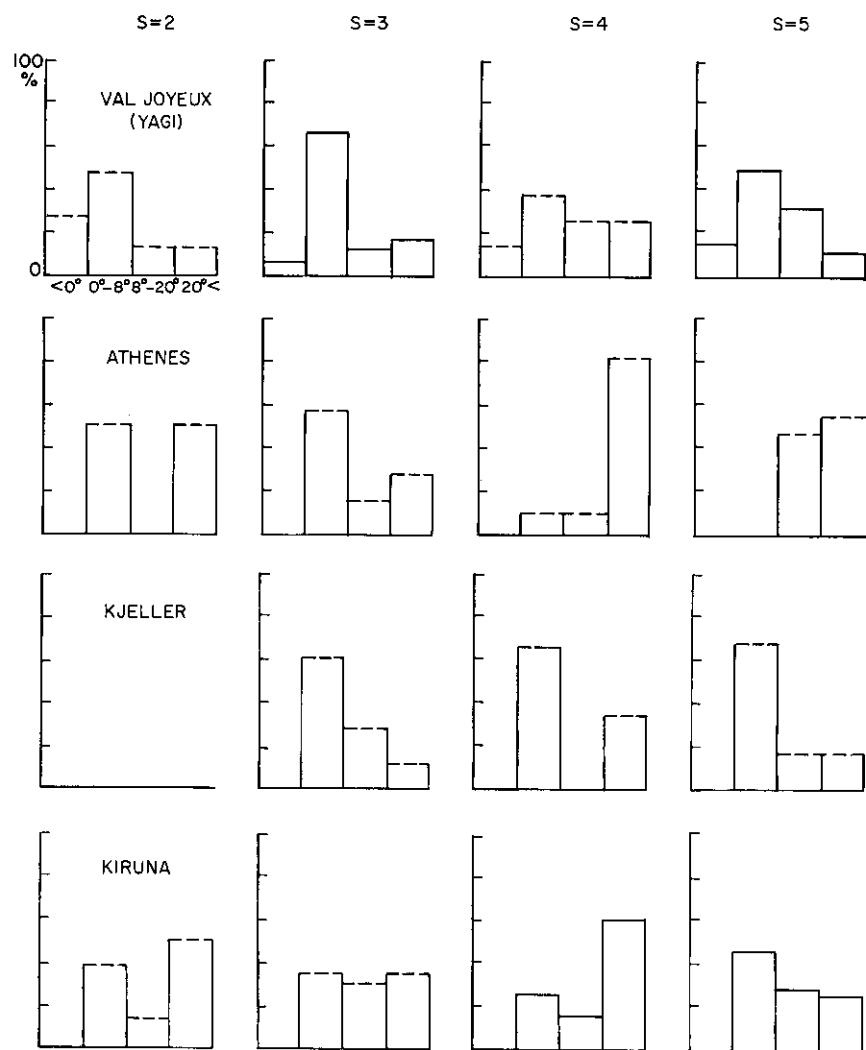


FIG. 13 Occurrence des scintillations en % pour chaque type de scintillation en fonction de l'angle d'élévation pour  $K = 0$ . En pointillé : le nombre de cas est inférieur à 20

présentent des scintillations de même type ou de types différents vues de deux ou trois stations différentes; mais ceci d'une manière statistique à l'intérieur d'un groupe horaire. La zone principale se situe au Nord du Val-Joyeux entre  $53^\circ$  et  $63^\circ$  de latitude Nord et entre  $0^\circ$  et  $13^\circ$  de longitude Est. Elle intéresse les observations de Kiruna, Kjeller et du Val-Joyeux. La deuxième zone se trouve dans le Sud-Est de Paris entre  $40^\circ$  et  $44^\circ$  de latitude Nord entre  $19^\circ$  et  $22^\circ$  de longitude Est.

Une autre façon de rechercher une représentation géographique des scintillations, consiste à utiliser un graphique semblable à ceux des Figs. 9 et 10, mais en se limitant à une seule révolution du satellite. Les figures 10, 11, 12 donnent trois exemples d'une telle représentation. Les trois révolutions utilisées ont presque la même longitude Ouest à l'équateur, donc des trajectoires presque semblables, mais avec des intervalles de temps de plusieurs semaines. Si l'on superpose ces trois figures, on trouve alors des zones relativement étroites où la répétition des scintillations enregistrées. Evidemment, ces zones sont aplaties, puisque les calculs ont été faits avec une hauteur d'ionosphère constante. Quoiqu'il en soit, le fait d'utiliser des hauteurs différentes, conduirait à un élargissement de la zone, mais non pas à une extension le long de la trajectoire subionosphérique.

#### DISTRIBUTION STATISTIQUE EN FONCTION DE L'ANGLE D'ELEVATION ET DU TYPE

Pour chaque valeur de  $K$  d'une part et pour chaque type de scintillation d'autre part, nous avons tracé une série d'histogrammes pour chacune des stations suivant la valeur de l'angle d'élévation  $E$  compris dans les tranches suivantes :

$$E < 0^\circ, 0 < E < 8^\circ, 8^\circ < E < 20^\circ, E > 20^\circ$$

La première série est faite pour  $K = 0$ , Fig. 13, la seconde est faite pour  $K = 1$ , Fig. 14, et la dernière est faite sur la totalité des cas sans tenir compte de l'individualité des stations d'observations, Fig. 15.

D'après les Figs. 13 et 14 nous constatons que seule la station du Val-Joyeux possède des enregistrements de scintillations lorsque les angles d'élévation sont négatifs. La majeure partie des enregistrements de scintillations ont lieu dans cette station sous des angles d'élévation plus petit que  $8^\circ$ , quelque soit la valeur de  $K$ .

La station d'Athènes possède une répartition assez peu marquée sauf dans le cas  $S = 4$  qui apparaît le plus souvent pour les angles d'élévation très élevés quelque soit la valeur de  $K$ , mais, il faut noter une tendance d'apparition des scintillations plus importante vers les angles d'élévation faibles pour  $K = 0$ . La station de Kjeller possède peu de scintillations du type  $S = 2$  et  $S = 4$ . Pour les autres types l'occurrence est nettement plus forte vers les angles d'élévation faible. Pour Kiruna, quelque soit le type de scintillation ou la valeur de  $K$ , la répartition est beaucoup plus uniforme que dans les autres stations. Il faut cependant noter une tendance d'occurrence plus marquée pour  $S = 2$  et  $S = 4$  vers les grandes valeurs d'élévation et pour  $S = 3$  et  $S = 5$  vers les faibles valeurs de celle-ci.

On remarque sur la Fig. 15 une répartition presque identique des types  $S = 3$  et  $S = 5$  quelle que soit la valeur de  $K$  avec un maximum

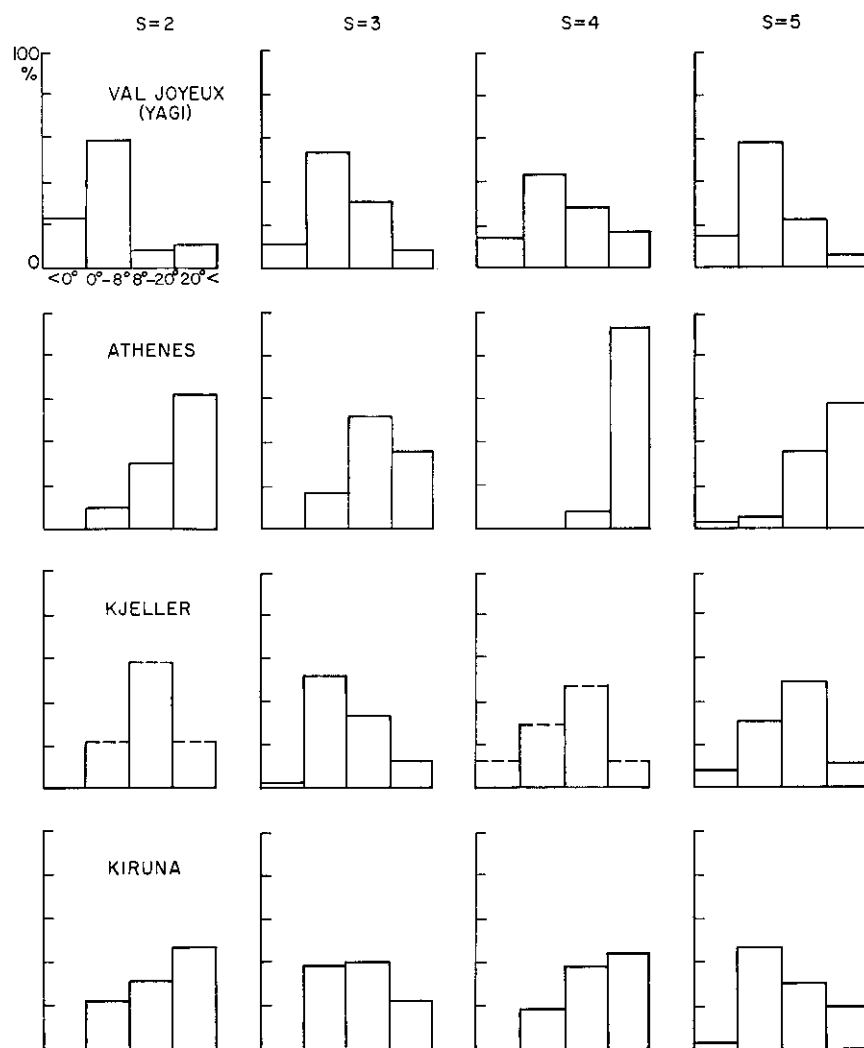


FIG. 14 Occurrence des scintillations en % pour chaque type de scintillation en fonction de l'angle d'élévation pour  $K = 1$ . En pointillé : le nombre de cas est inférieur à 20

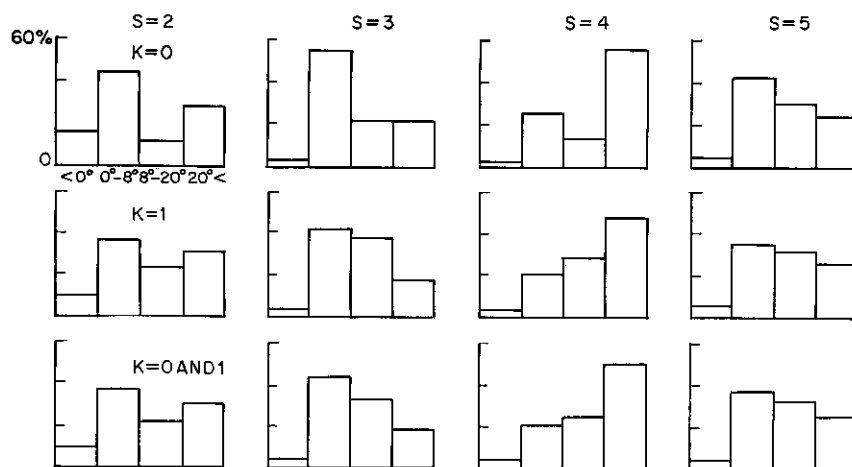


FIG. 15 Occurrence des scintillations en % pour chaque type en fonction de l'angle d'élévation. Les stations ne sont pas ici particularisées

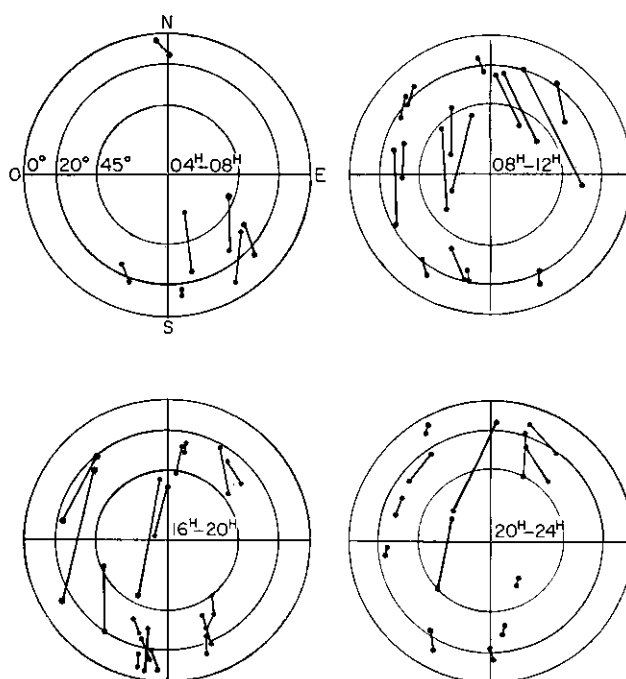


FIG. 16 Exemple de représentation en coordonnées polaires des zones de scintillations, pour la station d'Athènes pour  $K = 1$ , du type  $S = 5$ . Angle d'élévation en fonction de l'angle d'azimut

d'occurrence dans la zone comprise entre 0 et 8°. La zone pour laquelle l'angle d'élévation est négatif apparaît sous une faible occurrence du fait que seule la station du Val-Joyeux possède des enregistrements sous ces angles. Pour le type  $S = 2$  on trouve un maximum entre 0 et 8° et un maximum secondaire pour les angles plus grands que 20°, tandis que l'on observe un minimum pour la zone 8 — 20°. Pour les scintillations du type  $S = 4$ , on remarque une tendance semblable à la précédente, le maximum et le maximum secondaire étant inversés. Mais ceci n'a lieu que pour  $K = 0$  ; pour  $K = 1$ , on observe un maximum pour les grandes valeurs de l'angle d'élévation et une diminution de l'occurrence au fur et à mesure de la décroissance de l'angle d'élévation.

La répartition des cas de scintillations étant plus importante pour  $K = 1$  que pour  $K = 0$ , la répartition totale est donc plus proche de celle de  $K = 1$  que celle de  $K = 0$ .

#### CONCLUSION

Dans ce mémoire, nous avons surtout exposé les résultats bruts que l'on peut obtenir en comparant les données de plusieurs stations européennes dont les zones d'écoute sont recoupées par celle de la station du Val-Joyeux. Il est bien évident qu'une analyse plus fine devrait porter sur un plus grand nombre de cas, c'est à dire sur une période d'écoute s'étendant au moins sur une année. Quoiqu'il en soit, nous avons observé des tendances plus ou moins marquées qu'il était intéressant de signaler dès maintenant. En particulier, le renforcement des scintillations lorsque l'indice d'activité magnétique journalier est important. Cette tendance générale n'est pas incompatible avec le fait que nous avons relevé concernant l'indice d'activité magnétique par tranche horaire. Nous avons en effet remarqué que dans une zone azimutale située entre le Sud-Est et le Sud de la station les scintillations disparaissent pour des angles d'élévation de faible valeur. De même en ce qui concerne la différence de nature entre les scintillations qui apparaissent au Nord et au Sud des stations situées au Sud de l'Europe, par rapport aux stations situées au Nord de l'Europe. C'est ainsi que les scintillations du type  $S = 2$  sont très importantes au Sud puis au Nord de la Station du Val-Joyeux, lorsque les angles d'élévations sont faibles. Cette tendance est moins nette pour  $K = 1$ , avec une inversion du Nord au Sud. En revanche, les autres types de scintillations sont surtout vus dans le Nord de la station. Enfin, il est curieux de constater l'importance relative des types 3 et 5, quelque soit la valeur de l'indice d'activité magnétique journalier.

Nous tenons à remercier M. le Professeur Vassy qui nous a permis de mener à bien cette étude, ainsi que M. F. Bertin pour l'aide qu'il nous a apportée dans la conduite des calculs sur ordinateur. Nous tenons à remercier également les organismes qui nous ont fourni les moyens nécessaires à cette étude: l'Agard et le Centre National d'Etudes Spatiales.

#### DISCUSSION

M. ANASTASSIADES — Le cas d'Athènes au point de vue de l'apparition des scintillations se présente d'une façon particulière. Avez-vous une explication à donner?

J. PAPET-LEPINE — Nous n'avons pas encore trouvé une explication satisfaisante. Les singularités observées à Athènes par rapport aux autres stations

étaient particulièrement frappantes, il nous a semblé intéressant d'en présenter dès maintenant les principaux aspects.

K. RAWER – Je voudrais bien savoir si la scintillation et sa probabilité dépendent éventuellement de l'aspect, c'est à dire le l'angle entre le champ magnétique terrestre et la direction de propagation. On observe l'effet de scintillation par comparaison à un effet dépendant de cet angle, à savoir l'effet Faraday. Au cas où ceci aurait été étudié, il semblerait indiqué de ré-étudier l'influence du caractère magnétique en tenant compte de la distinction des angles d'aspect.

J. PAPET-LEPINE – Le calcul de l'angle  $\theta$  entre le champ magnétique terrestre et la direction de propagation est fait automatiquement par le programme sur ordinateur utilisé dans cet exposé en particulier, pour connaître les cas de propagation transversale. Une étude comparative avec cet angle nécessite un certain nombre de précautions. Quoiqu'il en soit, cette étude actuellement en soit, cette étude actuellement en cours tiendra compte non seulement de cet angle, mais également du produit  $B \cos \theta$  qui intervient précisément dans l'effet Faraday.

W. DIEMINGER – In recording the Faraday rotation of satellite signals we have observed quite frequently bursts of field strength when the satellite approached the horizon and smaller bursts when the satellite was already several degrees below the horizon. Probably similar observations have been made by other observers, but no explanation has been given in the literature so far. May I ask whether anyone in the audience can offer an explanation.

P. F. CHECCACCI – We have also observed this effect and we attribute it to reflections of the satellite signals from meteor trails in the ionosphere.

W. T. BLACKBAND – If this effect is due to meteor bursts, then it should show a diurnal variation with a maximum at 06 hours local time.

E. VASSY – A propos des recherches relatives aux hétérogénéités de l'ionosphère, il m'a été demandé de rappeler l'intérêt que présente le Join Satellite Studies Group.

Ce groupe prit naissance dès le lancement du 1er Sputnik en octobre 1957 sur l'initiative du Dr. Jules Aarons de l'U.S. Air Force Research Lab., de Cambridge Mass. Il comprenait à l'origine outre Cambridge, les équipes de Breisach (Allem. de l'W), Jodrell Bank (Grande Bretagne) Florence (Italie), Kjeller (Norvège), Kiruna (Suède) et Val-Joyeux (France). A l'origine il y avait aussi le Japon.

Notre rôle était alors d'enregistrer l'effet Doppler et d'envoyer chaque jour à l'U.S. Air Force Laboratory l'instant d'approche à la distance minimale et la pente de la courbe Doppler, de façon à permettre la restitution de la trajectoire. C'était le projet "Spacetrack".

Ces travaux durèrent près d'une année jusqu'à ce que le système Minitrack mis en place permette de faire le tracking d'une manière plus rapide et plus efficace.

Mais l'enregistrement des courbes Doppler avait montré les nombreuses irrégularités dues à des hétérogénéités de l'ionosphère. Aussi, libérées du tracking, les équipes du groupe ont pu se consacrer à une étude de l'ionosphère.

Il est en effet extrêmement précieux de disposer des enregistrements à l'aide d'appareillages standardisés de la courbe Doppler et du champ des satellites, présentant l'effet Faraday, et cela en des points convenablement



répartis, surtout en Europe. Il est alors possible par triangulation d'apprécier l'altitude et l'étendu des hétérogénéités.

Les travaux du groupe qui avaient été patronnés initialement par l'U.S.A.F., le furent ensuite par le Bureau des Affaires Scientifiques du NATO, puis par l'AGARD. Avec le temps, leur financement fut de plus en plus assuré avec des moyens nationaux. Ce patronnage efficace devait permettre un développement des travaux du groupe et du groupe lui-même. C'est ainsi que depuis longtemps déjà, fut ajoutée l'équipe d'Athènes, et depuis avril dernier nous sommes 14 avec une équipe au Danemark, une seconde en Grande Bretagne, une autre en Espagne, en Israel et même en Afrique.

Le travail des équipes est facilité par un bulletin de liason, édité par les soins de celle de Florence, dans lequel se trouvent consignées les données relatives aux révolutions étudiées en commun, et aussi par une réunion annuelle de travail où chaque équipe apporte des kilogrammes de papier, procède à la confrontation des enregistrements et prépare le travail à effectuer pendant l'année suivante.

Evidemment, chaque équipe conserve son individualité et se consacre à une spécialisation en accord avec l'ensemble du groupe. Mais surtout, les enregistrements de chaque équipe sont à la disposition des autres équipes. D'où des échanges fréquents, des déplacements des membres des équipes. Vous en avez eu une illustration par le travail présenté par le Dr. Papet-Lepine qui est allé étudier sur place les enregistrements d'Athènes, de Kjeller et de Kiruna. Il arrive fréquemment que des enregistrements spéciaux soient demandés par telle ou telle équipe. L'étude géographique de l'ionosphère est donc largement facilitée grâce à l'AGARD et le but de mon intervention est de signaler l'existence d'une masse considérable de données et de dire qu'elles peuvent être mises à la disposition des spécialistes intéressés.

J'ajouterai qu'en outre des laboratoires du Groupe préparent des équipements de satellites pour des études spéciales; ce fut le cas par exemple pour le satellite *Orbis* de l'USAF et le satellite Italien *San Marco*. D'autres sont en cours et en projet.

Il y a là un exemple d'étude coopérative de l'ionosphère, efficace parce qu'elle n'a pas la lourdeur d'une grande association internationale, et aussi parce que les relations de travail entre ses membres sont devenues rapidement des relations d'amitié.



## CHAPTER 3-3

IONOSPHERIC RESONANCE PHENOMENA AT VHF  
AND HF, AND THEIR EFFECTS ON SPACE TELE-  
COMMUNICATIONS

IRVINE PAGHIS

Radio Physics Laboratory  
Defence Research Telecommunications Establishment  
Ottawa, Ontario, Canada

## SUMMARY

A number of ionospheric resonance phenomena have been identified by experiments in the *Alouette I* satellite. Several of these resonances have not yet been observed in laboratory plasma experiments. Satellite experiments provide some direct information about the effects of ionospheric resonances on radio-wave propagation above the F-layer maximum. Such effects depend on:

- (1) The excitation mechanism of a particular resonance.
- (2) The scale size of the excited regions.
- (3) The intensity of the resonance oscillations.

More information is needed, particularly regarding the excitation processes. A rocket instrumentation program for exciting and measuring VLF ionospheric resonances has been started, and the frequency coverage of the planned resonance observations in *Alouette II* has been extended.

## INTRODUCTION

The existence of space telecommunications systems has raised many problems associated with the optimum design of space-borne transmitters and receivers. One problem of particular interest to communications engineers and radio physicists is the effect of the ionospheric plasma on the telecommunications terminals, as well as on wave propagation between these terminals. Theoretical analysis, based on relatively simple plasma models, indicates that the ionospheric plasma has a number of modes of oscillation, or resonances, at frequencies below about 15 Mc/s. Such resonances are obviously pertinent to the design of space telecommunications systems operating near the resonant frequencies. However, the degree of correspondence between the existence and properties of the theoretical resonances, and resonances in laboratory plasmas or in the actual ionospheric plasma, is largely undetermined. For a number of practical reasons, it is difficult to study these resonances in the laboratory, although some progress has been made.

During the past three years a considerable amount of data relating to ionospheric plasma resonances has been collected by the *Alouette I* earth satellite. The purpose of this paper is to describe these satellite observations,

and to discuss the probable effects of ionospheric resonances on space telecommunications systems, operating above the height of the F-layer maximum. It must be emphasized that the *Alouette I* experiments were not specifically designed for the study of plasma resonances, and the data therefore have many limitations.

*Alouette I* (1962 Beta Alpha) was designed and constructed by the Canadian Defence Research Telecommunications Establishment, and was launched into a 1000 km circular orbit by the National Aeronautics and Space Administration (U.S.A.) on September 29, 1962, as part of a long-term international program for studying the ionized constituents of the earth's upper atmosphere. The main experiment in *Alouette I* is a high-frequency (HF) pulsed ionosonde sweeping from 0.5 to 12 Mc/s. There are also three complementary experiments; a very-low-frequency (VLF) receiver to record natural and man-made radio emissions from 0.4 to 10 kc/s, circuitry to measure the intensity of radio noise from extra-terrestrial sources, and a number of detectors for measuring the flux of energetic particles. Three years after launch all the experiments are continuing to provide high-quality data and these data are pertinent to a number of telecommunication problems (1), (2), (3).

Information on ionospheric resonances may be obtained from the output of the HF and VHF receivers, and also from the automatic gain control (AGC) voltage on the HF receiver. No data are available from 10 kc/s to about 500 kc/s; and from 0.5 to 1.0 Mc/s the data are of relatively low quality, due to the low sensitivity of the HF sounder below 1.0 Mc/s. The sounder transmissions excite resonances that appear as vertical "spikes" on the topside ionograms and on the AGC voltage of the sounder receiver. The satellite does not transmit in the VLF band, but the existence of resonances may be deduced from the frequency dispersion of discrete VLF emissions and from the cutoff frequencies of VLF noise bands. Several of the ionospheric resonances, in particular the "lower-hybrid" resonance and the "resonance trace" at twice the electron gyrofrequency, had not previously been identified either in the laboratory or in space experiments.

#### OBSERVATIONS OF IONOSPHERIC RESONANCES BY ALOUETTE I

**High frequency** – A low-latitude *Alouette I* ionogram is shown in Fig. 1. The time delay between the transmitter pulse and a pulse at the receiver output is recorded on the vertical axis. Conventionally, the vertical scale gives the apparent distance of an echoing region from the satellite; this scale, however, is somewhat misleading when ionospheric resonances are recorded. For example, the spike appearing at about 2.8 Mc/s is due to a resonance excited by the sounder pulse (4) in the vicinity of the satellite. The length of the spike (from zero range to about 500 km) is an indication of the duration of the resonance. Note that there is no obvious change in the amplitude of the reflection traces near the frequency of this resonance.

Figure 2 shows the HF resonances in somewhat more detail. The following symbols are used to identify the resonances and the reflection traces:

$nf_H, n = 1, 2, 3$	electron gyrofrequency and harmonics
$f_N$	plasma frequency

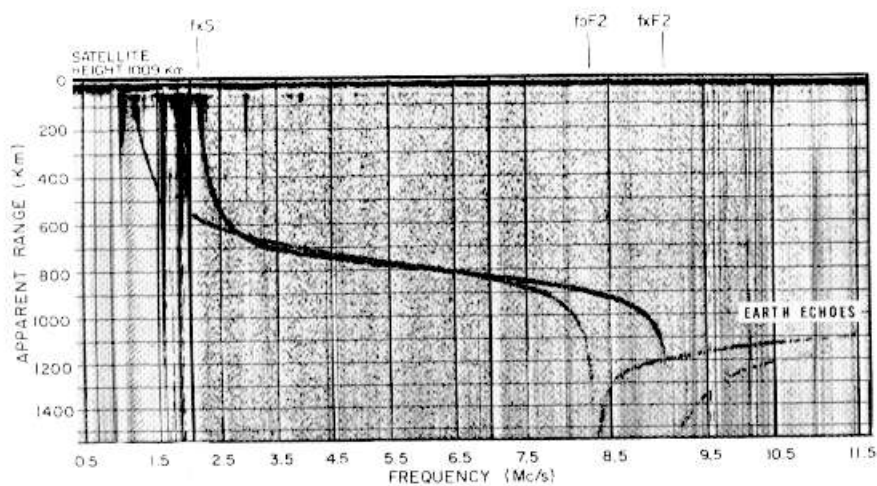


FIG. 1 *Alouette I* topside ionogram. (The vertical lines at 0.5, 1.5, 2.0, 2.5 . . . 7.0, 7.5 . . . etc. Mc/s are frequency markers)

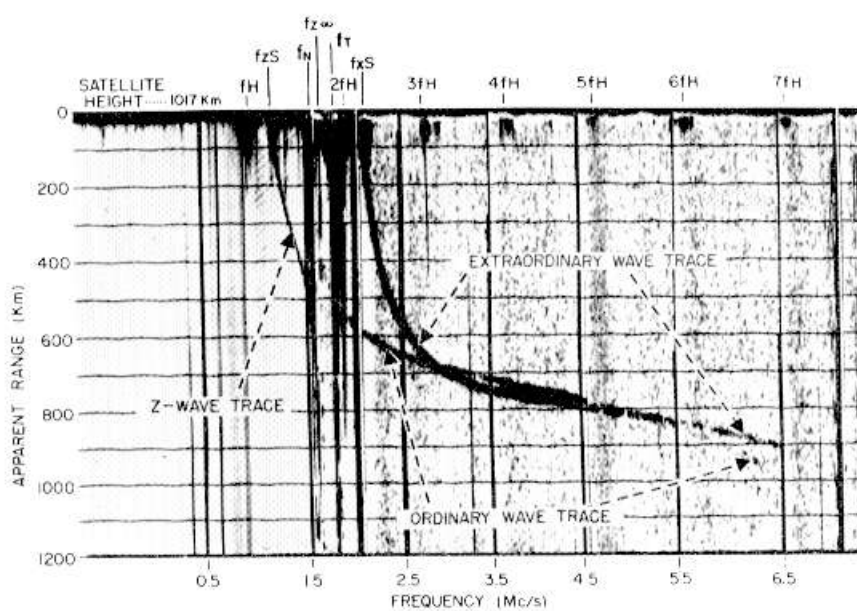


FIG. 2 Topside mid-latitude ionogram showing ionospheric resonances at the height of the satellite

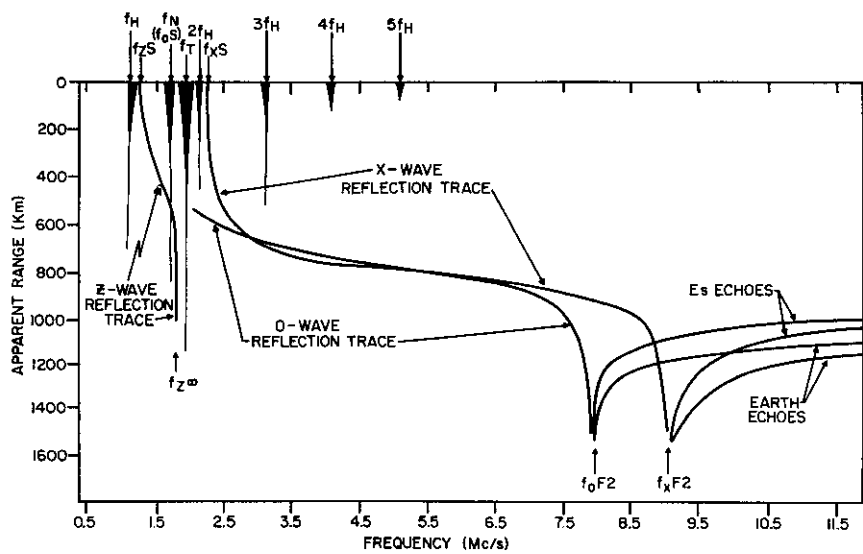


FIG. 3a Schematic equatorial ionogram

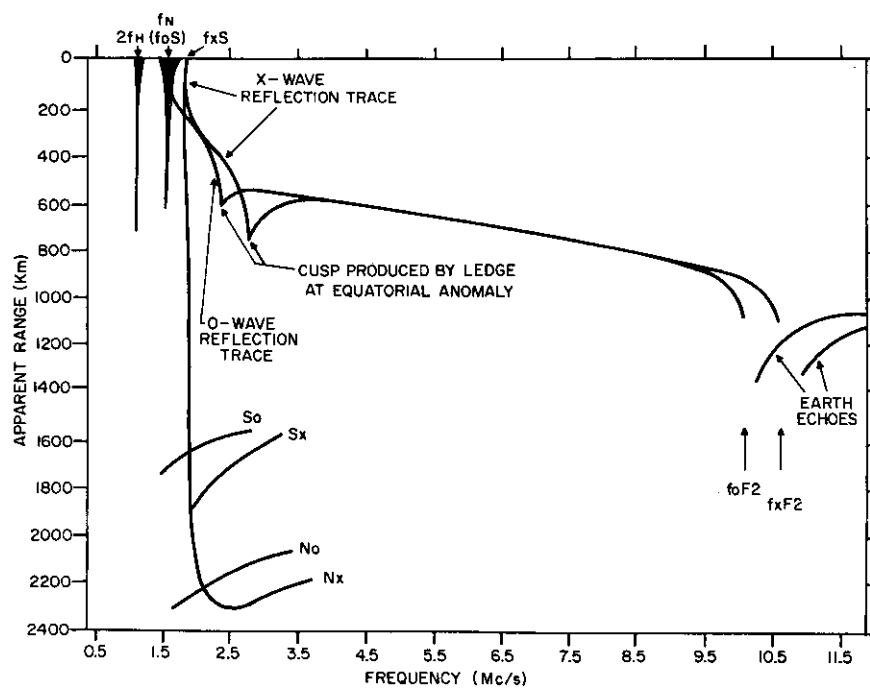


FIG. 3b Schematic mid-latitude ionogram

$f_T = (f_N^2 + f_H^2)^{1/2}$	upper hybrid resonance
$f_O S, f_X S, f_Z S$	the frequency of the ordinary ( <i>O</i> ), extraordinary upper branch ( <i>X</i> ), and extraordinary lower branch ( <i>Z</i> ) reflection traces at the satellite ( $f_O S \equiv f_N$ )
$f_{Z\infty}$	the frequency of large retardation of the <i>Z</i> wave.

When  $f_H/f < 1$ , the Appleton-Hartree magneto-ionic equations yield an infinity for the refractive index at a frequency slightly above  $f_N$ . Ray path computations for topside ionograms indicate that the *Z* reflections trace near this infinity is produced by a ray whose initial direction is nearly horizontal. The ray direction changes gradually towards the vertical until the refractive index approaches zero and reflection occurs. The symbol  $f_{Z\infty}$  has been assigned to the observed limiting frequency of the *Z* reflection trace. It should not, however, be assumed that the Appleton-Hartree equations are necessarily valid very near to  $f_{Z\infty}$ . See (5) for more detailed discussion.

Each resonance is visible over an appreciable frequency band and, even with the help of the labels at the top of the ionogram, it is difficult to pick out the resonances near the low-frequency end of the ionogram. Moreover, the relative amplitudes of the spikes depend on the orientation of the satellite with respect to the earth's magnetic field. The satellite is not orientation stabilized, and the spike amplitudes vary markedly from ionogram to ionogram. In practice, the identification and details of the HF resonances are most readily established by examining sequences of consecutive *Alouette I* ionograms (6). Some of the results of such studies are summarized in the schematic ionograms of Fig. 3.

In the equatorial ionogram, Fig. 3a, strong  $2f_H$  resonance spike appears at about 1.3 Mc/s and a plasma frequency spike  $f_N$  at 1.6 Mc/s. The  $f_H$  resonance is not visible, probably because of the greatly reduced receiver sensitivity below 1.0 Mc/s. The upper hybrid resonance, and higher harmonics of the gyrofrequency do not appear on this ionogram. The mid-latitude ionogram, Fig. 3b, shows  $f_H$  and its harmonics, up to  $5f_H$ . On this ionogram  $f_N$  is less than  $2f_H$ , and a strong upper hybrid resonance spike  $f_T$  appears between  $f_N$  and  $2f_H$ . Note that these three resonances occupy most of the frequency band between about 1.6 to 2.2 Mc/s, and that the *O*-wave reflection trace is not visible below about 2.1 Mc/s (or at apparent ranges less than 550 km). In Fig. 3c, spread-*F* is a dominant feature of the high-latitude reflection traces (7) at all heights. A strong  $2f_H$  spike appears at the height of the satellite, emerges from the bottom edge of the spread reflection traces, and extends to an apparent range of about 850 km. The most striking feature of Fig. 3c, however, is that the "resonance trace" that emerges from the *X*-wave reflection trace at a frequency corresponding to  $2f_H$  at the height of reflection (8).

Additional information on the HF plasma resonances may be obtained from the AGC voltage of the sounder receiver. This receiver is cut off during the transmitter pulses, and the AGC circuit has an integration time of 20 ms. As a result, normal ionospheric echoes are suppressed, and the AGC voltage records the background noise level. Spurious spikes at fixed frequencies

(caused by the satellite instrumentation) and ionospheric resonance spikes (9) appear superimposed on this noise background. The receiver, moreover, may be operated with the sounder transmitter either on or off, as in Fig. 4. When the transmitter is on, voltage spikes appear with maxima precisely at the ionospheric resonance frequencies, to within the experimental accuracy. On the high frequency side of each resonance spike the AGC voltage drops below the normal background noise level; this effect is particularly marked in the case of the  $f_T$  resonance shown in Fig. 4. When the transmitter is switched off the resonance spikes disappear; thus confirming other evidence that the resonances are excited in the vicinity of the satellite. The decrease in AGC level just above the  $f_T$  resonance frequency persists even when the transmitter is off.

Detailed analysis of the electron gyrofrequency resonances,  $nf_H$ , and comparison with magnetic data extrapolated from ground level, has established that they occur at accurate multiples of the electron cyclotron frequency. These spikes therefore provide a convenient and accurate method of measuring the strength of the earth's magnetic field at the height of the satellite (10). Figure 5 shows the field intensity at 1000 km altitude over North America and the North Atlantic, measured to an accuracy of better than 1 per cent.

The probability of occurrence of the higher harmonics of  $nf_H$  on *Alouette I* ionograms is increased when the exciting antenna is aligned approximately with the earth's magnetic field (11). (This statement is strictly applicable only to the daytime ionograms. At night the ionospheric critical frequencies are lower, and interference from ground-based transmitters severely restricts the observation of the higher harmonics.) The topside sounder antenna system consists of two crossed dipoles, 75 feet and 150 feet in length, permanently connected by a 4.7 Mc/s crossover network. The higher-frequency cyclotron harmonics, i.e. above about 5 Mc/s, are observed only when the angle between the short antenna and the magnetic field is within the range  $\pm 15^\circ$ . This point is illustrated in Fig. 6, showing data taken when the spin vector of the satellite was perpendicular to the magnetic field. The slope of the dashed line joining one set of harmonics arises from the fact that there is an appreciable rotation of the satellite during the 12-second frequency sweep of the sounder. It is evident from the figure that harmonics above the 10th were observed only when the short antenna was approximately aligned with the magnetic field.

The preceding discussion has been concerned with HF ionospheric resonances excited by sounder transmitter pulses in the immediate vicinity of the satellite. In principle, resonances may also be excited at any distance from the transmitter, and one remote resonance phenomenon, called the "resonance trace", has been identified on the *Alouette I* ionograms (8), (12). The resonance trace, Figs. 3c and 7, appears as a nearly vertical spur emerging from the X-wave reflection trace, at a frequency corresponding to  $2f_H$  at the height of reflection. It has been observed that a necessary condition for the occurrence of a resonance trace is that spread F occur at least up to the height of the satellite. As a result the vast majority of the observations are at high latitudes. From May 2-11, 1963, resonance traces were found on one-quarter of the 4000 topside ionograms recorded by the telemetry stations at Resolute Bay, N.W.T. and College, Alaska.



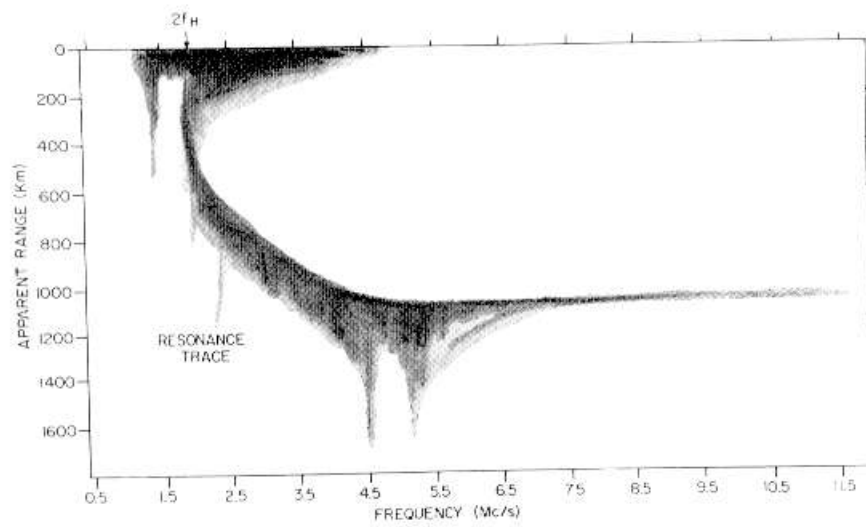


FIG. 3c Schematic high-latitude ionogram

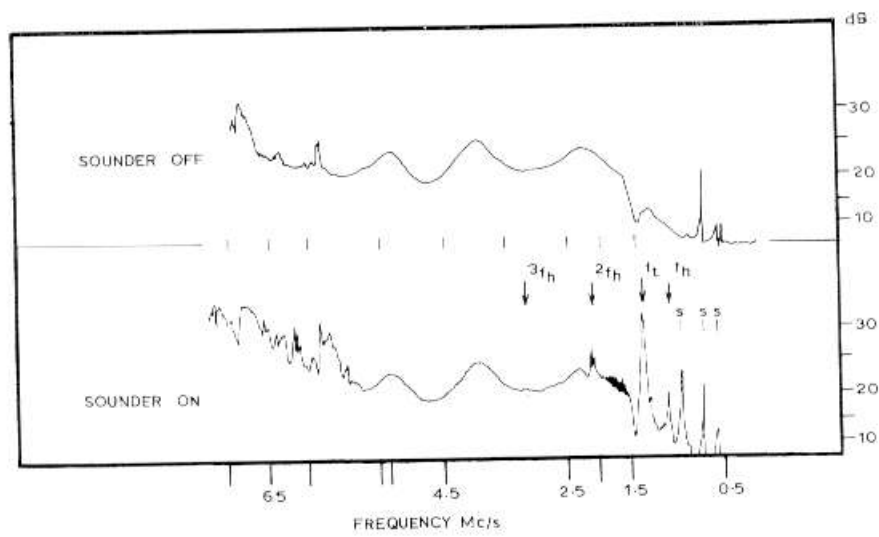


FIG. 4 Ionospheric resonance spikes

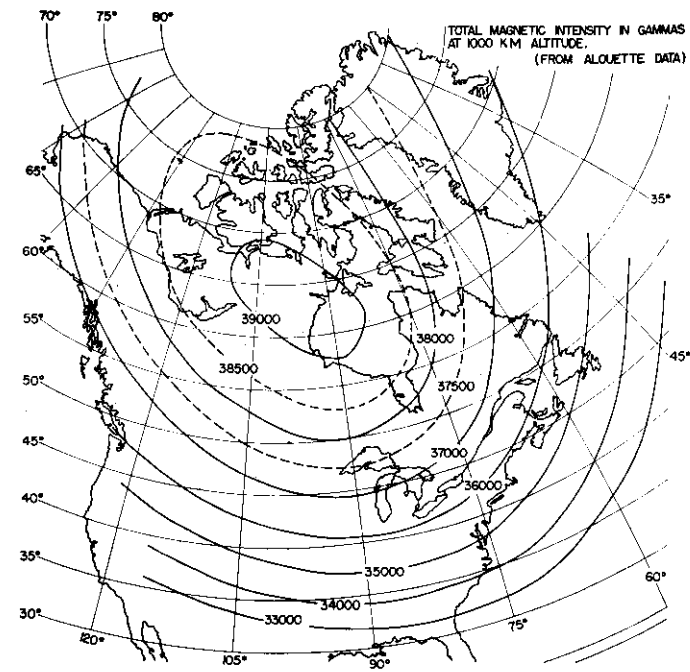


FIG. 5 The field intensity at 1000 km altitude over North America and the North Atlantic, measured to an accuracy of better than 1 per cent

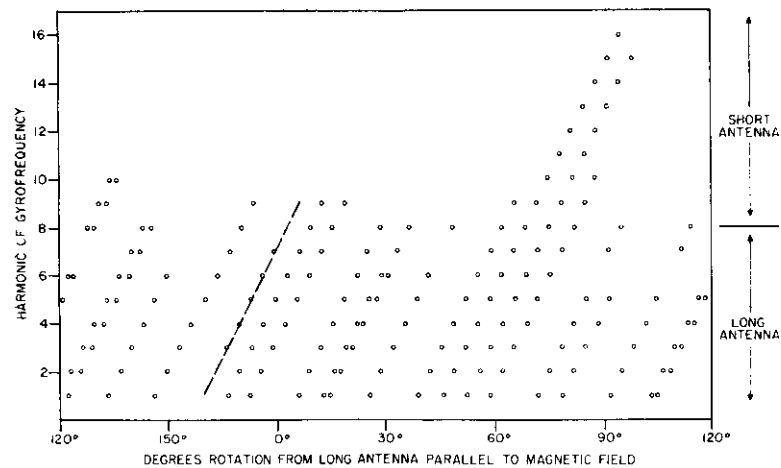


FIG. 6 Data taken with spin vector of satellite perpendicular to magnetic field

The intersections of the resonance trace with the  $X$ -wave reflection trace have been used to compute the plasma frequency at the height of reflection (12). Such values of plasma frequency are independent of the usual assumptions made in computing profiles of electron number density  $v$ . height, and are therefore of value in assessing the accuracy of  $N(h)$  profiles.

HF resonances corresponding to those observed by *Alouette I* are also seen by the fixed frequency topside sounder in *Explorer XX* (13), launched in August 1964. There may be discrepancies between the satellite observations and earlier rocket tests of a fixed frequency sounder (14). The rocket sounder records show spikes at  $f_N$ , and at the cut off frequencies of the  $X$ -waves; but there are no spikes at  $f_T$ . (Further rocket tests may be required to establish that the observed "spikes" are caused by ionospheric resonances.)

**Very-low-frequency** – Two VLF resonance phenomena, the so-called "proton whistlers" and the lower hybrid resonance, have been identified from the *Alouette I* data.

In both the *Alouette I* and the *Injun III* satellites, slightly dispersed lightning impulses (often called "short-fractional-hop (SFH) whistlers") are occasionally followed at low frequencies by a slowly rising tone. In Fig. 8, for example, two SFH whistlers are followed by tones that start at about 400 c/s, and rise asymptotically toward a frequency of about 500 c/s. This asymptotic frequency is, to within the experimental accuracy, the proton cyclotron frequency  $f_{Hp}$ , in the vicinity of the satellite (15). The duration of these rising tones, or "proton whistlers", is normally determined by cyclotron damping (16), and may exceed 5 seconds.

Certain VLF noise bands observed by *Alouette I* are not recorded by ground-based receivers and have a number of characteristic features that distinguish them from other emissions received at the satellite (17), (18). Brice and Smith (19) suggested that the lower cutoff frequency of these unusual bands is identical with the theoretical lower hybrid resonance;

$$f_{LHR} = \frac{f_N f_H}{(f_N^2 + f_H^2)^{1/2}} \left( \frac{1}{m} \frac{m_e}{m_p} \right)^{1/2}$$

where:

$m_e$  is the mass of an electron

$m_p$  is the mass of a proton

$$\frac{1}{m} = \sum_i \frac{\alpha_i}{m_i} m_p$$

and  $\alpha_i$  is the fractional abundance of the  $i^{\text{th}}$  ion species

$m_i$  is the mass of the  $i^{\text{th}}$  species.

This suggestion arose from the observation that whistlers and atmospherics can trigger the generation of the noise bands or increase their intensity, and that the low-frequency cutoff of the noise bands often shows a marked dependence on the geomagnetic field, as shown in Fig. 9, between geomagnetic  $L$  values of about 2 to 4. In this example, the cutoff frequency increases with decreasing latitude in both hemispheres, until these noise bands vanish at about 9 kc/s. On other occasions the noise bands persist until they are cut off by the upper frequency limit (10 kc/s) of the VLF receiver.

Detailed analysis of simultaneous observations by the *Alouette I* VLF receiver and the HF topside sounder (20) strongly supports the identification of the lower cutoff frequency of these noise bands with  $f_{LHR}$ . Data were available from 200 satellite passes during a two-year period. It was tentatively assumed that  $f_{LHR}$  and the VLF cutoff frequencies are identical; the data were then inserted into the formula for  $f_{LHR}$ , and values of  $\bar{m}$  were obtained. The results of the analysis were entirely plausible. Over 400 values of  $\bar{m}$  were computed; all values were within the limits 1 and 16, and the variations of  $\bar{m}$  with local time and with latitude were not inconsistent with data from other experiments.

#### WAVE PROPAGATION IN THE IONOSPHERIC PLASMA

The preceding section has described the *Alouette I* observation of ionospheric resonance phenomena. Before discussing the probable effects of these resonances on space telecommunication systems, it is convenient to review some of the pertinent theory of wave propagation in the ionosphere.

**Wave modes in an anisotropic plasma** – The integrated result of individual interactions between charged particles and waves in an anisotropic plasma is conveniently discussed in terms of a dispersion equation that gives the relation between the frequency and wavelength of plane waves in an infinite homogeneous plasma. In the following discussion non-linear effects and acoustic and quasi-acoustic waves are neglected. The dispersion equation may then be written in the form see, for example, (21):

$$An^4 - Bn^2 + C = 0$$

$$\text{where } n = \frac{c}{u}$$

$$\text{and } n = \text{refractive index of the plasma}$$

$$c = \text{velocity of light in vacuum}$$

$$u = \text{phase velocity of a wave.}$$

In the general case, the thermal motions and interactions of all the charged particles with a wave must be taken into account. If  $N$  is the number of charged components of the anisotropic plasma, there are  $N + 2$  independent solutions of the dispersion equation, consisting of two electromagnetic wave modes, and  $N$  electrostatic waves.

The complexity of this general case has led to a number of approximate solutions. Two special cases are of particular interest here. The first case is a "cold" plasma, in which thermal motions can be neglected. In this approximation the electrostatic wave solutions vanish, leaving only the two electromagnetic waves. The second case is a "high-frequency approximation", where the effect of ions on wave propagation becomes negligible, and the only charged particles that need to be considered are the free electrons. The plasma is no longer necessarily "cold", since the effects of collisions between electrons and other constituents, and of the thermal spread of electron velocities, may be included in the analysis. The high-frequency approximation is similar to the cold plasma approximation in that there are only two wave solutions, frequently referred to as the "ordinary" and "extraordinary" modes.

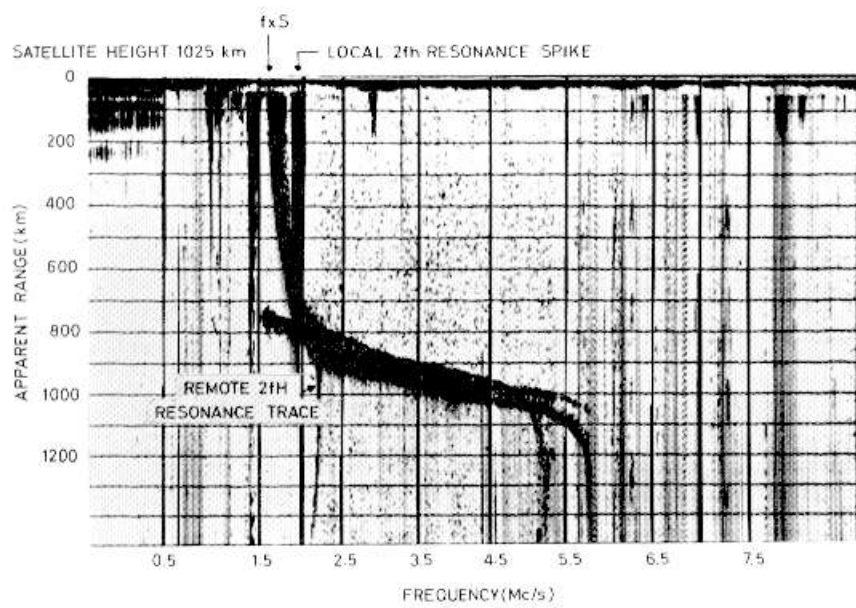


FIG. 7 A  $2f_H$  resonance trace

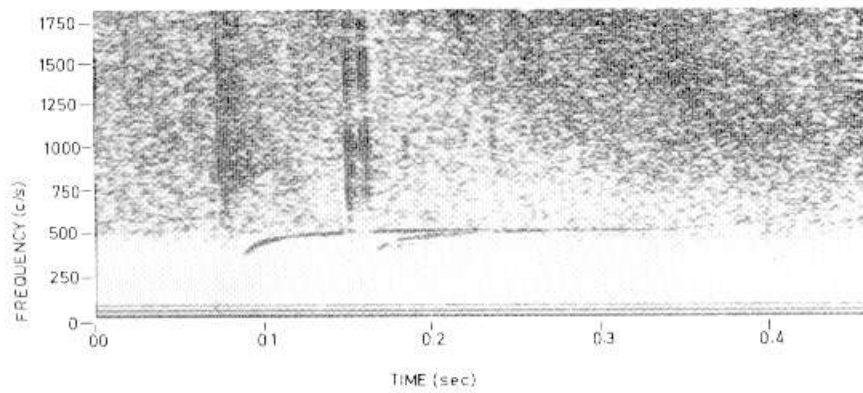


FIG. 8 Proton whistlers

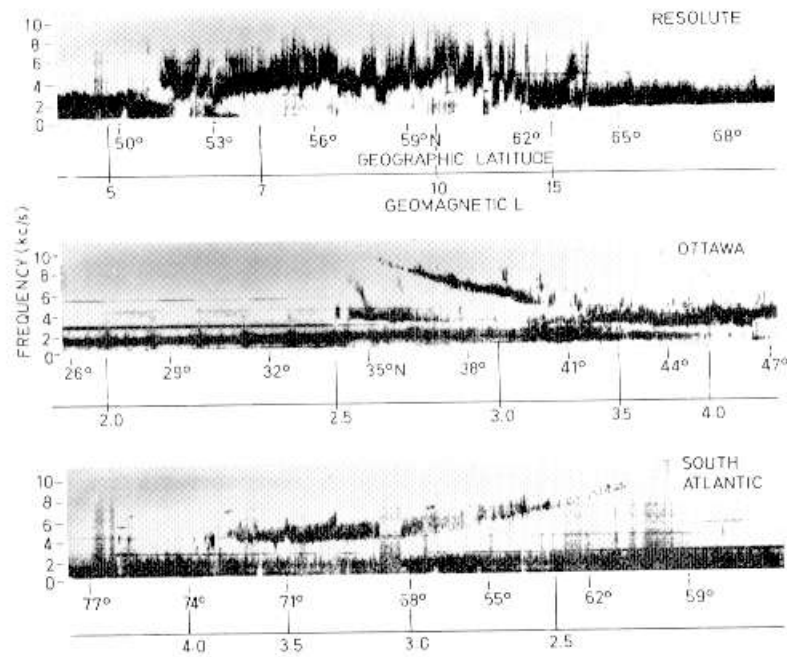


FIG. 9. Spectrogram of VLF emissions recorded by *Alouette I* at 1057–1148 U.T. on Jan 31, 1963. The captions on the three segments refer to the telemetry stations where the data were recorded (after Barrington *et al.* 20)

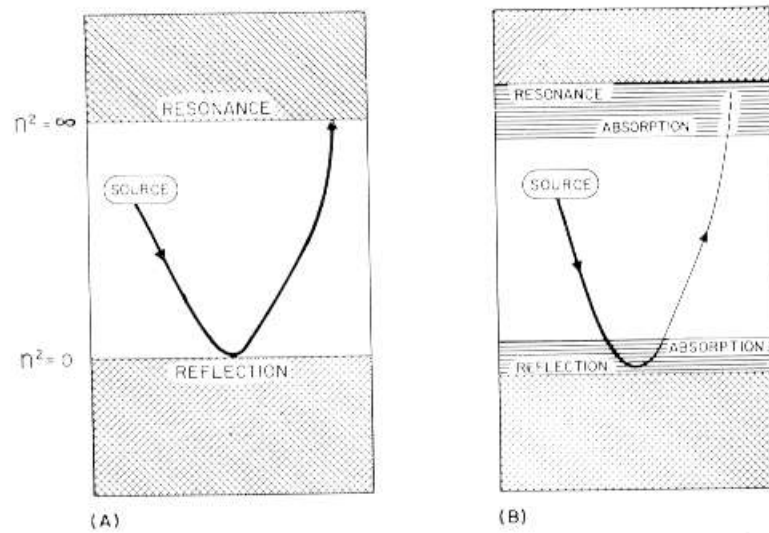


FIG. 10. Schematic representation of a single wave mode in a continuously varying plane-stratified plasma.  
 (a) Sharp boundaries at  $n^2 = 0$  and  $n^2 = \infty$   
 (b) Diffuse boundaries where  $n^2$  approaches zero and infinity

A third approximate solution is frequently used for a "warm" plasma in which the velocity of light is taken to be infinite. The electromagnetic wave solutions vanish, leaving only the electrostatic waves. This approximation is not included in the following review, to avoid excessive complication. (See "OMISSIONS".)

**Reflection and absorption; cutoff and resonance** – The refractive index  $n$  of a given electromagnetic wave mode in a collisionless plasma is entirely real, or entirely imaginary. The boundaries between the real and imaginary values are the surfaces  $n^2 = 0$  and  $n^2 = \infty$ , and these are precisely the boundaries for the regions of propagation and non-propagation of each mode. When the effect of collisions and the temperature spread of velocities is included (for example, in the high-frequency approximation) the refractive index becomes complex and the boundaries between regions of propagation and non-propagation are not as sharp as in the collision-free case.

In regions where propagation is possible the ray trajectory in an anisotropic plasma depends on the direction of the external magnetic field and, in general, the ray trajectory and the wave normal are not in the same direction. Consider a plane-stratified plasma in which there is a continuous variation of, say, plasma density, as illustrated in Fig. 10. Regions in which  $n^2$  is negative cannot support wave propagation; these regions are cross-hatched in the diagram. A source of electromagnetic waves is shown in the region where propagation is possible and (for simplicity) the ray trajectory and the wave normal are assumed to be in the same direction. In this special case a wave propagating in the direction of decreasing  $n$  is refracted away from the surface  $n^2 \approx 0$ . If the boundary surface is sharp, as in Fig. 10a, the wave is totally reflected; if it is diffuse, as in Fig. 10b, some of the wave energy is absorbed near the boundary. This reflection phenomenon is also known as "cutoff", because it often occurs at frequencies above (or below) a well-defined limit. Similarly, a wave propagating in the direction of increasing  $n$  is refracted toward the surface  $n^2 \approx \infty$  and reaches it at normal incidence. If the boundary is sharp, the wave energy is stored at the boundary in the form of currents in the plasma, oscillating at the wave frequency. This phenomenon is usually called "resonance", because it often occurs over a narrow range of frequencies. If the boundary is diffuse, some of the wave energy is absorbed near the boundary, and the resonant oscillations are damped.

In an anisotropic plasma, when the ray trajectory and the wave normal are in different directions, the ray trajectories may become quite complex. Detailed analysis (5) shows that, in spite of the added complexity, the reflection and absorption processes are still associated with surfaces  $n^2 \approx 0$  and  $n^2 \approx \infty$ .

**The electromagnetic principal waves** – Each of the two electromagnetic wave modes may propagate in any direction with respect to the magnetic field. Detailed solutions for the general case are complex and it is convenient, instead, to consider the special case of waves that propagate along and across the magnetic field direction. If  $\theta$  is the angle between the wave direction and the magnetic field direction, principal waves are defined as those waves for which  $\theta = 0$  and  $\theta = \pi/2$ . Results obtained for the two principal waves of a given wave mode can often be applied (at least, qualitatively) to waves travelling in arbitrary directions.

There is no generally accepted standard nomenclature for electromagnetic wave modes. In this paper the four principal waves are named according to the polarization of their electric fields with respect to the positive direction of the static magnetic field. The two waves with  $\theta = 0$  are circularly polarized and the electric fields rotate in opposite directions. Accordingly they are called the left-handed ( $L$ ) and right-handed ( $R$ ) principal waves. One of the waves with  $\theta = \pi/2$  is linearly polarized along the magnetic field and has a dispersion equation that is independent of the field strength; this is the ordinary ( $O$ ) principal wave. The second wave with  $\theta = \pi/2$  is either left- or right-handed elliptically polarized and its dispersion equation depends on the magnetic field strength; this is the extraordinary ( $X$ ) wave. The polarization sense of the ( $R$ ), ( $L$ ), and ( $X$ ) waves is such that the ( $R$ ) wave interacts primarily with negatively charged particles, the ( $L$ ) wave with positively charged particles, and the ( $X$ ) wave may interact with either or both. A wave mode (when it exists) may have one or two principal waves; i.e. one of the principal waves may disappear because of resonance or cutoff conditions, while the other principal wave continues to propagate.

Table 1 lists the theoretical ionospheric resonance and cutoff conditions for each electromagnetic principal wave. The normalized parameters:

$$X = \left(\frac{f_N}{f}\right)^2, X_j = \left(\frac{f_N}{f} \frac{m_e}{m_j}\right)^2, Y = \frac{f_H}{f}, Y_j = \frac{f_{Hj}}{f}$$

are used and the subscript  $j$  is omitted for free electrons. Harmonic resonances and related cutoffs are neglected in this theoretical table;  $M$  is the ratio of ion to electron mass for the special case of a single dominant ion.

#### OMISSIONS

The above review considered only the electromagnetic wave modes, and neglected possible electrostatic modes. No attempt was made to consider the mechanisms by which ionospheric resonances are generated, and there was no discussion of harmonic resonances and the related cutoff conditions. These are indeed vital issues, but, in the author's opinion, the progress made to date does not justify a general theoretical review here. Instead, electrostatic modes, resonance generation mechanisms and harmonic resonances are discussed below, in connection with specific experimental results.

**The resonant frequencies** – The theoretical plasma frequencies for the electromagnetic wave modes, Table 1, are in good agreement with the *Alouette I* observations of HF spikes and of VLF wave dispersion and cutoff phenomena. (The multiple-ion resonance frequencies and the  $O^+$  and  $H_e^+$  cyclotron frequencies are below the low-frequency cutoff of the VLF receiver and have not been observed.) This agreement is encouraging, but it should not therefore be assumed that the physical nature of the resonances necessarily corresponds to the theoretical model.

It is probably worth while to elaborate on this point. Resonance conditions for the collisionless "high-frequency" model, and for the collisionless "cold" plasma model, occur when  $n^2 = \infty$ ; at the same time the group velocity of the wave goes to zero. When losses are included in these models, the refractive index remains finite at resonance, and the group velocity (although small) never reaches zero; these losses, however, produce only



TABLE I

## PRINCIPAL WAVES

Mode	Resonances	High-frequency approximations
(L)	ion gyrofrequencies $\gamma_j = 1$	
(R)	electron gyrofrequency $\gamma = 1$	
(O)	none	
(X)	Multiple-ion and electron-ion $\frac{X}{1 - \gamma^2} + \frac{X_1}{1 - \gamma_1^2} + \frac{X_2}{1 - \gamma_2^2} = 1$	$X = 1 - \gamma^2$
	<b>Lower hybrid resonance</b> (for one dominant ion)	$\frac{1}{M} = \frac{1}{\gamma^2} + \frac{1}{X}$
<b>Cutoff conditions</b>		
(L)	$\frac{X}{1 + \gamma} + \frac{X_1}{1 - \gamma_1} + \frac{X_2}{1 - \gamma_2} = 1$	$X = 1 + \gamma$
(R)	$\frac{X}{1 - \gamma} + \frac{X_1}{1 + \gamma_1} + \frac{X_2}{1 + \gamma_2} = 1$	$X = 1 - \gamma$
(O)	(for one dominant ion) $X = 1 - \frac{1}{M}$	$X = 1$
(X)	Same as (L) and (R) above	$X = 1 \pm \gamma$

relatively slight changes in the resonance frequencies. If now, similar computations are made for a plasma model in which the effects of the thermal distribution of velocities are included, the group velocity near resonance may be quite substantial. (The group velocity may, for instance, be comparable with the orbital velocity of *Alouette I*.) The analysis is considerably simplified in this latter model if it is assumed that the wave magnetic field is negligible compared with the electric field – this is the so-called “electrostatic” approximation. Even in the electrostatic limiting case, the resonance frequencies are not necessarily greatly altered from the collisionless “cold” plasma case.

The question to be answered is this: are the parameters of a specific ionospheric resonance consistent with the limiting case of the electrostatic plasma model, or is it necessary to use an electromagnetic model including losses? I suggest that we do not yet know the answers, and that it will be necessary to make detailed comparisons between experiment and theory to resolve this issue. Such comparisons would have to include the resonance generation and decay processes. Progress to date has been limited by the complexity of the analysis (22), as well as by a lack of appropriate experimental data. In these circumstances, the following remarks concerning the effects of ionospheric resonances on the propagation of electromagnetic waves are necessarily tentative.

Suppose that radio waves are generated by a variable-frequency transmitter within the ionosphere above the height of the *F*-layer maximum, and

that  $O^+$ ,  $H_e^+$ , and  $H^+$  are the only ions present in significant quantities. As an illustration, the ratio of  $f_N$  to  $f_H$  is taken as about 1.7. Table 2 summarizes the probable effects of ionospheric resonances and the associated cutoff conditions on the propagation of the principal electromagnetic waves in a slowly varying plasma. Extrapolation from the *Alouette I* observations of harmonic resonances suggests that the plasma in the vicinity of a powerful VLF transmitter might also oscillate at harmonics of the ion cyclotron and multiple ion resonances. The frequencies of 2nd harmonics are shown, but higher harmonics are omitted. In the column headed "Principal Waves", the two electromagnetic waves are separated by a colon. When both principal waves of a mode are shown, this means that propagation may also occur for other values of  $\theta$ , between  $\theta = 0$  and  $\theta = \pi/2$ . (In the latter circumstance, and especially at HF, the entire wave mode is often labelled as "ordinary" or "extraordinary".)

Note that phenomena such as the remote resonance trace, at  $2f_H$ , that occur only when ionospheric irregularities are present, are not included in Table 2.

TABLE 2

Operating frequency (approx.)	Principal Waves	Remarks
$< 25$ c/s	$(R, X) : (L)$	
25		cyclotron and collisional damping of $(L)$ near $Y_{(O^+)} = 1$
	$(R, X)$	
30		damping of $(X)$ by multiple-ion $(O^+, H_e^+)$ resonance
	$(R)$	
40	$(R, X) : (L)$	transmission of $(L)$ and $(X)$
(50)	?	(possible 2nd harmonic of $O^+$ gyro-frequency)
(60)	?	(possible 2nd harmonic of $O^+, H_e^+$ resonance)
100		cyclotron and collisional damping of $(L)$ near $Y(H_e^+) = 1$
	$(R, X)$	
150		damping of $(X)$ by multiple-ion $(H_e^+, H^+)$ resonance
	$(R)$	
180		transmission of $(L)$ and $(X)$
	$(R, X) : (L)$	
(200)		(possible 2nd harmonic of $H_e^+$ gyro-frequency)
	?	
(300)		(possible 2nd harmonic of $H_e^+, H^+$ resonance)
	?	

Operating frequency (approx.)	Principal waves	Remarks
400		cyclotron damping of (L) near $Y_{(H^+)} = 1$
(800)	(R, X)	(possible 2nd harmonic of $H^+$ gyro-frequency)
	?	
5,000		damping of (X) by electron-ion (lower-hybrid) resonance
	(R)	
(10,000)		(possible 2nd harmonic of lower-hybrid resonance)
	?	
1.0 Mc/s	No transmission	cyclotron damping of (R) near $Y = 1$
1.3		transmission of (L) and (X) (At $X = 1 + Y$ , the Z-trace appears on topside ionograms)
	(L, X)	
1.7		At the plasma frequency, $X = 1$ , the (O)-trace does not normally appear on the topside ionograms. (See following text for further details)
	(L, O(?)) : (X)	
2.0		2nd harmonic of electron gyrofrequency at satellite height
	?	
2.1		damping of (X) near upper hybrid resonance, (At $X = 1 - Y^2$ the O-trace appears (in full strength) on the topside ionograms)
	(L, O)	
2.6		transmission of (R) and (X). (At $X = 1 - Y$ , the X-trace appears on topside ionograms)
	(L, O) : (R, X)	

Several portions of Table 2 merit further discussion. No observations of multiple-ion resonances, or of  $H_e^+$  and  $O^+$  whistlers, have yet been reported, either in laboratory or in space experiments, and the relative importance of various forms of damping is not certain. In the ion whistler case, the smaller the ion density the more likely it is that cyclotron damping will dominate collisional damping (16).

The relative strength of the higher harmonics of the electron gyro-frequency are much greater, on occasion, than would be predicted for synchrotron radiation by electrons spiralling around the earth's magnetic field

lines. The *Alouette I* observations have stimulated a number of theoretical studies, and some progress has been made in separate considerations of the excitation and loss processes. The generation of the harmonic resonances (4), (24) can be explained qualitatively in terms of energy bunching of the gyrating electrons in phase with the electric field of the wave. The duration of the harmonics appears to be consistent with the assumption that the harmonic resonances arise from electrostatic oscillations of the electrons across the magnetic field direction (24). The frequencies of the members of the harmonic series are integral multiples of the electron gyrofrequency, to within the experimental error (25). This result apparently differs from current interpretations of laboratory experiments (26) based on solutions of Bernstein's dispersion of relation (27) for electrostatic waves. There appear to be significant differences between the satellite and laboratory experiments, and it has been suggested that the results could be reconciled by taking into account the large difference in the ratio of antenna length to electron gyro radius in the two cases.

It was noted earlier, in connection with Fig. 2, that the *O*-trace on topside ionograms does not start near zero range, at the plasma frequency  $f_N$ , but appears on the ionogram at a substantial range, near the upper hybrid frequency  $f_T$ . On occasion, however, a relatively weak reflection trace is visible between  $f_N$  and the frequency of great retardation of the  $Z$  trace,  $f_{Z\infty}$ . This observation has been interpreted as due to coupling between the  $Z$  wave and the *O* wave (28), since the segment of weak trace appears to be a reasonable extrapolation of the stronger *O*-trace. The weak trace is bounded in frequency by the lowest frequency for *O*-wave reflections and the highest frequency for  $Z$ -wave reflections.

A complete explanation of the absence of *O*-reflection traces between  $f_{Z\infty}$  and  $f_T$ , and of the occurrence of occasional weak traces between  $f_N$  and  $f_{Z\infty}$ , is still lacking. One possible complication arises from the observation, by the UK-2 satellite (29) and other experimenters, is that the background noise level is substantially enhanced in two bands; between  $X = 1 + Y$  and  $f_N$ , and between  $f_N$  and  $f_T$ . The sensitivity of the HF receiver in *Alouette I* falls rapidly below about 1.5 Mc/s, so that this increase in noise is not particularly evident on the AGC records. It therefore seems unlikely that the *O*-trace observations are directly connected with the occurrence of enhanced noise bands. The preceding discussion, however, assumes that the only pertinent solutions of the dispersion equation are the two electromagnetic wave modes: this assumption may not be justified. In a recent paper on the production of thermal noise in the ionosphere Budden and Daniell (30) found that, in the frequency band between  $X = 1 + Y$  and  $f_T$ , the effect of temperature on the spatial dispersion of waves must be included in the noise analysis. When this is done a plasma wave solution is added to the two electromagnetic waves, and when the refractive index of the  $Z$  wave becomes very large it is very strongly coupled to the plasma wave. The implications of this noise analysis on the *O*-trace observations is not yet clear.

**The resonating regions** - The frequencies of the theoretical plasma resonances listed in Table 1 and the HF resonances observed by *Alouette I* at 1000 km agree to within the experimental error, if the assumption is made that the resonating region is not significantly perturbed by the presence of the

satellite. It follows that the scale size of the resonating regions must be substantially larger than the plasma sheath formed around *Alouette's* 150-foot dipole antennas. It is more difficult to set an upper limit on the size of the HF resonances, but the bandwidth of the  $f_N$  and  $f_T$  resonant spikes is not inconsistent with a vertical dimension of about  $10^2$  km.

The size of the region responsible for the remote resonance trace at  $2f_H$  may be estimated from the sharpness of the trace, Fig. 7. This estimate is based on the assumption that the wave paths are as illustrated in Fig. 11. A radio pulse of frequency  $f$  is transmitted in the ( $X$ ) mode from the satellite. Field-aligned ionization irregularities guide the wave along the direction of the magnetic field, and this guidance maintains sufficiently high signal levels to permit observation of the resonance trace by the *Alouette I* receiver. The wave propagates downward through the height  $A$ , where  $f = 2f_H$ . A fraction of the pulse energy is absorbed by the free electrons in a small range of heights around  $A$ . The absorbed energy is not significantly dissipated by collisions. Instead, at a time  $\tau$  after the initial pulse passed through  $A$ , a second  $X$ -mode pulse is generated at  $A$ . The delay time  $\tau$  depends on the index of refraction of the wave, and the plasma and gyrofrequencies at height  $A$ . The analysis (31) shows that a delayed pulse is generated at  $A$  only if the initial pulse is propagating in the direction of increasing magnetic field and that the delayed pulse can only propagate in the direction of decreasing field. Remote resonance traces computed on this model are consistent with the observations. The vertical extent of the resonating region is then found to be less than 50 km.

The scale size of the lower hybrid VLF resonance may be deduced from sonograms similar to Fig 9. and 12. Significant variations of the lower cutoff frequency with latitude can be measured, within less than one second. Moreover, when the LHR noise bands are triggered or enhanced, Fig. 12, the measured cutoff frequencies are nearly identical, whether that triggering is by upgoing atmospherics (SFH whistlers) or by downgoing whistlers (33). Although the LHR noise bands may be triggered by whistlers travelling along the magnetic field direction, the noise band signals propagate across the field. Such considerations indicate that the scale sizes of the lower-hybrid resonance source regions observed by *Alouette I* are less than 10 km.

In spite of the above observations of triggered and enhanced LHR noise bands, the generation process is not understood. There is a marked temporal variation in the frequency of occurrence of the LHR noise bands; during 1963 the occurrence frequency at Ottawa increased by a factor of about three from January to July, and declined again by December. The variation of occurrence frequency with magnetic invariant latitude has two maxima at  $59^\circ$  and  $69^\circ$ , and a minimum inbetween at  $65^\circ$ . The maxima are about five times and three times, respectively, as great as the  $65^\circ$  minimum (34).

The theory of propagation of proton whistlers has been examined in detail by Gurnett *et al* (35). Proton whistlers are evidently generated by SFH whistlers, and the crossover frequency at which this process occurs depends on the number density of protons (36). This process is shown schematically in Fig. 13. The solid curves represent the VLF emissions recorded by *Alouette I*; the broken portions of the curve would have been recorded by a VLF receiver with improved low-frequency sensitivity.

A single lightning impulse accounts for both the SFH ( $R$ ) whistler and the

proton ( $L$ ) whistler. The crossover occurs between the  $H^+$  and  $H_e^+$  (or  $O^+$ ) gyrofrequencies, and is the frequency at which both the ( $R$ ) and ( $L$ ) modes become linearly polarized and have the same refractive index. The vertical dashed line at time zero indicates the sferic that produces the VLF emissions, and the horizontal dashed line at about 450 c/s is the proton gyrofrequency  $f_{Hp}$ , at the height of the satellite.

The transmission bandwidth of the proton whistler at a given height depends on the crossover frequency and the proton gyrofrequency. This crossover frequency (about 200 c/s in Fig. 13) in turn depends on the number density of protons; it decreases with height and determines the low-frequency limit of the proton whistler. The proton gyrofrequency determines the upper-frequency limit, and this limit also decreases with height. The ( $L$ ) whistler has a smaller propagation velocity than the ( $R$ ) whistler, and the delay time  $\tau$  between the arrival of the two waves at the satellite is indicated in Fig. 13. When  $\tau = 0$  the crossover occurs at the height of the satellite.

Note that the attenuation of the ( $R$ ) whistler extends to a frequency  $F$  above the proton gyrofrequency at the satellite. The attenuation between  $F$  and  $f_H$  is due to conversion of ( $R$ ) to ( $L$ ) waves at heights below the satellite; the ( $L$ ) waves within this bandwidth are absorbed as the proton gyrofrequency decreases with height. The long-enduring "tail" of a proton whistler has a frequency dispersion that depends on the difference between the whistler frequency and the proton frequency near the satellite, and on the number density of protons. From measurements of the crossover frequency and the frequency dispersion of the proton whistler tail, electron densities at the satellite may be computed (37). The dispersion data may also be used to obtain the proton gyrofrequency (and hence magnetic field strength) at the satellite. Plots of the square root of the difference between a constant oscillator frequency  $\Omega_{osc}$  and the frequency of a proton whistler are shown in Fig. 14. The theory predicts that such plots will be linear when the oscillator frequency is set at the proton gyrofrequency. Evidently, the proton gyrofrequency here is close to 498 c/s. This technique permits the measurement of magnetic field strength to an accuracy of about 0.2 per cent, and proton number density to about 20 per cent (38).

The duration of proton whistlers observed at 1000 km is normally determined by cyclotron damping, and in this case the proton temperature can be computed. Preliminary results indicate that the computation depends critically on the assumed amount of cyclotron absorption. For example, a proton whistler with a duration of 3.34 seconds yielded proton temperatures in the range 715°–815°K for an assumed absorption of 30 dB, and temperatures of 855°–985°K for an assumed absorption of 40 dB (16). (In *Alouette I* there is no provision for measuring the amplitude of the VLF signals.)

**Future experiments** – More experimental information on the ionospheric resonances is obviously desirable. At the moment, it seems that results obtained from laboratory experiments cannot be readily applied to the ionosphere. At DRTE several rocket experiments are planned to investigate the VLF plasma resonances. The main program is a cooperative one with the Goddard Space Flight Center, Washington, D.C., in which ion data obtained from a VLF rocket experiment will be compared with data from ion mass spectrometers and other types of ion probes on the same rocket. The VLF

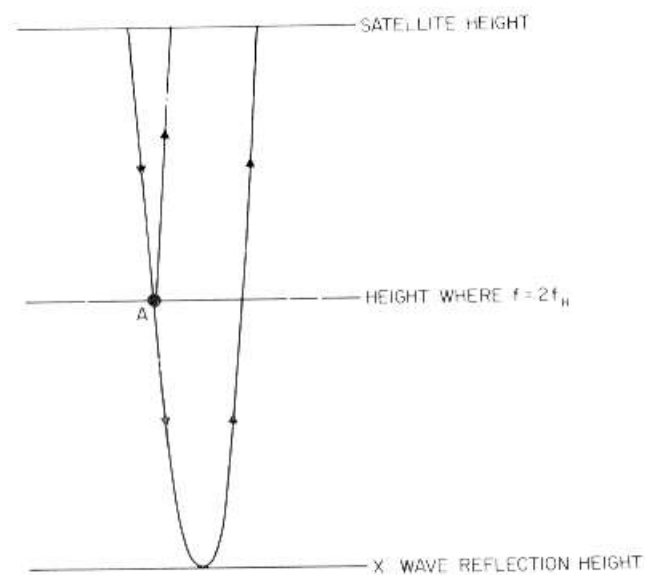


FIG. 11 Mode of propagation assumed for the radio energy responsible for producing the resonance trace. After Muldrew and Hagg (12)

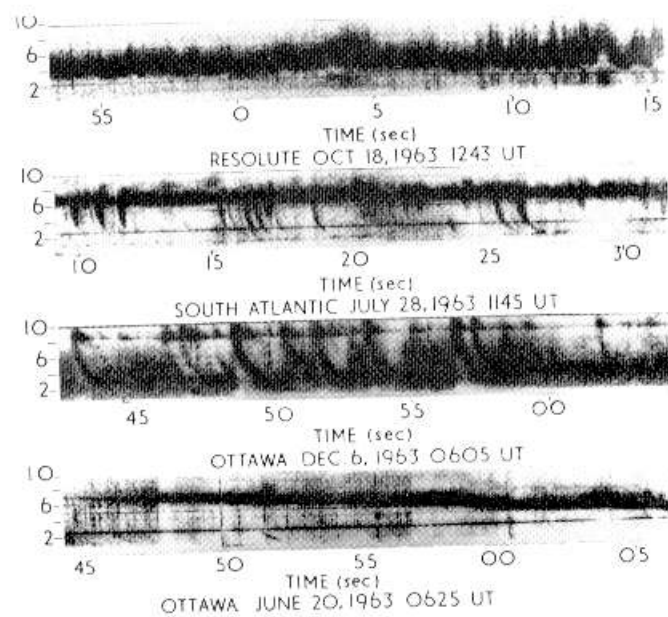


FIG. 12 ULF spectrograms of lower-hybrid resonance noise bands recorded by *Alouette I*. After Belrose *et al* (33)

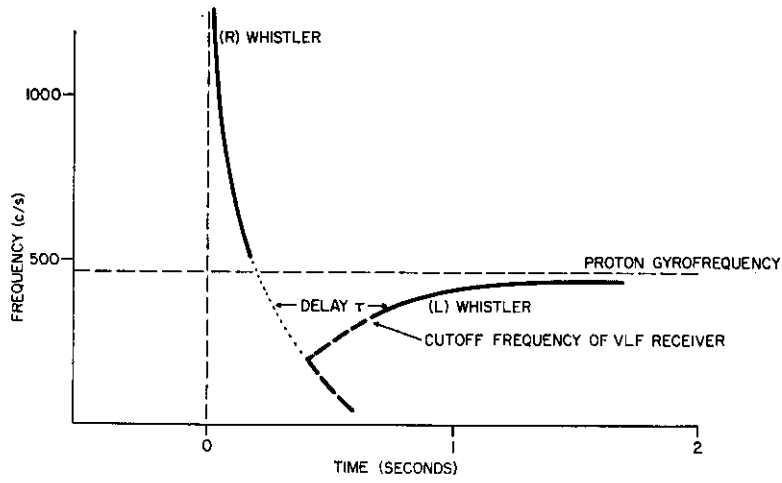


FIG. 13 Schematic representation of the partial conversion of a R-mode SFH whistler to a L-mode proton whistler

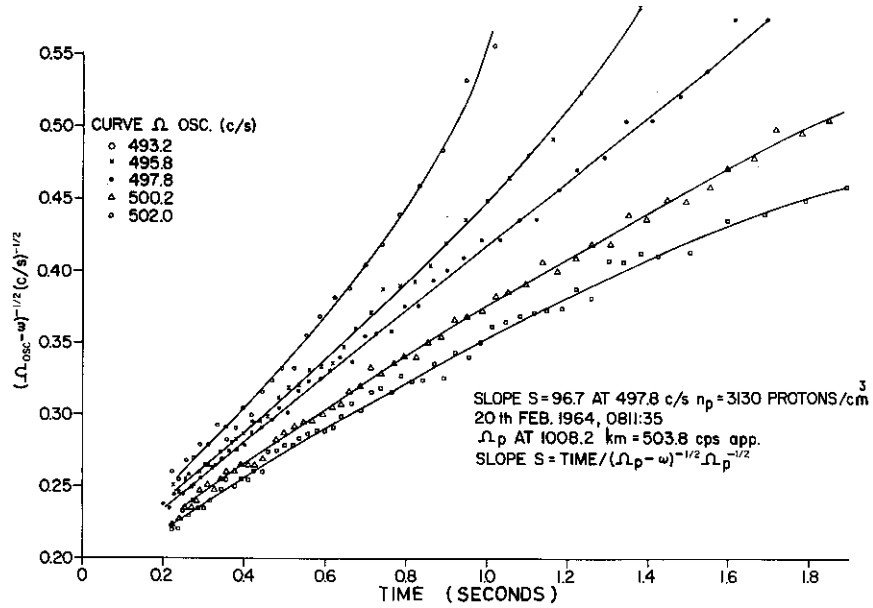


FIG. 14 Curves showing the square root of the period plotted against time for a wave form which is the difference in frequency between a pre-set oscillator frequency and a proton whistler. A straight line indicates that the oscillator frequency was equal to the proton gyrofrequency at the satellite when the proton whistler was recorded, and the slope of this line yields the number density of protons. After Brice (39)



rocket experiments consists of a receiver covering the band 50 c/s to about 15 kc/s, and an exciter unit that alternately sweeps in frequency from 50 c/s to 10 kc/s in a 2-second interval, and emits pulses of 100-volt amplitude and durations of  $10^{-3}$  and  $10^{-4}$  seconds. After each frequency sweep, there will be a 2-second silent period for listening. A similar VLF receiver will also be flown in the next Alouette satellite, scheduled for launch in late 1965.

#### SUMMARY

The frequencies and some of the parameters of a number of ionospheric plasma resonances have been measured by experiments in the *Alouette I* satellite. Most of the data pertain to the height region near 1000 km. The measurements extend over the frequency bands 0.4 to 10 kc/s and 0.5 to 12 Mc/s. The observed resonance phenomena include: the proton gyrofrequency, the lower-hybrid (ion-electron) resonance, the electron gyrofrequency and its harmonics, the plasma frequency, the upper-hybrid resonance, and a remote resonance trace at twice the electron gyrofrequency.

The observed resonant frequencies are in excellent agreement with the theoretical resonances of a homogeneous anisotropic plasma, with the possible exception of the harmonic resonances. The theory for a plasma containing only  $O^+$ ,  $H_e^+$  and  $H^+$  ions predicts the existence of the following additional resonances below the lower-frequency limit of the *Alouette I* VLF experiment:

the  $O^+$  and  $H_e^+$  gyrofrequencies  
the  $(O^+, H_e^+)$  and  $(H_e^+, H^+)$  multiple-ion resonances.

Extrapolation from *Alouette I* observations indicates that it may also be possible to excite harmonic resonances of appreciable amplitude.

The probable effects of the ionospheric resonances on telecommunication systems operating above the *F*-layer maximum may be qualitatively deduced from Table 2. Note that, for the ratio of  $f_N$  to  $f_H$  selected in this illustration, only one principal wave, the (*R*) wave, is transmitted between 5 kc/s and 1.0 Mc/s. Between 1.0 and 1.3 Mc/s electromagnetic waves do not propagate at all. This region of non-propagation disappears for smaller ratios of plasma to gyrofrequency.

Two frequency bands should probably be avoided except for very specialized telecommunication systems, i.e. frequencies below the proton gyrofrequency, and the frequency band between  $f_H$  or  $f_N$  (whichever is lower) and  $2f_H$  or  $f_T$  (whichever is higher).

#### REFERENCES

1. "Alouette, Canadian - U.S. Ionospheric Topside Sounder Satellite." IG Bulletin 65, 9, 1962.
2. "Alouette Topside Ionosphere Studies. Results from studies conducted by the Canadian Defence Research Telecommunications Establishment during the satellite's first year in orbit." IG Bulletin 79, 1, 1964.
3. "Alouette I (The First Three Years in Orbit). Part I: Ionospheric Studies." DRTE Report (in press), 1965.

4. LOCKWOOD, G. E. K., "Plasma and cyclotron spike phenomena observed in topside ionograms" *Can. J. Phys.* 41, 190, 1963.
5. BUDDEN, K. G., "Radio Waves in the Ionosphere". Cambridge University Press, London, 1961.
6. CALVERT, W. and GOE, G. B., "Plasma resonances in the upper ionosphere". *J. Geophys. Res.* 68, 6113, 1963.
7. PETRIE, L. E., "Topside spread echoes". *Can. J. Phys.* 41, 194, 1963.
8. HAGG, E. L., "An Alouette remote cyclotron resonance phenomenon" (in press). *Nature*, 1965.
9. HARTZ, T. R., "Observations of the galactic radio emission between 1.5 and 10.0 Mc/s from the Alouette satellite". *Ann. d'Astrophys.* 27, 823, 1964.
10. HAGG, E. L. (private communication).
11. LOCKWOOD, G. E. K., "Excitation of cyclotron spikes in the ionospheric plasma". *Can. J. Phys.* 43, 291, 1965.
12. MULDREW, D. B., and HAGG, E. L., "A novel cyclotron resonance phenomenon observed on Alouette data" (in preparation). *Can. J. Phys.*, 1965.
13. CALVERT, W., "Observations of ionospheric irregularities and plasma resonances by the fixed-frequency topside sounder, satellite", presented at NATO Advanced Study Institute, Finse, Norway, April 1965.
14. KNECHT, R. W., VAN ZANDT, T. E., and RUSSELL, S., "First pulsed radio soundings of the topside of the ionosphere". *J. Geophys. Res.* 66, 3078, 1961.
15. SMITH, R. L., BRICE, N. M., KATSUFRAKIS, J., GURNETT, D. A., SHAWHAN, S. D., BELROSE, J. S., and BARRINGTON, R. E., "An ion gyrofrequency phenomenon observed in satellites". *Nature* 204, 274, 1964.
16. BRICE, N. M., and GURNETT, D. A., "Duration of proton whistlers". Oral presentation at Fall URSI Meeting, Hanover, New Hampshire, October 4-6, 1965.
17. BARRINGTON, R. E., and BELROSE, J. S., "Preliminary results from the very-low-frequency receiver in Canada's Alouette satellite". *Nature* 198, 651, 1963.
18. BARRINGTON, R. E., BELROSE, J. S., and KEELEY, D. A., "Very-low-frequency noise bands observed by the Alouette I satellite". *J. Geophys. Res.* 68, 6539, 1963.
19. BRICE, N. M., and SMITH, R. L., "Recordings from satellite Alouette I. A very-low-frequency plasma resonance". *Nature* 203, 926, 1964.
20. BARRINGTON, R. E., BELROSE, J. S., and NELMS, G. L., "Ion composition and temperature at 1000 km as deduced from simultaneous observations of a VLF plasma resonance and topside sounding data in the Alouette I satellite". *J. Geophys. Res.* 70, 1647, 1965.
21. ALLIS, W. P., BUCHSBAUM, S. J., and BERS, A., "Waves in Anisotropic Plasmas". M.I.T. Press, Cambridge, 1963.
22. SHKAROFSKY, I. P., and JOHNSTON, T. W., "Cyclotron harmonic resonances observed by satellites". *Phys. Rev. Letters* 15, 51, 1965.
23. JOHNSTON, T. W., and NUTTAL, J., "Cyclotron harmonic signals received by the Alouette topside sounder". *J. Geophys. Res.* 69, 2305, 1964.

24. FEJER, J. A. and CALVERT, W., "Resonance effects of electrostatic oscillations in the ionosphere". J. Geophys. Res. 69, 5049, 1964.
25. BARRINGTON, R. E., and HERZBERG, LUISE, "Frequency variation in ionospheric cyclotron harmonic series obtained by the Alouette I satellite". Submitted to Can. J. Phys., 1965.
26. CRAWFORD, F. W., KRINO, G. S., and WEISS, H. H., "Transmission characteristics of cyclotron harmonic waves in plasma". Phys. Rev., 1965 (in press).
27. BERNSTEIN, I. B., "Waves in a plasma in a magnetic field". Phys. Rev. 109, 10, 1958.
28. WARREN, E. S., "Some preliminary results of sounding of the topside of the ionosphere by radio pulses from a satellite". Nature 197, 636, 1963.
29. HARVEY, C. C., "Results from the UK-2 satellite". Ann. d'Astrophys. 28, 248, 1965.
30. BUDDEN, K. G., and DANIELL, G. J., "The theory of thermal noise in the ionosphere" (private communication).
31. MULDREW, D. B. (private communication).
32. BELROSE, J. S., and BARRINGTON, R. E., "VLF noise bands observed by the Alouette I satellite". Radio Science 69D, 69, 1965.
33. BRICE, N. M., SMITH, R. L., BELROSE, J. S., and BARRINGTON, R. E., "Recordings from satellite Alouette I. Triggered very-low-frequency emissions". Nature 203, 926, 1964.
34. BARRINGTON, R. E., and McEWEN, D. J. (private communication).
35. GURNETT, D. A., SHAWHAN, S. D., BRICE, N. M., and SMITH, R. L., "Ion cyclotron whistlers". J. Geophys. Res. 70, 1665, 1965.
36. SHAWHAN, S. D., and GURNETT, D. A., "Determination of fractional concentration of  $H^+$  from proton whistler measurements". Submitted to J. Geophys. Res. 1965.
37. GURNETT, D. A., and SHAWHAN, S. D., "Determination of electron densities from the dispersion of proton whistlers" (in preparation).
38. BRICE, N. M., "Ion effects observed in radio wave propagation in the ionosphere". In Proc. of URSI Symposium on Electromagnetic Wave Theory, Delft, Holland, 1965 (in press).

#### ACKNOWLEDGEMENTS

I am indebted to the Staff of the RADIO PHYSICS LABORATORY, OTTAWA, for their constructive suggestions and for experimental data provided in advance of publication.

#### DISCUSSION

K. DAVIES — Have the resonances observed by *Alouette I* been used to determine the earth's magnetic field strength and electron density? Resonances are less sensitive to electron collision effects than are ion probes, for example, and should therefore provide a good means of determining electron density in the D- and E-regions.

B. BURGESS – Could you give us some more information about the extent of the areas of resonances?

I. PAGHIS – Perhaps the clearest example is the lower hybrid resonance (LHR). When the LHR noise bands are triggered or enhanced, Fig. 12, the measured cutoff frequencies are nearly identical whether the triggering is by upgoing atmospherics or by downgoing whistlers. Although the LHR noise bands may be triggered by whistlers travelling along the direction of the magnetic field, the noise-band signals propagate across the field. Such considerations indicate that the scale sizes of the LHR source regions observed by *Alouette I* are less than 10 km.

K. RAWER – In one of the top-side ionograms a symbol  $f_{z\infty}$  is shown. Could you please explain its meaning and whether or not there is some relation with the pole (infinity of refractive index) in the Appleton-Lassen dispersion formula?

I. PAGHIS – The frequency at which the apparent range of the  $z$ -reflection trace becomes very large is called  $f_{z\infty}$ . This large apparent range is due to large values of the refractive index, but I do not recall any analysis having been made to check whether  $f_{z\infty}$  occurs at precisely the frequency predicted from the dispersion equation for a loss-free plasma.

K. DAVIES – The  $f_{z\infty}$  does, I think, correspond to the infinity of refractive index in the Appleton formula.

K. RAWER – The generation mechanism which is indicated in the text of your paper and in Fig. 10 alludes to “strong currents in the plasma near the surface of infinite refractive index” by which the resonance phenomena could be produced. This reminds me of the “fourth reflection condition” supposed by Budden at the same interface. However, computations which I made together with Sughy (1), (2) many years ago have shown that in a real ionosphere this condition cannot be supposed to give an appreciable return. If one takes account of a temperature which is as low as 500 deg. K, the level mentioned above is found to be of conversion of (transverse) electromagnetic wave energy, into an acoustic wave in the electron gas. This coupling occurs just at the pole of the Appleton-Lassen dispersion formula, so that it becomes finite if account is taken of the acoustic electron waves. It is therefore felt that the hypothesis of a cold plasma is unrealistic at ionospheric heights where the electron temperature is between 1 000 and 2 000 deg. K.

Another point where the approach seems unrealistic is the hypothesis of a homogeneous medium, as it is well known (from whistlers and other effects) that a rather important structure of the electron concentration must be present at those heights.

1. RAWER, K., and SUCHY, K., “Longitudinal-und Transversal-Wellen im Lorentz-Plasma”. *Ann. der Phys.* 7, 3, 155-170, 1959.
2. RAWER, K., and SUCHY, K., “La ‘quatrième condition de réflexion’ d’ondes électromagnétiques dans un plasma”. *Comptes Rend.* 246, 3428-30, 1958.

I. PAGHIS – The main question appears to concern the validity of ignoring plasma wave modes in the discussion of HF ionospheric resonance. I agree with DR RAWER that this is a vital issue and have stated in my paper:

“The preceding discussion, however, assumes that the only pertinent

solutions of the dispersion equation are the two electromagnetic wave modes; this assumption may not be justified. . . . The implications of this noise analysis (Budden's analysis that includes a plasma wave mode) on the *O*-trace observations is not yet clear."

Plasma waves, it seems, may be required for an adequate discussion of some aspects of the reflection traces. The main purpose of the present paper, however, is to discuss ionospheric resonances, and we are not particularly concerned with the reflection traces. The frequencies of the HF resonances measured by *Alouette I* correspond to the resonant frequencies (and harmonics thereof) of a homogeneous anisotropic cold plasma to within the experimental error. The plasma sheath around the satellite, and other inhomogeneities in the medium do not apparently cause a measurable change in the resonant frequencies. This is the reason why the discussion of wave propagation in this paper was restricted to the two electromagnetic wave modes.

An adequate discussion of the excitation of HF resonances and of the resonance amplitude will probably require the use of a more complex plasma model which includes the thermal dispersion of electron velocities. This has already been found to be necessary in analysis of the production of the remote resonance trace at  $2f_H$ .

With regard to Dr Rawer's remarks on the fourth reflection condition, I have no specific comment, but would like to point out that the sketch in Fig. 10 does not indicate any reflection condition except at or near  $n^2 = 0$ . This corresponds to three reflection conditions for the two electromagnetic wave modes.



## CHAPTER 3-4

# IRREGULARITIES AND PLASMA RESONANCES OBSERVED BY THE FIXED FREQUENCY TOPSIDE SOUNDER SATELLITE

W. CALVERT and T. E. VAN ZANDT

Central Radio Propagation Laboratory,  
Boulder, Colorado, U.S.A.

## SUMMARY

The fixed frequency topside sounder on *Explorer 20* satellite (also known as S-48 and *Topsi*) sounds on each of six frequencies between 1.50 and 7.22 Mc/s every 105 m/s, as the satellite moves about 800 m. This sounding pattern has proven very useful for the study of field-aligned irregularities and plasma resonances on the topside of the ionosphere.

In high latitudes the irregularities are of two distinct types. One type causes continuous spread-*F* near the normal reflection levels. Most of the spread-*F* seen on bottomside soundings are of this type. The other type consists of sheets of irregularities, only 10 to 50 km thick, which extend upwards from below the normal reflection levels to far above the satellite, whose mean height is 950 km. There is evidence that these sheets are correlated with visible aurora.

The echoes from both of these types of irregularities are "back-scattered", i.e. they are reflected almost perpendicularly to the field-aligned irregularities.

On the other hand, in middle and low latitudes most of the echoes from irregularities are ducted along the irregularities and reflected from the normal reflection level. Although these ducted echoes are quite common, usually individual ducts can be seen. Occasionally, echoes of pulses ducted along the magnetic lines of force to the conjugate region are received. Such echoes have been identified up to magnetic inclinations of  $65^\circ$  or *L*'s of 2.3.

The fixed-frequency sounder has also provided important new observations of the structure of plasma resonances. On these records the resonances exhibit complicated, spin-modulated interference fringes, which should stimulate further theoretical and laboratory studies on their excitation and propagation.

This paper was also presented at the Nato Advanced Study Institute, Finse, Norway, April 1965, and will be published with the Proceedings of that meeting.





## CHAPTER 3-5

ELECTRON CONTENT MEASUREMENTS WITH  
A STATIONARY SATELLITE

E. HARNISCHMACHER

Ionosphären-Institut Breisach

After the launch of the U.S. satellite *Early Bird* on June 6, 1965, we tried to monitor the beacon signal on 136.980 Mc/s. As the orbit is equatorial and the orbital period is twenty-four hours, the satellite is at a fixed position for any ground station. It is thus possible with this satellite to determine the total electron content in the direction  $225^\circ$  azimuth and  $26^\circ$  elevation from Freiburg continuously, day and night. Knowing from ground soundings the behaviour of the inner layers of the ionosphere, we may be able to discover short- and longtime changes even in the outer region of the ionosphere.

We had got an announcement that the above frequency would be radiated by *Early Bird* at least during the month of May and probably much longer. This stimulated us to build up a special arrangement for the recording of Faraday rotations. It is, however, not enough on this frequency to observe the Faraday fading only. The number of rotations being rather small, angles inferior to  $180^\circ$  should be observable. In order to be able to distinguish the sense of the Faraday rotation we used two antennae with different orientation. The first antenna  $A_1$  is a ten-element Yagi. The axis is towards the satellite, the antenna elements are vertical. The second antenna is composed of four dipoles, each dipole being at  $45^\circ$  to the vertical. The normal to the plane of the four dipoles is directed towards the satellite. A relay allows the commutation of the antennae at the receiver input. The commutation is arranged in a way that the connection to the antenna  $A_1$  lasts for 4 minutes, whilst  $A_2$  is connected only for 1 minute to the receiver. Thus the two traces with the different antennae are easily identified.

With this system it is easy to give a quick estimate of the rotation angle in multiples of  $45^\circ$  (quarters of  $\pi$ ), just by marking the different maxima and minima on the field-strength curves. Moreover, we can take into account the instant of crossing-over of both traces or any other characteristic configuration of the curves. It is thus easy to read the rotation angle from both curves with an accuracy of about  $20^\circ$ . The indicative figures at the bottom of Fig. 1 identify: the minimum of  $A_1$  by "0", the minimum of  $A_2$  by "1", the maximum of  $A_1$  by "2" and the maximum of  $A_2$  by "3", so that "... 01230 ..." is a half-left turn and "... 32103 ..." a half-right turn of the Faraday rotation. In other words, the unit angle of this system of designation is  $\pi/4$ .

Figure 2 gives a typical example for this kind of record. At the top of the film we have the hour. At the bottom the evaluation in quarters of  $\pi$  is indicated. In this example we observe a rather fast right-hand rotation. This means that the electron content was decreasing. The sharper minima and the

broad maxima of the field-strength curves are quite well marked.

Figure 3 summarizes the results of our measurements for the period July 9 to August 12, 1965 with subdivision in epochs of 3 days. The average Faraday rotation as function of the hour is given for each 3-day period. Every morning we observe a deep minimum whilst a maximum occurs in the late evening. It should be remembered that the shape of the curves is rather variable from period to period. A summary is given in Fig. 4 which contains all observed data and permits estimation of the dispersion for all our measurements from July 9 to August 12.

We shall now check, in a rather crude manner, whether the variations in the critical frequencies of the F2 layer are of the same order. It is well known that the Faraday rotation  $\Omega$  is given in good approximation by:

$$\Omega = k_1 \cdot M \cdot \mathcal{I}_N$$

where:

$$k_1 = \text{constant}$$

$M$  is the magnetic-geometrical factor which is also more or less a constant in this particular case. It depends on three parameters:

the direction to the satellite,  
the earth's magnetic field and its direction,  
the height of the ionosphere.

$\mathcal{I}_N$  is the electron content:

$$\mathcal{I}_N = k_2 \cdot \int ds f_N^2$$

where:

$$k_2 = \text{constant}$$

If in a very first approximation we take thickness and shape of the  $F_2$  layer as being independent of the hour, we can write:

$$\Omega \approx k_3 \cdot f_0 F_2^2$$

where:

$$\begin{aligned} f_N &= \text{plasma frequency} \\ f_0 F_2 &= \text{critical frequency of the } F\text{-region} \\ k_3 &= \text{constant} \end{aligned}$$

For our intended comparison we need the geographical location of the ionospheric penetration point of the ray to the satellite. Figure 5 is a map on which the direction to the satellite is marked with an azimuth angle of  $225^\circ$ . As the elevation angle is  $26^\circ$ , we can mark the points on this ray, where the heights of 100, 200, 300 and 400 km are crossed. Ionospheric stations in this region are Freiburg, Garchy, Bern and Genova. As we have not yet the latest data, we used for all these stations critical frequencies for the month of July 1964; these have been plotted in Fig. 6. There is no doubt that the critical frequencies of the  $F_2$  layer for all the four stations are very similar. Thus, for a rough estimation and a quick comparison with the results of Faraday

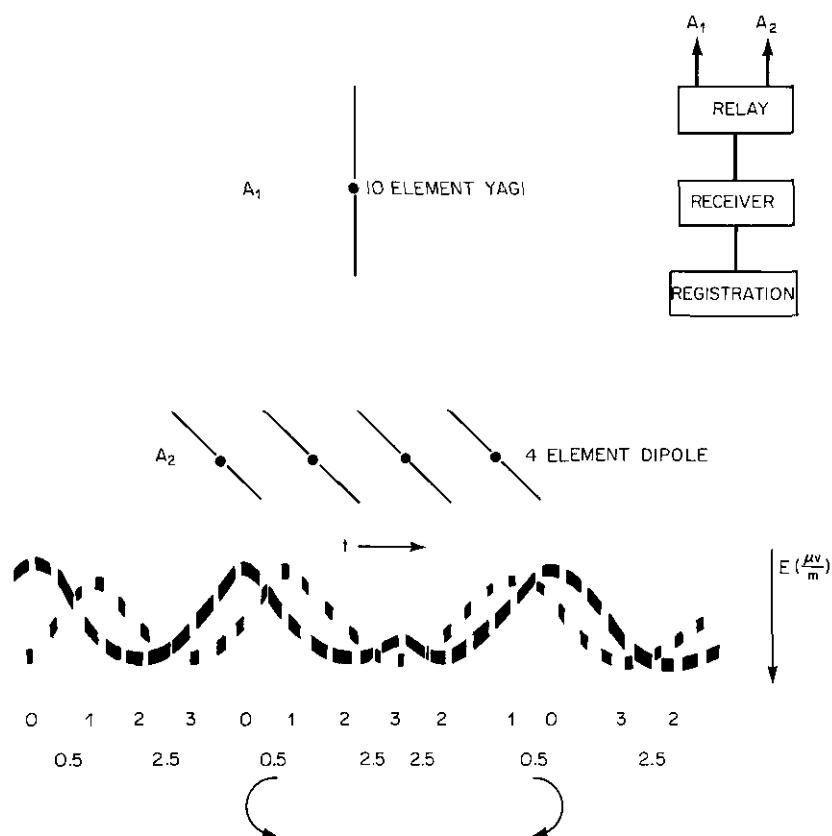


FIG. 1 Antennae arrangement and principle of measurements

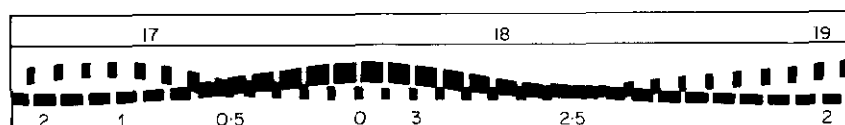


FIG. 2 Sample record (hour on top, rotation in 01230 scale on bottom)

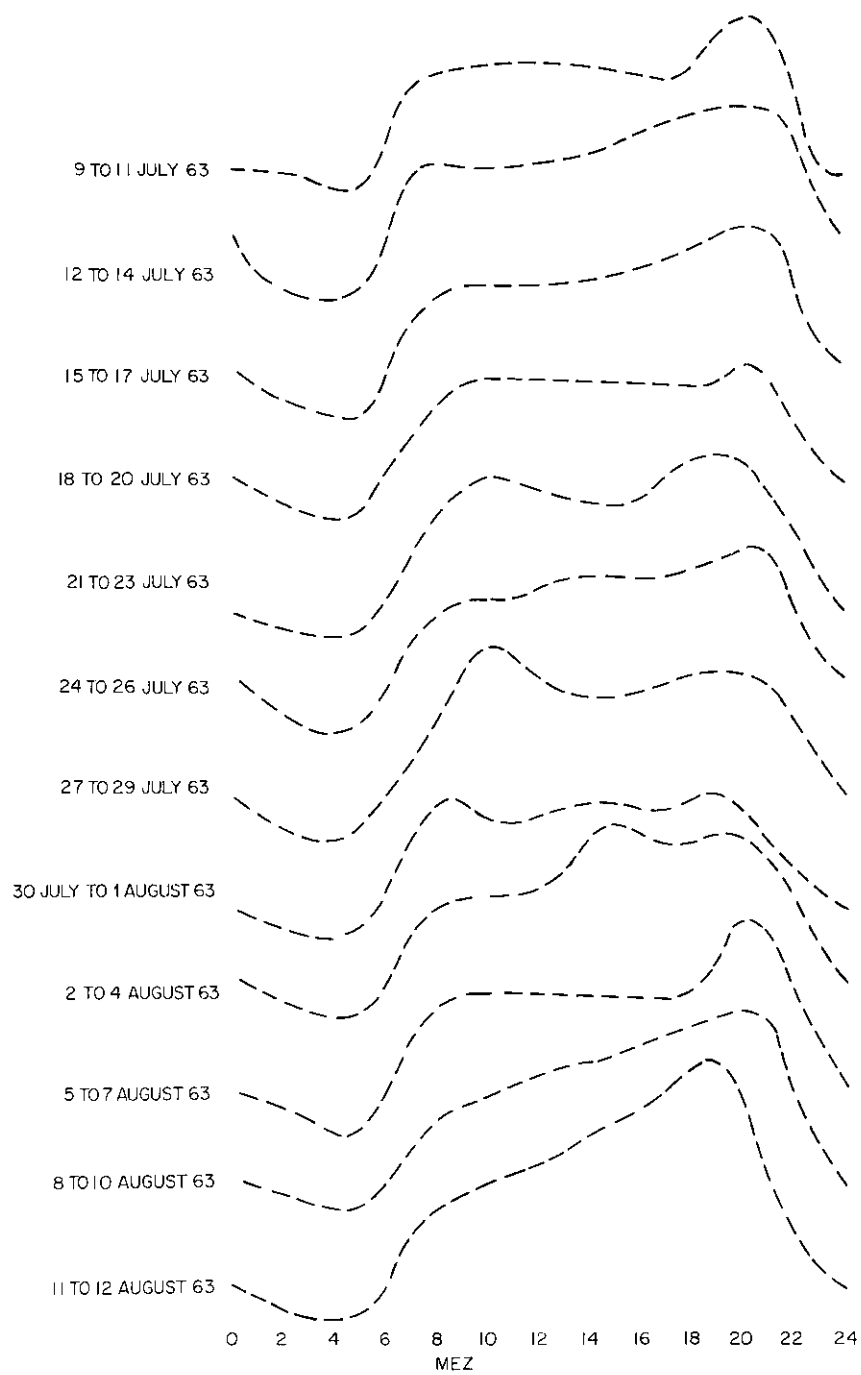


FIG. 3 Relative Faraday-rotation as function of the hour; averages for periods of three days. (Frequency 136 Mc/s)

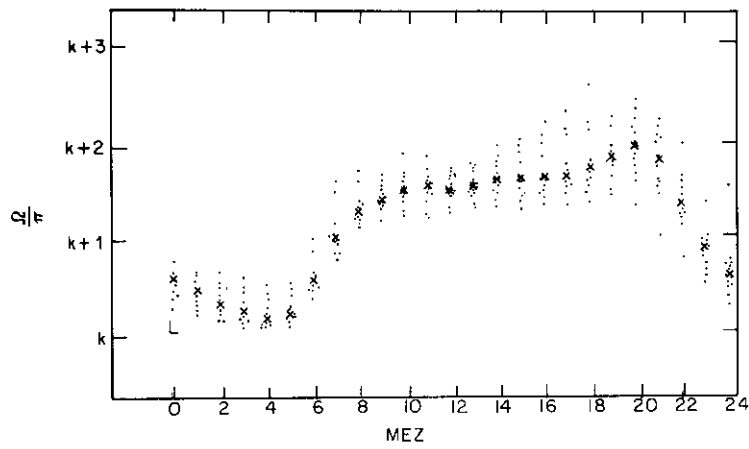


FIG. 4 Mass-plot of all Faraday data obtained from July 9 through August 12, 1965 (frequency 136 Mc/s)

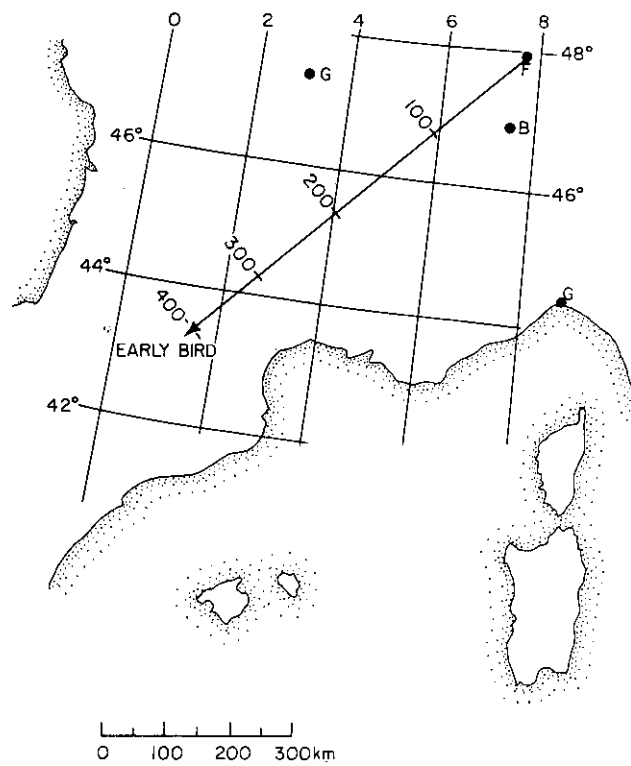


FIG. 5 Map of southern France with ray towards the satellite and penetration points at heights of 100, 200, 300 and 400 km above ground

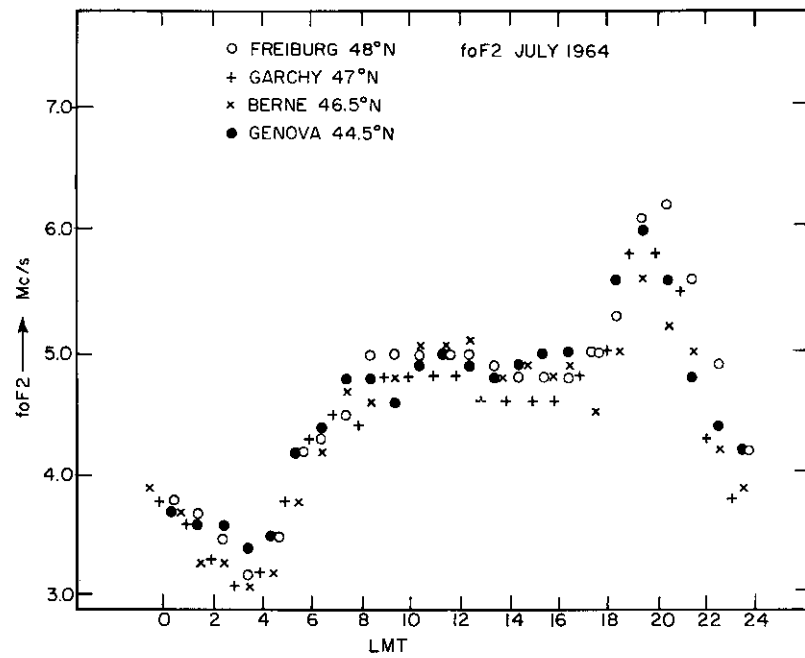


FIG. 6 Comparison of monthly median ionospheric critical frequencies for four neighbouring stations

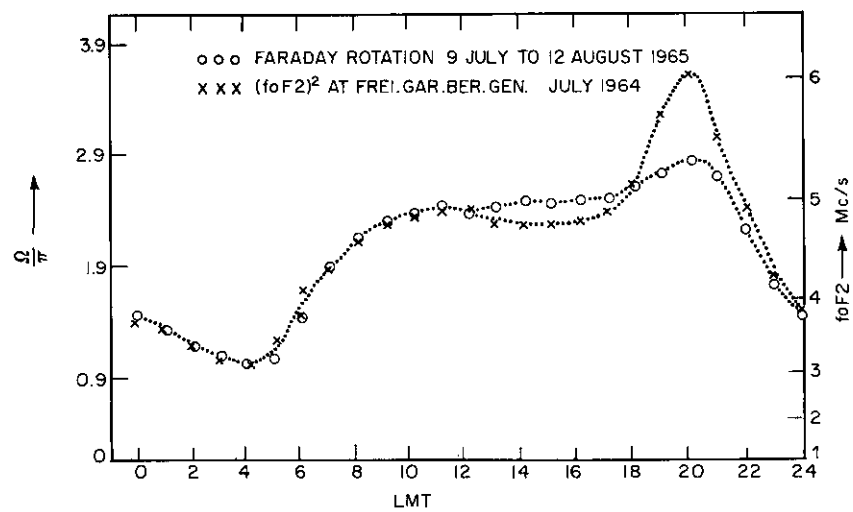


FIG. 7 Median diurnal variation of the critical frequency (crosses, right hand scale - squared) and of the observed Faraday-rotation (circles, left hand scale, adjusted by best fit method)

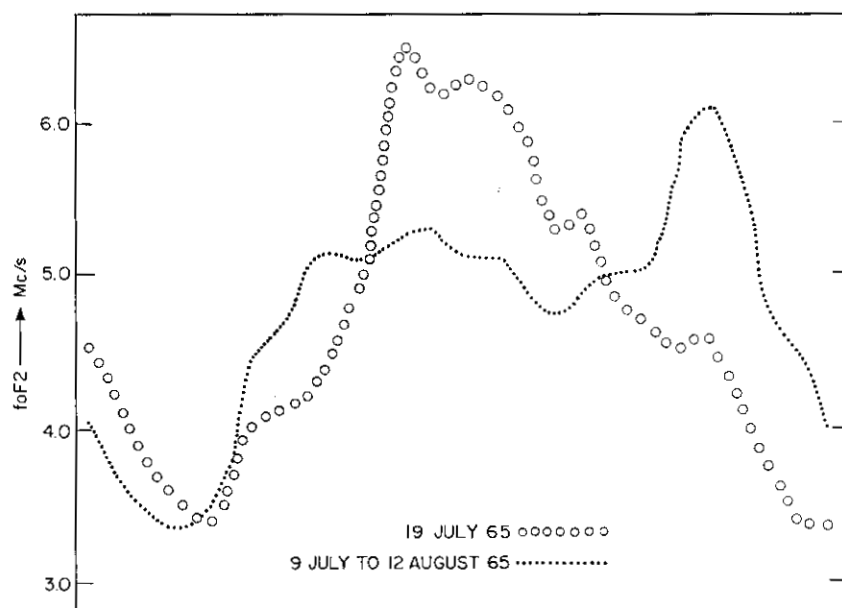
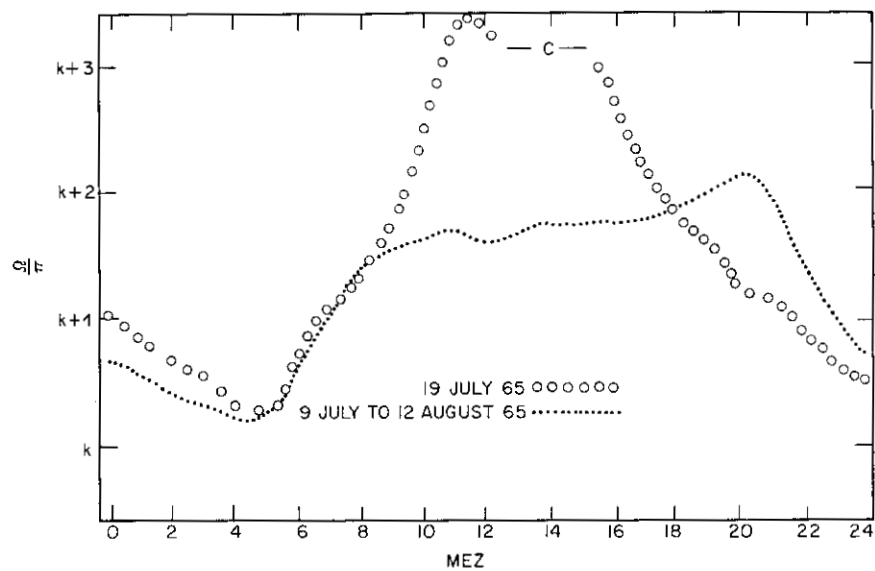


FIG. 8 Comparison of a disturbed day with the monthly median top for Faraday-rotation data, bottom for critical frequency (Freiburg)

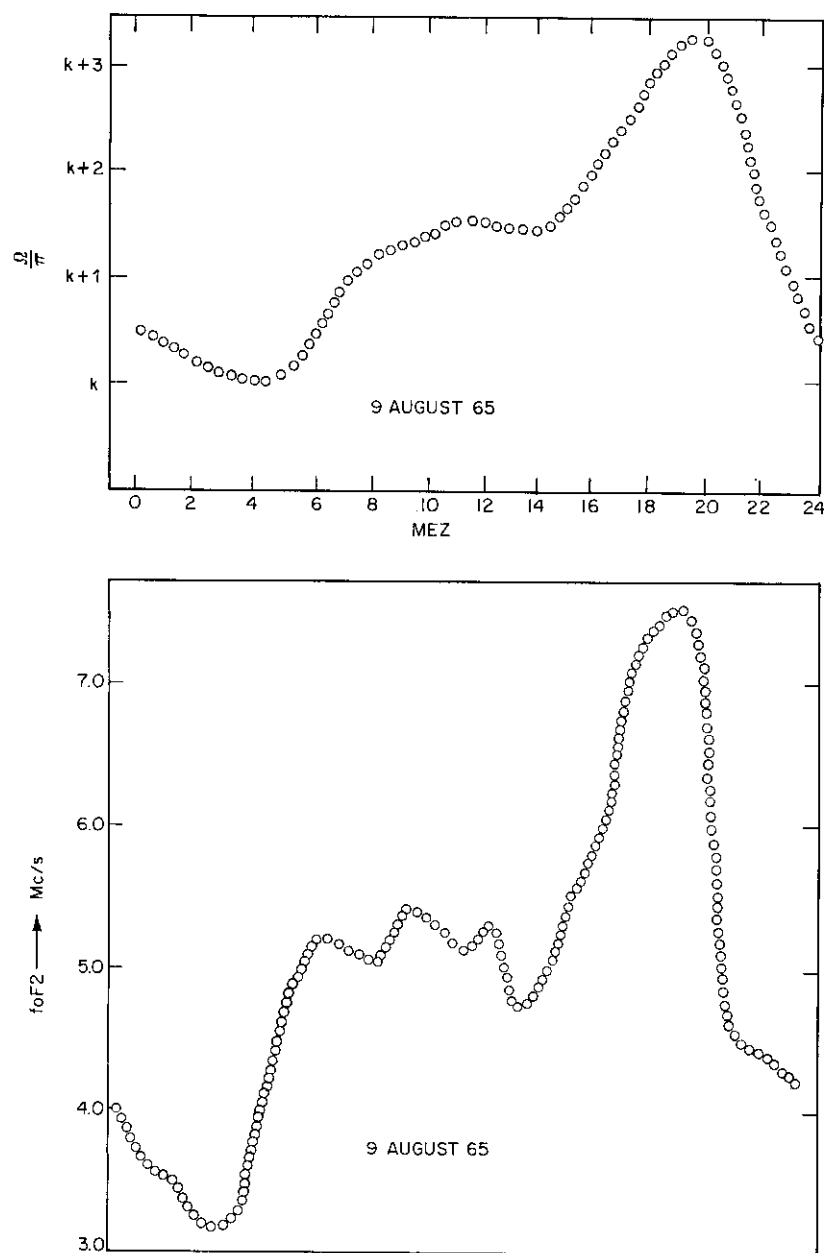


FIG. 9 Diurnal variation for a day with important evening increase; top: Faraday-rotation; bottom: critical frequency



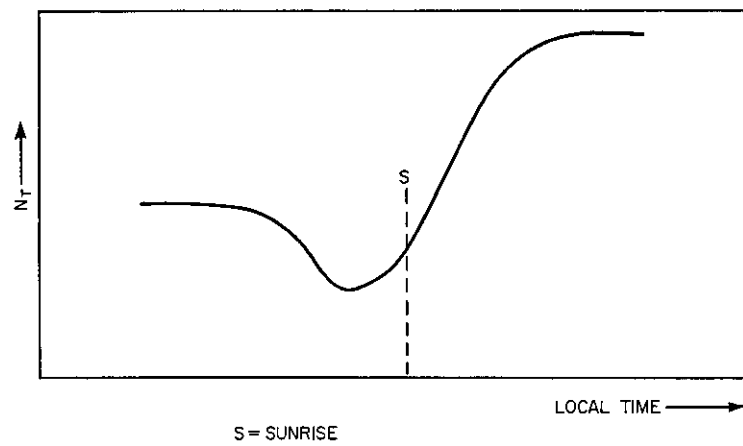


FIG. 3-A The pre-sunrise dip

rotation, we may use either the mean of the four stations or the values observed at Freiburg alone.

Figure 7 gives this comparison for the average of the Faraday data (circles) and the average out of the critical frequencies for the four stations (crosses). A linear scale for  $\Omega$  is shown at the left side and a square scale for the frequencies at the right side. In order to determine the right shift between both axes, before plotting we looked for the best fit for the two curves by trial and error, changing one of the two scales. This can, for example, be done by comparing night and morning values. We see from Fig. 7 that the behaviour of the curves is rather similar. As to the deviations in the afternoon and the evening hours we must admit that at these hours thickness and shape of the  $F_2$  layer are quickly changing and the above approximation is not justified.

As a physical result of the "best fit" operation we have the origin of the square scale for the critical frequencies, marking a certain angle on the linear scale for the Faraday rotations. This "zero angle" is given by the angle between the terrestrial and the satellite antenna. It is the angle under which we would see the great axis of the elliptic field of the satellite's turnstile antenna under the condition that there are no electrons between our station and the satellite. In our case this angle is found from the record to be about  $0.1 \pi \approx 18^\circ$ . On the other hand, with the data of the satellite *Early Bird* we found it should be  $26^\circ$ . The difference is not great.

To see whether for a given day the measurements of the Faraday rotation and the critical frequencies are similar, we selected one day with a strange behaviour. July 19 was a day with almost no evening maximum. Figures 8 and 9 give Faraday rotation at the top,  $f_0F_2$  at the bottom. Figure 8 shows nearly the same shape for both curves, for the elected day (circles) as well as for the average of the period (dots). Figure 9 shows another day with a marked evening maximum. This is August 9, 1965. Here also the similarity is rather good, except for the change in shape of the layer during the evening period.

We regret very much that since August 12, 1965, the transmission on 136.980 Mc/s from this satellite has been stopped. For this reason our simple and useful tool for controlling the topside ionosphere is no more at hand.

#### DISCUSSION

E. VASSY – In connection with the Joint Satellite Studies Group, we have started observations in the same way as the Breisach Group.

This method only permits measurements of the variations of total electron content; but its interest lies in the comparison of results obtained from stationary and orbiting satellites. This allows a check of the accuracy of the method by avoiding the difficulties due to the motion of the satellite.

K. RAWER – It appears from this paper that the use of the concept of "total electron content" might be better replaced by that of "equivalent thickness" of the ionosphere. This would lead to the comparison of the measured data with those from ionosondes, thus revealing more information than comes from electron content measurements alone.

K. DAVIES – The diurnal variation in  $N_T$ , the total electron content as measured by the *Syncom III* satellite over the Pacific, shows a marked pre-sunrise dip as in Fig. 1. Has Dr Harnishmacher observed this in Europe and has he an explanation?

K. C. YEH – It is proposed that the pre-sunrise dip in electron content, as in the case of the sunset peak in electron content, is due to a change in the electron temperature. In the post-sunset period the relaxation of electron temperature to ion temperature causes electrons to flow downward along the magnetic lines of force and hence enhance the  $f_oF_2$  and the content. It is possible that in the sunrise period the electron temperature exceeds the ion temperature. This causes the electrons to flow outward along the lines of force and also possibly a decrease in  $f_oF_2$  and the total content.

H. SOICHER – With regard to the pre-dawn dip we have data of a post-midnight enhancement with a Transit satellite.

#### ACKNOWLEDGEMENT

This work has been undertaken in the framework of a series of investigations supported by BUNDESMINISTERIUM FÜR WISSENSCHAFTLICHE FORSCHUNG, Grant No. J459.



## CHAPTER 3-6

USING IONOSPHERIC PREDICTION CHARTS TO  
TENTATIVELY FORECAST VLF SIGNAL INTENSITY  
IN SATELLITE COMMUNICATIONS

H. J. ALBRECHT

Forschungsinstitut für Hochfrequenzphysik, 5321 Werthhoven,  
Federal Republic of Germany

Experiments conducted by means of the *Lofti I* satellite have proved that the very low frequencies may possibly be useful for communication between the earth's surface and satellites. Reference is here made to the basic paper by J. P. Leiphart *et al.*, (1) who have published the first results of this experiment and their interpretation. The *Lofti I* satellite was launched on February 21, 1961; its last transmission occurred on March 30, 1961. Details of orbital parameters, instrumentation, etc., may be found in the paper mentioned. J. P. Leiphart and his co-authors also compared, on a general basis, the results obtained with some theoretical deductions. In their theoretical work and with regard to the ionospheric absorption experienced by a VLF wave travelling in the ionosphere, they assumed the angle of inclination of the wave normal to the geomagnetic field to be zero. Up to a certain degree this assumption may approach the true condition; it definitely simplifies the evaluation of the absorption coefficient calculated by means of the complex refractive index. (2). In a note published in 1963, C. Altman and H. Cory (3) have pointed out that the assumption mentioned does not necessarily coincide with the angle of minimum absorption loss.

It is the purpose of these notes to indicate some steps towards forecasting the VLF signal intensity at satellite positions above the lower edge of the so-called D-layer which is supposed to be the lowest effective ionized region. The objective is a general prediction procedure yielding approximate signal level at any possible position in the upper atmosphere and using the prediction methods employed for ordinary world-wide communications in the high-frequency range. In other words, the CRPL-D prediction charts (4), (5) issued by the U.S.-N.B.S. are regarded as basic world-wide information on ionospheric parameters. It should be emphasized that any prediction method obviously refers to average conditions for the prediction period. On the other hand, attention has to be paid to selecting these average conditions such that discrepancies are kept to a minimum. This short contribution represents an attempt to arrive at a useful method. Most likely, corrections will have to be applied in the future, although this is primarily a question of the availability of data. Only the final results of a comparison are to be mentioned here.

As a first approach, a VLF signal is considered to be propagated in the generally accepted mode between the lower ionosphere and earth surface. Parameters for such VLF propagation have been dealt with by many

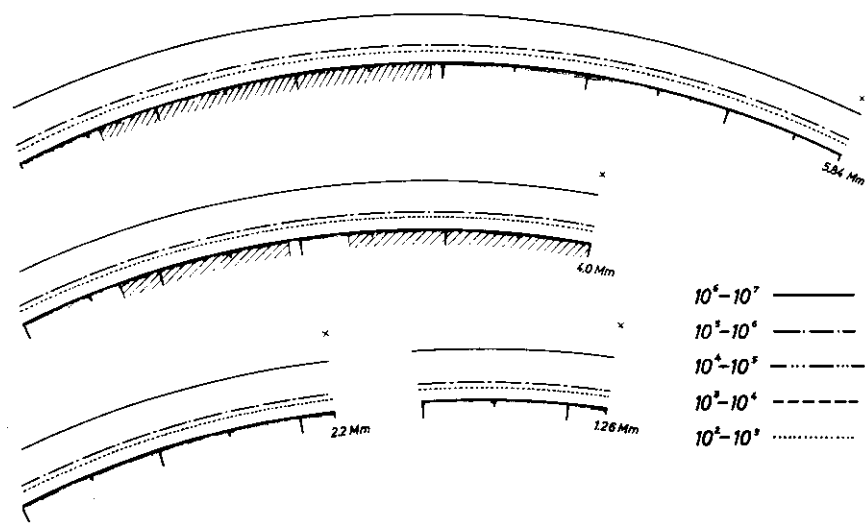


FIG. 1 Ionospheric parameters relative to the great circle distance from a ground transmitter

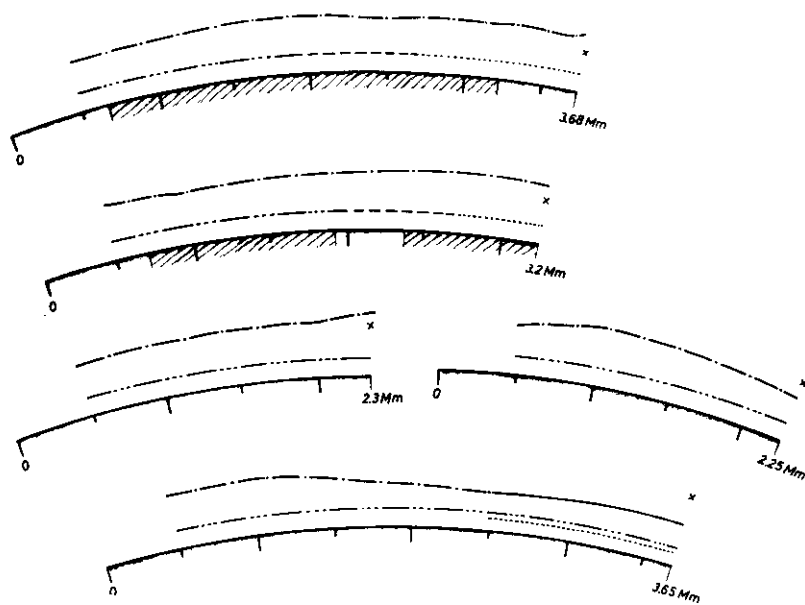


FIG. 2 Dawn path parameters

research workers in a large number of publications. To be mentioned are basic papers by Watson (6) and Wait (7) and a very useful comparison of theoretical and experimental investigations published by Watt and Croghan (8). Depending upon ionospheric parameters, some portion of the transmitted energy may penetrate through the lower region of the ionosphere. To determine approximately the signal intensity reaching the satellite, it seems to be necessary to take into account only rays penetrating the layer relatively close to the satellite position. In a further step to simplify the procedure, a circuit control point may be defined, as in some high-frequency prediction methods which utilize parameters at two control points to forecast the behaviour of a long-range transmission circuit. The probable signal intensity at the satellite position may now be predicted by considering, up to the control point, the attenuation due to propagation within the belt between the two boundaries, ionosphere and earth's surface, and, thereafter, the ionospheric absorption on an assumed passage of some 70 km length. Figure 1 illustrates the ionospheric parameters relative to the great circle distance from a ground transmitter. It shows several path diagrams for signals actually measured with the *Lofti I* experiment. Basically, the path diagrams are similar to those used by the author several years ago to analyse long-range propagation paths on high frequencies (9), (10). In the case on hand, ionospheric prediction charts issued by the CRPL for March 1961 have been employed as a basis of information. Figure 2 shows parameters encountered on a dawn path of *Lofti I*. As an initial step the control point has been assumed to be located about 500 km from the satellite position, both with respect to surface distance. Beyond the control point, attenuation may be expected to be given, in a first approach, with a simplified relationship obtained by equating the angle of inclination to zero, similar to the way indicated by Leiphart and his co-authors. The attenuation for a path length of 70 km would then be represented by:

$$\delta_i = 1.26 \times 10^{-6} \sqrt{N\nu} \quad (1)$$

where  $N$  and  $\nu$  represent the electron density in el/cm<sup>3</sup> and the collision frequency, respectively. The main contribution to attenuation is supposed to occur in the lowest ionospheric region. On the other hand, the prediction charts available contain only values of the E-2000-MUF. This parameter may be re-converted to  $f_oE$ , the appropriate value of maximum electron density may be determined, and a collision frequency around an average value of  $10^5$  collisions per second can be assumed. On the other hand, the parameter  $f_oE$  may be calculated directly without the use of prediction charts using a method due to Harnischmacher (11), (12). The probable VLF signal intensity can now be computed by applying a balance equation of the usual type where:

$$E_{[\text{dB above } 1\mu\text{V/m}]} = E_R - \delta_p - \delta_g - \delta_i \quad (2)$$

with the signal reference  $E_R$  including the power of the transmitter, spreading term, and the distance-dependent attenuation for the first megameter;  $\delta_p$  represents the path loss for the remaining megameters and  $\delta_g$  is the loss due to ground conditions. Results obtained for the conditions experienced during the *Lofti I* experiment are compiled in Table 1. It may be mentioned that,

TABLE I

Lofti position	signal intensity in dB above $\mu\text{V/m}$	
	measured $\pm 5$ dB	computed
Orbit 421 21 March		
Local time 8.05 a.m.	14	9.8
9.10 a.m.	14	8.3
10.15 a.m.	6	7.9
11.20 a.m.	6	6.1
Orbit 434 22 March		
Local time 5.55 a.m.	43.5	44.8
7.00 a.m.	23.5	28.1
8.05 a.m.	12	16.2

in computing the signal intensity, an eventual non-reciprocity in the path loss may be taken into account by considering relevant data given by Watt and Croghan (8) for the transmission loss per unit length. The effect of the ground may be accounted for by a chart of the kind published by Wait (7) if only a small portion of the path covers land surface. If this effect is considered to be essential, changes in climatic ground conditions can be accounted for by calculation methods and a chart published by the author some time ago (13), (14). The ionospheric loss is computed as shown above, employing the  $f_oE$  parameter at 500 km from the satellite position.

Considering the measurement accuracy indicated in by Leiphart *et al.* (1), there seems to be reasonable agreement between values computed and measured. It appears that more measurements are definitely desirable for a more conclusive comparison.

## REFERENCES

1. LEIPHART, J. P., ZEEK, R. W., BEARGE, L. S., and TOTH, E., "Penetration of the Ionosphere by very-low-frequency radio signals - interim results of the *Lofti I* experiment". Proc. I.R.E. 50, 6-17, 1962.
2. Appleton-Hartree formula published, e.g., in K. G. BUDDEN, Radio waves in the ionosphere, Cambridge, 1961.
3. ALTMAN, C., and CORY, H., "Comments on 'penetration of the ionosphere by very-low-frequency radio signals - interim results of the *Lofti I* experiment'". Proc. I.E.E.E. 51, 250, 1963.
4. "Basic Radio Propagation Predictions". CRPL Series D.
5. N.B.S., U.S., "Instructions for the use of basic radio propagation predictions".
6. WATSON, G. N., "The transmission of electric waves round the earth". Proc. Roy. Soc. (A) 95, 546-63, 1919.
7. WAIT, J. R., "The attenuation vs. frequency characteristics of VLF radio waves", Proc. I.R.E. 47 768-71, 1957.
8. WATT, A. D., and CROGHAN, R. D., "Comparison of observed VLF



- attenuation rates and excitation factors with theory". J. Res. Nat. Bur. Stand. 68D, 1-9, 1964.
9. ALBRECHT, H. J., "Further studies on the chordal-hop theory of ionospheric long-range propagation". Arch. Met. Geoph. Biokl. Ser. A 11, 84-92, 1959.
  10. ALBRECHT, H. J., "Analysis of ionospheric paths in long-range propagation". Indian J., Met & Geoph. 11, 57-63, 1960.
  11. HARNISCHMAGHER, E., C.R., Paris, 1301, 1950.
  12. RAWER, K., Die Ionosphäre, Noordhoff, 1953.
  13. ALBRECHT, H. J., "Näherungsformeln für die Berechnung einer physikalischen Beeinflussung der elektrischen Erdbodencharakteristik im Rahmen fernmeldetechnischer Anwendungen". Inter. Elektr. Rundsch 17, 451-2, 1963.
  14. ALBRECHT, H. J., "Variable ground characteristics and their effect on signal attenuation between 10 and 20 kc/s". Proc. I.R.E.E. Austr. 25, 534-6, 1964.

#### ACKNOWLEDGEMENTS

MR. H. REPPERMUND for assistance with some of the numerical calculations.



## CHAPTER 3-7

LARGE-SCALE IRREGULARITIES AND HORIZONTAL  
GRADIENT OF THE IONOSPHERE FROM ACTIVE  
SATELLITES TRANSMISSIONS MEASUREMENTS

M. ANASTASSIADES and D. MATSOUKAS

Ionospheric Institute, National Observatory, Athens

## SUMMARY

A spaced receiver technique is used between the tracking centres of Athens and of the Island of Crete, some 320 km apart, in order to investigate large irregularities and variations in the electron content at mid-latitudes.

Amplitude recordings of signals from the satellites *S-66* and *DE-C* were used for this purpose and the horizontal gradients of the electron content were determined.

The higher values of the electron content were generally observed to the south, which is in good agreement with the previous observations, but some characteristic discrepancies from this behaviour were in evidence.

The variations of the horizontal gradient of the electron content from day to night and from one period to another during several months are discussed. Sizes and heights of large irregularities as deduced by means of the spaced receiver technique are also presented and discussed.

## INTRODUCTION

Several papers on small- or large-scale irregularities have been published in which radio stars, vertical sounding or amplitude recordings from active satellite were used, in order to get information on their occurrence, size, densities, etc. (1), (2), (3), (4). In the present paper some results on large-scale irregularities are discussed and a new method to calculate the ionospheric horizontal gradient in electron content is presented.

**Observations** – The amplitude of the 40 Mc/s signal from a satellite was recorded simultaneously by three tracking centers, forming the Greek satellite tracking network, Fig. 1. Tracking centers are situated at Penteli Hill (38° 02' lat. 23° 51' long.), Crete Island (35° 2' lat. 23° 3' long.) and Alexandroupolis (40° 45' lat. 25° 52' long.). Signals were received on horizontal dipole aerials, orientated N-S. All receivers of Motorola type have a bandwidth of 4 kc/s to accommodate the Doppler frequency shift. Unitron d.c. amplifiers were used and the Sefram recorder speed was 6 cm/min.

**Method of analysis** – It is well known that Faraday rotation is given by the relation:

$$\Omega = kMN \quad (1)$$

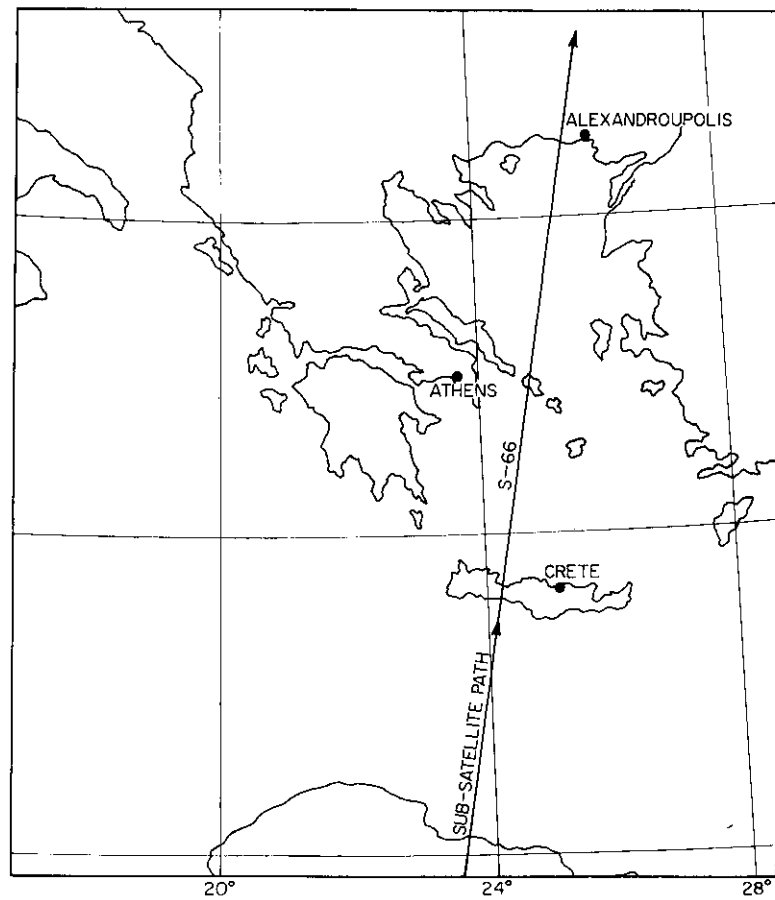


FIG. 1 Greek satellite tracking network

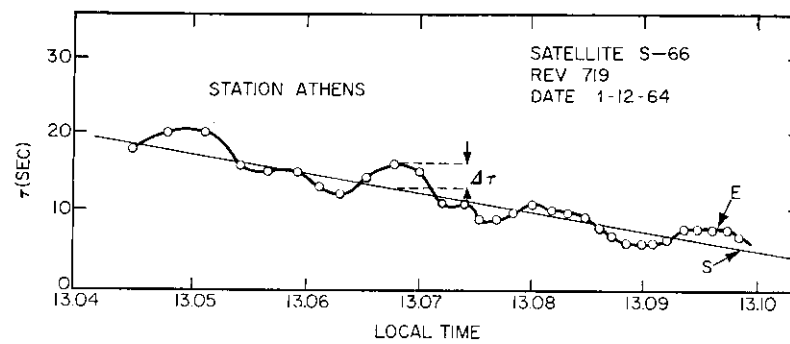


FIG. 2 Variation  $T$  versus  $t.E.$  gives the measured Faraday period and  $S$  is the smoothed curve

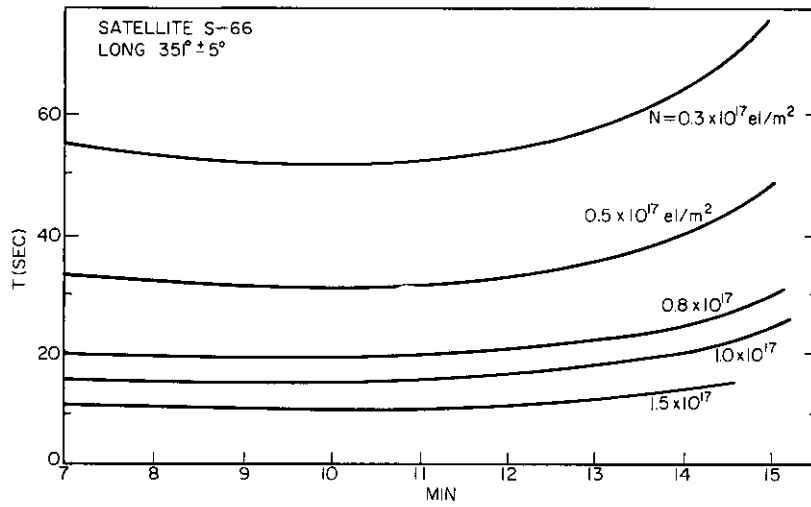


FIG. 3 A set of reference curves  $T(t)$  for a zone between  $346^\circ$ - $356^\circ$  long. W: The horizontal axes give the time distance of sub-satellite point from equator

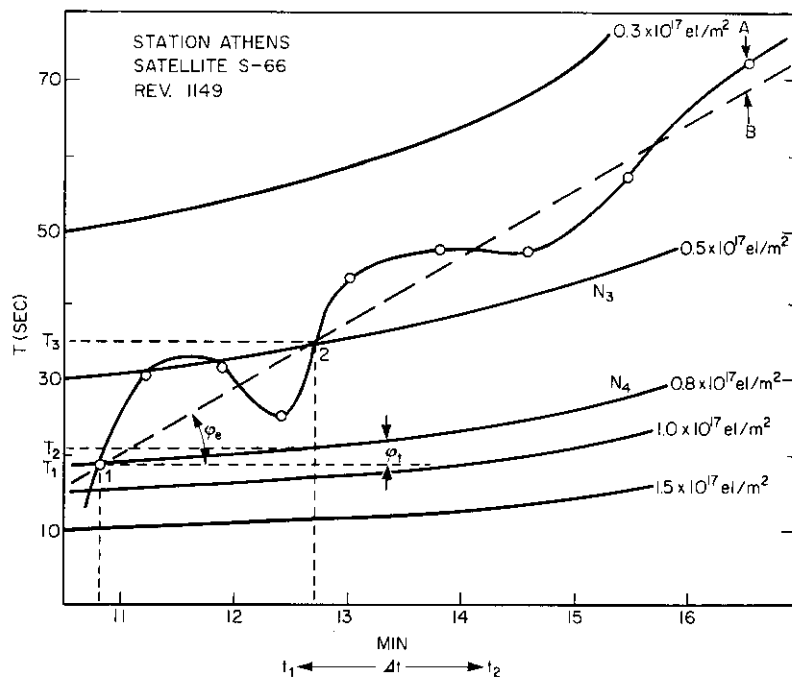


FIG. 4 Reference curves with experimental one (A) of the same zone B as the smoothed curve

where:

- $k = 0.00473/f^2$  in mks units
- $f$  = the wave frequency in c/s
- $M$  = magnetic field function
- $N$  = the electron content in a column between the observer and satellite.

Since for one rotation we have two nulls in the amplitude of the received signal, we have:

$$2 \frac{d\Omega}{dt} = 2k \left( \frac{dM}{dt} N + \frac{dN}{dt} M \right) = \frac{1}{T} \quad (2)$$

where  $T$  is the time difference between the successive Faraday nulls and  $\frac{1}{T}$  is the Faraday fading rate.

In order to investigate large-scale irregularities in an ionospheric area, it is possible to plot for each amplitude recording the curve  $\Omega$  versus  $t$  or  $T$  versus  $t$ , as in Fig. 2. Plotting  $T(t)$  is more sensitive to ionospheric irregularities as compared to the curve  $\Omega$  versus time  $t$ . The average relative deviation  $\frac{\Delta T}{T}$  of the experimental curve from the smoothed one, drawn by hand, has been shown by Liszka to be a sensitive indication of the appearance and of the magnitude of irregularities. Approximately 450 amplitude recordings from one center only (Penteli – near Athens) were analysed using the above method.

In order to simplify Eq. 2 we start in assuming that  $\frac{dN}{dt} = \Omega$  i.e. that the ionosphere has not any gradient. Equation 2 is then simplified to  $\frac{1}{T} = 2KN \frac{dM}{dt}$  or  $T = \frac{1}{2KN \frac{dM}{dt}}$

For every satellite pass the variation of  $\frac{dM}{dt}$  may be derived from existing tables giving the  $M$ -magnetic factor. In selecting different values of electron content  $N$  for an ionosphere without gradient, and for paths within a longitudinal zone of  $10^\circ$ , a set of reference curves  $T(t)$  can be plotted. For every  $10^\circ$ -width zone a definite set of curves can be plotted. Figure 3 shows a set of such reference curves for one of the zones.

In comparing reference curves with experimental ones of the same zone, useful information can be derived on a horizontal gradient as in Fig. 4. Amplitude recordings give  $T(t)$  curve, like  $A$ . The smoothed curve like  $B$ , drawn by hand, indicates an ionosphere presenting a definite gradient. Irregular fluctuations of curve  $A$  from  $B$  indicate variation of electron content superimposed on an ionosphere with a constant gradient. It can be easily shown that the difference in slope between the smoothed curve  $B$  and the reference curve is proportional to the above-mentioned horizontal constant gradient.

The difference in slopes  $D$  from Fig. 4 is:

$$D = tg\phi_e - tg\phi_i = \frac{T_3 - T_2}{\Delta t}$$

$$D = \frac{\frac{1}{2k \bar{M}_2 \bar{N}_3} - \frac{1}{2k \bar{M}_2 \bar{N}_4}}{\Delta t} = \frac{\bar{N}_4 - \bar{N}_3}{\Delta t \bar{N}_4} \cdot T_3 \quad (3)$$

At point 1 we have:

$$\frac{1}{2k \bar{M}_1 \bar{N}_4} = \frac{1}{2k (\bar{M}_1 \bar{N}_{e1} + \bar{N}_{e1} \bar{M}_1)}, \bar{N}_4 - \bar{N}_{e1} = \bar{N}_{e1} \frac{\bar{M}_1}{\bar{M}_1} \quad (4)$$

where  $\bar{N}_{e1}$ ,  $\bar{N}_{e1}$  are the electron content and the gradient in the smoothed ionosphere at the position 1.

At point 2 we have:

$$\frac{1}{2k \bar{M}_2 \bar{N}_3} = \frac{1}{2k (\bar{M}_2 \bar{N}_{e2} + \bar{M}_2 \bar{N}_{e2})}$$

$$\bar{N}_3 - \bar{N}_{e2} = \bar{N}_{e2} \frac{\bar{M}_2}{\bar{M}_2} \quad (5)$$

Subtracting Eq. 5 from Eq. 4 and under the condition that  $\bar{N}_{e1} = \bar{N}_{e2} = \bar{N}$

we have:  $\bar{N}_4 - \bar{N}_3 = \bar{N}_{e1} - \bar{N}_{e2} + \bar{N} \left( \frac{\bar{M}_1}{\bar{M}_1} - \frac{\bar{M}_2}{\bar{M}_2} \right)$

and

$$D = -\bar{N} \left( 1 + \frac{\bar{M}_2/\bar{M}_2 - \bar{M}_1/\bar{M}_1}{\Delta t} \right) T_3/\bar{N}_4 \quad (6)$$

The difference of slope then can be used as an index of the order of magnitude of a constant horizontal gradient which is associated with the irregularities.

#### EXPERIMENTAL RESULTS ON LARGE IRREGULARITIES - SEASONAL VARIATION OF $\frac{\Delta T}{T}$

During the period October 1964 to July 1965 amplitude recordings on 40 Mc/s from satellite *S-66* were obtained. For the present analysis we used recordings chosen to be without interferences and with a not-too-slow fading rate. For each recording we compute the average value of irregularity index  $\frac{\Delta T}{T}$ . Seasonal variation on large irregularities has been examined by several authors, (3), (4), (6). They have found that there is no very significant variation. On the other hand, Fooks found that large irregularities detected with vertical sounding technique are larger during the winter. Following our observations, our material has been divided into two periods: winter (November–December–January) and summer (May–June–July).

Figure 5 shows the probability of occurrence of various values of irregularities index for the two seasons. It seems that there exists a slight difference of distribution with season irregularities having larger amplitude during the winter period than during the summer. However, it is difficult to decide if there is any characteristic behaviour of irregularities with season.

#### DIURNAL VARIATION OF $\frac{\Delta T}{T}$

The diurnal variation of large irregularities has been investigated by

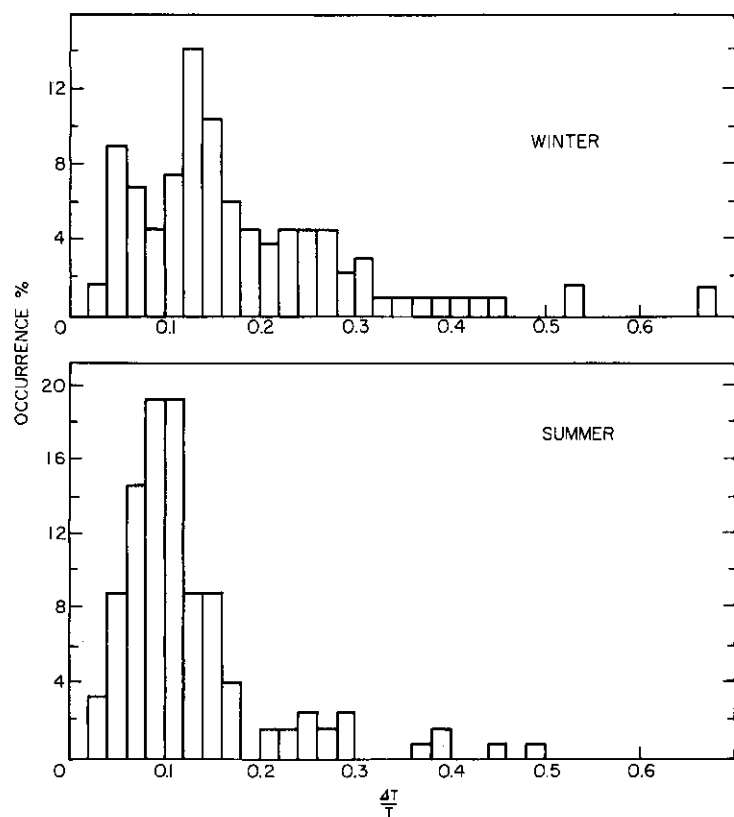


FIG. 5 Histogram of occurrence of various values of the irregularity index observed at Athens during the two seasons winter 1964, summer 1965

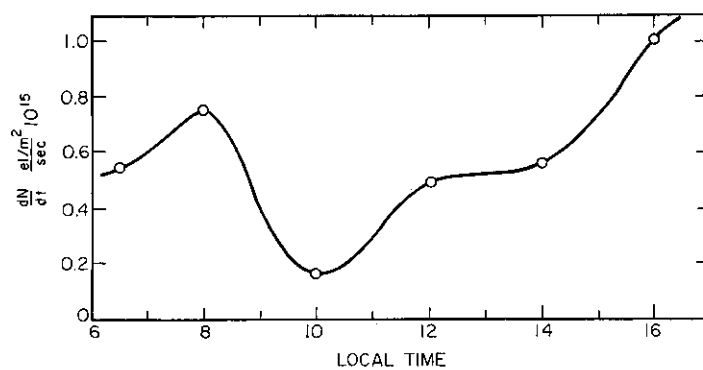


FIG. 6 Daytime variation of the measure horizontal gradient



several authors. Titheridge (3) (New Zealand) found that there was no diurnal variation of the occurrence of large irregularities. He observed only a tendency for irregularities to be less common during the early morning. On the contrary Merrill (6) *et al.* have found a clear variation. Results from Liszka (4) (Kiruna) are of special importance to us because they refer to observations in high latitudes but of the same longitude as Athens.  $\frac{\Delta T}{T}$  is slightly larger than the average during the early morning and the late evening. Merrill (6) found that this variation is more evident. Diurnal variations have been examined separately for winter and summer periods. The average  $\frac{\Delta T}{T}$  for each hour of day are shown in Fig. 7 and the number of values is given under each point.

We can conclude as a preliminary result that a diurnal variation is evident during the summer. We observe two maxima, one in the early morning 0600–0700, local time, and the second during the first hours of night. A minimum, almost constant, appears during day-time. The daily distribution  $\frac{\Delta T}{T}$  during the winter appears less clear, but still there are maxima, in the early morning and in the early night hours, as well as a clear minimum during the day. It is evident, therefore, that all these maxima, on the daily distribution of  $\frac{\Delta T}{T}$  happen after sunrise and sunset.

From Fig. 7 we can also observe a slight seasonal variation of  $\frac{\Delta T}{T}$ , which is larger during winter than during summer time.

#### HORIZONTAL GRADIENT

Using the above-described method, for the calculation of horizontal gradient we are able to measure the gradient along the part of the ionosphere which is parallel to the direction of satellite motion and is controlled by one station. This value is only the component of the total gradient along the direction of satellite motion.

From *S-66* amplitude recordings, and for the period November–December 1964 and January 1965, horizontal gradients were calculated.

Figure 6 shows the distribution of calculated values during the day hours only. Owing to the rather limited number of recordings available, it is difficult to reach conclusions about the diurnal variation of horizontal gradient. We can, however, accept that it is at a minimum around 10.00 hrs, which is in accordance with the general diurnal ionospheric variation. From all examined records, an increase of electron content was found for decreasing latitude. This result is in accordance with other measurement on electron content using the two-frequency technique at 40 and 41 Mc/s.

#### CORRELATION OF THE HORIZONTAL GRADIENT WITH IONOSPHERIC PARAMETERS

The order of magnitude of the computed values of horizontal gradient is approximately  $0.5 \times 10^{-5} \text{ el/m}^2, \text{ sec}^{-1}$ . However, there are several values greatly exceeding the above-mentioned average value.

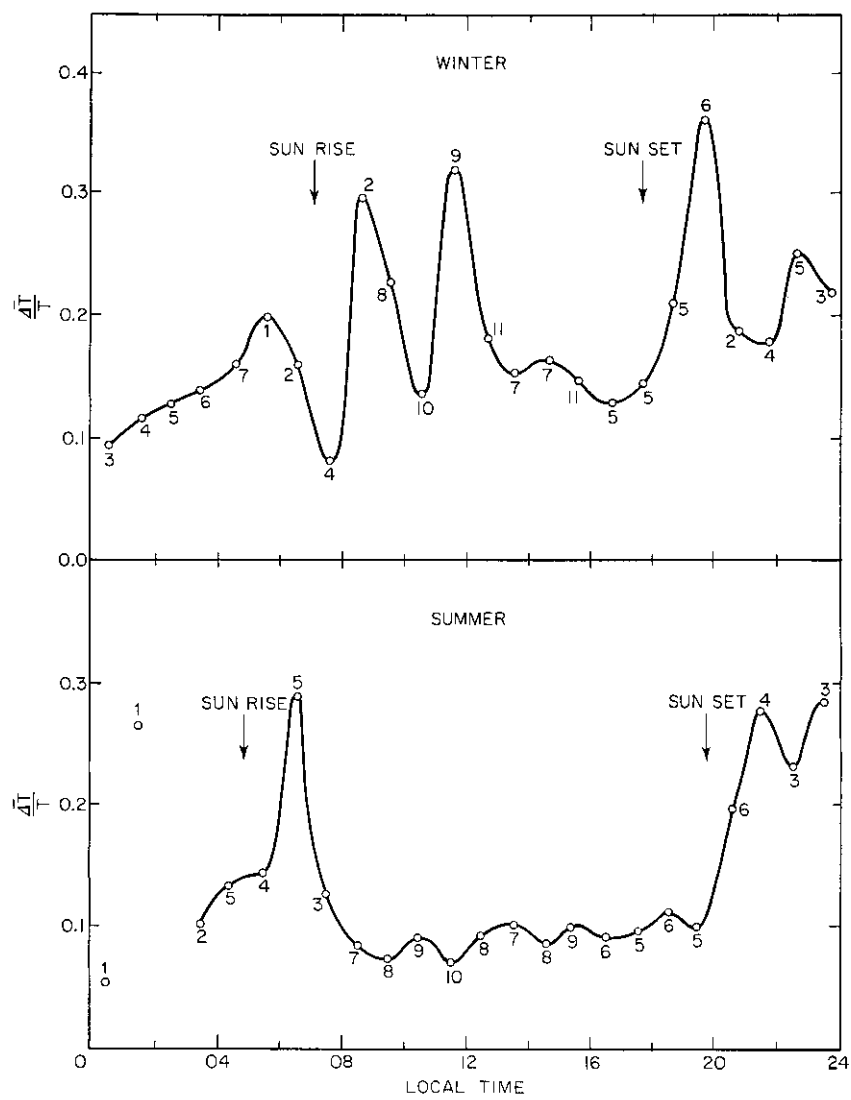


FIG. 7 The average irregularity index  $\frac{\Delta T}{T}$  versus local time

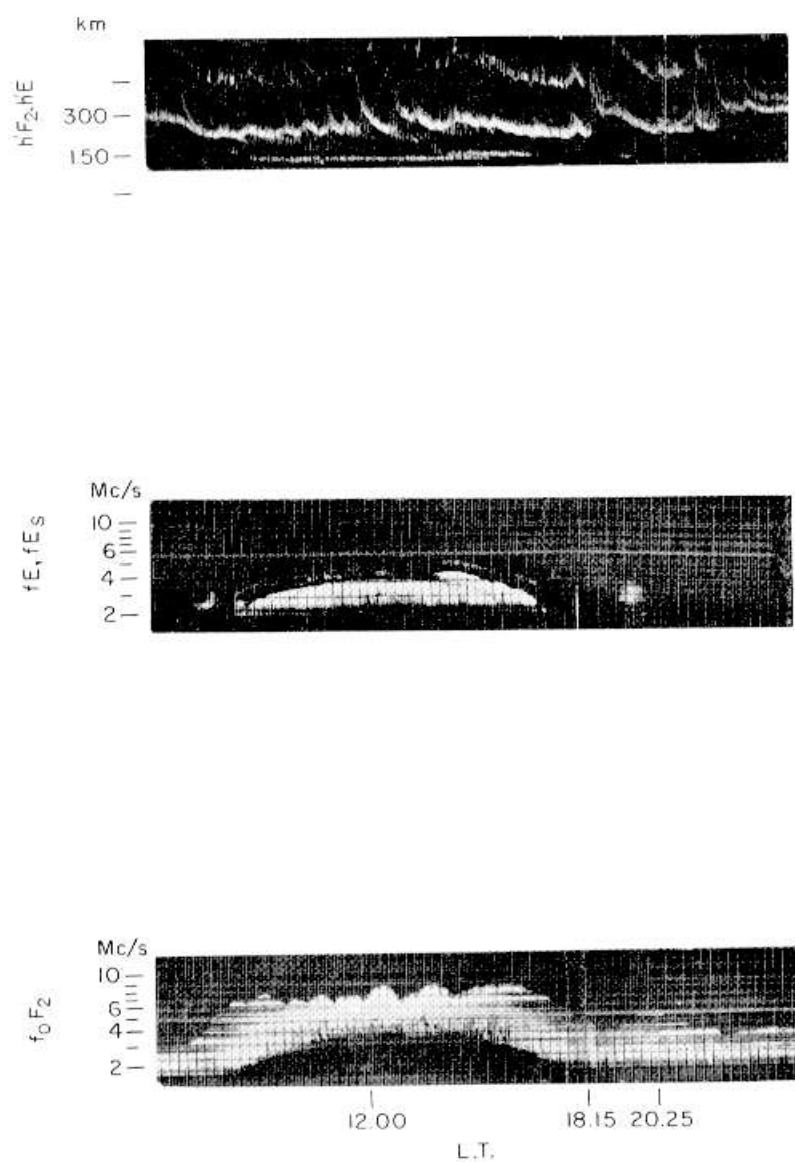


FIG. 8 Continuous recordings of ionospheric parameters  $h'F_2$ ,  $hE$ ,  $fE_s$ ,  $f_0F_2$  measured by vertical sounding technique, January 14, 1965

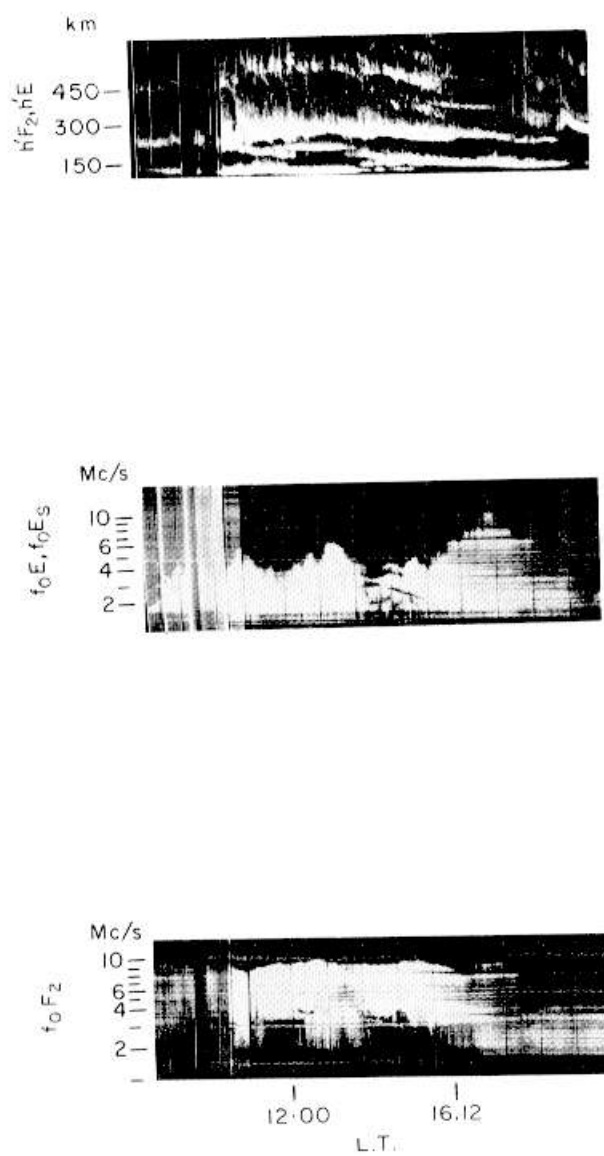


FIG. 9 Continuous recording of ionospheric parameters  $h'F_2$ ,  $h'E$ ,  $f_oE$ ,  $f_oE_s$ ,  $f_oF_2$  measured by vertical sounding technique, November 11, 1964

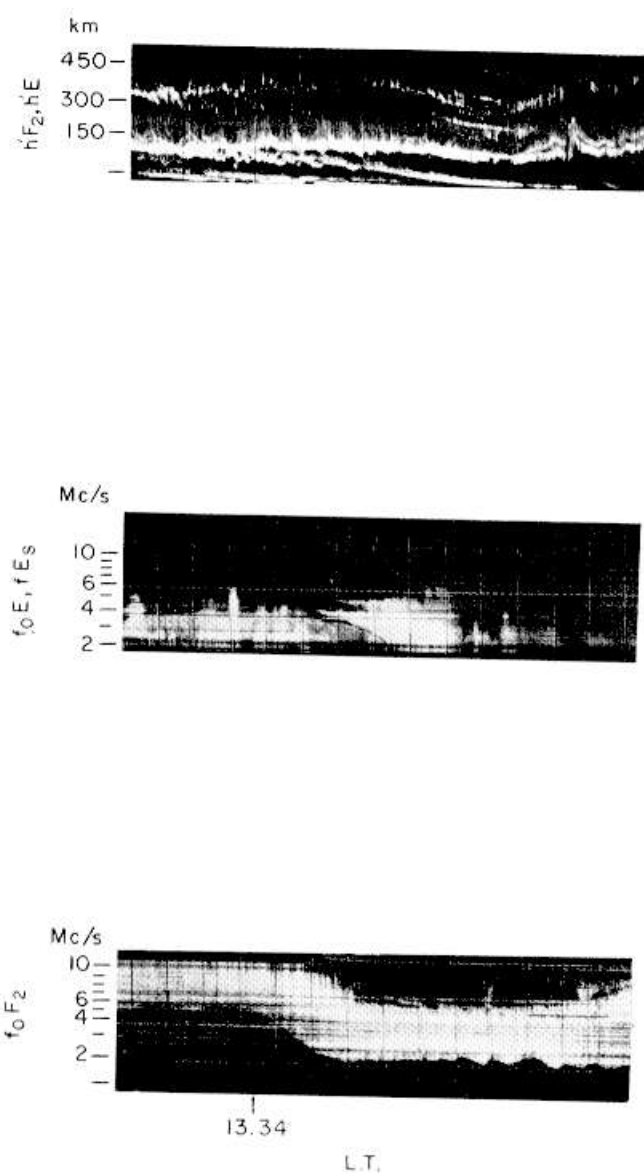


FIG. 10 Continuous recording of ionospheric parameters  $h'F_2$ ,  $h'E$ ,  $f_oE$ ,  $fE_s$ ,  $f_oF_2$  measured by vertical sounding technique November 13, 1964

An attempt was made to compare these excess values with ionospheric parameters. Taking into consideration that the horizontal gradient is the gradient of the ionosphere at the near approach of satellite path, we can compare these values, in a first approximation, with the ionospheric parameters taken from continuous recordings of vertical sounding of Scaramaga station, near Athens.

Figure 8 presents the continuous recordings of ionospheric heights and critical frequencies for the layers  $E$  and  $F$ . In this figure, at 2025 hrs an increase of critical frequency  $f_0F_2$  is observed as well as a variation of the height of the layers  $F_2$ . At the same recordings and at 1815 hrs is observed a value of  $f_0F_2$  smaller than the previous one. During the above two periods, the calculated horizontal gradient is  $9.9 \times 10^{15}$  and  $0.27 \times 10^{15}$  respectively. We observe then a simultaneous increase of  $f_0F_2$  with horizontal gradient. The increased value of the gradient corresponds also with some anomalous behavior of height. Some correlation also can be established with the appearance of sporadic  $E$ . Figure 9 is a continuous recording of  $f_0E$  obtained by vertical sounding, in which we can observe at 1612 hrs an intense increase of  $f_0E_s$  which corresponds to an increased value of horizontal gradient of the order of  $4.15 \times 10^{15}$  much in excess of the above-mentioned average value. Figure 10 is another case in which nothing particular is observed on the vertical sounding continuous recordings of  $f_0E$  and  $f_0F_2$ , but the observed high horizontal gradient at 1334 hrs is associated with an abnormal decrease of height which indicates a travelling wave in the ionosphere.

All the above-mentioned cases are but first attempts to correlate horizontal gradient with various characteristic ionospheric parameters. Many data on horizontal gradient, covering all periods and all hours, are needed to determine the parameter with the closest correlation.

#### CONCLUSIONS

Large ionospheric irregularities are investigated in a more sensitive and simple way, by using  $T$ , rather than  $\Omega$  versus time. Seasonal variation of large irregularities is not very clearly established, but it seems that there is a slight tendency for them to appear more frequently during winter.

Diurnal variation seems to be associated with sunrise and sunset, presenting around those hours more than one maximum. In winter time there are two maxima during sunrise, greater in value than the corresponding early-morning maximum observed in summer. Minima are present for both seasons after midnight. As a general rule, large irregularities in our middle latitudes are correlated with the sun's zenith-angle variation.

Measured values of horizontal gradient show an increase of electron content with decreasing latitude. This is in good agreement with many other results obtained by other techniques and methods on electron content in middle latitudes.

All the above results are obtained from observations from one tracking center (Penteli – near Athens). Amplitude recordings, simultaneously obtained for definite satellite paths, are now under investigation. It is expected that more information, not only on horizontal gradient, but also on size, heights and structure of large-scale irregularities, will be discussed in a subsequent chapter.

## REFERENCES

1. LITTLE, G. C., and LAWRENCE, R. S., "The use of polarisation fading of satellite signals to study the electron content and irregularities in the ionosphere". J. Res. Nat. Bur. Stand. 64D, 335, 1960.
2. EVANS, J. V., and TAYLOR, G. N., "The electron content of the ionosphere in winter". Proc. Roy. Soc. A263, 189, 1961.
3. TITHERIDGE, J. E., "Large scale irregularities in the ionosphere". J. Geophys. Res. 68, 3399, 1963.
4. LISZKA, L., "Report of Joint Satellite Group", p. 45.
5. LISZKA, L., and TAYLOR, G. N., "A synoptic study of large scale ionosphere irregularities using observations of the Faraday rotation of satellite signals". J. Atmos. Phys. 27, 843, 1964.
6. MERRILL, R. G., LAWRENCE, R. S., and ROPER, N. J., "Synoptic variations and vertical profiles of large scale ionospheric irregularities".





## CHAPTER 3-8

DIFFRACTION OF RANDOM WAVES IN A  
HOMOGENEOUS ANISOTROPIC MEDIUM

K. C. YEH

Electrical Eng. Res. Lab., University of Illinois

## SUMMARY

This paper considers the diffraction of random waves in a homogeneous anisotropic medium. These random waves are produced, for example, by reflection from a rough surface such as the moon or by transmitting through the ionosphere containing irregularities. Due to anisotropy both depolarization effect and the modification of spectral density functions of the wave by the medium may occur. Both effects may be important in certain ionospheric applications. In the forward scatter approximation it has been found that the sum of spectra of orthogonally polarized waves is uninfluenced by the medium.

## INTRODUCTION

The study of wave propagation in the magneto-ionic medium is concerned with solving the wave equation of the form

$$\nabla \times \nabla \times (\vec{F} \cdot \vec{D}) - \omega^2 \mu_0 \epsilon_0 \vec{D} = 0 \quad (1)$$

where  $\vec{F}$  is the relative inverse dielectric tensor. In Eq. 1 the electric displacement vector  $\vec{D}$  is used rather than the usual electric field intensity  $\vec{E}$ , since it is known that  $\vec{D}$  is transverse while  $\vec{E}$  is, in general, not (1). The plane wave solution of Eq. 1 has been studied quite extensively especially its refractive indices known as the Appleton-Hartree formula. Exp  $j\omega t$  time dependence is assumed throughout. All quantities are in rationalized MKS units.

The present investigation is concerned with the study of propagation of random waves in such a medium. Specifically the statistical properties of the wave are given at an initial plane. Through diffraction the fields propagate in the half space. The statistical properties of the wave at a plane parallel to the initial plane are desired. The method used is similar to that used by others who assumed the medium to be isotropic (2). Hence this study represents a slight generalization of the earlier work. However, it is found that due to anisotropic nature of the medium the additional effects such as depolarization of the wave and the modification of spectral density of the field by the medium will appear.

## BRIEF REVIEW

The purpose of this section is to briefly review those aspects and properties of the plane wave solution useful to later analysis. In the meantime, the conventions and notations are also explained.

Following notations will be used (as recommended by URSI) for the plasma frequency, the gyrofrequency and the normalized dimensionless quantities:

$$\begin{aligned}\omega_p^2 &= N e^2 / m \epsilon_0 & \vec{\omega}_H &= - |e| \vec{B}_0 / m \\ X &= \omega_p^2 / \omega^2 & \hat{Y} &= \vec{\omega}_H / \omega\end{aligned}\quad (2)$$

Orient the coordinate axes so that the propagation vector  $\vec{k}$  is along  $z$ , the steady magnetic field and hence also  $\vec{Y}$  in the  $yz$  plane. Assume that the radio frequency is much larger than the gyrofrequency. This permits us to ignore  $Y^2$  terms and this is done consistently in this investigation. With this approximation the relative inverse dielectric tensor is given by:

$$\vec{F} = \frac{1}{(1 - X)^2} \begin{bmatrix} 1 - X & -jXY_L & jXY_T \\ jXY_L & -1 - X & 0 \\ -jXY_T & 0 & 1 - X \end{bmatrix} \quad (3)$$

where  $Y_L$  and  $Y_T$  are respectively the longitudinal and transverse components of  $Y$ . For plane waves Eq. 1 is reduced to:

$$(-\vec{k}\vec{k} \cdot \vec{F} + k^2 \vec{F} - \omega^2 \mu_0 \epsilon_0 \vec{I}) \cdot \vec{D} = 0 \quad (4)$$

where  $\vec{I}$  is the identity matrix. The immediate conclusion when Eq. 3 is substituted into Eq. 4 is the vanishing of  $D_z$ , hence the electric displacement is polarized entirely in the plane transverse to  $\vec{k}$ . With this simplification the remaining equations expressed in the matrix form are:

$$\begin{bmatrix} \frac{1}{1 - X} - \frac{\omega^2 \mu_0 \epsilon_0}{k^2} & -\frac{jXY_L}{(1 - X)^2} \\ \frac{jXY_L}{(1 - X)^2} & \frac{1}{1 - X} - \frac{\omega^2 \mu_0 \epsilon_0}{k^2} \end{bmatrix} \begin{bmatrix} D_x \\ D_y \end{bmatrix} = 0 \quad (5)$$

In order for the equation to have non-trivial solution the determinant of the coefficient matrix must vanish. If again  $Y^2$  and higher-order terms are ignored, the following expressions for the refractive indices are obtained.

$$k^2 / \omega^2 \mu_0 \epsilon_0 = 1 - X \mp XY \cos \theta \quad (6)$$

where  $\theta$  is the angle between the propagation vector and the steady magnetic field. The wave with the upper sign in Eq. 6 as the refractive index is designated as the ordinary wave and is circularly polarized in the left-handed sense; the wave with the lower sign is designated as the extraordinary wave and is circularly polarized in the right-handed sense. Now Eq. 6 is nothing more than the usual expression used in connection with the study of Faraday effect and it is valid under the quasi-longitudinal approximation. Fuller analysis shows that such approximation is valid for nearly all directions of propagation except the region at which the direction of propagation is but a few degrees from exactly perpendicular to the steady magnetic field. Later development assumes Eq. 6 is valid for all regions and such an assumption makes sense only if the quasi-transverse region makes negligible contribution to the total effect.

Let  $k^{(0)}$  and  $k^{(x)}$  denote the propagation constants of the ordinary and the extraordinary waves respectively. Their mean and difference can be found as:

$$(k^{(0)} + k^{(x)})/2 = \omega[\mu_0\epsilon_0(1 - X)]^{1/2} \equiv k_0 \quad (7)$$

$$k^{(0)} - k^{(x)} = -\omega^2\mu_0\epsilon_0 XY \cos \theta/k_0 \quad (8)$$

It is known that a wave of any polarization can be decomposed into two characteristic waves; each will propagate independently in the medium with its corresponding propagation constant and polarization. The resultant is the sum of these two waves. In the present case the resultant wave is particularly simple if it is assumed that the resultant is polarized linearly at some initial position. The resultant wave will propagate with a propagation constant equal to the mean of the propagation constants of the characteristic waves and its polarization is kept linear with the plane of polarization rotated continuously along the direction of propagation (Faraday effect). As computed in Eq. 7, the mean of the propagation constants is just the propagation constant of the corresponding isotropic medium (i.e. in the absence of the steady magnetic field). The rotation of the polarization is through an angle equal to one-half of the difference of the propagation constants multiplied by the distance of travel. For a plane wave propagating in  $z$  direction with the electric displacement polarized in  $y$  direction at  $z = 0$  the resultant takes the form:

$$D_x = -D_0 \sin \Omega \cdot \exp j(\omega t - k_0 z) \quad (9)$$

$$D_y = D_0 \cos \Omega \cdot \exp j(\omega t - k_0 z)$$

where the rotational angle is

$$\Omega = -\frac{\omega^2\mu_0\epsilon_0 XY \cos \theta}{2k_0} \cdot z \quad (10)$$

In general if the wave is assumed to be polarized in  $yz$  plane at  $z = 0$  and the direction of propagation has a polar angle  $\alpha$  and azimuthal angle  $\beta$  the field is given by:

$$\begin{aligned} D_x &= -D_0 (\sin^2 \beta + \cos^2 \beta \cos^2 \alpha)^{1/2} \sin \Omega \exp j(\omega t - \vec{k}_0 \cdot \vec{r}) \\ D_y &= D_0 (\sin^2 \beta + \cos^2 \beta \cos^2 \alpha)^{-1/2} (\cos \alpha \cos \Omega + \\ &\quad + \sin^2 \alpha \sin \beta \cos \beta \sin \Omega) \exp j(\omega t - \vec{k}_0 \cdot \vec{r}) \\ D_z &= D_0 (\sin^2 \beta + \cos^2 \beta \cos^2 \alpha)^{-1/2} \cos \beta \cos \alpha \sin \alpha \sin \Omega - \\ &\quad - \sin \beta \sin \alpha \cos \Omega \exp j(\omega t - \vec{k}_0 \cdot \vec{r}) \end{aligned} \quad (11)$$

For cases of small polar angles Eq. 11 can be approximated by:

$$\begin{aligned} D_x &= -D_0 \sin \Omega \exp j(\omega t - \vec{k}_0 \cdot \vec{r}) \\ D_y &= D_0 \cos \Omega \exp j(\omega t - \vec{k}_0 \cdot \vec{r}) \\ D_z &= 0 \end{aligned} \quad (12)$$

The Faraday rotational angle  $\Omega$  appeared in Eq. 11 and 12 is the same as that given by Eq. 10 except  $z$  is to be replaced by  $r$ . Since  $\Omega$  plays an important role in the diffraction, its discussion will be postponed until later.

## DIFFRACTION OF RANDOM WAVES

The problem assumes that the statistical properties of the fields are given at some initial plane, say at  $z = 0$ . Our interest is in learning the statistical properties of the displacement vector at some plane parallel to the initial plane after propagating in the kind of medium discussed in the Brief Review. This suggests the use of the notation  $\vec{D}(\vec{r}_\perp; z)$  which stresses the fact that statistical properties are desired for various values of  $z$  in the two dimensional space  $\vec{r}_\perp = (x, y)$ , when their properties at  $z = 0$  are known. The problem is explicitly posed when the following (boundary) conditions are assumed.

(1)  $D(\vec{r}_\perp; 0)$  is polarized in  $yz$  plane. However, we are most interested in the case of small polar angles; it will be assumed the approximate expression of Eq. 12 is valid for all plane waves. This means that at  $z = 0$ , the wave can be assumed to be polarized entirely along  $y$  axis.

(2)  $D(\vec{r}_\perp; 0)$  is a complex homogeneous random field (3) with zero mean and known correlation functions that are absolutely integrable over all  $\vec{r}_\perp$ . This assures the existence of the spectral density functions.

(3) For  $z > 0$ , the displacement vector satisfies Eq. 1, at least approximately.

(4) As  $z \rightarrow \infty$ , the retarded solution is taken.

The method used here follows that used in the theory of time-series analysis. Like the theory of time-series analysis, the Fourier transform of  $D(\vec{r}_\perp; 0)$  does not in general exist because of the condition 2. This difficulty can be overcome as done by Wiener (4) by truncating  $D(\vec{r}_\perp; 0)$ . Therefore, let:

$$D_R(\vec{r}_\perp; 0) = \begin{cases} D(\vec{r}_\perp; 0) & \vec{r} \in R \\ 0 & \vec{r} \notin R \end{cases} \quad (13)$$

where  $R = \{x, y | X/2 < x < -X/2, Y/2 < y < -Y/2\}$ .<sup>\*</sup> Define in the mean square sense the amplitude spectral density function.<sup>†</sup>

$$\begin{aligned} D_R(\vec{\kappa}; 0) &= \int_{-\infty}^{\infty} \int D_R(\vec{r}_\perp; 0) e^{+j\vec{\kappa} \cdot \vec{r}_\perp} d^2r_\perp \\ &= \int_R \int D(\vec{r}_\perp; 0) e^{-j\vec{\kappa} \cdot \vec{r}_\perp} d^2r_\perp \end{aligned} \quad (14)$$

Then through Fourier inversion:

$$D_R(\vec{r}_\perp; 0) = \frac{1}{(2\pi)^2} \int_{-\infty}^{\infty} \int D_R(\vec{\kappa}; 0) e^{-j\vec{\kappa} \cdot \vec{r}_\perp} d^2\kappa \quad (15)$$

Note that since  $D_R(\vec{r}_\perp; 0)$  is assumed to have zero mean, so is  $D_R(\vec{\kappa}; 0)$ . The autocorrelation is obtained by:

$$K(\xi, \eta; 0) = \langle D(x, y; 0) D(x + \xi, y + \eta; 0) \rangle \quad (16)$$

<sup>\*</sup> Note that here  $X$  and  $Y$  are specific values of  $x$  and  $y$  respectively, not those defined by (2).

<sup>†</sup> Fourier transform pairs are distinguished by their arguments, same symbols are used here.

where the angular brackets are used to denote the ensemble average. Since  $K$  is assumed to be absolutely integrable over the infinite range, there exists a non-negative spectral density function defined by:

$$S(\vec{r}; 0) = \lim_{\substack{X \rightarrow \infty \\ Y \rightarrow \infty}} \frac{1}{XY} < D_R(\vec{r}; 0) D_R(\vec{r}; 0) > \quad (17)$$

By Wiener-Khinchine theorem  $K(\xi, \eta; 0)$  and  $S(\vec{r}; 0)$  form a Fourier transform pair (5). In case  $D(\vec{r}_\perp; 0)$  is additionally ergodic the autocorrelation function defined by Eq. 16 can be obtained through spatial average

$$K(\xi, \eta; 0) = \lim_{\substack{X \rightarrow \infty \\ Y \rightarrow \infty}} \frac{1}{XY} \int_{-\infty}^{\infty} \int_{-\infty}^{\infty} D_R(x, y; 0) D_R(x + \xi, y + \eta; 0) dx dy \quad (18)$$

with probability 1. In Eqs. 16, 17 and 18  $X$  and  $Y$  are specific values of  $x$  and  $y$  respectively, not those defined by (2).

The problem assumes that  $S(\vec{r}; 0)$  (or equivalently  $K(\xi, \eta; 0)$ ) is given and the expressions of the spectral densities and the autocorrelations for some finite values of  $z$  are desired. Now in the half-space  $z > 0$ , the fields are given by the superposition of many plane waves of the form of Eq. 12. With  $\exp j\omega t$  factor suppressed, these are given by:

$$\begin{aligned} D_{xR}(\vec{r}_\perp; z) &= -\frac{1}{(2\pi)^2} \int_{-\infty}^{\infty} \int_{-\infty}^{\infty} D_R(\vec{k}_\perp; 0) \sin \Omega(\vec{k}_\perp; z) e^{-j\sqrt{k_0^2 - k_\perp^2} z} \\ &\quad e^{-j\vec{k}_\perp \cdot \vec{r}_\perp} d^2 k_\perp \\ D_{yR}(\vec{r}_\perp; z) &= \frac{1}{(2\pi)^2} \int_{-\infty}^{\infty} \int_{-\infty}^{\infty} D_R(\vec{k}_\perp; 0) \cos \Omega(\vec{k}_\perp; z) e^{-j\sqrt{k_0^2 - k_\perp^2} z} \\ &\quad e^{-j\vec{k}_\perp \cdot \vec{r}_\perp} d^2 k_\perp \quad (19) \end{aligned}$$

where  $\vec{k}_\perp = (k_x, k_y)$ . Above expressions are certainly valid when  $z = 0$  at which, since  $\Omega = 0$ , Eq. 19 reduces to Eq. 15. This sets  $\vec{k} = \vec{k}_\perp$ . The first property of  $D_{xR}(\vec{r}_\perp; z)$  and  $D_{yR}(\vec{r}_\perp; z)$  can be obtained by averaging Eq. (19) over the ensemble, it concludes that both components have zero mean for any value of  $z$ . As indicated earlier the case of interest is when all component waves propagate in the forward direction like the consideration of Fresnel diffraction problems. In other words,  $D_R(\vec{k}_\perp; 0)$  has appreciable value only over the region  $k_0^2 < k_\perp^2$  (corresponding to evanescent waves) can be ignored. Therefore, the elements of the spectral matrix are obtained as

$$\begin{aligned} S_{xx}(\vec{k}_\perp; z) &= S(\vec{k}_\perp; 0) \sin^2 \Omega \\ S_{xy}(\vec{k}_\perp; z) &= S_{yx}(\vec{k}_\perp; z) = S(\vec{k}_\perp; 0) \cos \Omega \sin \Omega \\ S_{yy}(\vec{k}_\perp; z) &= S(\vec{k}_\perp; 0) \cos^2 \Omega \end{aligned} \quad (20)$$

For the special case of isotropic medium Eq. 20 shows that there is no depolarization effect; and the spectral density and hence also the autocorrelation function are independent of  $z$  as found by others (2). When the medium

is anisotropic these are no longer true. However, it is interesting to note that the sum:

$$S_{xx}(\vec{k}_\perp; z) + S_{yy}(\vec{k}_\perp; z) = S(\vec{k}_\perp; 0) \quad (21)$$

which is independent of  $z$ . This has some practical importance, since it means that the sum of spectral densities of orthogonally polarized waves is uninfluenced by the medium.

Since the Faraday rotation angle plays a dominant role in determining the spectral density functions it will be discussed later.

#### DEPENDENCE OF ROTATION ANGLE

Let  $\Omega_z$  be the Faraday rotation angle suffered by a wave propagating in  $z$  direction. From Eq. 10,

$$\Omega_z = - \frac{\omega^2 \mu_0 \epsilon_0 X Y_z z}{2k_0} \quad (22)$$

For a wave propagating in a general direction with propagation constant  $k_o = (\vec{k}_\perp, \sqrt{k_o^2 - k_\perp^2})$ , the polarization of the wave will rotate in the right-handed sense from  $y$ -axis through an angle

$$\Omega(\vec{k}_\perp; z) = \Omega_z - \frac{\omega^2 \mu_0 \epsilon_0 X z}{2k_o} \frac{\vec{k}_\perp \cdot \vec{Y}}{\sqrt{k_o^2 - k_\perp^2}} \quad (23)$$

Note that for a fixed  $z$ ,  $\Omega_z$  is a constant. Hence the dependence on  $\vec{k}_\perp$  of the rotational angle is through the second term in Eq. 23. Because of the appearance of the dot product it suggests that it is advantageous to rotate the coordinates about  $z$  axis so that  $y'z$  plane is parallel to the plane of magnetic meridian and  $x'z$  plane perpendicular to it. For this coordinate system  $\vec{k}_\perp \cdot \vec{Y} = k_{y'} Y_{y'}$ . Further, consistent with the forward propagation assumption  $k_\perp$  can be ignored when compared with  $k_o$ . This results in an expression for the rotational angle which is only a function of  $k_{y'}$ . Let  $\phi$  be the angle between the displacement vector at  $z = 0$  and the magnetic meridian plane. Then:

$$\Omega(k_{y'}; z) = \phi + \Omega_z - \frac{\omega^2 \mu_0 \epsilon_0 X Y_{y'} z}{2k_o^2} \cdot k_{y'} \quad (24)$$

Let:

$$z_c = \frac{2k_o^2}{\omega^2 \mu_0 \epsilon_0 X |Y_{y'}| k_b} = \frac{2n_o^2}{X |Y_{y'}| k_b} \quad (25)$$

where  $k_b$  is the spectral width of  $S(k; 0)$  in the plane of magnetic meridian plane (i.e.  $y'$  component). Then Eq. 24 can be written as:

$$\Omega(k_{y'}; z) = \phi + \Omega_z + \frac{z}{z_c} \frac{k_{y'}}{k_b} \quad (26)$$

Equation 26 indicates that in the region  $z \ll z_c$ ,  $\Omega(k_{y'}; z)$  is nearly constant over the spectral width of interest and the spectral density of the field is not affected appreciably by the medium. When  $z$  has the same order of magnitude as  $z_c$  or even larger than  $z_c$ , the spectral densities of the fields are expected to be strongly affected by the medium.

## CORRELATION FUNCTIONS

The elements of the correlation matrix can be calculated by taking the Fourier inversion of the respective elements of the spectral matrix. As seen from Eq. 20, since the spectral densities are given in the product form the convolution theorem can be used to compute the correlation functions. Assume that the approximate expression Eq. 26 is valid the convolution integrals can be carried out easily, obtaining:

$$\begin{aligned}
 K_{x|x_1}(\xi^l, \eta^l; z) &= \frac{1}{2} K(\xi^l, \eta^l; 0) - \frac{1}{4} K(\xi^l, \eta^l + 2z/z_c k_b; 0) e^{j2(\phi + \Omega_z)} \\
 &\quad - \frac{1}{4} K(\xi^l, \eta^l - 2z/z_c k_b; 0) e^{-j2(\phi + \Omega_z)} \\
 K_{x|y_1}(\xi^l, \eta^l; z) &= K_{y|x_1}(\xi^l, \eta^l; z) = \frac{1}{4} K(\xi^l, \eta^l + 2z/z_c k_b; 0) e^{j2(\phi + \Omega_z)} \\
 &\quad - \frac{1}{4} K(\xi^l, \eta^l - 2z/z_c k_b; 0) e^{-j2(\phi + \Omega_z)} \\
 K_{y|y_1}(\xi^l, \eta^l; z) &= \frac{1}{2} K(\xi^l, \eta^l; 0) + \frac{1}{4} K(\xi^l, \eta^l + 2z/z_c k_b; 0) e^{j2(\phi + \Omega_z)} \\
 &\quad + \frac{1}{4} K(\xi^l, \eta^l - 2z/z_c k_b; 0) e^{-j2(\phi + \Omega_z)} \quad (27)
 \end{aligned}$$

By addition, it is seen that  $K_{x|x_1}(\xi^l, \eta^l; z) + K_{y|y_1}(\xi^l, \eta^l; z) = K(\xi^l, \eta^l; 0)$ . Since the Fourier transform is unique this is just the special case of Eq. 21.

## DISCUSSIONS

As an example take  $f = 20$  Mc/s,  $f_p = 10$  Mc/s,  $f_{Hz} = 1$  Mc/s, and  $k_b = 0.1/m$ , the critical distance comes out to be approximately 1200 km. Hence it seems that the effect of anisotropic nature of the medium may be important in ionospheric studies of irregularities and in studies of moon reflections. As suggested under "Diffraction of Random Waves" one possible way of eliminating the influence of anisotropic nature of the medium is through addition of spectra obtained on orthogonal antennas as shown by Eq. 21.

The method described here can be extended to studying the scattering from irregularities and from rough surfaces and other diffraction problems.

## REFERENCES

1. LANDAN, L. D., and LIFSHITZ, E. M., "Electrodynamics of Continuous Media". Pergamon, 1959.
2. BOOKER, H. G., RATCLIFFE, J. A., and SHINN, D. H., "Diffraction from an Irregular Screen with Applications to Ionospheric Problems". Phil. Trans. Roy. Soc. A 242, 579-607, 1950.
- RATCLIFFE, J. A., "Some Aspects of Diffraction Theory and Their Application to the Ionosphere". Reports on Progress in Physics 19, 188-267, 1956.

3. YAGLOM, A. M., "Theory of Stationary Random Functions". Chap. 3, Prentice-Hall, 1962.
4. WIENER, N., "Extrapolation, Interpolation and Smoothing of Stationary Time Series". 37, John-Wiley, 1949.
5. MIDDLETON, D., "Introduction to Statistical Communication Theory", Chap. 3, McGraw-Hill, 1960.



## CHAPTER 3-9

TOPSIDE SPREAD-F AND SATELLITE RADIO  
SCINTILLATIONS

JAMES L. JESPERSEN

CRPL, National Bureau of Standards  
Boulder, U.S.A.

## SUMMARY

Over the last decade many workers have studied the relation between spread- $F$ , detected by ground-based ionospheric sounders, and the scintillation of a radio signal either from a radio star or from an artificial earth satellite. In this paper the relation between scintillations and spread- $F$  detected by the topside sounder satellite, *Alouette I*, near College, Alaska, is studied. The scintillations are correlated with small-scale irregularities in the vicinity of the satellite. This supports the view that high-latitude irregularities extend from near  $h_{\max}$  to as high as 1000 km. Simultaneous topside and bottomside soundings of the ionosphere, taken together with the scintillation observations, suggest that on occasion the ionospheric disturbance, associated with the irregularities, extends below  $h_{\max}$  into the  $D$  region.

## INTRODUCTION

Very soon after the discovery of radio star scintillations it was established that the scintillations are correlated with spread- $F$  detected by ground-based ionospheric sounders (1). Briggs (2) discussed the influence that irregularities located above the height of maximum ionization in the ionosphere,  $h_{\max}$ , may have in producing scintillations. In this paper the relation between irregularities above  $h_{\max}$  and scintillations is studied directly by comparing spread- $F$  on ionograms from the topside sounder satellite, *Alouette I*, with scintillation of the *Alouette I*, 136 Mc/s tracking beacon.

## REVIEW

**Topside spread-F** – The *Alouette* ionograms (3) have a different appearance depending upon whether the width of the irregularities  $d$  is larger or smaller than the sounding wavelength,  $\lambda$ . If  $\lambda \ll d$ , the sounding signal may be ducted down the irregularities to a point where the electron density is sufficiently high to reflect the signal back along the duct to the satellite. If  $\lambda \gtrsim d$ , the sounder signal will be scattered back to the satellite. For this case the position of the echoes on the ionograms is different depending upon whether the irregularities are near the satellite (direct scattered echo) or at some distance (oblique scattered echo).

**Scintillation observations** – Diffraction theory (4) shows that irregularities which are half-way between the satellite and the ground should be most

effective in producing amplitude scintillations. Irregularities either near the satellite or near the ground will not produce appreciable amplitude scintillations. Since *Alouette I* is in a nearly circular 1000 km orbit, irregularities near the 500 km level should be the most important in producing amplitude scintillations, assuming that the irregularities are uniformly distributed in height. However, radio star scintillation observations (5) indicate that the irregularities are more intense near  $h_{\max}$  so that we might expect, in fact, the region between 300 and 500 km to be the most effective. Because of this, the irregularities primarily responsible for the amplitude scintillations may be further away from the satellite than the irregularities responsible for the scattered echoes observed at the satellite. For this reason, one would not necessarily expect a correlation between topside spread- $F$  and scintillations, unless the irregularities which produce topside spread- $F$  extend down into the ionosphere near  $h_{\max}$ .

**Structure of the irregularities** – There is evidence from different types of experiments that the irregularities are continuously distributed from somewhat below  $h_{\max}$  to an altitude of at least 1000 km. An analysis based upon ionograms from the fixed frequency topside sounder satellite (6), *Explorer 20*, reveals sheets of field-aligned irregularities whose width in the north-south horizontal plane is of the order of 100 km. These sheets extend at least from the vicinity of the satellite, near 1000 km, down to  $h_{\max}$ . In general, it is not possible to tell from the *Explorer 20* ionograms if the irregularities extend below  $h_{\max}$ . However, by measuring the drift velocity of the scintillation diffraction pattern across the ground and knowing the height and velocity of the satellite, it is possible to deduce the height of the irregularities. Using this method, Jespersen and Kamas (7) have observed structures similar to the sheets described by Calvert, *et al.* (6). On these occasions the irregularities were continuously distributed in altitude from below  $h_{\max}$  to 700 km in a region 100 to 300 km in width in the north-south horizontal plane. As mentioned previously, however, the irregularities could extend up to the satellite and also considerably below  $h_{\max}$  and not be detected because of diffraction effects.

It is not possible to tell from the topside sounder observations what the cross-sectional shape of the irregularities is. They could either be thin sheets or tubular irregularities aligned along the earth's magnetic field. However, spaced-station correlation measurements of the ground scintillation diffraction pattern indicate that the irregularities are tubular.

Figure 1 is a diagrammatic representation of the structure of the irregularities which these various observations suggest. The figure shows that even though the region primarily responsible for the amplitude scintillations is only a portion of the total structure, there should nevertheless be a correlation between the direct scattered echoes and the amplitude scintillations, since these two effects are both manifestations of the same group of irregularities.

#### OBSERVATIONS AND DISCUSSION

During the period October 1962 through September 1963, *Alouette I* ionograms recorded at the College, Alaska, satellite-tracking station were compared with the 136 Mc/s *Alouette I* tracking beacon, recorded simultaneously. The study was limited to passes which were within 15 deg. of the

local zenith. Table 1 shows the distribution of direct scattered echoes and amplitude scintillations.

TABLE 1

**Direct Scattered Echoes**

		Yes	No	$r = 0.78$
Amplitude scintillations	Yes	10	14	
	No	6	114	

Pearson's cosine correlation coefficient (9),  $r$ , for this distribution is 0.78. Table 2 shows the distribution of ducted echoes and amplitude scintillations; for this distribution  $r = -0.22$ .

TABLE 2

**Ducted Echoes**

		Yes	No	$r = -0.22$
Amplitude scintillations	Yes	3	21	
	No	24	96	

The *Alouette I* sounder transmits frequencies whose wavelengths range from 25 to 600 meters. Since a good correlation is found between the scintillations and the scatter-type ionograms, but not the ducting type, the implication is that the scintillations are associated with irregularities near the satellite whose sizes are of the order of hundreds of meters rather than of kilometers. Sizes of hundreds of meters are in agreement with previous scintillation observations (10) at high latitudes.

The slight negative correlation between the ducted echoes and scintillations is probably due to a masking of the ducted echoes by the scattered echoes (3).

There are two factors which may affect the correlation between the amplitude scintillations and direct scattered echoes which should be considered. First, since passes up to 15 deg. away from the local zenith are included in the study, there may be occasions when irregularities exist in the vicinity of the satellite, but not near  $h_{\max}$ , along the oblique path from the satellite to the tracking station and vice versa. Either of these cases would lower the correlation. Second, there may be irregularities below  $h_{\max}$  which will produce scintillations, but will not produce any effects on the topside ionograms. For example, Brenan (11) at Halley Bay, Antarctica, found a correlation between sporadic- $E$  and scintillations.

Both bottomside and topside ionograms were available for eight of the passes which contained amplitude scintillations. On half of these ionograms there was a blackout (that is, the ionospheric trace was removed by absorption). On the other half, the average spread of the  $F$  region trace was 0.97 Mc/s compared with 0.24 Mc/s when there were no scintillations. The average values of the spread are given because spread- $F$  is nearly a permanent feature of high-latitude bottomside ionograms and therefore it would not be meaningful to make a correlation study.

Table 3 shows the distribution of blackouts, when scintillations were present, and direct scattered echoes.

TABLE 3

**Blackout and Scintillations**

		Yes	No
Direct scattered echoes	Yes	4	2
	No	1	75

 $r = 0.97$ 

Since blackouts are produced primarily by absorption in the  $D$  region, the observations suggest that the ionosphere is in a disturbed condition from the  $D$  region, considerably below  $h_{\max}$ , up to the vicinity of the satellite at 1 000 km.

**CONCLUSION**

At College, Alaska, a good correlation is found between amplitude scintillations of the *Alouette I*, 136 Mc/s tracking beacon and topside spread- $F$  produced by small-scale irregularities in the vicinity of the satellite. No significant correlation is found between scintillations and larger-scale irregularities. These results support the view, suggested by the previously reported observations of different satellites, that the irregularities extend from near  $h_{\max}$  to at least as high as 1 000 km. In addition, simultaneous bottom- and topside soundings give evidence that on occasion the ionospheric disturbances extends below  $h_{\max}$  into the  $D$  region.

**REFERENCES**

1. LITTLE, C. G., and LOVELL, A. C. B., "Origin of the fluctuations of the intensity of radio waves from galactic sources". *Nature* (London) 165, 423-4, 1950.
2. BRIGGS, B. H., "Observations of radio star scintillation and spread- $F$  echoes over a solar cycle". *J. Atmos. Terr. Phys.* 26, 1-23, 1964.
3. CALVERT, W., and SCHMID, C. W., "Spread- $F$  observations by the *Alouette* topside sounder satellite". *J. Geophys. Res.* 69, 9, 1839-52, 1964.
4. LAWRENCE, R. S., LITTLE, C. G., and CHIVERS, H. J. A., "A survey of

- ionospheric effects upon earth-space radio propagation". Proc. IEEE 52, 1, 1965.
5. LAWRENCE, R. S., JESPERSEN, J. L., and LAMB, R. C., "Amplitude and angular scintillations of the radio source Cygnus-A observed at Boulder, Colorado". J. Res. Nat. Bur. Stand. 65D, 4, 333-49, 1960.
  6. CALVERT, W., KNECHT, R. W., and VAN ZANDT, T. E., "Ionosphere Explorer I satellite: First observations from the fixed-frequency topside sounder". Science 146, 3642, 1964.
  7. JESPERSEN, J. L., and KAMAS, G., "Satellite scintillation observations at Boulder, Colorado". J. Atmos. Terr. Phys. 26, 457-73, 1964.
  8. SPENCER, M., "The shape of irregularities in the upper ionosphere". Proc. Phys. Soc., B68, 1955.
  9. ARKIN, H., and COLTON, R. R., "Statistical methods". College Outline Series, College, Alaska, 1956.
  10. LITTLE, C. G., REID, G. C., STILTNER, E., and MERRITT, R. P., "An experimental investigation of the scintillations of radio stars observed at frequencies of 223 and 456 megacycles per second from a location close to the auroral zone". J. Geophys. Res. 67, 1962.
  11. BRENNAN, P. M., "Radio star scintillation observations". The Roy. Soc., I.G.Y. Antarctic Exp., Halley Bay, Coates Land, Falkland Islands Dependencies, 2, 1960.

## ACKNOWLEDGEMENTS

MR JOHN MILLER for providing the *Alouette I* tracking beacon data.  
 DRS WYNNE CALVERT and THOMAS E. VAN-ZANDT for stimulating discussions.

## DISCUSSION

K. DAVIES - Could you give any idea of the changes in electron density and the order of size of the observed irregularities?

J. L. JESPERSON - It is not easy to estimate, but from the depth of amplitude the change in electron density would be a few per cent. There is a whole range of sizes from tens of meters to tens of kilometers, amplitude scintillations are from the small and phase scintillations from the large ones. At high latitudes there is a residual structure of irregularities.

J. M. LANSINGER - Changes in columnar content of  $0.2 \times 10^{15}$  have been measured; this would be about 1 per cent of the total content.

I. PAGHIS - Analysis of spread-*F* data from *Alouette I* by Petrie has revealed a regular variation with geomagnetic latitude. As the satellite moves to higher latitudes the spread-*F* first appears near the peak of the *F*-layer, and gradually spreads upward until at auroral-zone latitudes the spread-*F* may extend above the 1000 km height of the satellite. At still higher latitudes the reflection traces again become discrete at the smaller apparent ranges.

The fixed-frequency sounder has the virtue of high spacial resolution; the sweep-frequency sounder provides detailed information concerning variations with respect to frequency. It may be profitable to compare in some detail the data on irregularities obtained from these two forms of experiment.



## CHAPTER 3-10

POLARIZATION VARIATION OF SATELLITE-EMITTED  
RADIO SIGNALSH. SOICHER, G. VOGT, P. R. ARENDT, W. H. FISCHER, and  
J. GRAU

U.S. Army Electronics Command, Fort Monmouth, New Jersey

## INTRODUCTION

Satellite signals have been widely used to study the structure and the variation of the ionosphere and related radio propagation effects. So far, the interest has been centered on amplitude scintillations and on frequency scintillations, the latter observations being a by-product of precise Doppler-shift frequency measurements of satellite radio signals. These Doppler scintillations reflect the general status of the ionosphere (its fine structure and variations). The apparent momentary variation of the total ionospheric electron content as indicated by Doppler scintillations is of the order of 0.1 per cent of the total integrated content (1). It was anticipated that precise measurements of the Faraday polarization angle rotation would indicate similar variations.

A linearly polarized wave may be considered as a resultant of two circularly polarized waves rotating in opposite senses with the same angular velocities. Since these waves have different phase velocities as they traverse the birefringent ionosphere, the plane of polarization of the resultant linearly polarized wave rotates gradually. Measurements of the total angle of rotation of the polarization plane or its rotation rate yield electron-content values (2), (3), (4), (5).

Conventional polarization measurements are usually performed by means of polarization-sensing elements (one or two dipole antennas) placed in a plane orthogonal to the incident wave. For example, one uses two half-wave-length dipoles crossed at right-angles and electrically insulated from each other. Two corresponding receiving systems amplify and record the incoming signal amplitudes. If the input wave exhibits slow changes (due to Faraday rotation) in its linear-polarization orientation, the antennas will receive signals of varying amplitudes. A fading (or minimum) occurs when the polarization vector is perpendicular to the dipole; thus two minima occur in each antenna during one complete revolution of the polarization vector. Because of unavoidable instabilities and noise, only the minima positions can be used to determine the polarization angle as a function of time. Lack of accuracy and the relatively low rate of polarization rotation of VHF signals call for an improved system, especially when fine-structure measurements are desired.

## POLARIZATION-FOLLOWER SYSTEM

In an effort to improve these shortcomings the Polarization-Follower System was developed, which determines the polarization angle every other second for two closely spaced frequencies (40 and 41 Mc/s). Since a detailed description of the system is given elsewhere (6), (7), we present only a brief abstract of its function. In Fig. 1, the polarization-sensing dipoles  $x$  and  $y$  are the same as in the conventional system. However, the two-branch input is converted to one branch at the input of the receiver. The polarization processor is actually an electronic goniometer which consists of a double multiplier and a function generator. The input to the function generator is a d.c. voltage  $V_c$ , the magnitude of which defines an orientation angle  $\beta$ . This angle is a spatial angle and represents an equivalent shaft rotation when compared to a mechanical goniometer. The function generator delivers two plus or minus d.c. voltages, representing the cosine and the sine of  $\beta$ , respectively. These two voltages multiply or modulate the two VHF antenna signals, and the products are then added.

This method results in a polarization pattern similar to that of a single dipole with the added capability of changing the polarization pattern by variation of the control voltage  $V_c$ . In order to obtain an automatic polarization-follower system, this electronic (and therefore low-inertia) device can be simply complemented with a servo system. By introduction of an electronic scan  $f_s$  (i.e. 27 c/s) the pattern is swept  $\pm 90^\circ$  and 27 times per sec over the angle  $\beta$  set by  $V_c$ . The scan causes a modulation of the signal similar to that shown on the screen of the Pattern Monitor, Fig. 1, which modulation contains the difference  $\alpha - \beta$ . This wave shape when demodulated and compared by the phase corrector with the initial scan frequency, activates the servo system by means of an error detector called Phase Comparator, Fig. 1. The resulting error voltage  $\pm e$  is proportional to  $\alpha - \beta$ ; it is zero for  $\alpha - \beta = 45^\circ$ . The mechanical gear driven by the servo motor rotates a potentiometer delivering a voltage that is used as the control voltage  $V_c$ . Thus the loop is closed. In this closed-loop operation the voltage  $V_c$  determines the center of the sweep or an angle  $\beta$  which now is kept in coincidence with the incident polarization angle  $\alpha$  by means of the error voltage  $e$  and the servo system. The slightest deviation of  $\alpha$  changes the wave shape at the output of the receiver, and thus the speed and sense of rotation of the servo. Since  $V_c$  is proportional to  $\alpha$ , this voltage can be recorded by a strip-chart recorder, Fig. 2, or after conversion by means of a digital voltmeter in binary coded form punched on tape or printed out in form of a table.

The following modifications were necessary for the system employed in the S-66 experiment:

(a) A double-branch converter featuring equal phase and amplitude behavior was added in front of the processor, in order to convert 40 and 41 Mc/s, alternately, in one-second intervals, to the processor's IF of 10 Mc/s.

(b) The time-division multiplier for the two frequencies required two servo systems, but only one scan system.

(c) A memory device was added that permits a second-by-second readout of both frequencies, alternately related to measuring periods of 0.8 ms.



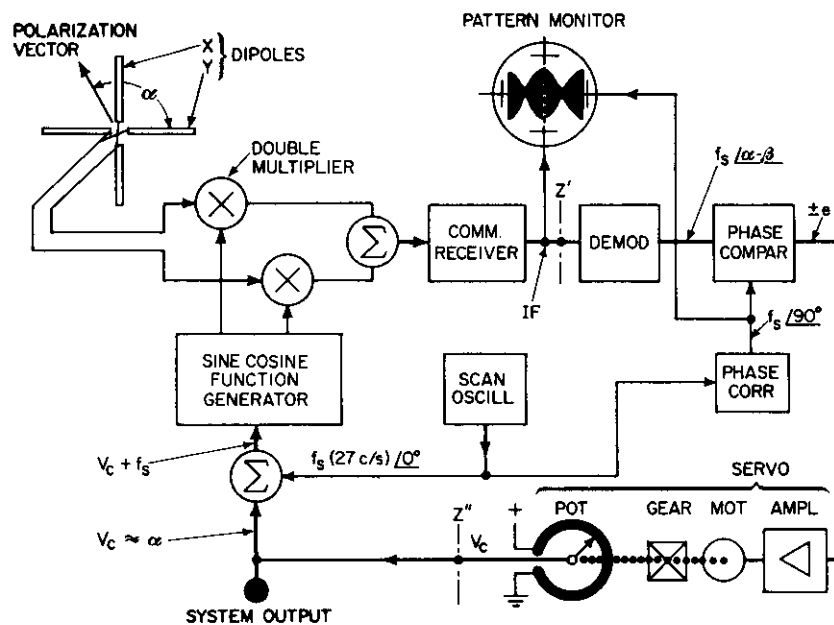


FIG. 1 Polarization follower – principle

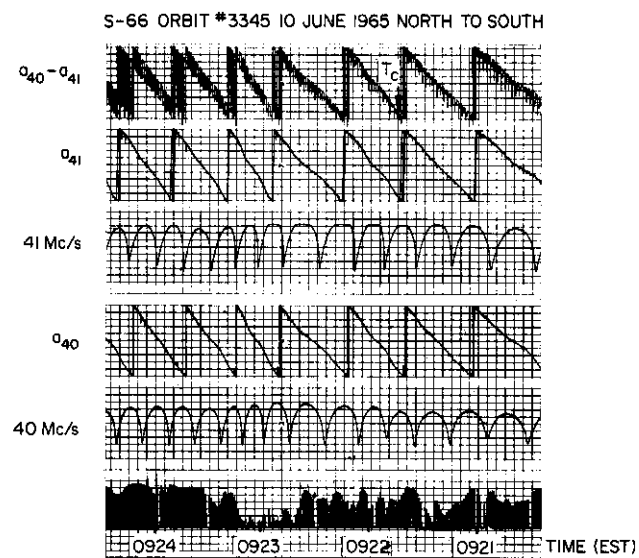


FIG. 2 Faraday rotation – conventional fading recording and continuous recording by polarization followers

## DESCRIPTION OF DATA

The data are illustrated in Fig. 2, where the conventional signal level fadings for 40 and 41 Mc/s are shown, as well as the output of the polarization follower indicating the rate of change of the polarization angle  $a_{40}$ ,  $a_{41}$  and their instantaneous difference. The conversion of these data to absolute angles of rotation is based on a method utilizing closely spaced satellite transmissions proposed by Blackband (8). Generally, the absolute number of rotations can be determined if the relevant orbit of the satellite includes the point in space where the ray path is perpendicular to the magnetic field (transverse point). In this case one has a reference point of zero fade. If we assume that the angle of rotation is monotonic and mostly dependent on ray path-magnetic field geometry, the total change between the transverse point and any point in space would correspond to the total angle of rotation at that point. The horizon of our receiving station at  $40^{\circ} 15' 30''$  N.,  $74^{\circ} 01' 30''$  W. does not include the transverse point for polar orbits, and hence we cannot utilize the conventional method. Blackband's method proposes that at the transverse point (the point of zero fade), the polarization angles of both frequencies must be in phase. If during the received portion of the satellite's orbit we measure a specific phase difference or observe phase coincidence, we can easily count back and locate the transverse point. In the case of Orbit No. 3345, Fig. 2, the point ( $T_c$ ) of phase deviation of  $\pi$  occurs at 09:21:42 EST. Note that  $\pm \pi$  ambiguity in our measuring system for the location of the polarization vector can easily be eliminated since an error of one  $\pi$  in the difference ( $\Delta a$ ) would lead to unrealistic values of the total content (at our latitude error of about 100 per cent) in comparison to electron-content values known from other methods. However, an ambiguity of one  $\pi$  in the absolute angles leads to a much smaller error in the electron-content measurements (about 5 per cent), and hence is much harder to eliminate. Using first-order theory, we have for  $\Delta a = \pi$ :

$$a = \frac{K}{f^2} \int NH \cos \theta \sec \delta \, dh \quad (1)$$

where:

- $a$  = total polarization rotation angle (in radians)
- $f$  = operating frequency
- $K = 2.36419 \times 10^4$  cgs units
- $H$  = magnetic field intensity in gauss
- $\theta$  = angle between magnetic field and ray path
- $\delta$  = ray zenith angle
- $dh$  = element of vertical height

$$\frac{a_{40}}{a_{41}} = \frac{f_{41}^2}{f_{40}^2} = \frac{1681}{1600} = 1.05062$$

$$a_{40} - a_{41} = \pi = 1.05062 a_{41} - a_{41} = .05062 a_{41} = .04818 a_{40}$$

$$a_{41} = 19.7530\pi$$

$$a_{40} = 20.7530\pi$$

Accordingly, for any  $\Delta a$  as a multiple of  $\pi$ , we have:

$$a_{41} = 19.7530 (\Delta a)\pi \quad (2)$$

$$a_{40} = 20.7530 (\Delta a)\pi \quad (2a)$$

Thus, at any point of known phase difference, the absolute values of  $a_{41}$  and  $a_{40}$  are known. Utilizing a new reference point for each observation, one can measure the relative increase or decrease of the absolute angles and determine the instantaneous value unambiguously.

An inherent uncertainty in Blackband's closely spaced frequency method, and in all methods utilizing the zero-fade transverse point, stems from the fact that the total angle is determined through an integrated process during which the satellite scans a large portion of the ionosphere. The assumption that the polarization angle is a monotonic function necessitates the existence of a well-behaved ionosphere. The existence of strong electron-density gradients and large-scale irregularities during the unobservable portion of the orbit (starting at the transverse point and ending at any point during the observed section of the orbit) would alter the absolute angle value, since the angle could have varied non-monotonically during a portion of the orbit.

The utilization of the difference value ( $\Delta = a_{40} - a_{41}$ ) for electron-content measurements overcomes this uncertainty, provided we can assume that at the satellite the position of the polarization vector is always identical for the two frequencies. This assumption is also required by the transverse-point measurement. Hence, the absolute value of the polarization angles  $a_{40}$  and  $a_{41}$  should be derived at each second from the observed value of their difference using Eqs. 2 and 2a respectively. We have found that it is incorrect to use a once-determined absolute value of  $a_{40}$  or  $a_{41}$  (say at  $\Delta a = \pi$ ) as a reference point from which other values of the angle are derived by merely observing the variation of the angle. This method leads to different values for the electron content if either  $a_{40}$  or  $a_{41}$  is applied. Thus, such integrated polarization angles should not be used in the calculation of the electron content. Having the absolute values of  $\Delta a$ , we can construct the curve to total variation of the polarization angle in a point-by-point fashion during the time of the orbit's observation, Fig. 3 and 4.

The observed non-monotonic change of  $\Delta a$  requires the investigation of contributing errors and irregularities.

#### PHYSICS OF FARADAY IRREGULARITIES

The oscillatory nature of the  $\Delta a$  curve has led us to examine the details of possible ionospheric effects. The polarization angle is given by:

$$a = \frac{\pi}{\lambda_0} \int_0^s (n_0 - n_e) ds \quad (3)$$

where:

$\lambda_0$  = wavelength in free space

$n_0$  = refractive index for ordinary component

$n_e$  = refractive index for extraordinary component

$ds$  = element of distance along path

This expression is true only for the case where collisions are neglected,

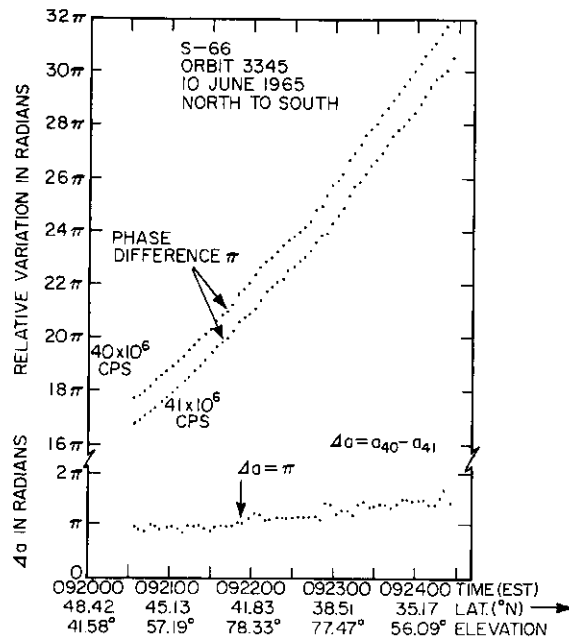


FIG. 3 Accumulated Faraday rotation of 40 and 41 Mc/s and their instantaneous difference (June 10, 1965)

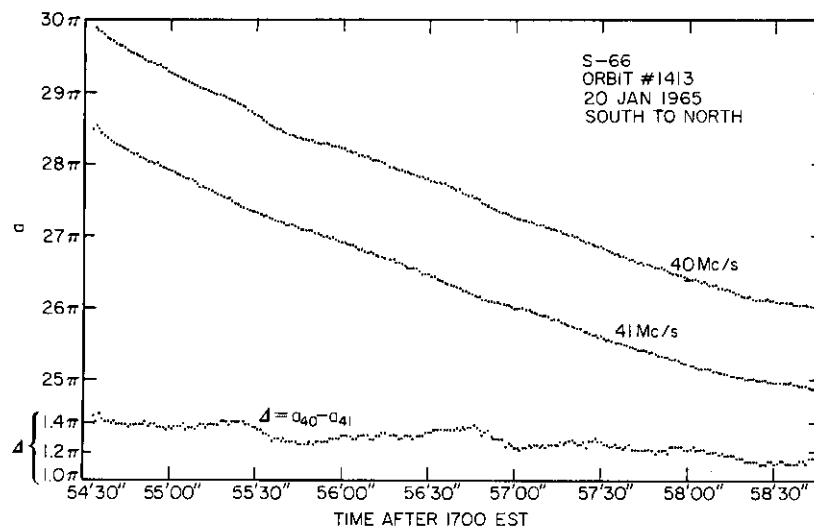


FIG. 4 Accumulated Faraday rotation of 40, 41 Mc/s and their instantaneous difference (January 20, 1965)

and quasi-longitudinal (QL) approximation holds. In the Appleton-Hartree formula, the QL approximation holds for:

$$\frac{f^2 - f_N^2}{f} \gg \frac{\sin^2 \theta}{\cos \theta} f_H \quad (4)$$

where  $f$  is the operating frequency,  $f_N$  is the plasma frequency,  $f_H$  is the gyrofrequency and  $\theta$  is the angle between the ray path and the magnetic field. For a weakly ionized medium  $f \gg f_N > f_H$ , the QL inequality will always hold except in the immediate vicinity of the transverse position. In such media the ordinary and extraordinary waves are right and left circularly polarized waves for most  $\theta$  values.

At our latitudes the conditions of the QL inequality are satisfied to a ratio of 3:1 for the elevation angles used in our experiments. This fact is obtained from the work of Potts (9), who plotted the maximum allowable angle of arrival (satellite elevation) against the frequency for various critical frequencies. In the case of a specific critical frequency of 5.1 Mc/s, applicable to Orbit No. 2826, Fig. 5, he obtains for frequencies in the 40 Mc/s range, a maximum allowable angle of arrival of  $45^\circ$ . However, the observed oscillations occur well within a cone of  $45^\circ$  and cannot be attributed to a misinterpretation of the QL condition.

Another assumption inherent in Eq. 3 is that the propagation paths of the ordinary and extraordinary modes be nearly identical and may be approximated by the mean isotropic ray path. Garriott (10) upon examining the phase difference in ray paths for flat earth and an ionosphere represented by homogeneous semi-infinite media found that the approximation of using mean isotropic ray path is valid up to an angle of  $45^\circ$  elevation. Potts (11) has shown the validity of the approximation for an ionospheric model of spherical slab of finite thickness having two anisotropic refractive indices. From his numerical calculation it is concluded that for the 40 Mc/s frequency range and gyrofrequencies in the order of 1 Mc/s, the relative path-length difference (with respect to the isotropic path) is smaller than  $1 \times 10^{-3}$ . This means that for an assumed effective ionospheric path length of 300 km we have to consider a maximum possible path-length difference smaller than 0.3 km. Now, assuming a typical Faraday rotation of  $20\pi$  radians we have on the "average"  $\pi$  rotations during 15 km of path. A 0.3 km path difference would yield an error smaller than  $0.02 \pi$ , which is much smaller than the observed effect. In addition, since we are examining the difference between  $a_{40} - a_{41}$ , and there is no reason for the path splitting being different on the two closely spaced frequencies, the effect should be eliminated. Also, the effect should be approximately the same for the entire passage of the satellite (since the total angle does not change much, from  $18$  to  $32\pi$ ). Any residual error should merely be additive to the  $\Delta a$  curve at all points. Thus, it seems that the errors introduced by ionospheric assumptions are much too small to account for the observed oscillatory irregularities in the differential Faraday curve.

#### IRREGULARITIES OF THE OBSERVATION PROCEDURE

The readout error of our system is of the order of  $\pm 0.02\pi$  when the charts shown in Fig. 2 are evaluated by an operator. The automatic data readout

contains an average error of  $\pm 0.01\pi$ . However, a comparison of momentary polarization angles at 40 and 41 Mc/s made during the center part of over-head satellite passages show marked deviations (in the order of  $0.1\pi$ ) from the expected inverse frequency-squared relation that are larger than the errors of the recording system.

In addition to these large variations shown by Fig. 3 through 6, there are also small variations. The momentary amount of this scintillation type of variation has been found in the order of  $\pm 0.0115 \pi/s$  by comparison of the momentary  $\Delta a$  values with a smoothed average (running average over five second-by-second data readouts) during a time interval when large deviations (greater than  $0.1\pi$ ) were absent. It is not possible to correlate directly this scintillation of  $0.0115\pi/s$  to Doppler-frequency scintillations observed simultaneously at the same frequencies. A polarization scintillation of this value would correspond to about 1 per cent scintillation of the total electron content, whereas Doppler scintillations indicate only a 0.1 per cent variation of the content. It is assumed therefore that such a differential polarization scintillation must eventually include an instrumental uncertainty that could be explained by the limited hunting capabilities of the servo system.

Being presented with this overall scintillation uncertainty, we have tried to reduce the pertinent error by smoothing the data readout. Figures 5 and 6 give a comparison of the direct readout of the polarization angle difference with running averages over three or five sequential data points. With the five-point averages (see the curves marked AVG5) the small scintillations disappear, but deviations of a pronounced oscillating character still exist. These large oscillations correspond to different slopes of the polarization (*vs* time) curves of 50 and 41 Mc/s, respectively. One could assume that these relative polarization variations at 40 and 41 Mc/s are attributable to different variations of the individual path geometries within the ionosphere and with respect to the geomagnetic field. This assumption would question the applicability of the Faraday-rotation method in the S-66 experiments. However, it is not in agreement with the above estimate of possible path deviations.

A further investigation of the possible errors in Faraday-rotation measurements has disclosed two major sources:

(1) A geometric error produced by the fact that the plane of the polarization of the incoming wave changes its attitude relative to the fixed antenna plane because of the changing azimuth and elevation of the satellite vehicle. This type of error is common to most types of polarization measurements of satellite-emitted signals.

(2) A non-linearity of the specific error function of our recording system. The absolute value of the angular error oscillates between zero and a maximum value every  $\pi/2$  of the measured angle. The maximum error is small; it depends on the equalization of the two measuring channels (the  $x$  and the  $y$  parts of our system); normally it is in the order of less than  $\pm \pi/30$  (or  $\pm 6^\circ$  for each  $180^\circ$  polarization change).

A detailed evaluation of the above two error sources was made and can be summarized as follows. First, the geometric error: the relation between the measured polarization angle  $\alpha'$  and the true or actual polarization angle  $\alpha$  is given by:

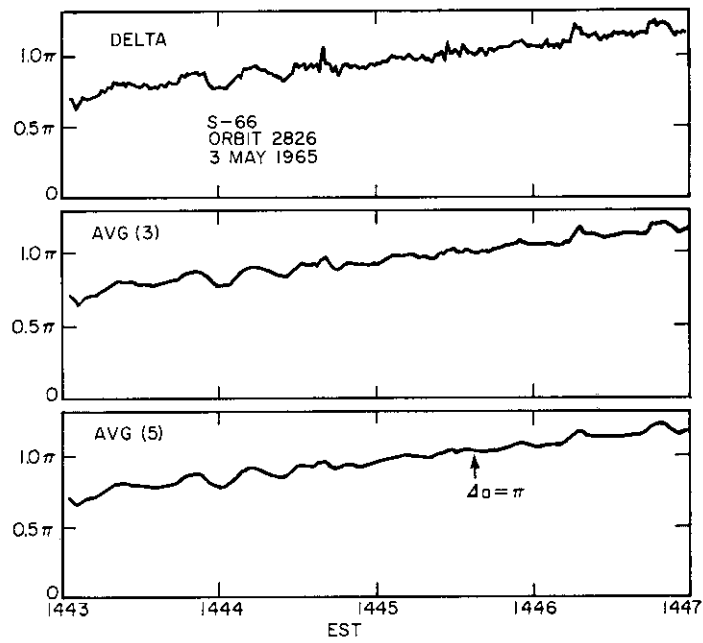


FIG. 5 Instantaneous values of  $a_4 - a_{41}$  (top); running average of top data over three sequential data (middle); running average of top data over five sequential data (bottom)

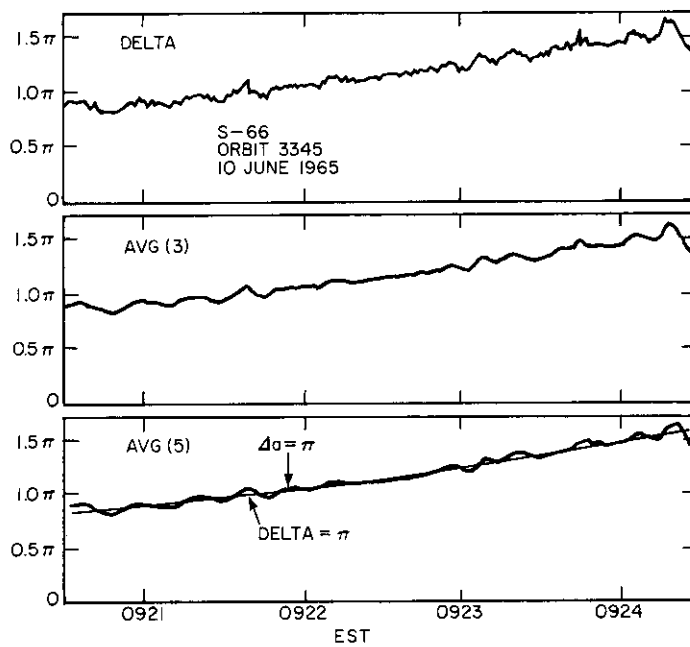


FIG. 6 Instantaneous value of  $a_{40} - a_{41}$  (top); running average of top data over three sequential data (middle); running average of top data over five sequential data (bottom)

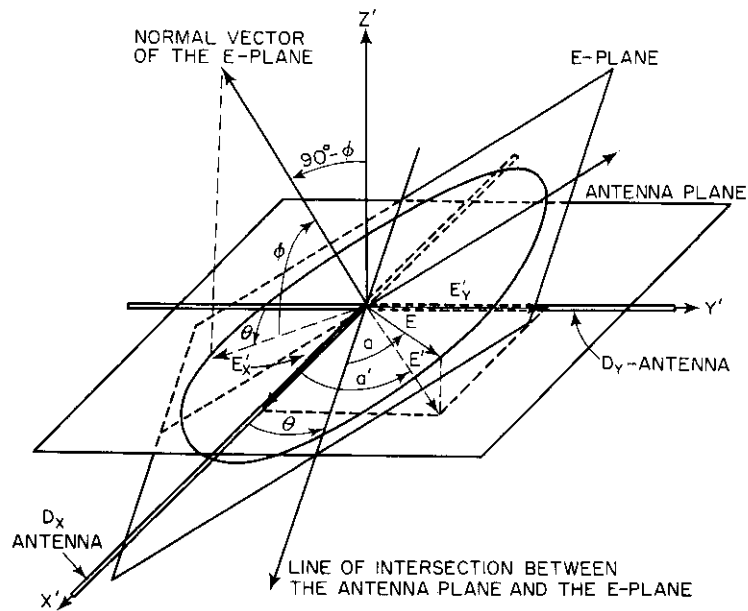


FIG. 7 The projection of the polarization vector incident at elevation  $\phi$  and azimuth  $\theta$  into the antenna plane

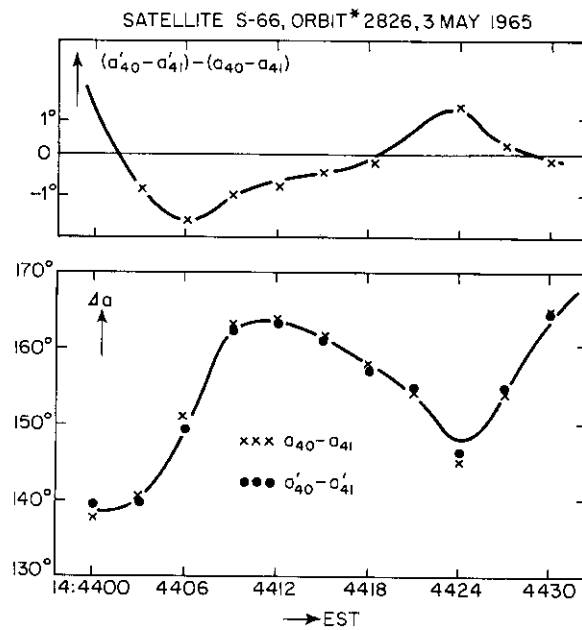


FIG. 8 Comparison of instantaneous measured values of  $\Delta a$  with values corrected for the geometric error (data refer to FIG. 6)



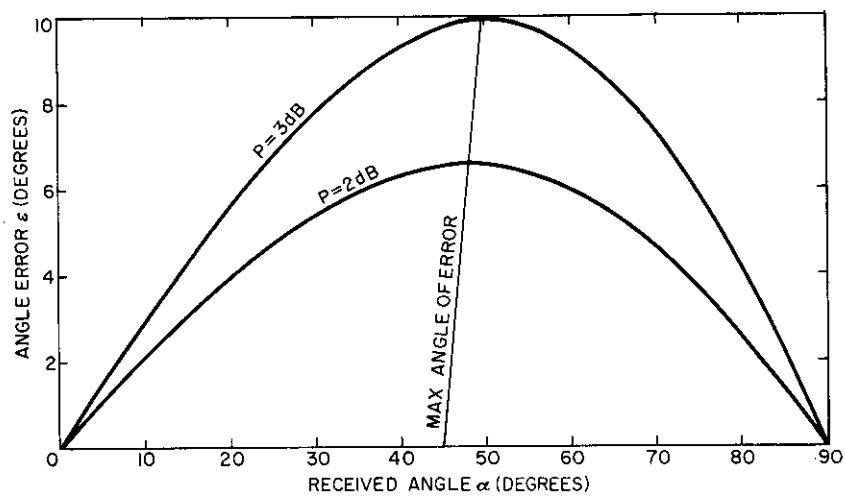


FIG. 9 Half wave section of non-linear error curve for differences of 2 and 3 dB in the  $x$  and  $y$  branches

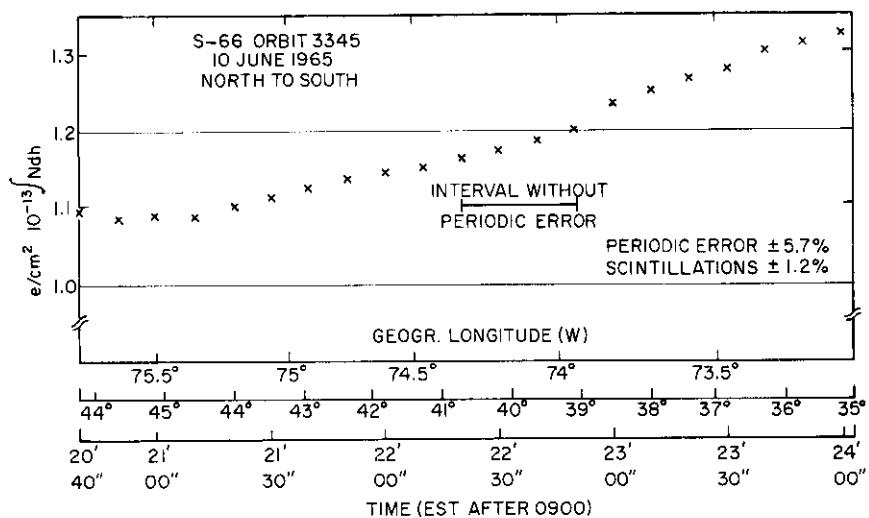


FIG. 10 Latitudinal variation of electron content derived from average variation of Faraday rotation angle differences

$$\alpha = \tan^{-1} \frac{\tan(\alpha' + A\mathcal{Z} - 315^\circ)}{\sin EL} \quad (5)$$

where  $A\mathcal{Z}$  and  $EL$  are the azimuth and elevation angles, respectively, and where  $315^\circ$  defines the azimuth position of the antenna. Figure 7 shows the pertinent geometric relations which are self-explanatory; they are explained elsewhere (12). For the center part of close to overhead passages  $\sin EL$  is close to unity and  $\alpha$  is equal to  $\alpha'$  minus the azimuth correction ( $-A\mathcal{Z} + 315^\circ$ ). Consequently, the geometric error is equal for both frequencies. Thus, it is completely eliminated when the difference  $\Delta a$  is utilized for the evaluation of the polarization measurements. Figure 8 compares  $\Delta a$  data measured during Orbit 2826, Fig. 5, with values corrected for the geometric error devised from azimuth and elevation. For practical conditions the residual error in  $\Delta a$  is less than  $2^\circ$  (below  $0.011\pi$ ). It should be noted that the scintillation uncertainty mentioned above is of the same order.

This cancellation of the geometric error possible in overhead passages makes it mandatory to utilize the differential polarization method for precision purposes. For single-frequency polarization measurements, the geometric error becomes substantial even with a  $45^\circ$  vertical cone. Therefore, we have restricted our work on polarization-data evaluation to the application of the differential method. The information about the possible magnitude of the geometric error also demands the rejection of the application of single-frequency polarization measurements (obtained by fixed antennas) for the so-called hybrid methods which combine Doppler and Faraday data for a calculation of the electron content. The hybrid methods must use Faraday data that are derived from differential measurements. The great importance of the S-66 satellite experiments is related to the fact that these beacon satellites permit the simultaneous application of differential Doppler and differential Faraday methods.

The effects of the non-linear error were also analyzed. They center about the unavoidable small differences observed in the gain of the two frequency converters in the  $x$  and  $y$  branches of the receiving system. Again, this error would cancel out for measurements applying only differences ( $a_{40} - a_{41}$ ) provided, however, that the two single polarization values for  $a_{40}$  and  $a_{41}$  were equal. Since this is not the case, the single momentary values of  $a_{40}$  and of  $a_{41}$  are related to errors of different magnitude and eventually of different sign. In forming the difference  $a_{40} - a_{41}$  the two errors cancel when both are of equal sign and of equal absolute value. This fact is realized close to the maximum of the error curve shown in Fig. 9. Due to the oscillating character of this error, the cancellation becomes better the closer the difference  $a_{40} - a_{41}$  comes to a specific value in the neighborhood of  $\pi$ . If both rotation angles  $a_{40}$  and  $a_{41}$  would follow the same rate of change, the error cancellation would occur strictly at the difference  $\pi$ . However, since  $a_{40}$  is changing faster than  $a_{41}$ , the error cancellation is shifted towards  $1.2\pi$  or towards  $0.8\pi$ . On the other hand, the resulting error becomes a maximum when the single errors have opposite signs. This case is realized when the  $a_{40}$  error has passed the zero point of the error curve and when the  $a_{41}$  error is still related to the opposite of the oscillating curve. It can be shown that the period of this oscillating error is twice the difference of the rate of change of the two single

polarization angles  $a_{40}$  and  $a_{41}$ . This period coincides with the large deviations observed. Since the absolute value of these deviations (measured between maximum and minimum) is of the magnitude predicted from the observed gain differences in the converters, the conclusion has to be drawn that the observed deviations cannot be ascribed to the ray path geometry or to the medium. The best results for differences  $a_{40} - a_{41}$  will be obtained when the observed oscillations are smoothed by the application of a best-fitting curve as shown in the lower part of Fig. 6. It is noteworthy to consider the center part of this curve (around  $\Delta a = 1.2\pi$ ) where the oscillating error has disappeared and where the actual data are identical with the smoothed curve. We will use this section of undisturbed data for a comparison of the various method for calculating the integrated electron content.

#### INTEGRATED ELECTRON CONTENT

Final data from Fig. 6 have been converted to integrated electron-content values using the smoothed curve at the bottom of Fig. 6, which curve excludes all scintillation, geometric and non-linear errors. The applied effective geomagnetic-field components pertinent to the position of the satellite and an assumed effective geomagnetic altitude of 450 km was taken from a table. The magnetic-field component was calculated by NASA for the coordinates of our station. The result is shown in Fig. 10, which indicates the latitudinal variation of the electron content close to the meridian of our station. The shape of the curve (increase towards the south) coincides well with our own data from topside-sounder evaluation over the same geographical area. (13). The results shown by Fig. 10 still contain one uncertainty that is related to the assumption of the pertinent altitude for the effective geomagnetic component. Obviously, this altitude depends upon the actual shape of the altitude profile of the electron density in the areas through which the radio ray passes on its way from the satellite to the observer. It is generally assumed that this profile is actually the same during the entire observation, and it is also assumed that the effective altitude is constant, but somewhat higher than the true height of the  $f_0F_2$  maximum. However, all these values may change during observation. The effective altitude depends mainly on the thickness of the  $f_0F_2$  layer and its altitude. For example, a change of the effective altitude from the assumed 450 km to 300 km, would reduce the data from Fig. 10 by about 7 per cent.

Finally, we must consider the various methods that might be utilized for the conversion of polarization data into electron-content values. In Fig. 10 we used the smoothed data from Fig. 6. However, if we restrict ourselves to the period around  $\Delta a = 1.2\pi$ , where all errors are minimized, one might use the original raw data (before smoothing procedures) and compare the results when using either  $a_{40}$  and  $a_{41}$  or both in first-order or in second-order terms for the Faraday effect. The results of such a comparison is given in Fig. 11. The absolute values of  $a_{40}$  and  $a_{41}$  were measured from the point  $\Delta a = \pi$  obtained from the smoothed curve in Fig. 6 (see the upper arrow on the lower curve). The enlarged scale of Fig. 11 shows that the electron-content values ascribed to either  $a_{40}$  or  $a_{41}$  are similar. This is to be expected because both contain the same but small geometric and non-linear errors besides scintillations. The magnitude of the residual geometric and

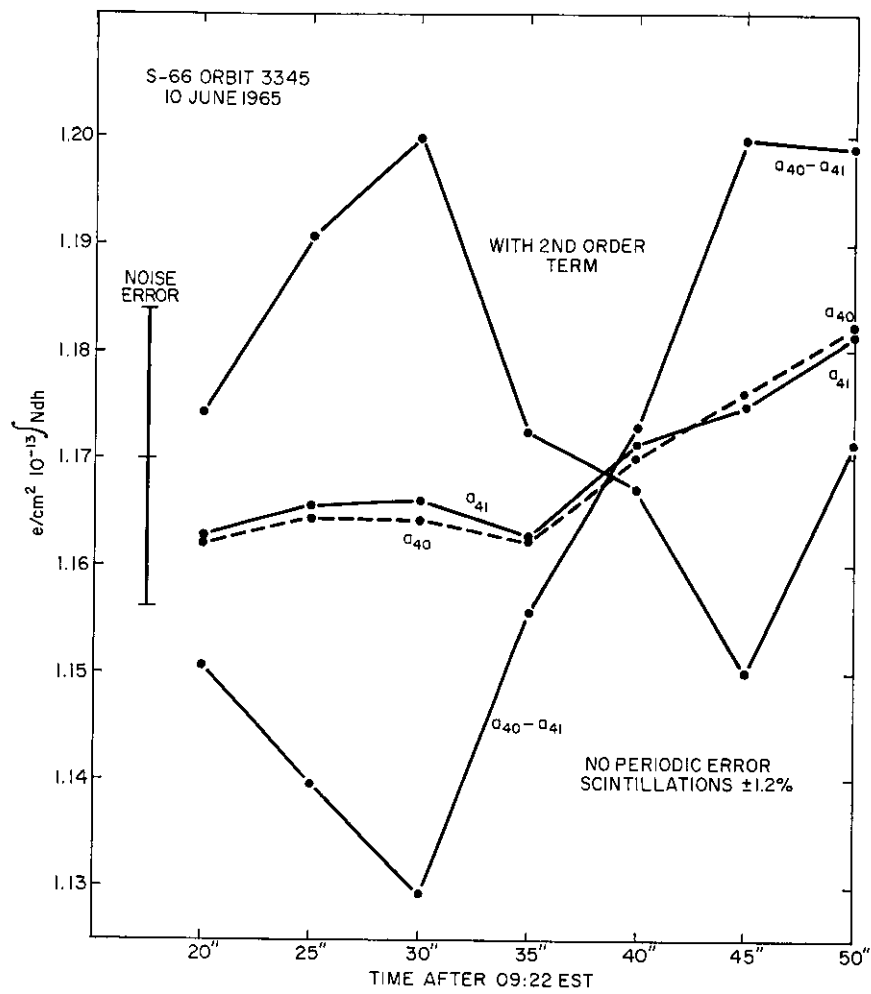


FIG. 11 Electron content from various applications of Faraday rotation data (enlarged scale)

non-linear error is explained by the deviation between  $a_{40}$  and  $a_{41}$  curves and the curve for  $a_{40} - a_{41}$ .

Although the  $\Delta a$  evaluation deserves higher confidence, it still contains the scintillation error because unsmoothed raw data were applied. (Note the error mark at the left of Fig. 11.) The oscillating character of the  $a_{40} - a_{41}$  evaluation justifies the otherwise applied smoothed data (see the straight curve in the lower part of Fig. 6). A similar discrepancy is observed when second-order terms (4) are introduced in the evaluation. In this case the absolute values for  $a_{40}$  and  $a_{41}$  that appear in the pertinent equation (in the form  $a_{41}f_{41} - a_{40}f_{40}$ ) must be utilized. Consequently, even small residual errors in the absolute angles are magnified. This fact can be seen clearly when the trend of the second-order evaluation is compared with the relative change of the  $a_{40}$  and  $a_{41}$  evaluation in Fig. 11. From the comparison of the curves in Fig. 11, we conclude that best results for the electron content will be obtained when  $a_{40} - a_{41}$  data are used and smoothed as described above.

#### CONCLUSION

A system has been developed and tested that delivers reliable and precise data for second-by-second Faraday-rotation measurements of satellite-beacon signals. The precision of the data, when restricted to difference values and to a center interval, is better than  $\pm 1$  per cent. This is better than the overall  $\pm 3.5$  per cent uncertainty in the electron content related to the variable choice of applicable components of the geomagnetic field. The uncertainty of this effective field component is due to the lack of knowledge of the electron-density *vs* height profiles which are transversed by the continuously changing ray paths between satellite and observing antenna. This uncertainty is mainly a function of the elevation angle. It becomes very large for close to the horizon observations. It is also large in the east-west directions during sunrise or sunset. It is further disturbed by tidal or other motions in the ionosphere which produce gradients (14). Consequently, the application of the Faraday-rotation method for measurement of the electron content has to be restricted to overhead passages of the beacon satellites in order to reduce the inherent uncertainty. In fact, differential polarization angle data and the related electron-content values obtained from the S-66 satellite are superior to measurements at low elevation angles either by moon radar or from 24-hour stabilized satellites. The basic prerequisite of all Faraday-effect methods is bound to a "close-to-vertical" geometry when precision is to be obtained. So far the precision reached by the various methods is not high enough to establish criteria on small-scale ionospheric irregularities.

#### REFERENCES

1. ARENDT, P. R., "The Non-Relativistic Doppler Shift in the Ionosphere". Proc. International Conference on the Ionosphere, London, Inst. Phys. and Phys. Soc., 331-5, 1962.
2. BROWNE, I. C., EVANS, J. V., HARGREAVES, J. K., and MURRAY, W. A. S., "Radio Echoes from the Moon". Proc. Phys. Soc. B, 69, 901, 1956.

3. DANIELS, F. B., and BAUER, S. J., "The Ionospheric Faraday Effect and Applications". J. Franklin Inst. 267, 3, 187, 1959.
4. YEH, K. C., and SWENSON, G. W., Jr., "Ionospheric Electron Content and Its Variations Deduced from Satellite Observations". J. Geophys. Res. 66, 4, 1061-8, 1961.
5. BOWHILL, S. A., "The Faraday Rotation Rate of Satellite Radio Signal". J. Atmos. Terr. Phys. 13, 1-2, 175-6, 1958.
6. VOGT, G., "An Analogue Polarization Follower for Measuring the Faraday Rotation of Satellite Signals". Radio Electr. Eng. (England) 28, 4, 1964.
7. VOGT, G., "An Electronic Method for Steering the Beam and Polarization of H.F. Antennas". Trans. I.R.E. AP-10 2, 193-200, 1962.
8. BLACKBAND, W. T., "The Observation of Ionospheric Electron Content by Observations of Faraday Fading". J. Geophys. Res. 65, 7, 1960.
9. POTTS, B. C., "Mean Ionospheric Scale Heights Deduced from Faraday Rotation Measurements". J. Geophys. Res. 70, 11, 2651-63, 1965.
10. GARRIOT, O. K., "The Determination of Ionospheric Electron Content and Distribution from Satellite Observations". J. Geophys. Res. 65, 4, Pt I, 1139-50; Pt II, 1151-7; 1960.
11. POTTS, B. C., "Utilization of the Faraday Effect in Ionospheric Studies". Antenna Laboratory, The Ohio State University, 1963.
12. ARENDT, P. R., *et al.* "Polarization Variation of Satellite-Emitted Radio Signals". USAECOM Tech. Report to be published. (An amplified version of this paper to be published at a later date.)
13. ARENDT, P. R., and PAPAYOANOU, A., "Structure and Variation of the Topside Ionosphere Close to the Fort Monmouth Longitude". J. Geophys. Res. 70, 15, 1965.
14. KING, J. W., and KOHL, H., "Movements in the Atmosphere and Ionosphere". Int. Mem. 207, Radio and Space Research Station, Slough, England.

## ACKNOWLEDGEMENTS

BLUMBLE, L. J., NASA Goddard Space Flight Center, for the geomagnetic data.

NASA, for furnishing World Map data on satellite positions.

POTTS, B. C., Rand Corp., Santa Monica, California, for helpful discussions.

ROSATI, V. J., and STRIMPLE, G., for Institute Exploratory Research, for their contributions to the error analysis of the system.

## CHAPTER 3-11

EFFECTS OF IONOSPHERIC IRREGULARITIES ON  
SPACE DATA ACQUISITION IN THE AURORAL ZONE

EDWARD J. FREMOUW

Geophysical Institute, University of Alaska

## SUMMARY

Some scattering effects of ionospheric irregularities on tracking and data acquisition from trans-auroral-zone satellites are discussed. Particular attention is paid to severe scattering associated with active auroral displays. Signal strength fluctuations in excess of 20 dB have been recorded at 136 Mc/s by NASA's Gilmore Creek data acquisition facility near Fairbanks. The scintillations often are caused by distinct patches or arcs of irregular ionospheric structure, which the College all-sky camera shows to be associated with visible auroral forms.

A combination of Gilmore Creek records and radio-star interferometer recordings obtained at College indicates that the most severe scattering is caused by irregularities with scales of the order of a few hundred meters. A photometer mounted on one of the tracking interferometer antennas shows that small-scale ionospheric structure is enhanced by entry into the ionosphere of aurora-producing particles. The small-scale structure apparently begins to collapse immediately upon cessation of the particle bombardment, but takes many minutes to return to its previous condition. Both the radio-star and satellite records show evidence of larger irregularities associated with auroral forms. The larger irregularities can produce shifts in apparent satellite position of several degrees of arc.

Comparison of current radio-star records with similar records collected at College during the IGY suggests that severe scintillation of trans-auroral-zone satellite signals may be expected on frequencies up to at least 400 Mc/s near solar maximum. On frequencies below about 200 Mc/s, severe scatter conditions may be expected, on the average, for from a few minutes to over 1 hour per 24-hour period.

## INTRODUCTION

As with many ionospheric phenomena, the scintillation of radio stars and satellites is especially frequent and complex in the auroral zones. It has been known since the very early days of ionospheric radio astronomy that scintillation increases considerably when a source is viewed through the auroral ionosphere (1). More recently, world-wide satellite surveys have shown the existence of an often sharply defined zone of enhanced scintillation at auroral and subauroral latitudes (2), (3). That scattering in these regions may be of

consequence to space communications is evident upon noting the location of ground stations such as NASA's data acquisition facility at Gilmore Creek, Alaska, and ESRO's forthcoming network.

Among the important and only partially answered questions concerning auroral-zone scintillation is its relation to other high-latitude geophysical phenomena. The satellite surveys have shown a weak dependence of the scattering zone's equatorward boundary latitude on geomagnetic activity (3). Radio-star observations at College, Alaska, imply also that the poleward boundary moves toward the equator under moderate to high magnetic activity conditions (4). Moorcroft and Forsyth (5) found a close relation between radio-star scintillation and auroral activity at Saskatoon, Saskatchewan. Owren, Fremoux, and Hunsucker (6) reported a direct relation between fractional fluctuation in received radio-star flux and line-of-sight auroral intensity.

Despite the evidence for a close relation between scintillation and auroral disturbance phenomena, it is inescapable that the latter are not necessary for the existence of scintillation-producing irregularities in the auroral zone. That such irregularities are essentially omnipresent is evident from observations currently being carried out at College on 68 Mc/s. Similar records obtained at College during the IGY on 223 Mc/s imply that the omnipresence of scintillations may be expected in the auroral zones on increasingly higher frequencies as the new solar cycle progresses.

From a geophysical point of view, the quiescent background of ionospheric irregularities in and near the auroral zones may turn out to be the most important. From the point of view of space communications, however, scattering during periods of special disturbance is of prime interest. Recent radio-star and satellite observations in Alaska indicate that significant scatter and refraction of VHF waves takes place during propagation through irregularities directly associated with individual auroral forms. In some cases the auroral scattering belt can be located well past sunrise by virtue of its scintillation production. It is the intent of this paper to describe the observed effects of such aurorally associated scattering.

The Geophysical Institute at College operates several radio-star interferometers and maintains close liaison with NASA's space data acquisition facility at Gilmore Creek, located about 20 km to the north-east. From the combined radio-star and satellite observations available from the two observatories plus satellite observations made at the College minitrack station, two periods of special interest during the 1964-5 northern auroral observing season have been selected for review. These occurred near the equinoxes, one in mid-September and the other in mid-April.

At Gilmore Creek, tracing and data acquisition are carried out on *Nimbus*, *Tiros*, and other satellites. Two 85-foot paraboloids are used independently, that is, not as a interferometer. Each dish employs multiple offset feeds so that angle information is available for automatic tracking of satellites. In addition to autotrack, several other modes of operation are available. These include a program mode in which the dish is controlled by a tape containing predicted satellite position information. Aside from telemetry, received signal strength (in the form of a.g.c. voltage) and angular information (in the form of servo error and dish velocity voltages) are recorded in all operational modes.



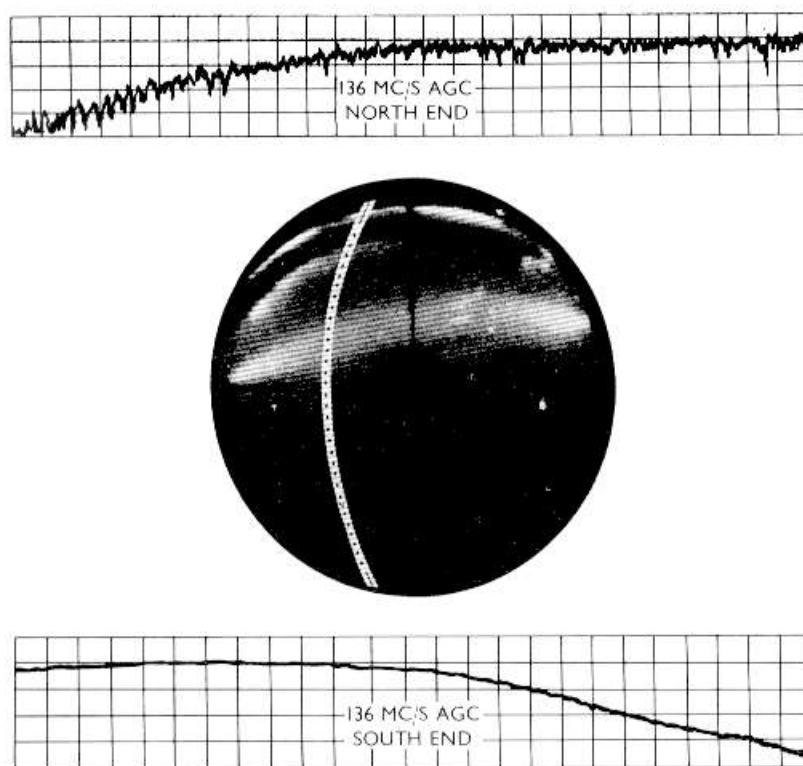


FIG. 1 Nimbus orbit 280 north-south pass from 0107 to 0116, September 16, 1964

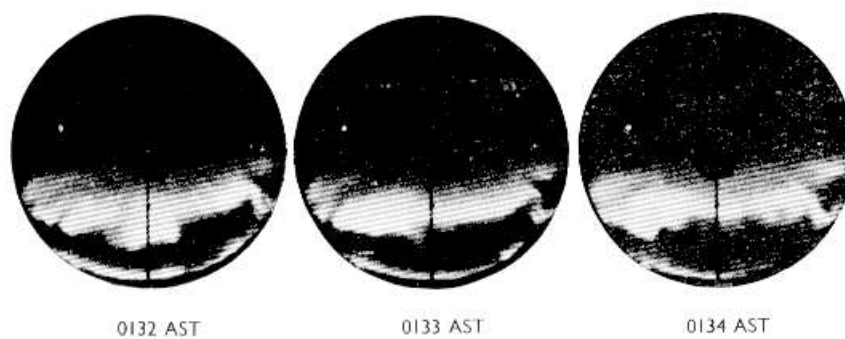


FIG. 2 Nimbus orbit 280 auroral break-up September 16, 1964

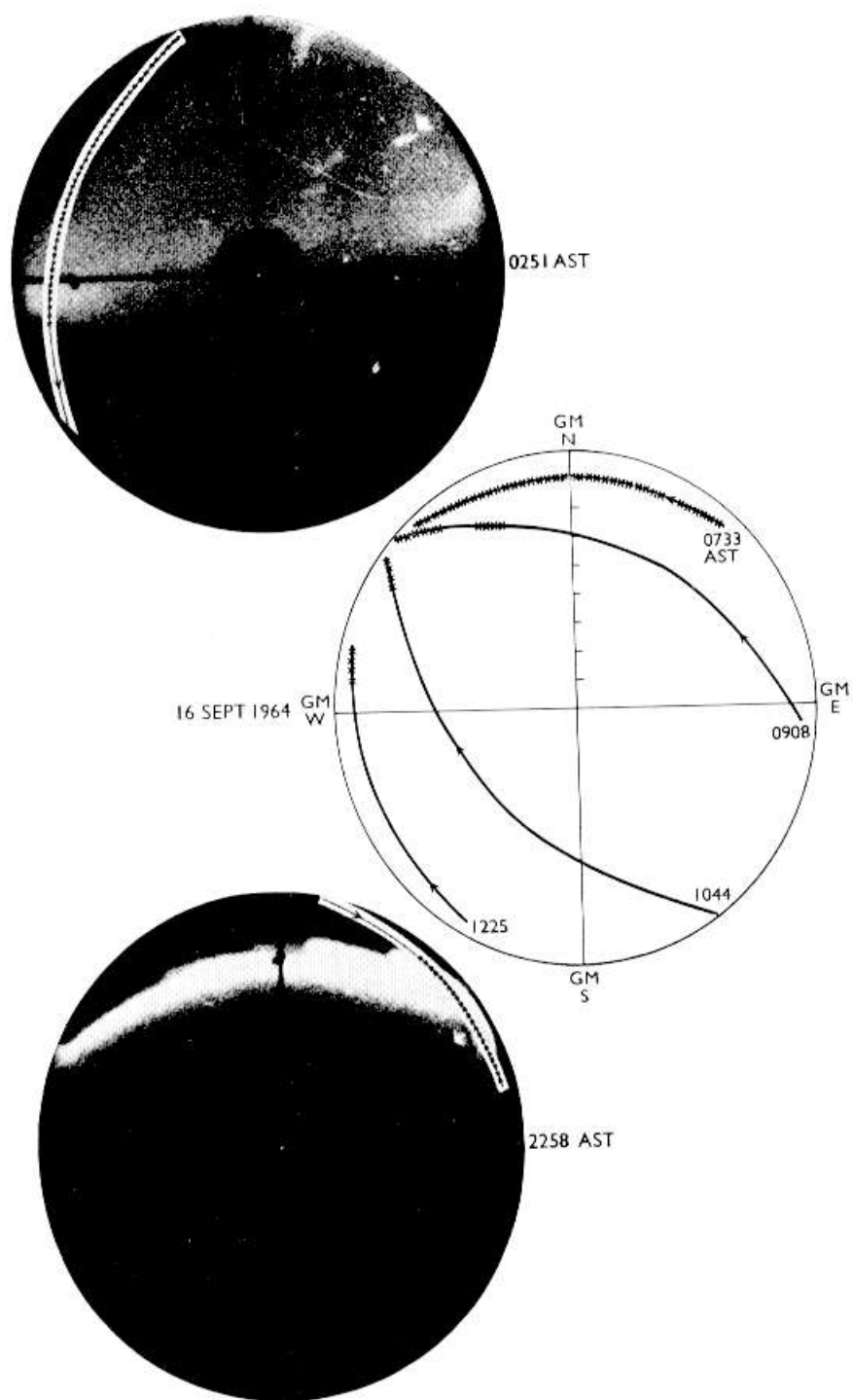


FIG. 3 Nimbus orbits 281, 284 to 287 and 293

## OBSERVED EFFECTS

In selecting periods of interest for the present study, some use was made of the operators' log from Gilmore Creek. On the local nights of September 15-16 and 16-17, for instance, one finds comments indicating that difficulties were encountered in the presence of visible aurora, and that the operational crews inferred a relationship. Later comparison of the satellite records from the period with all-sky camera photographs from the Geophysical Institute corroborates this on-the-spot appraisal of the situation.

Figure 1 typifies the a.g.c. records obtained on 136 Mc/s at Gilmore Creek under conditions of auroral scatter. The upper record strip corresponds to the first 2 minutes of a *Nimbus* pass, when the satellite was rising in the north. The scale bears an approximately logarithmic relationship to received signal strength, with one large division representing about 6 dB. Thus, amplitude scintillations on the order of 6 dB, peak to peak, were observed to the north. The lower record strip corresponds to the last 2 minutes of the pass, when the satellite was setting in the south. No amplitude scintillations are in evidence. The zenith angle of the satellite was very nearly equal for the two strips.

An all-sky camera frame, exposed during the satellite pass also is shown, the top of the frame corresponding to geomagnetic north. The track of the satellite has been drawn on the all-sky photograph, with the regions relating to the record strips designated by the two solid end portions. Thus, the disturbed record strip was obtained as the line of sight to the satellite passed through a bright auroral arc. The smooth record strip was obtained from an auroral-free part of the sky. We shall return later to a more detailed discussion of this pass.

Figure 1 relates to *Nimbus* orbit 280, the Gilmore Creek pass taking place between 0107 and 0116 Alaska Standard Time (150° west meridian time) on the morning of September 16, 1964. Figure 2 is a sequence of all-sky photographs exposed at College at 0132, 0133 and 0134 (left to right), about 10 minutes before a message was sent from Gilmore Creek which stated in part, "This station is at present unable to track anything due to excessive aurora." The all-sky photographs show an auroral breakup in progress.

By the time *Nimbus* returned, in orbit 281, the aurora had quietened to a diffuse glow in the northern half of the sky, and Gilmore Creek again was able to track. Figure 3 shows the sequence of events for this and the next five *Nimbus* passes. The all-sky camera frame on the left relates to orbit 281, with the satellite track shown in the west. The x's demark the region of observed amplitude scintillation, which ceased as the satellite entered the auroral-free part of the sky south of the station.

Orbits 282 and 283 did not bring *Nimbus* within view of Gilmore Creek. Orbit 284 produced a pass in the geomagnetic north between 0733 and 0739 AST. The satellite tracks for this and the following daytime *Nimbus* passes are shown in the center diagram of Fig. 3. Again the x's indicate amplitude scintillations. Pass 284 displayed scintillations in excess of 6 dB throughout. Orbits 285, 286 and 287, which produced south-to-north passes, displayed scintillations only at their extreme northern ends. It is submitted that the indicated regions of scintillation probably demark daytime locations of the aurora over Alaska on September 16, 1964.

*Nimbus* next came into view at Gilmore Creek during orbit 293, making a north-to-south pass, east of the station, between 2228 and 2234 AST. By this time, a bright auroral band was visible, the satellite rising north of the form. As indicated in the all-sky camera frame on the right of Fig. 3, the satellite signal was steady until the line of sight reached the aurora. Thereafter, amplitude scintillations were observed through the end of the pass.

Detailed comparison of all-sky photographs and Gilmore Creek records reveals a general tendency for amplitude scintillations to be stronger when the aurora is brighter. On occasion it even appears that small, relatively bright features within a large auroral form can be related to short enhancements of scintillation. This relationship of scintillation strength and auroral brightness, however, is far from being consistent. Some clearly visible forms do not appear to produce any appreciable amplitude scintillation at all, and patches of scintillation occur without any accompanying visible form in the immediate vicinity. For an example, let us return to *Nimbus* pass 280.

Figure 4 again shows the all-sky camera frame exposed at College at 0112 on the morning of September 16, together with the track of *Nimbus* over Gilmore Creek. The x's denote amplitude scintillations on the order of 6 dB, the slashes considerably less intense scintillations. Thus, of the three arcs visible on the all-sky camera frame, only one produced appreciable amplitude scintillations. On the other hand, a short burst of rather intense scintillation was observed somewhat to the south of the southernmost visible arc.

The amplitude scintillations observed at Gilmore Creek often are accompanied by angle scintillations of a fraction of a degree. In addition, occasional angular deviations which can be attributed to large-scale refraction near auroral forms are observed. On *Nimbus* pass 280, four such effects occurred in the regions marked with solid ovals on the satellite track. Records corresponding to the center pair of these four regions also are shown. The upper strip is a portion of the 136 Mc/s AGC record. The lower strip is the corresponding record of one of the two angular servo error voltages. Two regions of significant angular error voltage are evident. These correspond to the two center ovals marked on the all-sky camera frame. The angular deviations indicated by the error voltage reached peaks of greater than  $+2^\circ$  and  $-1^\circ$ , respectively. The error voltage from the orthogonal angular servo showed slightly smaller deviations at the same times.

It will be noted that the two angular deviations were accompanied by loss of signal. The first signal loss, on the left, is small and can be accounted for almost entirely by the off-axis arrival of the wave as indicated by the angular error voltages. The second signal loss, however, is approximately 20 dB and far exceeds that to be expected on the basis of the antenna polar diagram alone. This signal loss resulted from severe defocusing by an ionospheric lens associated with the southern border of the broad auroral arc shown in the all-sky photograph. The other refractive effects also were associated with border regions of visible auroral forms, except for the southernmost one.

The southernmost refracting region and the southernmost region of scintillation do not appear associated with a visible form. However, a long-exposed spectrograph operated at College indicated that a fourth arc crossed the sky a few degrees south of the zenith near the time of *Nimbus* pass 280.

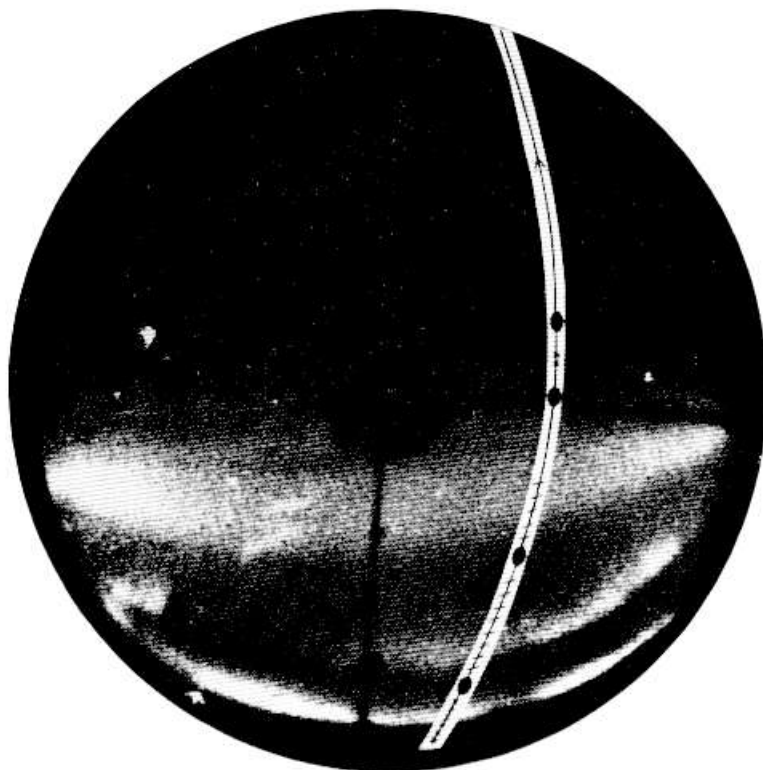
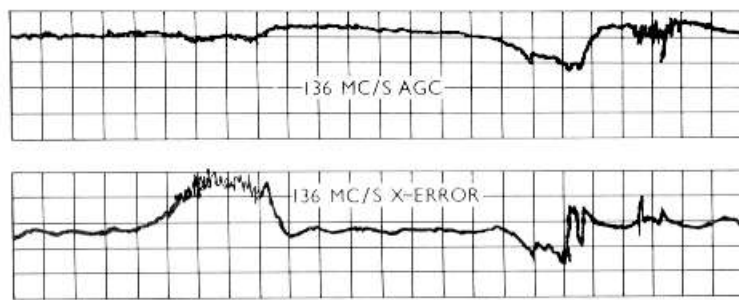


FIG. 4 Nimbus orbit 280, at 0112, September 16, 1964

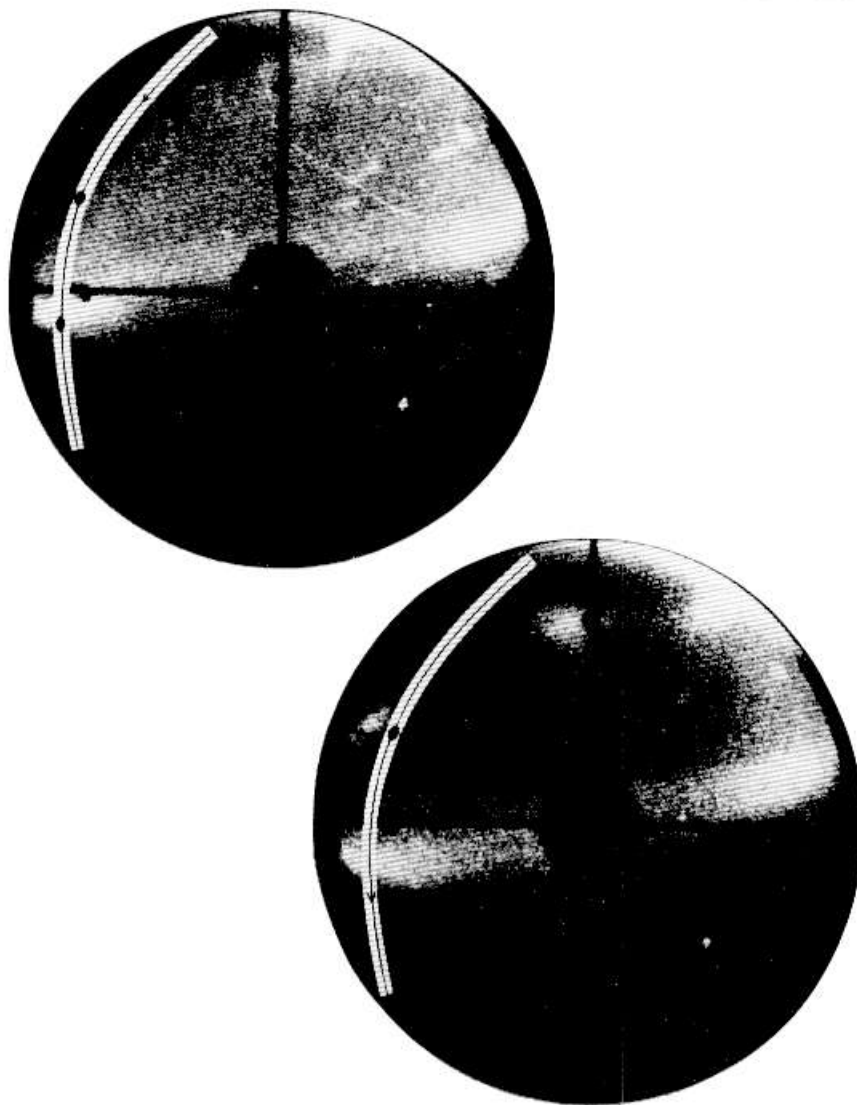
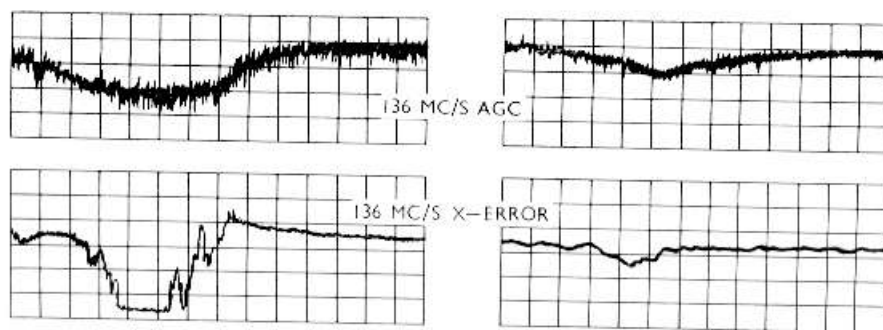


FIG. 5 Nimbus orbit 284, refractive effects

The spectrograph showed hydrogen alpha emission from the region of interest in the early-morning hours of September 16. An  $H_\alpha$  photometer, directed at the local geomagnetic zenith, also produced an appreciable output at the time in question. Comparison with the appropriate all-sky camera frames shows that even at its peak, the hydrogen emitting form was too weak to be detected by the all-sky camera. Thus the southernmost effects noted on the *Nimbus* pass probably were produced by a subvisual hydrogen arc resulting from proton bombardment. The more northerly effects were caused by visible auroral forms resulting from electron bombardment.

The relationship between scintillation and visible auroral forms is complicated not only in the spatial domain but also in the time domain. Not only do apparently aurorally associated effects occur outside the spatial boundaries of individual forms but also radio effects sometimes are observed from a given direction before and after distinct visible features can be discerned in the region. An example of this behavior occurred on September 16, during and following *Nimbus* pass 281.

Figure 5 again shows an all-sky camera frame on the left exposed during the pass, together with strips of 136 Mc/s a.g.c. and angle-error records. The refractive effects evident on the record occurred at the oval-marked positions on the all-sky photograph. The smaller refractive effect, on the right, corresponds to the lower oval-marked region. Thus it occurred as the satellite crossed a well-defined boundary from an auroral-filled to an auroral-free part of the sky. The larger refractive effect, on the left, is only vaguely associated with what might be termed a border region. The right-hand all-sky camera frame shows how the sky appeared 10 minutes after the satellite passed the more strongly refracting region. The region again is indicated by an oval. It can be seen that during the intervening period, the diffuse auroral light coalesced into more clearly defined arc structure with a border region between two arcs becoming evident near the region of observed refraction.

While satellite records such as those described above can give intermittent information on the position of refracting and scattering regions, no direct observation of the lifetime of the regions is afforded. On a few occasions the opportunity arises to combine such records with the results of radio-star observations, allowing determination of both spatial and temporal characteristics of the regions. Such an opportunity arose under auroral conditions on the night of April 17-18, 1965. Between 2352 and 0015 AST that night, *Tiros 9* passed over Gilmore Creek on orbit 1040, approaching within a fraction of a degree the angular position of *Cassiopeia A*, which was under track by several radio interferometers at the Geophysical Institute. At the time of the *Tiros* pass the interferometers were recording the waning phase of a radio-star visibility fade which had commenced some 20 minutes earlier. (For discussion of visibility fades, see Little *et al.* (7), Moorcroft (8), Flood (9), (12), and Fremouw and Owren (4), in preparation.)

The College all-sky camera recorded extensive aurora on the night in question. The sky was intermittently overcast, but bright and changing forms are discernible on the film. At the time of present interest, the sky was clear in the direction of the radio star, as noted by visual observation at the time from the interferometer site. The all-sky camera shows that an auroral break-up brought on the visibility fade in question. An auroral band located

near the local zenith swept northward across the radio-star position within the period of a few minutes, changing form in a complicated manner. The time resolution of the all-sky camera was not sufficient to give a complete description of the break-up development. Accordingly, we shall rely on photometric measurements to discuss the auroral effects on the radio-star signal.

Two line-of-sight photometers, with approximately  $1^\circ$  fields of view, were mounted on one of the tracking interferometer antennas. The photometers recorded auroral intensity at 5577 Angstroms in the green and 4278 Angstroms in the blue, in the immediate vicinity of the radio star. The 5577 Angstrom photometer was complemented by the 4278 Angstrom instrument in order to provide more direct information concerning primary auroral electron bombardment. As a matter of incidental interest, in no record inspected to date has there been sufficient difference between the two photometer records to associate scintillation effects any more directly with one than with the other.

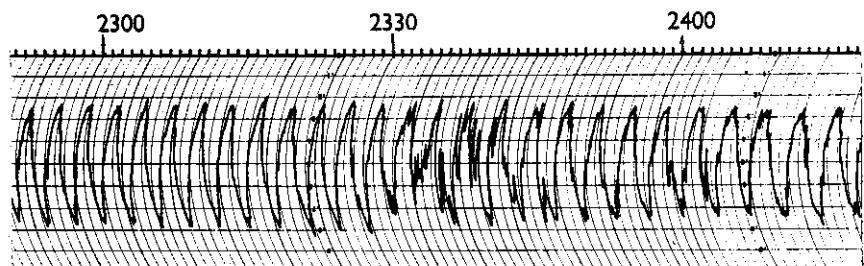
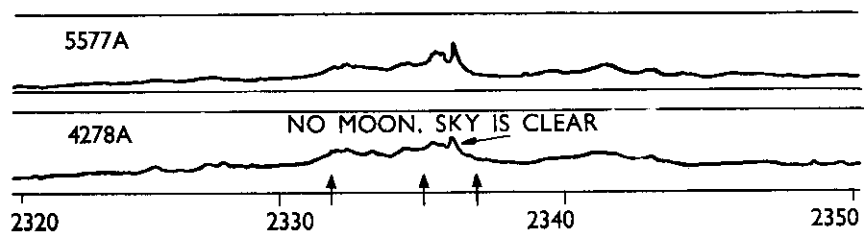
Figure 6 shows the photometer records for the period of interest along with records from three of the five phase-switch interferometers which were tracking *Cas. A*. The top pair of record strips is from the photometers. The interferometer records, from top to bottom, are from 223, 137 and 68 Mc/s, respectively, all with east-west baselines of approximately 220 m. Note that the photometer chart speed was about three times that of the interferometers. The records are aligned in time at the center of the strips. It is to be noted also that the photometer outputs are related approximately logarithmically to auroral intensity.

The 68 Mc/s record shows considerable scintillation activity throughout the period shown. Between about 2330 and 2400, the interference fringes are essentially lost, which constitutes the occurrence of a radio-star visibility fade. The time of commencement of the fade is most readily determined from the 223 Mc/s record, it being the least sensitive to prior scintillation activity. The 223 Mc/s interference fringe starting approximately at 2332 is the first one to be reduced in average amplitude. The time at which the amplitude reduction appears to have begun is marked by the leftmost arrow on the photometer trace. This is seen to correspond closely with a brightening of the line-of-sight auroral intensity.

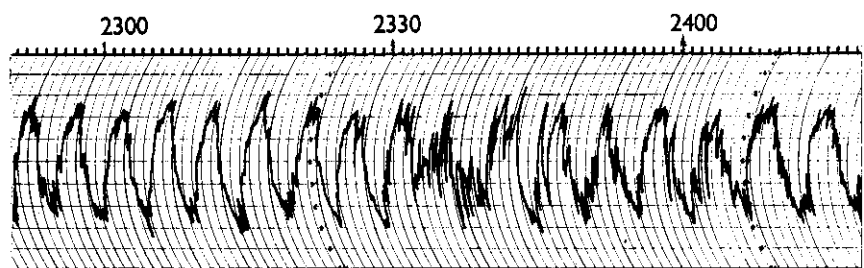
The next 223 Mc/s lobe recovered amplitude, but within a few seconds of 2335 the major fade effect commenced. The major effect lasted for  $1\frac{3}{4}$  minutes, the period between the center and rightmost arrows on the photometer trace. This period corresponds closely to the period of brightest line-of-sight aurora. Recovery from the main fade effect began within 20 seconds of the time at which the aurora returned to the intensity existing just before the main-effect commencement. By 2345 the auroral intensity had declined essentially to its pre-fade value, but the visibility fade on 68 Mc/s persisted until approximately 0015. The 223 Mc/s record, then, implies that the fade-producing ionospheric structure began to decay within seconds after cessation of the associated enhanced auroral electron influx, while the 68 Mc/s record implies a decay time constant on the order of minutes. The decay period, however, is complicated by continued faint auroral luminosity.

Besides the 220-m-baseline interferometers, two additional interferometers were in operation, on 68 Mc/s. These have east-west baselines of 110 and 330

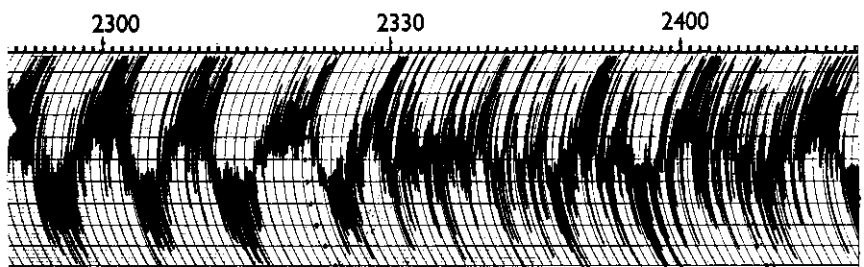




223 Mc/s



137.6 Mc/s



68 Mc/s

FIG. 6 Tiros 9 orbit 1040, April 17-18, 1965

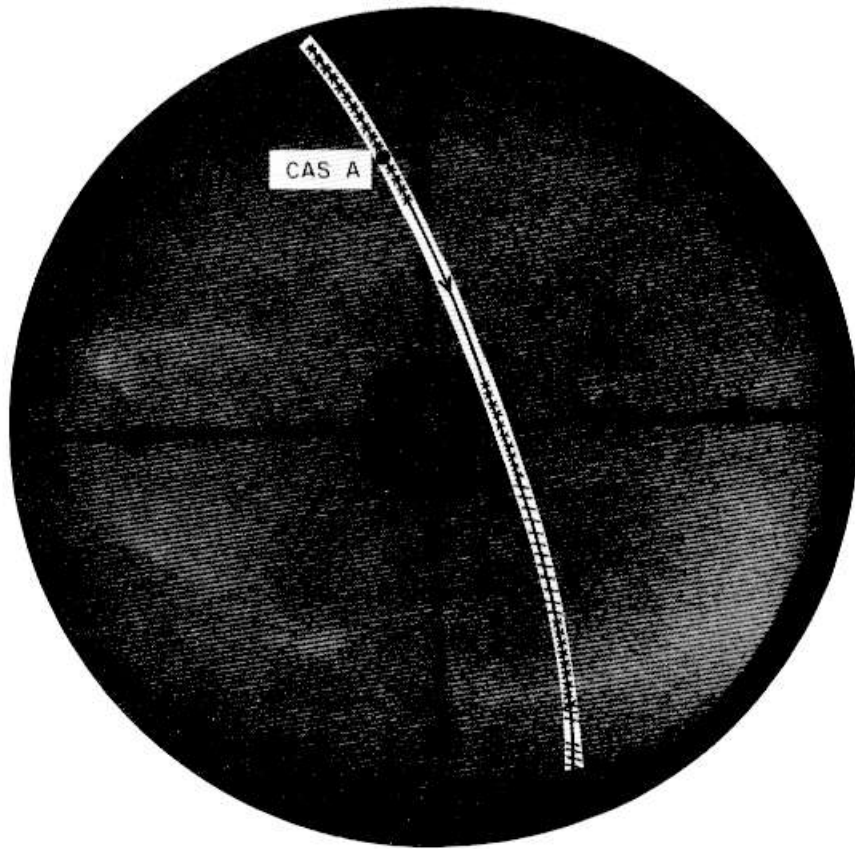


FIG. 7 Tiros 9 orbit 1040 on night-sky frame exposed at 0007, April 18, 1965

respectively. In addition to records of the type shown in Fig. 6, all the phase-switch interferometer outputs were recorded on rectilinear charts after integration to smooth out individual scintillations. The smoothed records show that coherence in the 68 Mc/s wavefront arriving at the ground was completely lost over a distance of less than 110 m between 2335 and about 2340. The work of Bramley (10) shows that loss of complete coherence requires scattering of 100 per cent of the radio-star flux.

At approximately 2353 AST, *Tiros 9* appeared in the north on a pass roughly paralleling the geomagnetic meridian of College and Gilmore Creek, as shown in Fig. 7. At about 2356, the satellite passed very near the angular position of *Cas. A* and thus through the part of the sky being observed by the radio-star interferometers. Scaling of the smoothed 68 Mc/s phase-switch records shows the radio-star visibility fade to be still in progress, although considerably reduced in severity compared with the period of maximum line-of-sight auroral intensity. In addition to the phase-switch interferometers, a phase-sweep interferometer giving independent phase and amplitude information was being operated on one of the 68 Mc/s antenna pairs, in co-operation with Boeing Scientific Research Laboratories. Combination of the phase-switch and phase-sweep data allows calculation of the size of ionospheric structure responsible for the visibility fade. The method used, which has not yet been published, does not require the usual approximations based on the somewhat arbitrary distinction between "single" and "multiple" scatter events. The method is based on a generalization of the work of Bramley (10), (11).

The combined radio-star interferometer data imply that a gaussian autocorrelation function provides a reasonably accurate statistical description of the fade-producing ionospheric structure. For the 5 minutes following passage of the satellite signal through the fade-producing region, the radio-star observations yield a scale of  $275 \pm 50$  m. The  $\pm 18$  per cent uncertainty arises when the scale is calculated independently from two different phase-switch interferometer spacings, assuming a gaussian autocorrelation function in each case, and thus gives an estimate of the error arising from this assumption. The observations indicate r.m.s. phase fluctuations across a plane at the base of the ionospheric scattering layer of just under 1 radian for the 68 Mc/s signal.

The x's on the satellite track of Fig. 7 indicate three discrete regions of strong scintillation. Peak-to-peak fluctuations in 136 Mc/s signal strength in excess of 6 dB were general in these regions, with some scintillation nulls dipping 20 dB to the recording threshold. The first two scintillation regions are separated by a region of essentially smooth signal reception, the second two by a region of reduced scintillation, as indicated by hatches. During the satellite pass, the sky was generally but thinly overcast. Rapidly changing auroral forms are evident on the all-sky camera film during the first half of the pass. Significant auroral changes took place during the 1-minute intervals between exposures.

A few minutes after midnight, near the middle of the pass, the aurora dimmed for about a minute and then entered a new and temporarily more stable phase. The dominant form of the new phase was a structured arc south of the zenith, as shown in the frame of Fig. 7, which was exposed at 0007 AST on April 18. At the time of exposure the satellite signal was passing

through the arc and displaying amplitude scintillations in excess of 20 dB, peak to peak. Random phase scintillations of a fraction of a degree also were experienced. In addition, short spikes of phase confusion at the time of amplitude scintillation nulls resulted from loss of signal in the tracking receiver. No large refractive effects were noted. During most of the pass the satellite was tracked in program mode. Two periods of autotrack were carried out, however, during which the servo velocity voltage showed moderate ionospheric effects. The dish departed from a smooth track at velocities up to a maximum of about  $1^\circ$  per second.

#### CONCLUSION

The combination of radio-star, satellite, and optical observations carried out at College during the past winter have shown a very close relation between severe radio scatter events and bright active auroral displays. The close directional correspondence of satellite scintillation regions and certain individual auroral forms suggests that a significant contribution to scattering may be made by E-layer irregularities. In this case, the scatter regions show north-south extents of from a few tens of kilometers to several hundred kilometers. They often appear to form into east-west arcs in the daytime as well as at night and may well afford a means of locating the auroral belt during the day. The most severe scatter events appear to be caused by ionospheric structure with scales of a few hundred meters.

At present, severe scattering effects noted on satellite records usually are limited to the lower half of the VHF band. However, effects have been noticed at Gilmore Creek on 235 Mc/s telemetry receivers. These data are much more limited in number than tracking data at 136 Mc/s. At least one instance of amplitude scintillations at 400 Mc/s has been noted at Gilmore Creek. Comparison of current radio-star records with similar records obtained at College on 223 and 456 Mc/s during the IGY indicates that scattering of VHF and UHF waves by the auroral ionosphere may be expected to increase considerably in severity and occurrence frequency between now and the next solar maximum period.

#### REFERENCES

1. LITTLE, C. G., and MAXWELL, A., "Fluctuations in the Intensity of Radio Waves from Galactic Sources", *Phil. Mag.* 42, 267, 1951.
2. AARONS, J., "Geophysical Aspects of Radio Star and Satellite Ionosphere Scintillations". *Spread F and its Effects upon Radiowave Propagation and Communication*, Technivision, Maidenhead, England, pp. 247, March 1967.
3. YEH, K. C., and SWENSON, G. W., "F-Region Irregularities Studied by Scintillation of Signals", *Spread F and its Effects upon Radiowave Propagation and Communication*, Technivision, Maidenhead, England, pp. 217, March 1967.
4. FREMOUW, E. J., and OWREN, L. (in preparation), "Radio Star Visibility Fades Observed in the Auroral Zone at Solar Maximum". To be submitted for publication in *Rad. Sci.*

5. MOORCROFT, D. R., and FORSYTH, P. A., "On the Relation between Radio Star Scintillations and Auroral and Magnetic Activity". J. Geophys. Res. 68, 117, 1963.
6. OWREN, L., FREMOUW, E. J., and HUNSUCKER, R. D., "Radio Star Scintillations and Spread F in the Auroral Zone". Spread F and its Effects upon Radiowave Propagation and Communication, Technivision, Maidenhead, England, pp. 217, March 1967.
7. LITTLE, C. G., REID, G. C., STILTNER, E., and MERRITT, R. P., "An Experimental Investigation of the Scintillation of Radio Stars Observed at Frequencies of 223 and 456 Megacycles per Second from a Location Close to the Auroral Zone". J. Geophys. Res. 67, 1763, 1962.
8. MOORCROFT, D. R., "Radio Star Fadeouts on Phase-Switching Interferometer Records". J. Geophys. Res. 68, 111, 1963.
9. FLOOD, W. A., "A Study of Radio Star Fadeouts and their Application to Radar Resolution". J. Geophys. Res. 68, 4129, 1963.
10. BRAMLEY, E. N., "Diversity Effects in Spaced-Aerial Reception of Ionospheric Waves". Proc. IEE 98, Pt 3 and 4, 19, 1951.
11. BRAMLEY, E. N., "Some Aspects of the Rapid Directional Fluctuations of Short Radio Waves Reflected at the Ionosphere". Proc. IEE 102, Pt B, 533, 1955.
12. FLOOD, W. A., "Radio Star Fadeouts and Radio Propagation". Spread F and its Effects upon Radiowave Propagation and Communication, Technivision, Maidenhead, England, pp. 267, March 1967.

## ACKNOWLEDGEMENTS

The author gratefully acknowledges the guidance of Professor Leif Owren, now of the Radiophysics Laboratory of Dartmouth College, in establishing the current radio-star observing program in Alaska. Thanks are due to Mr John Lansinger of Boeing Scientific Research Laboratories for technical assistance and to Mr Robert Hisamoto of RCA Service Co. for help in selecting satellite records. This work was funded by Goddard Space Flight Center of NASA under research contract NAS 5-3940.



## CHAPTER 3-12

AURORAL ZONE RADIO STAR SCINTILLATION  
MEASUREMENTS AND INTERPRETATIONS

JOHN M. LANSINGER

Boeing Scientific Research Laboratories, Seattle, U.S.A.

## SUMMARY

A quantitative evaluation and comparison are made of angular and amplitude scintillation data received at the College, Alaska, experimental station on 68 Mc/s with a lobe-sweep interferometer. The data are reduced with an automatic data-processing system. A description is presented of a phase-compensation system which allows readily interpretable measurements to be made which represent the difference between the predicted and apparent position of the radio source. A lead/lag correlation analysis is made between ionospheric absorption, magnetic variation and the angular and amplitude scintillation data. Some results are presented which show an association between short-term absorption events and the enhancement of scintillation activity. Power spectral analysis and cross-correlation analysis are made of the experimental data. Given several ionization models, the computed ground diffraction patterns are compared with experimental data. A comparison is made between the predicted variation of scintillation depth versus zenith angle, based upon a theoretical model for field-aligned irregularities and some earlier experimental results.

## INTRODUCTION

Much of the past experimental work in the field of radio-star scintillations has relied on subjective means for reduction of data and has dealt almost exclusively with the measurement of amplitude fluctuations. Most of the equipment used in the past studies have been phase-switch interferometer systems of the type described by Ryle (1). Such equipment provides an output which is a function of both amplitude and phase. Because of this, it has been difficult to separate out the phase and amplitude variations on a continuous basis.

This paper describes some preliminary results of continuous phase and amplitude radio-star scintillation measurements obtained from a lobe-sweep system operating at 68 Mc/s. The measurements were taken near College, Alaska, using an east-west interferometer with approximately a 50 wavelength spacing. The results given in this paper cover scintillation measurements using the source *Cygnus A* in November 1964, and the source *Cassiopeia A* for the following 4-month period. Automatic data processing was employed in the determination of the scintillation activity indices and the magnetic activity index obtained from a magnetic pick-up coil.

## INSTRUMENTATION

The equipment employed for radio-star scintillation studies is a lobe-sweep interferometer system which is similar in nature and operating principle to that described by Hanbury Brown, *et al.* (2), Little, *et al.* (3), and Adgie (4). The unique aspect of the system is that the output of the phase-measuring channel represents the difference between the predicted position of the source and the observed position as measured in the direction of the interferometer baseline. The essentials of the interferometer system and associated equipment are given in the simplified block diagram shown in Fig. 1.

As shown in Fig. 1, the local oscillator signals feeding the mixers used in the antenna legs are phase locked to a difference frequency of 1 kc/s. This results in a 1 kc/s signal at the detected i.f. output, the amplitude of which is a measure of the coherent signal received by the two interferometer antennas, and the phase of which, relative to the internal 1 kc/s reference, is a measure of the path difference between the receiving antennas.

It can be shown that the phase difference of the received signal between the receiving antennas is given by  $K \sin (HA + \alpha)$ . The hour angle of the source is given by  $HA$ , and  $K$  and  $\alpha$  are constants which depend upon antenna survey data, operating wavelength, and the source declination. The phase compensator shown in Fig. 1 is a digitally operated device which introduces into the 1 kc/s reference signal a time-varying phase equal to  $-K \sin (HA + \alpha)$ . The recorded output of the phase channel is therefore the difference between the observed phase variations and the theoretically expected phase variations. A brief discussion relating to the compensator is given in the appendix.

Amplitude and angular scintillation and magnetic data were recorded on paper chart recorders, a slow-speed magnetic tape-recorder, and were sampled with an analog-to-digital converter and punched on paper tape using an 8-bit binary word format.

The routine analysis consisted of a programmed computation and print-out of indices which are measures of scintillation (amplitude and phase) and magnetic activity over 5- or 10-minute periods (depending upon the basic sample rate). Hourly averages of the various indices were punched on IBM cards which were used in the later studies. The indices computed are defined as follows: amplitude index,  $\left(\frac{\Delta A}{A}\right)^2$ ; power index,  $\left(\frac{\Delta P}{P}\right)$ ; angular index, given by the mean squared angular variations (minutes<sup>2</sup>); and magnetic index, given by the mean squared variations obtained from the magnetic pick-up coil. Chart records containing the scintillation data were visually scanned, and the hourly data cards were appropriately coded to take account of equipment malfunctions, interference, etc., in the subsequent analysis of the processed data.

## INTERPRETATION OF THE AMPLITUDE SCINTILLATION DATA

Implicit in the manner in which the amplitude scintillation index is determined is the assumption that the fluctuations received at the two antennas are correlated. It is useful to know the error in the determination of the amplitude variations between the receiving antennas in order to ascertain a limit in determination of this index.



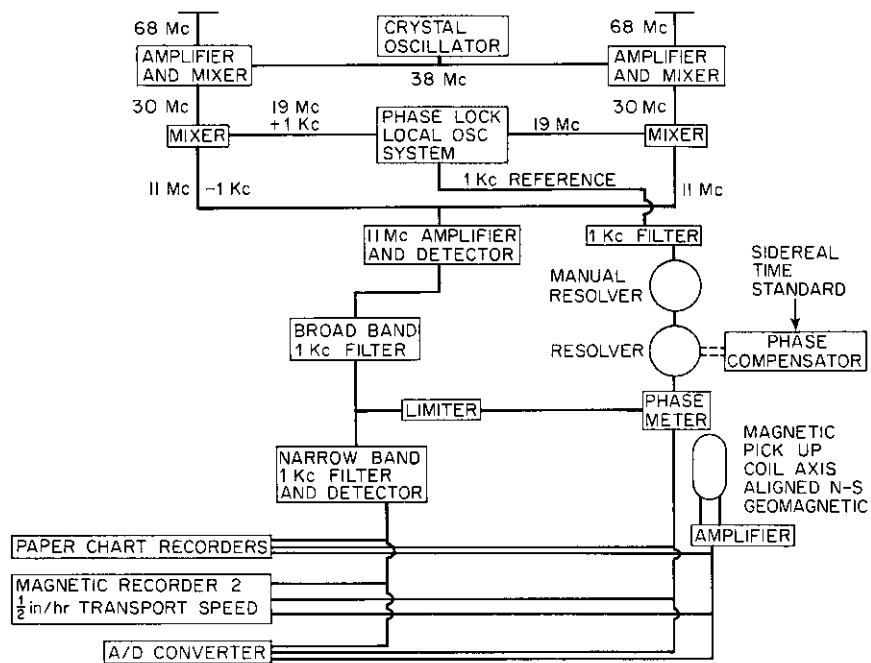


FIG. 1 College, Alaska instrumentation block diagram

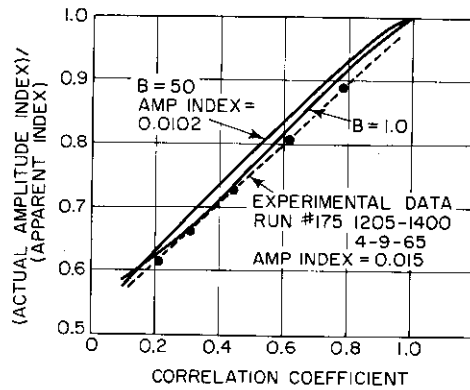


FIG. 2 A plot of the expected error in the apparent amplitude index as a function of the correlation of the amplitude variations between the two antennas

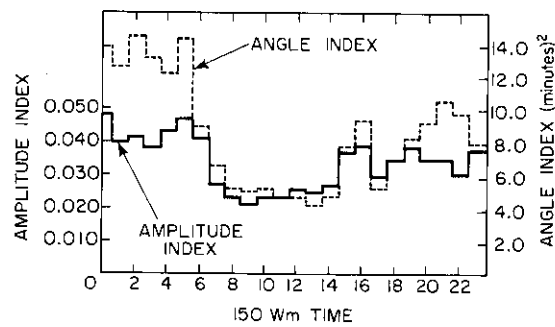


FIG. 3 Local time variation of 68 Mc/s amplitude and angular scintillations, December 1964–March 1965, College Alaska

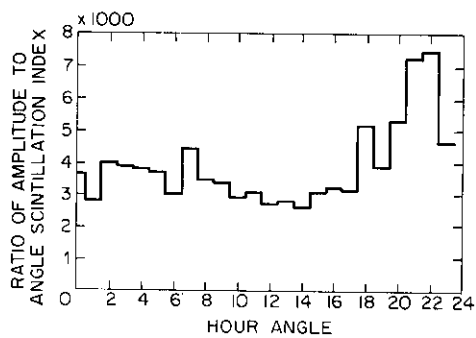


FIG. 4 Sidereal dependence of the ratio of amplitude to angular index for the source Cassiopeia A, December 1965–March 1965

Using computer-generated random numbers, a pair of data arrays having a given cross-correlation coefficient were generated. These represented the signal amplitude having a Rice probability distribution at two points on the ground. The recorder response in the lobe-sweep system is linear with the product of the amplitudes of the signals at the two antennas. The apparent amplitude is therefore obtained by taking the square root of this reading. The computer-generated arrays were used to represent the experimental data arriving at the receiving antennas and the resulting true and apparent amplitude scintillation indices were computed. The ratio of the actual amplitude index to apparent index was evaluated for various values of scattering ratio  $B$  (the ratio of non-scattered power to scattered power) and cross-correlation coefficients. For fully developed amplitude variations a given amplitude index will correspond to a particular value of  $B$ .

Given  $B$  equal 50 and 1 with the respective true amplitude indices 0.01 and 0.228, the results are represented by the solid lines given in Fig. 2. Using experimental data and assuming that the amplitude variations are correlated on the two receiving antennas given an apparent amplitude index of 0.015, similar calculations were performed and the results are indicated by the dashed lines in the same figure.

It is seen from Fig. 2 that the apparent value of amplitude index represents a lower limit in the determination of the true amplitude index and that the error in measurement is relatively insensitive to the degree of activity, but can be appreciable for small cross-correlation coefficients.

#### COMPARISON OF AMPLITUDE AND ANGULAR ACTIVITY INDICES

The results of a 4-month observation of the source *Cassiopeia A* of angle index and amplitude index as a function of local time are summarized in Fig. 3. Since 12 months of data are required to separate the sidereal and solar dependence, this limited amount of data is not sufficient to indicate the true solar dependence. From the plot of the ratio of amplitude index to angular index as a function of hour angle given in Fig. 4, it is apparent that this ratio reaches a peak approximately 2 hours prior to upper culmination. For a uniform layer at constant height, with transition or near zone irregularity sizes, it would be expected that the above ratio should be a maximum near lower culmination, since the amplitude variations would be more fully developed at the greater range.

A possible explanation for the observations is that a geographical dependence exists for the distribution of sizes and heights of the irregularities responsible for the scintillations. From satellite observations at College, Alaska, Basler and DeWitt (5) have reported the presence of irregularities at heights of 145 to 1000 km with the most frequent heights occurring between 250 and 650 km. Observing satellite scintillations at the same location, Hook and Owren (6) have reported the presence of irregularities from the satellite height of approximately 275 km down to heights of about 90 km. From both sets of observations the observed height distribution of irregularities appears to vary for different satellite passes. Liszka (7) has reported from high latitude satellite observations, variations in the height distribution of irregularities, with the presence of low-altitude irregularities down to 100 km occurring preferentially during the nighttime.

It is shown later, from an examination of the temporal phase and amplitude autocorrelation functions, that ionospheric gradients may be present an appreciable fraction of the time. The presence of such gradients in addition to a random diffracting region both of which may have a geographical, seasonal, and diurnal dependence may be responsible for the above-noted peak in the ratio of amplitude to angular index 2 hours before upper culmination for the *Cassiopeia A* data.

#### CORRELATION STUDIES

Correlation evaluation was made using hourly values for all combinations of amplitude and angular scintillation data, magnetic data obtained from the pick-up coil, and ionospheric absorption data. The absorption data were scaled from 30 Mc/s riometer records obtained at College, Alaska. The correlation coefficients for zero lag for the various combinations are summarized in Table 1.

TABLE 1

SUMMARY OF COMPUTED CORRELATION COEFFICIENTS

Date	Angular vs. power index	Angular vs. absorption	Power index vs. absorption	Angular vs. magnetic	Power index vs. magnetic	Absorption vs. magnetic	Radio Source observed
Nov. 1964	0.805	0.239	0.292	—	—	—	Cyg A
Dec. 1964	0.754	0.454	0.194	0.491	0.177	0.580	Cass A
Jan. 1965	0.878	0.483	0.501	0.457	0.358	0.693	Cass A
Feb. 1965	0.780	0.641	0.525	0.586	0.398	0.684	Cass A
Mar. 1965	0.848	0.497	0.434	0.466	0.338	0.595	Cass A

"Angular" is the r.m.s. angular variation, "absorption" is the absorption measured at 30 Mc/s, "magnetic" is the r.m.s. value of the output of the field coil.

The magnitude of the observed correlation of amplitude index with magnetic activity given in Table 1 is comparable to the high-latitude correlation of amplitude index and local K index reported by Little *et al.* (3), and Ryan (8), using scintillation data obtained from observations of *Cassiopeia A* and *Cygnus A*. Liszka (7) has reported somewhat higher correlations averaging approximately 0.45 between the scintillation index from satellite transmissions and magnetic  $A_p$  index. A typical lead/lag plot of correlation of scintillation activity with ionospheric absorption and scintillation activity with magnetic activity is given in Fig. 5a and 5b. The non-symmetry of the correlation about the zero lag is seen to be roughly similar in comparisons using magnetic or absorption data. The non-symmetry of the correlation coefficient about zero lag is similar to that previously noted by Little *et al.* (3) at the same station in the comparison of 223 Mc/s power index with magnetic index. Magnetic activity indices used in the present correlation computations were the r.m.s. value of the magnetic field variations obtained with the induction coil. Since the magnetic data were processed automatically along with the scintillation data, it was more convenient to use this form of magnetic measurement of magnetic activity rather than the usual K index measurement. For the month of December 1964 it was found that the correlation between the

FIG. 5(a) Lead/lag correlation of 68 Mc/s scintillations with 30 Mc/s ionospheric absorption, Feb. 1965

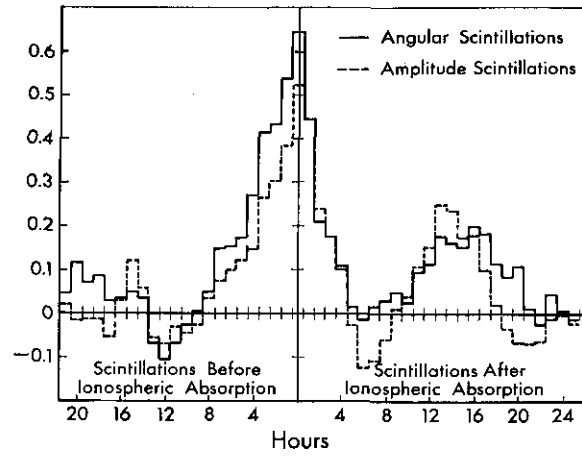


FIG. 5(b) Lead/lag correlation of 68 Mc/s scintillations with magnetic activity, Feb. 1965

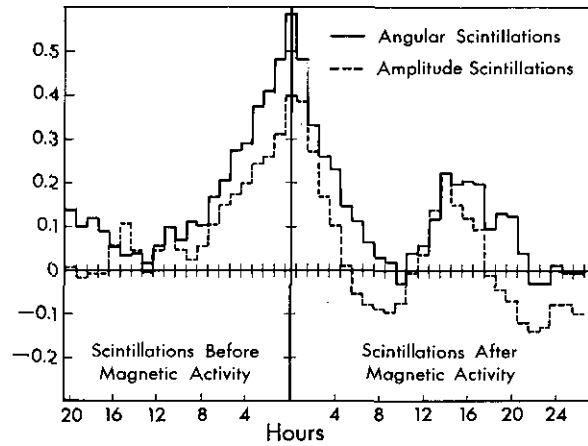
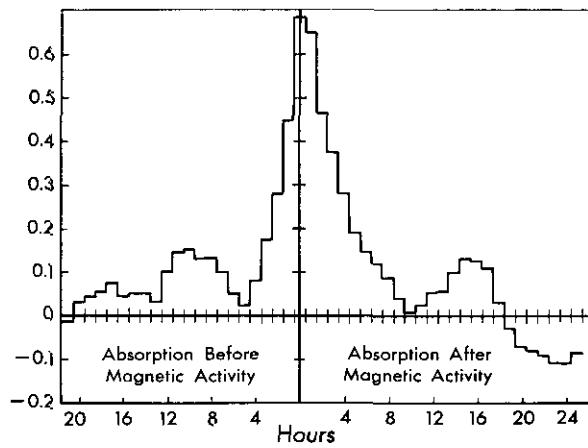


FIG. 5(c) Lead/lag correlation of 30 Mc/s ionospheric absorption with magnetic activity



r.m.s. field coil measurements and the College K index was 0.739.

From Table 1 it is clear that angular scintillations consistently have a greater association with either magnetic or absorption activity than do amplitude scintillations. Magnetic and absorption activity, however, are seen to be more closely associated to each other than they are to scintillation activity. From the lead/lag correlation evaluation of absorption versus magnetic activity given in Fig. 5c it is noted that there is a tendency for ionospheric absorption to be greater following magnetic activity rather than preceding it.

Cross-correlation studies of amplitude versus angular scintillations have shown that, over the period of observation, symmetry exists about zero lag. From Table 1 it is evident that the correlation coefficient remains consistently around 0.8. A correlation coefficient of less than unity is consistent with the presence of transition or near zone irregularity sizes. For this condition, the ratio of angular to amplitude index will change as the distance to the irregularities varies due to the changing geometry.

During the course of investigation it was noted that at times of a sudden increase in ionospheric absorption, as noted on the 30 Mc/s College riometer recording, there frequently were increases in scintillation activity. A short-term absorption event is defined here as a sudden increase in absorption of 0.5 dB or greater in which the absorption reaches a maximum within 15 minutes from the time of onset. During the period between December 11, 1964, and March 25, 1965, forty-four such events were noted during times when scintillation data were available. During this period thirty-two, or about 73 per cent, of the short-term absorption events appeared to be associated with a maximum in scintillation activity. An association was assumed to exist if the time of maximum of amplitude index came within 10 minutes of the time of maximum absorption. The data used for comparison were the computed 5-minute print-out values of scintillation amplitude index.

#### POWER SPECTRUM ANALYSIS

The majority of the scintillation data was digitized at a rate of fifteen samples per minute. Sampling rates as fast as 120 samples per minute were available, but because of data-handling limitations the lower rate was used for the majority of the data runs. Computed amplitude, phase and magnetic spectra using the method of Blackman and Tukey (9) were obtained from a few runs at the faster sample rate, and from selected periods of scintillation activity at the lower sampling rate. Lead/lag cross-correlations between the phase and amplitude data sets were computed during these same periods.

Valid results require that the sample data frequency components must not exceed half cycle per sample to avoid aliasing, and the data must remain stationary. The first requirement was satisfied by selecting only those data runs (obtained at the slow sample rate) which, from visual inspection, had sufficiently low frequency components. The statistics of the data were considered stationary if a data run when divided into two segments produced essentially identical power spectra. Low-pass filters internal to the system limit the frequency response to 0.45 c/s. Phase and amplitude components so far noted have been well below this limit.

Several typical examples of the phase and amplitude scintillation spectra and the corresponding autocorrelation functions are given in Fig. 6. Most of

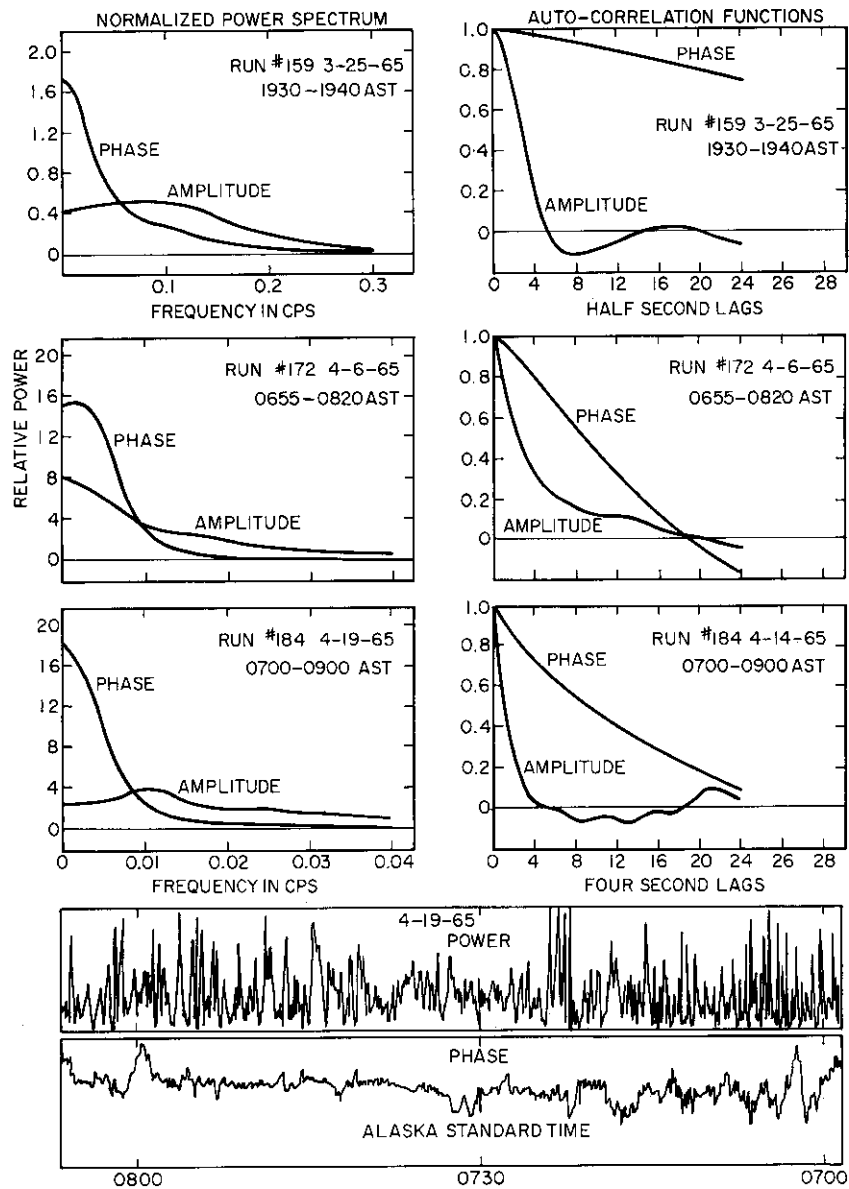


FIG. 6 Some examples of computed phase and amplitude power spectra. The full computed range is not shown, it goes to 1 c/s in the upper graph and to 125 c/s in the remaining two. The 68 Mc/s data shown correspond to a period covered by the spectra and correlations shown directly above the data

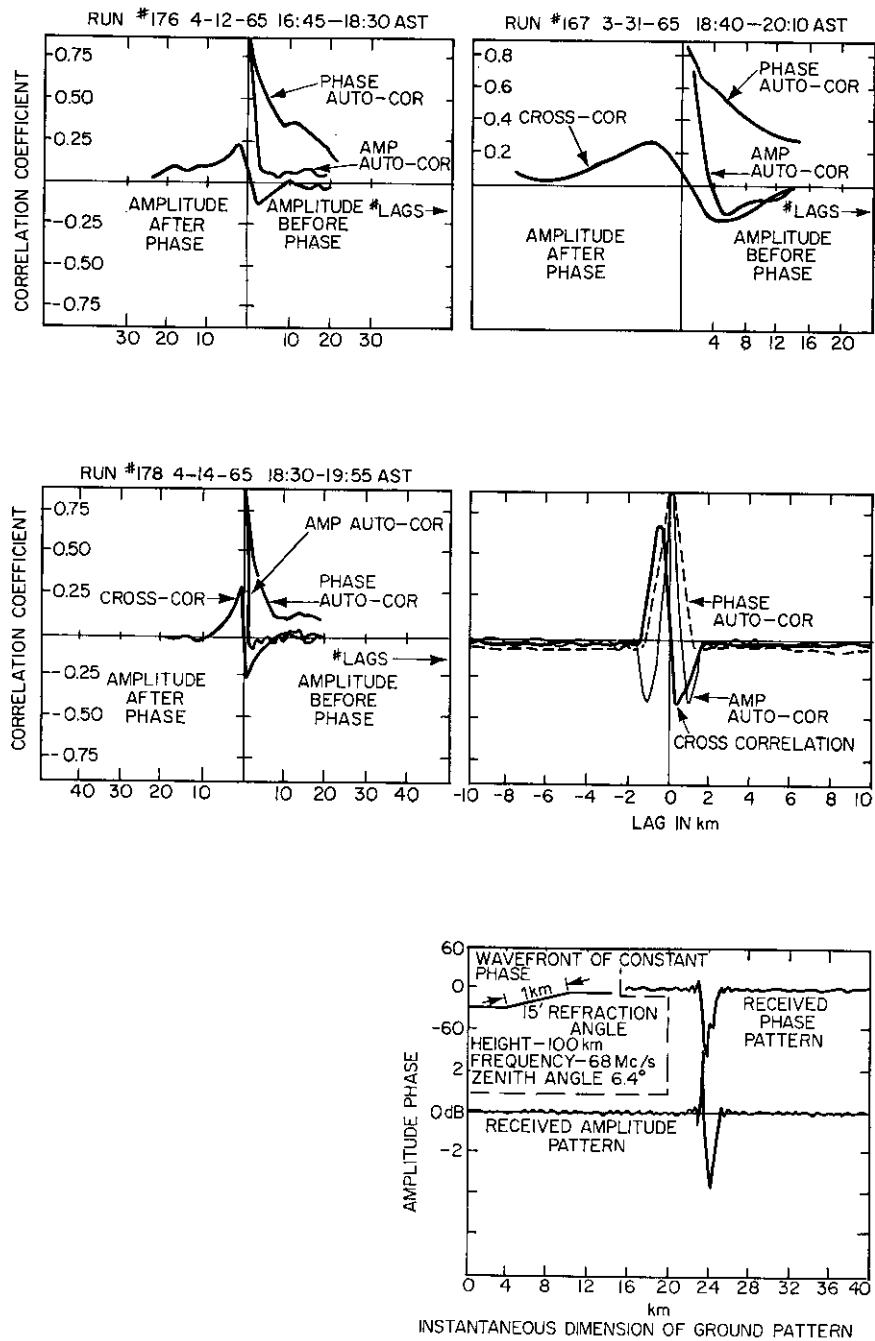


FIG. 7 Experimental temporal lead/lag correlation of amplitude with phase together with the theoretical correlation of amplitude with phase resulting from a simple wedge ionization



the spectra so far obtained have been characterized by a comparatively smooth spectrum with the high-frequency portion dropping off differently from one activity period to the next. As shown in the representative examples, the phase spectrum has greater emphasis at the low end of the spectrum. Broad peaks have been noted similar to those shown in the lower graph in Fig. 6.

Qualitative scintillation spectral data have also been routinely obtained electronically by playing back the data directly recorded on magnetic tape with an appropriate speed-up factor and analyzing the results with a Kay spectrum analyzer. The electronically obtained spectra also are characterized by an absence of peaks and appear in general to agree with the computed spectra obtained from the digitized records. Previous temporate-latitude observations of star scintillations by Gruber (10) and satellite scintillations by Jespersen and Kamas (11) have indicated the presence of both single and complex peaks in the scintillation spectrum. Gruber's observations, which included both phase and amplitude spectra, did not indicate a preponderance of low-frequency phase variations.

The low end of the spectrum work discussed by Gruber, however, was attenuated below about  $1/60$  c/s. The lowest spectral increment made for the observations reported here is 0.0025 c/s, which corresponds to roughly one cycle in 7 minutes. The duration of the data run for the slow sample rates was usually  $1\frac{1}{2}$ –2 hours. Spectral estimates made at frequencies as low as 0.0025 c/s are considered statistically significant due to the relatively long data record obtained. The bias at the low end of the phase spectrum is evident from an inspection either of the chart record covering a portion of a data run or of the corresponding computed spectrum of the phase and amplitude fluctuations shown in Fig. 6 for a typical period of activity. It was shown by Gruber (10) that a velocity component of the ground diffraction pattern along the direction of the interferometer baseline will result in the emphasis of the higher frequency components in the phase spectrum. Since the converse has been observed, it is of interest to explore possible explanation for this observation. Because the relative emphasis between amplitude and angular variations changes with the irregularity size and distance to the observer, it is conceivable that a thick region, which may have a complex structure varying with height, may be responsible for the observations. Another possible explanation for the enhancement of the low-frequency phase components may be the presence of lens- or wedge-type ionizations which have been reported by Wild and Roberts (12), Lawrence, *et al.* (13), and more recently by Warwick (14), and Liszka (15).

#### COMPARISON OF THE DATA WITH THEORETICAL RESULTS OBTAINED FROM IONIZATION MODELS

Most of the computer-processed records did not show any evidence of a statistically significant cross-correlation between the amplitude and phase variations. There were periods, however, when the cross-correlation was significant, and some representative examples are shown in Fig. 7. cursory inspection of the chart records did not reveal any obvious difference between these anomalous periods and normal periods which evidence zero cross-correlation.

The presence at times of non-independent statistics for the amplitude and angular scintillations suggests that non-random ionizations may be present causing ground-diffraction patterns having an ordered structure. To test this hypothesis a numerical method reported by Gagnon (16) was used to compute the amplitude and phase pattern as received by an interferometer system for various one-dimensional ionization models. A particular model along with the computed phase and amplitude cross-correlation, and autocorrelation functions evaluated for a 68 Mc/s, 220 m interferometer are shown in Fig. 7 together with some of the experimental results.

It is noted that a marked similarity exists between the experimental data and computed results for a ramp ionization model. This model requires an electron density gradient a kilometer wide that results in a refraction angle of 15 minutes on a segment of the incoming wavefront. Using a more complicated model which is comprised of a number of similar ramps going in the positive and negative directions results in a more complex display of the amplitude and phase components without altering significantly the shape or form of the computed cross-correlation function. It has been found that varying the model and/or the height of the wedges results in appreciable changes in the form of the correlation functions. It is noted, however, that the experimental autocorrelation function of the phase appears somewhat extended compared to the best theoretical model fit.

There are times when the phase recording is characterized by prominent excursions having a quasi-saw-tooth appearance with a period varying from 1 to 5 minutes. A reproduction of a series of such events is given in Fig. 8, along with the computer-determined amplitude and phase recordings of a complex model of the form indicated and which were located at a height of 100 km.

The above models giving the best match with the experimental data all have typical refraction angles ranging from 5 to 15 minutes which are maintained over distances of 1–5 km. An angular change of 15 minutes (at 68 Mc/s) over a distance of 5 km requires a change in total electron columnar content of about  $2 \times 10^{14}/\text{m}^2$ . When compared to the minimum observed total columnar electron content of about  $10^{17}/\text{m}^2$  observed at middle latitudes (17), the model values appear to represent a small fraction of the total expected electron columnar content. From analysis of Faraday-rotation records using a satellite source signal, Merrill, *et al.* (18) have reported the presence of mid-latitude large-scale irregularities having horizontal sizes of 50–400 km, an average size of 300 km was reported. Within the reported range in sizes the observations indicate variations in the electron columnar content of 1–2 per cent.

The reader is to be cautioned that for any apparent match between the model and the experimental results, uniqueness has not been established and the similarity obtained serves only to indicate the plausibility of a given model. No feasible approach has been developed to go from the experimental measurements to a model. One requirement for such an approach would seem to be the determination of the phase structure along the ground. In practice complications occur due to the fact that the measured phase comes from a difference measurement from two points along the ground. For a fixed antenna configuration in which the diffraction pattern along the ground has a

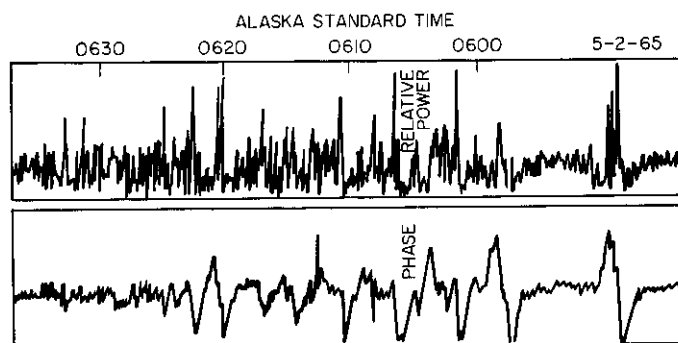
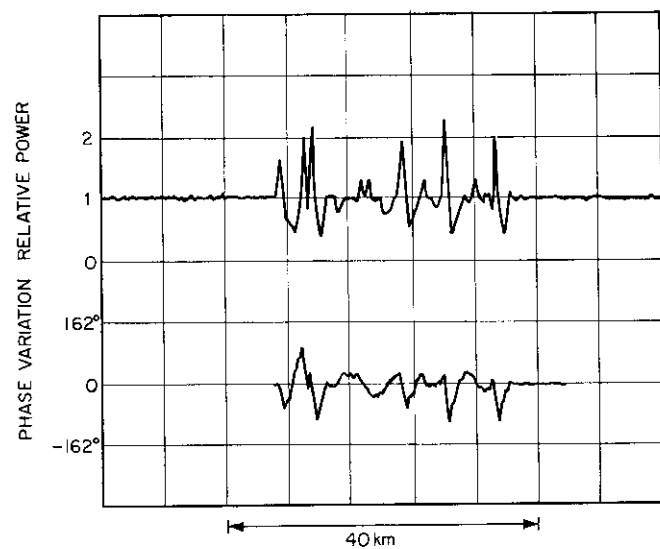
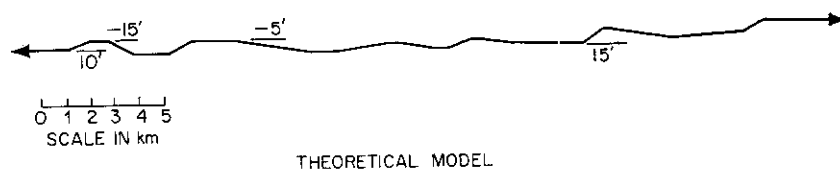


FIG. 8 Experimental data, showing large phase variations which are compared to the theoretical amplitude and phase variations resulting from a model consisting of a series of ionospheric gradients

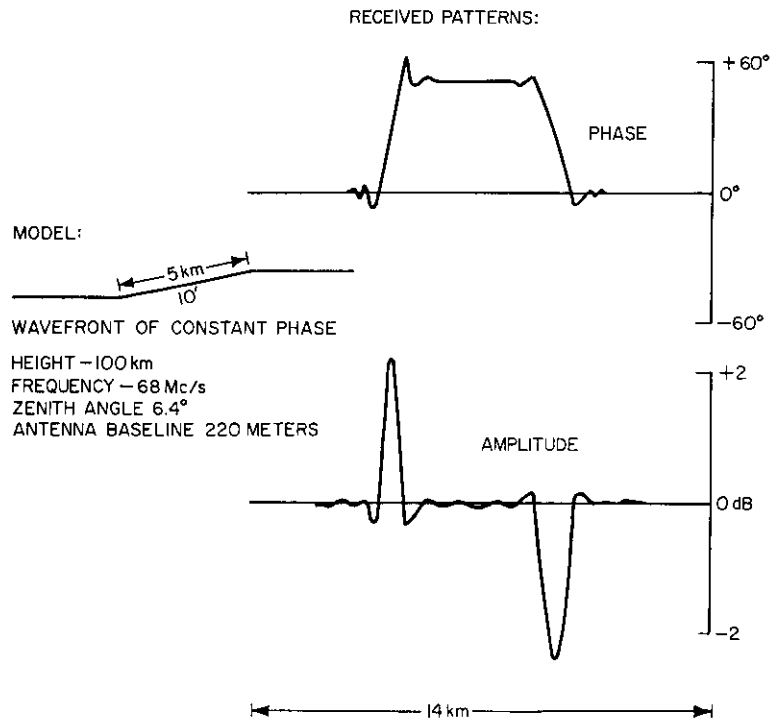


FIG. 9 The computed ground pattern for a 5 km model ramp producing a ten minute refraction angle

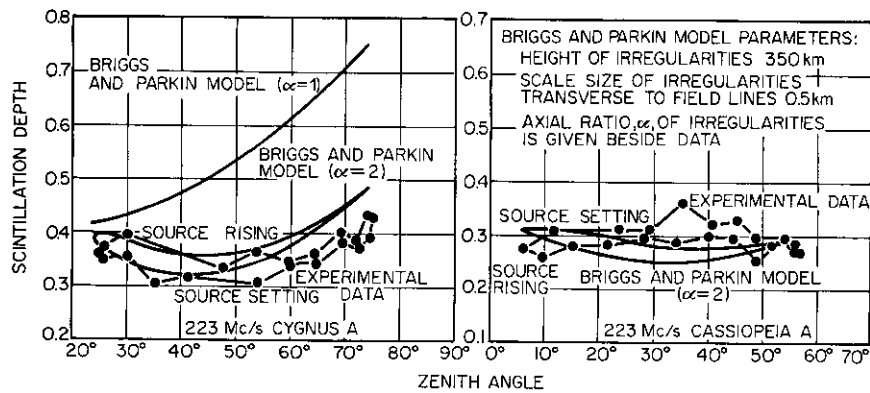


FIG. 10 Comparison between the measured and theoretical zenith angle scintillation dependence for the Cygnus A and Cassiopeia A radio sources at 223 Mc/s. The source rising and setting directions refer to the experimental observations. For the theoretical model the direction of source setting corresponds to the upper portions of the curves

finer structure than the antenna separation, there appears to be no straightforward way to determine the structure of the phase pattern.

As anticipated from the theory, using sufficiently large-scale models, the maximum computed phase deviation is linearly related to the gradient given in the model. The phase and amplitude resulting from a 5 km ramp are shown in Fig. 9. As seen in the figure, the variation of the received amplitude appears to be proportional to the derivative of the phase pattern, which implies that the cross-correlation function of amplitude and phase will be proportional to the first derivative of the phase autocorrelation function. Such a cross-correlation function will have a zero at zero lag and will be anti-symmetric about the zero lag. This form of the cross-correlation of amplitude and phase was found to be characteristic of certain ionization models.

A study has been made of the correlation of the experimental phase and amplitude data for times when a significant cross-correlation was evident. The experimental cross-correlation functions have all been similar to those shown in Fig. 7 which have the form discussed above.

From Fig. 9, it is clear that the presence of certain electron density gradients can result in higher-frequency components in the amplitude variations than in the phase variations, implying a difference in the shape of the amplitude and phase autocorrelation functions. The correlation functions from several model gradients have been studied. The results of this study have indicated that the difference in the shape of phase and amplitude autocorrelation functions becomes pronounced for irregularities of 5 km or larger in size. As the irregularity size is decreased the discrepancy between the autocorrelation functions decreases until, for sizes of around 500 m and less, the autocorrelation functions are similar.

A tentative explanation, therefore, for the previously noted dominance of low-frequency components in the phase spectrum together with the usual negligible cross-correlation between the amplitude and phase variations is that the ground-diffraction pattern results from the superposition of a pattern due to a random screen and that due to ordered ionizations. The cross-correlation is negligible since the dominance of the irregular screen is responsible for most of the observed amplitude variations, yet the presence of the ordered ionization structures results in the observed bias in the low-frequency end of the phase spectrum.

#### ELEVATION ANGLE DEPENDENCE OF AMPLITUDE SCINTILLATION

Using the theory developed by Briggs and Parkin (19), the scintillation depth (this number has been experimentally determined to be directly proportional to the power index or the square root of the amplitude index) was computed as a function of zenith angle for various heights of the scintillation-producing layer and degree of field alignment. Given an irregularity scale size of one km along the field line and  $\frac{1}{2}$  km transverse to the field line (axial ratio of 2) at a height of 350 km, the computed 223 Mc/s zenith angle dependence at the College, Alaska, station for an assumed earth-centered magnetic dipole is given in Fig. 10 for the *Cygnus A* and *Cassiopeia A* radio sources. Included are the 223 Mc/s experimental observations taken at the College station reported by Little, *et al.* (3), during the past sunspot maximum.

The computed curves (being relative in value) were shifted in the vertical

direction to provide the best correspondence with the observations. The non-symmetry in the variation of scintillation depth about transit results from the non-symmetry of the angle between the line of sight and the field line about transit. The effect of having the line of sight nearly parallel to the long dimension of the irregularities near upper culmination results in a relative enhancement of the degree of scintillation. This causes the slight increase in scintillation depth following the time of transit. Using greater axial ratios will result in an enhancement at times when the line of sight is nearly parallel to the direction of the field line. It was found that the match between the model and experimental results was relatively insensitive to scale size and height. The greatest sensitivity to the match was that of the variation of axial ratio.

From Fig. 10 it is seen that the rise and set directions of the experimental *Cygnus A* data are opposite to the theoretical model. Although the theoretical model of  $\frac{1}{2}$  km scale size, with an axial ratio of 2, appears to provide the best fit, it should be pointed out that the experimental data indicate a relative increase in scintillation depth with the *Cygnus A* source over that observed for the *Cassiopeia A* source for the same elevation angle. Also, from the experimental data it is seen for *Cassiopeia A* that there is a trend for the scintillation activity to decrease for an increase in zenith angle.

A possible explanation for the difference in shape of the *Cassiopeia* elevation dependence curve and difference in relative activity may be due to the greater angular size of the *Cassiopeia A* source. It was shown by Briggs (20) that the scintillation depth can be reduced as a result of finite source size. This occurs when the difference between the projected diffraction pattern from opposite edges of the source approaches an appreciable fraction of the scale size of pattern on the ground. For this condition Briggs derived the relation

$$\phi_1(\sec i)^{3/2} \sim L/h\theta \quad (1)$$

where:

- $\theta$  = angular source size =  $1.2 \times 10^{-3}$  radian (*Cassiopeia A*)
- $h$  = height of region
- $L$  = irregularity scale size
- $\phi_1$  = r.m.s. phase variation at normal incidence
- $i$  = zenith angle  $\cong 56.6^\circ$  at lower culmination for *Cassiopeia A* at College, Alaska.

Given the values used by Briggs (20) of  $L = 4$  km (four times the scale size to obtain the estimated distance between scintillation maxima),  $h = 350$  km, it is found from Eq. 1 that the r.m.s. phase deviation must be roughly 4 radians for the scintillation depth to be reduced due to the finite source size of *Cassiopeia A*. Since the comparisons given in Fig. 10 are made for data taken in the auroral zone at sunspot maximum, reported by Little *et al.* (3), a 4-radian r.m.s. phase variation at 223 Mc/s does not seem unrealistic.

#### CONCLUSIONS

Comparisons of amplitude and angular scintillation activities with magnetic activity and magnetic absorption has indicated scintillation activity is controlled to an important extent by geophysical factors. The association between scintillation activity and magnetic activity appears greater than the

association between scintillation activity and ionospheric absorption. In general, it appears that angular rather than amplitude scintillation is more closely associated with absorption and magnetic activity.

There has been observed a relative change in the ratio of amplitude to angular scintillations as a function of hour angle. This is interpreted as resulting from a geographical dependence of irregularity size and height distribution and/or the presence of ionization gradients which also have a geographical dependence.

Amplitude and phase power spectral results have indicated that the low frequencies are more emphasized in the phase spectrum. It has been shown that the presence of ionization gradients can be responsible for this observation.

#### APPENDIX

**Phase compensator** – The principle of operation of the phase compensator is outlined in Fig. A. As shown in the figure, a pulse train is developed each second of sidereal time which is proportional to the change in  $\sin(HA + \alpha)$  over a sidereal second interval. This is accomplished by storing on punched paper tape a  $90^\circ$  sine function made up of binary numbers which represent the change in  $\sin(X)$ , with the argument  $X$  varying in angular increments of 15 seconds. The pulses thus developed are subsequently divided and are used to drive a stepping-motor. This in turn drives a resolver which varies the phase of the 1 kc/s reference signal. The total amplitude of the phase correction is determined by  $K$  which is proportional to the total number of pulses desired to be passed over a 6-hour interval of sidereal time. It is necessary to divide the total number of available pulses by a number (a function of survey data, source declination, and operating wavelength) to obtain the phase correction required to compensate for the expected phase variation due to the rotation of the earth. This is accomplished by using a coarse binary divider, which divides the input pulses by the factor of  $(\frac{1}{2})^m$  followed by a fine divider. The fine divider consists of an inhibit circuit operating in conjunction with a chain of fourteen stages of a binary counter. Depending upon the circuit connection between the respective binary stage given by  $j$  and the inhibit circuit, the fine divider passes the fraction of pulses  $F$  given by:

$$F = \sum_{j=1}^{j=14} \frac{\sigma_j}{2^j}, \text{ with } \sigma_j = 0 \text{ or } 1$$

Thus, the total division given by  $F(\frac{1}{2})^m$  is set up by appropriate switches so that the total phase correction is nearly equal to that required for phase compensation. It can be shown that the error due to digitization is given by half times the number of counts passed by the fine divider. In the system described, this error for the source *Cassiopeia A* corresponds to approximately one part of 19000.

In practice the start time of the tape reader and the necessary switch settings of the phase compensator is determined by computer, and in routine operation a check of the position of the tape in the tape reader and the position of the resolver at a given instant will indicate proper operation of the

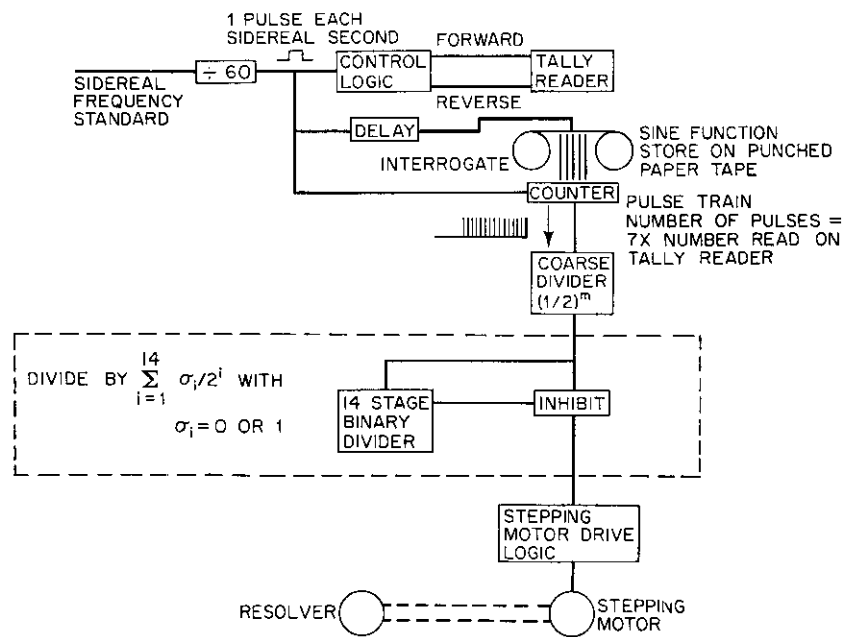


FIG. A Block diagrams of phase compensator



phase-compensation equipment. The equipment described has appropriate built-in logic which reverses the direction of the stepping-motor at one end of the sine reader tape. The tape transport is automatically reversed each end of the tape. In this manner operation of the compensator is continuous without the need of an operator. For a more detailed discussion relating to the phase compensator the reader is referred to an earlier report on the subject (21).

# REFERENCES

1. RYLE, M., "A New Radio Interferometer and its Application to the Observation of Weak Radio Stars". Proc. Roy. Soc. Lon. A211, 351-75, 1952.
2. BROWN, HANBURY, R., PALMER, H. P., and THOMPSON, A. R., "A Rotating-Lobe Interferometer and its Application to Radio Astronomy". Phil. Mag. Ser. 7 46, 379, 857-66, 1955.
3. LITTLE, C. G., REID, G. C., STILTNER, E., and MERRITT, R. P., "An Experimental Investigation of the Scintillation of Radio Stars Observed at Frequencies of 223 and 456 Mc/s from a Location Close to the Auroral Zone". J. Geophys. Res. 67, 5, 1763-84, 1962.
4. ADGIE, R. L., "A Phase-Sweep System for R.R.E. Radio Interferometer". R.R.E. Journal 50, 23-45, 1963.
5. BASLER, R. P., and DEWITT, R. N., "The Heights of Ionospheric Irregularities in the Auroral Zone". J. Geophys. Res. 67, 2, 581-93, 1962.
6. HOOK, J. L., and OWREN, L., "The Vertical Distribution of E-Region Irregularities from Scintillations of Satellite Radio Signals". J. Geophys. Res. 67, 13, 5853-6, 1962.
7. LISZKA, LUDWICK, "A Study of Ionospheric Irregularities in the Auroral Zone Using Satellite Transmissions at 54 Mc/s". Space Research IV, Proc. of the 4th Int. Space Sci. Symp., Warsaw, June 3-12, 1963, 399-406. North Holland, Amsterdam, 1964.
8. RYAN, W. D., "Radio Star Scintillation Near the Auroral Zone". Can. J. Phys. 42, 458-64, 1964.
9. BLACKMAN, R. B., and TUKEY, J. W., "The Measurement of Power Spectra". Dover Pub. Inc., 1959.
10. GRUBER, S., "Statistical Analysis of Radio Star Scintillation". J. Atmos. Terr. Phys. 20, 59-71, 1961.
11. JESPERSEN, J. L., and KAMAS, G., "Satellite Scintillations at Boulder, Colorado". Nat. Bur. Stand Rep. 7915, 1963.
12. WILD, J. P., and ROBERTS, J. A., "The Spectrum of Radio Star Scintillations and the Nature of Irregularities in the Ionosphere". J. Atmos. Terr. Phys. 8, 55-75, 1956.
13. LAWRENCE, R. S., JESPERSEN, J. L., and LAMB, R. C., "Amplitude and Angular Scintillations of the Radio Source *Cygnus A* Observed at Boulder, Colorado". J. Res. Nat. Bur. Stand 65D, 4, 333-49, 1961.
14. WARWICK, J. W., "Radio Star Scintillations from Ionospheric Waves". Radio Sci. NBS/USNC-URSI 68D, 2, 179-88, 1964.

15. LISZKA, L., "Investigations of Properties of the Auroral Zone Ionosphere by Means of a Radio Astronomical Swept-Frequency Interferometer, Covering the Frequency Band 35-65 Mc/s". Rep. 4 contribution from Kiruna Geophys. Obs., 1962.
16. GAGNON, R. J., "An Approximate Method for Computing Diffraction Patterns Caused by Ionospheric Irregularities". Radio Sci. NBS/USNC-URSI 68D, 6, 737-42, 1964.
17. LAWRENCE, R. S., POSAKANY, D. J., GARRIOTT, O. K., and HALL, S. G., "The Total Electron Content of the Ionosphere at Middle Latitudes Near the Peak of the Solar Cycle". J. Geophys. Res. 67, 7, 1889-98, 1963.
18. MERRILL, R. G., LAWRENCE, R. S., and ROPER, N. J., "Synoptic Variations and Vertical Profiles of Large-Scale Ionospheric Irregularities". J. Geophys. Res. 68, 19, 5453-9, 1963.
19. BRIGGS, B. H., and PARKIN, I. A., "On the Variation of Radio Star and Satellite Scintillations with Zenith Angle". J. Atmos. Terr. Phys. 25, 334-65, 1963.
20. BRIGGS, B. H., "The Correlation of Radio Star Scintillations with Geomagnetic Disturbances". Geophys. J. 5, 306-17, 1961.
21. LANSINGER, J. M., and GAGNON, R. J., "Boeing Lobe Sweep Interferometer". Boeing document D1-82-0122, 1961.

## ACKNOWLEDGEMENTS

The results given in this paper are based on data taken at a field site operated by the Geophysical Institute of the University of Alaska and are a result of a joint program between the Geo-Astrophysics Laboratory of the Boeing Scientific Research Laboratories and the Geophysical Institute made possible by PROFESSOR L. OWREN. Special thanks go to the following staff members of the Geophysical Institute: E. FREMOUW, for technical help; PROFESSOR V. HESSLER, for the generous loan of the magnetic pick-up coil; R. DOMKE, for the operation and maintenance of the equipment; and Dr R. PARTHASARATHY, for making available reduced 30 Mc/s riometer data.

Of the members of Boeing Scientific Research Laboratories, thanks go to W. COOK for considerable computer programming relating to spectral analysis, T. DEATON and J. HAYAKAWA for equipment development and construction, and to Dr J. C. NOYES and R. SCHWITTERS for helpful suggestions and technical assistance.

## CHAPTER 3-13

EFFECTS ON NON-INVERSE-FREQUENCY-SQUARED  
ABSORPTION EVENTS

S. M. BENNETT and G. F. ROURKE

Research and Advanced Development Division AVCO Corporation,  
Wilmington, U.S.A.

## SUMMARY

Attenuation computations utilizing theoretical D-region electron density profiles during solar proton events (PCA) has been extended through the VHF band. The generalized Sen-Wyller (12) magnetoionic absorption equation for the quasi-longitudinal case is employed throughout, and the collision frequency is taken to correspond to summer in the polar cap region. The effect of steady-state recombination coefficients due to Adams and Masley (7), Webber (3), (20), Weir, and Bailey (19) on the attenuation is evaluated by choosing particular theoretical production rates (various proton-to-alpha particle ratios are considered). Non-inverse-squared frequency dependence exists throughout the frequency range considered (3 to 300 Mc/s) and the significance of the departure depends on the steady-state coefficient and spectral form chosen. The trend found for the more recent determinations of recombination coefficients is to yield greater deviation from inverse square.

## INTRODUCTION

The attenuation effects resulting from bombardment of the polar D-region by high-energy protons generated by solar flares is often discussed in the context of the riometer, which records cosmic radio noise received by an antenna of finite beamwidth. Until the measurements reported by Parthasarathy *et al.* (1) this technique was restricted to a single frequency at each observatory (normally a nominal 30 Mc/s) and the frequency dependence of the attenuation was either unspecified or presumed to be the inverse square relation following from the quasi-longitudinal approximation to the Appleton-Hartree formula. Particular emphasis has been placed on interpretation of the riometer data in a manner which would yield D-region reaction rates. Both the day-night ratio and twilight variations have been studied in this respect (see, for example, Reid (2), Webber (3), Hultquist (4)). Computations utilizing both theoretical and experimental spectra in conjunction with selected values of D-region reaction rates have been reported; often these measurements have been compared with attenuation measured by the riometer. The latitudinal dependence of riometer attenuation and balloon-borne counter and emulsion results have been discussed by Freier and Webber (5) who deduced that a one-parameter system of the form:

$$\mathcal{J}(\geq P) = \mathcal{J}_0 \exp [-P/P_0] \quad (1)$$

best represents the spectra of solar-flare particles where  $\mathcal{J}_0$  is the flux of particles above zero rigidity and  $P_0$  is a characteristic  $e$ -folding rigidity at a particular time (3). It was also found that the alpha and proton components have similar rigidity spectra (5), (6) but the proton-to-alpha ratio ( $P/\alpha$ ) for each individual flare is characteristic yet highly variable, see Table 1.

Multifrequency riometer measurements obtained at College, Alaska, during the sequence of solar proton events in July 1961 indicated that the inverse square frequency dependence was not valid within the range of frequencies measured (10 to 50 Mc/s). The reduced, pencil-beam attenuation as a function of frequency plus local longitudinal gyrofrequency is shown in Fig. 1. These data have been inverted to yield a D-region electron density profile by least squares analysis of a cubic function by Parathasarathy *et al.* (1). While providing only a gross picture of the D-region electron density profile during a solar proton event, the electron-density profiles have led to a new determination of the daytime steady-state coefficient by Adams and Masley (7). We shall present some computations utilizing steady-state coefficients due to Webber, Weir, and Bailey (19), based on an evaluation of experimental and theoretical reaction rates, but the bulk of this analysis rests on the empirical coefficient of Adams and Masley. We should, therefore, review briefly the derivation of this empirical relationship.

The time derivative of electron density in the daytime D-region, considering the relevant reactions, is (e.g. Reid):

$$\frac{dN}{dt} = \frac{Q}{(\lambda + 1)} - (\alpha_d + \lambda\alpha_i)N^2 \quad (2)$$

where:

$$\lambda = \frac{\eta f_0^2 n^2}{\kappa f_0 n + \rho s} \quad (3)$$

and:

- $Q$  = rate of production of electron-ion pairs by collisional ionization
- $f_0$  = fraction of the neutral molecules which are  $O_2$
- $n$  = number density of neutral molecules
- $S$  = solar photon flux which contributes to photodetachment of electrons from  $O_2$
- $\rho$  = rate of photodetachment of electrons from  $O_2$
- $\eta$  = 3-body non-radiative attachment coefficient
- $\alpha_i$  = ion-ion neutralization coefficient
- $\alpha_d$  = dissociative recombination coefficient

and

- $k$  = collisional detachment coefficient

The relationship between the production rate  $Q$  and the steady-state electron density  $N$  is given from Eq. 2 as:

$$Q(z)/N^2(z) = (\lambda + 1) (\alpha_d + \lambda\alpha_i) \equiv \psi(z) \quad (4)$$

where  $\psi$  is the steady-state coefficient and is a function of altitude ( $z$ ) in the D-region. Provided that both  $Q(z)$  and  $N(z)$  are known for a particular geographical location and time, the steady-state coefficient may be determined empirically. Adams and Masley utilized the electron densities deduced by Parthasarathy *et al.* (1) from multifrequency riometer measurements of the July 1961 events in conjunction with particle data due to Pieper *et al.* (8), Hofmann and Winckler (9), and Keppler *et al.* (10); a proton-to-alpha ratio of 6 was used throughout by Freier (11).

Some confusion in terminology exists in the literature. Adams and Masley (7) define a steady-state coefficient  $\psi$  from Eq. 4 as the proportionality between the production rate and the square of the electron density in a unit volume and also define an effective recombination coefficient  $\alpha_{eff} = (\alpha_a + \lambda\alpha_i)$  such that:

$$\psi = (1 + \lambda) \alpha_{eff} = (1 + \lambda) (\alpha_a + \lambda\alpha_i)$$

but Webber (3), for example, alludes to the simple recombination formalism resulting in  $Q = \alpha_{eff} N^2$

$$\alpha_{eff} = (\lambda + 1) (\alpha_a + \lambda\alpha_i)$$

We have chosen to utilize the former definition throughout this discussion.

The production rate was deduced by summation of the specific ionization production rates over the energies of interest and  $\psi(z)$  deduced from Eq. 4. This function is compared with previous results based on evaluation of Eqs. 3 and 4 with reaction rates selected and justified by the various workers shown in Fig. 2. The empirical result differs substantially from previous steady-state coefficients and, as we shall observe, leads to greater deviation from inverse square behavior. Of course, this result is not unexpected, since the College riometer data, Fig. 1, exhibit substantial deviation from inverse square.

#### ATTENUATION

The computation of attenuation resulting from deduced electron density profiles during model PCA events is made in one kilometer steps. The attenuation coefficient is computed from the generalized magnetoionic formula of Sen and Wyller (12), in the quasi-longitudinal approximation

$$n\kappa = \frac{5}{4} \frac{\omega_0^2}{c\nu_m} C_{5/2} \left( \frac{\omega \pm \omega_L}{\nu_m} \right) \quad (5)$$

where:

- $\omega_0$  = plasma frequency
- $c$  = velocity of light in vacuo
- $\omega$  = wave angular frequency
- $\omega_L$  = longitudinal component of the gyrofrequency
- $\nu_m$  = electron-neutral collision frequency
- $n$  = refractive index which, in the D-region, is essentially unity

and  $C_{5/2}(x)$  is a tabulated semiconductor integral, see Dingle *et al.* (13), or Hara (14).

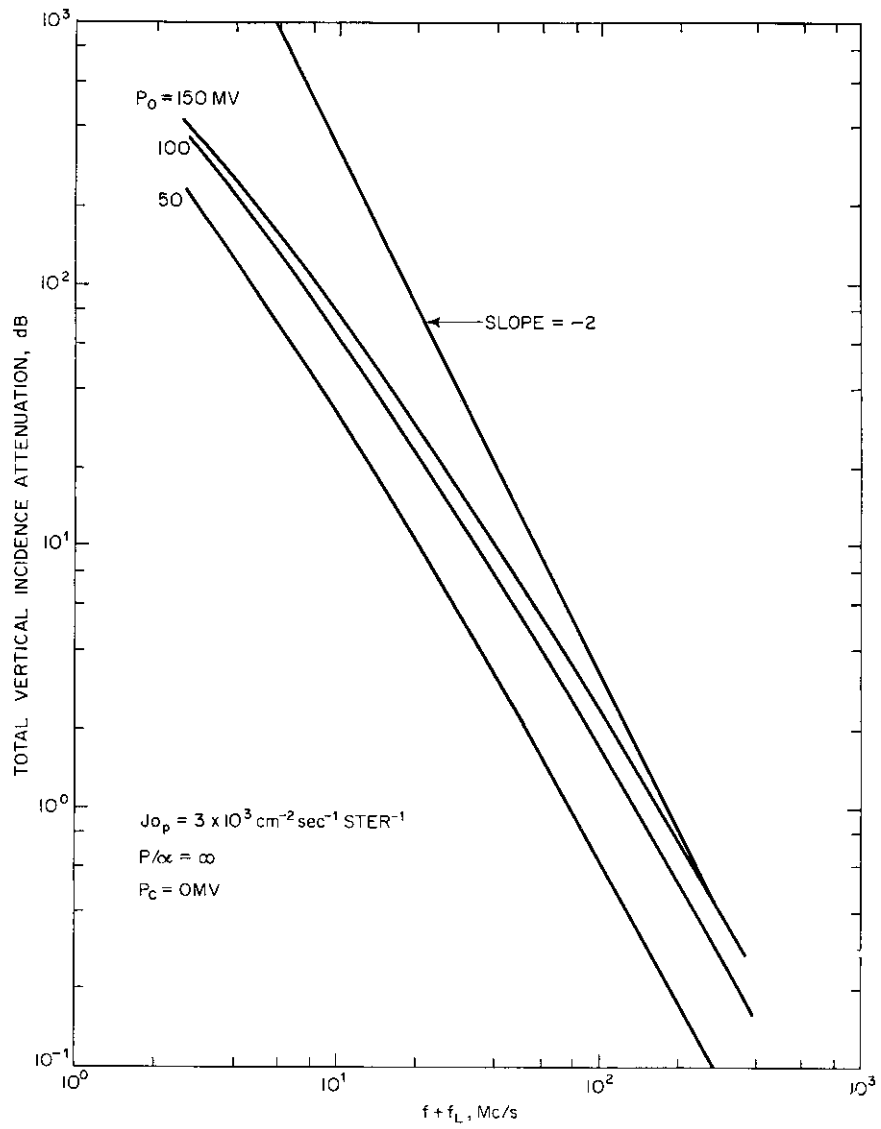


FIG. 3 Total vertical incidence attenuation versus frequency for purely proton events of various characteristic rigidities ( $P_0$ ) but constant flux at zero rigidity  $J_{0p} = 3 \times 10 \text{ cm}^{-2} \text{ sec}^{-1} \text{ ster}^{-1}$ . The geomagnetic cut-off is 0 Mv, corresponding to a geomagnetic latitude of  $90^\circ$  (65-11510)

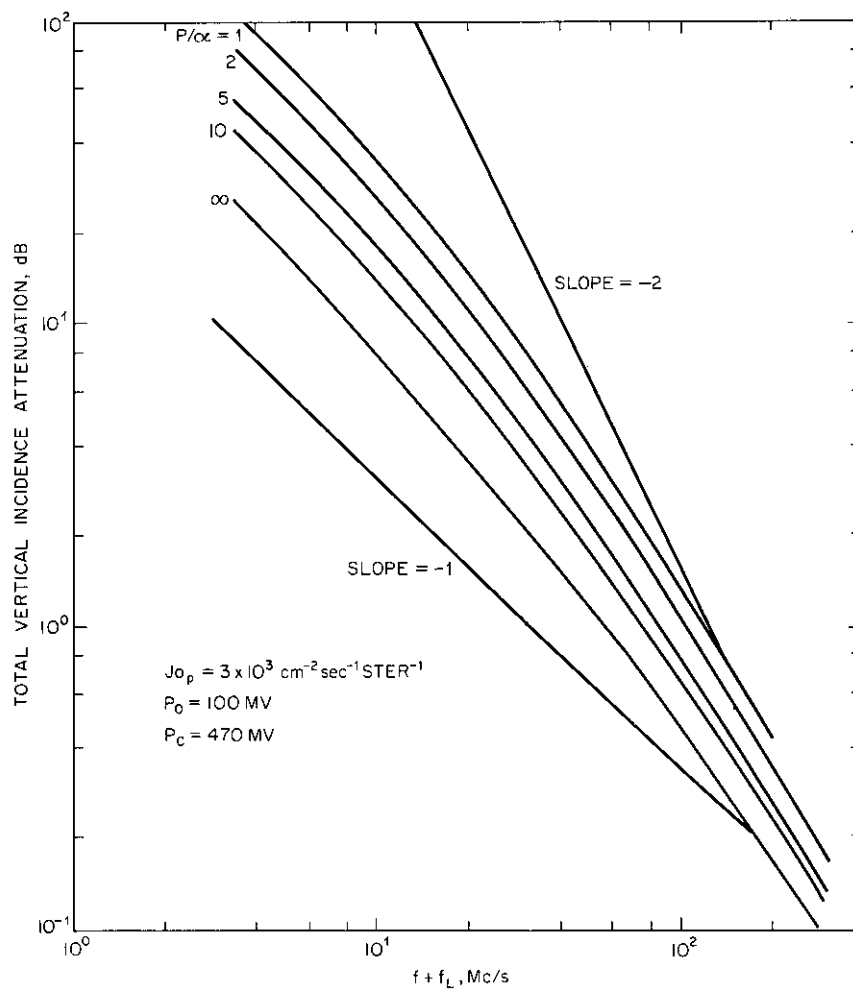


FIG. 4 Total vertical incidence attenuation versus frequency for various proton-to-alpha ( $P/\alpha$ ) ratios at constant characteristic rigidity ( $P_p$ ) and proton flux at zero rigidity,  $J_{0p} = 3 \times 10^3 \text{ cm}^{-2} \text{ sec}^{-1} \text{ ster}^{-1}$ . The geomagnetic cut-off is 470 Mv, corresponding to a geomagnetic latitude of  $65^\circ$  (65-11509)

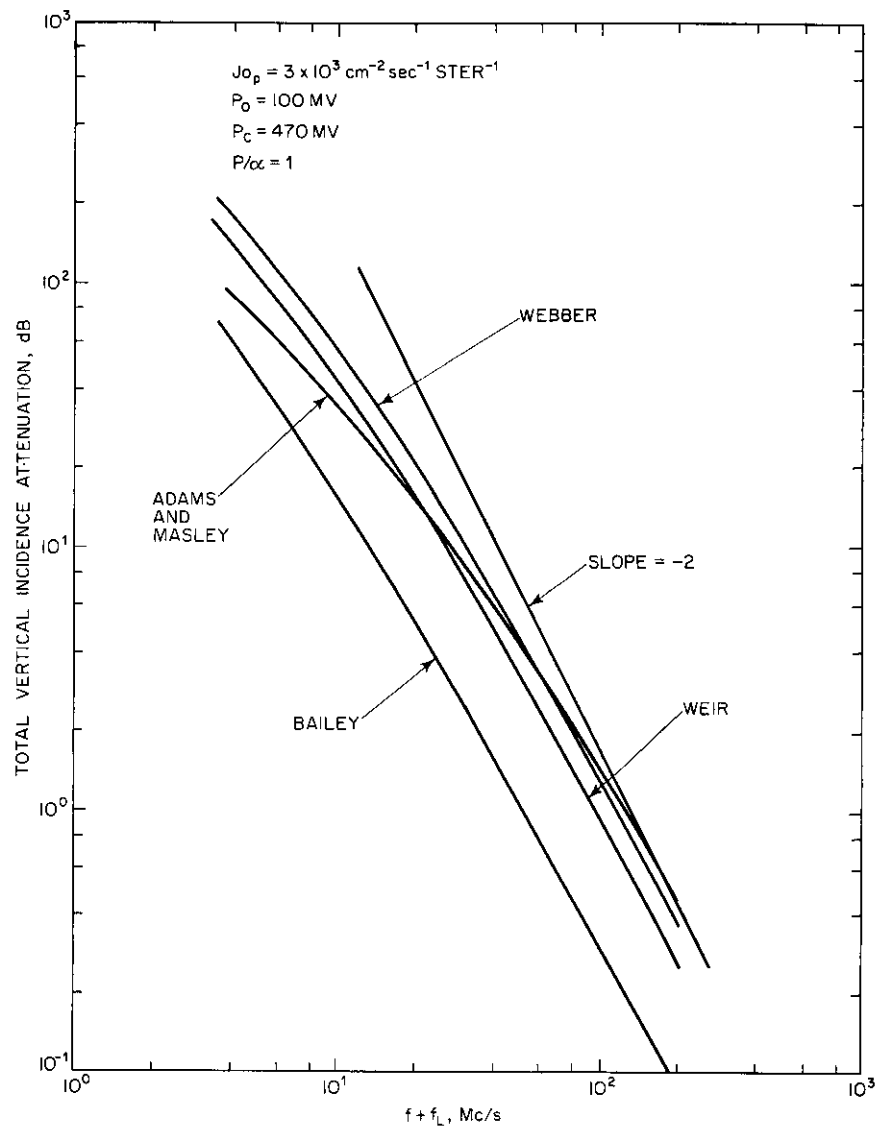


FIG. 5 Comparison of total vertical incidence attenuation versus frequency characteristics resulting from the adoption of alternate steady-state coefficients (65-11508)



The attenuation at a given frequency is:

$$A(f, z) = 2 \times 10^6 \cdot (\log_{10} e) \cdot \kappa(f, z), \text{ db}/\kappa m \quad (6)$$

and the total D-region attenuation is the summation of Eq. 6 over the altitudes of significant attenuation. An electron-neutral collision frequency was chosen to correspond to daylight conditions during local summer by Nordberg (15).

#### MODEL PCA SPECTRA

To provide an adequate survey of solar proton and alpha effects, we have chosen a series of spectra defined by Eq. 1 and summarized in Table 2. The steady-state electron density profiles are computed from Eq. 4 and the integrated D-region attenuation calculated for a number of frequencies throughout the HF and VHF bands. The resulting ordinary-mode attenuation values are presented versus  $(f + f_L)$  in Fig. 3 and 4 to provide results directly comparable to the inverse-square relationship which results from the quasi-longitudinal Appleton-Hartree equation when the wave frequency is considerably greater than the local collision frequency throughout the region of significant D-region attenuation. A line of slope  $-2$  is included in the figures as reference. For a full spectrum (no geomagnetic cutoff effect, Fig. 3), deviation from inverse-square behavior is apparent for the hard spectra throughout the frequency range investigated, but the soft (50 Mv) spectrum exhibits noticeable deviation only within the HF band. When the geomagnetic cutoff effectively hardens the spectrum, the deviation from the inverse-square relationship becomes pronounced, Fig. 4, especially when the event is purely proton in nature. A power law representation of the frequency dependence of the absorption is not possible except over a limited frequency range. Within the frequency range 10 to 100 Mc/s the  $P/\alpha = \infty$  event may be approximated by  $f^{-1.6}$ . All of the remaining events affected by geomagnetic cutoff have an alpha contribution which effectively softens the spectrum Adams and Masley (16), and results in a moderation of the deviation from the inverse-square behavior.

#### COMPARISON OF VARIOUS STEADY COEFFICIENTS

It is of some interest to compare qualitatively several of the steady-state coefficients which have been extensively utilized in previous solar-flare particle-attenuation studies and which were deduced from Eq. 3 and 4 by consideration of the numerical values of the relevant reaction rate coefficients. From Fig. 2 the empirical relation deduced by Adams and Masley (7) is seen to differ fundamentally from previous results, leading to an electron-density profile skewed towards lower altitudes for each production rate. Since such a circumstance favors the violation of conditions necessary for inverse-square behavior, the steady-state coefficient employed in the foregoing sections represents the worst case.

We compare the attenuation resulting from a spectrum  $J_0 = 3 \times 10^3$   $P_0 = 100$  Mv,  $P_e = 470$  Mv,  $P/\alpha = 1$ , for the steady-state coefficients displayed in Fig. 2 and the results are given in Fig. 5. The computation utilizing Bailey's coefficient deviates least from inverse-square behavior, while that due to Adams and Masley yields the greatest discrepancy. Webber and Weir

(17, 18) yield almost identical results lying between the two extremes. It should be noted, however, that particle spectra utilized are lacking in the low energies and thus the characteristics of the lower D-region are of greater significance than in the inner polar cap where the peak electron density occurs at a somewhat greater altitude.

#### CONCLUSIONS

Deviations from the elementary inverse-square frequency dependence are found at all frequencies within the HF and VHF frequency bands for solar proton events. The empirical steady-state coefficients due to Adams and Masley result in more substantial discrepancies than those which are deduced by evaluating Eq. 3 and 4, by considering the best available reaction-rate coefficients. In all instances, a pure solar proton spectrum results in greater functional deviation from inverse-square than an event which contains an admixture of alpha-particles, since these alphas effectively result in a softening of the bombardment spectrum due to their smaller penetrating power. Although it appears that the exponential representation of the flare-particle spectrum is superior to a power law, the existence of a power-law spectrum would result in a substantial enhancement of low-energy particles. In the inner polar cap, where geomagnetic cutoff effects do not exclude the low-energy portion of the spectrum, the altitude of peak electron density and attenuation will be increased, but with a corresponding reduction in the deviation from inverse-square behavior.

#### DISCUSSION

K. RAWER – In the equations shown at the beginning it appeared to me that the longitudinal approximations of the Appleton–Lassen dispersion formula was used. May I inquire whether this equation or that of Sen and Wyller has been used for the numerical work?

S. M. BENNETT – The quasi-longitudinal approximation to the Sen-Wyller generalized magnetoinic formula for attenuation was used throughout. We did not use the Appleton formula at any altitude. For completeness it should be stated that the semiconductor integral  $C_{5/2}(x)$  is approximated by

$$C_{5/2}(x) = x^{-2} \text{ for } x \geq 20,$$

which is equivalent to taking the quasi-longitudinal Appleton formula to be valid at all greater altitudes.

#### REFERENCES

1. PARTHASARATHY, R., LERFALD, G. M., and LITTLE, C. G., "Derivation of Electron Density Profiles in the Lower Ionosphere Using Radio Absorption Measurements at Multiple Frequencies". J. Geophys. Res. 68, 3581, 1963.
2. REID, G. C., "A Study of the Enhanced Ionization Produced by Solar Protons During a Polar Cap Absorption Event". J. Geophys. Res. 66, 4071, 1961.

TABLE 1  
PROTON-TO-ALPHA PARTICLE RATIO FOR VARIOUS EVENTS  
AFTER FREIER AND WEBBER (20)

Event	$J_p/J_\alpha$
23 March 1958	$1 \pm 0.5$
10 May 1959	$1 \pm 0.5$
10 July	$1.4 \pm 0.3, 5.0 \pm 1.0$
14 July	$1.0 \pm 0.5$
16 July	$1.0 \pm 0.5$
4 May 1960	$\geq 50$
3 September	40, 30
12 November	$1 \pm 0.5$
15 November	$1 \pm 0.5, 2 \pm 1$
18 July 1961	$6 \pm 1$

TABLE 2  
IDEALIZED EVENT CHARACTERISTICS

$J_p$	$P_0(\text{Mv})$	$P/a$	Reference	Geomagnetic cut-off latitude
$3 \times 10^3$	50	$\infty$	W	$90^\circ$
$3 \times 10^3$	100	$\infty$	W	$90^\circ$
$3 \times 10^3$	150	$\infty$	W	$90^\circ$
$3 \times 10^3$	100	$\infty$	WB	$65^\circ$
$3 \times 10^3$	100	1	WB	$65^\circ$
$3 \times 10^3$	100	2	WB	$65^\circ$
$3 \times 10^3$	100	5	WB	$65^\circ$
$3 \times 10^3$	100	10	WB	$65^\circ$

W = Webber (3); WB = Weir and Brown (18).

3. WEBBER, W., "The Production of Free Electron in the Ionospheric D Layer by Solar and Galactic Cosmic Rays and the Resultant Absorption of Radio Waves". J. Geophys. Res. 67, 5091, 1962.
4. HULTQUIST, B., "The Height Distribution of the Ratio of Negative Ion and Electron Densities in the Lowest Ionosphere". Sci. Rep. 2, Kiruna Geophysical Observatory, May 6, 1962.
5. FREIER, P. S., and WEBBER, W. R., "Exponential Rigidity Spectrums for Solar Flare Cosmic Rays". J. Geophys. Res. 68, 1605, 1963.
6. BISWAS, S., FICHEL, C. E., and GUSS, D. E., "Study of the Hydrogen, Helium and heavy nuclei in the November 12, 1960, solar cosmic ray event". Phys. Rev. 128, 2756, 1962.
7. ADAMS, G. W., and MASLEY, A. J., "Production Rates and Electron Densities in the Lower Ionosphere Due to Solar Cosmic Rays". J. Atmos. Terr. Phys. 27, 289, 1965.
8. PIEPER, G. F., ZMUDA, A. J., BOSTROM, C. O., and O'BRIEN, B. J., "Solar Protons and Magnetic Storms in July 1961". J. Geophys. Res. 67, 4959, 1962.
9. HOFMANN, D. J., and WINCKLER, J. R., "Simultaneous Balloon Observations at Ft. Churchill and Minneapolis during the Solar Cosmic Ray Events of July 1961". J. Geophys. Res. 68, 2067, 1963.
10. KEPPLER, E., EHMERT, A., and PROTZER, G., "Solar Proton Injections During the Period from July 12 to July 28, 1961, at Balloon Altitudes in the Auroral Zone". Space Research III, ed. W. Priester, J. Wiley, New York, 1963.
11. FREIER, P. S., "Emulsion Measurements of Solar Alpha Particles and Protons". J. Geophys. Res. 68, 1805, 1963.
12. SEN, H. K., and WYLLER, A. A., "On the Generalization of the Appleton-Hartree Magnetoionic Formulas". J. Geophys. Res. 65, 3931, 1960.
13. DINGLE, R. B., ARNDT, D., and ROY, S. K., "The Integrals  $C_p(x)$  and  $D_p(x)$  and their Tabulation". Appl. Sci. Rev. 6B, 155, 1957.
14. HARA, E. H., "Approximations to the Semiconductor Integrals  $C_p(x)$  and  $D_p(x)$  for Use with the Generalized Appleton-Hartree Magnetoionic Formulas". J. Geophys. Res. 68, 4388, 1963.
15. NORDBERG, W., "Density and Pressure Data in COSPAR International Reference Atmosphere". North-Holland, Amsterdam, 54, 1961.
16. ADAMS, G. W., and MASLEY, A. J., "Theoretical Study of Cosmic Noise Absorption Due to Solar Cosmic Radiation". Douglas Paper 3112, 1956.
17. WEIR, R. A., "A Study of Ionospheric Absorption Produced by Solar Cosmic Rays". University of Calif. at Berkeley, undated.
18. WEIR, R. A., and BROWN, R. R., "On the Contribution of Solar-Flare Alpha Particles to Polar-Cap Absorption Events". J. Geophys. Res. 69, 2193, 1964.
19. BAILEY, D. K., "Abnormal Ionization in the Lower Ionosphere Associated with Cosmic-Ray Flux Enhancements". Proc. IRE 47, 225, 1959.
20. WEBBER, W. R., and FREIER, P. S., "Electron Density Profiles in the Lower Ionosphere Due to Solar Cosmic Rays". J. Geophys. Res. 68, 6223, 1963.

CP-3

PART 4

RE-ENTRY PLASMA-SHEATH EFFECTS

---



## CHAPTER 4-1

# IONOSPHERIC EFFECTS OF SOLAR X-RAY ENHANCEMENTS

TUDOR B. JONES

Univ. of Leicester, England

### SUMMARY

Measurements of the solar X-ray spectrum during a number of solar flares have been used to evaluate the changes produced by these events in the D-region electron density profile. By combining these profiles with estimates of the total electron content changes, deduced from observations of sudden frequency deviations (SFD), some indication can be obtained of the ionization changes above the D-region. The limitations of the X-ray data at present available are described. Some of the effects produced by these changes in ionization density on radio waves propagated through the ionosphere are discussed.

### INTRODUCTION

The marked association between sudden ionospheric disturbances and solar flares has been known for some time, but until recently it was thought that these disturbances probably resulted from an enhancement of the solar Lyman  $\alpha$  radiation and that the production of additional ionization was confined to the D-region of the ionosphere. Lindsay (1) has shown that little change occurs in the Lyman  $\alpha$  flux during flare conditions, but marked increases have been reported in the solar X-ray flux (2), (3), (4). Ionization by cosmic ray primaries is thought to occur in the lower D-region, but only small variations have been observed in cosmic-ray intensities even during large flares. It appears therefore, that the additional ionization produced in the ionosphere during solar flares is due almost entirely to the increase in X-ray flux.

The purpose of this paper is to examine some recent measurements of flare-enhanced spectra and to show how the changes in the D-region electron-density profile may be calculated from these results. Measurements of the sudden frequency deviation (SFD) of an HF radio wave are available during one of the flares considered and these data have been used to estimate the total electron content change below the reflection level of the wave. Some of the effects produced by the flare-enhanced ionization on a 100 Mc/s radio wave propagated through the ionosphere have been evaluated.

### CALCULATION OF THE CHANGES IN THE ELECTRON DENSITY- HEIGHT PROFILE

The rate of ion production  $q$  at any height  $h$  by X-rays of wavelength  $\lambda$

can be expressed as

$$q = n_j I_j \exp \tau \quad (1)$$

where  $n_j$  is the number of molecules of the species  $j$ ,  $\tau$  is the optical depth and  $I$  is the ionization rate coefficient given by

(number of photons) $_{\lambda}$  (absorption cross section) $_{\lambda}$  (efficiency of ionization for X-rays of wavelength  $\lambda$ ).

It can be seen from the above that in order to compute  $I$  and hence  $q$  at all heights of interest a detailed knowledge of the spectral-energy distribution is required. In addition, the height variation of the atmospheric constituents must be known.

The rate of ion production is related to the rate of change of ionization density  $n_e$  and may be expressed as

$$\frac{dn_e}{dt} = \sum \frac{q_j}{1 + \lambda} - \alpha n_e^2 \quad (2)$$

where  $\alpha$  is the effective recombination coefficient and  $\lambda$  the ratio of negative ions to electrons. The effective recombination coefficient can be written as

$$\alpha = \alpha_D + \lambda \alpha_i \quad (3)$$

where  $\alpha_D$  is a constant related to the recombination coefficient of positive ions with electrons and  $\alpha_i$  is the recombination coefficient of positive ions with negative ions.

The rate of change of ionization can be expressed in terms of these two recombination coefficients as

$$\frac{dn_e}{dt} = \frac{\sum q_i}{1 + \lambda} - (\alpha_D + \lambda \alpha_i) n_e^2 \quad (4)$$

If it is assumed that at flare maximum the rate of change of ionization density is small, then  $\frac{dn_e}{dt} = 0$  and  $n_e$  can be determined at all heights from Eq. 4.

A computer has been programmed to evaluate  $n_e$  at 5 km intervals in the height range 50–100 km for any X-ray energy distribution. It is assumed in the calculation that oxygen and nitrogen are the major atmospheric constituents ionized by the X-rays and similar concentrations have been taken here to those assumed by Nicolet and Aiken (5) in the investigation of the formation of the D-region.

#### X-RAY DATA

The long series of solar X-ray measurements made using high-altitude rocket flights have shown that the X-ray flux is greatly enhanced during some solar flares (6). More recently the Naval Research Laboratories' N.R.L. satellite experiments have detected bursts of X-rays of wavelength less than 8 Å during flares (2). The U.K. experiments on board the *Ariel* satellite (7) measured spectral changes in the wavelength range 4–14 Å with a resolution of about 2 Å. Recently the *Vela* series of satellite experiments (8) have made measurements of X-ray enhancements in two wavelength bands  $\frac{1}{2}$ –4 Å and  $\frac{1}{2}$ –10 Å.



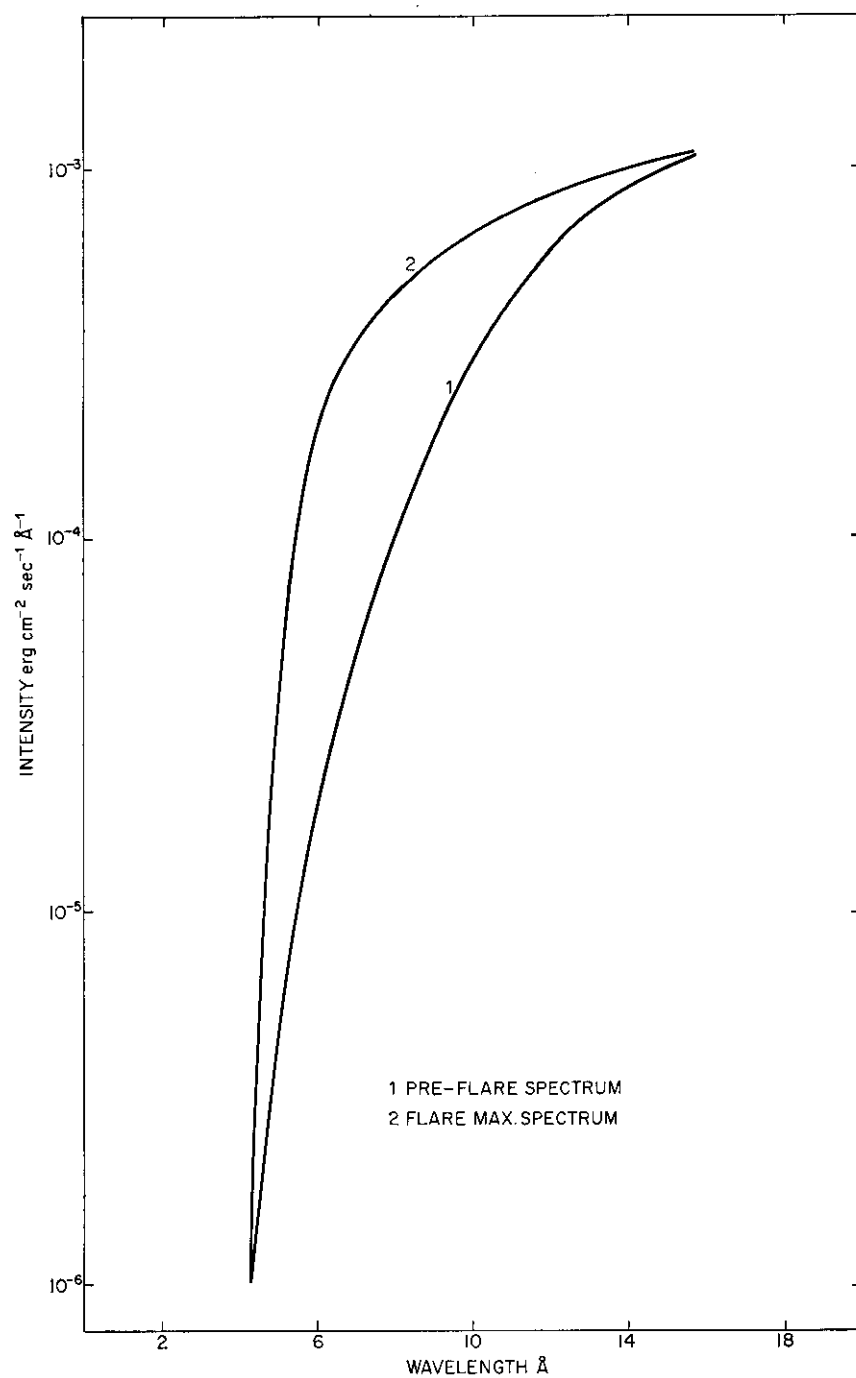


FIG. 1 X-ray entrancement associated with Class 1 M flare 23-05 U.T. April 27, 1962

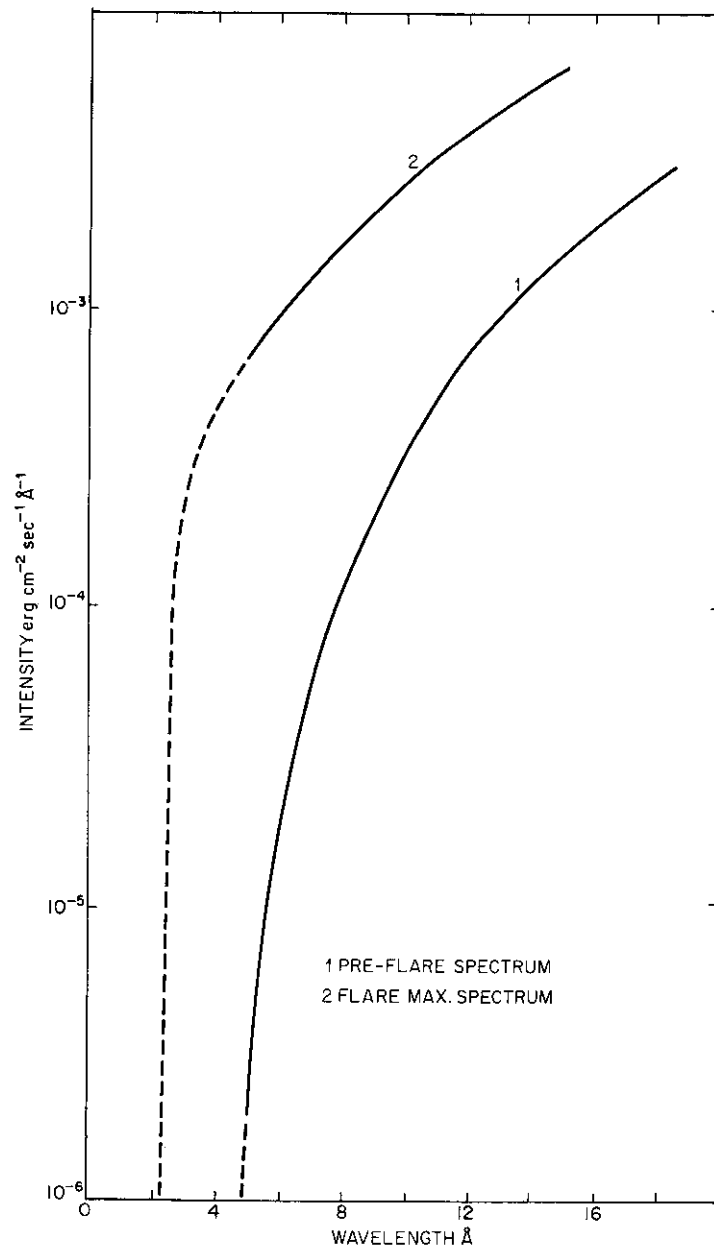


FIG. 2 X-ray entrainment associated with Class 2 flare 14-13 U.T. April 27, 1962

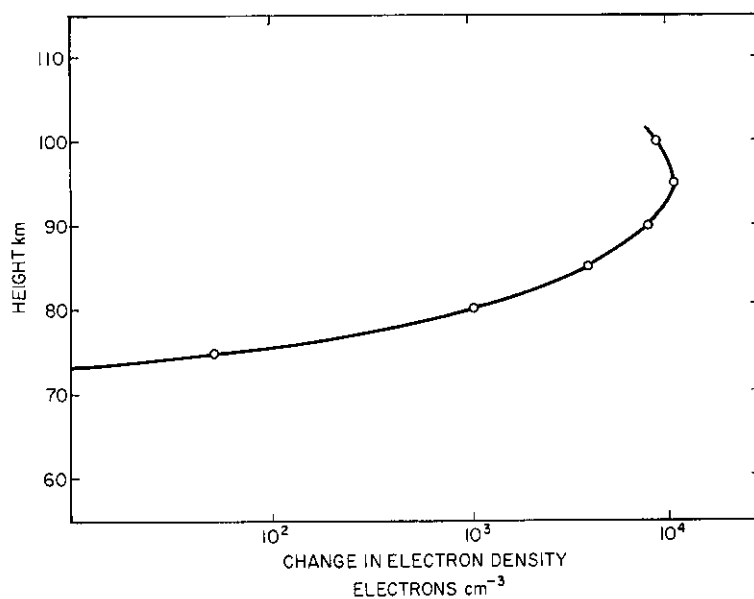


FIG. 3 Calculated electron density increase produced by the Class 1 flare 23-05 U.T. April 27, 1962

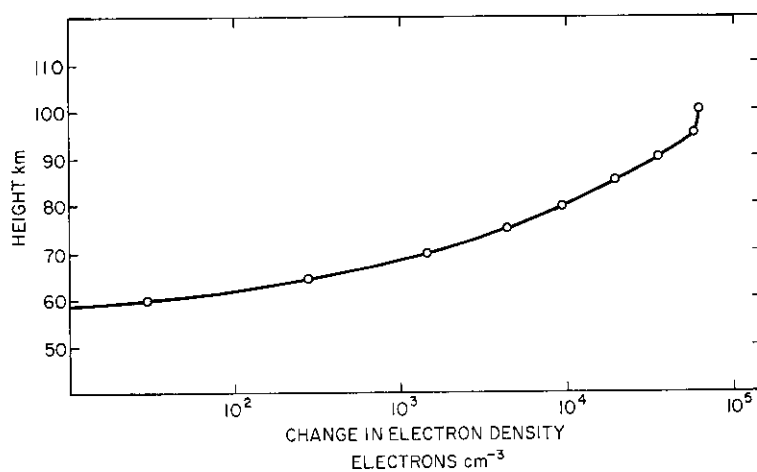


FIG. 4 Calculated electron density increase produced by the Class 2 flare 14-13 U.T. April 27, 1962

It has already been shown that in order to calculate the electron density-height profile produced by the X-ray flux a detailed knowledge of the spectral energy distribution is required. As most of the experimental measurements have up until now been made with low resolution it has been necessary to assume some form of energy wavelength distribution, usually that of a grey-body. The *Ariel* results show that the spectral distribution does not always approximate to the grey-body case and that different flares can produce significantly different changes in the X-ray spectrum. In view of this, the present calculations have been confined to the *Ariel* results for which the spectral shape is known to some degree of accuracy. Examples of pre-flare and flare-enhanced spectra for a Class 1 — and a Class 2 flare are shown in Fig. 1 and 2 respectively. This Class 2 flare produced a sudden ionospheric disturbance (SID).

It was not necessary to extrapolate the spectrum of the Class 1 — flare, as the pre-flare flux values at both short- and long-wavelength limits of the spectrum are almost unchanged at flare maximum. Thus the whole of the X-ray enhancement lies within the range 4–14 Å. This is not the case for the Class 2 flare and the spectrum at flare maximum shows enhanced values throughout the wavelength range. In order to estimate the increase in flux at wavelengths which ionize the atmosphere at D-region heights the spectrum has been extrapolated below 4 Å, illustrating an important limitation in the presently available flare X-ray data. In this respect it is of interest to note the potential value in ionospheric analysis of the new Leicester X-ray spectrometer to be flown in the OSO-D satellite in 1966, covering the wavelength band 1–70 Å with resolution into twenty-six energy intervals.

The electron-density changes calculated for the Class 1 — and Class 2 flares of April 27, 1962, are shown in Fig. 3 and 4 respectively. In both cases maximum enhancement occurs around 90–95 km, but in the case of the larger flare the increase is still considerable at 100 km. The calculation could not be extended to greater heights due to lack of X-ray data at wavelengths greater than 14 Å. The ionization increase produced by the Class 1 — flare decreases rapidly between 95 and 100 km and it would appear that for this flare the ionization enhancement is confined to the D-region.

#### SUDDEN FREQUENCY DEVIATIONS (SFD) AND X-RAY ENHANCEMENTS

The Class 2 flare of April 27, 1962, produced a marked SFD which was observed at the National Bureau of Standards, Boulder, on the 10 Mc/s signal received there from the transmitter WWV, Washington. From these measurements the change in the total electron content below the reflection level has been calculated and this event produced a columnar increase of  $2.3 \times 10^{15}$  el/m<sup>2</sup> up to a height of 150 km. An increase of  $7.9 \times 10^{14}$  el/m<sup>2</sup> in the D-region content is obtained from the profile of Fig. 4. The difference between these two values suggests that considerable ionization has taken place above 100 km. This is in agreement with the curve of Fig. 4, which indicates that the electron-density change with height does not decrease rapidly with increasing height above 100 km as in the case of the Class 1 — flare, Fig. 3.

#### IONOSPHERIC EFFECTS

The propagation characteristics of a radio wave of frequency greater

than the penetration frequency of the ionosphere will be modified by the changes in electron density produced by solar flares. The present section is devoted to an investigation of the possible effects of the two flares of April 27, 1962, on a radio wave propagated through the ionosphere.

During the Class 2 flare a sudden cosmic noise enhancement (SCNA) event having a peak absorption of 1.7 dB was recorded on 18 Mc/s at Boulder. As radio waves of this frequency penetrate the ionosphere, it can be assumed that the absorption will be entirely non-deviative and can therefore be expressed as

$$\text{absorption (dB)} = \frac{4.6 \times 10^{-5}}{(\omega + \omega_L)^2} \int_0^S N \nu ds \quad (5)$$

where

- $N$  = the electron density
  - $\nu$  = the collision frequency
  - $\omega$  = the angular wave frequency
  - $\omega_L = 2\pi f_L, f_L$  the gyro-frequency
  - $S$  = the total path length.
- All quantities are in M.K.S. units.

The additional absorption during the flare will thus be proportional to the increase in  $\int N \nu ds$ . The variation of  $\nu$  with height is known and the change in  $\int N \nu ds$  can therefore be calculated from the profile of Fig. 4. This corresponds to an increase in absorption of 1.4 dB for an 18 Mc/s radio wave.

The small discrepancy between measured and calculated values could be due to absorption in the ionization formed above 100 km. An estimate of the electron-density change up to 150 km has already been made from the SFD results, but unfortunately this gives no information regarding the height distribution of the ionization. A mean value of  $\nu$  for the height range 100–150 km must therefore be assumed in order to evaluate the absorption. A surprisingly small value is obtained amounting to only 0.05 dB at 18 Mc/s, and it would appear that most of the additional attenuation observed during the flare results from the increase in D-region electron density. At 100 Mc/s the absorption is, of course, much smaller and the total attenuation for a wave of this frequency is 0.045 dB.

Lawrence *et al.* (9) have considered some of the effects produced by the ionosphere on a 100 Mc/s radio wave propagated through it. Similar calculations have been made for the electron-density enhancements of Fig. 3 and 4, and the results are given in Table 1, together with the values of Lawrence *et al.* for a typical normal ionosphere. Both flares increase the attenuation of the 100 Mc/s wave and the effect of the Class 2 flare is an order of magnitude greater than that of the smaller flare. It is interesting to note that the increase in absorption produced by the larger flare is nearly equal to the attenuation produced by the undisturbed ionosphere. The relative changes in the other parameters are considerably smaller and for the Class 2 flare amount to only about one-fiftieth of the total ionospheric effect. The Class 1 — flare produces even smaller changes, these being about twenty times less than those of the Class 2 flare.

Finally, the effect of the flares on the apparent position of a vehicle in the

TABLE I  
MAGNITUDES OF IONOSPHERIC EFFECTS AT 100 MC/S

Ionospheric propagation factor	Change produced by Class 1 — flare	Change produced by Class 2 flare	Normal ionospheric effect
Absorption = $\frac{8.7 \times b}{(w + w_L)^2 c} \int NvdL$	.004 dB	.045 dB	.05 dB
Phase path change = $-\frac{b}{w^2} \int Ndl$ (— $\Delta l$ )	— 0.6 m	— 10.0 m	— 400 m
Polarization rotation = $\frac{b}{w^2 c} \int Nw_L dl$	.01 rad.	0.15 rad.	6.6 rad
Group path delay = $\frac{\Delta l}{c}$	.002 $\mu s$	.03 $\mu s$	1.3 $\mu s$
Differential phase path = $\frac{2b}{w^3} \int Nw_L dl$	.01 m	.15 m	6.4 m
Frequency change = $\frac{b}{2\pi w c} \frac{d \int Ndl}{dt}$ $b = 1.6 \times 10^3$ (M.K.S.)	.002 c/s	0.04 c/s	Zero

ionosphere as measured by radio means is investigated. It has been shown by Burgess (10) that the horizontal distance  $d$  between the apparent and true positions of such a vehicle is given by

$$d = \tan \theta \sec^2 \theta \frac{c^2}{2\pi m f^2} \int_{h_0}^H Ndh \quad (6)$$

where  $\theta$  is the angle of incidence of the radio wave of frequency  $f$  on the ionosphere and  $H$  and  $h_0$  are the heights of the vehicle and the base of the ionosphere respectively,  $e$  and  $m$  being the charge and mass of the electron. For a vehicle at a height of 200 km observed by means of a 100 Mc/s radio wave at an angle of incidence of  $70^\circ$  a change of 3.5 m is produced by the Class 2 flare and 0.2 m by the Class 1 — flare. These changes will be in addition to the normal ionospheric effect which gives rise to an apparent displacement of about 20 m. Although these perturbations are quite small their magnitude increases with decreasing frequency and their effects could become significant if lower frequencies are to be employed.

#### CONCLUSIONS

Satellite measurements of the solar X-ray flux show marked enhancements of the spectrum during flare conditions. The magnitude of the increase varies considerably for different flares and is not necessarily related to the size of the visible flare. For the Class 1 — flare considered in this paper, the X-ray enhancement was confined to the wavelength range 4–14 Å and additional ionization will be produced in the D-region only. The Class 2 flare of April 27

is a typical example of a larger disturbance which has increased the flux throughout the measured spectral range. It appears from the spectral distribution of this flare that increases in flux have occurred both below 4 Å and above 14 Å. The enhancement of the longer wavelengths will produce ionization in the higher regions of the ionosphere and this is confirmed by the SFD results. A detailed study of the ionization production at heights greater than about 100 km cannot be undertaken until measurements are available at wavelengths greater than 14 Å. It must be noted that no measurements of the X-ray spectrum have been made during very large flares (Class 3+) and considerable enhancement over large wavelength ranges might be expected for these events.

At present the calculations of the height distribution of flare-enhanced ionization are limited by lack of X-ray data of adequate resolution over a sufficiently large wavelength range. Furthermore, there is considerable uncertainty regarding the recombination rate coefficients in the various regions of the ionosphere. Another source of error arises from the assumption that  $\frac{dn_e}{dt} = 0$ , which is probably not valid even at flare maximum. In spite of these difficulties it has been possible to calculate changes in the electron density-height profiles which yield values of absorption in fairly good agreement with experimental results.

The greatest effect of flare-enhanced ionization on VHF radio waves propagated through the ionosphere will probably be the increase in absorption. The changes produced in other parameters are smaller, but these could become significant if these parameters are to be measured to high degrees of accuracy.

## REFERENCES

1. LINDSAY, J. C., "Orbiting Solar Observatory (OSO-1)". Trans.-Amer. Geophys. Union 44, 722, 1963.
2. KREPLIN, R. W., CHUBB, T. A., and FRIEDMAN, H., "X-ray and Lyman  $\alpha$  emission from the sun as measured from the NRL SR-1 satellite". J. Geophys. Res. 67, 2231-53, 1962.
3. MANDELSTAM, S., VASILYEV, B., VORONKO, Y., TINDO, I., and SHURYGIN, A., "Measurements of solar X-ray radiation". Space Research III, North Holland, Amsterdam, 1963.
4. BOWEN, "Measurement of the solar spectrum in the wavelength band 4-14 Å". Proc. Roy. Soc. A 281, 538-52, 1964.
5. NICOLET, M., and AIKEN, A. C., "The formation of the D-region of the ionosphere". J. Geophys. Res. 65, 1469, 1960.
6. CHUBB, "Measurements made of high energy X-rays accompanying three Class 2+ solar flares". J. Geophys. Res. 65, 1831, 1960.
7. CULHANE, J. L., WILLMORE, A. P., POUNDS, K. A., and SANFORD, P. W., "Variability of the solar X-ray spectrum below 15 Å". Space Research IV, North Holland, Amsterdam, 1964.
8. CONNER, J. P., EVANS, W. D., and SINGER, S. F., "Solar flare X-ray emission measurements and plasma observations at 10<sup>5</sup> km". Space Research V, 546 North Holland, Amsterdam, 1964.

9. LAWRENCE, R. S., LITTLE, G. C., and CHIVERS, H. J. A., "A survey of ionospheric effects upon earth-space radio propagation". Proc. I.E.E.E. 52, 1, 2, 1964.
10. BURGESS, B., Private Communication, 1965.
11. POUNDS, K. A., "Recent solar X-ray studies in the United Kingdom". Ann. Astrophys. 28, 1, 132-45, 1965.

## ACKNOWLEDGEMENTS

DR K. DAVIES for the use of SFD measurements made at Boulder.  
 DR B. BURGESS for the use of unpublished material.  
 DR K. POUNDS for the very helpful discussions during the preparation of this work.

## DISCUSSION

K. DAVIES - The Doppler technique mentioned by Dr Jones for measuring sudden frequency deviations (SFD) has been developed at the CRPL.

The instantaneous frequency shift of an ionospheric radio signal is proportional to the rate of change of phase, i.e. it measures the rate of change of some characteristic of the ionosphere. It is therefore a very powerful tool for the study of the dynamic ionosphere - it is of no use in the study of the steady state.

I should like to advance some evidence which illustrates that during some SFD's most of the ionization is produced above the D-region. Over the WVV-to-Boulder path (2400 km) the signal consists of both E and F echoes as in Fig. A. The corresponding frequency deviation record is shown in Fig. B. It will be seen that the effect on the F echo is very much larger than that on the E echo. Thus most of the electrons must be produced above the 110 km level. With this technique we cannot, of course, tell what happens above the reflection level.

When the E echo is not deviated in frequency we find that the D-region effects such as absorption, sudden phase anomalies, etc., are small, and vice versa. We conclude that the electrons above the D-region are produced mostly by X-radiation of wavelengths longer than those presented by Dr Jones (i.e.  $> 16 \text{ \AA}$ ).

A second point to which I would like to draw your attention is the fine structure in the time variation of the SFD. If the loss processes are small compared with the production, the frequency deviation  $\Delta f$  follows the production rate, which in turn is proportional to the flux of ionizing radiation. In order to ascertain that these fluctuations are not due to local effects set up in the ionosphere, we have compared SFD's recorded simultaneously in Accra, Ghana, Boulder, Colorado, and Honolulu, Hawaii. The fine structure is reproduced in all records, including different carrier frequencies to an amazing degree of detail.

E. THRANE - During the Class 2 + flare of October 22, 1963, the Norwegian Defence Research Establishment in collaboration with the Ionospheric



Institute of Athens measured ionospheric cross-modulation (1) of Crete 230 km south of Athens. The flare was received in Greece at a zenith angle of about  $70^\circ$ . The measurements during the maximum of the flare made it possible to set upper and lower limits to the electron densities in the height range 55 to 75 km. Our conclusions are that there was little change from normal conditions below 70 km, but that the electron density between 70 and 75 km was enhanced by a factor between 5 and 10 compared with normal conditions. The excess ionization started to disappear at the same time as the intensity of the hard component of the X-ray spectrum as measured by the Vela satellite decreased ( $0.5 - 4 \text{ \AA}$ ). According to Swift (2) X-rays with wavelengths  $< 2 \text{ \AA}$  will produce appreciable electron densities below 70 km. Since such electron densities were not observed, we conclude that the enhanced ionization on this particular occasion was probably produced by X-rays in the range  $2 < \lambda < 4 \text{ \AA}$ .

K. RAWER – It must be remembered that with these methods it is the absolute value of the additional ionization that is compared. Due to the large undisturbed electron density above 100 km the relative effect compared with the normal ionosphere is, of course, much larger in the lower ionosphere where the undisturbed electron density is small.

W. DIEMINGER – I should like to stress a point brought forward already by Prof. Rawer. Considering the column content of electrons the contribution of the higher layers may be greatest; however, considering the relative increase in the different layers the effect is most significant in the D-region without any doubt. For the E-region, the increase in electron density during a SID may be observed directly. It has been proved on many occasions that the critical frequency increases distinctly during the SID. The reason that this effect has been detected only late in the history of ionospheric study is that the older ionosondes were not very efficient on the lower frequencies. For this reason the lower limit of detectable echoes  $f_{\min}$  was higher than the critical frequency  $f_0E$  during a SID, and the variation was not observable. Using high-power ionosondes and efficient antenna systems one can measure  $f_0E$  even during SID's. In nearly all cases a jump in the diurnal variation is observed corresponding to an increase of maximum electron density of up to 40 per cent. There are a very few cases when an increase in the critical frequency of the F layer was also observed, but this is a rare phenomenon occurring only during extremely strong disturbances, whereas the increase for the E region is a regular effect.

#### REFERENCES

1. BARRINGTON, R. E., and THRANE, E. V., "The determination of D-region electron densities from observations of cross-modulation". J. Atmos. Terr. Phys. 24, 1, 31-42, 1962.
2. SWIFT, D. W., "Radio Wave Absorption in the Ionosphere", ed. N. C. Gerson. AGARDograph 53, 29, Pergamon Press, 1962.

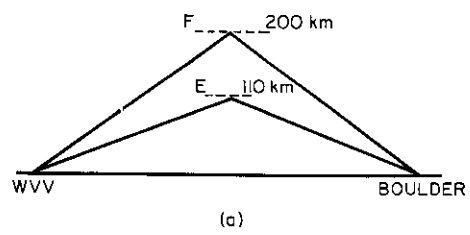


FIG. 4-A

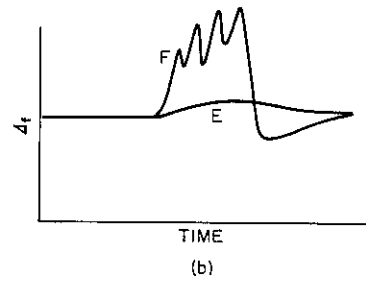


FIG. 4-B

## CHAPTER 4-2

RADIO-WAVE PROPAGATION THROUGH RE-ENTRY  
PLASMA SHEATHS

M. P. BACHYNSKI

RCA Victor Research Laboratories, Montreal, Canada

## SUMMARY

Laboratory experiments have been conducted on the use of magnetic fields to alter the plasma characteristics in order to achieve communications during re-entry using an appropriate magneto-ionic mode. In the geometrical arrangement the applied static magnetic field is aligned along the direction of propagation.

Both circularly polarized (left-hand and right-hand) and linearly polarized waves have been used. For the right-hand mode at radio frequencies above the electron cyclotron frequency, cut-off occurs at much lower electron densities than in the absence of a magnetic field. Transmission is readily achieved, however for radio frequencies below the electron cyclotron frequency. For the left-hand wave, both the phase change and attenuation decrease with magnetic field and the wave is affected much less by the plasma than the right-hand wave over the range of parameters encountered in the experiments. For the linearly polarized wave, both the phase and intensity of the components of electric field parallel and cross-polarized to the incident field show wide variation with plasma density.

Comparison of the measurements with theory show good agreement.

## INTRODUCTION

A shock-induced layer of ionized gas surrounds a space vehicle moving at hypersonic velocities within a planetary atmosphere. This enveloping ionization, or plasma sheath, can have a profound influence on communications and telemetry to and from the vehicle, resulting in very high signal attenuation or "blackout" of the radio signal. The magnitude of this effect depends upon the shape of the vehicle. Over typical flight parameters the electron density in the stagnation region (1) can vary from a few electrons/cm<sup>2</sup> to 10<sup>18</sup> electrons/cm<sup>3</sup>, while the electron-collision frequency can be as high as 10<sup>13</sup> sec<sup>-1</sup>. The ratio of plasma frequency to collision frequency can range from very large to very small compared to unity. The thickness of the plasma sheath again depends on vehicle shape, velocity and altitude, but as an order of magnitude estimate for a blunt body, is 5 to 10 per cent of the body radius at the stagnation point and somewhat larger at positions off the stagnation region. In the stagnation region, under conditions of thermal equilibrium, the electron density distribution may be relatively uniform, but outside the stagnation region the electron density enveloping the body is very

non-uniform and can vary several orders of magnitude along a normal from the body to the bow shock created by the vehicle. The corresponding variation in collision frequency is quite small and for most purposes can be considered uniform along a given normal. Both electron density and collision frequency vary at different distances along the body.

It is these extreme values of the electron density and collision frequency in the plasma sheath and their variation during a flight which affect the interaction of an electromagnetic wave with the plasma and hence seriously interfere with the normal performance of data telemetry, monitoring and command, and control systems operating between the space craft and the ground or between vehicles in flight. Elimination, or at least minimization, of these effects is essential, particularly during predetermined positions along the flight path in order to maintain communications with the re-entering vehicle.

A number of techniques have been suggested (2) in order to alleviate the "blackout" situation and permit a radio signal to penetrate through the re-entry sheath of plasma, such as using very high-frequency radio waves, low-frequency radio waves, imposing static magnetic fields to create magneto-ionic mode "windows", and modifying the plasma by chemical seeding or aerodynamic shaping of the vehicle. No single technique appears to offer universal advantages over the others, and considerable experimental data, both laboratory and free flight, are yet required in order to establish the feasibility of a given technique under flight conditions.

This paper is concerned with laboratory studies on the use of magnetic fields to alter the plasma characteristics in order to achieve communication during re-entry using an appropriate magneto-ionic mode. In the geometrical arrangement the applied static magnetic field is aligned along the direction of propagation. The following sections discuss the theory of magneto-ionic wave propagation, followed by a description of the experimental arrangement. Experimental results using both circularly polarized and linearly polarized plane waves are presented later in this Chapter under Experimental Measurements of Transmission and compared with theory. The final section summarizes the results and implications of this investigation.

#### MAGNETO-IONIC MODES FOR PROPAGATION ALONG MAGNETIC FIELD

For e.m. wave propagation in plasmas along the direction of the applied static magnetic field the dielectric coefficient is given by:

$$K_{\pm} = 1 - \frac{X(1 \pm Y)}{(1 \pm Y)^2 + Z^2} - j \frac{XZ}{(1 \pm Y)^2 + Z^2} = K_{r\pm} - jK_{i\pm} \quad (1)$$

where:

$$X = \omega_p^2/\omega^2; Y = \omega_b/\omega; Z = \nu/\omega$$

$$\omega_b = \frac{e}{m} B_0 \text{ is the electron cyclotron or gyro frequency}$$

$$B_0 \text{ is the imposed static magnetic field}$$

$$\omega_p = (ne^2/m\epsilon_0)^{1/2} \text{ is the plasma frequency}$$

$$\nu \text{ is the collision frequency}$$

$n$  is the number density of electrons  
 $e, m$  are the electron charge and mass respectively  
 $\epsilon_0$  is the permittivity of free space  
 $\omega$  is the radian radio frequency

As is well known, a plasma in the presence of a magnetic field is doubly refracting and can simultaneously support two wave modes – the so-called “ordinary wave” and “extraordinary wave”. The polarization of the wave modes for these values of dielectric coefficient can be obtained from the ratios of the electric field components arising in the wave equation, which can be written (for propagation in the  $z$ -direction)

$$\left(\frac{E_x}{E_y}\right)_{\pm} = \pm j \quad (2)$$

The waves are thus circularly polarized; the right-hand circularly polarized wave ( $+j$ ) rotating in the same direction as electrons gyrate in the presence of the static magnetic field corresponds to a dielectric coefficient  $K_-$ , the left-hand circularly polarized wave ( $-j$ ) rotating in the opposite sense to the electron motion and in the same direction as positive particles gyrate under the influence of the magnetic field corresponds to a dielectric coefficient  $K_+$ .

For the propagation of plane waves in a uniform plasma chosen to be along the  $z$ -direction, the electromagnetic fields are of the form:

$$E = E_0 e^{j\omega t} e^{-\gamma z}$$

$$H = H_0 e^{j\omega t} e^{-\gamma z}$$

where  $\gamma$  is the propagation constant given by:

$$\gamma = jkK^{\frac{1}{2}}$$

where  $k = 2\pi/\lambda$  is the free-space wave number

$\gamma$  is complex, and of the two solutions for  $\gamma$  which differ in sign, the solution yielding a negative real part is chosen in order to insure attenuation as the wave propagates. Thus:

$$\gamma = \alpha + j\beta$$

where:

$$\alpha/k = \frac{|K| - K_r}{2} \quad (3)$$

$$\beta/k = \frac{|K| + K_r}{2} \quad (4)$$

$$|K| = \sqrt{K_r^2 + K_i^2}$$

$\alpha$  is the attenuation coefficient and  $\beta$  the phase coefficient. Many of the features of propagation along the direction of the magnetic field are most readily obtained by considering the collisionless case ( $Z = 0$ ) so that:

$$\mu^2 = K_{\pm} = 1 - \frac{X}{1 \pm Y} \quad (5)$$

For a lossless plasma, ( $Z = 0$ ) conditions exist whereby the refractive

index of the plasma is infinite (i.e. there is a "pole" in the expression for the refractive index). Under these conditions the phase velocity of an e.m. wave in the plasma is zero. This "resonance" condition corresponds to a very high (infinite in the limiting case) value of the conduction current in the plasma and is associated with strong absorption of e.m. energy in the plasma.

Conditions for a lossless plasma also exist whereby the refractive index of the plasma can be zero (i.e. there is a "zero" in the expression for the refractive index). The phase velocity of a wave in the plasma is then infinite. At such cutoff conditions the conduction current is just cancelled by the displacement current. This condition corresponds to a strong reflection of the electromagnetic fields from such a medium.

Thus when the plasma parameters and the frequency are varied, the refractive index (and hence the wave-phase velocity) will vary through these values. In the case where collisions are present, the resonances and cutoffs are not as sharp as for the lossless case. The refractive index (and phase velocity) in the presence of collisions may, however, pass near the zero and infinite values as the plasma parameters and frequency are varied. When the collision frequency is high ( $\nu \sim \omega_p$ ) most of this behaviour is obscured by high attenuation. For propagation in a plasma along the direction of a static magnetic field, the resonance condition exists only for the right-hand wave and occurs at:

$$1 - Y = 0 \text{ or } \omega = \omega_b \quad (6)$$

The "cutoffs" correspond to:

$$1 = X/(1 \pm Y) \quad (7)$$

or  $\omega_p/\omega = (1 \pm \omega_p/\omega)^{\frac{1}{2}}$  for the left-hand wave and right-hand wave respectively.

The poles and zeros of the dielectric coefficient separate the values of the plasma properties where the dielectric coefficient is negative or positive. In regions between adjacent poles and zeros (resonance and cutoff) where the dielectric coefficient is negative, transverse electromagnetic waves cannot penetrate without severe attenuation. These regions thus designate "stop-bands" for the propagation of e.m. waves in a plasma.

A schematic diagram showing the variation of the opaque and transparent regions of an anisotropic plasma with plasma parameters for both the ordinary and extraordinary wave corresponding to the two values of the refractive index is shown in Fig. 1. These "pass" regions depend upon the radio frequency, polarization and angle of incidence of the electromagnetic wave and upon the electron density and applied static magnetic field. Hence an electromagnetic wave of any frequency can be made to penetrate through the plasma provided a sufficiently strong magnetic field is applied to the plasma. The value of magnetic field required to open these "windows" in the plasma is defined through the magnitude of the electron cyclotron frequency namely:

$$\omega_b = \left| \frac{e}{m} B_0 \right| = 17.6 \times 10^6 B_0 \text{ (gauss)} \quad (8)$$

The actual magnitude of field necessary will depend upon the wave mode used, the radio frequency of operation and the electron density of the plasma

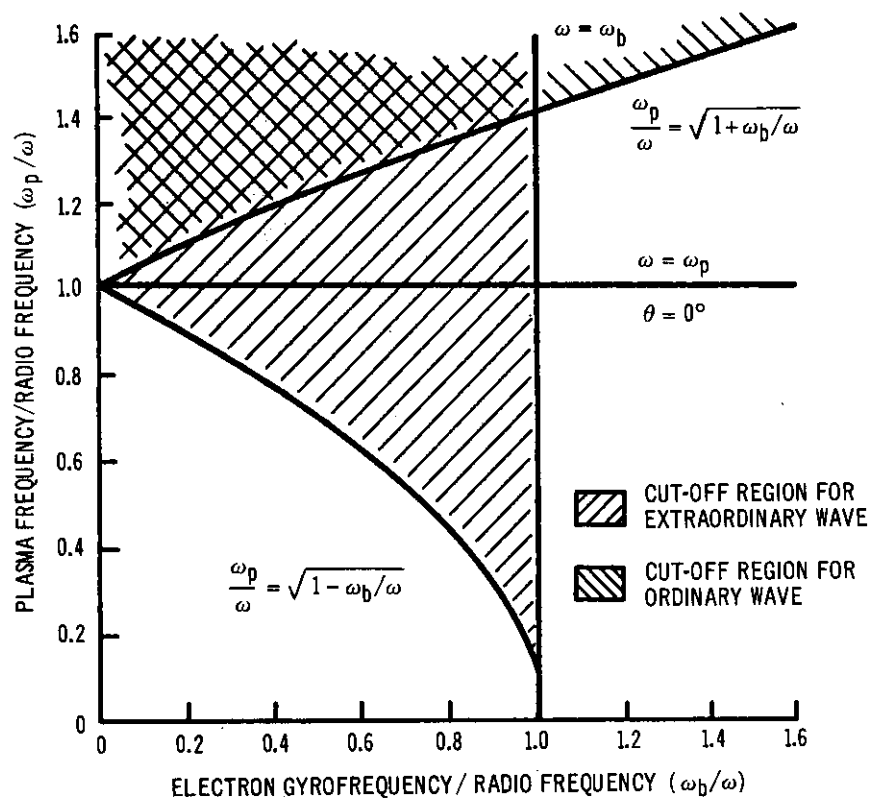


FIG. 1 Dependence of "cut-off" regions of magneto-ionic wave modes in plasma parameters for propagation along the direction of magnetic field

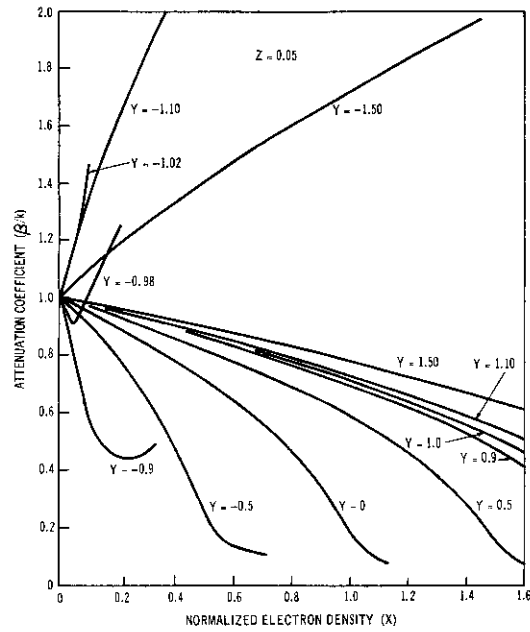


FIG. 2a Variation of the normalized phase coefficient ( $\beta/k$ ) with electron density ( $X$ ) for circularly polarized wave propagation along the direction of the magnetic field in a plasma for  $Z = 0.05$

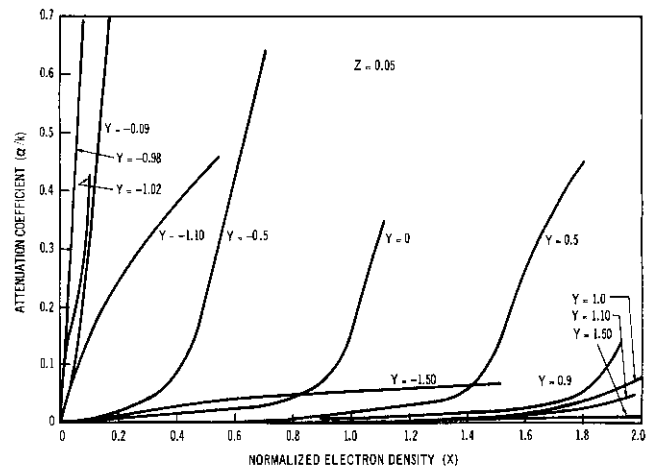


FIG. 2b Variation of the normalized attenuation coefficient ( $\alpha/k$ ) with electron density ( $X$ ) for circularly polarized wave propagation along the direction of the magnetic field in a plasma for  $Z = 0.05$



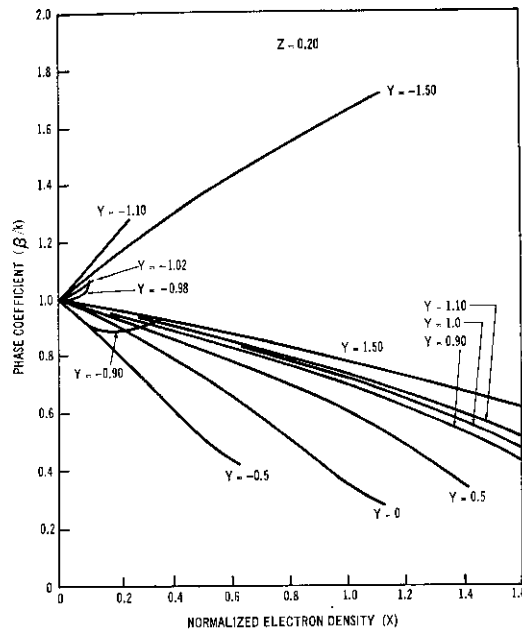


FIG. 3a Variation of the normalized phase coefficient ( $\beta/k$ ) with electron density ( $X$ ) for circularly polarized wave propagation along the direction of the magnetic field in a plasma for  $\zeta = 0.20$

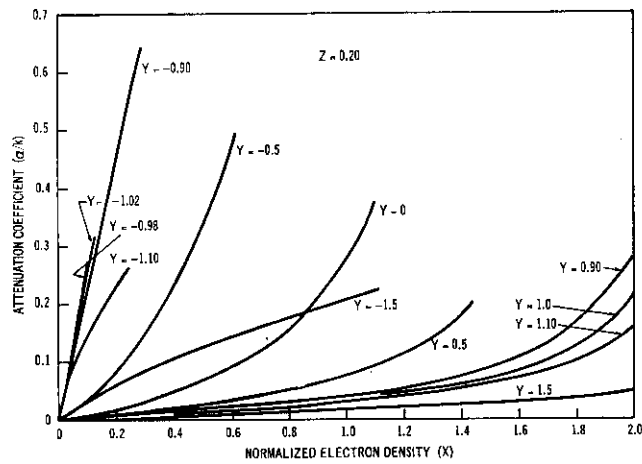


FIG. 3b Variation of the normalized attenuation coefficient ( $\alpha/k$ ) with electron density ( $X$ ) for circularly polarized wave propagation along the direction of the magnetic field in a plasma for  $\zeta = 0.20$

and can readily be calculated. Hodara (3) has presented numerical results for the case of the right-hand circularly polarized wave.

Plots of the variation of the phase coefficient and attenuation coefficient for a normalized collision frequency  $\mathcal{Z} = \nu/\omega$  of 0.05 with normalized electron density are shown in Fig. 2a and 2b. The deviations of the phase coefficient from one (free-space) is considerably greater for the right-hand wave  $K-$  than the left-hand wave  $K+$ . In particular around  $Y \sim 1$ , i.e.  $\omega \sim \omega_b$ , very rapid variations of the phase coefficient occur. For  $Y < 1$ , the phase coefficient is less than one (corresponding to a refractive index less than one) and for  $Y > 1$  the phase coefficient is greater than one (corresponding to a refractive index greater than one). The attenuation coefficient for the left-hand mode is always less than if no magnetic field is present and decreases with increasing magnetic field. Very high attenuation occurs for the right-hand mode, particularly in the region  $Y \sim 1$  corresponding to electron-cyclotron resonance. A corresponding effect would be expected to occur for the left-hand mode at the ion-cyclotron frequency. In practice, however, this frequency is so low that in most cases collisional effects mask this phenomenon. The attenuation decreases the farther the magnetic field values are from  $Y = 1$  and can be quite small for  $Y > 1$  (the whistler mode).

Collision effects have a marked influence on the behaviour of the propagation coefficients as can be seen from Figs. 3a and 3b which show the variation of the phase and attenuation coefficients with normalized electron density for  $\mathcal{Z} = 0.20$ . It is interesting to note that the increase in collision frequency increases the attenuation for all ranges of parameters except for the right-hand wave in the immediate region of  $Y = 1$ . In this region in the vicinity of the electron cyclotron frequency the attenuation coefficient is actually decreased. The total attenuation that a wave suffers in propagating a distance  $d$  in a plasma is given by:

$$A_{\pm} = \frac{2\pi d}{\lambda} (8.68) (\alpha_{\pm}/k) \text{ decibels} \quad (9a)$$

and the phase shift by:

$$\phi_{\pm} = \frac{2\pi d}{\lambda} (1 - \beta_{\pm}/k) \text{ radians} \quad (9b)$$

Thus in the real situation, i.e. in the presence of collisions, we do not get a sharp cutoff or stop region, but rather a region of greater or lesser attenuation. We can, however, still think in terms of the cutoff regions of Fig. 2, although these regions will be modified. Thus let us define cutoff to occur when the attenuation is "prohibitive" and that this prohibitive attenuation corresponds to an attenuation rate of 10 dB/free space wavelength of plasma. This is a reasonable value. However, what is prohibitive must relate to the particular application at hand. This rate is here arbitrarily chosen to illustrate the e.m. wave-plasma behaviour. Any other rate with corresponding behaviour could have been chosen. The modified cutoff region in the presence of collisions for  $\mathcal{Z} = 0.05$  and  $\mathcal{Z} = 0.20$  for propagation along the magnetic field direction are shown in Fig. 4. It is interesting to note that the presence of collisions can either increase or decrease the electron cyclotron required for cutoff. In particular, in the region around electron cyclotron resonance the

electron density required for cutoff is increased. In other regions, the cutoff electron density for the right-hand circularly polarized wave is decreased and in the whistler region, which is transparent in the lossless case, considerable attenuation can occur. The left-hand circularly polarized wave is not as markedly affected by collisional effects.

The above results are applicable to circularly polarized incident waves and to situations where the reflections from the plasma boundaries are insignificant. When the boundaries of the plasma are included in the analysis the results for a uniform sharply bounded infinite plasma of thickness  $d$ , for normally incident circularly polarized plane waves propagating along the direction of magnetic field are:

$$T_{\pm} = [\cosh(\alpha_{\pm}d + j\beta_{\pm}d) + (\mathcal{Z}_{r\pm} - j\mathcal{Z}_{i\pm}) \sinh(\alpha_{\pm}d + j\beta_{\pm}d)]^{-1} \quad (10)$$

$$R_{\pm} = T_{\pm} \left[ \mathcal{Z}_{i\pm} \left( \frac{\beta_{\pm}/k}{\alpha_{\pm}/k} \right) + j\mathcal{Z}_{r\pm} \left( \frac{\alpha_{\pm}/k}{\beta_{\pm}/k} \right) \right] \sinh(\alpha_{\pm} + j\beta_{\pm})d \quad (11)$$

where:

$$\mathcal{Z}_{r\pm} = \frac{1}{2}(\beta_{\pm}/k) \left( \frac{|K_{\pm}| + 1}{|K_{\pm}|} \right)$$

$$\mathcal{Z}_{i\pm} = \frac{1}{2}(\alpha_{\pm}/k) \left( \frac{|K_{\pm}| - 1}{|K_{\pm}|} \right)$$

$T_{\pm}$ ,  $R_{\pm}$  are the amplitude transmission and reflection coefficients for the  $+$  wave and  $-$  wave modes respectively.

The power transmission coefficient  $T_{\pm}T_{\pm}$  and reflection coefficient  $R_{\pm}R_{\pm}$  are:

$$T_{\pm}T_{\pm} = [(\mathcal{Z}_{r\pm}^2 + \mathcal{Z}_{i\pm}^2) (\sinh^2 \alpha_{\pm}d + \sin^2 \beta_{\pm}d) + 2\mathcal{Z}_{r\pm}\cosh \alpha_{\pm}d \sinh \alpha_{\pm}d + \sinh^2 \alpha_{\pm}d + \cos^2 \beta_{\pm}d + 2\mathcal{Z}_{i\pm} \sin \beta_{\pm}d \cos \beta_{\pm}d]^{-1} \quad (12)$$

$$R_{\pm}R_{\pm} = T_{\pm}T_{\pm} (\sinh^2 \alpha_{\pm}d + \sin^2 \beta_{\pm}d) \left[ \left( \frac{\beta_{\pm}}{\alpha_{\pm}} \mathcal{Z}_{i\pm} \right)^2 + \left( \frac{\alpha_{\pm}}{\beta_{\pm}} \mathcal{Z}_{r\pm} \right)^2 \right] \quad (13)$$

As can be seen the calculations for bounded anisotropic plasmas are lengthy and tedious. An important point to notice is that existing calculations for isotropic uniform plasma slabs are equally applicable to the anisotropic slab with normal incidence propagation along the direction of the applied static magnetic field by a transformation of variables such that:

$$(X \text{ isotropic})_{\pm} \rightarrow \frac{X}{1 \pm Y} \quad (14a)$$

$$(\mathcal{Z} \text{ isotropic})_{\pm} \rightarrow \frac{\mathcal{Z}}{1 \pm Y} \quad (14b)$$

where  $X$  isotropic,  $\mathcal{Z}$  isotropic are the values of  $X, \mathcal{Z}$  used in the isotropic plasma slab calculations; the  $\pm$  sign corresponds to applications of the isotropic slab results to the  $+$  or  $-$  circularly polarized wave mode.

For an initially linearly polarized wave, the transmitted power resulting

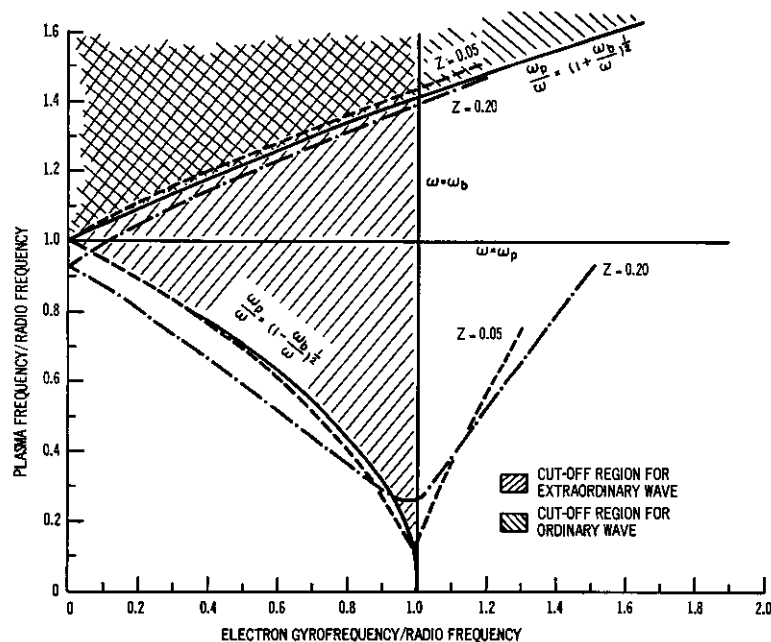


FIG. 4 Dependence of the "cut-off" regions for circularly polarized waves propagating along the direction of magnetic field in a plasma on collision frequency. ("Cut-off" is defined to correspond to an attenuation of 10 dB per free-space wavelength of the plasma)

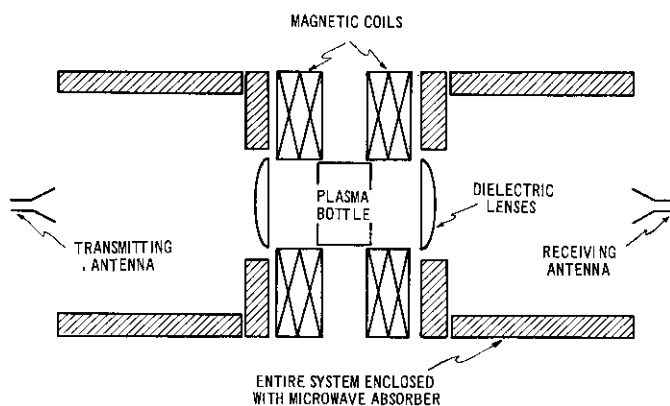


FIG. 5 Schematic diagram of experimental arrangement for investigation of effect of magnetic field in propagation through a plasma along the direction of a static magnetic field

from the fields parallel to the original polarization  $P_{\parallel}$  and cross-polarized to the original polarization  $P_{\perp}$  along with the respective phases of signal  $\phi_{\parallel}$  and  $\phi_{\perp}$  are given by;

$$P_{\parallel} = \frac{1}{2}[\frac{1}{2}(e^{-2\alpha+d} + e^{-2\alpha-d}) + e^{-(\alpha_++\alpha_-)d} \cos(\beta_+ - \beta_-)d] \quad (15)$$

$$P_{\perp} = \frac{1}{2}[\frac{1}{2}(e^{-2\alpha+d} + e^{-2\alpha-d}) - e^{-(\alpha_++\alpha_-)d} \cos(\beta_+ - \beta_-)d] \quad (16)$$

$$\tan \phi_{\parallel} = \frac{e^{-\alpha+d} \sin \beta_+d + e^{-\alpha-d} \sin \beta_-d}{e^{-\alpha+d} \cos \beta_+d + e^{-\alpha-d} \cos \beta_-d} \quad (17)$$

$$\tan \phi_{\perp} = \frac{-e^{-\alpha+d} \cos \beta_+d + e^{-\alpha-d} \cos \beta_-d}{e^{-\alpha+d} \sin \beta_+d - e^{-\alpha-d} \sin \beta_-d} \quad (18)$$

The total power is the sum of Eq. 15 and 16, namely,

$$P_{\text{total}} = \frac{P_0}{2} \{e^{-2\alpha+d} + e^{-2\alpha-d}\} \quad (19)$$

where:  $P_0 = \frac{E_0 H_0}{2}$  the power carried by the incident wave at  $d = 0$ . The two terms in Eq. 19 correspond to the fraction of the power in the left-hand circularly polarized wave mode  $e^{-2\alpha+d}$  and the fraction of the power in the right-hand circularly polarized wave mode  $e^{-2\alpha-d}$  respectively. For a bounded plasma and incident linear polarization, the power flow or transmission coefficient is:

$$(TT)_L = \left\{ \text{Re} \left[ \left( \frac{T_- + T_+}{2} \right) e^{j\omega t} \right] \right\}^2 + \left\{ \text{Re} \left[ j \frac{T_- - T_+}{2} e^{j\omega t} \right] \right\}^2 \quad (20)$$

The first term is the transmission coefficient for the wave received which has the same orientation (polarization) as the incident wave. The second term corresponds to the cross-polarized power. For the reflected wave, the parallel polarized and cross-polarized components of the reflection coefficient are obtained from:

$$(RR)_L = \left\{ \text{Re} \left[ \left( \frac{R_- + R_+}{2} \right) e^{j\omega t} \right] \right\}^2 + \left\{ \text{Re} \left[ j \left( \frac{R_- - R_+}{2} \right) e^{j\omega t} \right] \right\}^2 \quad (21)$$

where:  $\text{Re}$  means "the real part of".

#### EXPERIMENTAL ARRANGEMENT

In order to obtain detailed quantitative measurements on the propagation of electromagnetic waves in an anisotropic plasma it is necessary that the experimental arrangement conform as closely as possible with the requirements of theory (4). Thus, it is essential that the appropriate range of parameters is achieved. The interesting interactions for propagation in a plasma along the direction of magnetic field occur in the regions of electron cyclotron frequency/radio frequency ( $\omega_b/\omega$ ) of unity. If X-band ( $\sim 10$  Gc/s) is selected as the radio frequency, then magnetic fields in excess of 3800 gauss and electron densities greater than  $10^{12}/\text{cc}$  are required. Furthermore, the volume of plasma should be large enough so that diffraction effects do not predominate and preferably the plasma should be uniform, with well-defined boundaries and reproducible. The thermal kinetic properties of the plasma must be

well known, so that the electrical properties of the plasma can be predicted by theory. If possible, plane electromagnetic waves should be used in the investigations and all undesirable interactions between the incident waves with the experimental system either eliminated or minimized (5).

An experimental system designed to meet all the above requirements is sketched in Fig. 5 and the remainder of this section will be devoted to a description of the various units of this experimental arrangement.

**Magnetic field facility** – The magnetic field facility consisted of two magnetic coils arranged in a Helmholtz configuration. This facility is capable of generating magnetic fields in excess of 4500 gauss with a working area of 7 inches diameter. This enables ratios of  $\omega_b/\omega$  of up to 1.4 (when  $\omega \sim 10$  Gc/s) and volumes of plasma sufficient to minimize diffraction effects if proper precautions are taken. For a coil spacing of  $4\frac{1}{2}$  inches and a longitudinal working length of 2 inches the magnetic field is uniform to about 2 per cent.

The vacuum and gas-handling system is built into the supporting framework of the magnetic coils. A symmetrical input and output manifold arrangement, with pressure gauges, vacuum valves and diffusion pump, provides a suitable high-vacuum system and at the same time a convenient support for the plasma bottle.

The entire system is situated in an anechoic chamber. The apparatus itself is surrounded with microwave absorbing material to eliminate reflections.

**Microwave system** – The microwave system for performing the measurements of transmission of e.m. waves through the plasma operates at a frequency of 9.195 Gc/s ( $\omega = 5.78 \times 10^{10} \text{ sec}^{-1}$ ,  $\lambda = 3.26 \text{ cm}$ ). The transmitting section consists of a circular horn mounted on a turnstile transition. By adjusting the phase of the signal being fed into each arm of the turnstile, any desired polarization (from linear to circular) can be launched (6), (7). The transmitter is located at the focus of a dielectric microwave lens, so that a plane wave emanates from the lens and is incident on the plasma. A second microwave lens collimates the energy passing through the plasma into the aperture of a rectangular linearly polarized horn. The linearly polarized horn, in the case of a circularly polarized transmitted wave loses 3 dB of the power. However, rotating the horn by  $90^\circ$  should result in the same signal and hence a check as to whether the transmitted wave is indeed circularly polarized.

The microwave measurements are made with the multiple probe system (8), which permits the simultaneous display of the phase and amplitude of the transmitted wave at a predetermined repetition rate. This makes it possible to follow the continuous changes of the plasma characteristics in the afterglow of a decaying plasma. The display is in polar form (radius vector = amplitude and polar angle = phase change) with timing markers.

**Plasma generation and containment** – The major problem in the study of plasmas in the presence of magnetic fields is the generation of a suitable, controlled, reproducible plasma. The generation of plasma in helium was made in a cylindrical container with flat faces (in order to simulate a slab of plasma) and a grid electrode configuration such that it was possible to propagate an electromagnetic wave along the direction of the static magnetic field. In order to eliminate the  $\vec{j} \times \vec{B}$  forces arising from the current density

( $\vec{j}$ ) generated in the plasma, it is necessary that the current in the plasma should flow in the direction of propagation and hence that the electrodes are arranged normal to the incident wave (i.e. the e.m. wave must pass through the electrodes). In order to achieve this, electrodes were constructed from a fine, loosely spaced, thin wire mesh or grid and placed within the plasma container parallel to the flat faces of the container. The plasma was generated by a capacitor discharge in which the plasma is pulsed and measurements made in the afterglow.

**Display marker system** – Once the plasma is generated it decays in time, and at the time of “crowbarring” of the capacitor bank the electron density is usually too high to permit transmission measurements (i.e. the electron density is higher than required for cutoff). Hence a variable marker delay triggered by the firing of a thyatron was introduced. The variable marker is followed by a 10 kc/s brightening modulation which permits the normal marker points in the polar type display used in recording the output of the four-probe microwave measuring system. In the very late afterglow the microwave properties of a plasma change very slowly and the marker points tend nearly to coincide, resulting in a time history which is difficult to decipher. Therefore, a “cutoff gate” has been introduced to cutoff the display at a predetermined time.

#### EXPERIMENTAL MEASUREMENTS OF TRANSMISSION THROUGH ANISOTROPIC PLASMAS

**Measurements of Transmission of circularly polarized electromagnetic waves** – Measurements of the propagation of circularly polarized electromagnetic waves through anisotropic plasma along the direction of the static magnetic field were made using the arrangement shown in Fig. 5 and the various systems described under the heading “Experimental Arrangement”. The measurement sequence consisted of setting the magnetic field at a known fixed value, generating the plasma by discharging a capacitor bank, “crowbarring” the capacitors, waiting a predetermined time (usually 0.5 ms) for the plasma to thermalize, and then performing microwave measurements of the phase and amplitude of the signal transmitted through the plasma at time intervals of  $10^{-4}$  seconds as the plasma decayed. The microwave system operated at a frequency of 9.195 Gc/s and a change from left-hand circular polarized incident signal to right-hand circular polarized wave (or vice versa) was accomplished by reversing the direction of the static magnetic field without altering any adjustments in the physical arrangement. The use of a linearly polarized receiver permitted a check on whether or not the signal was still circularly polarized after passing through the plasma, by repeating the measurements with the receiver at  $90^\circ$  to its original orientation.

A complete set of data as recorded by the multiple probe unit is shown in Fig. 6. Each display shows phase (polar angle) and amplitude (radius vector) versus time (timing markers) as the plasma decays. A complete sequence for various values of magnetic field for both the right-hand circularly polarized wave and the left-hand circularly polarized wave is shown. Even from the “raw” data a number of qualitative conclusions can be drawn.

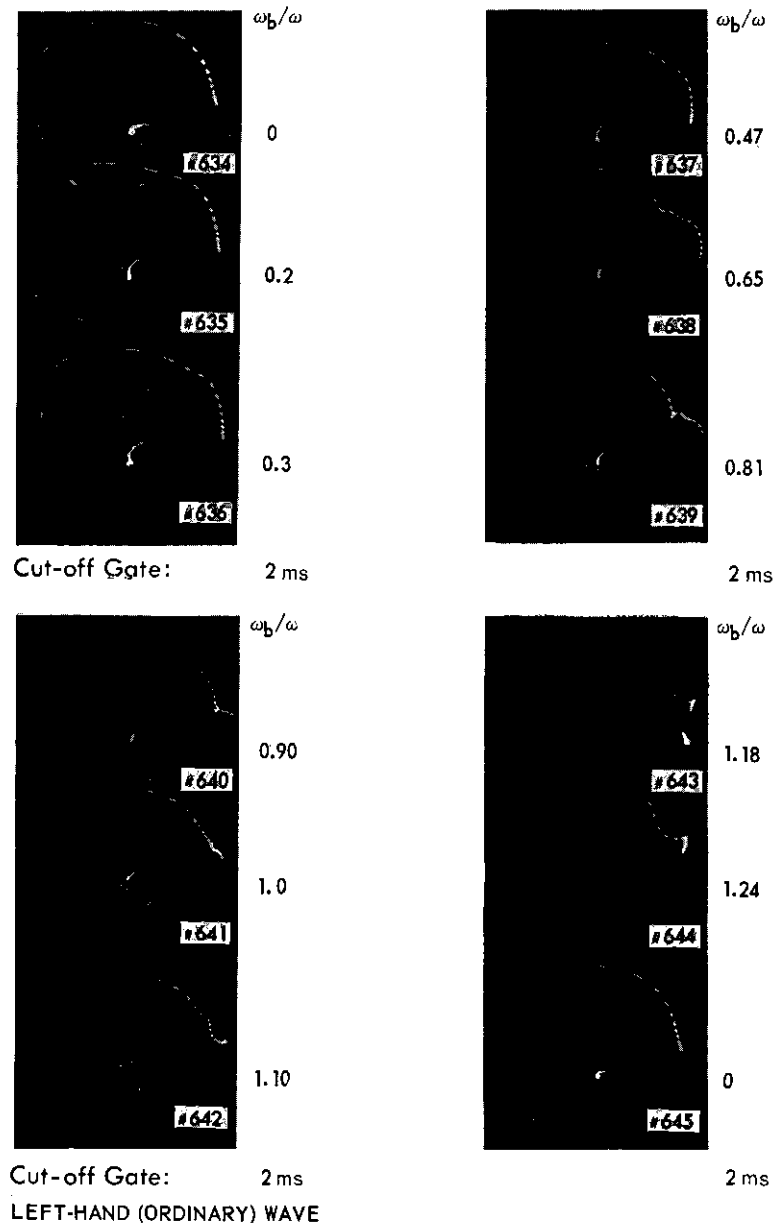


FIG. 6a Series of measurements using multiple-probe system for left-hand circularly-polarized waves in helium discharge. (Phase = polar angle, attenuation - 2 dB/div. of radius vector). (Pressure 0.6 torr, crowbar delay 1.3 ms, marker length 0.5 ms, sampling rate 10 kc/s coil spacing 4.5 inches inner diameter)



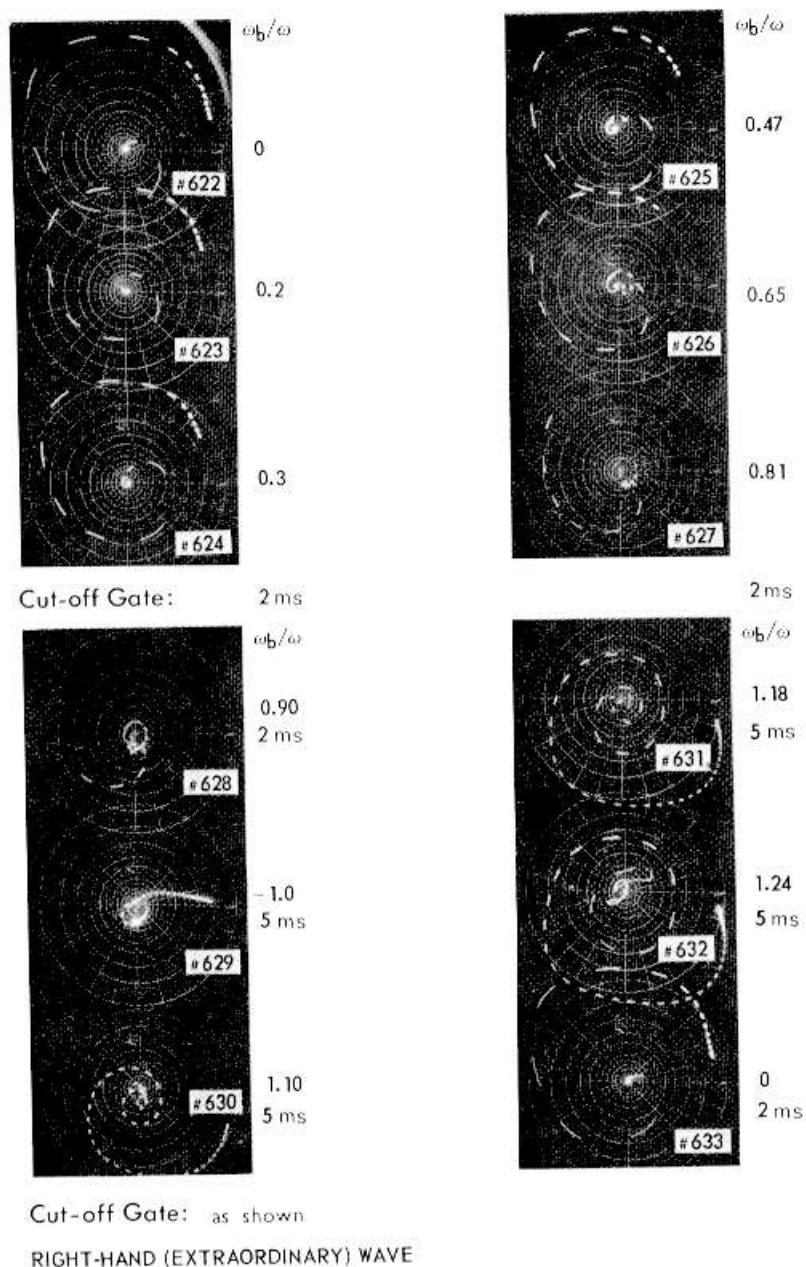


FIG. 6b. Series of measurements using multiple-probe system for right-hand circularly polarized waves in helium discharge. (Phase — polar angle, attenuation — 2 dB/div. of radius vector). (Pressure 0.6 torr, crowbar delay 1.3 ms, marker length 0.5 ms, sampling rate 10 kc/s, coil spacing 4.5 inches inner diameter)

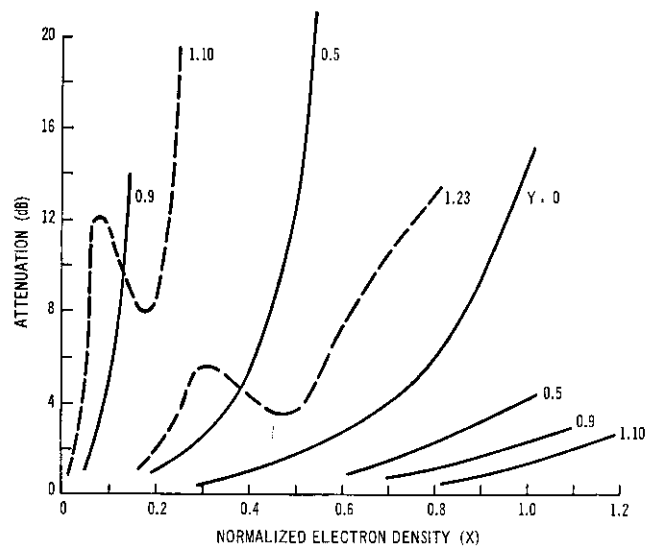


FIG. 7 Experimentally determined variation of attenuation of the signal transmitted through the plasma with electron density for different magnetic field strength

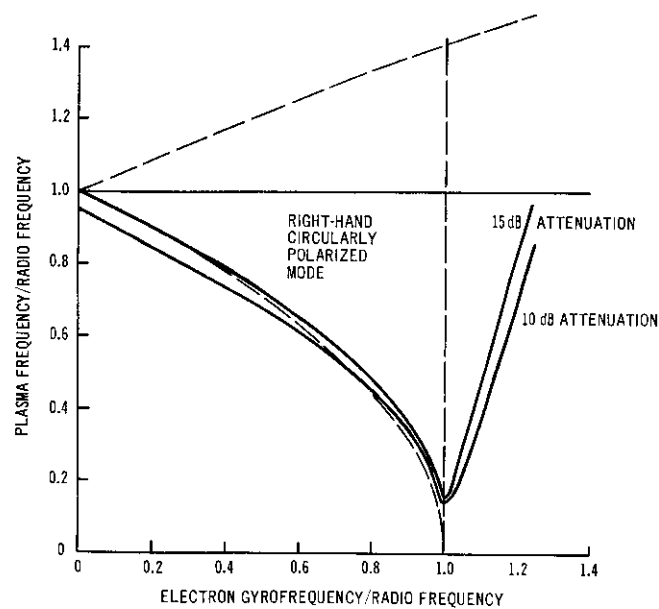


FIG. 8 Experimentally determined "cut-off" regions for circularly polarized waves propagating along direction of magnetic field

These include:

- (a) With no magnetic field the wave is initially well cut off, indicating that electron densities in excess of  $10^{12}\text{cm}^{-3}$  are generated in the plasma.
- (b) The plasma container is well "matched" to the incident radiation, as can be seen from the  $\mathcal{V} = 0$  trace which does not exhibit reflection type of undulations.
- (c) For the right-hand circularly polarized wave
  - 1 in the region  $0 < \mathcal{V} < 1$  cutoff occurs at much lower electron densities than in the absence of a magnetic field;
  - 2 in the region  $\mathcal{V} \sim 1$  a very strong interaction occurs in which the wave experiences severe attenuation and very little phase shift;
  - 3 in the region  $\mathcal{V} > 1$  (whistler region) the sign of the phase change is reversed (direction of rotation of the recorded data is reversed). This is a direct observation of the fact that for  $\mathcal{V} > 1$  the dielectric coefficient of the plasma is greater than one, while for  $\mathcal{V} < 1$  the dielectric coefficient is less than one. For  $\mathcal{V} > 1$  the wave experiences large-phase shifts (corresponding to large values of the dielectric coefficient) and the attenuation decreases rapidly as the magnetic field strength is increased. Also, as the attenuation decreases the received signal "undulates" as the electron density changes due to the interference effects resulting from multiple reflections within the plasma.
- (d) For the left-hand circularly polarized wave
  - 1 the wave is affected much less by the plasma than the right-hand circularly polarized wave over the range of parameters encountered in the experiment;
  - 2 both the phase change and attenuation decrease with increasing magnetic field;
  - 3 there is no significant change in the wave properties in the region  $\mathcal{V} \sim 1$ .

The electron densities of the plasma can be determined from the phase shift of the signal using the theory presented under the heading "Magneto-ionic Modes". In determining the interaction it is necessary to include the variation of the collision frequency with electron density due to the effect of electron-ion collisions. It is found that at the high electron densities, electron-ion collisions dominate, while at low electron densities electron-neutral encounters determine the collision frequency. Ascertaining the electron density in this manner and plotting the corresponding attenuation measured at the same instant in time gives the variation of the attenuation of the signal with electron density for various values of the magnetic field. These are shown in Fig. 7. For the range of parameters encountered in the experiment the effect of the magnetic field in reducing the attenuation is most apparent for the left-hand circularly polarized wave and in the whistler region ( $\mathcal{V} > 1$ ) for the right-hand circularly polarized wave. This latter case requires large magnetic field strengths and hence is strongly dependent on progress being made in the use of super-conducting materials to provide

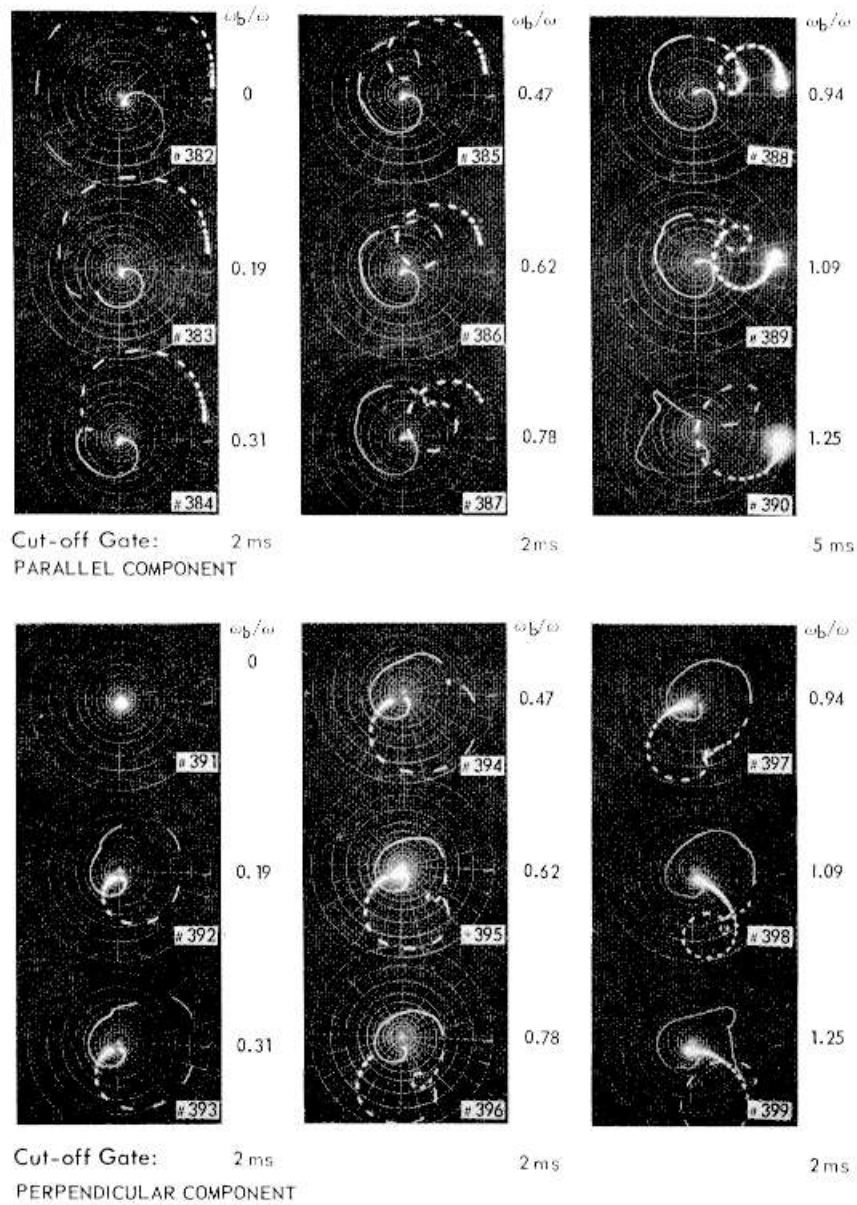


FIG. 9 Series of measurements using multiple-probe system of the components parallel and perpendicular to the incident linearly-polarized wave transmitted through a helium plasma (phase — polar angle, attenuation — 2dB/div. of radius vector). (Pressure 0.6 torr, crowbar delay 1.3 ms, marker length 0.5 ms, data sampling rate 10 kc/s, coil spacing 5 inches inner diameter)

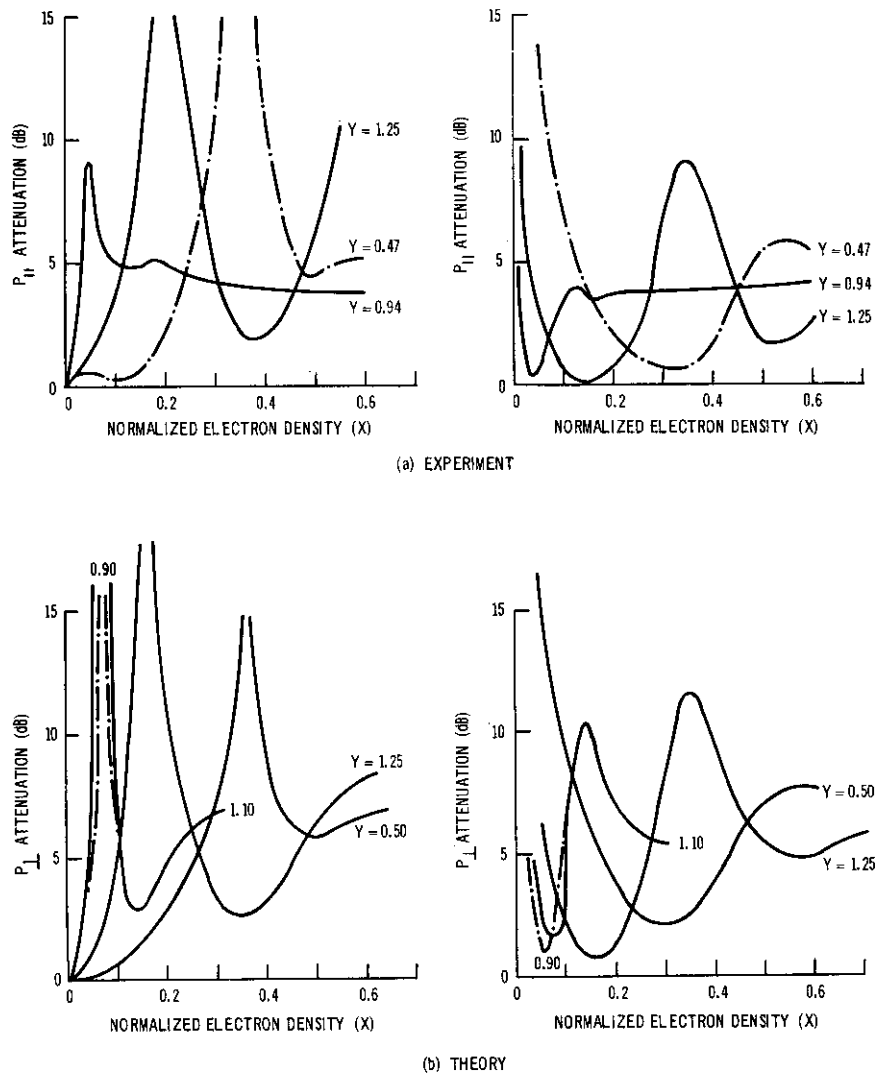


FIG. 10 Variation of transmitted signal through a plasma with electron density for a linearly polarized incident wave. Both components oriented in the same direction as the incident field ( $P_{11}$ ) and cross-polarized to the incident field ( $P_{\perp}$ ) are shown

the field strength within the weight, size and power supply requirements compatible with space missions.

The above attenuation results can be put in a form similar to the cutoff diagrams of Fig. 1 and 4. This is done in Fig. 8. A comparison with Fig. 4 and 8 shows quite reasonable agreement between theory and experiment.

In the experiments, the reflection coefficient was found to be less than 10 per cent in the absence of a magnetic field and to decrease with increasing magnetic field to small values, thus making quantitative measurements difficult. The importance of reflections and the resulting mismatch has been raised by Mullin (9). The effect of the mismatch is to reduce the apparent advantage of the extraordinary wave mode over the ordinary wave mode for propagation along the magnetic field and to cause the transmission properties of the extraordinary wave mode to exhibit sharp peaks (when the optical thickness of the plasma is  $m(\lambda/4)$ ,  $m$  being an integer) with changing plasma density. In the re-entry case, the plasma boundaries will not be infinitely sharp, so that this effect may not be so severe. Nevertheless it could be appreciable. Schemes to vary the strength of the magnetic field in order to minimize the mismatch and to shape the magnetic field to compensate for the plasma non-uniformity have also been suggested (10).

#### **Measurements of transmission of linearly polarized electromagnetic waves**

Measurements of the transmission of linearly polarized plane electromagnetic waves through an anisotropic helium afterglow plasma along the direction of the static magnetic field were made in the same manner as described for the circularly polarized waves. The notable changes from the previous arrangement and procedure were that a 5-inch (inner diameter) coil spacing was used in the magnets and a linearly polarized wave was launched at the transmitter. The phase and intensity of the components of the signal transmitted through the plasma in the same orientation as the incident polarization and cross-polarized ( $90^\circ$  to the incident polarization) were measured. In addition, a set of measurements for the right-hand and left-hand circularly polarized wave modes over the same range of parameters as the linearly polarized waves was taken.

A complete set of data as recorded by the multiple probe unit is shown in Fig. 9. The data show the phase and intensity variation of the component oriented parallel to the incident field and the corresponding component perpendicular (cross-polarized) to the incident field. The features from the "raw" data to note are:

- (a) With no applied static magnetic field (isotropic plasma), the cross-polarized component is zero.
- (b) At low values of magnetic field ( $\mathcal{F} < 0.5$ ) there is a relatively uniform variation of the phase with electron density for both components. The intensity of the parallel component continues to increase with decreasing electron density. The cross-polarized component increases as first with decreasing electron density and then decreases to zero at no plasma.
- (c) At intermediate values of magnetic field ( $0.5 < \mathcal{F} < 1.0$ ) a reversal in phase and undulations in intensity occur for both components as the electron density varies.

- (d) In the region  $\gamma \sim 1$  (see  $\gamma = 0.94$  and  $1.09$  measurements) for large electron densities the right-hand wave mode is cut off and both traces show a signal approximately 6 dB down from the free space value corresponding primarily to the left-hand wave mode.
- (e) For magnetic fields such that  $\gamma > 1.0$  the reversal in phase and undulations in intensity still occur for both components, but the direction of the phase reversal is opposite to that when  $\gamma < 1.0$  (corresponding to a change in direction of the Faraday rotation).

The variation of the signal levels of the parallel polarized fields  $P_{\parallel}$  and cross-polarized fields  $P_{\perp}$  due to Faraday rotation with electron density are shown in Fig. 10a. The corresponding theoretically calculated variations are shown in Fig. 10b. The agreement between theory and experiment is quite reasonable. As can be seen, large undulations in transmitted power occur at the lower electron densities. At the higher densities and for magnetic field values such that  $\gamma < 1$ , the right-hand mode is cut off, so that only the left-hand mode is measured. At high magnetic field values both modes are transmitted and again variations of the transmitted signal with electron density occur.

#### CONCLUSIONS

A detailed quantitative investigation of the propagation of both circularly polarized and linearly polarized electromagnetic waves in an anisotropic plasma along the direction of an applied static magnetic field has been conducted. Experimental measurements of electron density and attenuation show good agreement with theory over all ranges of parameters.

For the right-hand mode for  $\gamma < 1$ , cutoff occurs for much lower electron densities than in the absence of a magnetic field. This range of parameters is to be avoided in attempts to use magnetic fields to aid re-entry communications. For  $\gamma > 1$  the direction of phase shift is reversed, showing that the dielectric coefficient of the plasma is greater than one and the large phase shifts indicate high values of dielectric coefficient. The use of magnetic fields reduces the attenuation greatly in this region, but strong magnetic fields are required. Practical magnetic fields for this region must make use of superconductors.

For the left-hand wave, both the phase change and attenuation decrease with increasing magnetic field and the wave interacts much less with the plasma than the right-hand wave over the range of parameters used in the experiments. Significant reductions in attenuation of this wave mode can be achieved using magnetic fields. Practical utilization of this wave mode could be made by selecting sufficiently high frequencies which are just marginal for a given mission and then using magnetic fields to insure their penetration through the plasma sheath.

For a linearly polarized incident wave, large undulations in the power received by a linearly polarized antenna due to Faraday rotation occur as expected.

## REFERENCES

1. BACHYNSKI, M. P., JOHNSTON, T. W., SHKAROFKY, I. P., "Electromagnetic Properties of High Temperature Air". *Proc. IRE* 48, 347-56, 1960.
2. BACHYNSKI, M. P., "Electromagnetic Wave Penetration of Re-entry Plasma Sheaths". *Radio Science* 69D, 147-54, 1965.
3. HODARA, H., "The Use of Magnetic Fields in the Elimination of Re-entry Radio Blackout". *Proc. IRE* 49, 1825-30, 1961.
4. BACHYNSKI, M. P., GRAF, K. A., "Electromagnetic Properties of Finite Plasmas", *RCA Rev.* XXV, 3-53, 1964.
5. BACHYNSKI, M. P., CLOUTIER, G. G., "Free Space Microwave Techniques for Plasma Measurements". *RCA Rev.* XXV, 168-99, 1964.
6. OSBORNE, F. J. F., BACHYNSKI, M. P., "A Turnstile Multiple Probe Polarimeter for Plasma Diagnostics". *RCA Victor Res. Report* 7-801-17, 1962.
7. BACHYNSKI, M. P., OSBORNE, F. J. F., "Microwave Techniques for Measurements of Transient Plasma Properties". *Gas Discharges and the Electrical Supply Industry*, - ed. J. S. Forrest, P. R. Howard, D. J. Little, 553-64. Butterworth, London, 1962.
8. OSBORNE, F. J. F., "A Multiple Probe Microwave System for Plasma Studies". *Can. J. Phys.* 40, 1620-5, 1962.
9. MULLIN, C. R., HODARA, H., "Elimination of Re-entry Radio Blackout". *Proc. IRE* 50, 2108-10, 1962.
10. FISCHER, S. T., "Magnetoplasmas and Re-entry Radio Blackout". *Proc. IEEE* 51, 1029-30, 1963.



## CHAPTER 4-3

ELECTRO-MAGNETIC WAVE PROPAGATION  
THROUGH AN IONIZED GAS LAYER AS AN OPTIMAL  
PROCESS

M. Z. V. KRZYWOBLOCKI

Michigan State University

## SUMMARY

The author attacks analytically the following problem: Suppose a spaceship enters the atmosphere around a planet at a very high speed. Presumably, there develops around the spaceship a layer of an ionized gas. Obviously, the technique proposed below refers to any kind of atmosphere and gas, i.e. neutral as well. The wave-propagation from and to the inside of the ship interferes with the layer around the ship. The problem is to calculate the e.m. wave-propagation through the layer with a minimum possible energy loss of the e.m. character. The problem is attacked by means of the most recent techniques developed in the theory of optimal processes, particularly those referring to continuous media. The problem consists of two parts. First, the flow of the gaseous medium around a body is described by means of a hydrodynamic system of partial differential equations. In the case of a highly rarefied gas (hypersonics) the dynamics of the gas may be described by means of the tool of the kinetic theory of gases followed usually by an averaging process. This implies that in the final form equations describing the hydrodynamic phenomena are partial differential equations involving continuous functions (for illustrative example one can mention Burnett-Enskog, Grad equations, etc.). This system is subject to some (usually two-curve) boundary conditions. On this system there is superimposed the system of electromagnetic equations (Maxwell's) satisfying again some prescribed boundary conditions. A solution of this e.m.-hydrodynamic system furnishes the distribution of the characteristic variables of the ionized layer around the body: velocity, pressure, density, temperature, intensities of the induced magnetic and electric fields, degree of the ionization (which may depend upon the temperature, say), electric conductivity, etc. The above takes care of the phenomena outside the body. The second part of the problem is the following: Inside the body there exists a source of e.m. waves, moving outward and passing through the ionized layer. Equations governing this part of the complex phenomenon in question are the Maxwell equations. These, after a certain modification and recombination, are representable as a single second-order linear partial differential equation (see Bremmer's works, electric and magnetic solutions, previous works of the present author, etc.). The important factor in this part of the problem is the permittivity of the medium, which parameter depends upon the variables (like temperature, degree of

ionization, etc.) of the layer outside the body and is the main link between the two parts of the problem: hydrodynamic and e.m. wave-propagation. The permittivity and the frequency of the wavy motion are the two important parameters which are considered to be the control parametric functions of the problem as a whole. On this base, we can now approach to the main part of the mathematical analysis, namely to the optimization technique. Assume a certain dynamic system governed by some laws of motion, continuity and energy, equipped with certain control functions on whose position and magnitude the status of the system depends. The governing equations are partial differential equations, the functions occurring in the problem are continuous or at most, of bounded variations. The system of equations is subject to certain boundary conditions (two-curve initial or boundary-value problems). The fundamental problem can be formulated as follows: In the function space  $W$ , two points  $w_0$  and  $w_1$  are given. Among all the admissible control functions which transfer the (function) point from the position  $w_0$  to the position  $w_1$  (if such control functions exist), find one for which the functional (integral) of the known and given form takes on the least possible value. The functional in question (to be minimized) involved the integrand which assures the optimum conditions for the propagation of the e.m. wave through the layer of the plasma. The author may mention the possible mathematical tools available today to solve a problem of this nature (calculus of variations, optimum processes, etc.). He concentrates on the "General Optimum Principle", applicable to continuous media. One may consider it to be some sort of a generalization of the well-known Pontryagin Maximum Principle, which is applicable only to discrete point systems (ordinary differential equations). The author presents and discusses thoroughly this principle in some of its details and phases. To demonstrate its applicability, the author presents an example of a spherical (for simplicity's sake) space vehicle, provides all the necessary equations of the e.m.-hydrodynamic character as well as the equation for the wave-propagation and the functional to be optimized. A demonstration of how to approach the problem of solving the final system closes the work.

#### MATHEMATICAL FORMULATION OF THE GENERALIZED PROBLEM OF OPTIMUM CONTROLS

##### **Mathematical formulation of the generalized optimum principle –**

Consider the behavior of a dynamic system or sub-system of a matter-full or matter-less continuous medium whose state at any instant of time is characterized by  $n$  real numbers,  $w^1, w^2, \dots, w^n$  (these may be velocity components, coordinates, density, pressure, energy of any kind, etc.). The function space  $W$  of the variable  $w = (w^1, w^2, \dots, w^n)$  is the function space of the system under consideration. The state (motion) of the system consists of the fact that variables  $w^1, w^2, \dots, w^n$  change with position. It is assumed that the state (motion) of the system can be controlled, i.e. that the system may be equipped with controllers on whose state (location, characteristic properties, etc.) the state (motion) of the dynamic system depends. The state of the controllers is characterized by vector  $u$ , of a certain control region  $U$ , which may be any

set in some function space  $E_r$ . Giving a vector  $u = (u^1, u^2, \dots, u^r)$  is equivalent to giving a numerical system of parametric functions  $u^1, u^2, \dots, u^r$ . Often the region  $U$  may be a closed region in  $E_r$  (a closed and bounded set in the  $r$ -dimensional function space  $E_r$ ). We call  $U$  the control region. Thus,  $U$  is a certain set in the function space of the variables  $u^1, u^2, \dots, u^r$ , and  $u = (u^1, \dots, u^r)$  is its vector located arbitrarily in  $U$ . We call every function  $u = u(x^1, x^2, \dots, x^m)$ , where  $x = (x^1, \dots, x^m)$  are space coordinates, defined in a space region  $x_0^1 \leq x^1 \leq x_1^1; x_0^2 \leq x^2 \leq x_1^2, \dots$ , with  $u \in U$ , a control. We assume some conditions superimposed upon  $u(x)$  like piecewise continuity, differentiability (admissible controls). The admissible control functions are continuous for all  $(x)$  under consideration, with the exception of only a finite number of  $(x)$ , at which  $u(x)$  may have discontinuities of the first kind, i.e. there is assumed the existence of finite limits.

We assume that the laws of motion of the dynamic system can be given in the form of a system of partial differential equations:

$$L(w) = \frac{Dw^i}{Dt} = f^i(w^1, \dots, w^n, u^1, \dots, u^r) = f^i(w, u) \quad (1)$$

where the partial differential operator  $L(w)$  is of the form (in coordinates of a three-dimensional space  $X(x^1, x^2, x^3)$ ):

$$\frac{D}{Dt} = \frac{\partial}{\partial x} \frac{dx}{dt} + \frac{\partial}{\partial y} \frac{dy}{dt} + \frac{\partial}{\partial z} \frac{dz}{dt} \quad (2)$$

with the symbols  $dx/dt$ , etc., denoting from the physical standpoint the velocity components in the corresponding directions:

$$dx/dt = V_1; dy/dt = V_2; dz/dt = V_3 \quad (3)$$

Eq. 1 can be written in a vector form:

$$Dw/Dt = f(w, u) \quad (4)$$

where  $f$  is the vector with the components  $f^1(w, u); f^2(w, u); \dots; f^n(w, u)$ . The functions  $f^i$  are defined for  $w \in W$  and for  $u \in U$ . They are assumed to be continuous in the variables  $w^1, w^2, \dots, w^n, u^1, u^2, \dots, u^r$  and continuously differentiable with respect to  $w^1, w^2, \dots, w^n$ .

Suppose an additional function  $F^0(w^1, w^2, \dots, w^n, u) = F^0(w, u)$  is given which is defined and is continuous together with  $\partial F^0 / \partial w^i, i = 1, 2, \dots, n$ , on  $W \times U$ . Then the problem of finding the optimum controls can be formulated as follows: In the function space  $W$  there are given  $w_0$  and  $w_1$ . Among all the admissible control functions  $u = u(x)$ , which transfer  $w(x)$  from  $w_0$  to  $w_1$  (provided that such control functions exist), find one for which the functional

$$J = \int_{x_0}^{x_1} F^0(w(x), u(x)) dx \quad (5)$$

takes the least possible value. Obviously, here  $w(x)$  is the solution of Eq. 4 with the initial conditions  $w(x_0) = w_0$  corresponding to the control  $u(x)$  and passing through  $w(x_1)$ . Let us note that for fixed  $w_0$  and  $w_1$  the upper and lower limits in Eq. 5 are not fixed numbers, but depend upon the choice of

the control function  $u(x)$  which transfers  $w(x)$  from  $w_0$  to  $w_1$ . Problems with fixed  $(x_0, x_1)$  and given  $(w_0, w_1)$  present particular cases of this type of problem. The control  $u(x)$  which furnishes the solution of the problem cited above is called an optimal control function corresponding to a transition from  $w_0$  to  $w_1$ .

We may reformulate the problem. Let us introduce a new coordinate into the system of coordinates  $w^1, w^2, \dots, w^n$  in  $W$ , namely  $w^0$  defined in the following way:

$$w^0 = \int_{x_0}^x F^0(w(x'), u(x')) dx' = K \quad (6)$$

One can calculate the derivatives  $\partial K / \partial x^i$  and construct a function:

$$f^0(w, u) = V_1 \frac{\partial K}{\partial x} + V_2 \frac{\partial K}{\partial y} + V_3 \frac{\partial K}{\partial z} = \frac{DK}{Dt} \quad (7)$$

Then we can write:

$$\frac{Dw^0}{Dt} = f^0(w^1, w^2, \dots, w^n, u) \quad (8)$$

Introducing the vector:

$$w = (w^0, w^1, w^2, \dots, w^n) = (w^0, w) \quad (9)$$

in the  $(n+1)$ -dimensional function space  $W$ , we consider the system of differential equations:

$$Dw/Dt = f(w, u) \quad (10)$$

where  $f(w, u)$  is the vector in  $W$  with coordinates  $f^0(w, u), f^1(w, u), \dots, f^n(w, u)$ ; Eq. 10 can be written in the form:

$$Dw^i/Dt = f^i(w^1, w^2, \dots, w^n, u^1, \dots, u^r), i = 0, 1, \dots, n \quad (11)$$

where the right-hand side does not depend upon the coordinate  $w^0$  of the vector  $w$ .

Let  $u(x)$  be an admissible control function transferring  $w_0$  to  $w_1$ , and let  $w = w(x)$  be the corresponding solution of Eq. 4 with initial condition  $w(x_0) = w_0$ . We denote the point  $(O, w_0) = (O, w_0^1, \dots, w_0^n)$  of  $W$  by  $w_0$  with  $(w_0^1, w_0^2, \dots, w_0^n)$  being coordinates of  $w_0$  in  $W$ . Then the solution of Eq. 10 with the initial condition  $w(x_0) = w_0$ , corresponding to the control  $u(x)$ , is defined in the entire region  $x_0 \leq x \leq x_1$  and has the form:

$$w^0 = \int_{x_0}^x F^0(w(x'), u(x')) dx' \quad (12)$$

$$w = w(x) \quad (13)$$

For  $x = x_1$ , one has:

$$w^0 = \int_{x_0}^{x_1} F^0(w(x), u(x)) dx = J, w = w_1 \quad (14)$$

which means that the solution  $w(x)$  of Eq. 10 with the initial condition  $w(x_0) = w_0$  passes through  $w = (j, w_1)$ . Assume in  $W$  a line "k" passing through the point  $w = (0, w_1)$  and parallel to the  $w^0$  axis; to construct it we find the locus of points in  $W$  passing through the point  $w = (0, w_1)$  and having coordinates  $(\xi, w_1)$  where the number  $\xi$  is arbitrary. The solution  $w(x)$  passes through a point on "k" having the coordinates  $w^0 = j$  for  $w = w_1(x = x_1)$ . On the other hand, suppose that  $u(x)$  is an admissible control of such a character that the corresponding solution  $w(x)$  of Eq. 10 with initial condition  $w(x_0) = w_0 = (0, w_0)$  for some  $(x_1)$  passes through  $w_1 \in k$ , which has the coordinate  $w_0 = j$  and  $w = w_1(x = x_1)$ . Then, the control function  $u(x)$  transfers  $w \in W$  from  $w_0$  to  $w_1$  and the functional Eq. 5 takes on the value  $j$ . We can express the above problem in the following form:

In the  $(n + 1)$ -dimensional function space  $W$  the point  $w_0 = (0, w_0)$  and the line "k" are given. The line "k" is assumed to be parallel to the  $w^0$  axis, and to pass through the point  $(0, w_1)$ . Among all the admissible controls  $u = u(x)$ , having the property that the corresponding solution  $w(x)$ , of Eq. 10 with initial condition  $w(x_0) = w_0$  intersects the line "k" find the one whose point of intersection with "k" has the smallest coordinate  $w^0$ .

The formulation of the optimal problem, cited above, is similar to the formulation of the optimal problem in Pontryagin's maximum principle. There is a difference in the structure of the function spaces. In Pontryagin's maximum principle one deals with processes which can be described by a system of ordinary differential equations. We operate here in the vector space  $W$  of the vector variable  $w = (w^1, \dots, w^n)$ . The state of the object at any instant of time is characterized by "n" real numbers  $w^1, \dots, w^n$ . The space  $W$  is the phase space of the object under consideration, and  $w = w(t)$  are functions of only one variable,  $t$ . The optimal trajectories  $w(t)$  are curves. In the present problem the function spaces  $W$  (or  $W$ ) refer to the variable  $w = (w^1, \dots, w^n)$ , where  $w^i = w^i(x^1, \dots, x^m)$ , are functions of  $m$  variables  $x^m(t)$ . The control functions are of the analogous forms,  $u = u(x(t))$ . Both  $w^i$  and  $u$  are hypersurfaces of the corresponding order. The control function  $u(x)$  which yields the solution of the optimal problem, an optimal control corresponding to a transition from  $w_0$  to  $w_1$ , represents geometrically an optimal hypersurface. Thus, the generalized problem of controls consists of finding the optimum control function and of the corresponding optimal hypersurfaces.

Equations describing the system discussed above may possess partial derivatives of any order. By the proper substitutions we may always include the derivatives into the system of functions themselves. For example,  $\partial^2 w^2 / \partial x \partial y$  may be treated in the following way:

$$\partial w^2 / \partial x = w^p; \partial^2 w^2 / \partial x \partial y = \partial w^p / \partial y = w^{p+1} \quad (15)$$

where the new functions  $w^p, w^{p+1}, (p > n)$ , have to be added to the set of functions  $w^1, \dots, w^n$  in Eq. 1. In this case the differential operator  $D/Dt$ , Eq. 2, should refer to the representation in the form of Eq. 2 and to any other form like  $\partial/\partial x$ , etc. Hence, we may remodel Eq. 2 in the sense:

$$\begin{aligned} D/Dt &= \partial/\partial x(dx/dt) + \partial/\partial y(dy/dt) + \partial/\partial z(dz/dt) \text{ or} \\ &= \partial/\partial x, = \partial^2/\partial x \partial y, \text{ etc.} \end{aligned} \quad (16)$$

The generalized problem of the optimal processes as formulated above (generalized optimum principle) may have no solution in some cases. The reason is the following: In the classical formulation of the mathematical theory of optimal processes by Pontryagin and his co-workers (5) one deals with ordinary differential equations. In this approach there appear convex cones as the essential element of the mathematical formalism. When dealing with the partial differential equations, having prescribed boundary conditions, the cones in question may be concave. This would result in an invalidation of the maximum principle. On the other hand, we demonstrate below that for our purposes we need to reformulate the generalized optimum principle cited above. This reformulation may remove the discussed difficulties.

**Generalized optimum boundary value principle** – Assume that the control functions are functions of the boundary conditions, or of the boundary and initial conditions. Moreover, they have to be functions of the variable  $w(x)$ .

Briefly:

$$\mathcal{J} = \int_{x_0}^{x_1} F^0\{w(x), u(w_0(x_0), w(x))\} dx = \int_{x_0}^{x_1} F^0(w(x), w_0(x_0)) dx \quad (17)$$

We assume that  $V_0$ , called the boundary value region, is a certain set in the function space of the variables  $w_0^1, w_0^2, \dots, w_0^n$ , and  $w_0 = (w_0^1, \dots, w_0^n)$  is its vector located in  $V_0 \in W$ . We call every function  $w_0 = w(x_0^1, x_0^2, \dots, x_0^m)$ , where  $x_0 = (x_0^1, \dots, x_0^m)$  are space coordinates, with  $w_0 \in V_0$  a boundary condition. Since  $V_0$  is a set in the function space of the functions  $w^1, w^2, \dots, w^n$ , each boundary condition  $w(x_0) = (w_0^1(x_0), \dots, w_0^n(x_0))$  is a vector function whose region is in  $V_0 \in W$ . Obviously, we deal with admissible boundary conditions. We specify that  $w_0^{(1)} \leq w_0 \leq w_0^{(2)}$  with  $w_0^{(1)} \in V_0, w_0^{(2)} \in V_0$ , but that  $w_1$  is not in  $V_0$ . Briefly, the parametric boundary conditions are specified in a certain subdomain  $V_0$  which does not contain  $w_1$ , i.e.  $w_1$  is located outside  $V_0$ . The remaining part of the reasoning, presented earlier in this chapter concerning the Generalized Optimum Principle preserves its validity. Thus, we can formulate the generalized optimum boundary-value principle: In the  $(n+1)$ -dimensional function space  $W$  the set  $V_0 = (O, w_0^1, w_0^2, \dots, w_0^n) = (O, V_0)$  with  $(w_0^1, w_0^2, \dots, w_0^n)$  being coordinates of  $w_0$  in  $V_0 \in W$  and the line “ $k$ ” are given. The line “ $k$ ” is assumed to be parallel to the  $w^0$  axis (this line “ $k$ ” is made up of all the points  $(\xi, w_1)$  where the number  $\xi$  is arbitrary) and to pass through the point  $(O, w_1)$ . Among all the admissible boundary conditions  $w_0$ , having the property that the corresponding solution  $w(x)$  of the system of equations in question with the boundary condition (to be found)  $w(x_0) = w_0$  intersects the line “ $k$ ”, find the one whose point of intersection with “ $k$ ” has the smallest coordinate  $w^0$ . Returning to the particular case of a tri-fluid plasma, one may see very easily that the boundary conditions should be admissible, i.e. they should be limited to some appropriate values in  $V_0$  (boundary-value region). For example, if the temperature of plasma during re-entry is too high, the neutral component fluid cannot be in a stable status, i.e. the neutral fluid will be ionized.

**Generalized upper bound optimum principle** – We shall briefly discuss the third possible technique in attacking the problem of the controllability

of plasma. Assume that we deal with the neutral fluid which is a component of a three-fluid plasma. Assume that we select the upper bounds for the dependent variables (pressure, temperature, etc.) characterizing the neutral fluid. The upper bounds are chosen so that the neutral fluid will not be subject to the ionization process. The equations governing the motion of the neutral fluid are the electromagneto-hydrodynamic equations. The neutral fluid may be subject to the transport phenomena (mass, heat, etc.) from the neighboring fluids. The integral functional to be satisfied states that the square of the difference between the temperature, existing in the domain, and its upper bound, should be a minimum. The integral, to be optimized, may extend over the entire domain and the entire interval of time.

Below, we present the mathematical formalism of the generalized optimum principle.

**Formulation of the theorem** – We proceed to formulate the theorem which yields the solution to the problem in question. Consider the system Eq. 11 and the additional system in the variables  $\psi_i$ 's ( $i = 0, 1, \dots, n$ ):

$$\frac{D\psi_i}{Dt} = - \sum_{\alpha=0}^n \frac{\partial f^\alpha(w, u)}{\partial w^\alpha} \psi_\alpha, i = 0, 1, \dots, n \quad (18)$$

Suppose, we choose an admissible control  $u(x)$ ,  $x_0 \leq x \leq x_1$ , and have the corresponding trajectory  $w(x)$  of the system Eq. 11 with the initial conditions  $w(x_0) = w_0$ , then the system Eq. 18 takes the form:

$$\frac{D\psi_i}{Dt} = - \sum_{\alpha=0}^n \frac{\partial f^\alpha(w(x), u(x))}{\partial w^\alpha} \psi_\alpha, i = 0, 1, \dots, n \quad (19)$$

The homogeneous system may be linear or not, depending upon the form of the operator  $D/Dt$ . We may attempt to combine Eqs. 11 and 19 by choosing a function  $M$  of the variables  $w^1, \dots, w^n; \psi_0, \psi_1, \dots, \psi_n; u^1, \dots, u^r$ :

$$M(\psi, w, u) = (\psi, f(w, u)) = \sum_{\alpha=0}^n \psi_\alpha f^\alpha(w, u) \quad (20)$$

Then the systems Eq. 11 and 19 can be written in the form:

$$Dw^i/Dt = \partial M / \partial \psi^i, i = 0, 1, \dots, n \quad (21)$$

$$D\psi^i/Dt = - \partial M / \partial w^i, i = 0, 1, \dots, n \quad (22)$$

Taking an arbitrary admissible control  $u(x)$  and the initial conditions  $w_0$ , we can find the corresponding trajectory  $w(x(t))$  from Eq. 21. After that we can find solutions to the system Eq. 22  $\psi(x) = (\psi_0(x), \psi_1(x), \dots, \psi_n(x))$  corresponding to the functions  $w(x)$  and  $u(x)$ . For fixed values of  $\psi$  and  $w$  the function  $M$  is a function of  $u \in U$ . We denote the least upper bound of this function by  $M_m(\psi, w)$ , i.e.:

$$M_m(\psi, w) = \sup M(\psi, w, u) \quad (23)$$

Thus, when the (continuous) function  $M$  achieves its upper bound on  $U$ , then  $M_m$  is the maximum of the values of  $M$  for fixed  $\psi$  and  $w$ . We propose the theorem: Theorem A. Let  $u(x)$ ,  $x_0 \leq x \leq x_1$ , be an admissible control chosen

so that the corresponding trajectory  $w(x)$  begins at the point  $w_0$  at the location  $x_0$  and passes at a  $x_1$  through a point on the line "k". In order that  $w(x)$  and  $u(x)$  be optimal it is necessary that there exists a continuous vector function  $\psi(x) = (\psi_0(x), \psi_1(x), \dots, \psi_n(x))$ , which is different from zero, which corresponds to  $w(x)$ ,  $u(x)$  in question, and such that:

(a) for every  $x$ ,  $x_0 \leq x \leq x_1$ , the function  $M(\psi(x), w(x), u)$  of the variable  $u \in U$  attains its maximum at the point  $u = u(x)$ :

$$M(\psi(x), w(x), u) = M_m(\psi(x), w(x)) \quad (24)$$

(b) at the terminal position,  $x_1$ , the following relations are fulfilled:

$$\psi_0(x_1) \geq C_1; M_m(\psi(x_1)) \leq C_2 \quad (25)$$

where the constants  $C_1, C_2$  will be determined in the proof of the theorem A, which is now under investigation. Theorem A allows us to get, from the trajectories which begin at  $w_0$  and end on some point of "k", those trajectories and controls which satisfy all the conditions. We have  $2n + 3$  relations Eqs. 21, 22 and 24 for  $2n + 3$  variables  $w, \psi, u$ . The relation Eq. 24 is not in a differential form, and the number of differential equations is equal to  $2n + 2$ ; hence, solutions depend upon  $2n + 2$  parameters (i.e. initial conditions). However, one of these parameters is redundant; namely, from Eqs. 19 and 20 one may see that the functions  $\psi_i$  are defined only up to a common multiple; the function  $M$  is homogeneous in  $\psi_i$ . Moreover, one of the parameters is determined by the condition Eq. 25: thus the number of parameters is  $2n$ . Since the trajectory  $w(x)$  passes through  $w_0$  at  $x = x_0$  and through a point on "k" for  $x_1 > x_0$ , the difference  $x_1 - x_0$  is also a parameter and the number of parameters is equal to  $2n + 1$ .

#### EQUATIONS OF MOTION AND WAVE PROPAGATION IN THE IONIZED SHEATH ON THE SURFACE OF THE SPACE VEHICLE

**Equations of motion outside the space vehicle** – Let us assume the following dynamic system: a space vehicle of a spherical shape moves uniformly in a rarefied gaseous medium with a high speed. The motion is considered to be steady and the problem is divided into two parts. The first system of equations refers to the motion of the ionized medium outside the space vehicle. The second system of equations describes the physical phenomenon of the electromagnetic wave propagation from a source located in the center of the spherical vehicle. At first we consider the motion of the ionized medium outside the vehicle. Assume, for illustrative examples, a fully ionized plasma. In a steady motion the equation of motion derived from the Boltzmann equation, (9), becomes for ions:

$$\vec{v}_i \cdot \nabla \vec{v}_i = \zeta e (cm_i)^{-1} (\vec{E} + \vec{v}_i \times \vec{B}) - (m_i n_i)^{-1} (\nabla \cdot \vec{p}_i - \vec{P}_{ie}) - \nabla \phi \quad (26)$$

where the used symbols denote:

- $\zeta e c^{-1}$  = particle charge;  $c$  = speed of light;
- $m_i$  = ion mass;
- $\vec{v}_i$  = ion velocity;
- $\vec{E}, \vec{B}$  = electric and magnetic fields;
- $\zeta$  = particle charge, in units of the proton charge;
- $e$  = charge of proton;



- $n_i$  = particle density;  
 $\phi$  = gravitational potential;  
 $\vec{\psi}_i$  = the stress tensor;  
 $\vec{P}_{ie}$  = the total momentum transferred to the ions per unit volume by collision with the electrons.

The mean velocity of the particles in an element of unit volume is given by:

$$\vec{v}_i = n_i^{-1} \sum \vec{\omega}_i \quad (27)$$

$\vec{\omega}_i$  = particle velocity, and

$$\vec{\psi}_i = m_i \sum (\vec{\omega}_i - \vec{v}_i) (\vec{\omega}_i - \vec{v}_i) \quad (28)$$

the summation extending over the unit volume. The equation of motion for electrons is obtained from Eq. 26 with  $\vec{v}_e$ ,  $n_e$ ,  $m_e$ ,  $\vec{\psi}_e$  and  $\vec{P}_{ei}$  replacing  $\vec{v}_i$ ,  $n_i$ ,  $m_i$ ,  $\vec{\psi}_i$  and  $\vec{P}_{ie}$  respectively, and with  $\mathcal{Z}$  set equal to  $-1$ . As it is well known in the simplest case  $\nabla \cdot \vec{\psi} = \nabla p$  ( $p_i$  or  $p_e$ ). For a gas containing only electrons and one type of positive ion, the macroscopic quantities  $\vec{v}$  and  $\vec{j}$  (current density) are defined by:

$$\vec{v} = \rho^{-1} (n_i m_i \vec{v}_i + n_e m_e \vec{v}_e) \quad (29)$$

$$\vec{j} = ec^{-1} (n_i \mathcal{Z} \vec{v}_i - n_e \vec{v}_e) \quad (30)$$

$$\rho = n_i m_i + n_e m_e \quad (31)$$

The equation of motion (for the macroscopic  $\vec{v}$ ) has the form:

$$(\vec{v} \cdot \nabla) \vec{v} = \rho^{-1} (\vec{j} \times \vec{B} - \nabla p - \rho \nabla \phi) \quad (32)$$

The generalized Ohm's law:

$$\vec{E} + \vec{v} \times \vec{B} + c(en_e)^{-1} (\nabla p_e - \vec{j} \times \vec{B}) - \eta \vec{j} = 0 \quad (33)$$

where  $\eta$  = electrical resistivity. Eqs. 32 and 33 have to be supplemented by the equations of continuity of matter and electric charge or the electrical equation of continuity of the plasma:

$$\nabla \cdot (\rho \vec{v}) = 0; \nabla \cdot \vec{j} = 0 \quad (34)$$

and by the Maxwell equations (in their most simplified forms):

$$\nabla \cdot \vec{E} = 4\pi c^2 \sigma; \nabla \times \vec{E} = 0; \nabla \cdot \vec{D} = \sigma \quad (35)$$

Or:  $\nabla \cdot \vec{E} = 4\pi ec(n_i \mathcal{Z} - n_e)$ .

$$\nabla \cdot \vec{B} = 0; \nabla \times \vec{B} = 4\pi \vec{j} \quad (36)$$

where  $\sigma$  = the density of electric charge. In the system above we have ten unknown variables:  $\vec{v}_i$ ,  $\vec{v}_e$ ,  $n_i$ ,  $n_e$ ,  $p_i$ ,  $p_e$ ,  $\vec{v}$ ,  $\vec{j}$ ,  $\rho$  and nine equations: Eqs. 26, 29, 30, 31, 32, 33, and 34. For  $B$  and  $E$  one has to use Eqs. 35 and 36. The equation of state for a perfect gas may be used to determine the temperature  $T$  of the gas as a total single fluid. The energy equation can be used in the form (7):

$$\begin{aligned} \frac{dE_{in}}{dt} + p \frac{d}{dt} (\rho^{-1}) - \vec{B} \cdot \frac{d}{dt} (\vec{B}^{(1)} \rho^{-1}) - \vec{E} \cdot \frac{d}{dt} (\vec{D} \rho^{-1}) = \\ = \rho^{-1} [\nabla \cdot (\partial \nabla T) + \Phi_d + j^2/g + W_r] \end{aligned} \quad (37)$$

$$\Phi_d = \mu \left\{ -\frac{2}{3} \operatorname{div} \vec{v} + 2 [(\vec{v}_{1,x1})^2 + (\vec{v}_{2,x2})^2 + (\vec{v}_{3,x3})^2] + \right. \\ \left. + (\vec{v}_{3,x2} + \vec{v}_{2,x3})^2 + (\vec{v}_{1,x3} + \vec{v}_{3,x1})^2 + (\vec{v}_{2,x1} + \vec{v}_{1,x2})^2 \right\} \quad (38)$$

where:

- $E_{in}$  = internal energy per unit volume;
- $\vartheta$  = heat conductivity coefficient;
- $W_r$  = intensity of the energy source;
- $\mu$  = coefficient of viscosity;
- $\vec{B}^{(1)}$  = magnetic induction =  $\mu_m \vec{B}$ ;
- $\mu_m$  = magnetic permeability;
- $\vec{D}$  = electric displacement (or induction) vector =  $\epsilon \vec{E}$ ;
- $\epsilon$  = permittivity (dielectric coefficient).

Eq. 37 allows us to select one more unknown variable,  $T$  say. The systems 26, 29, 30, 31, 32, 33, 34, 37 is now a determinate one. The internal energy is given by:

$$E_{in} = \frac{3}{2} (1 + \beta_E) n_K k_B T \quad (39)$$

$\beta_E$  = ratio of the energy contained by the internal degrees of freedom of the species over the energy of the external (translational) degrees of freedom;

$n_K$  = number density of species  $K$ ;

$k_B$  = Boltzmann's constant.

We divide the system of equations, derived above into two subsystems:

The main subsystem consists of Eqs. 26, 32 and 34, written in the form:

$$D\rho/Dt = -\rho \operatorname{div} \vec{v}, \quad (40)$$

and Eq. 37.

This subsystem of eleven equations can be remodelled so that it is representable in form of Eq. 11. On this subsystem there are superimposed the appropriate two-curve boundary conditions, corresponding to the boundary conditions in a boundary layer, i.e. zero or a finite slip velocity and the wall temperature at the surface of the body and the uniform flow conditions at infinity.

The auxiliary subsystem consists of all the remaining equations, including the Maxwell system.

**Electromagnetic wave propagation from a source inside the space vehicle** – We begin with the system of Maxwell's equations in the free space:

$$(a) \operatorname{curl} \vec{H} = c^{-1} \vec{D}_{,t} \quad (b) \operatorname{curl} \vec{E} = -c^{-1} \vec{B}_{,t} \quad (41)$$

$$(c) \operatorname{div} \vec{B} = 0; \quad \operatorname{div} \vec{D} = 0 \quad (42)$$

$$\vec{D} = \epsilon \vec{E}; \quad \vec{B} = \mu_m \vec{H}; \mu_m = 1 \quad (43)$$

Let us assume a monochromatic wave and the forms:

$$\vec{H} = \vec{h} \exp(-i\omega t); \vec{E} = \vec{e} \exp(-i\omega t); \omega = \text{constant} \quad (44)$$

$$\epsilon \equiv n^2(r), r^2 = x^2 + y^2 + z^2 \quad (45)$$

which says that the permittivity is only a function of the distance from the

center of the source located at the center of the sphere. Then one gets from Eqs. 41 to 43:

$$\text{curl } \vec{h} + i\omega c^{-1} n^2(r) \vec{e} = 0 \quad (46)$$

$$\text{curl } \vec{e} - i\omega c^{-1} \vec{h} = 0 \quad (47)$$

Bremmer (2), (3) has shown that the system (46), (47) has two particular solutions (called electric and magnetic), respectively:

$$\vec{e}_e = ic(\omega n^2(r))^{-1} \text{curl curl } [n(r) \Pi_e \vec{r}] \quad (48)$$

$$\vec{h}_e = \text{curl } [n(r) \Pi_e \vec{r}] \quad (49)$$

$$\vec{e}_m = i\omega(c n^2(r))^{-1} \text{curl } [n^2(r) \Pi_m \vec{r}] \quad (50)$$

$$\vec{h}_m = \text{curl } \{ (n^2(r))^{-1} \text{curl } [n^2(r) \Pi_m \vec{r}] \} \quad (51)$$

Inserting Eqs. 48 to 51 into the systems 46, 47 furnishes:

$$\text{curl } \vec{e}_e - i\omega c^{-1} \vec{h}_e = -ic\omega^{-1} \text{curl} \left\{ \vec{r} [n^{-1} \nabla^2 \Pi + (\omega^2 c^{-2} n - \frac{d^2}{dr^2} (n^{-1})) \Pi] \right\} \quad (52)$$

$$\text{curl } \vec{h}_m + i\omega c^{-1} n^2 \vec{e}_m = -\text{curl} \{ \vec{r} [\nabla^2 \Pi + \omega^2 c^{-2} n^2 \Pi] \} \quad (53)$$

Maxwell equations are satisfied if the scalar function  $\Pi$  satisfies an equation of the form:

$$\nabla^2 \Pi + \omega^2 c^{-2} n^2_{eff}(r) \Pi = 0, = f(r) \quad (54)$$

since  $\text{curl } [\vec{r} f(r)] = 0$ , where the so-called effective refractive index is:

$$n^2_{eff}(r) = n^2 - c^2 \omega^2 n \frac{d^2(n^{-1})}{dr^2} \quad (55)$$

for the electric solution,

$$n^2_{eff}(r) = n^2, \text{ for the magnetic solution.} \quad (56)$$

We use a notation for Eq. 54:

$$\nabla^2 \Pi + F(r^2) \Pi = 0, = f(r), \quad (57)$$

where  $F(r^2) \equiv \omega^2 c^{-2} n^2_{eff}(r)$  is only a function of  $r^2$ . This can be easily achieved by putting  $r = (t^2)^{1/2}$  and avoiding the possible singular points (like branch-points) by taking the positive sign in front of the square root and by using a single sheet from a multiple-sheet surface. Equation 54 is subject to boundary conditions for the variable function  $\Pi$  on the surface of the sphere ( $r = a$ ) and at infinity. These may be accepted in the form proposed by Bremmer (3):

$$\frac{\partial}{\partial r} (r \Pi) = a^{-1} \Gamma(r \Pi), \quad \text{at } r = a \quad (58)$$

$$\Gamma = \Gamma_e = i\omega(4\pi)^{-1} a n^2(a) \mathcal{Z}_e - a[n(a)]^{-1} n'(a) \quad (59)$$

$$\Gamma = \Gamma_m = 4\pi a \omega (ic^2 \mathcal{Z}_m)^{-1} \quad (60)$$

$n(a)$  = the atmospheric (gaseous) refractive index at the sphere's surface. The magnitudes  $\mathcal{Z}_e$  and  $\mathcal{Z}_m$  (the surface impedance,  $\mathcal{Z} = 4\pi c^{-1} E_1(H_0)^{-1}$  at  $r = a$ , depend on the ratio of the tangential components of the electric and

magnetic vectors at the solid body surface) must be known and given. For  $r = \infty$ ,  $\Pi = 0$ . Using the identity:

$$\operatorname{div}(\vec{v}\Pi) = \Pi \operatorname{div} \vec{v} + \vec{v} \cdot \operatorname{grad} \Pi \quad (61)$$

and multiplying Eq. 57 by  $\operatorname{div} \vec{v}$ , furnishes an equation which is nonlinear (in contrast to Eq. 57, which is linear) and more complicated than Eq. 57, but may be included into the system Eq. 11.

$$\frac{D\Pi}{Dt} = F^{-1}(r^2) \operatorname{div} \vec{v} \nabla^2 \Pi + \operatorname{div}(\vec{v} \Pi) \quad (62)$$

with the B. C., Eq. 58, and  $\Pi(r = \infty) = 0$

**Electrical resistivity** – Let us assume, for illustrative purposes, the simplest possible form for the electrical resistivity (9):

$$\eta = c(ne)^{-1} P_{ei} j^{-1} \text{ or } = me^2 \nu / (ne^2) \quad (63)$$

where  $\nu$  is the collision frequency for each electron. This elementary equation for  $\eta$  is only an approximation. With this definition,  $\eta$  is directly related to the heating effect produced by the flow of current through a resistive medium. The power dissipated into heat per unit volume equals the force on the electrons, resulting from ion impact, times the mean drift velocity of electrons relative to the ions. The first of these two quantities is simply  $\vec{P}_{ei}$ , while the latter is  $cj(ne)^{-1}$ . Use of the definition gives us directly the rate of Ohmic, or Joule, heating, equal to  $\eta j^2$ . Thus the coefficient  $\eta$  has a simple physical meaning in terms of the dissipation of energy by an electric current. Since the inverse of  $\eta$  is the electric conductivity,  $\sigma$ , we may refer to the calculation of the conductivity tensor  $\vec{\sigma}$  in (1) ( $\vec{j} = \vec{\sigma} \cdot \vec{E}$ ) based upon the Boltzmann theory. From this it is seen that  $\vec{\sigma}$  depends upon the temperature of plasma. Allis (1) and his collaborators furnish the following formula for the value of  $\vec{\sigma}$  for a Maxwellian distribution:

$$\vec{\sigma} = \vec{U} \cdot \vec{\sigma} \vec{U}^{-1}; \quad \sigma' = U \cdot \sigma U^{-1} \quad (64)$$

$$U = 2^{-1/2} \begin{bmatrix} 1 & -j & 0 \\ 1 & j & 0 \\ 0 & 0 & 2^{1/2} \end{bmatrix}; \quad U^{-1} = 2^{-1/2} \begin{bmatrix} 1 & 1 & 0 \\ j & -j & 0 \\ 0 & 0 & 2^{1/2} \end{bmatrix} \quad (65)$$

$$\sigma'_{ij} = Ne^2(m\omega_b)^{-1}v_T^{-4} \int_0^\infty \exp\{-j[(\omega - j\nu)\omega_b^{-1} \mp 1]2x\} - \\ - 2k_\parallel^2 v_T^2 \omega_b^2 x^2\} dx \cdot \int_0^\infty w^3 \mathcal{J}_0(2k_\perp w \omega_b^{-1} \sin x) \exp(-\frac{1}{2} w^2 v_T^{-2}) dw \quad (66)$$

- $N$  = particle density;
- $m$  = particle mass;
- $\omega_b$  = cyclotron frequency =  $-em^{-1}\vec{B}_0$ ;
- $\vec{B}_0$  = static magnetic field;
- $v_T^2$  =  $eTm^{-1}$  (thermal speed);
- $j^2$  =  $-1$ ;
- $u, w, \phi$  = coordinate system in the velocity space;

$$\vec{v} = \vec{a}_x w \cos \phi + \vec{a}_y w \sin \phi + \vec{a}_z u; \quad (67)$$

$a_x, a_y, a_z$  = unit vectors along the  $x$ -,  $y$ -, and  $z$ - axes;

$\nu$  = collision frequency;

$\vec{k}$  = propagation vector;

$\parallel, \perp$  = parallel and perpendicular components of any field vector relative to  $\vec{B}_0$ ;

$\vec{B}$  = wave magnetic field;

$l, r$  = left and right for rotating components of any field vector relative to  $\vec{B}_0$ ;

$J_0(\zeta)$  = Bessel function.

The double sign  $\mp$  in Eq. 66 refers to  $(l)$  or  $(r)$ . The tensor dielectric coefficient has the form (1):

$$\vec{\epsilon} = \vec{I} + \vec{\delta}(j\omega\epsilon_0)^{-1} \quad (68)$$

$\vec{I}$  being the unity matrix and  $\epsilon_0$  the permittivity of free space. Using the tensor  $\vec{\epsilon}$ , Eq. (43)<sub>1</sub>, should be changed to  $\vec{D} = \vec{\epsilon} \cdot \vec{E}$ .

**Energy in a wave** – The energy can be supposed to be distributed throughout an electromagnetic field at the rate of:

$$G = (8\pi)^{-1} (\epsilon E^2 + \mu_m H^2) \text{ ergs per unit volume.} \quad (69)$$

The most important property of electromagnetic waves is that they convey energy at the rate indicated by Eq. 69. What is actually observable is usually not the energy density carried along with the waves, but the amount of energy that flows per second across unit area of a plane drawn perpendicular to the direction of propagation of the waves equal to  $I = cG$ ,  $c$  = the velocity of the wave.

**The final system** – The final system of equations consists of:

- (a) The subsystem of equations of motion in the ionized sheath on the surface of the space vehicle given under the heading Equations of Motion Outside the Space Vehicle with the B.C. at the surface of the body and at infinity; this includes both the main subsystem and the auxiliary subsystem;
- (b) the subsystem of the electro-magnetic wave propagation, Eq. 62, with the B.C., Eq. 58, and  $\Pi(r = \infty) = 0$ . Both subsystems (i), (ii) are interrelated by means of the  $n_{eff} = n_{eff}(\vec{\delta}(T))$ , and  $\omega$ .

#### FORMULATION OF THE PROBLEM

**Fundamental system** – A space vehicle of a circular shape possesses inside itself a source of electromagnetic waves. Suppose, due to the limitations in the weight increase of the space vehicle, the intensity of the source is bounded, i.e. we cannot cross a certain intensity limit. Consider the space vehicle and the surrounding rarefied gas being at rest. Let the surrounding atmosphere be spherically stratified. The task is to find a solution to the problem of the wave propagation through such a stratified rarefied atmosphere. This problem was attacked in the past by Pryce (6), Bremmer (3), and recently by v. Krzywoblocki (4) with the use of the Bergman integral operator. The starting equation is Eq. 54 with the B.C. given by Eqs. 58 to 60 for  $r = a$ ,

and  $\Pi_0 \rightarrow 0$  for  $r \rightarrow \infty$ . (All the variable dependent functions and parameters in the fundamental system are denoted by the subscript "o".) The coefficient  $n_{eff0}$  and the frequency  $\omega_0$  are parameters. We solve Eq. 48 for various values of  $n_{eff0}$  and  $\omega_0$ , and next we calculate the magnitude  $G_0$ , Eq. 69. This must be smaller or at most equal to the magnitude of the energy per unit volume which can be supplied by the mechanical unit inside the space vehicle. We call this dynamical system the "fundamental system". The final solution of the fundamental system may be represented in the form of tables and diagrams.

**Actual system** – The actual system of equations is shown under the heading Energy in a Wave with the corresponding B.C. This system is representable in the form Eq. 4. As the components of the vector "w" we choose the components of:  $\vec{v}_i$ ,  $\vec{v}_e$ , Eq. 26;  $\vec{v}$ , Eq. 32;  $\rho$ , Eq. 40;  $E_{in}$ , Eq. 37;  $\Pi$ , Eq. 62. Attention is called to the fact that we are using two different forms of the Maxwell system, Eqs. 35, 36 and 41 to 43. This is so since one system refers to the plasma flow near the body and the other to the electromagnetic wave propagation. In the system (35) it may be more appropriate to use the last form  $\nabla \cdot \vec{D} = \sigma$ . The remaining equations are auxiliary equations which are not included into the main system, but, of course, must be solved. The mathematical formalism, discussed below, explains the entire procedure in more detail. The system is subject to the boundary conditions given under the heading The Final System at the surface of the body (space-vehicle) and at infinity for both subsystems. The electromagneto-hydrodynamic subsystem has velocities  $\vec{v}_i$ ,  $\vec{v}_e$ ,  $\vec{v}$ , density  $\rho$ , internal energy or temperature  $T$  with prescribed values at the surface of the body and infinity. These boundary conditions are identical to those known from the theory of the boundary layer in the classical fluid dynamics of magneto-hydrodynamics and plasma dynamics. In addition to the variables of the hydrodynamic nature in the ionized layer around the vehicle there exists an induced electromagnetic field due to the phenomenon of the ionization of the layer. It is superimposed upon the electromagnetic field due to the signal-sending source inside the vehicle. The Maxwell equations are valid only in those points of the medium in question in whose neighborhood the physical properties of the medium vary continuously. On the boundary of the flow field, the physical properties of the media may exhibit discontinuities. At a solid boundary, the electromagnetic properties of the plasma change abruptly to those of the solid. Across such a surface of discontinuity of electromagnetic properties, the following four conditions hold:

- (a) the transition of the normal component of the magnetic induction,  $\vec{B} = \mu_m \vec{H}$ , is continuous, i.e.

$$(\vec{B}_2 - \vec{B}_1) \cdot \vec{n} = 0 \quad (70)$$

where  $\vec{n}$  is the unit normal to the surface of discontinuity. Subscripts 1 and 2 refer to the values immediately on each side of the surface;

- (b) at the boundary

$$\vec{n} \times (\vec{H}_2 - \vec{H}_1) = \vec{j}_s \quad (71)$$

$\vec{j}_s$  = surface density current. For a finite electrical conductivity,  $\vec{j}_s$  is zero,

whereas for an infinite electrical conductivity,  $\vec{j}_s$  may be different from zero;

(c) at the boundary

$$\vec{n} \times (\vec{E}_2 - \vec{E}_1) = 0; \vec{n} \cdot (\vec{D}_2 - \vec{D}_1) = \rho_{es}$$

$\rho_{es}$  = the surface-free charge density.

For most of the problems in the rarefied magneto-gasdynamics, we may often, but not always, neglect the surface current density,  $\vec{j}_s$ , and the surface-free charge density,  $\rho_{es}$ . Hence, the boundary conditions become that both the tangential components of  $\vec{H}$  and  $\vec{E}$ , and the normal components of  $\vec{B}$  and  $\vec{D}$  are all continuous across a surface separating a body and a fluid. The B.C. for  $\vec{B}$ ,  $\vec{D}$ ,  $\vec{E}$ ,  $\vec{H}$ , of the magneto-gasdynamic system must be in full agreement with the B.C. of the wave-propagation system given on page 320. Moreover, the B.C. of the electromagnetic nature must be satisfied by the total electric and magnetic fields which are the sums of two fields due to the electromagnetic source inside the body and to the ionization layer around the body, respectively.

We assume that the frequency  $\omega$  and the effective refractive index,  $\eta_{eff}$  are control parameters of the system in question. To complete the system of equations discussed at the beginning of this chapter, we have to construct the functional to be minimized. As such, we choose the condition that the square of the difference between the rate of the electromagnetic energy of the fundamental system,  $G_0$ , Eq. 69, and the rate of the electromagnetic energy of the actual system,  $G$ , should be a minimum, i.e.

$$I = \int_{vol} (G_0 - G)^2 d \text{Vol} = \min., \delta I = 0 \quad (73)$$

$G$  given by Eq. 69 and the integral is taken over the entire domain of the electromagnetic wave propagation, i.e. from the surface of the space vehicle up to infinity. This will assure us a correct solution which will be contained within the allowable limits. In such a way the problem is reduced to the problem of the kind of optimal processes in continuous media discussed earlier.

**Mathematical aspects** – The equations which govern the optimal process are nonlinear partial differential equations subject to two-curve boundary conditions. There does not exist up to now any mathematical theory involving such boundary-value problems. Hence, some technique has to be proposed involving a remodelling of the system from a nonlinear one to a linear one. Concerning the part referring to the e.m. wave propagation, Eq. 62 is a nonlinear one, but the original Eq. 57 is linear. Thus, either one can use Eq. 57 including it into the system of auxiliary equations or one may linearize Eq. 62. The hydrodynamic system is always a nonlinear one. Concerning a solution of the two-curve boundary-value problem involving Eq. 57, the author has shown in a previous paper that the Bergman technique of linear integral operators gives a very elegant solution. An application of the technique of integral operators to equations of the kind of Eq. 62 is now under study by the author of the present paper. Bergman's technique involves multiple expansions in convergent series. Each series may contain in front of it a constant coefficient, unknown for the time being. Analogously,

particular solutions of the hydrodynamic system may be found by iteration of successive approximation procedure, or by a linearization and series expansion (an association of a finite system of nonlinear partial differential equations with an infinite system of linear partial or ordinary differential equations, which procedure is very well known). Due to the linearity, particular solutions multiplied by constant coefficients may be superimposed each upon the other. All the particular solutions of the wave equation mentioned above, do not need to satisfy the boundary conditions on the surface of the vehicle, but should approach to zero for  $r \rightarrow \infty$ . This can easily be achieved by expansions in series of functions with powers  $r^{-n}$ , ( $n > 0, = 1, 2, \dots, \dots, n, \dots$ ) in front of them. All the particular solutions of the hydrodynamic equations should satisfy given values of the dependent variables when  $r \rightarrow \infty$ . These aspects are well known from the mathematical theory of the boundary layer.

Concerning the boundary conditions on the surface of the vehicle, we may propose more than one technique. The B.C. of the hydrodynamic system may be satisfied by the use of techniques known from the theory of the boundary layer. If these are not strong enough, we may use a variational principle. This may be illustrated on the function  $\Pi$  appearing in the e.m. wave propagation. Assume that the B.C. are given in the spherical coordinates  $(r, \theta, \phi)$  and are of the form (with " $a$ " being the radius of the spherical vehicle):

$$\Pi(r = a, \theta, \phi) = P(\theta, \phi; a), \quad 0 \leq \theta \leq 2\pi, \quad 0 \leq \phi \leq \pi \quad (74)$$

Assume that we obtained a particular solution for the function  $\Pi$  in form of a sum of series with constant coefficients in front of each, which coefficients,  $C_v$ , are unknown for the time being. We construct a functional:

$$I = f(C_v) = \int_{\theta=0}^{\theta=2\pi} d\theta \int_{\phi=0}^{\pi} d\phi [P(\theta, \phi; a) - \Pi(r = a, \theta, \phi)]^2 = \min \quad (75)$$

and require that  $f(C_v)$  be a minimum, i.e.  $\delta I = 0$ . Then we get:

$$\partial I / \partial C_v = 0, \quad v = 1, 2, \dots, N. \quad (76)$$

This represents an approximate solution of the boundary-value problem. The functional to be minimized, Eqs. 6 to 8, 73, has the form:

$$\frac{Dw^0}{Dt} = uK_x + vK_y + wK_z \quad (77)$$

$$K = \int_0^x dx' \int_0^y dy' \int_0^z dz' (G_0 - G)^2 \quad (78)$$

where possibly the lower limit maybe taken  $0 + \epsilon$ ,  $\epsilon$  small, to avoid a probable singularity in the center of the e.m. source. This completes the analytical formalism of the problem in question.

#### CONCLUDING REMARKS

The author presented the mathematical formalism of the problem of an electromagnetic wave propagation through an ionized gas layer as optimal



process with the use of continuous functions of several independent variables and partial differential systems. Due to the complexity of the system and the cost and time of programming of such a large system, involving series expansions and successive approximation or iterative procedures, no numerical example was calculated. The proof of the generalized optimum principle referring to partial differential systems and functions of several independent variables is not yet finished by the author. In practice the above system can be appropriately simplified. In a similar way one may formulate the Generalized Optimum Boundary Value Principle (see page 314), where the optimum initial values of dependent variables (temperature, velocity, etc.) must be found to assure the controllability of plasma.

## REFERENCES

1. ALLIS, W. P., BUCHSBAUM, S. J., and BERS, A., "Waves in Anisotropic Plasmas". M.I.T., Cambridge, Mass., 1963.
2. BREMMER, H., "Terrestrial Radio Waves - Theory of Propagation". Elsevier, London, 1949.
3. BREMMER, H., "On the Theory of Wave Propagation Through a Concentrically Stratified Troposphere With a Smooth Profile". J. Res., Nat. Bur. Stand. 64D, 5, 1960.
4. KRZYWOBLOCKI, V., M. Z., "Bergman's Integral Operator Method in the Theory of Wave Propagation through a Stratified Troposphere". (In press.)
5. PONTRYAGIN, L. S., BOLTYANSKII, V. G., GAMKRELIDZE, R. V., and MISHCHENKO, E. F., "The Mathematical Theory of Optimal Processes". Translated from the Russian by K. N. Trirogoff and L. W. Neustadt. Interscience Publishers, 1962.
6. PRYCE, M. H. L., "The Diffraction of Radio Waves by the Curvature of the Earth". Advances in Physics, Phil. Mag. Suppl. 2, 67-95, 1953.
7. SAMARAS, D. G., "Theory of Ion Flow Dynamics". Prentice Hall, 1962.
8. SLATER, J. C., FRANK, N. H., "Introduction to Theoretical Physics". McGraw-Hill, 1933.
9. SPITZER, L., Jr., "Physics of Fully Ionized Gases". Interscience Publishers, New York, 1956.

## ACKNOWLEDGEMENTS

MR JOHN W. HOFFMAN, Director, Research Division, M.S.U., PROF. DR CHARLES R. ST. CLAIR, JR., Chairman, M.E. Dept., M.S.U., and MR H. R. KIM, a Ph.D. candidate in the Space program of M.S.U. for their help in preparing the paper.

MISS CAROL LUNDBERG, secretary M.E. Dept., M.S.U., MISS PAM WELCHER, and MISS PATT HARNEY, secretarial office of the M.E. Dept., M.S.U., for the heavy task of typing the paper.



## CHAPTER 4-4

METHODS OF IMPROVING RADIO-WAVE  
PROPAGATION THROUGH THE PLASMA SHEATH

ROBERT RAWHOUSER

Air Force Avionics Laboratory Wright-Paterson AFB, Ohio, USA

The introduction of hypersonic vehicles has produced the problem of propagation of electromagnetic waves through an ionized medium. The electron density of the plasma sheath formed about the vehicle may be eight orders of magnitude greater than the maximum density of the ionosphere. Also the collision frequency may be many orders of magnitude greater than the collision frequency range in the ionosphere. These factors result in a much higher plasma resonance frequency, and much greater wave attenuation, phase shifts, reflections, and plasma-wave interaction. The severity of the conditions in the re-entry vehicle plasma leads one to consider possible methods of improving radio-wave propagation through the sheath.

There are two standard methods of solving the problem, or perhaps we should say of avoiding the problem. The first method is proper signal-frequency selection. Of course, using a frequency well above the plasma resonance frequency  $f_p$

$$(f_p \cong 8.9 \sqrt{N_e} \text{ where } N_e = \text{electrons/meter})^3$$

insures propagation through the sheath. However, there are practical limits to the freedom of choice of operating frequency. For example Fig. 1 illustrates the attenuation of transmission from a typical vehicle to ground. This is a hypothetical missile at 200000 feet altitude flying at a velocity of Mach 20. The figure shows that the plasma effect decreases with increasing frequency, but one soon gets into the region of attenuation in the troposphere due to oxygen and water vapor. Equipment and signal acquisition problems also limit the freedom of choice. A possibility of going toward a limit along this line is the use of a light beam for communications. There are no plasma problems for such a system, so we will not consider it.

Another possibility of frequency selection is to go to the very low frequency end of the spectrum. The figure shows that attenuation decreases as the frequency is lowered. This occurs because the attenuation factor for a plasma with loss depends on the number of wavelengths in the path length. For low frequencies the plasma sheath about a vehicle is only a fraction of a wavelength, so the signal loss is low. However, this solution is not very useful, because of the obvious antenna problems in trying to get a low-frequency antenna on a missile. There are problems both from the standpoint of efficiency and pattern formation.

The second method in use for avoiding the problem is aerodynamic shaping. A sharp-nosed cone has a physically thin shock-wave region and a

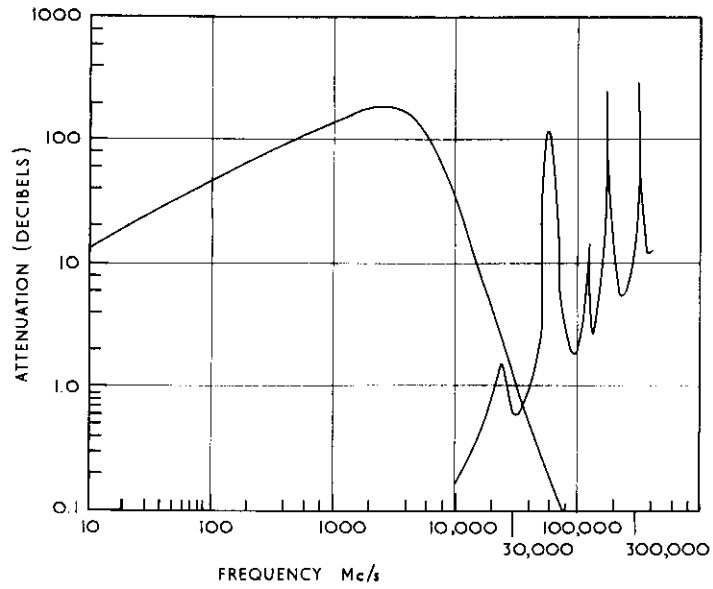


FIG. 1 Total attenuation of a signal from a hypersonic vehicle to ground. The left hand curve shows plasma absorption and the right curve the absorption in the troposphere

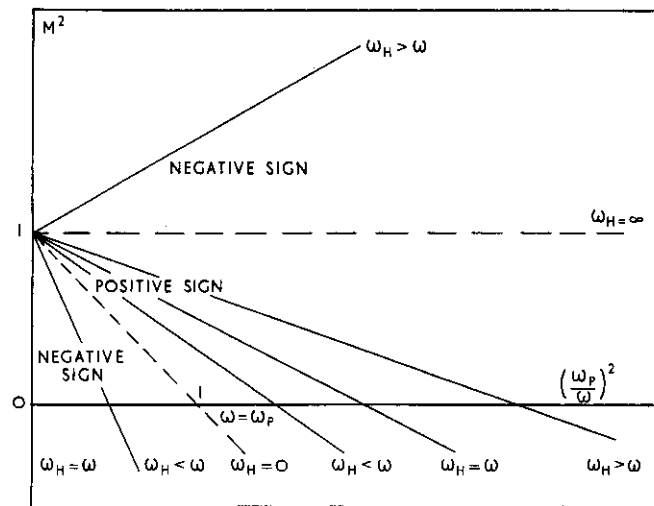


FIG. 2 Variation of index of refraction when a magnetic field is along the direction of propagation

less dense plasma sheath than a blunt body. Under this heading we can also include placement of antennas in a region of low plasma. There are also possibilities of placing antennas on or behind thin fins or other structure which protrude through the dense portion of the plasma sheath. The method should be useful for some missile requirements, but many missions require the use of a blunted spacecraft. Hence work is continuing on methods of either reducing the density of the plasma about a body or of finding ways to propagate a signal through the plasma at a frequency below the plasma resonance frequency.

One method of improving communications suggested by theory is to create a very strong magnetic field along the path of the waves. The equations show that the presence of the magnetic field converts the plasma into an anisotropic medium, that is, the properties of wave transmission depend on the direction of propagation (1, 2, 3). The mathematics is rather complicated. Not only is there an ordinary and extraordinary electromagnetic wave, but other modes of wave propagation – electrodynamic and hydromagnetic – are possible. A somewhat simplified case occurs when the direction of electromagnetic waves coincides with that of a uniform external field.

The Appleton-Hartree solution to the propagation constant in this case gives two solutions.

$$k_{\pm}^2 = \frac{\omega^2}{c^2} \left[ 1 - \frac{w_p^2}{w^2 \pm \omega\omega_H + j\omega\nu} \right]$$

where:

$k_{\pm}$  = wave propagation constant

$\frac{\omega}{2\pi}$  = signal frequency

$c$  = velocity of light in vacuum

$\omega_H = \frac{e B_0}{m}$  = gyro frequency

$e$  = electronic charge

$m$  = mass of the electrons

$B_0$  = static magnetic field flux

$\omega_p = \sqrt{\frac{e^2 N_e}{\epsilon_0 m}}$  = plasma resonance frequency

$\epsilon_0$  = permittivity of free space (MKS units)

$N_e$  = electron density

$\nu$  = electron collision frequency with neutral atoms

The wave is split into components, one with right circular polarization and the other with left circular polarization. These components travel through the plasma at different velocities. The combination results in a polarization shift called the Faraday rotation which accumulates with distances as the wave travels through the plasma. The effective cutoff frequencies are shifted from the cutoff frequency which is obtained without a magnetic field present. Figure 2 is a graph, for a lossless plasma ( $\nu = 0$ ), of the refraction index of the medium, which is related to the propagation constant by the simple formula

$$n = \frac{ck}{\omega}$$

The graph shows a marked difference between the behavior of the two types of circular polarization. The index for the case without the magnetic field is shown by the dotted line. The index becomes imaginary for frequencies below the critical frequency ( $\omega < \omega_p$ ) and propagation ceases. For frequencies above the critical, the index rapidly approaches unity. Now consider the case where the sign in the Appleton-Hartree equation is positive. The cutoff frequency is reduced to the value

$$\frac{\omega}{\omega_p} = \sqrt{\left(\frac{\omega_H}{2\omega_p}\right)^2 + 1} - \frac{\omega_H}{2\omega_p}$$

$$\approx \begin{cases} 1 - \frac{\omega_H}{2\omega_p} & \text{for } \omega_H \ll \omega_p \\ \frac{\omega_p}{\omega_H} & \text{for } \omega_H \gg \omega_p \end{cases}$$

Thus we see the cutoff frequency can be made considerably below the normal cutoff point and propagation of waves is possible in that region. For the negative sign the cutoff frequency is shifted to:

$$\frac{\omega}{\omega_p} = \sqrt{\left(\frac{\omega_H}{2\omega_p}\right)^2 + 1} + \frac{\omega_H}{2\omega_p}$$

$$\approx \begin{cases} 1 + \frac{\omega_H}{2\omega_p} & \text{for } \omega_H \ll \omega_p \\ \frac{\omega_H}{\omega_p} & \text{for } \omega_H \gg \omega_p \end{cases}$$

The attenuation for this type of polarized wave is increased.

Investigations have been made in laboratories on the effect of propagating through a plasma with the aid of a fixed magnetic field. One of these has been the subject of a previous paper (4).

The AF Avionics Laboratory is sponsoring an investigation to go a step further and demonstrate the use of a magnetic field. A flight package is being built for this purpose. For this demonstration a Trailblazer missile will be used (5). The Trailblazer missile is a vehicle developed for research purposes only. It consists of four stages, two of which fire upward at an 80° elevation angle and lift the final stages, called the velocity package, to about 200 miles altitude. After coasting over the apogee the third and fourth stages fire downward. The last stage consists of a 15-inch spherical solid-propellant motor together with a protective nose-cone and instrumentation. The re-entry package will have a velocity in the neighborhood of 18000 ft/s at 350000 feet altitude if the total re-entry weight (including the burned-out spherical motor) is 65 pounds. Trade-off can be made on velocity versus payload weight.

The particular re-entry shape we will use is a cone-sphere. The spherical nose cap has a 6-inch outer radius. This flares into a cone about 19 inches in diameter at the base with overall length of 27 inches. The weight-to-drag ratio is 80.

The experiment will be conducted at S-band (3 Gc/s) and the transmission will be made through the stagnation region. The plasma density

here is about  $10^{12}$  electrons/cm<sup>3</sup> at 250000 feet altitude and rises to a maximum around  $10^{14}$  at about 150000 feet. These densities correspond to plasma resonance frequencies over 9 Gc/s. The magnet to be flown will have a strength of 13000 gauss (1.3 webers/m<sup>2</sup>) at the nose of the missile. This gives an electron cyclotron frequency of 36 Gc/s. With such a field the lower cutoff frequency is reduced to 2.2 Gc/s. The attenuation through the plasma under those conditions is 1.7 dB per free-space wavelength. The plasma sheath is only a fraction of the wavelength, so that small attenuation should be observed. Another transmitter without benefit of a magnetic field is mounted on the side of the nose cap in a lower plasma environment as a comparison transmission.

In order to obtain the strong magnetic field desired a decision was made to use a superconducting coil. This became possible several years ago with the introduction of new superconducting alloys with relatively high critical magnetic fields. Of course, with these alloys cryogenic devices are required. In the equipment constructed, the magnetic field is produced by a coil of niobium tin cooled to the temperature of liquid helium (4° Kelvin). This coil will be energized on the ground and the current made self-sustaining at the desired level. At this point the leads will be withdrawn and the superconducting magnet will be flown without any power supply.

The antenna and magnetic field coil comprise a package almost cylindrical in shape 7 inches high and 6 inches in diameter. The antenna lies along the axis and is a 5-turn helix embedded in dielectric so as to be less than 1 inch in diameter. The pattern is broad, giving coverage over 160° and with ellipticity of 7:1 out at 71°.

The superconducting magnet package is essentially an airborne Dewar container designed to hold the coil at superconducting temperature for a period of several hours. The container is evacuated and contains inner and outer cold walls and insulation. In operation the inner container is filled with liquid nitrogen, cooling the interior down to 77° Kelvin. A vacuum pump lowers the boiling-point of the nitrogen and reduces the temperature further. At this point liquid helium is pumped through separate coils until the temperature is reduced to the neighborhood of 4° Kelvin. The nitrogen is frozen, as is also an outer jacket filled with alcohol. When the electric coil becomes superconducting the charging current is applied and the magnet is obtained in a sustained state. Before launch the cryogenic tubing to the outside of the missile is disconnected. Any liquid helium in the system soon boils away. However, the frozen nitrogen has satisfactory heat capacity and the vacuum spaces and radiation shield prevent convection and radiation heating. Contact points are kept to a minimum to cut down heat conduction. The flight itself takes only 8 minutes, so the practical consideration of flight is to avoid undue hold-time on the launch pad after the cryogenic lines are disconnected.

The missile will be launched from the NASA Wallops Station on the east coast of the United States. It will fly out over the Atlantic Ocean and the re-entry package will splash or burn up over a spot some 50 miles offshore. A network of stations along the coast will monitor the signals. The transmitted signals will be microsecond pulses with 300 pulses per second. The data must be analyzed in accordance with theory and comparison with other flights without a magnetic field as an aid to propagation. It would have been

desirable to have a means of turning the magnetic field on and off during the re-entry period, but this is impossible on the type of experiment flown. There is quite a lot of energy stored in the magnetic field and this cannot be diverted and then restored easily. The design of this package was influenced greatly by the necessity of keeping the weight low. The experiment is rather difficult to instrument and launch. It is expected that launch will occur early in 1966.

Another related idea may be mentioned as a means of aiding propagation through plasma. This is the use of a strong magnetic field to divert plasma flow away from an antenna in a desired protected region of a re-entry body. This effect does not enter into the experiment described because of the symmetry and the choice of the stagnation region for transmission. The use of a magnetic field for plasma flow diversion has not been considered in detail.

Another technique to aid propagation through the plasma sheath is the use of what has been termed an aerodynamic gas spike. This is closely related to the beforementioned use of a sharp-nosed body in order to modify the shock-wave front. It is also related to the method of additives which will be discussed later. In the gas-spike technique a jet of inert gas is injected forward in front of an antenna to be protected (6). Wind-tunnel tests have shown that with the proper gas pressure and nozzle the gas will penetrate the incoming airstream and maintain a pointed front. The shock wave formed is that of a sharp-nosed cone. Furthermore the gas spike is self-sustaining and does not wear away as would a material body. The gas can be ejected right through a spike antenna. Then instead of a dense plasma sheath around the antenna a lesser plasma environment will be created by the gas spike. The lowered critical frequency gives a wider choice of possible frequency selection. Cooling of the plasma by the injected gas undoubtedly plays a role in the action as well as the aerodynamic reshaping.

Studies have been made of some of the parameters involved in building a system and a flyable gas-storage container and control-valve device has been built. This one is an ellipsoid with 113 cubic inches gas capacity. It is designed to eject helium gas which is stored at 6700 pounds per square inch pressure. The gas ejects from the nozzle at about Mach 4 and forms a gas jet in an impinging hypersonic stream. It is planned to use this in a flight demonstration, but the time has not been set.

Injection of chemicals in the plasma sheath about the re-entry body to reduce the electron density has been suggested in numerous places. This idea has many variants due to the variety of mechanisms which possibly play a part. Mechanisms which have been considered are

- (a) cooling the plasma by an endothermic reaction,
- (b) electron attachment by atoms and radicals, and
- (c) recombination of ions by means of third-body droplets or refractory dust.

A number of investigations has been made in a variety of plasma facilities. It has been determined that cooling the plasma below 3000°K is required before an electron attachment process is effective. Water, benzene, ethanol, propanol are effective in reducing the plasma temperature. For electron attachment the halogens, carbon tetrachloride, carbon tetrafluoride, sulphur hexafluoride, oxygen, water and chemicals with the cyanogen radical are



possibilities (7), (8). For refractor dust, micron-size particles of hafnium dioxide, thorium dioxide or perhaps carbides or nitrides have been suggested (9), (10).

Most work has been done with water as the injectant. Studies have been made of the mechanisms involved. It has been determined that water is most effective dispersed in the plasma in the form of droplets. These droplets collect electrons and ions of both charges and recombination takes place on the droplets. Water injection is the only means which has actually been tried of *reducing plasma on re-entry vehicles* (11). Preliminary reports showed good restoration of the radio signal under blackout conditions when water was injected. Detailed results have not yet been released.

An investigation of an entirely different kind is an attempt to modulate the plasma sheath and use the sheath itself as a radiator. Theoretical studies have been conducted on *electron-beam and plasma-wave interaction* (12). A laboratory investigation is being made on the feasibility of using such a scheme for a communication system. The mechanism of the system is as follows: An electron gun sends its beam through a re-entrant microwave cavity which is energized by the signal to be transmitted. The electron beam is velocity-modulated and, as it drifts, becomes bunched. The bunched electron beam is injected into the plasma where it interacts and excites a space-charge plasma wave. This wave travels out along the beam until it meets the shock boundary. The shock boundary is sharp and is a discontinuity for the plasma wave. At this point transition radiation takes place out into space. Thus the problem of transmitting electromagnetic energy through a plasma is replaced by the shooting of an electron beam through the plasma and radiation from the discontinuity of the sheath.

The laboratory work has been done using a shock-tube facility. A shock is generated in a 6-inch-diameter shock tube triggered by the discharge of a bank of condensers. The plasma has a density above  $10^{12}$  electrons per cubic centimeter and a steady state of about 1 millisecond. The electron gun is placed in a cross-arm of the shock tube. It has a microperviance in the neighborhood of unity and is operated at an accelerating voltage of 10000. This gives a 1-ampere beam to shoot through the microwave cavity. The beam is pulsed to coincide with the generation of the plasma. After the beam is modulated by the microwave cavity at 1200 Gc/s it travels across the plasma column. The beam is collected by a Faraday cup in the opposite cross-arm and microwave radiation is picked up by an antenna outside the shock tube.

Measurements have been made of various modes of operation, namely

- (a) leakage radiation from the hole in the microwave cavity,
- (b) microwave radiation with the electron beam going through the activated cavity but no plasma present and
- (c) radiation with and without the beam operating and plasma present.

With the leakage radiation being taken as a base it is found that the electron beam alone increases the radiation by a factor of 15 dB, while the presence of the plasma brings the result up over 70 dB. It appears that the system is operating as expected from theory. Several details have been investigated. Transition radiation has been studied by shooting a bunched electron beam through a small hole in a metal plate (13). It is found that the

radiation from the exit hole is a function of the current density passing through the hole. Therefore, it is important that the electron beam be focused well and have small divergence. On this point the presence of the plasma sheath has a surprisingly good effect. Instead of scattering the beam excessively the plasma has a focusing effect (14), (15), (16). A positive ion sheath is formed around the electron beam and its integrity is maintained much better than originally expected. In fact, the plasma brings several bonuses. Not only does it help to focus the electron beam, but there is also amplification of the plasma wave as the beam progresses (17). Measurements have indicated an amplification of 1.5 to 4 dB in a travel distance of a centimeter. These figures correspond to pressures of 10.0 microns and 1.0 micron respectively. Thus the effect is dependent on the pressure, and the amplification is better at low pressures. Problems of plasma poisoning of the cathode of the electron gun and detuning of the microwave cavity have been overcome. A slight differential pressure of an inert gas in the region of the gun will protect an oxide cathode. A ruggedized tungsten cathode can be operated without the overpressure.

The big problem of such a system is the amount of power expended for the radiation output. In terms of efficiency of radiated power versus input microwave power to the cavity some very good efficiencies can be obtained particularly at specified altitudes. The difficulty comes when these figures are measured in terms of the power needed to form the electron beam. Obviously it will be necessary to have a pulsed transmission to bring the power down to a practical level for an aerospace vehicle.

Another problem is that what has been discussed is for transmission from a re-entry vehicle only, and only in the plasma formation régime. A suggestion has been made for a receiving system for the vehicle in plasma. This would involve the use of an electron beam and also a magnetic field to curve the beam around back to the vehicle. In this case the beam would be modulated by an incoming wave and the modulation detected from the returning beam. This has not been pursued.

A further suggestion for use of the plasma sheath in transmission is for the plasma to play the role of frequency mixing. In this scheme two frequencies would be transmitted side by side both above, but one of them near, the plasma resonance frequency of the sheath. In the plasma a mixing action would take place and the difference frequency would be radiated. The frequencies could be arranged so that the difference is the one desired for transmission. If one of the mixing frequencies is modulated, the modulation will appear on the heterodyned frequency. No work has been done on this idea.

A number of processes for getting electromagnetic waves through the plasma sheath have been discussed. These are given in the following outline:

- A Signal frequency selection
  - 1 E.M. waves above plasma-resonance frequency
  - 2 Light beams
  - 3 Very low frequency
- B Aerodynamic shaping
  - 1 Sharp-nosed vehicle
  - 2 Antenna placement

- C Static magnetic field
  - 1 Electromagnetic effect
  - 2 Plasma-flow diversion
- D Aerodynamic "gas spike"
  - 1 Cooling effect
  - 2 Shock-wave reduction
- E Chemical additives
  - 1 Cooling effect
  - 2 Electron attachment to atoms and radicals
  - 3 Recombination of ions on third bodies
- F Electron beam - plasma-wave interaction
- G Frequency mixing in plasma

Some of the work done on several of these topics has been discussed. It appeared that none of them was an unmixed blessing. Especially in the practical situation of using the techniques in an actual re-entry body the problems are very severe. The use of any of the techniques will depend on the particular mission and the type of vehicle. In the meantime the use of frequency selection, storage and playback when practical will be the primary method of attack.

## REFERENCES

1. MITRA, S. K., "The Upper Atmosphere". The Asiatic Society, 1952.
2. RATCLIFFE, J. A., "The Magneto-Ionic Theory and Its Application to the Ionosphere". Cambridge University Press, 1959.
3. ALLIS, W. P., BUCHSBAUM, S. J., and BERS, A., "Waves in Anisotropic Plasmas". MIT Press, 1963.
4. BACHYNSKI, M. P., "Radiowave Propagation through Re-entry Plasma Sheaths". See Chap. 4.2.
5. HARTSEL, J. E., and NEREM, R. M., "Predicted Re-entry Performance of a Trailblazer II Vehicle". Ohio State Univ. Res. Found. Rep. 1573-7, 1964.
6. ADAMS, R. H., and ROSSI, J. J., "Research of Aerodynamic Methods of Producing Antenna Windows in a Plasma Sheath". AFCRL Rep. 65-65, 1964.
7. CARSWELL, A. I., and CLOUTIER, G. C., "Supersonic Plasma Streams Seeded with Electronegative Gases". Phys. Fluids 7, 602, 1964.
8. CLOUTIER, G. G., and CARSWELL, A. I., "Plasma Quenching by Electronegative Gas Seeding". Phys. Rev. Letters 10, 327, 1963.
9. ROSEN, G., "Method for the Removal of Free Electrons in Plasma". Phys. Fluids 5, 737, 1962.
10. DIMICK, R. C., and SOO, S. L., "Scattering of Electrons and Ions by Dust Particles in a Gas". Phys. Fluids 7, 1638, 1964.
11. SIMS, T. E., "Re-entry Communications Research at Langley Research Center". IEEE Intern. Conv., 1965.
12. PARZEN, P., "Radiation from a Modulated Beam with a Plasma Background". J. Appl. Phys. 32, 2484, 1961.

13. DNESTROVSKI, YU. N., and KOSTOMAROV, "Radiation of a Modulated Beam of Charged Particles in Passing through a Round Opening in a Flat Screen". Soviet Phys. Doklady 4, 132, 1959.
14. MARKEVITCH and HURLBUT, "The Study of Electron Beam Attenuation in Air". Univ. of Cal. TR HE-150-142, 1957.
15. FIELD, L. M., SPANGENBERG, K., and HELM, R., "Control of Electron Beam Dispersion at High Vacuum by Ions". Elec. Comm. 24, 108, 1947.
16. LINDER, E. G., and HERNQUIST, K. G., "Space Charge Effects in Electron Beams and Their Reduction by Positive Ion Trapping". J. Appl Phys. 21, 1088, 1950.
17. BOYD, G. D., GOULD, R. W., and FIELD, R. W., "Interaction of a Modulated Electron Beam with a Plasma". Proc. IRE 49, 1906, 1961.

## DISCUSSION

K. DAVIES. Can you tell us the effects of the antenna site on the vehicle during re-entry?

R. RAWHOUSER. This question cannot always be answered simply. Along the side of a vehicle the plasma sheath may be separated from the skin in the neighbourhood of the antenna. This may constitute in effect a leaky wave guide. The electromagnetic energy may be propagated in a surface wave along the vehicle and be radiated away in a direction entirely different from that followed in the absence of the plasma.

## CHAPTER 4-5

## SURFACE WAVE PROPAGATION ALONG A DIELECTRIC ROD IMMERSED IN AN UNMAGNETIZED PLASMA AND ITS APPLICATION TO MEASURING ELECTRON DENSITY

P. N. ROBSON AND R. D. STEWART

The University of Sheffield, England

## SUMMARY

A microwave surface-wave probe which enables the electron density profile in an unmagnetized gaseous plasma to be measured is described.

The technique used is to measure the phase-change coefficient of an electromagnetic surface wave supported by a fused quartz rod which is inserted into the body of the plasma. An  $HE_{11}$  mode surface wave is established on the quartz rod by means of a small launching horn at the vessel wall; the wave travels along the rod and is reflected back by a small metal disk, attached to the end of the rod, to the launching (now receiving) horn. The phase of the reflected signal depends on the frequency of operation, the diameter of the rod, the dielectric constant of the rod and the electron density of the plasma enveloping the rod. The quartz rod waveguide and launching horn are designed so that the penetration of the rod into the plasma may be varied. Measurements of phase change for various penetrations enable the electron-density profile to be determined through the plasma.

Typical theoretical dispersion characteristics for the plasma-clad rod are presented and corrections for the Debye sheath forming at the surface of the rod are considered. Measurements made using such a probe at a frequency of 35 Gc/s in an argon afterglow plasma at 80 mTorr and with densities, at the time of measurement, in the range  $10^{12}$  to  $10^{14}$  electrons/cc are described. The profiles calculated are compared with those determined by electrostatic double-probe measurements.

## INTRODUCTION

The majority of microwave diagnostic techniques for determining electron densities in plasmas may be divided broadly into two classes: (a) resonant cavity measurements where the plasma and containing vessel are designed to be part of a tuned circuit (1) and (b) plane wave propagation through the plasma where reflection, transmission and, to a lesser extent, refraction measurements are made (2), (3), (4), (5). Most of these techniques measure the average electron density over the volume irradiated, the exception being the refraction-type measurements where the electron-density profile can be obtained (3), (4), (5). Refraction-type measurements, however, require

plasmas having considerable accessibility, which it is often difficult or impossible to provide.

A microwave diagnostic technique is described here which can provide both spatial and temporal resolution of electron density for an unmagnetized plasma and yet requires limited access to the plasma (6). Since it involves inserting a material probe, in the form of a thin quartz rod, into the plasma, it does not strictly provide an unperturbed measurement of electron density as do most microwave probing methods. Its role was seen therefore to be that of complementing the more usual electrostatic or r.f. probe techniques for determining electron density. The present account describes some of the initial calculations and experiments undertaken to assess the usefulness and accuracy of the method.

#### OUTLINE OF METHOD OF SURFACE-WAVE PROBING

The method can best be appreciated by reference to Fig. 1. A surface wave is launched at the side of the vessel containing the plasma and guided along the length of a fused quartz rod into the body of the plasma. At the end of the rod a small plate is placed to reflect the incident signal. The phase of the reflected signal depends upon the phase-change coefficient and path length of the signal along the dielectric rod. The phase-change coefficient is determined partly by the plasma density surrounding the rod. This reflected signal is combined with a portion of the incident reference signal in a phase-sensitive detector. Initially, the rod is inserted for a distance  $\Delta l_1$  into the plasma, sufficiently small that the plasma electron density  $N$  can be assumed to be spatially constant in the interval  $\Delta l_1$  and equal to  $N_1(t)$ , say. Associated with this constant density  $N_1(t)$  are a constant phase-change coefficient  $\beta_1(t)$  and plasma dielectric constant  $\kappa_{p1}(t)$ . If no plasma existed at time  $t = 0$  and  $\beta = \beta(0)$ , the overall phase change recorded at time  $t$ , with the plasma present, is  $\phi_1(t)$ , where:

$$\phi_1(t) = 2[\beta(0) - \beta_1(t)] \Delta l_1$$

$\phi_1(t)$  may be measured and  $\beta_1(t)$  calculated for any value of  $t$ .

$\kappa_{p1}(t)$  is then determined from calculated dispersion curves (see later in this chapter), and  $N_1(t)$  is found by using:

$$\kappa_{p1}(t) = 1 - [N_1(t)e^2 / \epsilon_0 m \omega^2]$$

For a second incremental insertion  $\Delta l_2$  of the rod into the plasma, the measured phase change  $\phi_2(t)$  is given by:

$$\begin{aligned} \phi_2(t) &= 2[\beta(0) - \beta_1(t)] \Delta l_1 \\ &\quad + 2[\beta(0) - \beta_2(t)] \Delta l_2 \end{aligned}$$

$$\text{or } \phi_2(t) = \phi_1(t) + 2[\beta(0) - \beta_2(t)] \Delta l_2$$

where  $\beta_2(t)$  is the constant phase-change coefficient for the interval  $\Delta l_2$ .  $N_2(t)$ , the electron density in the interval  $\Delta l_2$ , may be calculated from  $\beta_2(t)$ . Extending the notation, the phase change  $\phi_K(t)$  for a penetration  $l$  equal to

$$\sum_{j=1}^k \Delta l_j$$

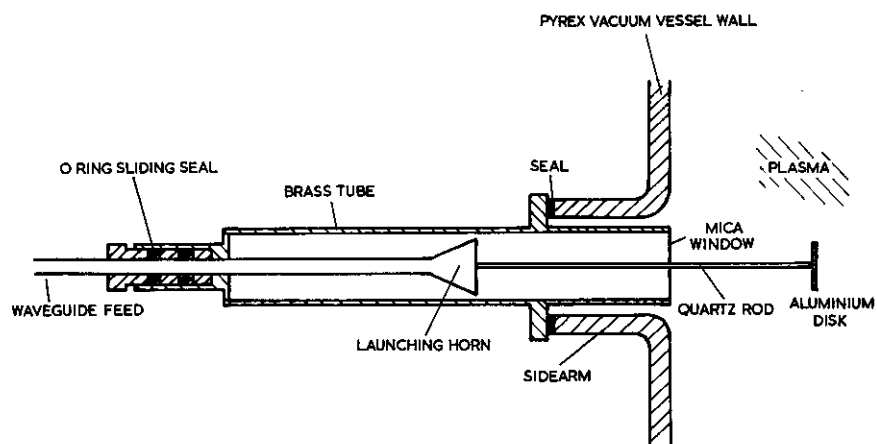


FIG. 1 Surface wave probe assembly

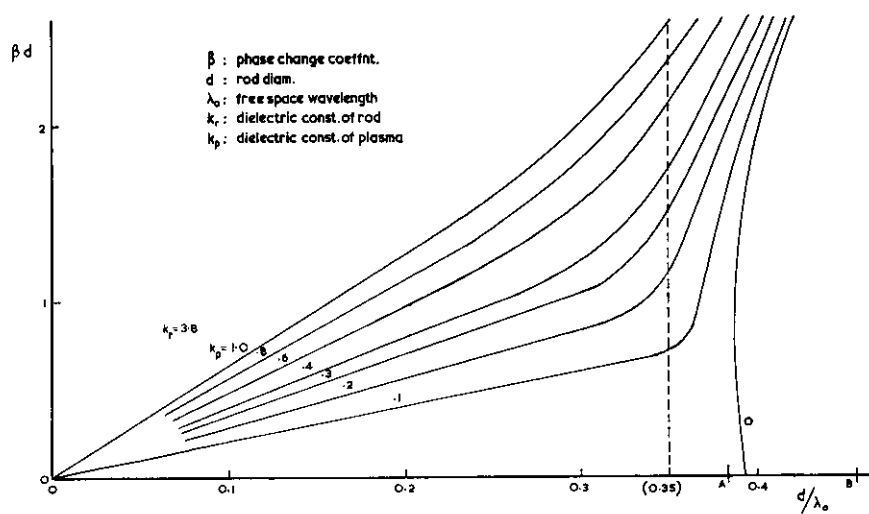


FIG. 2  $HE_{11}$  mode on dielectric rod

is given by:

$$\phi_K(t) = \phi_{K-1}(t) + 2[\beta(0) - \beta_K(t)] \Delta l_K$$

For the chosen sequence of intervals  $\Delta l_j$  we have an associated sequence of plasma electron densities  $N_j(t)$ , which will give a stepwise picture of the density profile along the axis of the rod.

This prescription assumes that the wave travelling along the rod has the properties of a progressive wave, that is, its wave function has an axial dependence of the form:

$$\exp \pm j \int_0^L \beta(l) dl$$

where  $\beta(l)$  is the phase constant along an infinitely long rod surrounded by plasma, whose density corresponds to that at  $l$ . We have not been able to obtain any exact solutions for propagation along a plasma-clad dielectric rod, in the mode to be considered, except when the density is constant in the direction of propagation. Thus no quantitative estimate of the error can be provided for a given profile. General considerations (7), however, suggest that the phase integral representation is a good approximation if:

$$\frac{1}{\beta^2} \left| \frac{d\beta}{dl} \right| \ll 1 \quad (1)$$

This requires the density gradient along the rod to be sufficiently small and also that the rod does not penetrate regions of plasma close to cutoff for the surface-wave mode (i.e.  $\beta = 0$ ).

#### CHOICE OF SURFACE-WAVE STRUCTURE

Many structures will support bound surface waves and it is necessary to consider the most suitable for the present purpose. Metallic guiding structures were not selected for a number of reasons. A continuous structure must perforce stabilize at a fixed potential and, since the local space potential in the plasma is not fixed, a space-charge sheath of varying thickness would form around the probe and possibly render interpretation of the results difficult. More serious, perhaps, is the fact that suitable metallic guiding structures normally have a periodically varying contour, and an exact solution of the boundary-value problem, even in the absence of plasma, is difficult. Again the disposition of the plasma contiguous to the structure is difficult to know in this case.

The guiding structure considered most satisfactory was a cylindrical dielectric rod. The dominant mode in the absence of plasma is the hybrid  $HE_{11}$ , which will propagate even at the lowest frequencies. For a range of plasma densities surrounding the rod this mode is still the dominant one, and is thus a natural choice, since the risk of mode conversion does not then appear. Moreover, a very suitable rod material exists in quartz or fused silica ( $\kappa_r = 3.8$ ), as its loss tangent at microwave frequencies is small ( $\tan \delta \approx 2.5 \times 10^{-4}$  at 25 Gc/s) and it is also very stable at high temperature.

The guiding structure in this case is an insulator and a positive ion sheath of thickness several Debye lengths will form around it when placed in the



plasma. As the sheath thickness depends on both the local electron density and temperature, and both are initially unknown, some assumption must be made about this dimension. The simplest is to neglect it completely and assume that the plasma extends up to the surface of the probe. As will be shown later, this assumption leads to negligible error over quite a large range of plasma densities and electron temperatures.

#### CALCULATION OF DISPERSION CHARACTERISTICS

The propagation of surface waves along a dielectric rod surrounded by another dielectric is fairly well documented, although it is not usual to present calculated data for any dielectric external to the rod other than free space.

The phase constant  $\beta$  and angular frequency  $\omega$  may be shown to satisfy the following transcendental equation for the hybrid  $HE_{11}$  mode if collisional damping is neglected:

$$\left[ \frac{\tilde{J}_1'(h_1 a)}{h_1 a \tilde{J}_1(h_1 a)} + \frac{K_1'(h_2 a)}{h_2 a K_1(h_2 a)} \right] \left[ \frac{\kappa_r \tilde{J}_1'(h_1 a)}{h_1 a \tilde{J}_1(h_1 a)} + \frac{\kappa_p K_1'(h_2 a)}{h_2 a K_1(h_2 a)} \right] = \frac{(\kappa_r h_2^2 + \kappa_p h_1^2)(h_1^2 + h_2^2)}{h_1^4 h_2^4 a^4} \quad (2)$$

where  $h_1^2 = \omega^2 \mu_0 \epsilon_0 \kappa_r - \beta^2$

$h_2^2 = \beta^2 - \omega^2 \mu_0 \epsilon_0 \kappa_p$

$2a = d = \text{diameter of rod}$

$\kappa_r = \text{dielectric constant of rod}$

$\kappa_p = \text{dielectric constant of plasma, assumed constant everywhere external to the rod.}$

A computer programme was written to solve Eq. 2. The dispersion characteristics are most conveniently plotted as  $\beta d$  versus  $d/\lambda_0$  for a fixed value of  $\kappa_r$  and varying  $\kappa_p$ . A typical characteristic is shown in Fig. 2. For  $\kappa_p > 0$ , the mode exhibits no cutoff frequency: however,  $\kappa_p \leq 0$ , there is a frequency below which no propagation takes place, and in the neighbourhood of this frequency backward waves can exist. When a frequency of operation and rod of given size and dielectric constant are chosen, the phase-change coefficient  $\beta$  depends solely on  $\kappa_p$ . To investigate unmagnetized plasmas whose dielectric constant lies in the range  $1 > \kappa_p \geq 0.1$ ,  $\kappa_r$  and  $d/\lambda_0$  are chosen so that a reasonable change in  $\beta$  may be expected for the change in  $\kappa_p$ . Also shown in Fig. 2 are the cutoff frequencies for the next higher-order modes, the  $E_{01}$  and  $H_{01}$  when there is no plasma present (B) and when the plasma permittivity is zero (A). The dotted line represents what is considered to be a suitable choice of  $d/\lambda_0$  in order to give a reasonable change in  $\beta d$  as  $\omega_p$  varies from  $0(\kappa_p = 1)$  to  $\omega_p \approx \omega(\kappa_p \approx 0)$ . The  $HE_{11}$  mode is still dominant under these conditions and thus no interference from other modes is likely.

As the plasma density approaches critical ( $\kappa_p = 0$ ) a larger fraction of the total transmitted energy resides outside the dielectric rod. This can be seen in Fig. 3, where the ratio of the power transmitted within a normalized radius  $\rho$ , to the total transmitted power, is plotted for two values of  $\kappa_p$  when  $\frac{d}{\lambda_0} = 0.35$ . In one case ( $\kappa_p = 1$ ) there is no plasma surrounding the rod, and in

the second case the plasma density is near critical ( $\kappa_p = 0.1$ ). It is important to recognize this behaviour, since it implies that:

- (i) As the wave propagates into regions of increasing density, the plasma is sampled to a larger transverse distance from the probe.
- (ii) Whilst the short-circuit termination will be of sufficiently large radius at low densities to reflect all the incident power, an increasing amount of power will be transmitted past it as the density increases.

We have not yet investigated the solutions of the dispersion Eq. 2 in detail below cutoff, when  $\kappa_p \leq 0$ . It seems unlikely, however, that solutions representing evanescent bound waves will be obtained. In this case radiation must occur from the rod.

#### MINIMUM AND MAXIMUM MEASURABLE DENSITIES

So far no frequency of operation has been specified. In order to ensure a high launching efficiency, the launching horn must be several wavelengths in diameter. Previous considerations in the foregoing suggest an optimum ratio of rod diameter to wavelength around 0.35 (see Fig. 2). Thus in order to maintain both rod and launcher dimensions conveniently small, an operating wavelength of around 1 cm or less is called for. The wavelength used in the experiments to be reported was approximately 8.6 mm, resulting in a rod diameter of 3 mm. The maximum measurable density is considered to correspond to  $\kappa_p \approx 0.1$ , since for higher densities diffraction effects around the short-circuit termination are becoming increasingly serious; also the inequality equation (1), is more difficult to satisfy. Reference to Fig. 3 suggests that for a rod diameter 0.3 cm, a short-circuit termination of 2.0 cm diameter ensures that only 60 per cent of the total power flux is intercepted when  $\kappa_p = 0.1$ . At  $\lambda_0 \approx 8.6$  mm,  $\kappa_p = 0.1$  corresponds to a density of  $n = 1.35 \times 10^{13}$  electrons/cc.

The minimum density that can be measured is determined principally by the smallest phase change that can be measured. Hotston and Seidl (8) have described a microwave interferometer which can detect phase changes as small as 5 deg., with an error of 6 per cent. For densities well below critical, the phase change along the dielectric rod in the  $HE_{11}$  mode becomes linearly dependent on number density, being about 1.5 deg. per cm of path length for  $n = 10^{11}$  electrons/cc. We conclude that this order of density represents the smallest measurable at  $\lambda_0 \approx 8.6$  mm.

The range of density quoted above, namely  $10^{11} < n < 10^{13}$  electrons/cm<sup>3</sup> can be moved upwards by working at shorter wavelengths and using a correspondingly smaller rod diameter.

#### THE EFFECT OF THE DEBYE SHEATH SURROUNDING THE PROBE

The thickness of the positive-ion sheath surrounding the probe,  $l_D$ , is given approximately by:

$$l_D \approx \left( \frac{\epsilon_0 k T_e}{n e^2} \right)^{\frac{1}{2}}$$

where  $T_e$  is the electron kinetic temperature, and  $n$  the electron density. Some

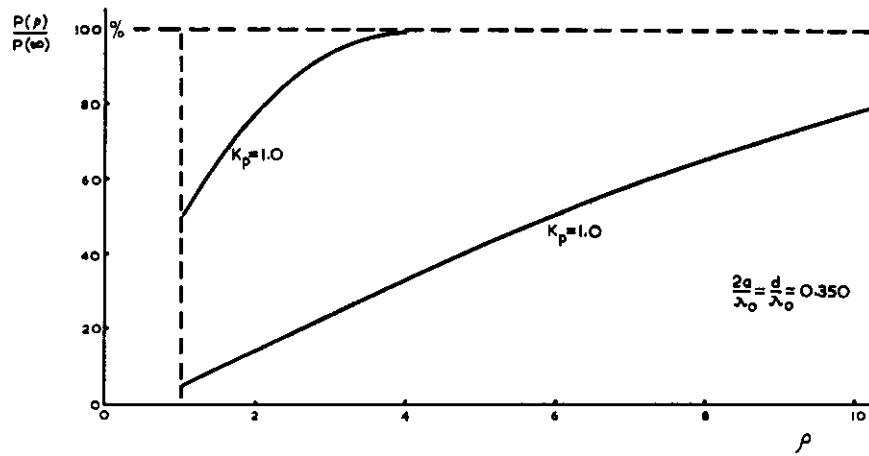


FIG. 3 Ratio of power transmitted within normalized radius  $\rho$ ,  $P(\rho)$ , to total power transmitted,  $P(\infty)$

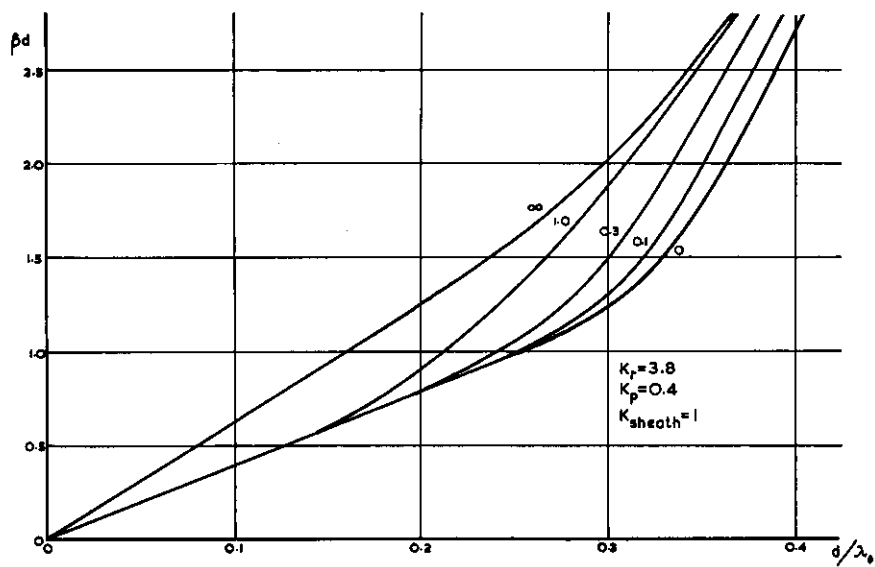


FIG. 4  $\beta d$  vs  $d/\lambda_0$ ; parameter  $t/d$

typical values for  $l_D$ , in cm, are given below for a range of appropriate temperatures and densities.

TABLE I

$n$	$T_e \text{ } ^\circ K$		
	$10^3 \text{ } ^\circ K$	$10^4 \text{ } ^\circ K$	$10^5 \text{ } ^\circ K$
$10^{12} \text{ cm}^{-3}$	$2 \times 10^{-4}$	$7 \times 10^{-4}$	$2 \times 10^{-3}$
$10^{13}$	$7 \times 10^{-5}$	$2 \times 10^{-4}$	$7 \times 10^{-4}$
$10^{14}$	$2 \times 10^{-5}$	$7 \times 10^{-5}$	$2 \times 10^{-4}$

If the Debye thickness is very much smaller than the reciprocal of the radial wave number  $h_2$ , then the error in neglecting the sheath should be small. It is important, however, to have a quantitative assessment of the error in order to establish just how thick a sheath can be tolerated. The sheath region is a transition region between the insulated surface (dielectric rod), where the normal components of electron and positive-ion currents are equal, and the plasma, where the electron and positive-ion densities are equal. In the sheath adjacent to insulated boundaries the positive-ion densities are greater than the electron densities. In order to estimate the perturbation due to the sheath a simplified model has been considered where the sheath is represented by a uniform layer of stationary positive ions, this sheath having a dielectric constant equal to 1.

Figure 4 shows the relationship between  $\beta d$  and  $d/\lambda_0$  for varying values of the parameter  $t/d$ , where  $t$  is the sheath thickness, when  $\kappa_r = 3.8$  and  $\kappa_p = 0.4$ . Similar curves are obtained for  $1 \geq \kappa_p \geq 0.1$ . From Table I, which covers temperature and densities of interest in the present experiment, we see that  $(t/d)_{\text{max.}} = 6.7 \times 10^{-3}$  for  $d = 3.0 \text{ mm}$  (i.e. the rod size chosen) and  $t = 2 \times 10^{-3} \text{ cm}$ , this corresponding to  $n = 10^{12} \text{ electron/cm}^3$  and  $T = 10^5 \text{ } ^\circ K$ . This sheath thickness causes a negligible perturbation, as reference to Fig. 4 shows.

#### EXPERIMENTAL WORK

In order to investigate the accuracy and usefulness of such probes, a number of experiments have been made, and are currently being set up. The experiments performed to date will now be described. The plasma investigated was an afterglow plasma in argon at a pressure of 80 mTorr. The plasma was established by discharging an 80  $\mu\text{F}$  capacitor bank with a terminal voltage of 3 kV between two plane 5 in. diameter electrodes 24 in. apart in a Pyrex cylinder of 6 in. internal diameter and 30 in. long. The tube had four side arms of 2 in. internal diameter arranged at right-angles to each other, lying in a plane at right-angles to the axis of the main discharge tube and 15 in. from one end. Two of the side arms were used to accommodate a surface-wave launching assembly and an electrostatic double-probe assembly, respectively.

The microwave phase bridge consists of a magic tee with the klystron connected in the shunt arm. This signal is shared equally between the remaining shunt arms, one of which is connected to the surface-wave probe and the other to a variable attenuator backed by a variable short circuit.

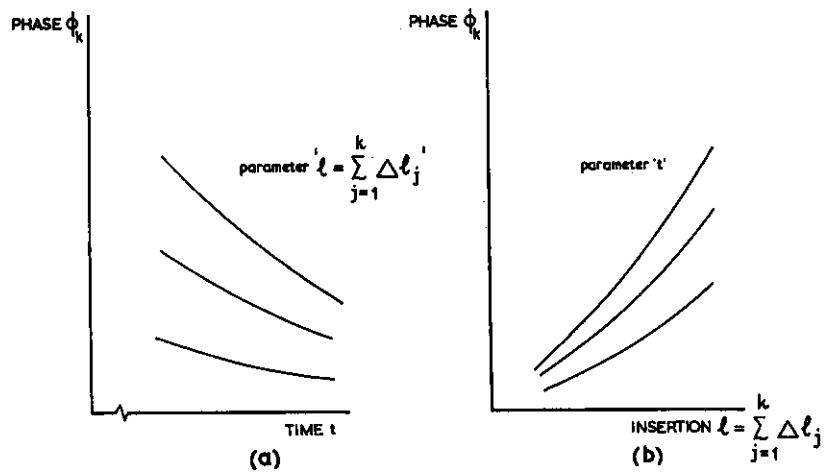


FIG. 5 Sketches of measured relationship  $\phi_k$  vs  $t = \sum_{j=1}^k \Delta \ell_j$

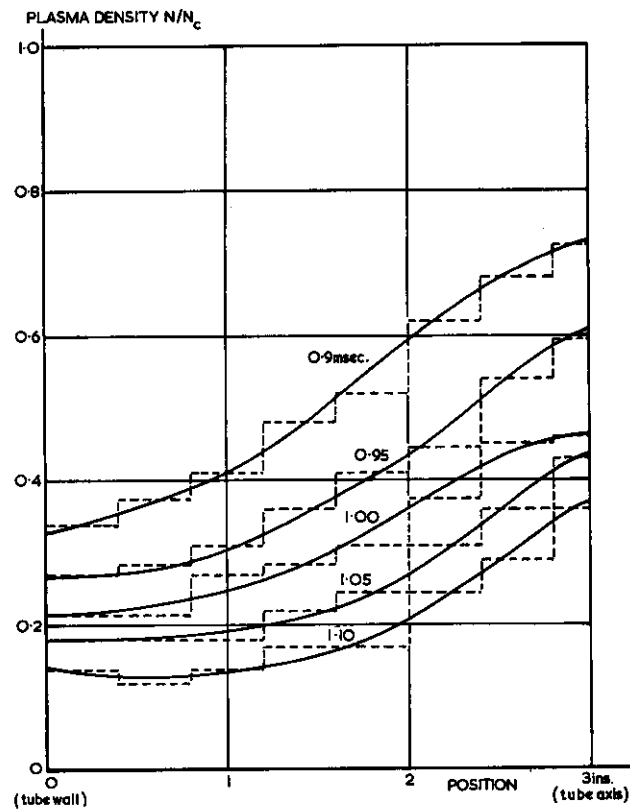


FIG. 6 Plasma density vs position

The crystal detector is connected to the series arm and the bridge is balanced in the absence of plasma. Using this arrangement, phase changes in steps of  $2\pi$  were noted during the period of the afterglow.

The surface-wave launcher consisted of a linear taper from WG22 (WR28) to a circular waveguide of 0.3282 in. internal diameter, which, in turn, was connected to a conical horn of 15 deg. semiangle and 1 in. diameter aperture. One end of a centreless ground silica rod of 3 mm diameter and dielectric constant  $\kappa_r = 3.8$  was supported concentrically in the throat of the horn by a tapered slug of PTFE. A thin aluminium disk  $\frac{1}{16}$  in. thick and  $\frac{3}{4}$  in. in diameter was bonded to the other end of the rod to form a reflecting plate. The whole launching assembly was located in one of the side arms of the vacuum vessel, the waveguide feed passing through an O-ring vacuum seal to allow axial displacement of the assembly. The length of the surface waveguide from the horn to the aluminium reflector was 8 in., and this length could be accommodated in the side arm. When the probe reflector was at the centre of the main discharge tube the length of the surface waveguide in the side arm was 8 in. — 3 in. = 5 in. The contribution to the phase change of this length of surface waveguide in the side arm was assumed to be constant for all penetrations (from zero to 3 in.) into the main vessel at any given instant of time. This launcher had a launching efficiency greater than 85 per cent and an input V.S.W.R. less than 1.1 when the dielectric rod was terminated by a matched load. To overcome the problem of plasma diffusing into the side arm, a second launching assembly has been designed. This is shown in Fig 1. The mica window is flush with the walls of the plasma vessel and thus prevents plasma entering the side arm.

From the interferometer oscillograms, the various phase changes  $\phi_k$  corresponding to the insertions

$$l = \sum_{j=1}^k \Delta l_j$$

are measured against time and plotted graphically. From the curve  $\phi_k$  vs.  $t$ , the curve  $\phi_k$  versus penetration depth, i.e.

$$l = \sum_{j=1}^k \Delta l_j$$

is drawn with  $t$  as a parameter. These two curves typically have the form shown in Fig. 5a and 5b. At this stage it is necessary to check the validity of the phase integral assumption. The inequality Eq. 1 can be recast as:

$$\frac{d^2 \phi}{dl^2} \ll 2\beta^2$$

where  $\phi$  is the total phase change at penetration distance  $l$ . Thus the curvature of the characteristics in Fig. 5b must be much less than the minimum value of  $\beta^2$  to be measured.

For a chosen time  $t_1$ , say,

$$\beta_1(t_1) = 2\pi/\lambda_{g0} - \phi_1(t_1)/2\Delta l_1$$

All the terms on the right hand-side of the equation for  $\beta_1(t_1)$  are known,  $\lambda_{g0}$  being the guide wavelength along the rod when  $\kappa_p = 1$ , and so  $\beta_1(t_1)$  may be found. Using the equation

$$\phi_k(t_1) = \phi_{k-1}(t_1) + 2[\beta(0) - \beta_k(t_1)] \Delta l_k$$

the quantities  $\beta_2(t_1)$ ,  $\beta_3(t_1)$ ,  $\beta_4(t_1)$  . . . can also be found.  $d$  and  $\lambda_0$  are known so that the quantities  $\beta_1(t_1)d$  and  $d/\lambda_0$  are readily calculated and a point on the dispersion curve may be located corresponding to  $\kappa_{p1}(t_1)$ , Similarly for  $\kappa_{p2}(t_1)$  etc. We now have a complete stepwise profile  $N_1$ ,  $N_2$ ,  $N_3$ , . . . for a chosen time  $t_1$ . This may be repeated for times  $t = t_2, t_3, \dots$ . In Fig. 6 a series of electron-density profiles are shown for varying times after the initiation of the discharge, calculated in the above manner. The density is not zero at the tube wall, since with the design of launching horn used in these experiments plasma was able to penetrate along the side arm containing the probe.

#### COMPARISON OF RESULTS WITH DOUBLE PROBE MEASUREMENTS

Measurements made using the surface-wave probe have been compared with those made using a double probe of the type described by Johnson and Malter (7). The table below is a presentation of normalized plasma density  $(N/N_c)_{swp}$ , where  $N_c (= \omega^2 m \epsilon_0 / e^2)$  is the critical plasma density as measured by the surface-wave probe, and normalized plasma density  $(N/N_c)_{dp}$ , as measured by the double probe at a point midway between the centre and wall of the tube, for times of 0.90–1.10 ms after the start of the discharge. If the double-probe densities are correct, the surface-wave-probe densities are some 30 per cent too high.

TABLE 2

$t(ms)$	$(N/N_c)_{dp}$	$(N/N_c)_{swp}$
0.90	0.36	0.49
0.95	0.26	0.38
1.00	0.20	0.29
1.05	0.17	0.23
1.10	0.13	0.17

This discrepancy has not yet been resolved and may, in fact, be genuine, since the double probe has a diameter several times larger than the surface-wave probe and thus presents a much greater surface area for recombination.

#### FUTURE WORK

It is intended to use the present technique on a much larger cylindrical afterglow plasma. This plasma has been diagnosed previously by independent free-space microwave methods (3) and it is hoped that some useful comparison may be made between the various methods. Work will be extended to investigate propagation when the plasma is above the critical density, this being possible with this particular surface-waveguide probe. The behaviour of the surface-wave fields at frequencies below cutoff calls for further study. Although

in the present work the attenuation introduced by the low collision frequency is very small, this would not be the case in a higher pressure, more weakly ionized plasma. Quantitative calculations of attenuation as a function of collision frequency therefore are required.

#### CONCLUSIONS

It is too early at present to make serious claims to great accuracy of the device as a probe. However, with this reservation in mind we conclude that the probe can be used to determine the electron density at any point along a straight path through the plasma and from these measurements profiles may be built up. The electron densities measured are those in the neighbourhood of the rod, that is, densities within a few radial decay distances (inverse of radial wave number) of the fields external to the rod.

#### REFERENCES

1. GOLDSTEIN, L., "Advances in Electronics and Electron Physics" VII, 437. Academic Press, N.Y., 1955.
2. WHARTON, C. B., SLAGER, D. M., J. Appl. Phys. 31, 428, 1960.
3. KHARADLY, M. M. Z., Proc. Inst. Elect. Engrs. 110, 7, 202, 1963.
4. SHMOYS, J., J. of App. Phys. 32, 4, 689.
5. ANICIN, B. A., Nat. Bur. of Stand. Rep., "Radio Science" (to be published).
6. ROBSON, P. N., STEWART, R. D., "Electronics Letters" 1, 1, 13, 1965.
7. BUDDEN, K. G., "Radio Waves in Ionosphere", Cambridge University Press, 1961.
8. HOTSTON, E., SEIDL, M., "A Microwave Interferometer for the Measurement of Small Phase Angles". U.K.A.E.A. Rep. CIM-P62.
9. JOHNSON, E. O., MALTER, L., "A Floating Double Probe Method for Measurements in Gas Discharges", Phys. Rev., 80, 58, 1950.

#### ACKNOWLEDGEMENTS

PROFESSOR A. L. CULLEN, University of Sheffield, for encouragement and interest in this work.

SCIENCE RESEARCH COUNCIL for financial support.

#### DISCUSSION

C. T. SWIFT – I would like to comment that we have developed, at Langley Research Center, numerical methods for handling computations involving cylindrical geometry. These techniques may be helpful for surface-wave computation for rods coated with a lossy plasma.

P. N. ROBSON – I will be very interested to study the techniques which you mention.

K. RAWER – May I mention here that we have developed an impedance



probe for measuring plasma densities in the ionosphere (1) which applies one of the principles mentioned by Dr Robson. We use a variable-frequency system with a large range. The impedance is not determined for the antenna itself, but for a combination of it with a series (and parallel) capacitor such that the resonance of the system occurs at some frequency below the plasma frequency. At that frequency the antenna in the plasma behaves like an inductance. The device thus avoids propagation waves and any disturbance of the measurement which could result from it.

I. PAGHIS – Could we have some amplification on the following points.

(a) To what extent do the experimental data and their interpretation depend upon the thickness of the plasma around the dielectric rod?

(b) With regard to the measurement of collision frequency; which collision frequency is it and what assumptions, if any, have to be made in the computation?

P. N. ROBSON – The plasma is sampled to a radial distance given approximately by the wavelength divided by the slowing factor, i.e. the ratio of the phase velocity to that of light. For the experiments described in the paper this distance is approximately 3 mm. However, as the plasma increases the fields extend further from the structure, as Fig. 3 shows. Thus the sampling radius is a rather complex function of the plasma density of the environment around the rod.

The collision frequency measured is some average between that for short-range electron-neutral collisions and long-range electron-ion collisions. In our experiments where the percentage ionization is small the former collisions are dominant.

Our calculations of attenuation at present, which are not included in this paper, are based on a perturbation technique in which the fields in the absence of collisions are used as trial fields. We intend to extend these calculations to collision frequencies where the ratio  $\nu/\omega$  is greater than unity, in which case the perturbation analogies will not be valid.

#### REFERENCES

1. JACOBS, K. G., and RAWER, K., "Electron density measurements in the ionosphere over the Sahara with a variable frequency impedance probe". Space Research V, Proc. 5th Intern. Space Sci. Symp., 1964.



## CHAPTER 4-6

EFFECTS OF THE PLASMA SHEATH ON ANTENNA  
PERFORMANCE

C. T. SWIFT

NASA Langley Research Center  
Langley Station, Hampton, Va., U.S.A.

H. HODARA

National Engineering Science Company  
Pasadena, Calif., U.S.A.

## INTRODUCTION

Many scientific investigations have been pursued in the past few years concerning the radiation characteristics of slotted antennas immersed in a plasma. This research has, of course, been prompted by attempts to explain or predict electromagnetic effects which may occur during the re-entry of space vehicles.

The analysis of the problem is conceptually simple, i.e. the wave equation is solved, and all unknown coefficients are found by applying the electromagnetic boundary conditions at the air-plasma interface and at the aperture. However, unless idealized models of the vehicle are chosen, the evaluation of the complicated solutions of the wave equation becomes a major obstacle. In order to avoid these problems, models chosen by most investigators have been of simple geometry, namely, the coated slot on the flat ground plane and the slot on a conducting cylinder. The former is applicable to the re-entry problem provided the dimensions of the vehicle are much greater than a wavelength, and the latter is a reasonable choice if the wavelength is comparable to vehicle dimensions.

Radiation pattern computations constituted the earlier work in this field. The slot on the flat ground plane, coated with a gyro-plasma was analyzed by Hodara (1), (2), and the coated cylinder was originally solved by Wait (3). Others (4), (5), (6), (7), (8), (9), (10) have also examined these geometries from different viewpoints or to extend the results. The final expressions for the patterns reduced to relatively simple forms because of certain asymptotic expansions which may be used in the far field. At least for plane geometry, patterns may be computed easily without the aid of electronic computing machines. The results are valuable because changes in the angular distribution of energy can be predicted.

However, the radiation patterns do not give a complete description of the problem. For instance, if the aperture is backed by a waveguide, the amount of power reflected back into the guide cannot be established by the patterns alone. Such information requires knowledge of the input admittance which

follows from a study of the near fields. Recently, excellent work on this subject has been done by Villeneuve (11), Galejs (12), (13), (14) and Compton (15). All three considered a waveguide opening on to a flat ground plane; however, the differences in the formulation and results made each effort a contribution. The only published near-field results for the cylinder is Wait's (3) treatment of the thin half-wave axial slot radiating into free space.

In this paper the near fields of both geometries are investigated via a transfer function which algebraically relates the unknown aperture fields to those in free space. This transfer function is a matrix of computable numbers which are specified entirely by the plasma parameters, regardless of whether the plasma is homogeneous or inhomogeneous. It is important to note that the matrix is independent of the aperture excitation. Therefore, when a given plasma condition is analyzed any aperture problem can be solved with no more degree of difficulty than the same aperture radiating into free space. The other advantage of this type of formulation is that better near-field approximations may be made without repeating the plasma solution.

To illustrate the use of these techniques, the admittance of long slots on cylinders and planes is computed. The results are compared, and the effects induced by the inhomogeneous plasma are noted. Although no computations for finite apertures are given, expressions are derived. An appendix is also included which outlines an exact treatment of this parallel plate waveguide opening on to a flat ground plane.

#### RADIATION FROM SLOT ANTENNAS ON A FLAT GROUND PLANE

**Infinite Slot with  $\text{TE}_x$  Polarization** – The model shown in Fig. 1 consists of a conducting ground plane on to which is cut a long radiating slot excited so that  $\vec{H}$  is directed along the slot. The fields are assumed to be uniformly distributed along the slot, and the exponential function  $e^{j\omega t}$  is chosen to describe the time dependence. The complex permittivity of the plasma is assumed to vary only in a direction normal to the ground plane. The scalar wave equation which describes the magnetic field in the inhomogeneous plasma is

$$\frac{\partial^2 H_x^I(y, z)}{\partial y^2} + \frac{\partial^2 H_x^I(y, z)}{\partial z^2} - \frac{1}{\epsilon} \frac{d\epsilon}{dz} \frac{\partial H_x^I(y, z)}{\partial z} + \omega^2 \mu_0 \epsilon(z) H_x^I(y, z) = 0 \quad (1)$$

The above equation is partially solved by expressing  $H_x^I$  as a Fourier integral, i.e.

$$H_x^I(y, z) = \frac{1}{2\pi} \int_{-\infty}^{\infty} \bar{H}_x(k_y, z) e^{jk_y y} dk_y \quad (2)$$

which leads to the total differential equation

$$\frac{d^2 \bar{H}_x}{dz^2} - \frac{1}{\epsilon} \frac{d\epsilon}{dz} \frac{d\bar{H}_x}{dz} + \left[ \omega^2 \mu_0 \epsilon(z) - k_y^2 \right] \bar{H}_x = 0 \quad (3)$$

The dielectric constant  $\epsilon$  is an arbitrary function of position; therefore Eq. 3 must be solved by numerical means. However, since Eq. 3 is a second-order differential equation, an initial value of  $\bar{H}_x$  and its first derivative must first be specified before any numerical work can be performed. These starting

conditions are found by constructing functional solutions of  $E_y$  and  $H_x$  in regions I and II, and requiring continuity of the components at the interface  $z = z_0$ .

In the plasma, the fields are of the form,

$$\left. \begin{aligned} H_x^I(y, z) &= \frac{1}{2\pi} \int_{-\infty}^{\infty} \bar{H}_x(k_y, z) e^{jk_y y} dk_y \\ E_y^I(y, z) &= \frac{1}{2\pi} \frac{1}{j\omega\epsilon(z)} \int_{-\infty}^{\infty} \frac{d}{dz} \bar{H}_z(k_y, z) e^{jk_y y} dk_y \end{aligned} \right\} \quad (4)$$

And, in unbounded free space;

$$\left. \begin{aligned} H_x^{II}(y, z) &= \frac{1}{2\pi} \int_{-\infty}^{\infty} H_T(k_y) e^{jk_z z} e^{jk_y y} dk_y \\ E_y^{II}(y, z) &= \frac{1}{2\pi} \frac{1}{j\omega\epsilon_0} \int_{-\infty}^{\infty} H_T(k_y) jk_z e^{jk_z z} e^{jk_y y} dk_y \end{aligned} \right\} \quad (5)$$

where:

$$k_z = \begin{cases} jk_0 \sqrt{\left(\frac{k_y}{k_0}\right)^2 - 1} & k_0 < |k_y| \\ -k_0 \sqrt{1 - \left(\frac{k_y}{k_0}\right)^2} & k_0 > |k_y| \end{cases} \quad (6)$$

The preceding choice of roots is required in order to assure outgoing, damped waves at  $z = \infty$ .

The boundary conditions at  $z = z_0$  requires that

$$\left. \begin{aligned} H_x^I(y, z_0) &= H_x^{II}(y, z_0) \\ E_y^I(y, z_0) &= E_y^{II}(y, z_0) \end{aligned} \right\} \quad (7)$$

Therefore the normalized initial value of  $H_x$  and its derivatives is:

$$\left. \begin{aligned} g(k_y, z_0) &= \frac{\bar{H}_x(k_y, z_0)}{H_T(k_y) e^{jk_z z_0}} = 1 \\ g'(k_y, z_0) &= \frac{dg(k_y, z)}{dz} \Big|_{z=z_0} = \frac{d}{dz} \left[ \frac{\bar{H}_x(k_y, z)}{H_T(k_y) e^{jk_z z}} \right]_{z=z_0} \\ &= j \frac{\epsilon(z_0)}{\epsilon_0} \begin{cases} jk_0 \sqrt{\left(\frac{k_y}{k_0}\right)^2 - 1} & k_0 < |k_y| \\ -k_0 \sqrt{1 - \left(\frac{k_y}{k_0}\right)^2} & k_0 > |k_y| \end{cases} \end{aligned} \right\} \quad (8)$$

If the differential Eq. 3 is now divided by  $H_T(k_y) e^{jk_z z_0}$ , normalized values of  $H_x$  can be numerically computed at  $z = 0$ .

The normalization constant,  $H_T(k_y) e^{jk_z z_0}$  is found by completing the boundary conditions at  $z = 0$ .

It is of interest to note the plasma problem has been solved without any detailed thoughts given to the aperture or the method of feeding the aperture.

The transforms of the external field at the aperture are:

$$\left. \begin{aligned} \bar{H}_x(k_y, 0) &= g(k_y, 0) H_T(k_y) e^{jk_z z_0} \\ E_y(k_y, 0) &= \frac{-j}{k_0 Y_0 \frac{\epsilon(0)}{\epsilon_0}} g(k_y, 0) H_T(k_y) e^{jk_z z_0} \end{aligned} \right\} \quad (9)$$

In matrix form, Eq. 9 becomes:

$$\begin{pmatrix} \bar{H}_x(k_y, 0) \\ E_y(k_y, 0) \end{pmatrix} = \begin{pmatrix} L_{11}(k_y) \\ L_{12}(k_y) \end{pmatrix} H_T e^{jk_z z_0} \quad (10)$$

where the matrix elements are known numbers which are defined through Eq. 9. Equation 10 is nothing more than a transfer function which relates the unknown fields at the aperture to the unknown free-space Fourier coefficient  $H_T(k_y)$ . Therefore when the matrix elements are specified the coated antenna is no more complicated to solve than the uncoated problem.

If the aperture is fed by a parallel plate waveguide, excited such that only  $TE_x$  modes exist in the guide, the formal solution follows by constructing interior ( $z < 0$ ) fields and requiring continuity of  $\bar{H}_x$  and  $\bar{E}_y$  at  $z = 0$ . The interior solution will contain one unknown, namely, the reflection coefficient; therefore, the boundary conditions should, in principle, give both  $\Gamma$  and  $H_T(k_y)$ . Such a general formulation is outlined in Appendix 1.

The general equation developed in Appendix 1 has not been programed; however, a first-order estimate of  $\Gamma$  and  $H_T$  can be achieved by intelligently guessing the electric field at the aperture. If a  $TEM$  mode is incident on the aperture, a reasonable guess for  $E_y(y, 0)$  is

$$E_y(y, 0) = \frac{V_0}{b} \quad (11)$$

A construction of the field solutions in the guide to relate the aperture voltage  $V_0$  to the reflection coefficient is the next natural step. Use of Eq. 10 would then give a first-order estimate of both  $\Gamma$  and  $H_T$ . However, it is more conventional to solve for the external admittance of the guide. This can also be done through use of Eq. 10.

The Fourier transform of Eq. 14 is

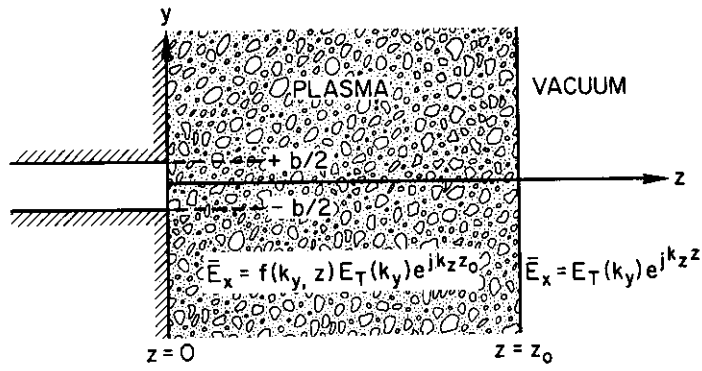
$$E_y(k_y, 0) = V_0 e^{-jk_y \frac{b}{2} \sin\left(k_y \frac{b}{2}\right)} \frac{1}{k_y \frac{b}{2}} \quad (12)$$

Therefore, Eq. 10 may be expressed in terms of  $V_0$  as follows:

$$\begin{pmatrix} \bar{H}_x(k_y, 0) \\ E_y(k_y, 0) \end{pmatrix} = \begin{pmatrix} L_{11} \\ L_{12} \\ 1 \end{pmatrix} V_0 e^{-jk_y \frac{b}{2} \sin\left(k_y \frac{b}{2}\right)} \frac{1}{k_y \frac{b}{2}} \quad (13)$$

The power per unit length radiated by the aperture is

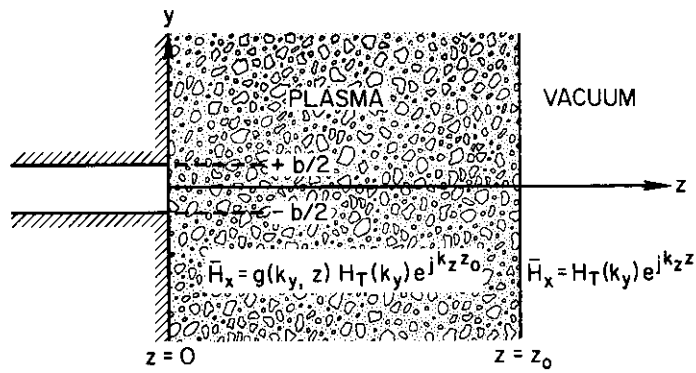
$$Pl = \frac{1}{2} \int_{-b/2}^{b/2} H_x(y, 0) E_y^*(y, 0) dy = \frac{1}{2} \frac{1}{2\pi} \int_{-\infty}^{\infty} \bar{H}_x(k_y, 0) E_y^*(k_y, 0) dk_y \quad (14)$$



$$\frac{d^2 f}{dz^2} + [\omega^2 \mu_0 \epsilon(z) - k_y^2] f = 0$$

$$\begin{Bmatrix} \bar{E}_x(k_y, 0) \\ \bar{H}_y(k_y, 0) \end{Bmatrix} = \begin{bmatrix} f(k_y, 0) \\ -f'(k_y, 0) \end{bmatrix} E_T(k_y) e^{jk_z z_0}$$

FIG. 1 Plasma-covered  $TE_x$  slot



$$\frac{d^2 g}{dz^2} - \frac{1}{\epsilon} \frac{d\epsilon}{dz} \frac{dg}{dz} + [\omega^2 \mu_0 \epsilon(z) - k_y^2] g = 0$$

$$\begin{Bmatrix} \bar{H}_x(k_y, 0) \\ \bar{E}_y(k_y, 0) \end{Bmatrix} = \begin{bmatrix} g(k_y, 0) \\ -jg'(k_y, 0) \end{bmatrix} H_T(k_y) e^{jk_z z_0}$$

FIG. 2 Plasma-covered  $TM_x$  slot

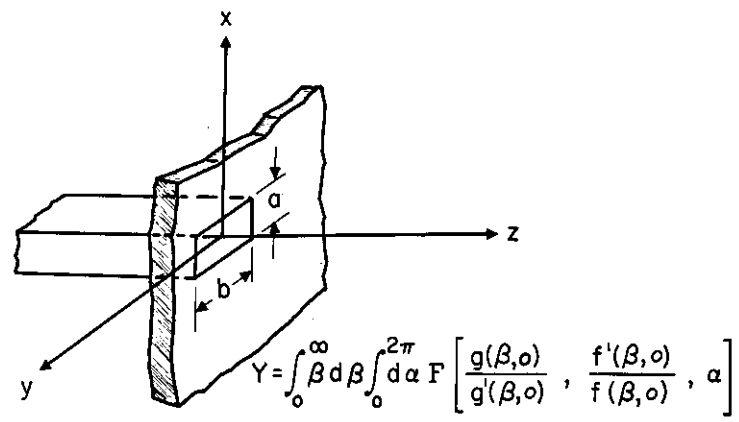


FIG. 3 Aperture coated with inhomogeneous plasma

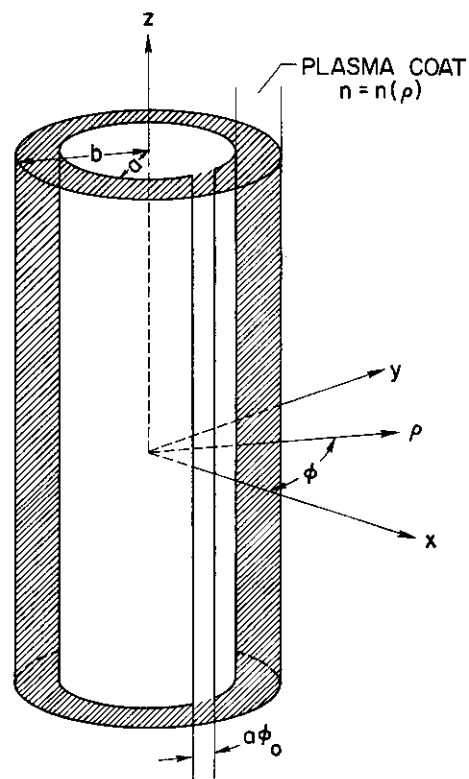


FIG. 4 Geometry of a coated slotted cylinder



where the dual integral representation is a statement of Parseval's theorem.

Using Eq. 13 and 14, the external aperture admittance per unit length is

$$\begin{aligned} Y_l &= \frac{2P_l}{|V_0|^2} = \frac{1}{2\pi} \int_{-\infty}^{\infty} \frac{L_{11}}{L_{12}} \frac{\sin^2\left(k_y \frac{b}{2}\right)}{\left(k_y \frac{b}{2}\right)^2} dk_y \\ &= \frac{j}{\pi} k_0 Y_0 \frac{\epsilon(0)}{\epsilon_0} \int_0^{\infty} \frac{g'(k_y, 0)}{g(k_y, 0)} \frac{\sin^2\left(k_y \frac{b}{2}\right)}{\left(k_y \frac{b}{2}\right)^2} dk_y \end{aligned} \quad (15)$$

In order to compute radiation patterns,  $H_x^{II}(y, z)$ , hence  $H_T(k_y)$ , must be evaluated at points far from the aperture. From Eqs. 10 and 12,

$$H_T(k_y) = \frac{V_0 e^{-j\left(k_y \frac{b}{2} + k_z z_0\right)} \sin\left(k_y \frac{b}{2}\right)}{L_{12}(k_y) k_y \frac{b}{2}} \quad (16)$$

Therefore, with the substitutions

$$\begin{cases} z = \rho \cos \phi \\ y = \rho \sin \phi \end{cases} \quad (17)$$

the expression for  $H_x^{II}(\rho, \phi)$  becomes

$$H_x^{II}(\rho, \phi) = \frac{V_0}{2\pi} \int_{-\infty}^{\infty} \left[ \frac{e^{-j\left(k_y \frac{b}{2} + k_z z_0\right)}}{L_{12}(k_y)} \right] e^{j\rho(k_z \cos \phi + k_y \sin \phi)} dk_y \quad (18)$$

where it has been assumed that

$$\frac{\sin\left(k_y \frac{b}{2}\right)}{k_y \frac{b}{2}} \cong 1 \quad (19)$$

The integral of Eq. 18 may be solved by the method of stationary phase. (See (1) for application to this geometry.) The result is

$$H_x^{II}(\rho, \phi) \cong \frac{e^{j\frac{3\pi}{4}}}{\sqrt{\rho\lambda_0}} e^{j(z_0 \cos \phi + \frac{b}{2} \sin \phi)} V_0 Y_0 \left\{ \frac{\epsilon(0)}{\epsilon_0} \frac{k_0 \cos \phi}{g\left(\frac{k_y}{k_0} - \sin \phi\right)} \right\} e^{-jk_0 \rho} \quad (20)$$

where the magnitude of the terms in parentheses is the pattern expression, i.e.

$$P(\phi) = k_0 \left| \frac{\epsilon(0)}{\epsilon_0} \right| \left| \frac{\cos \phi}{g\left(\frac{k_y}{k_0} - \sin \phi\right)} \right| \quad (21)$$

**Infinite Slot with TM<sub>x</sub> Polarization** – The geometry and appropriate field representation is shown in Fig. 2. If the fields are polarized such that the electric field  $E(y, z)$  is directed along the  $x$ -axis, the wave equation for  $E_x^I$  is

$$\frac{\partial^2 E_x^I}{\partial y^2} + \frac{\partial^2 E_x^I}{\partial z^2} + \omega^2 \mu_0 \epsilon E_x^I = 0 \quad (22)$$

As before,  $E_x^I(y, z)$  and  $E_x^{II}(y, z)$  are defined through the Fourier representation,

$$\left. \begin{aligned} E_x^I &= \frac{1}{2\pi} \int_{-\infty}^{\infty} F(k_y, z) e^{jk_y y} dk_y \\ E_x^{II} &= \frac{1}{2\pi} \int_{-\infty}^{\infty} E_T(k_y) e^{jk_y z} e^{jk_y y} dk_y \end{aligned} \right\} \quad (23)$$

Use of Eq. 23 then reduces Eq. 22 to the following equation, which must be solved numerically

$$\frac{d^2 f(k_y, z)}{dz^2} + [\omega^2 \mu_0 \epsilon(z) - k_y^2] f = 0 \quad (24)$$

subject to the starting conditions,

$$\left. \begin{aligned} f(k_y, z_0) &= 1 \\ f'(k_y, z_0) &= j \begin{cases} j k_0 \sqrt{\left(\frac{k_y}{k_0}\right)^2 - 1} & \left|\frac{k_y}{k_0}\right| > 1 \\ -k_0 \sqrt{1 - \left(\frac{k_y}{k_0}\right)^2} & \left|\frac{k_y}{k_0}\right| < 1 \end{cases} \end{aligned} \right\} \quad (25)$$

where

$$f(k_y, z) = \frac{F(k_y, z)}{E_T(k_y) e^{jk_y z_0}}$$

In matrix form, the transformed field solutions at  $z = 0$  are given by

$$\begin{pmatrix} E_x(k_y, 0) \\ H_y(k_y, 0) \end{pmatrix} = \begin{pmatrix} f(k_y, 0) \\ -\frac{1}{j\omega\mu_0} f'(k_y, 0) \end{pmatrix} E_T(k_y) e^{jk_y z_0} \quad (26)$$

Now, if the electric field at the aperture corresponds to a  $TE_1$  excitation, the following transform pairs are defined at  $z = 0$

$$\left. \begin{aligned} E_x^I(y, 0) &= E_0 \cos\left(\frac{\pi y}{b}\right) & -\frac{b}{2} \leq y \leq \frac{b}{2} \\ E_x(k_y, 0) &= E_0 \cdot 2\pi b \frac{\cos\left(k_y \frac{b}{2}\right)}{\pi^2 - (k_y b)^2} \end{aligned} \right\} \quad (27)$$

and the aperture admittance per unit length is

$$Y_l = \frac{2P}{|E_0|^2} = j \frac{k_0}{Y_0} 4\pi b^2 \int_0^\infty \frac{\cos^2 k_y \frac{b}{2}}{[\pi^2 - (k_y b)^2]^2} \frac{f^1(k_y, 0)}{f(k_y, 0)} dk_y \quad (28)$$

The radiation fields, as derived from a stationary phase evaluation of  $E_x^{II}$  is given by

$$E_x^{II}(\rho, \phi) \cong E_0 e^{j\frac{\pi}{4}} \frac{e^{-jk_0 \rho}}{\sqrt{\lambda_0 \rho}} e^{-jk_y z_0} \frac{2\pi b \cos\left(k_0 \frac{b}{2} \sin \phi\right)}{f\left(\frac{k_y}{k_0} = -\sin \phi, 0\right) [\pi^2 - (k_0 b \sin \phi)^2]} \quad (29)$$

**The General Aperture** – The development of a general aperture on a ground plane, shown in Fig. 3, parallels the development given above, except a double Fourier integral representation is necessary because the fields depend on all three cartesian coordinates. This problem was approached by superimposing *TE* and *TM* vector potentials. By a straightforward application of the boundary conditions, it can be shown that the pertinent differential equations are

$$\left. \begin{aligned} \frac{d^2 f}{dz^2} + k_0^2 \left[ \frac{\epsilon(z)}{\epsilon_0} - \beta^2 \right] f &= 0 \\ \frac{d^2 g}{dz^2} - \frac{1}{\epsilon(z)} \frac{d\epsilon(z)}{dz} \frac{dg}{dz} + k_0^2 \left[ \frac{\epsilon(z)}{\epsilon_0} - \beta^2 \right] g &= 0 \end{aligned} \right\} \quad (30)$$

With starting conditions

$$\left. \begin{aligned} f(z_0) &= 1 \\ f'(z_0) &= j \begin{cases} jk_0 \sqrt{\beta^2 - 1} & |\beta| > 1 \\ -k_0 \sqrt{1 - \beta^2} & |\beta| < 1 \end{cases} \\ g(z_0) &= 1 \\ g'(z_0) &= j \begin{cases} jk_0 n^2(z_0) \sqrt{\beta^2 - 1} & |\beta| > 1 \\ -k_0 n^2(z_0) \sqrt{1 - \beta^2} & |\beta| < 1 \end{cases} \end{aligned} \right\} \quad (31)$$

where  $\beta$  is defined through the transformation  $k_x = k_0 \beta \cos \alpha$  and  $k_y = k_0 \beta \sin \alpha$ .

Note that Eq. 30 and 31 are identical to the equations and starting conditions which were used for the infinite slot. It can therefore be concluded that when the external plasma problem is solved for the infinite slot of *TE* and *TM* polarization, it is automatically solved for the finite aperture.

The double Fourier transform of the aperture fields may also be set up in matrix form defining a transfer function which relates the aperture fields to the free-space fields. This relationship is

$$\begin{bmatrix} \bar{E}_x(k_x, k_y, 0) \\ \bar{E}_y(k_x, k_y, 0) \\ \bar{H}_x(k_x, k_y, 0) \\ \bar{H}_y(k_x, k_y, 0) \end{bmatrix} = \frac{1}{k_0 \beta^2} \begin{bmatrix} 0 & \frac{-jk_x g'(0) \epsilon_0}{\epsilon(0) k_0} & 0 & -k_y f(0) \sqrt{\mu_0 \epsilon_0} \\ 0 & \frac{-jk_y g'(0) \epsilon_0}{\epsilon(0) k_0} & 0 & k_x f(0) \sqrt{\mu_0 \epsilon_0} \\ 0 & k_y g(0) \sqrt{\epsilon_0 / \mu_0} & 0 & \frac{-jk_x f'(0) \epsilon_0}{k_0} \\ 0 & -k_x g(0) \sqrt{\epsilon_0 / \mu_0} & 0 & \frac{-jk_y f'(0) \epsilon_0}{k_0} \end{bmatrix} \begin{bmatrix} 0 \\ E_{TE} e^{jk_x z_0} \\ 0 \\ H_{TE} e^{jk_x z_0} \end{bmatrix} \quad (32)$$

If the aperture field corresponds to a *TE*<sub>01</sub> excitation, then

$$\left. \begin{aligned} E_x &= \frac{V}{a} \cos \frac{\pi y}{b} \\ E_y &= 0 \end{aligned} \right\} \quad (33)$$

The transforms of Eq. 33 are

$$\left. \begin{aligned} \bar{E}_x &= \frac{V_0}{a} \int_{-b/2}^{b/2} \int_{-a/2}^{a/2} \cos \frac{\pi y}{b} e^{-jk_y y} e^{-jk_x x} dx dy \\ &= V_0 \left[ \frac{2\pi b \cos \left( k_y \frac{b}{2} \right)}{\pi^2 - (k_y b)^2} \right] \left[ \frac{\sin \left( \frac{k_x a}{2} \right)}{\left( \frac{k_x a}{2} \right)} \right] \\ \bar{E}_y &= 0 \end{aligned} \right\} \quad (34)$$

And the aperture admittance is

$$\begin{aligned} Y &= \frac{2P}{|V_0|^2} = \frac{1}{(2\pi)^2} \int_{-\infty}^{\infty} \int_{-\infty}^{\infty} \frac{\bar{E}_x^*(k_x, k_y, 0) \bar{H}_y(k_x, k_y, 0)}{|V_0|^2} dk_x dk_y \\ &\equiv \frac{k_0^2}{(2\pi)^2} \int_0^{2\pi} \int_0^{\infty} \frac{\bar{E}_x^*(\alpha, \beta, 0) \bar{H}_y(\alpha, \beta, 0)}{|V_0|^2} \beta d\beta d\alpha \end{aligned} \quad (35)$$

Equations 32 and 34 may be used to express  $E_T$  and  $H_T$  in terms of  $V_0$ ; therefore,  $H_y(k_x, k_y, 0)$  may also be expressed in terms of  $V_0$ , i.e.

$$\bar{H}_y(k_x, k_y, 0) = \frac{j\bar{E}_x V_0}{k_x^2 + k_y^2} \left\{ -\left( \frac{k_x}{k_0} \right)^2 \left( \frac{k_0 g}{g^1} \right) \frac{\epsilon(0)}{\epsilon_0} + \left( \frac{k_y}{k_0} \right)^2 \left( \frac{f^1}{k_0 f} \right) \right\} \quad (36)$$

If Eqs. 34 and 35 are converted to polar coordinates and substituted into Eq. 35, the final admittance expression is:

$$\begin{aligned} Y &= jY_0 (k_0 b)^2 \int_0^{\infty} \int_0^{2\pi} \left[ \frac{\cos \frac{k_0 b}{2} \sin \alpha}{\pi^2 - (k_0 b \sin \alpha)^2} \right]^2 \left[ \frac{\sin \left( \frac{k_0 a}{2} \cos \alpha \right)}{\left( \frac{k_0 a}{2} \cos \alpha \right)} \right]^2 \\ &\quad \times \left\{ -\cos^2 \alpha \left( \frac{k_0 g}{g^1} \right) \frac{\epsilon(0)}{\epsilon_0} + \sin^2 \alpha \left( \frac{f^1}{k_0 f} \right) \right\} \beta d\beta d\alpha \end{aligned} \quad (37)$$

#### RADIATION FROM SLOT ANTENNAS ON A CYLINDRICAL GROUND PLANE

**The Infinitely Long Axial Slot on a Cylinder** – The geometry is shown in Fig. 4. An infinitely long slot is cut into a long conducting cylinder with  $H$  directed along the axis. The structure is coated with plasma, whose dielectric properties vary radially. It is assumed that the fields are independent of  $z$  so that  $H_z$  in regions I and II can be described by the following Fourier series in azimuth

$$\left. \begin{aligned} H_z^I(\rho, \phi) &= \sum_{m=-\infty}^{\infty} H_m^I(\rho) e^{-jm\phi} \\ H_z^{II}(\rho, \phi) &= \sum_{m=-\infty}^{\infty} C_m H_m^{(2)}(k_0 \rho) e^{-jm\phi} \end{aligned} \right\} \quad (38)$$

where the radial function,  $H_{mz}(\rho)$  satisfied the differential equation

$$\frac{1}{\rho} \frac{d}{d\rho} \left( \rho \frac{d}{d\rho} H_{mz} \right) - \frac{1}{\epsilon} \frac{d\epsilon}{d\rho} \frac{dH_{mz}}{d\rho} + k_0^2 \left[ \frac{\epsilon(\rho)}{\epsilon_0} - \frac{m^2}{(k_0\rho)^2} \right] H_{mz} = 0 \quad (39)$$

By normalizing with respect to  $C_m$ , Eq. 39 can be numerically integrated provided the boundary conditions are met at  $\rho = b$ . The continuity requirement for  $H_z$  and  $E_\phi$  gives

$$\left. \begin{aligned} h_{mz}(b) &= \frac{H_{mz}(b)}{C_m} = H_m(2)(k_0b) \\ h_{mz^1}(b) &= \left. \frac{d}{d\rho} \frac{H_{mz}(\rho)}{C_m} \right|_{\rho=b} = \frac{\epsilon(b)}{\epsilon_0} H_m(2)^1(k_0b) \end{aligned} \right\} \quad (40)$$

Equations 39 and 40 then yield normalized field solutions,  $h_m(a)$  and  $h_m^1(a)$  at the aperture.

Since the azimuthal component of the electric field in the plasma is given by

$$E_{\phi^I}(\rho, \phi) = \sum_{m=-\infty}^{\infty} E_{m\phi}(\rho) e^{-jm\phi} = -\frac{1}{j\omega\epsilon(\rho)} \sum_{m=-\infty}^{\infty} \frac{dH_{mz}(\rho)}{d\rho} e^{-jm\phi} \quad (41)$$

the field transforms at the aperture can immediately be written as

$$\begin{pmatrix} H_{mz}(a) \\ E_{m\phi}(a) \end{pmatrix} = \begin{pmatrix} h_{mz}(a) \\ -\frac{1}{j\omega\epsilon(a)} h_{mz^1}(a) \end{pmatrix} C_m \quad (42)$$

The power per unit length radiated by the aperture is

$$\begin{aligned} P_t &= \frac{a}{2} \int_{-\phi_0/2}^{\phi_0/2} E_{\phi^I*}(a, \phi) H_{z^I}(a, \phi) d\phi \\ &= \frac{a}{2} \sum_{m=-\infty}^{\infty} \sum_{m'=-\infty}^{\infty} E_{m'\phi}^{I*}(a) H_{m\phi^I}(a) \int_{-\pi}^{\pi} e^{+j(m'-m)\phi} d\phi \\ &= \pi a \sum_{m=-\infty}^{\infty} \sum_{m'=-\infty}^{\infty} E_{m'\phi}^{I*}(a) H_{mz^I}(a) \delta_{m'm} = \pi a \sum_{m=-\infty}^{\infty} E_{m\phi}^{I*} H_{mz^I}(a) \end{aligned} \quad (43)$$

where the equivalence of the integral over physical space to the sum over mode space is nothing more than Parseval's theorem in cylindrical co-ordinates.

It is now assumed that the electric field distribution at the aperture is

$$E_\phi(a, \phi) = \frac{V_0}{a} \quad (44)$$

whose transform is

$$\begin{aligned} E_{m\phi}(a) &= \frac{1}{2\pi} \int_{-\phi_0/2}^{\phi_0/2} E_\phi(a, \phi) e^{-jm\phi} d\phi \\ &= \frac{V_0}{2\pi a} \frac{\sin\left(\frac{m\phi_0}{2}\right)}{\left(\frac{m\phi_0}{2}\right)} \end{aligned} \quad (45)$$

From Eq. 42 and 45 the transform of  $H_z'$  at the aperture is

$$H_{mz}(a) = -j\omega\epsilon(a) \frac{V_0}{2\pi a} \frac{\sin\left(\frac{m\phi_0}{2}\right)}{\left(\frac{m\phi_0}{2}\right)} \frac{h_{mz}(a)}{h_{mz'}(a)} \quad (46)$$

Therefore, the admittance per unit length is:

$$Y_l = \frac{2P}{|V_0|^2} = -j \frac{k_0 Y_0}{2\pi a} \frac{\epsilon(a)}{\epsilon_0} \sum_{m=-\infty}^{\infty} \left[ \frac{\sin\left(\frac{m\phi_0}{2}\right)}{\left(\frac{m\phi_0}{2}\right)} \right]^2 \frac{h_m(a)}{h_{m'}(a)} \quad (47)$$

The radiation pattern expression is found by solving for  $C_m$ , substituting into the second of Eq. 38, and evaluating  $H_z''(\rho, \phi)$  in the far field (i.e. by asymptotically expanding the Hankel function). From Eqs. 42 and 45,

$$C_m = \frac{-j\omega\epsilon(a)}{2\pi a h_{m'}(a)} V_0 \frac{\sin\left(\frac{m\phi_0}{2}\right)}{\left(\frac{m\phi_0}{2}\right)} \quad (48)$$

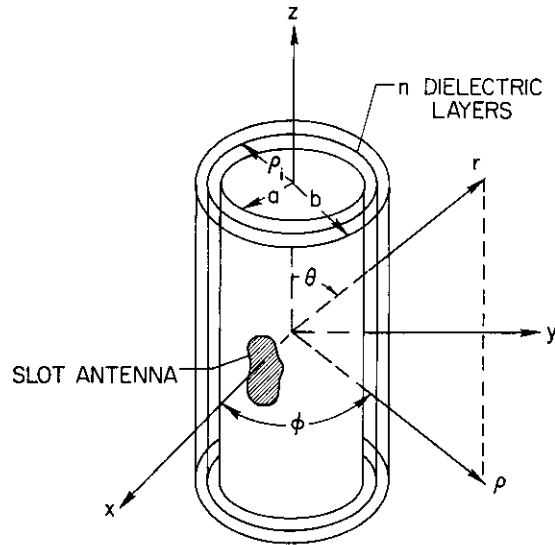
Therefore,  $H_z''(\rho, \phi)$  in the far field is given by

$$H_z(\rho, \phi) = -j \frac{V_0 Y_0}{2\pi a} \sqrt{\frac{2}{\pi k_0 \rho}} e^{-j(k_0 \rho - \frac{\pi}{4})} \left\{ \frac{\epsilon(0)}{\epsilon_0} \sum_{m=-\infty}^{\infty} \left[ \frac{\sin\left(\frac{m\phi_0}{2}\right)}{\left(\frac{m\phi_0}{2}\right)} \right] \frac{e^{-jm(\phi - \frac{\pi}{2})}}{h_{m'}(a)} \right\} \quad (49)$$

The pattern is computed by taking the magnitude of the term in brackets.

**The Arbitrary Aperture on a Cylindrical Ground Plane** – The preferable method of approaching the problem of a general aperture radiating into a radially varying plasma as shown in Fig. 5 would be to construct the fields from axial *TE* and *TM* components and numerically solve the differential equations. However, such an attempt fails because the Maxwell equations will not be satisfied. As an alternative approach (16), the inhomogeneous plasma was replaced by several homogeneous tandem layers judiciously chosen to fit the given distribution. The development of the problem follows from a straightforward generalization of Wait (3), and will therefore only be outlined here. Since each layer is homogeneous, the axial components of  $\vec{E}$  and  $\vec{H}$  completely specify the external problem, and can be written as follows:

$$\left. \begin{aligned} E_z(\rho, \phi, z) &= \frac{1}{j\omega\mu_0\epsilon_i} \sum_{m=-\infty}^{\infty} e^{-jm\phi} \int_{-\infty}^{\infty} u_i^2 F_m^i(k_z, \rho) e^{-jk_z z} dk_z \\ H_z(\rho, \phi, z) &= \frac{1}{j\omega\mu_0\epsilon_i} \sum_{m=-\infty}^{\infty} e^{-jm\phi} \int_{-\infty}^{\infty} u_i^2 G_m^i(k_z, \rho) e^{-jk_z z} dk_z \end{aligned} \right\} \quad (50)$$



$$\begin{Bmatrix} E_{mz}(a, k_z) \\ H_{m\phi}(a, k_z) \\ H_{mz}(a, k_z) \\ E_{m\phi}(a, k_z) \end{Bmatrix} = \begin{bmatrix} L_{jk}(m, k_z) \end{bmatrix}_{4 \times 4 \text{ MATRIX}} \begin{Bmatrix} 0 \\ c_m(k_z) \\ 0 \\ d_m(k_z) \end{Bmatrix}$$

FIG. 5 General aperture on a coated cylinder

Layer No.	1	2		i	i+1		n	n+1 (free space)
Diel. Const.	$\epsilon_1$	$\epsilon_2$		$\epsilon_i$	$\epsilon_{i+1}$		$\epsilon_n$	$\epsilon_{n+1} = \epsilon_0$
Permeability	$\mu_0$	$\mu_0$		$\mu_0$	$\mu_0$		$\mu_0$	$\mu_0$
$\sqrt{k_1^2 - k_z^2}$	$u_1$	$u_2$	...	$u_i$	$u_{i+1}$	...	$u_n$	$u_{n+1} = u_0$
Radius	a	$\rho_2$	$\rho_3$	$\rho_i$	$\rho_{i+1}$	$\rho_{i+2}$	$\rho_n$	b
Matrices	$[D_{jk}^1]$	$[C_{jk}^2]$	$[C_{jk}^3]$	$[C_{jk}^i]$	$[C_{jk}^{i+1}]$	$[C_{jk}^{i+2}]$	$[C_{jk}^n]$	$[C_{jk}^{n+1}]$

FIG. 6 Schematic for applying boundary conditions

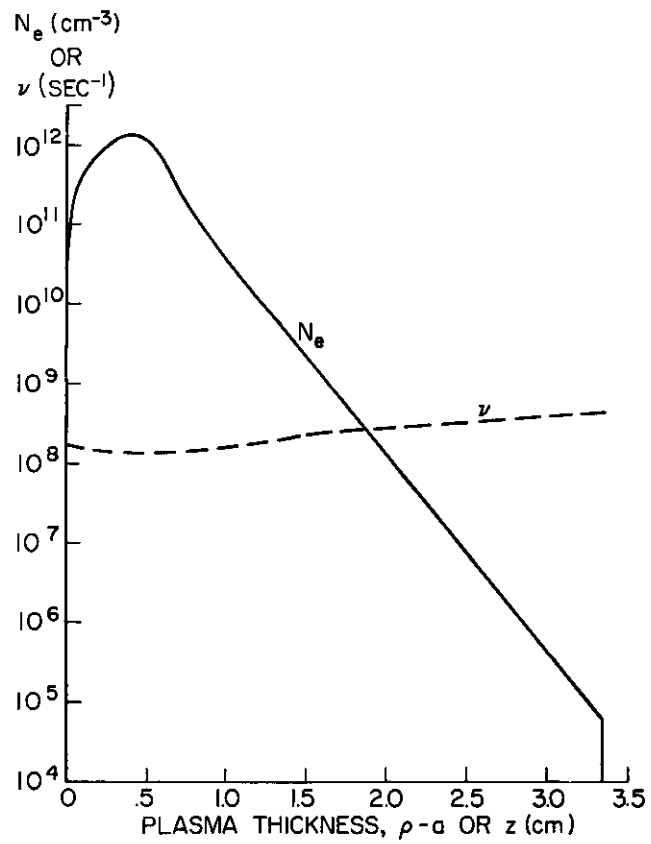


FIG. 7 Typical re-entry plasma profile

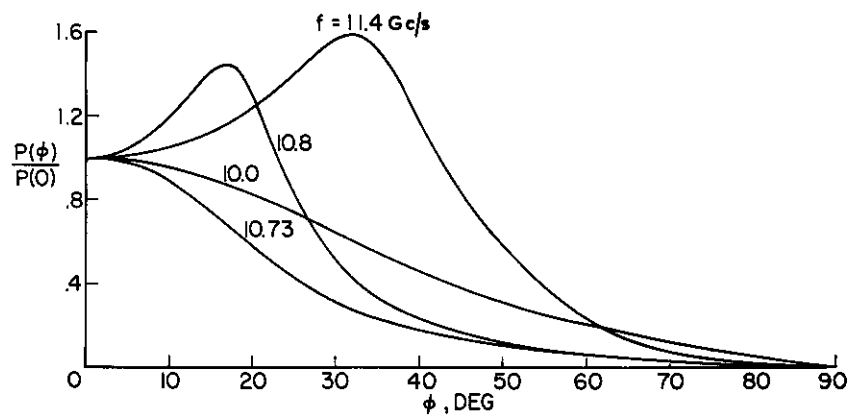


FIG. 8 Patterns of the coated slotted plane



where the superscript  $i$  refers to the fields in the  $i^{\text{th}}$  layer. When  $i = 1, 2, \dots, n$ , the radial solutions of Eq. 50 are:

$$\left. \begin{aligned} F_m^i(k_z, \rho) &= a_m^i J_m(u_i \rho) + A_m^i(u_i \rho) \\ G_m^i(k_z, \rho) &= b_m^i J_m(u_i \rho) + B_m^i(u_i \rho) \end{aligned} \right\} \quad (51)$$

No standing waves exist in free space ( $i = n + 1$ ); therefore,  $F_m^i$  and  $G_m^i$  are of the form:

$$\left. \begin{aligned} F_m^{n+1}(k_z, \rho) &= c_m H_m^{(2)}(u_0 \rho) \\ G_m^{n+1}(k_z, \rho) &= d_m H_m^{(2)}(u_0 \rho) \end{aligned} \right\} \quad (52)$$

If Eq. 50 is used in connection with the Maxwell equations, the azimuthal components of  $\mathbf{E}$  and  $\mathbf{H}$  can be computed, and the boundary conditions can therefore be stated at each interface. From the schematic shown in Fig. 6, the boundary conditions are at  $\rho = \rho_{i+1}$  are:

$$\left. \begin{aligned} E_\phi^i(\rho_{i+1}, \phi, z) &= E_\phi^{i+1}(\rho_{i+1}, \phi, z) \\ E_z^i(\rho_{i+1}, \phi, z) &= E_z^{i+1}(\rho_{i+1}, \phi, z) \\ H_\phi^i(\rho_{i+1}, \phi, z) &= H_\phi^{i+1}(\rho_{i+1}, \phi, z) \\ H_z^i(\rho_{i+1}, \phi, z) &= H_z^{i+1}(\rho_{i+1}, \phi, z) \end{aligned} \right\} \quad (53)$$

The fields are defined in terms of the unknown coefficients,  $a_m, b_m, A_m$ , and  $B_m$ ; therefore, Eq. 53 can be expressed in terms of  $4 \times 4$  matrices relating the unknowns in the  $i^{\text{th}}$  layer to those in the  $(i + 1)^{\text{th}}$  layer, i.e.

$$[A_{jk}^{i+1}] \begin{Bmatrix} a_m^i \\ A_m^i \\ b_m^i \\ B_m^i \end{Bmatrix} = [B_{jk}^{i+1}] \begin{Bmatrix} a_m^{i+1} \\ A_m^{i+1} \\ b_m^{i+1} \\ B_m^{i+1} \end{Bmatrix} \quad (54)$$

where the  $A$  and  $B$  matrices are given explicitly in Appendix 3.

If another  $4 \times 4$  matrix is defined such that  $[C_{jk}^{i+1}] = [A_{jk}^{i+1}]^{-1} [B_{jk}^{i+1}]$ , then it can easily be verified that

$$\begin{Bmatrix} a_m^1 \\ A_m^1 \\ b_m^1 \\ B_m^1 \end{Bmatrix} = [C_{jk}^2] [C_{jk}^3] \cdots [C_{jk}^{n-1}] [C_{jk}^n] \begin{Bmatrix} a_m^n \\ A_m^n \\ b_m^n \\ B_m^n \end{Bmatrix} \quad (55)$$

That is, the unknown coefficients in the first layer can be related directly to those in the last layer by multiplying similar  $4 \times 4$  matrices.

If the boundary conditions are completed at the air-plasma interface, and if  $a_m^1, A_m^1, b_m^1$ , and  $B_m^1$  are converted to field transforms at  $\rho = a$ , the following transfer function is defined

$$\begin{Bmatrix} E_{mz}(a, k_z) \\ H_{m\phi}(a, k_z) \\ H_{mz}(a, k_z) \\ E_{m\phi}(a, k_z) \end{Bmatrix} = [L_{jk}(m, k_z)] \begin{Bmatrix} 0 \\ c_m(k_z) \\ 0 \\ d_m(k_z) \end{Bmatrix} \quad (56)$$

where the  $4 \times 4$   $L$ -matrix is entirely composed of specified or computable

parameters (dielectric constant, Bessel functions, etc.). The  $L$ -matrix is symbolically defined in Appendix 3. The admittance and patterns can be found by completing the boundary conditions at the aperture, and algebraically solving for the unknowns.

#### RESULTS

In order to compare the radiating characteristics of slots on flat and cylindrical ground planes under typical re-entry conditions, the electron density and collision frequency profile shown in Fig. 7 was chosen as a coating. The slot on both ground planes was infinitely long, 0.4 inch wide (the width of a standard  $X$ -band waveguide), and polarized with the magnetic field directed along the slot. The patterns and input admittance were then computed via the method described under the headings "Infinite Slot with  $TE_x$  polarization" and "The Infinitely Long Axial Slot on a Cylinder".

The radiation patterns of the coated slot on a flat ground plane are shown in Fig. 8. The behavior of the patterns as a function of frequency is sharply divided at the peak plasma frequency of 10.76 Gc/s. Frequencies above this exhibit definite off-axis maxima which progress toward the axis as the frequency decreases. Whereas, below 10.76 Gc/s the maxima occur only at  $\phi = 0$  and the radiation rapidly decays as a function of angle. The shifting of the maximum and the differences in the pattern characteristics on either side of critical frequency are exactly what one would expect if the coating were homogeneous with a plasma frequency of 10.76 Gc/s. However, the location of the pattern maximum, which for a collisionless homogeneous plasma is given by the plane wave critical angle

$$\phi_c = \cos^{-1}(f_p/f)$$

does not correlate with the results of Fig. 8.

The radiation patterns of the coated cylinder are shown in Fig. 9. Again, the radiation patterns have strikingly different characteristics, depending upon whether the propagating frequency is greater than or less than the peak plasma frequency. There is also a progression of the pattern maxima above plasma resonance, but the location cannot be predicted as easily as in the plane case.

The external admittance of the cylinder is plotted as a function of frequency in Fig. 10. Nineteen admittance points were computed in the frequency interval of 10.0 to 11.8 Gc/s, yet this number was insufficient to establish a smooth curve because of small-scale fluctuations; none the less, some interesting features are revealed. The most striking effect occurs in the region of peak critical frequency, where the conductance and susceptance suddenly decrease. Based upon some recent work by C. M. Knop, low values of admittance should be expected at the critical frequency. At frequencies above resonance, the conductance rises rapidly, but the susceptance remains relatively constant. As the frequency increases, both curves smoothly approach the no-coating values, as they should. Below resonance the curves are fluctuating too much to make any general comments.

TABLE I

TABLES OF  $\frac{g(\beta, 0)}{g'(\beta, 0)}$  AND  $\frac{f'(\beta, 0)}{f(\beta, 0)}$  FOR THE INHOMOGENEOUS

PLASMA GIVEN IN FIGURE 7

1  $f = 10.00 \text{ Gc/s}$ 

$\beta$	$\frac{g(\beta, 0)}{g'(\beta, 0)}$	$\frac{f'(\beta, 0)}{f(\beta, 0)}$
0	0.035 + j0.163	- 0.424 - j0.844
0.050	0.034 + j0.164	- 0.427 - j0.842
0.100	0.030 + j0.166	- 0.433 - j0.836
0.150	0.023 + j0.168	- 0.444 - j0.825
0.200	0.014 + j0.171	- 0.460 - j0.811
0.225	0.009 + j0.172	- 0.469 - j0.803
0.250	0.003 + j0.174	- 0.480 - j0.793
0.275	- 0.004 + j0.175	- 0.492 - j0.783
0.300	- 0.011 + j0.176	- 0.504 - j0.771
0.325	- 0.018 + j0.176	- 0.518 - j0.759
0.350	- 0.026 + j0.176	- 0.534 - j0.746
0.375	- 0.034 + j0.176	- 0.550 - j0.732
0.400	- 0.042 + j0.175	- 0.568 - j0.716
0.425	- 0.050 + j0.173	- 0.586 - j0.700
0.450	- 0.058 + j0.171	- 0.606 - j0.684
0.475	- 0.067 + j0.169	- 0.627 - j0.666
0.500	- 0.074 + j0.166	- 0.650 - j0.647
0.550	- 0.089 + j0.159	- 0.698 - j0.608
0.600	- 0.103 + j0.150	- 0.752 - j0.565
0.650	- 0.114 + j0.141	- 0.810 - j0.520
0.700	- 0.124 + j0.131	- 0.874 - j0.471
0.800	- 0.138 + j0.111	- 1.016 - j0.364
0.900	- 0.147 + j0.093	- 1.180 - j0.240
1.000	- 0.152 + j0.082	- 1.364 - j0.002
1.200	- 0.156 + j0.048	- 2.027 - j0.001
1.400	- 0.150 + j0.031	- 2.508 - j0.001
1.600	- 0.144 + j0.021	- 2.966 - j0.001
1.800	- 0.138 + j0.014	- 3.413 - j0.001
2.000	- 0.133 + j0.010	- 3.855 - j0.001
2.500	- 0.121 + j0.005	- 4.946 - j0.000
3.000	- 0.110 + j0.002	- 6.028 - j0.000
3.500	- 0.101 + j0.001	- 7.102 - j0.000
4.000	- 0.092 + j0.001	- 8.171 - j0.000

1b  $f = 10.73 \text{ Gc/s}$ 

$\beta$	$\frac{g(\beta, o)}{g'(\beta, o)}$	$\frac{f'(\beta, o)}{f(\beta, o)}$
0	$0.049 + j0.191$	$- 0.293 - j0.970$
0.050	$0.043 + j0.195$	$- 0.295 - j0.967$
0.100	$0.026 + j0.205$	$- 0.302 - j0.960$
0.150	$- 0.002 + j0.215$	$- 0.315 - j0.948$
0.200	$- 0.041 + j0.221$	$- 0.332 - j0.931$
0.225	$- 0.062 + j0.220$	$- 0.343 - j0.921$
0.250	$- 0.083 + j0.216$	$- 0.355 - j0.909$
0.275	$- 0.103 + j0.210$	$- 0.368 - j0.897$
0.300	$- 0.122 + j0.201$	$- 0.382 - j0.883$
0.325	$- 0.138 + j0.190$	$- 0.398 - j0.868$
0.350	$- 0.152 + j0.179$	$- 0.415 - j0.852$
0.375	$- 0.164 + j0.166$	$- 0.434 - j0.835$
0.400	$- 0.174 + j0.154$	$- 0.453 - j0.817$
0.425	$- 0.181 + j0.142$	$- 0.474 - j0.798$
0.450	$- 0.187 + j0.131$	$- 0.497 - j0.778$
0.475	$- 0.192 + j0.120$	$- 0.521 - j0.757$
0.500	$- 0.195 + j0.110$	$- 0.546 - j0.735$
0.550	$- 0.199 + j0.092$	$- 0.601 - j0.688$
0.600	$- 0.200 + j0.078$	$- 0.662 - j0.637$
0.650	$- 0.200 + j0.066$	$- 0.728 - j0.584$
0.700	$- 0.199 + j0.056$	$- 0.801 - j0.527$
0.800	$- 0.196 + j0.041$	$- 0.964 - j0.403$
0.900	$- 0.191 + j0.031$	$- 1.152 - j0.262$
1.000	$- 0.187 + j0.024$	$- 1.364 - j0.002$
1.200	$- 0.178 + j0.014$	$- 2.095 - j0.001$
1.400	$- 0.169 + j0.008$	$- 2.626 - j0.001$
1.600	$- 0.161 + j0.005$	$- 3.128 - j0.001$
1.800	$- 0.153 + j0.003$	$- 3.616 - j0.001$
2.000	$- 0.145 + j0.002$	$- 4.097 - j0.000$
2.500	$- 0.128 + j0.000$	$- 5.281 - j0.000$
3.000	$- 0.114 + j0.000$	$- 6.448 - j0.000$
3.500	$- 0.102 + j0.000$	$- 7.606 - j0.000$
4.000	$- 0.092 + j0.000$	$- 8.756 - j0.000$

1C  $f = 10.8 \text{ Gc/s}$ 

$\beta$	$\frac{g(\beta, 0)}{g^2(\beta, 0)}$	$\frac{f'(\beta, 0)}{f(\beta, 0)}$
0	$0.070 + j0.200$	$-0.280 - j0.983$
0.100	$0.074 + j0.230$	$-0.290 - j0.973$
0.200	$0.055 + j0.349$	$-0.320 - j0.943$
0.250	$-0.020 + j0.446$	$-0.342 - j0.921$
0.300	$-0.188 + j0.498$	$-0.370 - j0.894$
0.350	$-0.364 + j0.410$	$-0.403 - j0.863$
0.400	$-0.422 + j0.261$	$-0.442 - j0.827$
0.450	$-0.402 + j0.153$	$-0.486 - j0.787$
0.500	$-0.365 + j0.093$	$-0.536 - j0.743$
0.530	$-0.344 + j0.070$	$-0.469 - j0.715$
0.570	$-0.320 + j0.050$	$-0.615 - j0.676$
0.600	$-0.304 + j0.039$	$-0.653 - j0.645$
0.630	$-0.291 + j0.032$	$-0.693 - j0.612$
0.670	$-0.275 + j0.024$	$-0.749 - j0.567$
0.700	$-0.266 + j0.020$	$-0.794 - j0.532$
0.725	$-0.259 + j0.017$	$-0.833 - j0.502$
0.750	$-0.252 + j0.015$	$-0.873 - j0.471$
0.775	$-0.246 + j0.013$	$-0.916 - j0.440$
0.800	$-0.241 + j0.011$	$-0.959 - j0.407$
0.820	$-0.237 + j0.010$	$-0.995 - j0.380$
0.840	$-0.233 + j0.009$	$-1.032 - j0.353$
0.860	$-0.230 + j0.008$	$-1.070 - j0.324$
0.880	$-0.226 + j0.008$	$-1.109 - j0.295$
0.900	$-0.223 + j0.007$	$-1.149 - j0.264$
0.920	$-0.221 + j0.006$	$-1.190 - j0.232$
0.940	$-0.218 + j0.006$	$-1.232 - j0.197$
0.960	$-0.215 + j0.005$	$-1.275 - j0.157$
0.970	$-0.214 + j0.005$	$-1.297 - j0.135$
0.980	$-0.213 + j0.005$	$-1.319 - j0.109$
0.990	$-0.212 + j0.005$	$-1.341 - j0.077$
0.995	$-0.211 + j0.004$	$-1.352 - j0.055$
1.000	$-0.210 + j0.004$	$-1.364 - j0.002$
1.200	$-0.191 + j0.002$	$-2.102 - j0.001$
1.500	$-0.172 + j0.001$	$-2.893 - j0.001$
2.000	$-0.148 + j0.001$	$-4.121 - j0.000$
2.500	$-0.129 + j0.000$	$-5.313 - j0.000$
3.000	$-0.114 + j0.000$	$-6.488 - j0.000$
3.500	$-0.102 + j0.000$	$-7.654 - j0.000$
4.000	$-0.092 + j0.000$	$-8.812 - j0.000$

1d  $f = 11.4 \text{ Gc/s}$  $\beta$  $\frac{g(\beta, \alpha)}{g'(\beta, \alpha)}$  $\frac{f'(\beta, \alpha)}{f(\beta, \alpha)}$ 

0	$0.030 + j0.194$	$- 0.168 - j1.099$
0.050	$0.031 + j0.196$	$- 0.170 - j1.096$
0.100	$0.003 + j0.202$	$- 0.178 - j1.087$
0.150	$0.037 + j0.212$	$- 0.192 - j1.073$
0.200	$0.041 + j0.228$	$- 0.211 - j1.053$
0.225	$0.044 + j0.238$	$- 0.222 - j1.041$
0.250	$0.046 + j0.251$	$- 0.235 - j1.028$
0.275	$0.048 + j0.265$	$- 0.250 - j1.013$
0.300	$0.050 + j0.283$	$- 0.266 - j0.997$
0.325	$0.050 + j0.304$	$- 0.283 - j0.979$
0.350	$0.049 + j0.329$	$- 0.302 - j0.960$
0.375	$0.044 + j0.358$	$- 0.322 - j0.940$
0.400	$0.035 + j0.392$	$- 0.344 - j0.919$
0.425	$0.019 + j0.431$	$- 0.367 - j0.897$
0.450	$- 0.008 + j0.474$	$- 0.392 - j0.873$
0.475	$- 0.049 + j0.518$	$- 0.418 - j0.849$
0.500	$- 0.108 + j0.558$	$- 0.446 - j0.823$
0.550	$- 0.277 + j0.588$	$- 0.507 - j0.768$
0.600	$- 0.449 + j0.502$	$- 0.575 - j0.710$
0.650	$- 0.529 + j0.346$	$- 0.649 - j0.648$
0.700	$- 0.520 + j0.210$	$- 0.730 - j0.582$
0.800	$- 0.429 + j0.071$	$- 0.914 - j0.441$
0.900	$- 0.353 + j0.024$	$- 1.125 - j0.283$
1.000	$- 0.303 + j0.002$	$- 1.364 - j0.002$
1.200	$- 0.239 + j0.001$	$- 2.160 - j0.001$
1.400	$- 0.208 + j0.001$	$- 2.737 - j0.001$
1.600	$- 0.187 + j0.000$	$- 3.279 - j0.001$
1.800	$- 0.170 + j0.000$	$- 3.805 - j0.000$
2.000	$- 0.157 + j0.000$	$- 4.322 - j0.000$
2.500	$- 0.133 + j0.000$	$- 5.589 - j0.000$
3.000	$- 0.115 + j0.000$	$- 6.836 - j0.000$
3.500	$- 0.101 + j0.000$	$- 8.069 - j0.000$
4.000	$- 0.091 + j0.000$	$- 9.294 - j0.000$

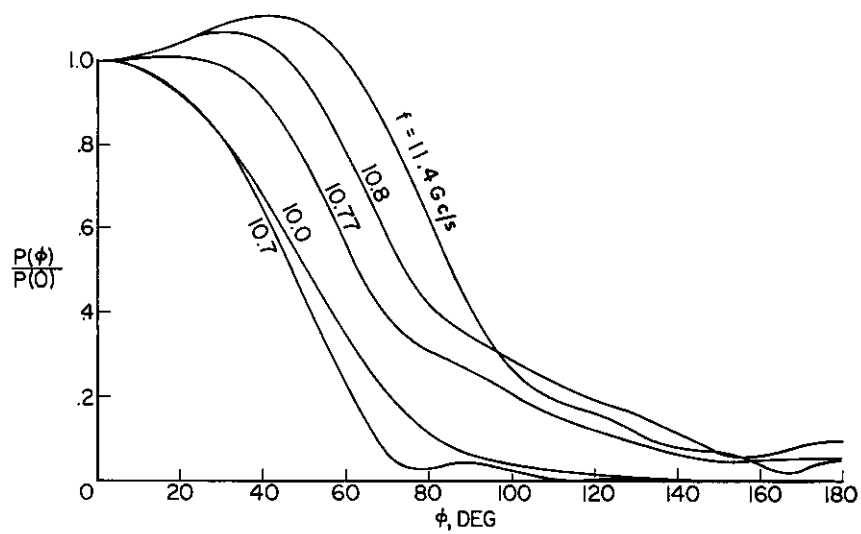


FIG. 9 Patterns of the coated slotted cylinder

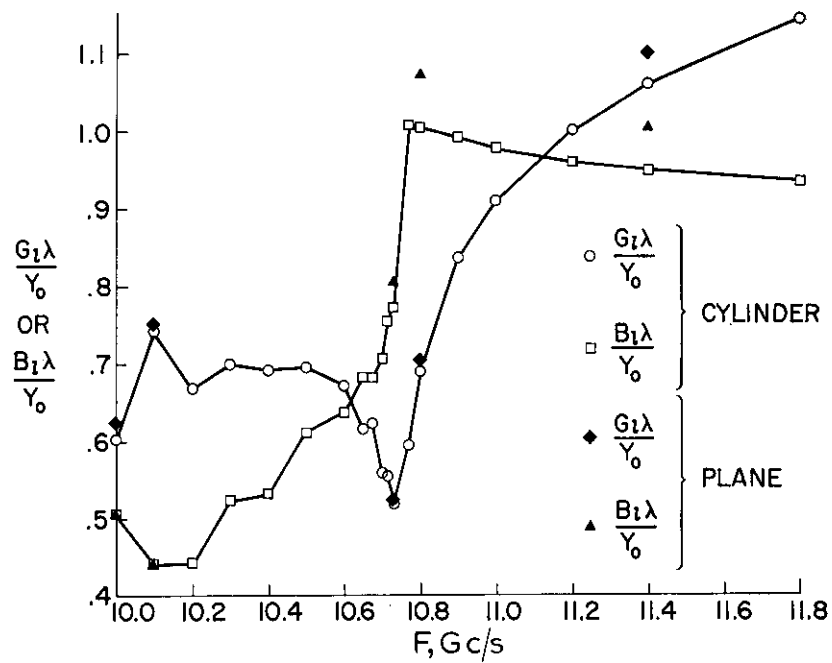


FIG. 10 Admittance of coated slots

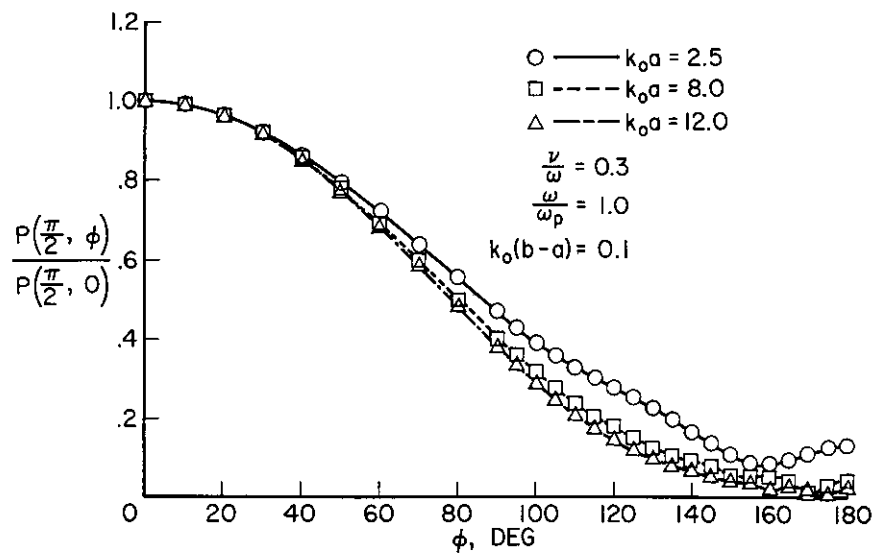


FIG. 11 Equatorial patterns of coated axially slotted cylinders

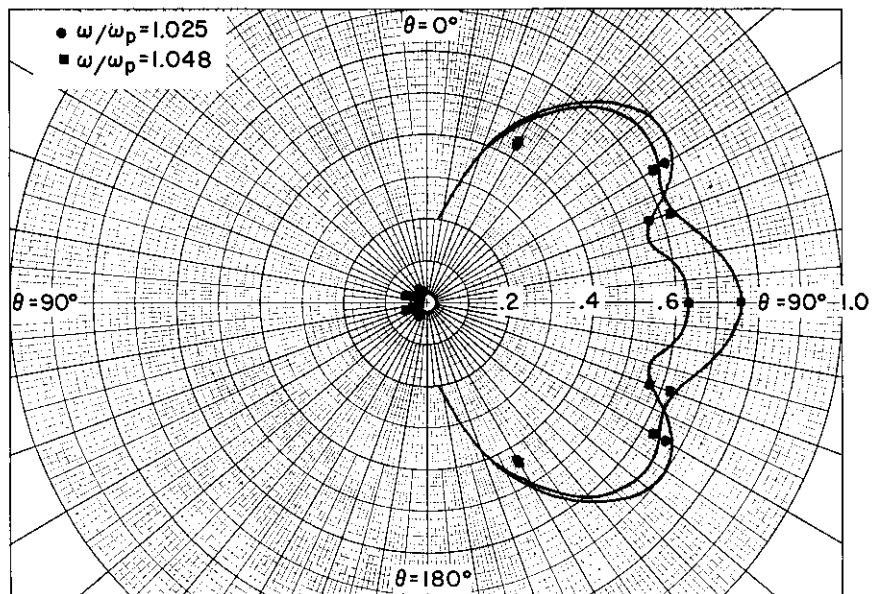


FIG. 12 Elevation patterns of a coated axially slotted cylinders



In order to save computer time, the plane results were confined to the five points shown in Fig. 10. The computations are not as extensive as those for the cylinder; nevertheless, there are sufficient data to conclude that for the parameters considered here, the admittance of a slot on a plane differs from the cylinder by only a few per cent over the entire frequency range.

If the losses are small (as they are for this plasma distribution), trapped waves in azimuth are supported by the cylindrical structure at frequencies above resonance. Therefore, it is conceivable that the wave interference within the cylindrical coating could be such that the difference between the admittance of this structure and that of a slot on a flat ground plane would be substantial. The results of Fig. 10 seem to indicate that this is not so, at least for the size cylinder considered here. It is of interest to note, however, that the greatest differences in the admittance occur at frequencies above resonance, which confirms the intuitive expectation.

The computations of the external admittance of a finite aperture, coated with the inhomogeneous plasma, have not been done; however, the ratios

$$\frac{g(\beta, 0)}{g'(\beta, 0)} \text{ and } \frac{f'(\beta, 0)}{f(\beta, 0)}$$

appearing in the integrand of Eq. 37 are given as a function of  $\beta$  in Tables 1a through 1d. Using these tables, the double integral which defines the admittance can be numerically evaluated.

The equatorial ( $\theta = \pi/2$ ) radiation patterns of a half-wave axial slot, coated with a homogeneous plasma, are shown in Fig. 11, and were derived by two independent methods. The points were derived from the bracketed term of Eq. 49, (in the equatorial plane, the patterns of a finite slot are identical to those of an infinitely long slot, see Knop (7)), and the solid curve was derived from the  $L$ -matrix, Eq. 56.

The explicit expression for equatorial pattern, in terms of the  $L$ -matrices from the stationary phase evaluation of Knop (7), is

$$P\left(\frac{\pi}{2}, \phi\right) = \frac{2\omega\zeta_0}{\pi^2} \left| \sum_{m=0}^{\infty} \frac{j^m \cos m\phi}{(1 + \delta_0^m) L_{44}} \right|$$

The agreement is good; therefore, one method substantiates the other.

The elevation patterns shown in Fig. 12 were taken directly from the results of W. V. T. Rusch (6), who based his treatment on a thin sheath approximation. The use of this approximation assures that the solution within the plasma may be expanded in a Taylor series about the thickness  $b-a$ . However, as the polar angle decreases from 90 deg. to 0 deg., this approximation becomes invalid. The points on Fig. 12 were computed from the expression

$$P\left(\theta, \frac{0}{\pi}\right) = \left[ \frac{2\omega\zeta_0 \cos\left(\frac{\pi}{2} \cos \theta\right)}{\pi^2 \sin \theta} \right] \left| \sum_{m=0}^{\infty} \frac{j^{\pm m} L_{12}}{(1 + \delta_0^m) [L_{12}L_{44} - L_{42}L_{14}]} \right|$$

(the positive or negative sign on  $j$  is chosen if  $\phi$  is 0 or  $\pi$ , respectively) and were normalized with respect to Rusch's on-axis value of  $\omega/\omega_p = 1.048$  curve. There is reasonably good agreement at  $\theta = 70$  deg. and  $\theta = 90$  deg.,

but the results begin to deviate as  $\theta$  decreases. However, this was expected, so it is reasonable to assume that the method can validly be extended to the admittance problem.

#### CONCLUDING REMARKS

Methods have been developed whereby the radiation patterns and near-field effects can be evaluated by solving the aperture and plasma problems independently. As a special application of these techniques, infinitely long slots on planes and cylinders, coated with a re-entry plasma were analyzed, and the following conclusions were noted:

(1) If the collision frequency is low, the peak value of the plasma frequency determines the radiating characteristics of the aperture. At critical, both the patterns and admittance undergo drastic changes.

(2) A homogeneous plasma "equivalent" of the inhomogeneous plasma coating given in Fig. 7 will give only general trends of pattern behavior.

(3) The external admittance of the particular slotted planes and cylinders considered here differs by only a few per cent.

Tables were also given whereby the external admittance of a finite aperture on a plane coated with the plasma of Fig. 7 can be computed by using these tables in connection with the double integral of Eq. 37.

The solution for a finite aperture on a cylinder was formulated in terms of matrix products and verified by comparing the radiation patterns with known results.

#### REFERENCES

1. HODARA, H., "Radiation from a Gyro-Plasma Coated Magnetic Line Source". Trans. Inst. Radio Engrs. AP-10, 5, 581-93, 1962.
2. HODARA, H., "Radiation from a Gyro-Plasma Sheathed Aperture". Trans. IEEE AP-11, 1, 2-12, 1963.
3. WAIT, JAMES R., "Electromagnetic Radiation from Cylindrical Structures". Pergamon, 1959.
4. TAMIR, T., and OLINER, A. A., "The Influence of Complex Waves on the Radiation Field of a Slot-Excited Plasma Layer". Trans. Inst. Radio Engrs. AP-10, 55-65, 1962.
5. OMURA, M., "Radiation Pattern of a Slit in a Ground Plane Covered by a Plasma Layer". Air Force Cambridge Res. Labs., Hanscom Field, Mass., Rep. AFCRL-62-958, 1962.
6. SENGUPTA, D. L., "The Radiation Field Produced by an Infinite Slot in an Infinite Cylinder Surrounded by a Homogeneous Plasma Sheath". Radar Lab., Univ. Mich., Ann Arbor, Rep. 4563-35T, 1963.
7. KNOPF, C. M., "The Radiation Fields from a Circumferential Slot on a Metal Cylinder Coated with a Lossy Dielectric". Trans. Inst. Radio Engrs. AP-9, 6, 535-45, 1961.
8. RUSCH, W. V. T., "Radiation from a Plasma-Clad Axially Slotted Cylinder". USCEC Rep. 82-201 (AFCRL 714), Univ. S. Calif., 1962.
9. HARRIS, J. H., "Radiation Through Cylindrical Plasma Sheaths". Sci. Rep. 2 (AFCRL-62-976), Hughes Aircraft Co., 1962.

10. SWIFT, CALVIN, T., "Radiation From Slotted-Cylinder Antennas in a Re-entry Plasma Environment". NASA Tech. Note D-2187, 1964.
11. VILLENEUVE, A. T., "Admittance of Waveguide Radiating into Plasma Environment". Sci. Rep. 6 (ARCRL-63-540), Hughes Aircraft Co., 1963.
12. GALEJS, J., "Admittance of Annular Slot Antennas Radiating into a Plasma Layer". Proj. No. 125, Appl. Res. Lab., Sylvania Electronic Systems, July, 1963.
13. GALEJS, J., "Admittance of a Waveguide Radiation into Stratified Plasma". Proj. No. 125, Appl. Res. Lab., Sylvania Electronic Systems, June 1963.
14. GALEJS, J., "Slot Antenna Impedance for Plasma Layers". App. Res. Lab., Sylvania Electronic Systems, July, 1963.
15. COMPTON, R. T., "The Admittance of Aperture Antennas Radiating Into Lossy Media". Ohio State Univ. Rep. 1691-5, 1964.
16. SWIFT, CALVIN T., "Radiation From Slotted-Cylinder Antennas, Coated with Concentric Layers of Dielectric Material". M.S. Thesis, V.P.I., April 1965.

## ACKNOWLEDGMENT

W. D. ALLISON, B. P. LATIMER, and P. HURST of NASA for their cooperation in arriving at the computations given in this paper.  
 CONTRACT NASI-4623 for sponsorship.

## DISCUSSION

K. RAWER - The curves presented showed some specific features about which the author seemed to be worried. I feel that such effects as rapid changes with frequency should be expected with coated surfaces. The problem resembles that of wave propagation through coated lenses where one arranges partial reflection to cancel for one particular frequency. In every case where steep gradients occur in a propagation problem the effects of partial reflection will depend critically on frequency. Besides, this is the reason why it is not normally possible to replace a given index profile by a "constant index coating" except for a very narrow frequency range.

## APPENDIX I

## List of Symbols

$a$	slot dimension along the $x$ -axis or radius of cylinder, as appropriate
$b$	slot dimension along the $y$ -axis or radial distance to air-plasma interface, as appropriate
$E$	electric field intensity
$\bar{E}, \bar{E}$	Fourier transforms of the electric field
$E_0$	electric field intensity at aperture of $TM_x$ slot
$f$	propagating frequency
$f_p$	plasma frequency, $8.97 \times 10^3 \sqrt{N_e}$
$H$	magnetic field intensity
$\bar{H}, \bar{H}$	Fourier transforms of magnetic field
$H_0$	field intensity of incident $TEM$ mode in waveguide
$j = \sqrt{-1}$	
$k_0$	free-space wave number
$k_x, k_y, k_z$	Cartesian mode numbers
$m$	azimuthal mode numbers
$n$	index of refraction or discrete mode number in waveguide, as appropriate
$N_e$	electron density
$P$	power
$r, \theta, \phi$	spherical coordinates
$u$	radial mode numbers
$V_0$	applied potential on slot
$x, y, z$	Cartesian coordinates
$Y_0$	admittance of free space, $\sqrt{\frac{\epsilon_0}{\mu_0}}$
$Y$	admittance
$Z_0$	impedance of free space, $\sqrt{\frac{\mu_0}{\epsilon_0}}$
$z_0$	plasma thickness
$\alpha = \arctan \frac{k_y}{k_x}$	
$\beta = \frac{1}{k_0} \sqrt{k_x^2 + k_y^2}$	
$\Gamma$	reflection coefficient
$\delta_m^n$	Kronecher delta $\begin{cases} 0 & (m \neq n) \\ 1 & (m = n) \end{cases}$
$\epsilon$	permittivity
$\epsilon_0$	permittivity of free space
$\lambda_0$	free-space wavelength
$\mu_0$	permeability of free space
$\nu$	collision frequency
$\rho, \phi, z$	cylindrical coordinates

$\phi_c$	plane-wave critical angle
$\phi_0$	angular width of slot
$\omega$	angular frequency
*	complex conjugate

Superscripts:

$I$	fields within the plasma
$II$	fields in free space
$i$	fields within the $i^{th}$ dielectric layer
$n$	fields within the $n^{th}$ dielectric layer

Subscripts:

$i$	physical parameters within the $i^{th}$ dielectric layer
$l$	per unit length
$x, y, z$	vector components in the principal Cartesian directions
$\rho, \phi, z$	vector components in the principal cylindrical directions

A prime denotes differentiation with respect to  $z$  or  $\rho$ , as appropriate.

## APPENDIX 2

**Exact Formulation of the Infinite Slot on the Ground Plane Radiating into an Inhomogeneous Plasma** – Assuming a *TEM* wave incident upon the aperture shown in Fig. 1, the pertinent internal fields at  $z = 0$  are given by

$$\left. \begin{aligned} H_x(y, 0) &= H_0 \left[ 1 + \sum_{n=0}^{\infty} A_n \cos \left( \frac{n\pi y}{b} \right) \right] \\ E_y(y, 0) &= \frac{1}{j\omega\epsilon_0} \frac{\partial H_y}{\partial z} = -\frac{H_0}{Y_0} \left[ 1 - \sum_{n=0}^{\infty} A_n \frac{k_{nz}}{k_0} \cos \left( \frac{n\pi y}{b} \right) \right] \end{aligned} \right\} \quad (2-1)$$

where

$$\left. \begin{aligned} k_{nz} &= \sqrt{k_0^2 - \left( \frac{n\pi}{b} \right)^2} & |k_0| > \frac{n\pi}{b} \\ k_{nz} &= j \sqrt{\left( \frac{n\pi}{b} \right)^2 - k_0^2} & |k_0| < \frac{n\pi}{b} \end{aligned} \right\} \quad (2-2)$$

The external fields at the aperture are, from Eq. 10

$$\left. \begin{aligned} H_x(y, 0) &= \frac{1}{2\pi} \int_{-\infty}^{\infty} L_{11}(k_y) H_T e^{jk_z z_0} e^{jk_y y} dk_y \\ E_y(y, 0) &= \frac{1}{2\pi} \int_{-\infty}^{\infty} L_{12}(k_y) H_T e^{jk_z z_0} e^{jk_y y} dk_y \end{aligned} \right\} \quad (2-3)$$

The continuity requirement on  $E_y$  gives

$$\frac{1}{2\pi} \int_{-\infty}^{\infty} L_{12}(k_y) H_T e^{jk_z z_0} e^{jk_y y} dk_y = -\frac{H_0}{Y_0} \sum_{n=0}^{\infty} (\delta_0^n - A_n) \frac{k_{nz}}{k_0} \cos\left(\frac{n\pi y}{b}\right) \quad (2-4)$$

Multiplying Eq. 2-4 by  $e^{-jk_y y} dy$ , and integrating with respect to  $y$  gives

$$L_{12}(k_y) H_T e^{jk_z z_0} = -\frac{H_0}{Y_0} \sum_{n=0}^{\infty} (\delta_0^n - A_n) \frac{k_{nz}}{k_0} \int_0^b \cos \frac{n\pi y}{b} e^{-jk_y y} dy \quad (2-5)$$

where the integration of the left-hand side of the above was extended over all space because  $E_y = 0$  on the ground plane.

It is now convenient to define

$$\frac{1}{b} \int_0^b \cos \frac{n\pi y}{b} e^{+jk_y y} dy = \frac{-jk_y b}{(k_y b)^2 - (n\pi)^2} [(-1)^n e^{jk_y b} - 1] = C_n(k_y) \quad (2-6)$$

which has the property

$$\int_{-\infty}^{\infty} C_n(k_y) C_l^*(k_y) dk_y = \frac{\pi}{b} \delta_n^l (1 + \delta_0^n) \quad (2-7)$$

that is,  $C_n(k_y)$  is an orthogonal function. Therefore, in terms of  $C_n(k_y)$ , the continuity of  $E$  gives the following equation

$$\frac{H_T}{H_0} e^{jk_z z_0} = \frac{-b}{Y_0 L_{12}(k_y)} \sum_{n=0}^{\infty} (\delta_0^n - A_n) \frac{k_{nz}}{k_0} C_n^*(k_y) \quad (2-8)$$

The boundary conditions for  $H_x$  is a little more difficult to apply because the magnetic field involves "mixed" boundary conditions, i.e.  $H_x$  is continuous at the aperture and equal to the unknown surface current on the ground plane. The boundary condition must therefore be applied only over the region where the aperture exists. This is done by expanding  $e^{jk_y y}$  in a cosine series over the aperture; i.e.

$$e^{jk_y y} = \sum_{n=0}^{\infty} B_n \cos \frac{n\pi y}{b} \quad 0 \leq y \leq b \quad (2-9)$$

Use of orthogonality gives

$$B_n = \frac{2}{(1 + \delta_0^n)} C_n(k_y) \quad (2-10)$$

Therefore,

$$e^{jk_y y} = \sum_{n=0}^{\infty} \frac{2}{(1 + \delta_0^n)} C_n(k_y) \cos \frac{n\pi y}{b} \quad (2-11)$$

Use of Eq. 2-11 in the boundary condition for  $H_x$ , gives

$$H_0 \sum_{n=0}^{\infty} (\delta_0^n + A_n) \cos \frac{n\pi y}{b} = \frac{1}{2\pi} \int_{-\infty}^{\infty} dk_y L_{11}(k_y) H_T e^{jk_z z_0} \sum_{n=0}^{\infty} \frac{2}{(1 + \delta_0^n)} C_n(k_y) \cos \frac{n\pi y}{b} \quad (2-12)$$

or

$$(\delta_0^n + A_n) = \frac{1}{\pi(1 + \delta_0^n)} \int_{-\infty}^{\infty} L_{11}(k_y) \frac{H_T}{H_0} e^{jk_z z_0} C_n(k_y) dk_y \quad (2-13)$$

By substituting Eq. 2-8 into Eq. 2-13,

$$(\delta_0^n + A_n) = \frac{b}{\gamma_0 \pi (1 + \delta_0^n)} \int_{-\infty}^{\infty} dk_y \frac{L_{11}(k_y)}{L_{12}(k_y)} C_n(k_y) \sum_{q=0}^{\infty} (\delta_0^q - A_q) \frac{k_{qz}}{k_0} C_q^*(k_y) \quad (2-14)$$

Now, let

$$\mathcal{J}_{nq} = \frac{b}{\gamma_0 \pi (1 + \delta_0^n)} \frac{k_{qz}}{k_0} \int_{-\infty}^{\infty} \frac{L_{11}(k_y)}{L_{12}(k_y)} C_n(k_y) C_q^*(k_y) dk_y \quad (2-15)$$

The Eq. 2-14 becomes:

$$(\delta_0^n + A_n) = \sum_{q=0}^{\infty} (\delta_0^q - A_q) \mathcal{J}_{nq} \quad (2-16)$$

or,

$$\sum_{q=0}^{\infty} (\mathcal{J}_{nq} + \delta_n^q) A_q = \mathcal{J}_{n0} - \delta_n^0 \quad (2-17)$$

Therefore, since the coefficient matrix  $\mathcal{J}_{nq}$  can be computed after  $L_{11}$  and  $L_{12}$  are specified, the problem reduces to solving an infinite matrix 2-16 in order to compute the unknown  $A_q$ 's.

### APPENDIX 3

**The Finite Aperture Radiating into Layered Dielectrics** - Upon applying the boundary conditions (53) at  $\rho = \rho_{i+1}$ , the matrix relationship between the coefficients in the  $i^{\text{th}}$  and the  $(i+1)^{\text{st}}$  layer can be expressed in many ways; however, if closed-form expressions are desired, the most profitable way seems to be

$$[A_{jk}^{i+1}] = \begin{bmatrix} \mathcal{J}_m(u_i \rho_{i+1}) & H_m^{(2)}(u_i \rho_{i+1}) & 0 & 0 \\ u_i \mathcal{J}_m'(u_i \rho_{i+1}) & u_i H_m^{(2)'}(u_i \rho_{i+1}) & 0 & 0 \\ 0 & 0 & \mathcal{J}_m(u_i \rho_{i+1}) & H_m^{(2)}(u_i \rho_{i+1}) \\ 0 & 0 & u_i \mathcal{J}_m'(u_i \rho_{i+1}) & u_i H_m^{(2)'}(u_i \rho_{i+1}) \end{bmatrix} \quad (3-1)$$

$$[B_{jk^{i+1}}] = \begin{bmatrix} \begin{matrix} \left(\frac{k_i u_{i+1}}{k_{i+1} u_i}\right)^2 \mathcal{J}_m(u_{i+1} \rho_{i+1}) & \left(\frac{k_i u_{i+1}}{k_{i+1} u_i}\right)^2 H_m^{(2)}(u_{i+1} \rho_{i+1}) \\ u_{i+1} \mathcal{J}_m'(u_{i+1} \rho_{i+1}) & u_{i+1} H_m^{(2)'}(u_{i+1} \rho_{i+1}) \end{matrix} & \begin{matrix} 0 & 0 \end{matrix} \\ \begin{matrix} -\frac{j\omega\epsilon_0 m k_z k_i^2}{k_0^2 u_i^2 \rho_{i+1}} \left(1 - \frac{k_i^2}{k_{i+1}^2}\right) \mathcal{J}_m(u_{i+1} \rho_{i+1}) & -\frac{j\omega\epsilon_0 m k_z k_i^2}{k_0^2 u_i^2 \rho_{i+1}} \left(1 - \frac{k_i^2}{k_{i+1}^2}\right) H_m^{(2)}(u_{i+1} \rho_{i+1}) \end{matrix} & \begin{matrix} 0 & 0 \end{matrix} \\ \begin{matrix} \frac{j\omega\mu_0 m k_z}{u_i^2 \rho_{i+1}} \left(1 - \frac{k_i^2}{k_{i+1}^2}\right) \mathcal{J}_m(u_{i+1} \rho_{i+1}) & \frac{j\omega\mu_0 m k_z}{u_i^2 \rho_{i+1}} \left(1 - \frac{k_i^2}{k_{i+1}^2}\right) H_m^{(2)}(u_{i+1} \rho_{i+1}) \\ \left(\frac{k_i u_{i+1}}{k_{i+1} u_i}\right)^2 \mathcal{J}_m(u_{i+1} \rho_{i+1}) & \left(\frac{k_i u_{i+1}}{k_{i+1} u_i}\right)^2 H_m^{(2)}(u_{i+1} \rho_{i+1}) \\ u_{i+1} \left(\frac{k_i}{k_{i+1}}\right)^2 \mathcal{J}_m'(u_{i+1} \rho_{i+1}) & u_{i+1} \left(\frac{k_i}{k_{i+1}}\right)^2 H_m^{(2)'}(u_{i+1} \rho_{i+1}) \end{matrix} \end{bmatrix}$$

where the  $[A_{jk^{i+1}}]$  and  $[B_{jk^{i+1}}]$  matrices are defined in Eq. 54. The C matrix was defined as

$$[C_{jk^{i+1}}] = [A_{jk^{i+1}}]^{-1} [B_{jk^{i+1}}] \quad (3-3)$$

where the inverse of the A-matrix is given by



$$[A_{jk^{i+1}}]^{-1} = \begin{bmatrix} j\frac{\pi}{2}u_i\rho_{i+1}H_m^{(2)*}(u_i\rho_{i+1}) & -j\frac{\pi}{2}\rho_{i+1}H_m^{(2)}(u_i\rho_{i+1}) \\ -j\frac{\pi}{2}u_i\rho_{i+1}\tilde{J}_m^*(u_i\rho_{i+1}) & j\frac{\pi}{2}\rho_{i+1}\tilde{J}_m(u_i\rho_{i+1}) \\ 0 & 0 \\ 0 & 0 \\ 0 & 0 \\ 0 & 0 \\ j\frac{\pi}{2}u_i\rho_{i+1}H_m^{(2)*}(u_i\rho_{i+1}) & -j\frac{\pi}{2}\rho_{i+1}H_m^{(2)}(u_i\rho_{i+1}) \\ -j\frac{\pi}{2}u_i\rho_{i+1}\tilde{J}_m^*(u_i\rho_{i+1}) & j\frac{\pi}{2}\rho_{i+1}\tilde{J}_m(u_i\rho_{i+1}) \end{bmatrix}$$

If Eq. 55 is carried one step further, it follows that

$$\begin{Bmatrix} a_m^1 \\ A_m^1 \\ b_m^1 \\ B_m^1 \end{Bmatrix} = [C_{jk^2}] [C_{jk^3}] \cdots [C_{jk^{n-1}}] [C_{jk^n}] [C_{jk^{n+1}}] \begin{Bmatrix} 0 \\ c_m \\ 0 \\ d_m \end{Bmatrix} \quad (3-5)$$

where use was made of the fact that

$$\begin{Bmatrix} a_m^{n+1} = d_m \\ A_m^{n+1} = 0 \\ b_m^{n+1} = c_m \\ B_m^{n+1} = 0 \end{Bmatrix} \quad (3-6)$$

describe outgoing waves in free space. From the explicit form of the field transforms, it can be shown that

$$\begin{Bmatrix} \tilde{E}_{mz}(a, k_z) \\ \tilde{H}_{m\phi}(a, k_z) \\ \tilde{H}_{mz}(a, k_z) \\ \tilde{E}_{m\phi}(a, k_z) \end{Bmatrix} = [D_{jk^1}] \begin{Bmatrix} a_m^1 \\ A_m^1 \\ b_m^1 \\ B_m^1 \end{Bmatrix} \quad (3-7)$$

where

$$[D_{jk^1}] = \begin{bmatrix} \left(\frac{u_1 k_0}{k_1}\right)^2 \frac{\mathcal{J}_m(u_1 a)}{j\omega\mu_0\epsilon_0} & \left(\frac{u_1 k_0}{k_1}\right)^2 \frac{H_m^{(2)}(u_1 a)}{j\omega\mu_0\epsilon_0} \\ -\frac{u_1}{\mu_0} \mathcal{J}_m'(u_1 a) & -\frac{u_1}{\mu_0} H_m^{(2)'}(u_1 a) \\ 0 & 0 \\ -\frac{k_z m k_0^2 \mathcal{J}_m(u_1 a)}{j\omega\mu_0\epsilon_0 k_1^2} & -\frac{k_z m k_0^2 H_m^{(2)}(u_1 a)}{j\omega\mu_0\epsilon_0 k_1^2 a} \\ 0 & 0 \\ -\frac{m k_z k_0^2 \mathcal{J}_m(u_1 a)}{j\omega\mu_0\epsilon_0 k_1^2 a} & -\frac{m k_z k_0^2 H_m^{(2)}(u_1 a)}{j\omega\mu_0\epsilon_0 k_1^2 a} \\ \left(\frac{u_1 k_0}{k_1}\right)^2 \frac{\mathcal{J}_m(u_1 a)}{j\omega\mu_0\epsilon_0} & \left(\frac{u_1 k_0}{k_1}\right)^2 \frac{H_m^{(2)}(u_1 a)}{j\omega\mu_0\epsilon_0} \\ \left(\frac{k_0}{k_1}\right)^2 \frac{u_1}{\epsilon_0} \mathcal{J}_m'(u_1 a) & \left(\frac{k_0}{k_1}\right)^2 \frac{u_1}{\epsilon_0} H_m^{(2)'}(u_1 a) \end{bmatrix}$$

Hence, the  $L$ -matrix of Eq. 56 is the product of the  $n + 1$  matrices

$$[L_{jk}] = [D_{jk^1}] [C_{jk^2}] [C_{jk^3}] \cdots [C_{jk^n}] [C_{jk^{n+1}}] \quad (3-9)$$

It is interesting to note that if the index of refraction of all the layers is unity, the  $C$ -matrices are unit matrices.

Excerpts from ref. 16 were used in this appendix.

## CHAPTER 4-7

NOISE PRODUCED BY TERRESTRIAL SOURCES  
IN THE NEAR-EARTH SPACE

K. RAWER

Ionosphären-Institut Breisach

## INTRODUCTION

This paper tries to give a provisional answer to the following question: How does the earth look, if seen by radio waves from outside, i.e. in near space. Our answer shall be given in a broad way, mainly by indicating some equivalent temperature values; these are, of course, colour temperatures, and thus variable with frequency. We need two considerations in this context:

**The propagation problems** – we shall describe the propagation through the troposphere and ionosphere which occurs in certain frequency ranges, the “propagation windows”. The main “radio window” has a lower frequency limit somewhere in the decameter waveband, due to ionospheric reflection phenomena. There is a transition range in frequency, extending from  $f_c$  to  $f_d$ ; in this range the transparency of the atmosphere increases more and more. It is very high in the window range, which goes from the decameter or meter waveband up to centimeter and millimeter waves where the upper frequency limit of the window is reached. It is due to tropospheric absorption phenomena and may be characterized by a transition range extending from  $f_e$  to  $f_f$ . Generally speaking the opacity of the atmosphere increases with frequency in this range; there is, however, a number of different absorption bands between  $f_e$  and  $f_f$ .

**The radiated energy** – may be of natural or of human origin and could be described either as a surface distribution, i.e. by maps of the planet earth, or by indicating an average value of total radiation emitted from the earth. For rather low satellite heights which we consider in the first instance, maps are more satisfactory. These may be labelled in colour temperatures. Separate maps should be used for the different noise sources, which could then be combined into an overall map (for a given frequency range).

Both considerations, though undertaken separately here, may sometimes be interrelated.

## THERMAL RADIATION

This is particularly true for thermal radiation, which therefore shall be considered first.

In ranges of vanishing propagation attenuation, thermal radiation from the earth's surface propagates through the atmosphere. Supposing a “black” surface, the earth radiates as a uniform disk according to Beer's law. The corresponding temperature is of the order of the reference temperature of

288°K. Whilst this is true inside the window range, the situation is different in frequency ranges where the atmosphere is more or less opaque.

Where propagation influences are predominant the temperature is mainly determined by that of the layer which, seen from outside, is most efficient for propagation effects. On UHF frequencies above  $f_f$ , tropospheric absorption is important and finally prevents ground emission at high frequencies from being visible. The efficient interface is now in the troposphere at a few kilometers above the earth's surface. The corresponding temperature is slightly lower than 288°K, down to about 240°K. In the transition range,  $f_f \dots f_e$ , some average between ground and tropospheric radiation determines the effective temperature. Figure 1 gives effective noise-temperature values of the troposphere as seen from below. Due to the decrease of temperature with height in the troposphere these values should become slightly lower when seen from above. In the frequency range where lower temperature values are indicated on Fig. 1 the atmosphere is nearly transparent, such that for ground-bound observations the "cold" sky looks through it. However, seen from above, the ground appears much warmer than the sky.

The situation is quite different in the range below  $f_a$ , where the ionosphere affects the propagation. Generally speaking, refraction effects are more important here than absorption effects. Effective temperature is determined by that layer where the radio waves coming from outside are mostly attenuated. As this attenuation is normally not total, the emissivity of the topside ionosphere has to be evaluated at heights between 300 and 1000 km roughly, according to the frequency. If the effective (energy) reflection coefficient of the top-side ionosphere is  $p$ , the energy absorption is  $(1-p)$  and this is also the emissivity. The true (electron) temperature of the ionospheric plasma must therefore be multiplied by a factor  $(1-p)$ , in order to obtain the effective colour temperature. Giving both, absorption and emissivity in dB, we have Table 1:

TABLE 1

<b>Absorption, dB</b>	0,1	0,2	0,5	1	2	5	10	20
<b>Emissivity, dB</b>	16,6	13,5	9,6	7,0	4,3	1,7	0,5	0,05

The outer ionosphere is not in thermal equilibrium. The temperature of the electron component must therefore be considered. It is between 800 and 2000°K, and largely variable; in particular, it has an important diurnal variation (1), (2). On frequencies where the absorption is rather large, the temperature of the earth's ionosphere as seen from outside may therefore be much higher than on frequencies in the window. In the transition range between  $f_a$  and  $f_e$  the ground looks through in certain directions whilst in others the ionosphere reflects radiation. These spots may be at higher temperature than the first ones.

Radio-wave absorption in the outer ionosphere is mainly due to electron-ion collisions (3). These are independent of the neutral density, but depend in a critical manner on the plasma density. The frequency law of this absorption (4) is rather different from that of lower ionosphere layers with prevailing neutral collisions. Absorption is rather important near the critical frequency, then decreases with decreasing frequency, but may again become

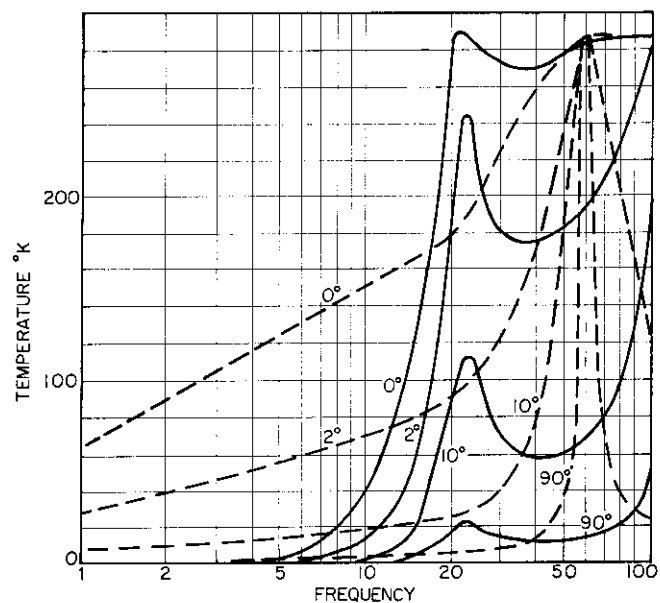


FIG. 1 Sky noise temperature due to oxygen and water vapour ( $10 \text{ g/m}^3$ ); parameter angle of elevation (CCIR Rep. 234(1963))

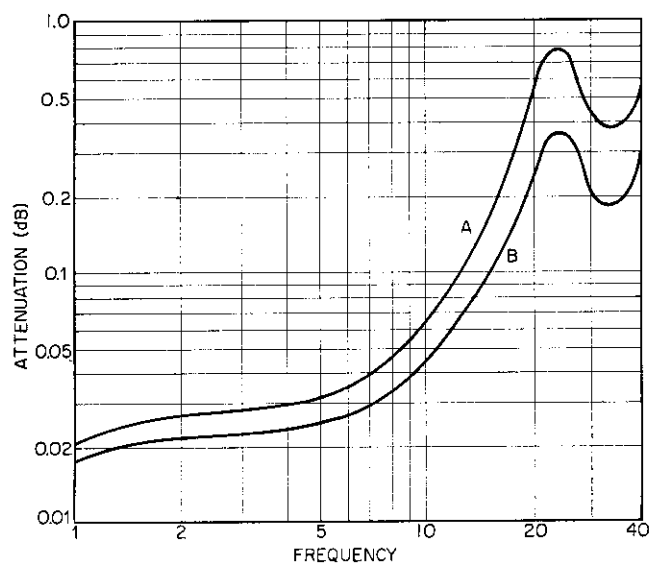


FIG. 2 Computed one-way attenuation for a vertical path in a moderately humid zone; A from sea level, B from 2 km above it (CCIR Rep. 205, 1963)

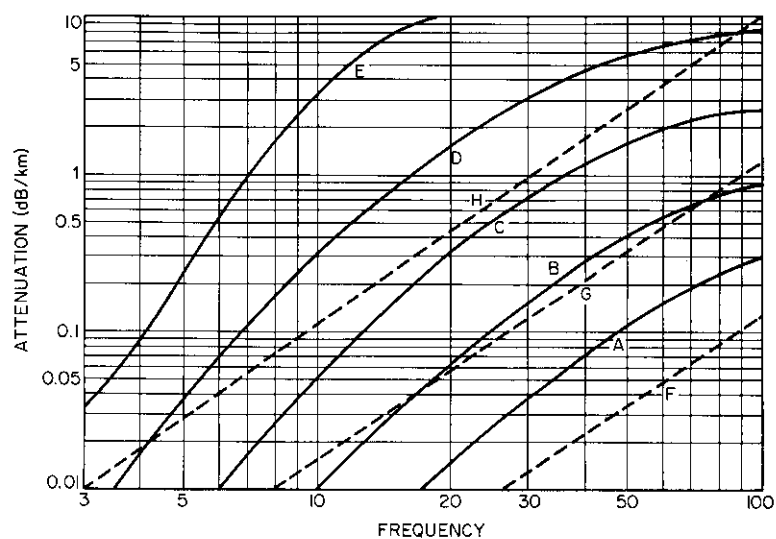


FIG. 3 Attenuation due to precipitation in a 1 km sheath, - Rainfall (A drizzle, B light, C moderate, D heavy, E very heavy rain). - Fog (visibility F 600 m, G 120 m, H 30 m) (CCIR Rep. 205, 1963)

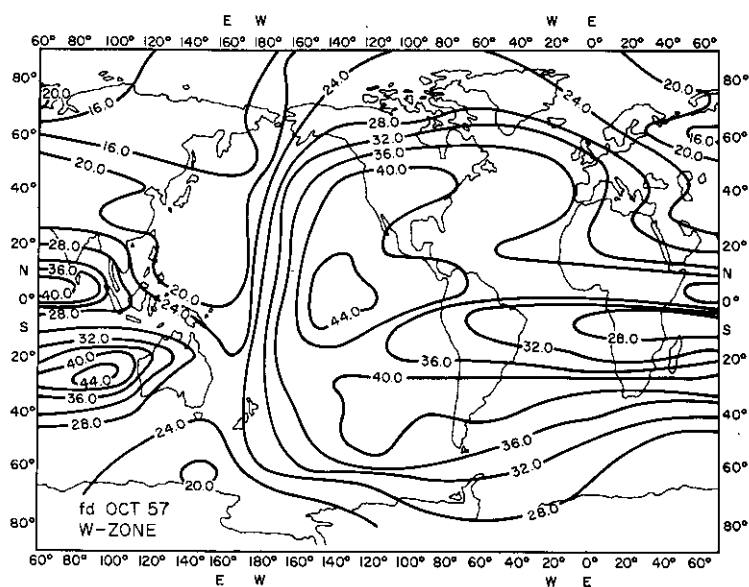


FIG. 4 Map of  $fd$ , median for October 1957, computed from maps of  $foF_2$  and  $M(3000)$  W-Zone

important on lower frequencies in the MF range. The corresponding variations in temperature should be quite important.

#### PROPAGATION EFFECTS

These must be described as function of the frequency  $f$ . We begin with the highest frequencies. In the UHF range where the absorption influence of the troposphere is most effective ( $f_e < f < f_f$ ) radiation coming from the earth surface is seriously attenuated.

Water vapour and oxygen absorption are effective above 16 Gc/s. The attenuation as shown by Fig. 2 is valid for vertical incidence; it is higher at oblique incidence. This has the effect that high elevation-angle radiation penetrates better, such that noise is best received from the subsatellite zone. With fog or rain conditions  $f_e$  decreases considerably and may occasionally become as low as 5 Gc/s with heavy rain. Some typical absorption curves are shown in Fig. 3, computed for an effective thickness of the rain zone of 1 km and for vertical incidence. Again, oblique incidence gives stronger attenuation, but as the rain zones on the earth are rather limited anyhow it was not felt worth while to give particular oblique incidence curves.

In the main range of the window, between 10 Gc/s and 50 Mc/s roughly ( $f_a < f < f_e$ ), only very small propagation attenuation occurs, some 0.1 ... 0.5 dB. Only at the lower end larger effects are to be expected, particularly during such disturbed conditions as: solar flare effects, auroral absorption, polar-cap absorption. These disturbance effects may reach up to 10 dB near  $f_a$  (as defined by refraction).

In the lower transition range,  $f_c < f < f_a$ , we have important ionospheric refraction and reflection phenomena. The higher frequencies go through the ionosphere, the lower ones are reflected. The limits  $f_c$  and  $f_a$  are widely variable with the ionospheric conditions, and so with time and location. As refraction phenomena give clear delimitations, the characteristic frequencies  $f_a$  and  $f_c$  are well defined at a given location. The upper limit  $f_a$  is the highest frequency for which ionospheric reflection (of waves coming from the ground) may just occur. To a good approximation it is found without ray-tracing from Bouguer's refraction law; the condition is that the ray with zero elevation angle at the ground becomes just horizontal at the peak altitude of the ionosphere, i.e. at maximum electron density. This leads to the following condition for the refraction index  $n_M$  at this level:

$$n_M = \rho_T / \rho_M \quad (1)$$

$\rho_T$  and  $\rho_M$  being the radius of the earth and the ionospheric peak, respectively. Introducing a general dispersion formula

$$n^2 = 1 - \mathcal{K}(f) \quad (2)$$

we may determine  $f_a$  from

$$\sqrt{1 - \mathcal{K}(f_a)} = \rho_T / \rho_M \quad (3a)$$

or with  $^{-1}\mathcal{K}$  being the inverse function of  $\mathcal{K}$ :

$$f_a = ^{-1}\mathcal{K} (1 - \rho_T^2 / \rho_M^2) \quad (3b)$$

In the easiest approximation we use the Sellmeier formula:  $\mathfrak{K} = X \equiv \frac{f_N^2}{f^2}$  where  $f_N$  is the plasma frequency, and obtain

$$f_a = f_{NM} (1 - \rho_T^2 / (\rho_T + H)^2)^{-1/2} \quad (4)$$

Normally  $f_N$  equals  $f_oF2$ , the critical frequency of the  $F2$  layer.  $H$  is the peak height of the layer which determines  $f_{NM}$ . From Eq. 4 maps of  $f_a$  can easily be obtained provided that maps of  $f_{NM} = f_oF2$  and  $H = h_M$  are available. Figure 4 gives an example ( $h_M$  has been taken from a M(3000)map using the well-known empirical relations). It is seen from this figure that  $f_a$  is widely variable over the world. It might be stated that the longitudinal effect has not correctly been taken into account in this example, as only maps for the American longitude zone were used. Also it has been supposed that  $f_oF2$  determines  $f_a$  everywhere; it might, however, occur that  $f_a$  may be determined by  $E_s$ -layers, particularly in the equatorial belt.

Figure 4 is only approximate, as it is known that the magnetic field exerts an influence. As this is anisotropic, the result of the determination depends on the azimuth because the dispersion formula (Appleton-Lassen formula) depends on the angle  $\Theta$  formed by the wave normal and the magnetic field. As the critical ray is horizontal at the peak of the ionosphere the value of  $\Theta$  is given by

$$\cos \Theta = \cos \Phi \cos \psi \quad (5)$$

where  $\psi$  is the magnetic dip at the place and  $\Phi$  is the (magnetic) azimuth which is considered.

There exists another complication due to the magnetic field; the magnetic double refraction. A radio ray with an arbitrary polarization, when entering the ionosphere, splits up into two rays of well-defined conjugate polarizations, the so-called characteristic polarizations. These are correctly labelled as ionic and electronic polarization, but it is general usage to call these "ordinary" and "extraordinary". As a result of double refraction we get two different  $f_a$  values for each azimuth, so that we should write

$$f_{ao}(\Phi) \text{ and } f_{ax}(\Phi).$$

Methods to compute these are given in the following paragraphs.

The lower limit  $f_c$  is the highest frequency that cannot penetrate the ionosphere. This is well known as the highest critical frequency; it is nearly always identical with  $f_oF2$ , the critical frequency of the  $F2$ -layer, but sometimes it may be given by  $E_s$ , at least instantaneously. As an example Fig. 5 shows the  $f_oF2$ -map which is basically used when Fig. 4 has been established. As it is known,  $f_oF2$  may go down below 3 Mc/s, in particular at night for high latitudes, but sometimes also at low ones. On the other side, the highest values reach up to 20 Mc/s roughly; these are found in the equatorial zone, particularly at dip values of  $\pm 20 \dots 30^\circ$ . In the transition range  $f_a > f > f_c$  higher-angle radiation from the earth penetrates the ionosphere, but lower-angle radiation is reflected down towards the ground. Effects such as penetration after multiple reflection between ionosphere and ground are certainly important as propagation phenomena, but may be neglected here to a first order. Their effects "devalue" the highest values of  $f_c$ ,  $f_a$  to some extent,



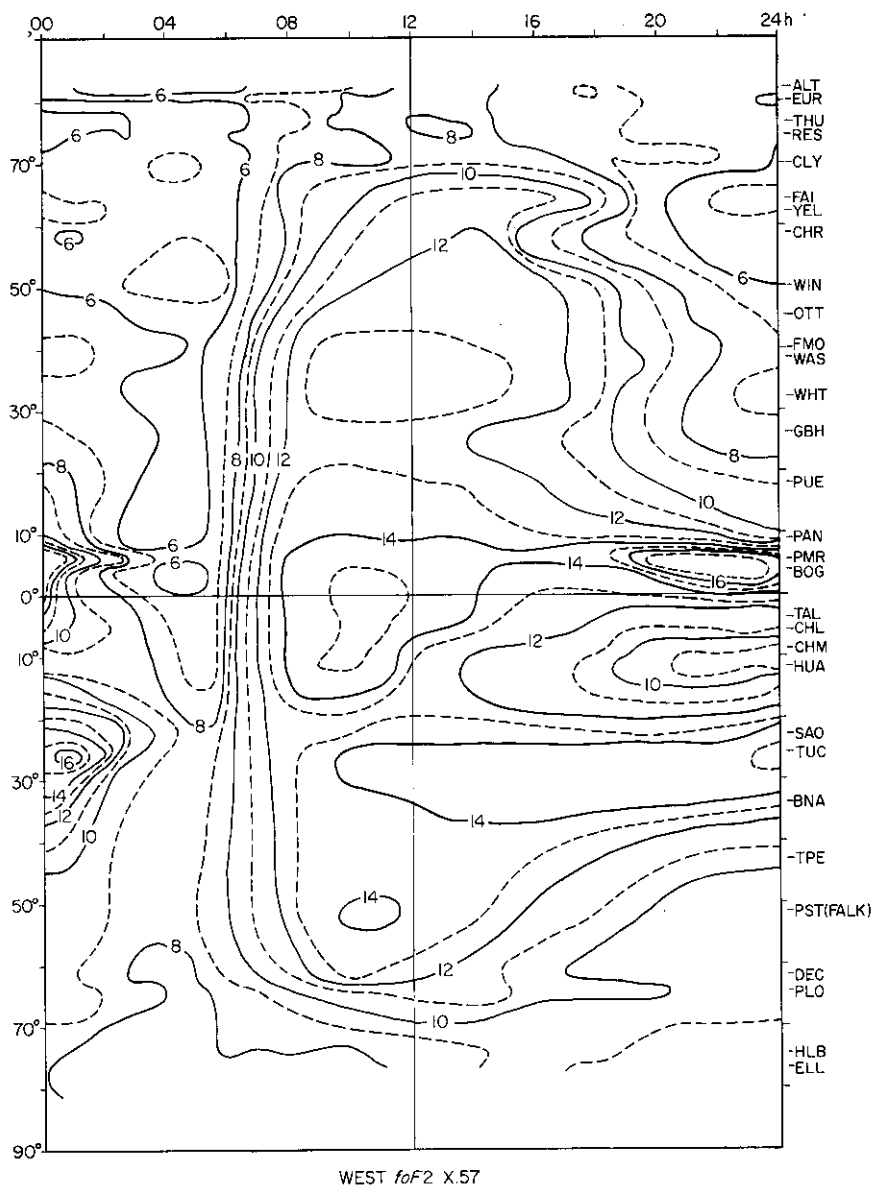


FIG. 5 Map of  $foF_2$ , median for October 1957 W-Zone (Report IIB No. 16)

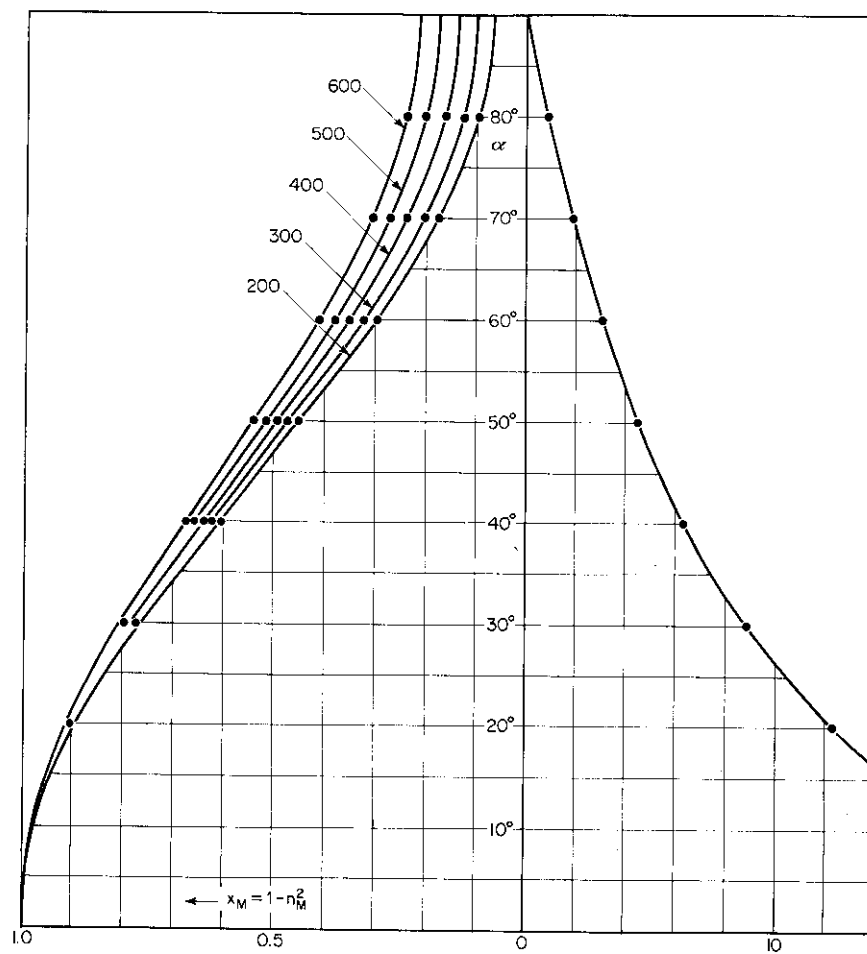


FIG. 6 Nomogram for determining effective loss by conal reflection, from  $\chi_M = 1 - n_M^2$ . Parameter peak altitude/km

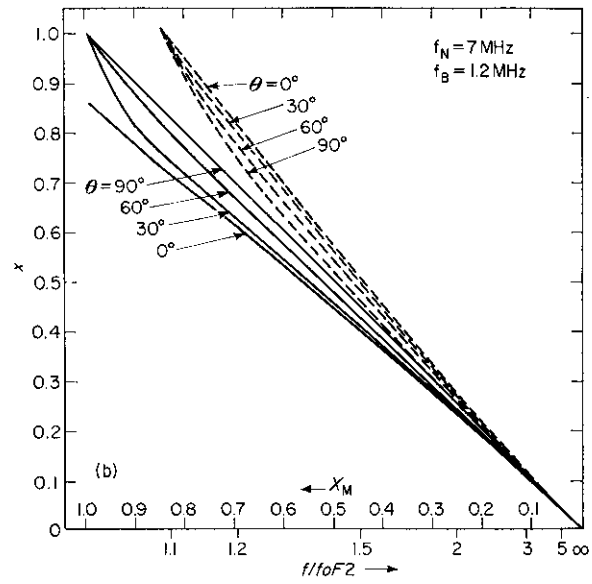
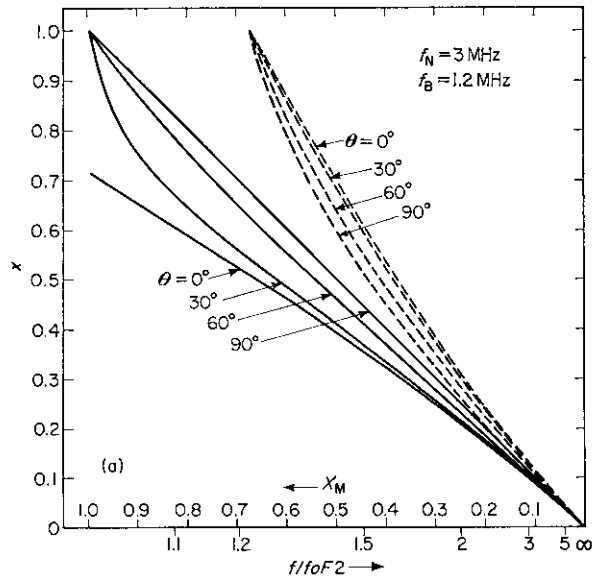


FIG. 7 Dispersive diagrams of  $X_M$  versus  $X_M = (f_0 F_2 / f)^2$  (lower scale:  $f / f_0 F_2$ );  
 Parameter: angle  $\theta$   
 (a) Plasma frequency  $f_N = 3 \text{ Mc/s}$ ; Gyro-frequency  $f_B = 1.2 \text{ Mc/s}$   
 (b) Plasma frequency  $f_N = 7 \text{ Mc/s}$ ; Gyro-frequency  $f_B = 1.2 \text{ Mc/s}$

because for these places the radiation "creeps out" by multiple reflection and finally leaves the earth.

Neglecting horizontal gradients, the opening angle of the penetration cone at the ground,  $\alpha_g$ , can be found from the condition that the ray starting with  $\alpha_g$  just becomes horizontal at the peak altitude. This is a generalized  $f_d$  condition. It allows  $\alpha_g$  to be determined if Bouguer's refraction law is applied, yielding

$$\alpha_g = \arcsin \left( \frac{\rho_M}{\rho_T} n_M \right) = \arcsin \left( \frac{(\rho_T + H)}{\rho_T} \sqrt{1 - \chi} \right) \quad (6)$$

As we try to establish a balance for the penetration of wave energy through the whole atmosphere it is sufficient to consider the rays at the transmitting site at ground. The refraction phenomena in the layer which may be interesting for other propagation problems are less important here. It has been shown (5) that by refraction any point in space is "desserved", however, with very different energy. Neglecting transmission with strong attenuation (by dilution of radiation) we may say that to the (well-defined) cone at the ground corresponds another (larger) cone of refracted rays.

The efficiency of the penetration in an energy balance,  $D$ , is given by the ratio between the spatial angle of the cone with  $\alpha_g$  and the surface of a half-sphere, viz.  $2\pi$ . Let  $\alpha_g$  be the opening angle of the cone, then

$$D = 1 - \cos \alpha_g \quad (7)$$

Instead of this ratio ( $< 1$ ) we may apply dB scales with

$$\delta = -10 \log_{10} D = -10 \log (1 - \cos \alpha_g) \quad (7a)$$

If account is taken of the magnetic anisotropy, Eq. 7 is no longer correct, as  $\alpha_g$  depends on the azimuth. However, with the accuracy needed, Eq. 7 may be used if a weighted average value of  $\alpha_g$  (over all azimuths  $\Phi$ ) is introduced.

Equations 6 and 7 have been combined in the nomogram of Fig. 6. The left side gives Eqs. 6, the right one 7a. The ordinate is  $\alpha_g$ , but this value need not necessarily be read out. One has to apply  $\chi$  on the left abscissa and go over to the left-side curve with the line  $H = h_M$  into the right-hand diagram and from that curve down to the required value of  $\delta$  (in dB) on the right abscissa. The influence of anisotropy due to the magnetic field can be accounted for by applying below the left-hand diagram of Fig. 6 a dispersive diagram of  $\chi$  v.  $S$ . Examples of such diagrams, deduced from the Appleton-Lassen formula, are found in Fig. 7a and 7b. At a given location one gets different values at different azimuths, as  $\theta$  is different, see Eq. 5. A median value is appropriate as entrance of the nomogram.

Diagrams as shown in Fig. 6 can also be used to determine  $f_d$  after Eq. 3. From this equation one has the input value,  $\chi_d$ , given by

$$\chi_d = 1 - \rho_T^2 / \rho_M^2 = (1 - \rho_T / \rho_M) (1 + \rho_T / \rho_M) = \frac{H (2\rho_T + H)}{(\rho_T + H)^2} \quad (8)$$

Of course, absorption mainly in lower ionospheric layers is present in the window, thus also in the transition range. As in general it increases quickly with decreasing frequency the phenomenon is particularly important at the

lowest frequencies of the window. The frequency variation of the absorption decrement is approximately given by  $1/f^2$ . Therefore absolute values of the attenuation depend largely on the absolute value of  $f_c$ . As both,  $f_c$  and the typical absorption are subject to a large diurnal variation, the range of possible cases is rather large. Details of ionospheric absorption data through the ionosphere should be established in a similar way as has been done for terrestrial propagation via ionospheric reflection (6) (7).

For practical application the transmission conditions must yet be introduced, i.e. the influence of the radiation diagrams on the ground. In the case of terrestrial transmitters most antennae are directed at rather low elevation angles (high  $\alpha_T$ ); it follows for this particular case that the increase of attenuation for  $f$  approaching  $f_c$  as shown in Fig. 5 right-hand side, is partially compensated by the antenna diagram. Probably industrial noise and atmospheric noise also are not isotropically distributed over the different elevation angles. For practical work, in particular for standard measurements, this may be of importance.

**The LF window** – On very low frequencies the ionosphere becomes again transparent for the simple reason that its thickness is finite. This happens in the ELF range, where the wavelength of the electromagnetic radiation is comparable with a few hundred kilometers, which is the order of the thickness of the ionosphere.

However, the presence of the earth's magnetic field makes the ionosphere partially transparent even in the VLF and LF range. This is due to the fact that at frequencies below the gyrofrequency the "electronic polarization" (also called "extraordinary mode") propagates through the ionosphere in a narrow cone around the direction of the magnetic field (8). The index of refraction corresponding to this so-called "whistler-mode" is great compared with unity. Hartree's dispersion formula (9) did not admit this propagation mode, as it has a polarization term by which the behaviour just at these low frequencies is different from that described by the correct dispersion formula first given by Lassen (10).

The possibility of the "whistler-mode" makes the ionosphere partially transparent, but with rather great attenuation in the statistical average of all possible cases. This "attenuation" increases with increasing frequency until it becomes infinite at the gyrofrequency. It is difficult to give a numerical estimation because the conditions for a wave to enter the lower ionosphere seem to be rather variable and, for the time being, unpredictable. A crude estimate of the statistical average attenuation for through propagation in the VLF range is the order of 30 dB. This attenuation increases considerably with increasing frequency, probably with  $1/f^2$ , i.e. with 20 dB per decade.

With penetration in the whistler mode the propagation roughly follows the magnetic field lines. This gives a very queer aspect of the earth's surface as seen from outside: the equatorial belt is "invisible" from outside; this belt depends on the satellite height, and it extends with increasing height. An example of the aspect for satellites moving on spherical shells around the earth is given in Fig. 8; the hatched regions alone are "visible" for a satellite at 1000 and 2000 km above the earth's surface. This figure has been drawn using recent NASA L-maps (11). In fact this particular mode of propagation from the ground is largely influenced by the "entrance condition" in the

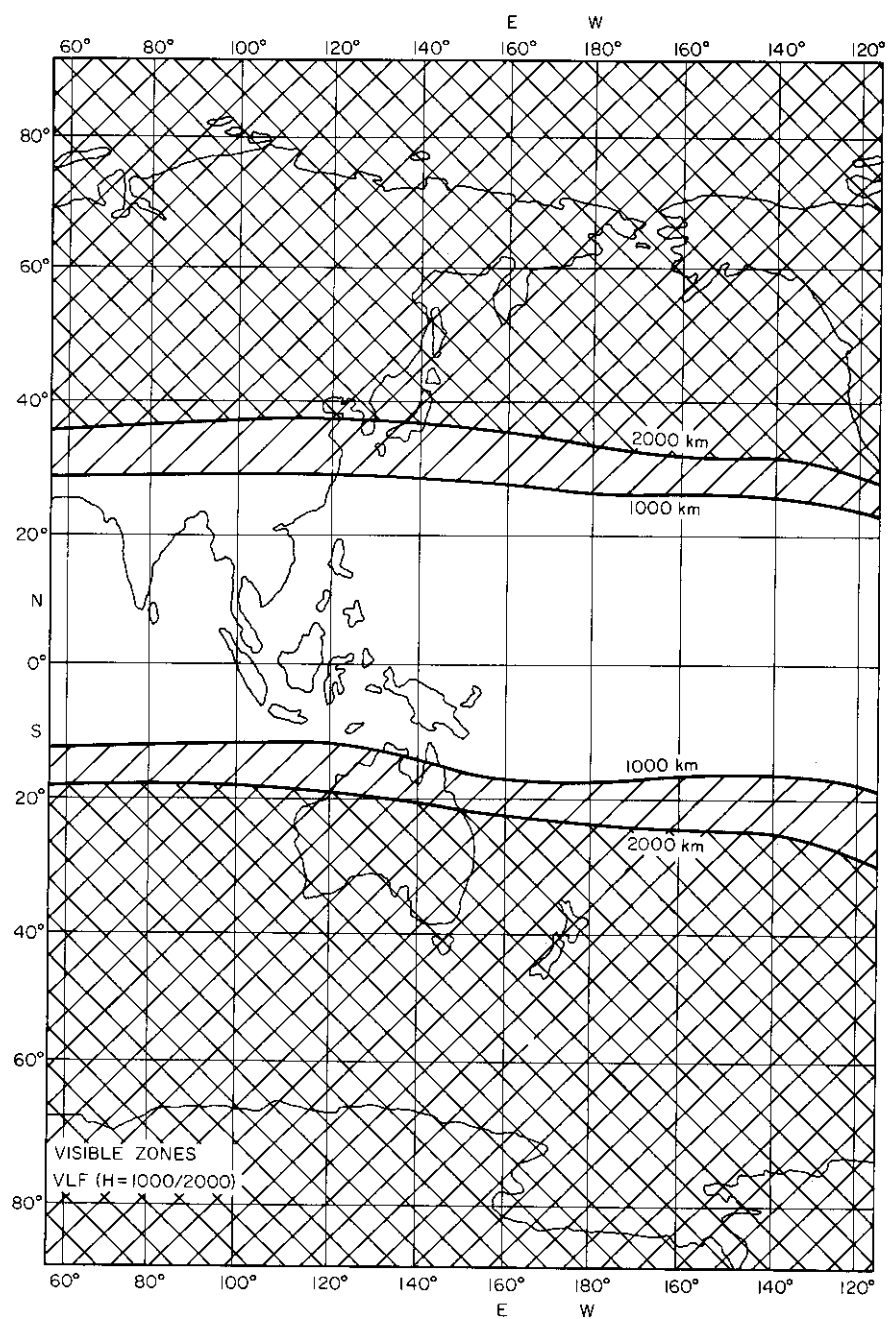


FIG. 8 "Visible" (Hatched) and "invisible" zones on the ground if the magnetic field lines are used as lines of sight. (Parameter: height of spherical shell in which the observer orbits)

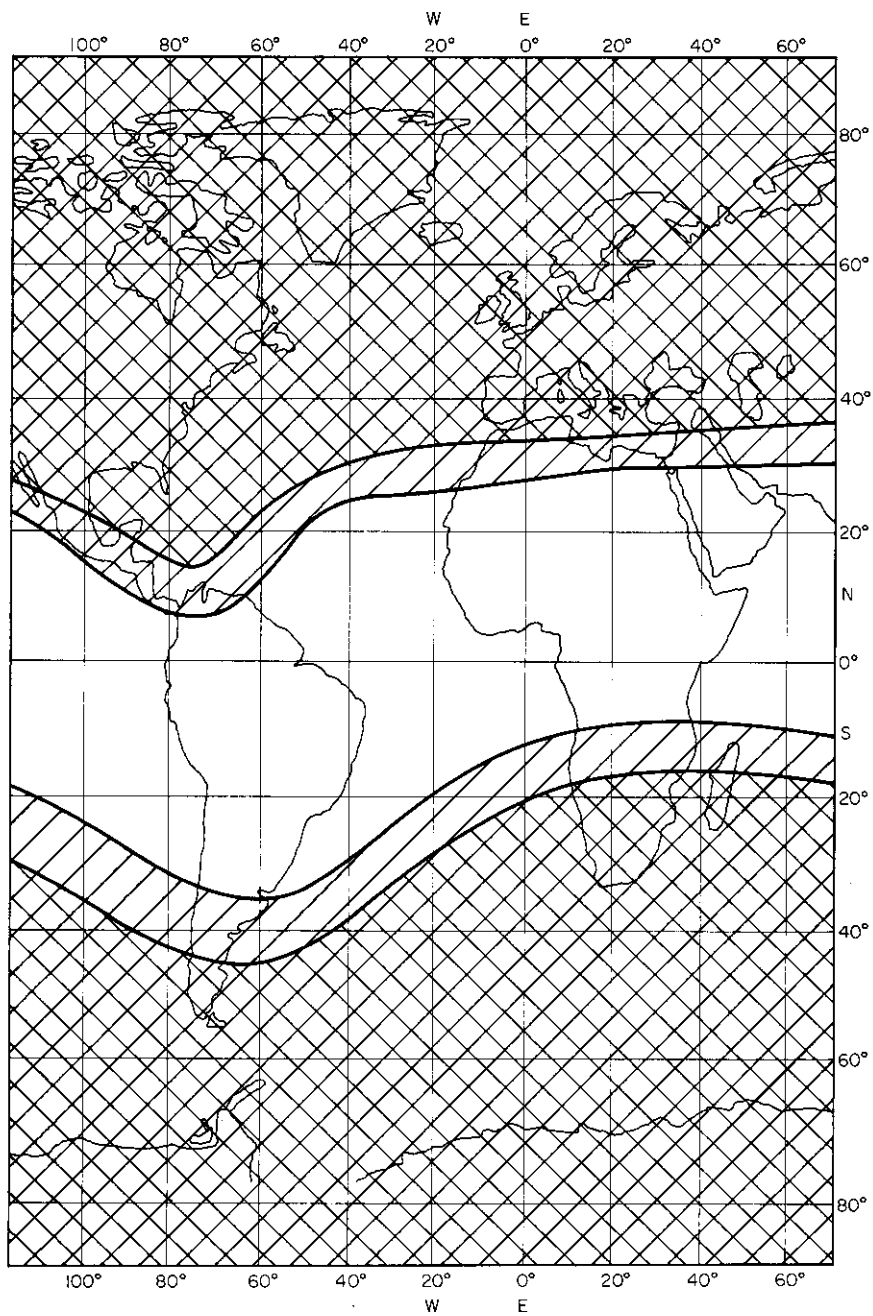


FIG. 8 "Visible" (Hatched) and "invisible" zones on the ground if the magnetic field lines are used as lines of sight. (Parameter: height of spherical shell in which the observer orbits)

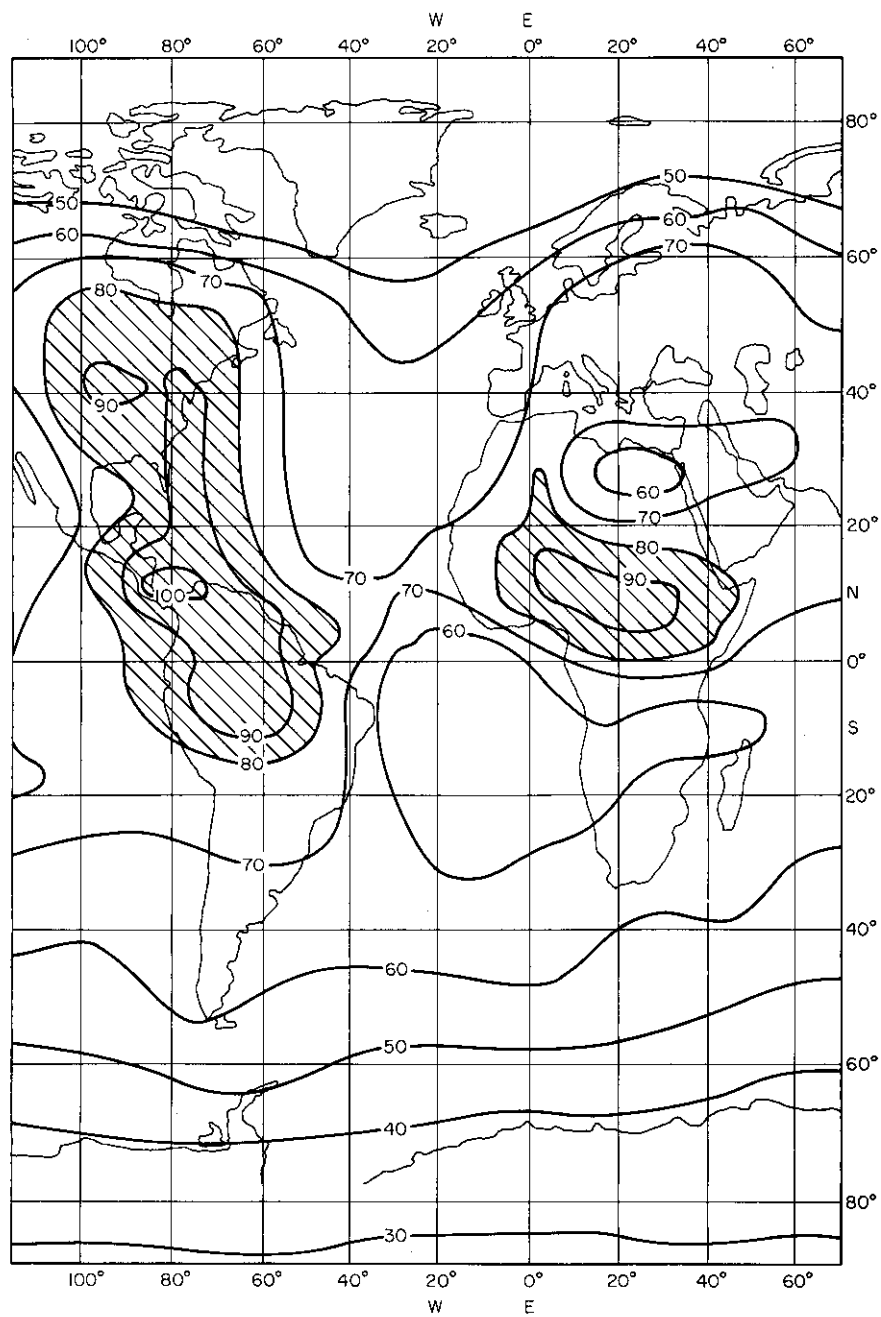


FIG. 9 World map of standard atmospheric noise power (dB above 288°K, at 1 Mc/s); valid of June . . . August, 00-04 h LMT. (CCIR Rep. 322, 1963)



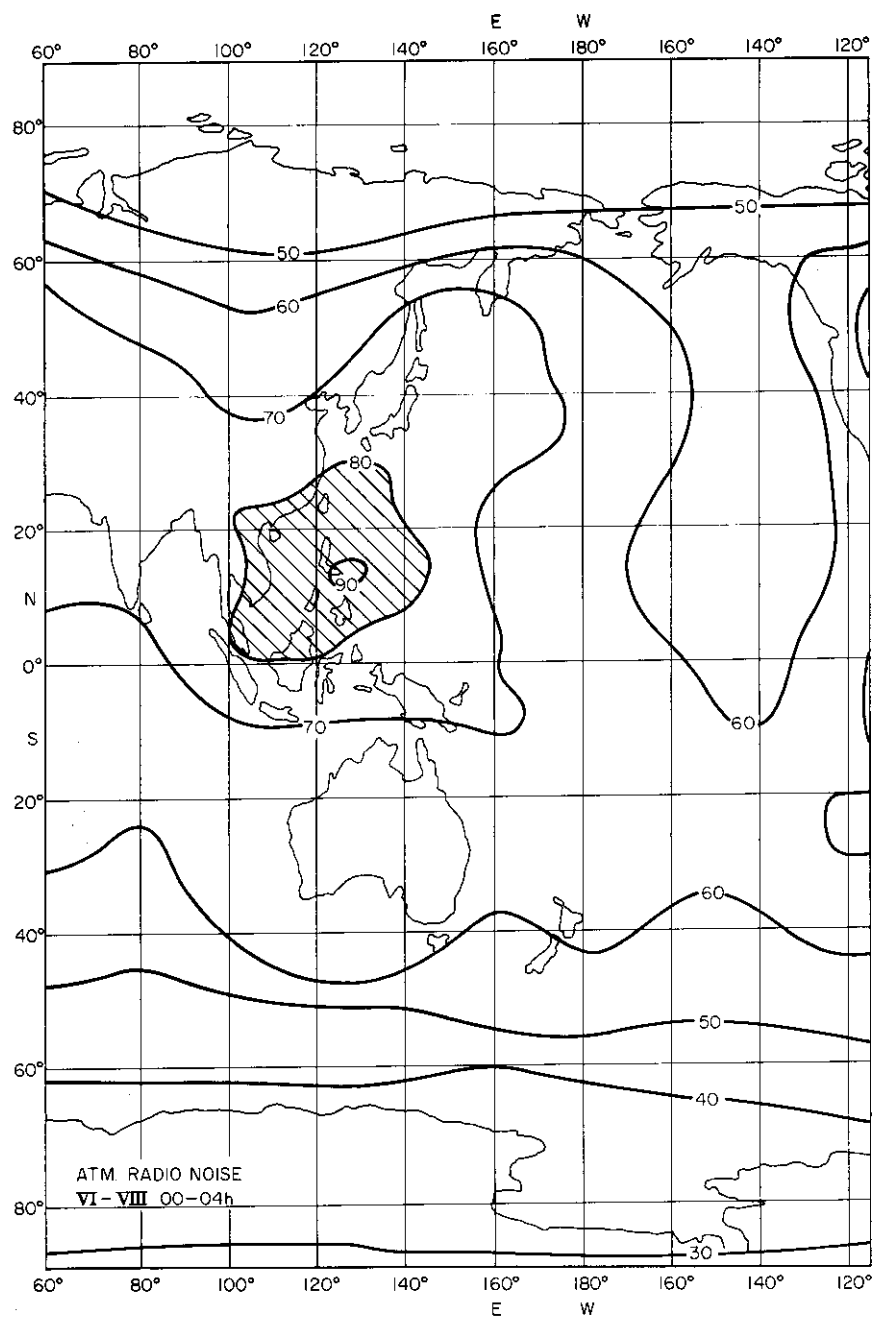


FIG. 9 World map of standard atmospheric noise power (dB above 288°K, at 1 Mc/s); valid for June . . . August, 00-04 h LMT. (CCIR Rep. 322, 1963)

D-region. Rays may often first propagate by ionospheric reflection thus reaching other magnetic latitudes as has been shown by whistler recordings. These possible reflections tend to "smear out" the clear picture given above.

#### SOURCES

Only terrestrial noise sources will be considered in the following. Their effect is mainly described by indicating a "temperature". This, of course, is a rather crude description for most of these emissions, the spectrum of which is far from being "white". So temperature values given in the following are all equivalent – or colour temperatures, thus relative to a limited frequency range which must be indicated.

It is understood that the average spectral power density,  $P_s$ , in the indicated frequency range is characterized by the value of the colour temperature  $T_s$ . Thus the relation between  $P_s$  and  $T_f$  is given by Planck's radiation law (for the differential of frequency  $f$ ):

$$P_s = \left| \frac{c_3}{\Omega_0} f^3 / (\exp c_4 f / T_f - 1) \right| \quad (9)$$

$$c_3 = 1.469 \cdot 10^{-50} \text{ W s}^4 \text{ m}^{-2}; c_4 = 0.479 \cdot 10^{-10} \text{ s} [^\circ\text{K}]; \Omega_0 = 1.57$$

from which

$$T_f = c_4 f \left| \ln \left[ 1 - \frac{c_3}{\Omega_0} f^3 / P_s \right] \right| \quad (9a)$$

In the cases we consider in the following, the low-frequency approximation applies, i.e. the radiation law of Rayleigh and Jeans, which gives

$$T_f \approx \frac{c_5}{f^2} P_s \quad (10)$$

with  $c_5 = c_4/c_3 = 0.326 \cdot 10^{40} [^\circ\text{K}] \text{ m}^2 \text{ W}^{-1} \text{ s}^{-3}$

The terrestrial sources of radiation are either natural or artificial. Thermal radiation and atmospheric must be considered in the first category, industrial noise and man-made emissions in the second. Thermal radiation has already been considered under the heading "Thermal Radiation". The three other main sources of terrestrial radiation are to be discussed in the following.

**Atmospherics** – These are mainly due to thunderstorms. Lightning flashes produce irregular pulse series with a broad spectrum, decreasing quickly towards higher frequencies. Ionospheric propagation influences considerably the spectrum which is observed at the earth's surface. The aspect in time is a background noise with superposed pulses. A report of CCIR (12) gives a description of the observed average field in terms of a temperature given in dB over 288°K (called  $F_{am}$  in the CCIR terminology). In this report world maps for different conditions are found, all valid for  $f = 1 \text{ Mc/s}$ . As an example we show in Fig. 9 the map for 0004 h, June–August. The values of  $F_{am}$  (at 1 Mc/s) are between 20 and 100 dB; three zones of high thunderstorms activity are prominent.

As to the variation with frequency CCIR gives a summary description by empirical diagrams which are different for different hourly and seasonal intervals. These curves are not free from ionospheric propagation influences:

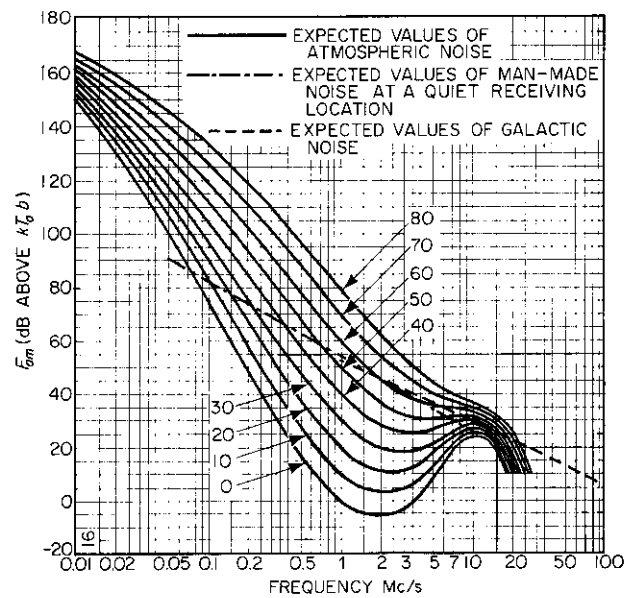
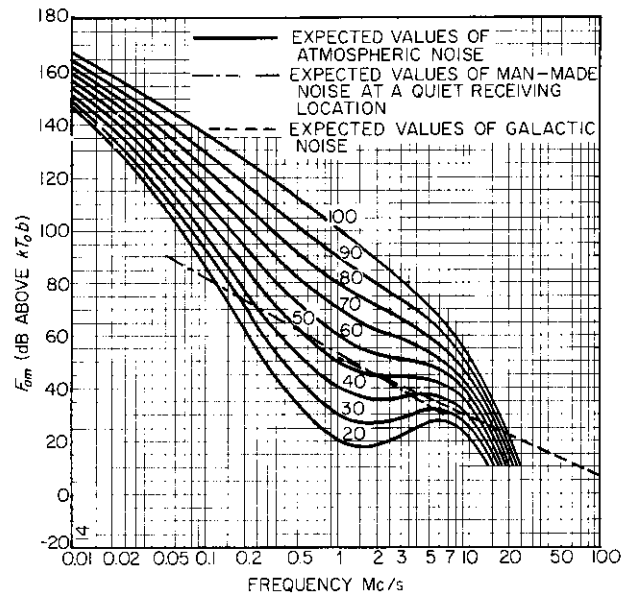


FIG. 10 Frequency variation of atmospheric noise  
 (a) Summer, 00-04 h LMT  
 (b) Summer, 08-12 h LMT (CCIR Rep. 322, 1963)

there is a high-frequency cutoff due to penetration of the ionosphere and on lower frequencies a range of attenuation due to absorption. This latter is particularly important during the day, as can be seen by comparison of Fig. 10a and 10b. It is clear that these curves give only an overall description of widely variable conditions. In particular the cutoff depends mainly on the ionization density of the  $F_2$ -layer, i.e. on geographic location on one side and on the solar cycle on the other. In fact, the curves of CCIR do not give the original radiation intensity of the sources, but the power density of radiation which is trapped in the duct between ground and ionosphere. As it is our aim to consider just the radiation which escapes from this duct, we need information about the effective topside emission of this duct. As explained above, the propagation conditions must be considered separately and in detail. Therefore we cannot use the CCIR curves as they stand.

But we could try to obtain from these curves an extrapolated value of the effective radiated power. This means that we should eliminate from the curves the propagation effects, viz. cutoff and absorption. Unfortunately at the reference frequency of 1 Mc/s the absorption effect is quite strong, so that the separation of the curves is larger on this frequency than it is on less attenuated frequencies. We therefore take the  $F_{am}$  values of CCIR only as a classification symbol. Our estimate for the extrapolation is that for the radiated power the difference between subsequent curves should be as small as on the lower frequencies, whilst the absolute values must certainly be higher. Considering the set of CCIR curves with this orientation we came to the following estimate for the effective power density, in the absence of propagation influences:  $F_0 = 62 + 0.4 F_{am}$  at 1 Mc/s, and a decrease of 40 dB per decade, thus:

$$F_{at} = F_0 - 40 \log_{10} \left( \frac{f}{\text{Mc/s}} \right) = 62 + 0.4 F_{am} - 40 \log_{10} \left( \frac{f}{\text{Mc/s}} \right) \quad (11)$$

The corresponding equivalent temperature would then be:

$$T_{at} = 4.50 \cdot 10^8 \cdot 10^{0.04 F_{am}} / \left( \frac{f}{\text{Mc/s}} \right)^4 \quad (11a)$$

The estimated relation for the frequency 1 Mc/s is shown in Table 2. The conversion for 1 Mc/s would then be

TABLE 2

$$F_0 = F_{at} (1 \text{ Mc/s})$$

$F_{am}$	100	80	60	40	20
$F_0 (1 \text{ Mc/s})$	102	94	86	78	70

For the conditions in space the higher frequencies of Table 3 are more important.

The values decrease rapidly with increasing frequency. However, at the lowest space frequency of 10 Mc/s the colour temperature is pretty high, between  $5 \times 10^8$  and  $3 \times 10^9$  K; on 100 Mc/s it is between 50 000 and 30°K.

TABLE 3

	$F_{at}(f)$				
Class $F_{am}$	100	80	60	40	20
Frequency $f/\text{Mc/s}$	3	83	75	67	59
	5	74	66	58	50
	10	62	54	46	38
	20	50	42	34	26
	30	43	35	27	19
	50	34	26	18	10
	100	22	14	6	-2
					-10

The highest of these values refer to the terrestrial zones of very high atmospheric noise level, i.e. to the tropical thunderstorm zones. Seen from outside, these appear as "hot spots" on the earth.

As explained above, on frequencies below 50 Mc/s only a part of the earth's surface may be "visible" from outside, "visibility" depending on the ionization distribution in the  $F_2$ -layer. But on higher frequencies certainly an integrated value over one hemisphere should reasonably be determined. On these frequencies one could introduce an equivalent temperature for the whole earth. Fortunately our estimate from Eq. 11a describes frequency and class influences by separate factors. Thus the effective value is obtained simply by integrating on the map over the surfaces of the different classes and summing up, taking account of the decrease in power which is 8 dB from class to class. This means that only the stronger classes are effective for the integrated value. Looking through the maps, we estimate that under these conditions something near class 70 should be the average class. With Eq. 11 and 11a this leads to equivalent integrated temperature values of

$$F_{aq} = 90 - 40 \log_{10} \left( \frac{f}{\text{Mc/s}} \right) \quad (12)$$

$$\bar{T}_{aq} = 2.9 \cdot 10^{11} / \left( \frac{f}{\text{Mc/s}} \right)^4 \quad (12a)$$

giving values between  $3 \times 10^7^\circ\text{K}$  at 10 Mc/s over  $3000^\circ\text{K}$  at 100 Mc/s down to only  $0.3^\circ\text{K}$  at 1 Gc/s.

In this context ionospheric propagation influences are particularly important. At the lowest frequencies of the "radio-window" ionospheric reflection occurs, particularly at the limb of the earth where the angle of incidence is large. Ionospheric absorption also is particularly strong for these angles such that a limb darkening is to be expected. This influence is superposed to the systematic ionospheric changes depending on geographic and diurnal position. The "aspect" of the earth is thus determined by three influences: distribution of noise sources – propagation effects depending on the position – limb darkening by propagation. Due to the last two influences the effective integrated temperature values given above may be slightly overestimated.

**Industrial noise** – This is due to unwanted man-made emissions, radiated

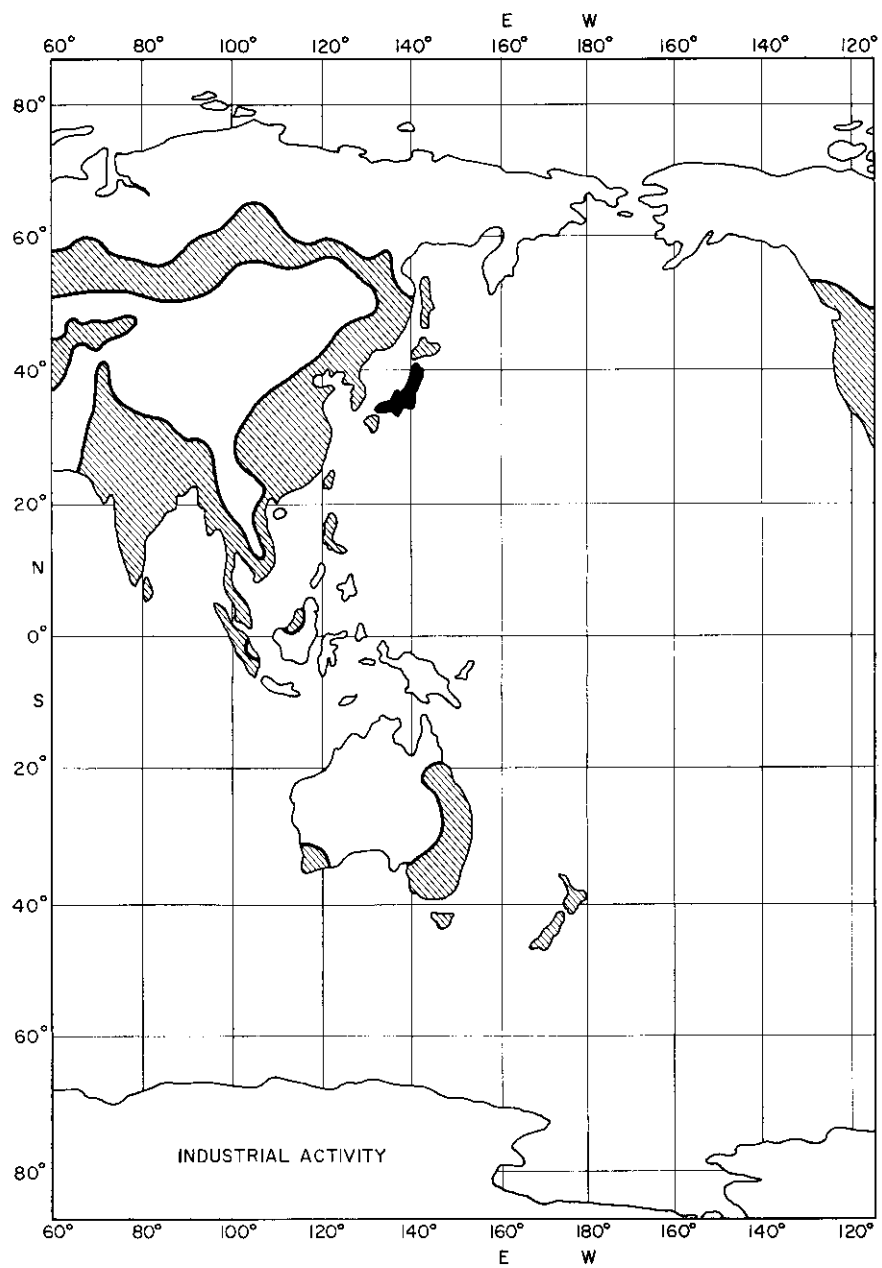


FIG. 11 Zones of industrial activity: I heavily active (black); II slightly active (hatched); III small activity (blank); IV deserts and oceans

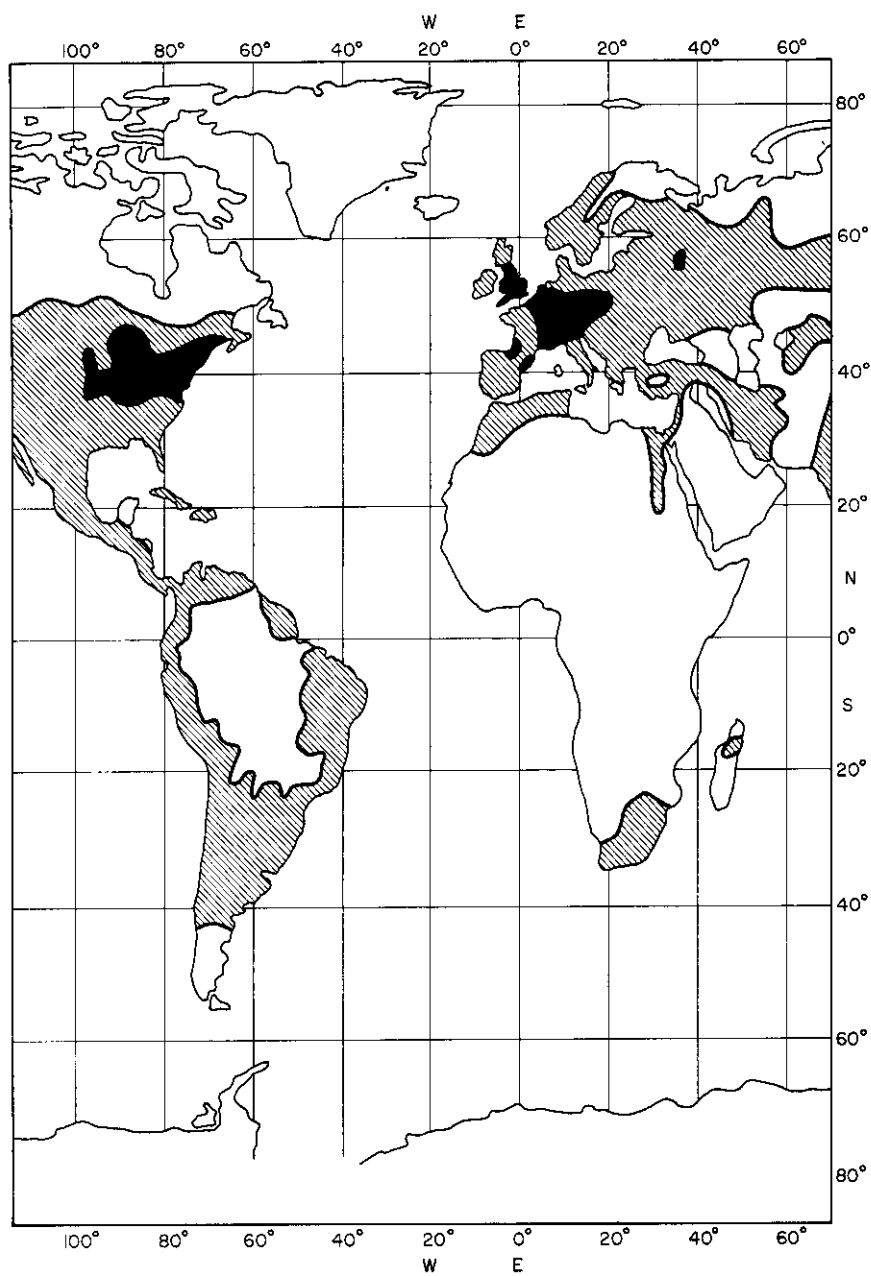


FIG. 11 Zones of industrial activity: I heavily active (black); II slightly active (hatched); III small activity (blank); IV deserts and oceans

mainly by power lines. Traffic noise may be important on the higher frequencies. CCIR data (13) exist over a few years. They have been established from measurements in civilized, i.e. rather noisy zones. The data are also given in terms of a noise factor  $F_{in}$  over the standard temperature of 288°K. The reference value at 1 Mc/s lies between 43 and 55 dB and the decrease with frequency is 28 dB per decade. In industrial regions one has, after (12):

$$F_{in}^{(I)} = 54 - 28 \log \left( \frac{f}{\text{Mc/s}} \right) \quad (13)$$

This expression is supposed to be valid as an average for the most active zones. The highest values found in the neighbourhood of big industries or highways are not interesting in this context, because only the integrated emission is considered. Noise in less-industrialized zones is surely considerably lower.

A subdivision of the earth according to industrial activity is therefore needed in connection with Eq. 13. As a very crude first estimation we introduce the four classes schedule of Table 4.

TABLE 4

## INDUSTRIAL NOISE CLASSES

Class	Description	Basic value	Reduction measure / dB
I	Heavily active	54	0
II	Slightly active	44	10
III	Small activity	34	20
IV	Deserts, oceans	14	40

(The reduction measure is the difference against Eq. 13 in dB.)

Figure 11 is a world map of industrial against other activity, taken from an atlas. It is quite evident that the "hot spots" are now rather small zones in Europe, U.S.A. and Japan. This should only be taken as a very first approximation. It is felt that better data could be obtained, for example, by plotting a map giving the production of electric (line) power per unit surface. With this at hand the classification could probably be replaced by a continuous formula. It is, however, doubtful whether the noise power could be supposed to be only proportional to the line power, because our expression also takes account of traffic noise. A series of measurements appears to be highly desirable.

Values of the colour temperature for industrial and other zones are found in Table 5, obtained from Eq. 13 with Table 4.

Even in the most industrial zone I the equivalent temperature goes from  $4 \times 10^6$ °K at 3 Mc/s to  $6,3 \times 10^3$ °K at 30 Mc/s and down to 170°K at 100 Mc/s. A comparison with Table 3 shows that only in the most industrial zone may industrial noise be stronger than atmospheric noise.



TABLE 5

		$F_{in}$			
Zone		I	II	III	IV
Frequency $f/\text{Mc/s}$	3	41	31	21	1
	5	34	24	14	-6
	10	26	16	6	-14
	20	18	8	-2	-22
	30	13	3	-7	-27
	50	6	-4	-14	-34
	100	-2	-12	-22	-42

Integrating in Fig. 10 over the earth the following surface distribution of the zones (Table 6) is found roughly:

TABLE 6

ABSOLUTE AND RELATIVE SURFACES OF ZONES  
OF DIFFERENT INDUSTRIALIZATION

Zone	I	II	III	IV	Total	Unit
Surface	1,8	56,9	76	375	509,7	$\text{mm}^2$
Relative						
surface 100 a	0,4	11,1	14,9	73,5	100	%
10 log a	-24,0	-9,5	-8,3	-1,3	0	dB

An integrated value for the earth depends certainly on the aspect (visible hemisphere), because the industrialized zones are all on the northern hemisphere, nearly at the same latitude. Taking the integral over the whole earth, we use the surfaces given in Table 6, in particular its last line. As power contributions must be summed up, the integrated temperature is given by

$$i\bar{T}_n = \sum_v a_v T_{in(v)} \quad (14)$$

This leads to Table 7.

TABLE 7

INTEGRATED EQUIVALENT TEMPERATURE OF INDUSTRIAL NOISE

Frequency $f$ (Mc/s)	3	5	10	20	30	50	100
$\bar{T}_{in}(f)$ (°K)	$5 \times 7.10^4$	$1 \times 1.10^4$	$1 \times 8.10^3$	275	89	18	3

These values are considerably lower than those found for atmospheric noise. **Terrestrial emissions** – These may sometimes be negligible for practical application, namely in the case where the frequency used is reserved for the space communication, such that interference from other terrestrial transmitters is excluded. However, very often this protection is far from being complete. Let us therefore consider here the bad case where terrestrial transmissions must be treated as a source of jamming. The worst case, where one has a single frequency from a strong terrestrial transmitter, is not taken into account, but terrestrial transmissions are smoothed out in frequency by using spectral power density values. With the radiation law Eq. 9 this leads directly to an equivalent temperature, after Eq. 10 in our case.

In order to apply Eq. 10 the spectral power density  $P_s$  must be known. We tried to make a guess, which, of course, is only a very crude estimation, by looking through frequency allocation lists for countries of high population density and industrial activity. We first considered the broadcasting band near 1 Mc/s and find for the U.S.A. a total radiated power of 1500 kW in a 100 kc/s range from a surface of nearly 1 mm<sup>2</sup>. With a time economy factor of 2/3 this gives

$$P_s'_{max} = 10 \text{ kW} / \text{mm}^2 \text{ kc/s} \quad (15)$$

The dash indicates that this power is radiated into the angle  $2\pi$  and not into 1 sr.

$P_s'_{max}$  is supposed to be the maximum value which occurs in the range near 1 Mc/s. It is known from experience with frequency-band recording that bands which are not allocated to broadcasting have much lower power density; our estimate is 15 dB less. There is also an overall decrease of the average radiated power with increasing frequency; we estimate it to be about 5 dB per decade. This corresponds to a frequency law with  $f^{-1}$ . The estimation, Eq. 15 corresponds to a heavily industrial zone. Having no better documentation at hand, we use the same activity zones I–IV as previously (Tables 4 and 6). The decreased intensity in the zones of lower activity is described by a factor  $B$  ( $< 1$ ) to be applied to Eq. 15; the corresponding dB value is called  $-b$ . We must now confess that the following estimate is a very crude one and should be corrected with better data in the future. Our guess of  $b$  for broadcasting (a) and other frequency band (b) is given in Table 10.

TABLE 8  
ESTIMATED DECREASE MEASURE B (IN dB) FOR ZONES  
OF DECREASING ACTIVITY

Zone	I	II	III	IV
<b>Service:</b>				
Broadcast	0	10	20	60
Other	15	20	30	60

The corresponding *absolute values* of  $P_s^1$  are given in Table 9.

TABLE 9  
SPECTRAL POWER DENSITY  $P_s^1$  RELATIVE TO 1 MC/S  
(dB over 1 kW mm<sup>-2</sup> kc/s<sup>-1</sup>)

Zone	I	II	III	IV
<b>Service:</b>				
Broadcast	10	0	-10	-50
Other	-5	-10	-20	-50

The equivalent temperature  $T_{em}$  is then found with the frequency law from Eq. 10, inserting  $P_s = P_s/2\pi sr$ , or  $\Omega_0 P_s = P_s^1/2\pi$ :

$$T_{em} = \frac{c_5}{2\pi f^2} P_s^1 = \frac{c_5}{2\pi} f^{-2} B P_s^1_{max} / \sqrt{f/Mc/s} \quad (16)$$

The evaluation in terms of a dB-factor  $F$  (over 288°K) is obtained from  $F_{em} = 10 \log (T_{em} / 288^\circ K)$  as

$$F_{em} \approx 132 - 25 \log \left( \frac{f}{Mc/s} \right) - b \quad (16a)$$

(the precise value of the constant being 132.5).

Values of  $F_{em}$  for different frequencies and zones are given in Table 10.

TABLE 10

Zone/Service	$F_{em}$							
	I		II		III		IV	
	(a)	(b)	(a)	(b)	(a)	(b)	(a)	(b)
Frequency Mc/s 3	120	105	110	100	100	90	60	60
5	115	100	105	95	95	85	55	55
10	107	92	97	87	87	77	47	47
20	100	85	90	80	80	70	40	40
30	95	80	85	75	75	65	35	35
50	90	75	80	70	70	60	30	30
100	82	67	72	62	62	52	22	22
1000	57	42	47	37	37	27	-3	-3

Service: (a) broadcasting; (b) other.

Comparing this table with Table 3 (for atmospheric noise) and Table 5 (for industrial noise), we come to the rather trivial statement that, except for deserts and oceans, the radiation from these latter sources is small against that of man-made emissions. Thus, due to human activity, the earth seen from outside has very "hot" spots.

It appears unwise in the present state of our basic data to give integrated

equivalent temperature values for the terrestrial emissions. More precise data about transmitting activity are needed at this end. It may only be mentioned that for future radio astronomy with observations on board of satellites or spaceships there may well be some interest in having such integrated temperature values.

#### ACKNOWLEDGEMENT

This work has been undertaken in the framework of a series of investigations supported by Bundesministerium für wissenschaftliche Forschung, Grant No. J 459.

#### DISCUSSION

D. MUHLEMAN – I believe that computations of this type with supporting observations looking back at the earth could be very valuable to our understanding of the radio spectrum of Jupiter and the other planets. In this regard, have you made any calculations of the radio spectrum that one would expect from non-thermal processes in the Van Allen radiation belts?

K. RAWER – No, as the present subject is limited to near-earth space. The Van Allen belt radiation would appear as originating in space.

D. MUHLEMAN – You reported that the temperature of the earth as seen in the radio window would be on the order of 300°K. Have you included deviations from unity in emissivity such as would occur over the oceans? I would expect the temperature to be closer to 30°K in this region in, say, the 2000 Mc/s region.

K. RAWER – I have not included this effect in my report, but I believe that it would be important in this special region. There should also occur deviations from Beer's law on the oceans, causing some "limb darkening".

G. H. MILLMAN – Noise measurements in the HF band are made with vertical oriented whip antennas or in other words vertical polarization. How does one convert these data for systems which use horizontal polarized antennas?

K. RAWER – It is felt that terrestrial observations with horizontal polarization would not be much better in our context. In fact, the polarization observed on the earth is largely affected by ionospheric propagation, in particular on higher frequencies which are of interest here. Our problem concerns the radiation escaping from the earth the polarization of which is also more or less influenced by ionospheric refraction. The main question in this context is whether the radiation from thunderstorms into higher angles compares with that at lower elevation angles as measured at the noise stations. It should also be of interest to know the relation between vertical and horizontal lightning strokes with respect to both probability and current intensity.

CP-3

PART 5

TROPOSPHERIC EFFECTS

---



ABSORPTION OF RADIO WAVES IN THE  
TROPOSPHERE

D. T. GJESSING

Norwegian Defence Research Establishment, Kjeller, Norway

## SUMMARY

The physical processes giving rise to absorption of radio waves will first be considered phenomenologically, discussing the various types of molecular absorption spectra in gases. Having determined which atmospheric constituents are responsible for the absorption of radio waves, the various absorption processes will be discussed quantitatively in some detail. In particular, one will discuss the absorbing effect on microwaves of the atmospheric gases and of liquid and solid particles in the troposphere.

## INTRODUCTION

We are concerned with propagation of radio waves in the troposphere. But before we proceed to consider in detail the particular absorption effect that a radio wave is subjected to when it passes through the troposphere, it is appropriate to relate our problem to that met in general when the troposphere is used as the medium for the propagation of electromagnetic waves.

Consider the radio power received as a function of distance over a practical communication circuit, as shown in Fig. 1. In the initial range (from 0 to  $D_1$  on Fig. 1) where the receiver is within optical sight of the transmitter, the field strength at the receiver is governed by two factors:

- (a) the absorbing effect of the troposphere determining the maxima of the field strength that "oscillates" with distance;
- (b) the reflectivity of the earth surface determining the minima of the field strength versus distance curve.

The distance  $D_1$  to the radio horizon is determined by the path geometry and by the refraction effect of the troposphere, i.e. by the rate at which the mean refractive index decreases with height. In the range interval  $D_1$  to  $D_2$  the field strength is primarily determined by obstacle-diffraction effects giving rise to a comparatively large decrease in field strength with distance. For ranges greater than  $D_2$ , tropospheric scattering effects are of dominating importance.

In this brief presentation we shall concentrate on the absorbing effect of the troposphere on radio waves. By radio waves we mean for this treatment electromagnetic waves with wavelengths greater than approximately 1 mm, or frequencies below approximately  $10^6$  Mc/s. The troposphere is confined to the lower atmosphere, where the propagation medium is non-ionized. When dealing with absorption effects in the troposphere it is appropriate to distinguish between the absorption presented by the tropospheric gases and

that of liquid and solid particles in the troposphere. Let us consider each of these in turn.

#### THE ABSORPTION BY GASES

In order to fully understand the mechanisms giving rise to absorption of radio waves, it is necessary to go into some detail and consider the micro-structure of the gas. Let us start with the atom.

**Atomic spectra** – In the range 1 to 500 Gc/s now covered by microwave sources direct transitions between fine or hyperfine levels of many atoms are theoretically observable. Because of the low intensity of micro-wave transitions of atoms these atomic absorption spectra are of very little practical importance in connection with atmospheric absorption. Then let us consider the next degree of smallness, the molecule.

**Molecular spectra** – There are four different mechanisms giving rise to molecular absorption spectra:

- (a) Pure rotational spectra – This category constitutes the principal class of microwave molecular spectra. The spectra arise from the transitions between quantized rotational energies of molecules in single electronic ground states. If the molecule is excited by an electromagnetic field of a frequency  $\nu$  corresponding to the energy difference between the ground state and the next energy level ( $h\nu = E_1 - E_0$ ), the molecule will absorb this energy difference from the electromagnetic field resulting in an absorption line at this very frequency. The main group of molecules giving rise to absorption lines within the range of microwave frequencies are the hydrogen halides which are of no importance when dealing with atmospheric gases. The only atmospheric gases offering absorption through the mechanism under consideration are  $\text{SO}_2$ ,  $\text{O}_3$  and  $\text{H}_2\text{O}$ .
- (b) Inversion spectra – Inversion may be described as the reflection of all the nuclei of a non-planar molecule at its center of mass. In this way a new equilibrium configuration of the molecule is obtained which in non-planar molecules cannot be obtained from the original one through any succession of simple rotations. To obtain the new equilibrium configuration, the molecule must pass through a potential barrier, a feat which in the quantum mechanics is described as “barrier tunnelling”. For  $\text{NH}_3$  (ammonia), the inversion frequency in the ground vibrational state falls in the radio-frequency region at about 24 Gc/s. It is on this phenomenon that the action of the ammonia maser is based. There is no important atmospheric gas possessing inversion spectra.
- (c) Vibrational spectra – Consider a molecule within which potential forces are acting; the atoms are thus bound together by elastic forces. If these atoms having a finite mass are excited by an alternating electromagnetic field, resonance will occur when the stimulating frequency equals that corresponding to the difference between two quantized vibrational energy levels. The vibrational spectra of importance all lie in the infra-red range of frequencies and thus outside the scope of this treatment.



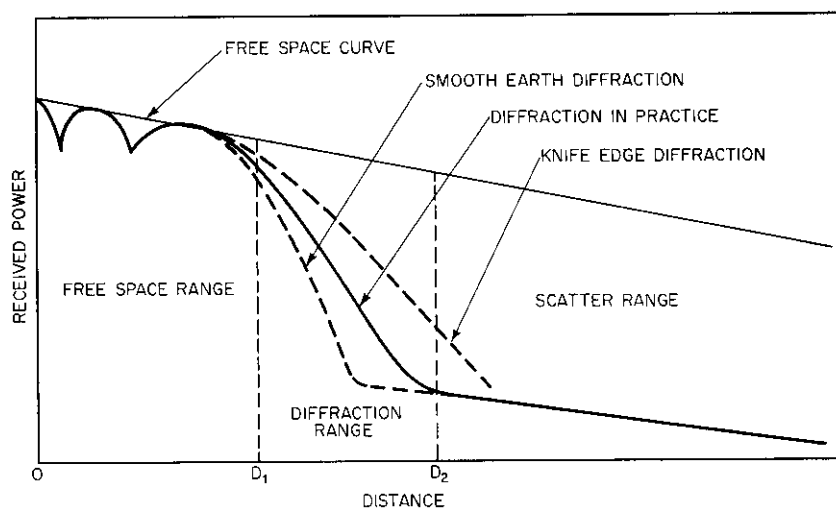


FIG. 1 Factors determining the path loss in tropospheric propagation

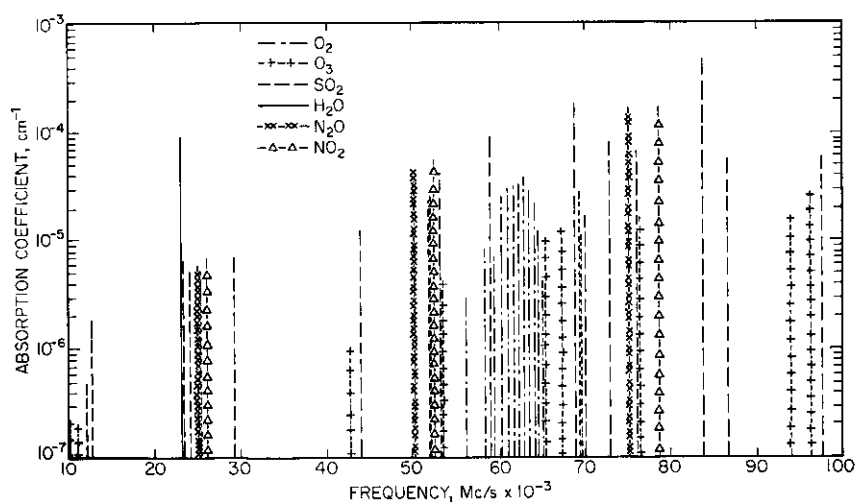


FIG. 2 Microwave absorption coefficients of atmospheric gases in the frequency range 10–1000 kMc/s (after Ghosh and Edwards)

It then only remains to consider one further type of molecular spectrum, namely that originating from paramagnetic resonances:

- (d) Paramagnetic Spectra – These spectra are of great importance in connection with atmospheric absorption. Let us now study the group of molecules which contain one or more unbalanced electron spins in the electronic ground state. The molecules  $O_2$ ,  $NO$ ,  $NO_2$  and  $ClO_2$  are examples. If the molecule is subjected to a magnetic field, the unbalanced spins will be weakly coupled to the magnetic momentum resulting from this field. Now, such a magnetic field will under certain circumstances be generated from the orbital motion of the electrons or from the end-over-end rotation of the whole molecule. This weak interaction between the spin magnetic moment  $S$  and the magnetic moment generated by the molecular rotation results in a splitting of each rotational level into  $(2S + 1)$  components, commonly known as the spin multiplets. Transitions between these triplets, brought about an external magnetic field of frequency  $\nu$ , will result in closely-spaced absorption lines for  $O_2$  in the 4 to 6 mm. region and to a single component in the 2.5 mm region (1).

Having now discussed the problem phenomenologically, let us proceed and give some quantitative results. Figure 2 shows a theoretical absorption spectrum for the most typical atmospheric gases at radio frequencies. The absorption coefficient at the peak resonance frequency is given by

$$\alpha_0 = \frac{8\pi^2 \nu_0^2 N f}{3CkT} (\mu_{ij})^2 \frac{1}{\Delta\nu} \quad (1)$$

$N$  = total number of molecules per ml

$f$  = fraction of the total molecules present in the lower state

$\mu_{ij}$  = matrix element of the dipole moment  $\mu$ , which gives rise to transition from  $i$  to  $j$  states

$\Delta\nu$  = half-width of absorption line

$\nu_0$  = peak resonance frequency

In terms of the conventional measure of attenuation dB/km, we have

$$\gamma = 10^6 \alpha_0 \log_{10} e \text{ dB/km}$$

Let us then consider the individual factors of Eq. 1.  $N$ , the number of molecules per ml is given by

$$N = \frac{P}{kT}$$

where

$P$  = partial pressure of the absorbing gas

$T$  = temperature

$k$  = Boltzman's constant

Herzberg has shown that  $f$ , the fraction of molecules present in the lower states is given by

$$f \approx \frac{1}{T} \text{ for diatomic and linear polyatomic molecules (O}_2 \text{ and N}_2\text{O)}$$

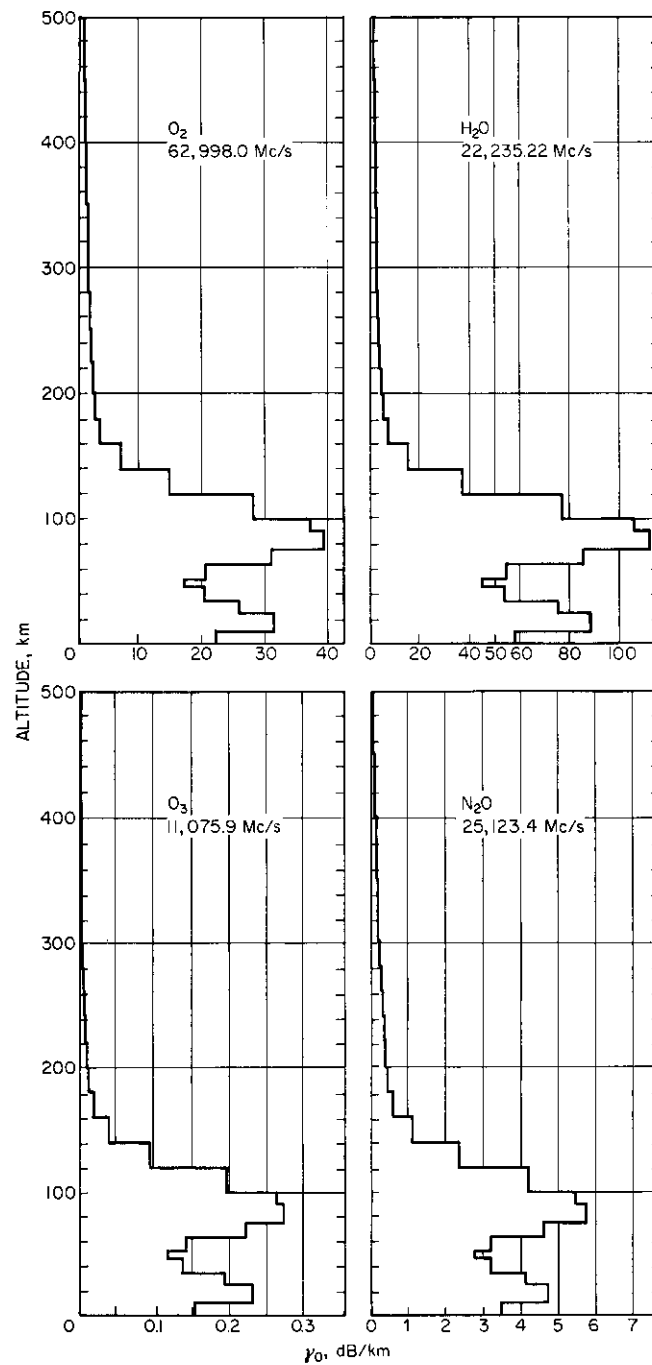


FIG. 3 Histograms showing the variations of peak absorption of different atmospheric gases with altitude (after Ghosh and Malaviya)

and

$$f \approx \frac{1}{T^{3/2}} \text{ for symmetric and asymmetric top molecules (H}_2\text{O and O}_2\text{)}$$

Finally the line-width  $\Delta\nu$  varies with temperature and pressure as follows:

$$\Delta\nu = (\Delta\nu)_{T=300^\circ K} P \left( \frac{300}{T} \right)^x$$

The value for  $x$  has been found experimentally (by Tinkham and Stradberg) for oxygen to be  $\frac{3}{4}$ . For  $\text{O}_3$ ,  $\text{H}_2\text{O}$ ,  $\text{N}_2\text{O}$ ,  $x$  has been assumed unity. Basing the calculations on an idealized height temperature distribution, the peak absorption of different gases as a function of height is obtained. This is shown in Fig. 3. Finally, let us consider the shape of the absorption curve near the resonance frequency. In terms of the resonance frequency  $\nu_0$ , the half-width of the absorption line  $\Delta\nu$  and the absorption coefficient at resonance, it can be shown (1)

$$\alpha = \alpha_0 \frac{\Delta\nu^2}{(\nu_0 - \nu)^2 + \Delta\nu^2} \frac{\nu^2}{\nu_0^2} \quad (2)$$

This expression is commonly known as the Lorentz factor. Figure 4 shows the total absorption round resonance for  $\text{O}_2$  and  $\text{H}_2\text{O}$ .

#### LIQUID AND SOLID PARTICLES

When dealing with this part of the problem, the procedure is to determine by exact electromagnetic theory the power absorbed and that lost by scattering when a plane wave passes over a single spherical droplet. The result is dependent only on the wavelength  $\lambda$ , the drop diameter  $D$  and its complex dielectric constant. The dielectric constant is a function of  $\lambda$  and also of the temperature  $T$ .

The effect of a uniform concentration of droplets, all of the same size, may then be determined and from this information the attenuation can be derived for any given droplet concentration, and size distribution applicable to particular meteorological conditions. The scattering particles are assumed to be distributed at random and the scattered radiation is considered as entirely non-coherent for the range of wavelengths under consideration. The effects of the passage of a plane wave over a sphere have been studied extensively in the past, generally with various restrictive conditions. The completely general and exact theory was first developed by Mie in 1908 and a compact presentation of the problem has been given by Stratton in 1941. On the basis of these earlier works, the effects produced by single drops of various diameters can be determined. The only fundamental physical information required for this is a knowledge of the complex dielectric constant  $\epsilon$  of the drop for the appropriate ranges of  $\lambda$  and  $T$ .

$$\epsilon = \epsilon' - j\epsilon''$$

The square root  $m$  of the dielectric constant may be written

$$m = n - j n \psi \quad (3)$$

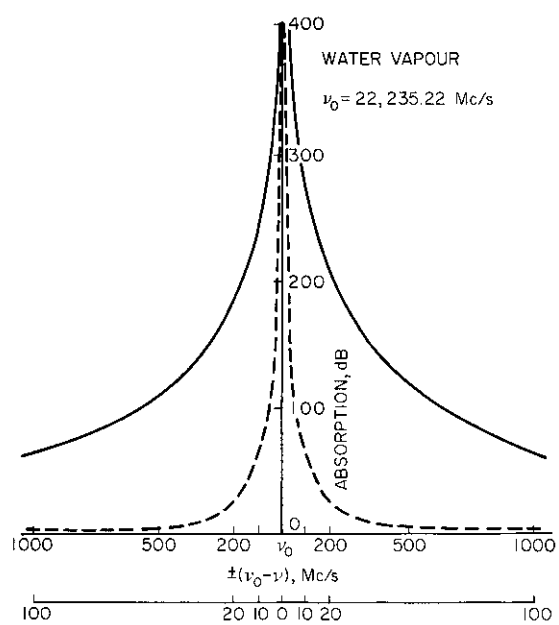
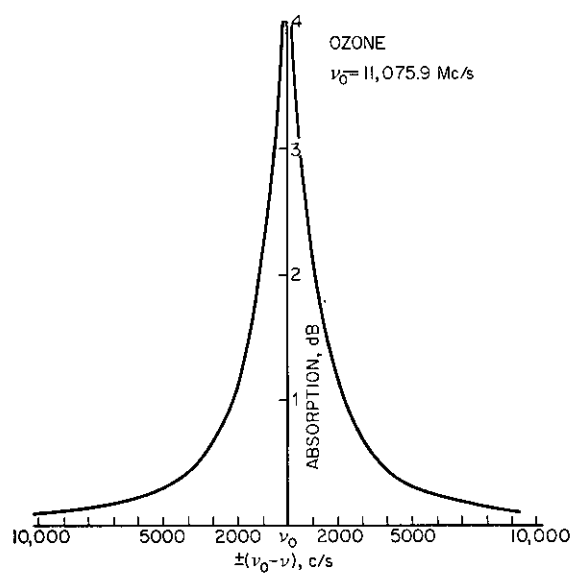


FIG. 4 Total absorption around peak resonance frequency for ozone and water vapour (after Ghosh and Malaviya)

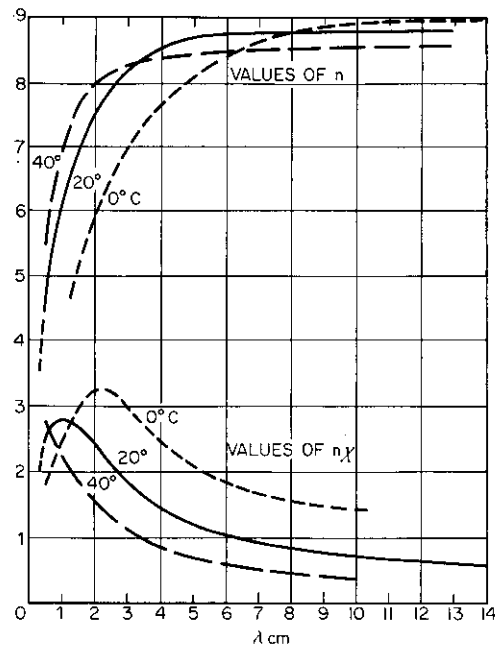


FIG. 5 Complex refractive index  $m = n - in\chi$  for water (Saxton)

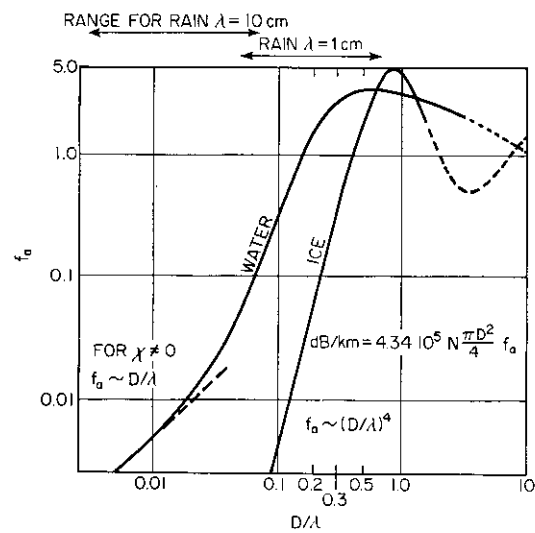


FIG. 6 The effective cross-section of a sphere for combined absorption and total scattering  $\pi D^2/4 f_a$  Schematic diagram:  $n$  and  $n\chi$  assumed constant at values corresponding to slightly greater than 1 cm (after Ryde)

where

$n$  = refractive index  
 $n\psi$  = absorption index

It is upon the values of these two parameters, for given  $\lambda$  and  $T$ , that the required absorption and scattering properties of a sphere of a given size will depend. The general form of the function relating  $n$  and  $n\psi$  to the wavelength  $\lambda$  and the temperature  $T$  is shown in Fig. 5.

Now let us consider the absorption effects of the liquid particles. On the basis of Mie and Stratton's work, it can be shown that the attenuation in dB/km is given by

$$\alpha(\text{dB/km}) = 10 \log_{10} e \cdot 10^5 \cdot N \frac{\pi D^2}{4} f_a \left( \frac{D}{\lambda}, m \right) \quad (4)$$

$N$  = number of drops

$D$  = diameter of drop

$f_a$  = function of  $\frac{D}{\lambda}$  and  $m$

$f_a$  may be regarded as the ratio of the total energy absorbed + scattered by a single drop, to that in the area of the wavefront equal to the projected area of the drop. In fact, the effective target-area of a sphere for combined absorption and total scattering is  $\frac{\pi D^2}{4} f_a$ .

The determination of  $f_a$  is simple when the drop diameter is very small in comparison with the wavelength. But, as  $D/\lambda$  exceeds about 0.06 the computations rapidly become lengthy, due to the fact that Riccati-Bessel and Hankel functions with complex arguments are involved. The general way in which  $f_a$  is found to vary with  $D/\lambda$  is shown in Fig. 6 for a constant value of  $m$  appropriate to a wavelength slightly greater than 1 cm and  $T = 18^\circ\text{C}$ .

Now let us consider the limiting case of fine-droplet clouds where  $D < 0.01$  cm. From Fig. 6 we see that, provided  $D/\lambda < 0.015$ ,  $f_a$  varies as  $D/\lambda$ . It may, in fact, be shown that for such small values of  $D/\lambda$  the function  $f_a$  reduces to

$$f_a = 2\pi C_1 D/\lambda \quad (5)$$

where  $C_1$  is a function of  $n$  and  $n\psi$  and therefore also of  $\lambda$ .

The expression for the attenuation then becomes

$$\alpha(\text{dB/km}) = 4.093 C_1 M/\lambda\rho \quad (6)$$

$\rho$  = density

$M$  = mass concentration of droplet, grams/ $M^3$

Note that the attenuation does not depend on drop size  $D$ . Figure 7 shows  $\alpha$  plotted to the basis of  $\lambda$  for different values of the visible range.

In this brief presentation, it does not appear to be pertinent to go into detail as regards the various types of liquid and solid particles in the troposphere. The attenuation produced by hail is calculated very much in the same way as that for rain droplets. As far as the absorption caused by snow and ice-clouds is concerned, Mie's theory developed specifically for spheres will no longer apply. The ice crystals appear in the form of stars, plates,

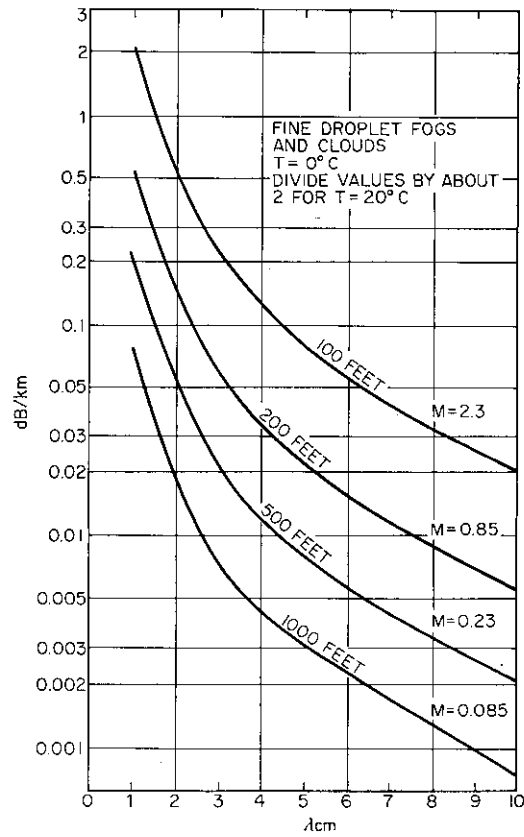


FIG. 7 Average attenuation in dB/km for given visual range in feet (after Ryde)

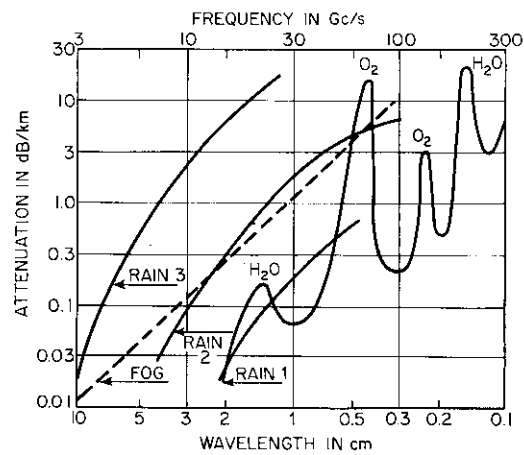


FIG. 8 Tropospheric absorption (after du Castel) Rain 1 = 1 mm/h, Rain 2 = 10 mm/h, Rain 3 = 100 mm/h, Fog = visibility 25 m



prisms and prismatic needles, according to the conditions under which they are formed. Gans in 1912 considered the case of ellipsoids, small in comparison with the wavelength, and from his work expressions relating to the limiting case of small disks and needles were derived.

It was found that for ice crystals, whose principal dimensions do not normally exceed a few millimeters, an expression of the form established above for fine water droplets, Eq. 6, will be sufficiently accurate for wavelength in the cm band. It is found that even for  $\lambda = 1$  cm the attenuation is extremely small.

#### CONCLUSIONS

The eighth and last figure summarizes the absorbing effect on radio waves of gases, solid and liquid particles in the troposphere. We see that the gases produce a very frequency-selective absorption, the general trend being an increase in absorption with increasing frequency. The solid and liquid particles in the troposphere produce a smooth curve relationship between attenuation and frequency; high frequency is associated with high attenuation.

#### REFERENCES

1. GORDY, W., "Microwave Spectroscopy, Handbuch der Physik", Band 28. Springer-Verlag, Berlin, 1957.
2. STRATTON, "Electromagnetic Theory", 1941.
3. RYDE, J. W., "The Attenuation and Radar Echoes Produced at Centimeter Wave-lengths by Various Meteorological Phenomena". The Physical Society, London, 1946.
4. DU CASTEL, "Propagation Troposphérique et Faisceaux Hertiens Transhorizon, Collection Technique et Scientifique de CNET". Editions Chiron, Paris, 1961.
5. GHOSH, S. N., and MALAVIYA, V., "Microwave absorption in the earth's atmosphere". J. Atmos. Terr. Phys. 21, 4, 1961.
6. BURROWS, C. R., "Radio Wave Propagation". Academic Press, New York, 1949.



## CHAPTER 5-2

TROPOSPHERIC REFRACTION AND ITS INFLUENCE  
ON THE COVERAGE OF LONG-RANGE RADARS

DAG T. GJESSING

Norwegian Defence Research Establishment, Kjeller-Lillestrøm, Norway

## SUMMARY

An investigation of the frequency of occurrence and the effect on radar coverage of anomalous radar propagation (in a given area) is given. The measured coverage diagram is compared with diagrams computed from a knowledge of the refractive index distribution in the troposphere. A method by which radio ducts can be predicted from synoptic weather data is discussed.

## INTRODUCTION

During the last decade technological progress in the field of radio and radar has been considerable. The performance of modern radio and radar systems developed with a high degree of sophistication for the purpose of measuring distance and direction is no longer limited by technological shortcomings; it is often the propagation medium itself, the troposphere, that is the limiting factor. Consequently, a detailed knowledge of the propagation properties of the troposphere is needed in order to meet the ever-increasing demands for accuracy.

It is the purpose of this brief note to describe an investigation currently in progress which has the following objectives:

- (a) Explore the frequency of occurrence of anomalous propagation conditions in a given area.
- (b) Investigate the effect that these anomalous atmospheric conditions have on the coverage diagram of a long-range air-traffic-control radar.
- (c) Compare the measured coverage diagrams with diagrams computed from the knowledge of the refractive index distribution in the appropriate part of the troposphere.
- (d) Discuss methods by which the refractive index distribution can be deduced from a knowledge of the synoptic weather situation.
- (e) Compare the weather analyses (d) with the experimental investigations (a).

## THE EXPERIMENTS

**Determination of the Existence of Anomalous Conditions by the Aid of Radio** – Air-control radars are designed so as to detect air targets at maximum range and at the same time cover a given height interval. In order to achieve this, it is undesirable to obtain echoes from ground targets. Under particular atmospheric conditions, however, these radars, having generally a

cosecant square antenna pattern, do receive distant ground echoes known as ground clutter. The existence of distant ground echoes suggests prevailing anomalous atmospheric conditions, although it is theoretically conceivable to have an anomalous atmosphere without this giving rise to distant ground clutter.

The current investigation makes use of the clutter observations. A simple ground-based receiver is placed far outside the normal range of the radar. Since the electromagnetic wave impinging on this receiver only suffers one-way attenuation, whereas the wave giving rise to radar ground clutter passes twice through the same part of the atmosphere, this receiver need not be very sensitive. Successive tests have been made with simple transistorized battery-driven video receivers. Under normal atmospheric conditions no radar signal could be detected using these receivers. Under ducting conditions strong signals were recorded. Over an approximately one and a half year period the signal from an operational radar was recorded using a sensitive ground-based superheterodyne receiver placed some 100 miles from the radar. Normally a weak, but persistent scatter signal of strength approximately 70 dB below 1 mW was received. Under ducting conditions this signal increased some 40 dB or more. If the signal strength were higher than approximately  $-40$  dBm, the propagation condition was classified as anomalous.

The results can be summarized as follows:

- (1) On the average there are 10 days (or parts of a day) with anomalous propagation conditions per month.
- (2) Generally the chances of having anomalous propagation conditions are smaller in winter than in summer.

**The Effect of Anomalous Propagation Conditions on the Radar Coverage Diagram** – The ability of a radar to detect a target is determined by several factors:

- (1) Transmitted power, receiver sensitivity, etc.
- (2) Shape and size of antenna.
- (3) Echoing area of target.
- (4) Transmission properties of troposphere.

For all practical purposes factors 1 and 2 can be considered as time independent. The remaining two factors however do vary with time; the echoing area is strongly dependent on the aspect of the target relative to the direction of the radar beam. Normally the aspect varies considerably with time, giving rise to variations in scattering cross-section of the target. The present investigation is concerned with changes in coverage volume resulting from tropospheric phenomena; it is important, therefore, to vary a minimum of parameters at the time. The effect of a changing target-scattering cross-section is excluded by equipping the target with a simple transponder. The transponder output power was kept constant during the tests and it was ensured that the transponder antenna gave a radiation diagram sufficiently wide to exclude the effect on the experimental results of normal and inherent changes in target aspect.

The power received from the transponder was displayed on c.r.o. with

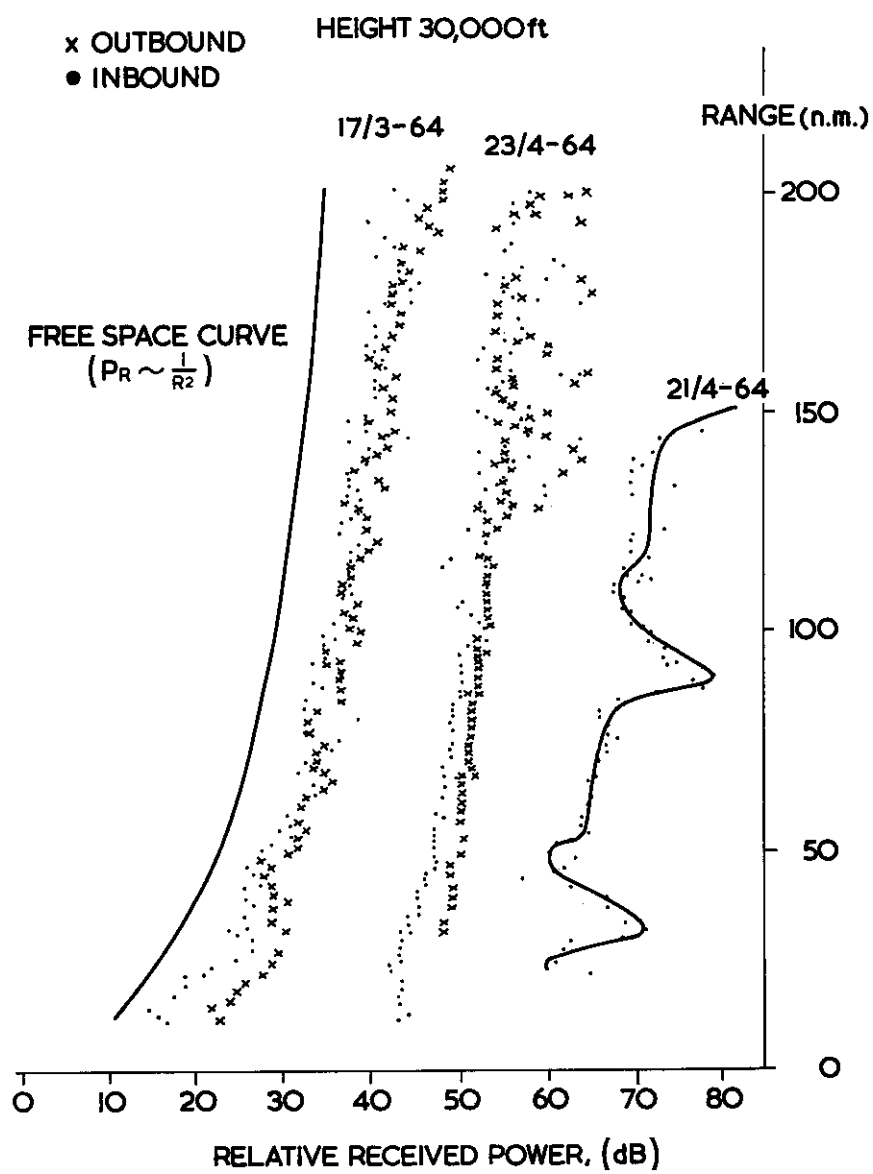


FIG. 1 Relative power received from aircraft transponder as a function of distance

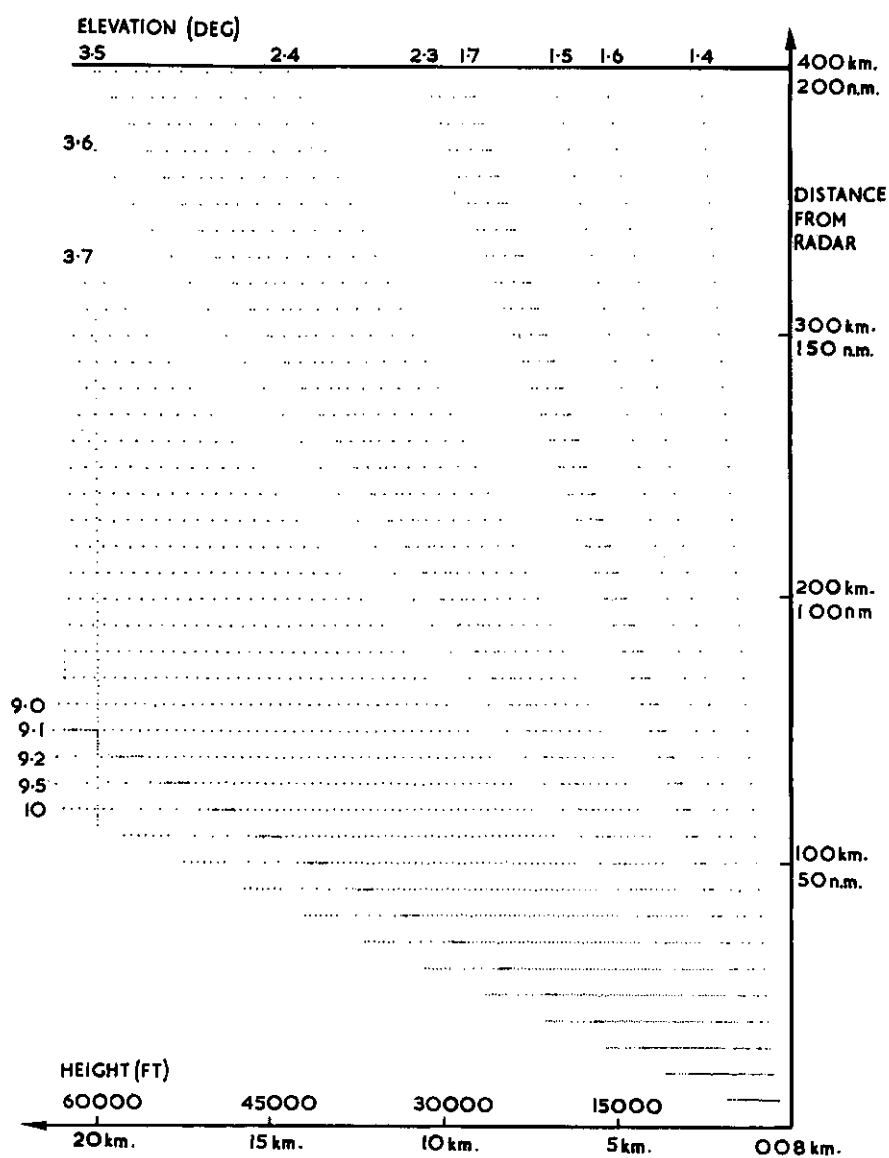


FIG. 2 Example of a ray-tracing analysis, sinusoidal layer wavelength 5 km mean height 400 m, amplitude 150 m and thickness 40 m

long afterglow. A calibrated reference signal was used as a means of assessing the magnitude of the received signal. Synchronizing the c.r.o. with the radar p.r.f., our c.r.o. display gives information of both distance to transponder and level of the signal received from this. The radar was operated in an anormal fashion, giving one reading of absolute received power per antenna revolution. In practice, with the particular aircraft-speed used, this amounts to approximately one power-reading for each nautical-mile range between radar and target.

Several tests were performed using the current method together with the conventional methods making use of the P.P.I. display by counting the number of antenna scans per 10 nautical miles and observing the number of detectable echoes (blips) received from these scans. It was observed that this "blip/scan" method was liable to give results that varied considerably with range, whereas the transponder method indicated a perfectly normal atmosphere. It appears to be very clear that many of the "anomalies" observed using the "blip/scan" method are determined solely by variations in the target aspect.

Figure 1 shows some typical results. (Note that the spacing between curves is arbitrary.) The 17/3-64 curve corresponds to a perfectly normal atmosphere; the power decreases according to the inverse-square law. The 23/4-64 curve represents the type of results most frequently encountered. The observed points follow a comparatively smooth curve up to a certain range; beyond this range the received signal power fluctuates considerably with distance. We see that in this particular case, the critical range is some 120 nautical miles when the height of the radio source is 30 000 feet.

The following explanation for this can be offered: As the distance to the radio source increases, the elevation angle of the ray relative to the earth tangent plane decreases, since the altitude of the source is kept constant. Now, the smaller the ray elevation angle is, the smaller refractive index gradients and the thinner layers does it take to establish a radio duct. It is conceivable that in the troposphere there are always weak small-scale changes in refractive index. Our current observations support the assumption of there existing thin and weak rippled layers in the troposphere.

Then consider the 21/4-64 curve of Fig. 1. This corresponds to a case where the troposphere is classified as anomalous as defined in the first section of the current note. We observe that there are "holes" in the coverage volume at 30 and 90 n.m. range and 30 000 feet elevation. Furthermore, we observe that on the far side of the "hole" there is an increase in received power. This is a feature exhibited in most of the ducting observation. Basing our discussion on the assumption that there exists an undulating sinusoidal layer in the troposphere, the current experimental results can readily be explained. In practice a layer with varying slopes can be generated by an internal gravity wave or it may be part of a lee wave or a "wave" resulting from a land-sea breeze.

Figure 2 shows the results of a ray-tracing analysis performed on a digital computer basing the computations on Snell's law. We have assumed that the undulating layer is sinusoidal, wavelength is 5 km, mean height is 400 m, amplitude is 150 m, and thickness is 40 m. A radar is located at the origin of the height-versus-range coordinate system of Fig. 2 and discrete rays with

initial elevation angles varying from 1.4 deg. to 10 deg. are plotted using an automatic  $x$ - $y$  plotter. The point density is thus a measure of the signal intensity in space. Note that the inverse-square law is not superimposed on the computed rays. Note also that, since different vertical and horizontal scales are used, the "holes" associated with small elevation angles appear to be "wider" than those associated with large angles. The ray-tracing figure based on our assumed layer configuration shows that if flying at 30000 feet one would experience holes at the ranges 30 and 90 n.m. This compares favourably with the aircraft observations. We also observe, again in agreement with the experiments, that the field strength just beyond a hole shows an increase.

#### THE PREDICTION OF CHANGES IN THE RADAR-COVERAGE VOLUME

This problem can conveniently be separated in two parts. The first deals with the forecasting of anomalous conditions, the second is concerned with the prediction of the specific effects of these anomalous conditions on the radar-coverage diagram.

**Forecasting of Anomalous Conditions** – Some 150 ducting events have been compared with the synoptic weather situation for the purpose of finding a simple meteorological parameter on the basis of which ducting predictions can be made. It is well known that the following three atmospheric mechanisms are liable to give rise to ducting (1).

- (a) Horizontal movement (advection) of warm dry air over a cool sea.
- (b) Radiative cooling over land resulting from nocturnal clear sky.
- (c) Subsidence occurring under anticyclonic conditions.

In seeking a suitable ducting parameter the following basic philosophy was adopted: In the lower troposphere above comparatively water-rich soil or above the sea, the humidity is generally considerable. If then a particular atmospheric mechanism (subsidence, advection) should give rise to dry air at a given altitude, say the 850 mb level, it is likely that this dry layer would constitute a humidity inversion and thus result in marked changes in the refractive index. The appropriate radar stations are supplied with two ducting probability maps every morning, one corresponding to the present-day situation, the second constituting the prognosis for the following day. Observed ducts compare very favourably with those forecast.

**Forecasting of Changes in Radar Coverage** – This forecasting problem requires very careful consideration. It is clear that the layers responsible for the coverage volume distortions are not flat. Hence one must predict the shape of the layer boundary relative to the radar station as well as the height of the layer, the thickness and the refractive index distribution through the layer (2, 3). The position of the radar "holes" depends critically on the shape of the layer and of its "phase" relative to the radar. Thus, if the rippled layer is a result of an internal gravity wave, the mentioned phase will vary and so will the position of the radar "holes". If, on the other hand, lee waves or a land-sea breeze is the origin, our rippled layer may be fixed in relation to a coastline or a mountain. The present state of the art does not offer a satisfactory solution to the detailed prediction of the changes in radar coverage induced by tropospheric disturbances. It is hoped, however, that



repeated aircraft experiments under ducting conditions will shine new light on the problem.

#### CONCLUSIONS

Anomalous tropospheric conditions may give rise to severe distortions of the radar-coverage diagram. The frequency of occurrence of such anomalous propagation conditions for a specific area have been investigated, and on the basis of this investigation radiometeorological methods for the prediction of anomalous conditions have been obtained. One knows the general effect on the radar-coverage diagram of an anomalous troposphere; at the present, however, it does not appear to be possible to offer a general solution to the problem of linking the shape of the distorted radar diagram with the synoptic weather condition. This problem is being investigated.

#### REFERENCES

1. APPLETON, SIR EDWARD, "The Influence of Tropospheric Conditions on Ultra-Short-Wave Propagation". Rep. Conf. held April 8, 1946 at The Royal Institution, London. Phys. Soc., London.
2. GJESSING, DAG T., and IRGENS, F., "On the Scattering of Electromagnetic Waves by a Moving Tropospheric Layer Having Sinusoidal Boundaries". IEEE, PTGAP, AP 12, No. 1, 1964.
3. GJESSING, DAG T., and IRGENS, F., "Scattering of Radio Waves by a Moving Tropospheric Rippled Layer: A Simpler Model-Experiment". IEEE, PTAGP, AP 12, No. 6, 1964.

#### ACKNOWLEDGEMENTS

ROYAL NORWEGIAN AIR FORCE for providing the aircraft and radar facilities and for their exceptionally helpful attitude whenever assistance was requested.

MR A. MOENE, Norwegian Meteorological Institute, for services rendered in connection with the ducting predictions.



## CHAPTER 5-3

ÉTUDE EXPÉRIMENTALE DE LA BAISSÉ DE GAIN  
D'ANTENNE DANS LES LIAISONS TRANSHORIZON

L. BOITHIAS and J. BATTESTI

CNET Issy-Les-Molineaux, Seine, France

The full text of this paper has been published in *Annales des Télécommunications*, Tome 19, No 9-10 Septembre-Octobre 1964.

La turbulence troposphérique déforme les surfaces d'onde de façon aléatoire, et par suite le gain d'une antenne défini à partir d'ondes planes n'est plus obtenu dans le cas de surfaces d'ondes déformées. Cette baisse de gain a déjà été estimée à partir de diverses théories, chacune partant d'un certain modèle de turbulence de l'atmosphère. Les résultats obtenus ont été extrêmement variés, contradictoires entre eux, et non vérifiés par l'expérience.

Une étude purement expérimentale de ce phénomène a été entreprise en France. Cette étude était spécialement destinée à l'établissement de projets de faisceaux hertziens transhorizon, mais les résultats obtenus sont d'un usage plus général. On a constaté qu'en première approximation, la baisse de gain était liée au gain de l'antenne, et qu'elle dépendait peu de la longueur du trajet, dans le cas d'une liaison terrestre. Ces conclusions doivent évidemment être un peu modifiées dans le cas d'une liaison terre-espace.

Tropospheric turbulence deforms the phase front of a wave in a random way. The gain of an antenna, which is defined in relation to plane waves, is not fully achieved with a deformed wave front. This loss of gain has been estimated by use of various theories, each based upon a special model for atmospheric turbulence. The results of these theories have been varied, contradictory between themselves and not verified by experiment.

A purely experimental study of this problem has been undertaken in France. This study was especially directed towards the establishment of microwave links, but the results obtained are of general application. It appears that to a first approximation the loss in gain is related to the gain of the antenna and that it depends but little upon the length of the path for terrestrial links. These conclusions should evidently be a little modified in the case of an earth-space path.



## CHAPTER 5-4

THE INFLUENCE OF WAVE-FRONT COHERENCE ON  
THE RADIATION PARAMETERS OF LARGE-SIZE  
ANTENNAS

C. COLAVITO

Istituto di Elettronica, Università di Roma

## SUMMARY

This paper deals with the calculation of the radiative parameters of antennas, when the received field is fluctuating in time and space. The theory of partially-coherent electromagnetic waves is employed to express these fluctuations by means of only one quantity, that is the complex "degree of coherence" which must be measured in the various points of the wave front. Using some suitable analytical expressions for the complex "degree of coherence", formulas for the gain factor and for other radiative parameters of antennas are obtained. The application of the experimental and calculation procedure to large-size antennas employed in satellite communication systems is illustrated.

## INTRODUCTION

The classical electromagnetic theory has been developed for coherent and monochromatic waves. Therefore, applying this theory to diffraction and antenna problems, the results obtained are valid only in the ideal case of coherent waves. However, when real propagation circuits are considered, the received electromagnetic field is fluctuating in time and space domains and to express its stochastic properties the theory of partially coherent electromagnetic waves may conveniently be used (1), (2).

Following the lines of the latter theory, it is possible to give the conventional definitions of the radiative parameters of antennas as the gain, the resolution and the diffraction pattern in a more general form, which takes into account also the statistics of the incident field. The relations obtained in that way are particularly useful when the characteristics of large-size antennas are analyzed for a statistical environment. Indeed, the larger the antenna the more difficult it is to separate its radiative parameters from the statistical behaviour of the wave front interacting with the antenna and therefore from the properties of the propagation medium.

In this paper the calculation of the gain of large-size antennas is developed employing the basic quantity of the coherence theory, that is, the complex "degree of coherence". For this reason, firstly the method of measuring of the complex "degree of coherence" is outlined, keeping in mind the applications to the antennas used in the earth stations of the satellite communication systems. It is worth noticing that the present study is not concerned with the

nature or the causes of the fluctuations of the electromagnetic field, but only with the statistical deformations of the received wave front. On the other hand, an analysis of the coherence accomplished in time and space domains can be a useful tool in the study of ionospheric and tropospheric irregularities, since it can supply much more information than the recordings of amplitude and phase fluctuations which are generally used in radio-propagation experiments.

#### THE MEASUREMENT OF THE "DEGREE OF COHERENCE"

The complex "degree of coherence" is a very useful quantity when the partial-coherence theory is applied to radio propagation problems; indeed, it has been shown in many previous works that it meets the following requirements:

- (a) it is representative of the statistical properties of the electromagnetic fields in radio propagation (1), (2);
- (b) it easily appears in the calculations related to diffraction problems (3), (4), (5);
- (c) it is directly measurable, in the microwave frequency spectrum (6).

The complex "degree of coherence" between two points  $P_1$  and  $P_2$  in space, is indicated by  $\gamma_{12}(\tau)$  where  $\tau$  is the time delay between the two signals. The complex degree of coherence is obtained by normalizing the mutual coherence function  $\Gamma_{12}(\tau)$  with respect to the mean power flows at the points  $P_1$  and  $P_2$  (see Appendix 1).

The measurement of the complex degree of coherence in the microwave frequency spectrum can be carried out by an interferometric device like the one outlined in Fig. 1. The antennas 1 and 2 have been previously located at the points between which the degree of coherence is required and their dimensions have been kept very small in order to minimize the effects of the statistical irregularities of the wave front. The two incoming powers  $I_1$  and  $I_2$  have been brought to interfere in the magic Tee 6; two equal interference power patterns, with a relative phase shift  $\pi$  have been obtained at the arms  $a$  and  $a'$  of the magic Tee, by the phase shifter 5.

The analytical expression of the interference power patterns is the same given by the formulae 1-8A of Appendix 1, except for a different value of the factors  $K_1$  and  $K_2$ . If the attenuators 3 and 4 are adjusted to equalize the two incoming powers (i.e.  $I_1 = I_2$ ), the interference power patterns become:

$$I = 2 I_1 \left\{ 1 + |\gamma_{12}(0)| \cos \left[ \phi_{12}(0) - \alpha \pm \frac{\pi}{2} \right] \right\} \quad (1)$$

where  $\phi_{12}(0)$  is the phase of  $\gamma_{12}(0)$  and  $\alpha$  is the phase delay introduced by the phase shifter 5. The maximum and minimum values of the interference power pattern are given by:

$$I_{\max, \min} = 2 I_1 [1 \pm |\gamma_{12}(0)|] \quad (2)$$

and can be detected at the same time at the arms  $a$  and  $a'$  of the magic Tee.

From Eq. 2 the modulus of the complex degree of coherence is obtained:

$$|\gamma_{12}(0)| = \frac{\frac{I_{\max}}{I_{\min}} - 1}{\frac{I_{\max}}{I_{\min}} + 1} \quad (3)$$

Also, the argument  $\phi_{12}(0)$  is measured by the interferometer shown in Fig. 1, reading on the phase shifter 5 the angular position corresponding to a minimum with respect to a reference angular position.

In practice, some difficulties arise in carrying out the steps of the measurement procedure and in particular in finding the minimum position and to determine exactly the ratio  $I_{\max}/I_{\min}$ . Indeed, all the quantities  $I$  are theoretically derived from averaging operations performed on infinite time intervals, but the time intervals during which the fields received in radio-propagation circuits can be considered stationary are rather short. Therefore, the measurement operations must be performed very quickly, and to obtain an acceptable precision some refined techniques discussed in a previously mentioned paper (6) are needed.

As far as the determination of the degree of coherence in the earth stations of a satellite communication system is concerned, the power received in this kind of link is so low that it does not allow in the interferometer the use of the small interferometric antennas which are necessary for an accurate analysis of the received wave front. To overcome this difficulty, pulse transmissions from spacecraft and continuous wave transmissions from aircraft or high mountains can be used. It goes without saying that in the last three cases only the lower zones of the troposphere influence the propagation.

#### THE COHERENCE CURVES

By varying the position of the interferometric antennas along different lines of the space, diagrams of the modulus of degree of coherence, or "coherence curves", can be obtained. The main problem encountered in applying the coherence theory to diffraction studies is the selection of a suitable analytical law for the "coherence curves" on the basis of the results of experimental investigations.

As a matter of fact, the experimental research work so far developed has been mainly concerned with line-of-sight radio links: the results obtained in this case show that the shape of the "coherence curves" is dependent on the characteristics of the link under examination and on the statistical properties of the fading through the course of the measurement time intervals. It has also been found that, when the received field shows rapid fluctuations or "scintillations" due to tropospheric turbulence, the "coherence curve" follows a nearly Gaussian law, over which an oscillating function is often superimposed. Since experimental results regarding the measurement of the degree of coherence on the wave front received in satellite communication links are so far not available, in the following a simple Gaussian law will be assumed for the coherence curve and the modulus of the degree of coherence will be given by the formula:

$$|\gamma(P_1, P_2, 0)| = e^{-\frac{d^2}{L^2}} \quad (4)$$

where  $d$  is the distance between the points  $P_1$  and  $P_2$  and  $L$  is the "distance

of coherence". For comparison purposes, the calculus of the gain reduction will be developed also for other kinds of coherence curves. Like the shape of the coherence curve, the value of the parameter  $L$  is also dependent upon the characteristics of the link and the type of fading; in experimental investigations carried out on line-of-sight radio links operating at a frequency of about 7000 Mc/s and with path lengths of 50 to 60 km, values of  $L$  ranging from 5 to 10 m have been found. Larger values of  $L$  are expected in communication satellite systems at angles of elevation greater than few degrees.

However, for an accurate computation of the antenna gain reduction satellite communication systems, direct measurements of the coherence curve in operational conditions are suggested as a function of the satellite elevation angle and of the distance between satellite and earth station.

#### THE ANTENNA GAIN FACTOR

To obtain the radiation parameters of an antenna in terms of the mutual coherence function on the antenna aperture, an expression for the propagation law of the mutual coherence is needed. Starting from Maxwell's equations, it has been proved by Wolf (7) that in free space the mutual coherence function obeys two wave equations:

$$\nabla_1^2 \Gamma_{12}(\tau) = \frac{1}{c^2} \frac{\delta^2 \Gamma_{12}(\tau)}{\delta \tau^2} \quad (5a)$$

$$\nabla_2^2 \Gamma_{12}(\tau) = \frac{1}{c^2} \frac{\delta^2 \Gamma_{12}(\tau)}{\delta \tau^2} \quad (5b)$$

and a rigorous formulation of the propagation law of the mutual coherence has been obtained by the same author. This law expresses the mutual coherence function for any two points in the space  $Q_1$  and  $Q_2$ , in terms of the value of the same function on a closed surface containing  $Q_1$  and  $Q_2$ . If  $Q_2 \rightarrow Q_1$  (see Appendix 1), one has the mean power intensity  $I(Q)$  at an arbitrary point in the space  $Q$ .

Indeed, a simpler radiation law had been previously formulated by Zernike (8) for quasi-monochromatic radiations and in the case when the time delay  $\tau$  is small compared with the coherence time of the radiation. The first of the two hypotheses means that  $\bar{\lambda} \gg \Delta \lambda$ , where  $\bar{\lambda}$  is the carrier wavelength and  $\Delta \lambda$  represents the bandwidth of the radiation; the second hypothesis brings as a consequence the dependence of the coherence function on  $\tau$  only through a harmonic term, i.e.:

$$\Gamma(P_1, P_2, \tau) \simeq \Gamma'(P_1, P_2, 0) e^{j2\pi f\tau}$$

Applying the Fraunhofer approximation in the Zernike formula, the mean power intensity at the point  $Q$  placed in the far zone of an extended primary source  $A$ , is obtained:

$$I(Q) = \frac{\cos^2 \theta}{\lambda^2 D^2} \int_A \int_A I_1^\dagger I_2^\dagger \gamma(P_1, P_2, 0) e^{-j\vec{k} \cdot \vec{r}(P_1 - P_2)} dA_1 dA_2 \quad (6)$$

where  $I_1$  and  $I_2$  are the mean power intensities at the points  $P_1$  and  $P_2$ ;  $\gamma(P_1, P_2, 0)$  is the complex degree of coherence on the diffraction aperture;  $\vec{k}$  is the mean wave number ( $\vec{k} = 2\pi/\bar{\lambda}$ ),  $\vec{r}$  is a unitary vector,  $dA_1, dA_2$  are



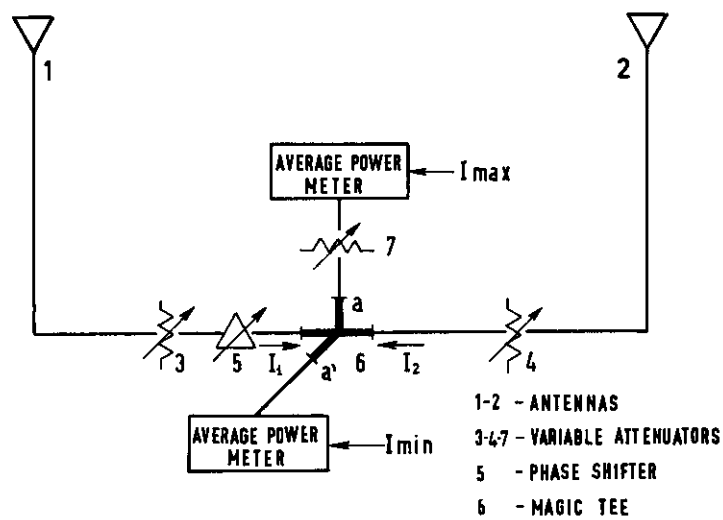


FIG. 1 The interferometric device for the measurement of the complex degree of coherence

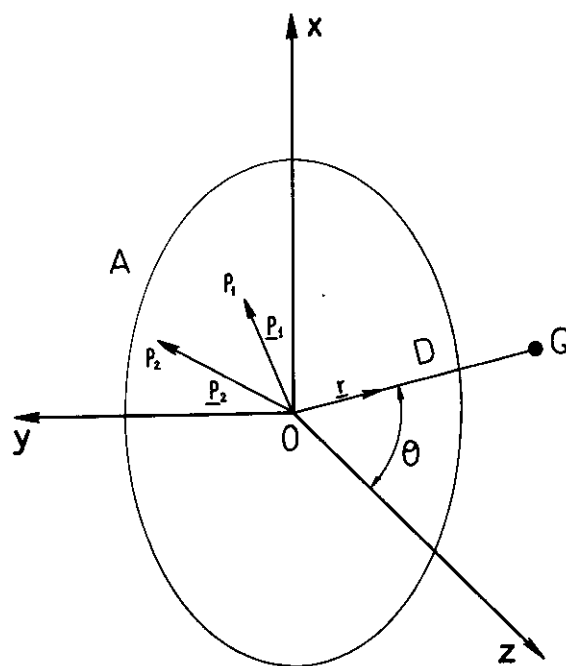


FIG. 2 The geometry of diffraction

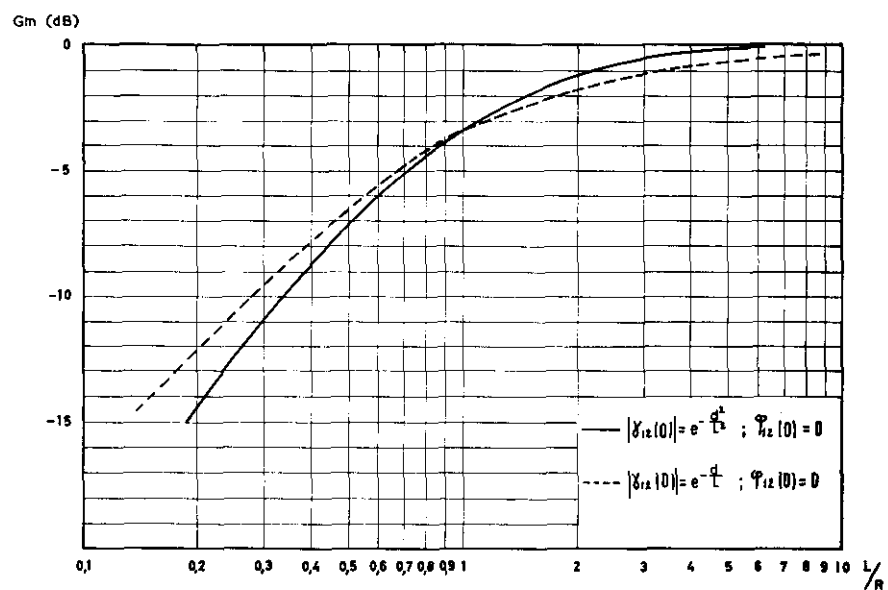


FIG. 3 The gain reduction vs  $L/R$

area elements of the aperture  $A$  and the significance of the other notations is explained in Fig. 2.

Equation 6 closely resembles the diffraction integrals in the Huygens-Frenel theory: in fact, from that equation the power-radiation pattern and the other radiative parameters of an antenna having an aperture  $A$  are easily secured. In Appendix 2 the antenna gain is derived under the following hypotheses: (a) the illumination of the aperture is uniform; (b) the phase  $\phi_{12}(O)$  of the complex degree of coherence between two arbitrary points of the aperture is equal to zero. The expression of the gain is:

$$G_m = \frac{4\pi}{\lambda^2} \frac{\int_A \int_A |\gamma(P_1, P_2, O)| dA_1 dA_2}{A} \quad (7)$$

where  $A$  is the area of the antenna aperture and the gain has been indicated by  $G_m$  to point out it is time average quantity, like all the radiative parameters which one can obtain following the previous procedure. The gain factor  $G_m$  has been computed for a circular aperture by means of the formulae 2-16A of Appendix 2, assuming different laws for the modulus of the degree of coherence. The results obtained are shown in Fig. 3, where  $10 \log G_m$  is given as a function of  $L/R$ , that is, the ratio of the distance of coherence and the radius of the antenna.

The calculation of the gain factor for other apertures having different geometrical shape and/or non-uniform illumination, etc. can be carried out in a similar way. It is worth noticing that all the properties of the complex degree of coherence are transferred to the radiative parameters which, therefore, are dependent upon the frequency of radiation and the characteristics of the propagation circuit where the antenna is installed (as the distance between the antennas, the influence of obstacles, etc.). These parameters are also changing in time following the variations of the statistical moments of the fluctuations; indeed, a certain statistical distribution of the wave-front irregularities takes place on the antenna aperture while a certain type of fading is present, and then it will change successively to another distribution according to the propagation conditions. To every distribution of the wave-front irregularities a well-defined law corresponds for the behaviour of the complex degree of coherence; from the knowledge of that behaviour, one can obtain by means of Eqs. 6 and 7 the radiation diagram and the gain for the diverse types of fading.

#### CONCLUSIONS

The problem of determining the radiative characteristics of the antennas when the received wave front is fluctuating in the time and space domains has been attacked applying the principles of the partial-coherence theory. A complete computation has been carried out for the gain factor of the circular parabolic antenna, but a formula suitable for the calculus of other radiative parameters of many kinds of antennas is also available. The results of the computation are dependent upon all the assumed hypotheses and, in particular, upon the chosen law for the modulus of the degree of coherence. A numerical computer programme is still under development to evaluate the influence of the previous law on the gain reduction.

All the research work so far carried out seems to lead to the conclusion that the quantities of the mutual coherence theory are a useful tool for a rigorous formulation of many diffraction problems when the incident wave front is fluctuating in space and time. Besides the radiation characteristics of antennas, the scattering cross-section of large reflectors and the properties of radio links which take advantage of particular kinds of propagation can be conveniently determined when the complex degree of coherence is employed. However, the experimental results so far obtained are not sufficient to supply satisfactory knowledge of the behaviour of the degree of coherence in the various propagation circuits and for the different types of fading. Further investigations and measurements are suggested to control the assumed hypotheses and to establish more exact values for the distance of coherence in the satellite communication links.

## REFERENCES

1. BERAN, M. J., and PARRENT, G. B., "Theory of Partial Coherence". Prentice Hall, 1964.
2. ZUCKER, F. J., "Introduction to Partially Coherent Electromagnetic Waves". Electromagnetic Theory and Antennas (ed. E. C. Jordan), Pergamon Press, 1963.
3. SHORE, R. A., "Partially coherent diffraction by a circular aperture". Electromagnetic Theory and Antennas (ed. E. C. Jordan), Pergamon Press, 1963.
4. SHORE, R. A., "Rigorous diffraction theory with partially coherent illumination". Paper presented at the URSI Symposium on Electromagnetic Theory, Delft, 1965.
5. COLAVITO, C., D'AURIA, G., "Statistical properties of radio-links using passive repeaters". Internal Report, Fondazione Ugo Bordoni, Roma, 1965 (in Italian).
6. COLAVITO, C., D'AURIA, G., "Coherence measurement in radio propagation" Paper presented at the URSI Symposium on Electromagnetic Theory, Delft, 1965.
7. BORN, M., WOLF, E., "Principles of Optics". Pergamon Press, 1965.
8. ZERNIKE, F., "Concept of degree of coherence and its application to optical problems". Physica, No. 5, 791-1938.

## APPENDIX I

**The Mutual Coherence Function** – If  $v(P, t)$  is a real function of point in space  $P$  and of time  $t$ , as a component of electric or magnetic field, the complex “analytic signal”  $V(P, t)$  comes from the relations:

$$\operatorname{Re} [V(P, t)] = v(P, t) \quad (1A)$$

$$\operatorname{Im} [V(P, t)] = \frac{1}{\pi} \int \frac{v(P, t')}{t - t'} dt' \quad (2A)$$

The second member of Eq. 2A is a Hilbert transform; also  $\operatorname{Re} [V(P, t)]$  can be obtained as a Hilbert transformation in  $\operatorname{Im} [V(P, t)]$ .

The “mutual coherence function” between the points  $P_1$  and  $P_2$  in space is defined as the second-order correlation of the complex “analytical signal” and is given by:

$$\Gamma(P_1, P_2, \tau) = \langle V(P_1, t + \tau) \cdot V^*(P_2, t) \rangle \quad (3A)$$

where the sharp brackets indicate the time average:

$$\langle \dots \rangle = \lim_{T \rightarrow \infty} \frac{1}{T} \int_{-T/2}^{+T/2} \dots dt \quad (4A)$$

$\Gamma(P_1, P_2, \tau)$  is often shown by the shortened notation  $\Gamma_{12}(\tau)$ .

If  $\tau$  goes to zero and  $P_2 \rightarrow P_1$ , or  $P_1 \rightarrow P_2$ , Eq. 3 becomes respectively:

$$\Gamma_{11}(0) = \langle V(P_1, t) \cdot V^*(P_1, t) \rangle = I_1 \quad (5Aa)$$

$$\Gamma_{22}(0) = \langle V(P_2, t) \cdot V^*(P_2, t) \rangle = I_2 \quad (5Ab)$$

When  $V(P, t)$  is properly normalized,  $I_1$  and  $I_2$  are the mean power flows through unity surface or, for analogy with optics, the “mean intensities” at the points  $P_1$  and  $P_2$ .

The complex degree of coherence is obtained normalizing  $\Gamma_{12}(\tau)$  with respect to the mean intensities  $I_1$  and  $I_2$  and is given by:

$$\gamma_{12}(\tau) = \frac{\Gamma_{12}(\tau)}{\sqrt{I_1 \cdot I_2}} \quad (6A)$$

where:

$$0 < |\gamma_{12}(\tau)| < 1 \quad (7A)$$

To explain the meaning of the degree of coherence, the case of the interference between two partially coherent beams is here considered.

If in  $P_1$  and  $P_2$  are placed two radiation sources, Fig. 1A having intensities  $I_1$  and  $I_2$ , it can be shown that the intensity at point  $Q$  is:

$$I(Q) = |k_1|^2 I_1 + |k_2|^2 I_2 + 2 |k_1 k_2| \sqrt{I_1 I_2} \gamma_{12}(\tau) \cos[\phi_{12}(\tau) - \alpha] \quad (8A)$$

where:  $\phi_{12}(\tau)$  is the argument of  $\gamma_{12}(\tau)$ ; the parameter  $\tau$  and the phase difference  $\alpha$  have the values:

$$\tau = \frac{r_2 - r_1}{c} \quad \alpha = \frac{2\pi}{\lambda} (r_2 - r_1) \quad (9A)$$

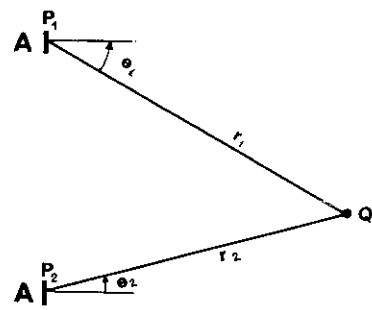


FIG. 1A Two beams interference

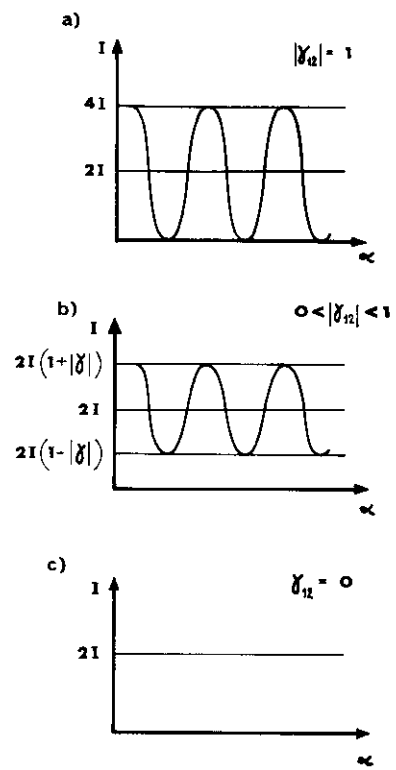


FIG. 2A The interference patterns for different degrees of coherence

with  $\bar{\lambda}$  equal to the mean wavelength of the radiation; if only the radiative components of the field are considered, the factors  $K_1, K_2$  have the values:

$$k_1 = \frac{A \cos \theta_1}{\bar{\lambda} r_1} \quad k_2 = \frac{A \cos \theta_2}{\bar{\lambda} r_2} \quad (10A)$$

with  $A$  equal to the area of a radiation source. The meaning of other notations used in Eq. 9A and Eq. 10A is given in Fig. 1A. Varying the position of point  $Q$ , i.e. the difference  $r_2 - r_1$ , an interference power pattern analytically expressed by the Eq. 8 is obtained.

In Fig. 2A the intensity distribution in the interference pattern is outlined for the three cases when the radiations at points  $P_1$  and  $P_2$  are: (a) coherent ( $|\gamma_{12}| = 1$ ), (b) partially coherent ( $0 < |\gamma_{12}| < 1$ ), (c) incoherent ( $\gamma_{12} = 0$ ). It is supposed  $I_1 = I_2$  and  $Q$  so far from  $P_1$  and  $P_2$  that:  $r_1 \simeq r_2$  and  $\theta_1 \simeq \theta_2$ . The above considerations suggest that the complex degree of coherence between two points  $P_1$  and  $P_2$  can be measured by means of an interferometric device. In the radio-frequency spectrum the two sources are substituted by the antennas of the radio interferometer.

## APPENDIX 2

**Some Calculations Regarding the Antenna Gain Factor** - The expression of the time-average gain factor is derived from Eq. 6 stating some suitable hypotheses. For  $\theta = 0$ , i.e. on the axis perpendicular to the antenna aperture, Eq. 6 becomes:

### THE ANTENNA GAIN FACTOR

$$I(Q) = \frac{I}{\lambda^2 D^2} \int_A \int_A \Gamma(P_1, P_2, 0) dA_1 dA_2 \quad (11A)$$

Bearing in mind Eq. 6A in the hypothesis of uniform illumination of the antenna aperture ( $I_1 = I_2 = I_P = \cos t$ ) and of  $\phi_{12}(0) = 0$  everywhere, one obtains from Eq. 11A the following:

$$I(Q) = \frac{I_P}{\lambda^2 D^2} \int_A \int_A |\gamma(P_1, P_2, 0)| dA_1 dA_2 \quad (12A)$$

The conventional definition of the gain of the radiator is:

$$G_m = \frac{4 \pi D^2}{A} \frac{I(Q)}{I_P} \quad (13A)$$

where  $A$  is the area of the antenna aperture and the subscript  $m$  indicates that the gain is a time-average quantity.

Substituting Eq. 12A in 13A one has:

$$G_m = \frac{4 \pi}{\lambda^2} \frac{\int_A \int_A |\gamma(P_1, P_2, 0)| dA_1 dA_2}{A} \quad (14A)$$

From Eq. 14A the gain factor is easily obtained:

$$gm = \frac{\int_A \int_A |\gamma(P_1, P_2, 0)| dA_1 dA_2}{A^2} \quad (15A)$$

The gain factor has been calculated for a circular aperture, in the hypothesis

that the modulus of the degree of coherence follows a Gaussian or an exponential law and therefore is only a function of the distance between the points  $P_1$  and  $P_2$ . In the first case, for symmetry of the circular aperture, Eq. 15A can be reduced to:

$$gm = \frac{4}{\pi R^4} \int_0^{+R} x_0 dx_0 \int_{-R}^{+R} e^{-\left(\frac{x-x_0}{L}\right)^2} dx \int_0^{\sqrt{R^2-x^2}} e^{-\left(\frac{y}{L}\right)^2} dy \quad (16A)$$

where:  $R$  is the radius of the aperture,  $x$  and  $y$  are Cartesian coordinates on the aperture. The integrals of Eq. 16A have been numerically evaluated varying the ratio  $L/R$ .



## CHAPTER 5-5

LASER WAVE PROPAGATION THROUGH THE  
ATMOSPHERE

H. HODARA

National Engineering Science Company, Pasadena, Calif., U.S.A.

## INTRODUCTION

Communication with coherent light through the atmosphere brings out new system limitations besides the ones imposed by attenuation and scattering normally associated with incoherent waves. This is so because the laser's high directionality and coherence on which are based the high channel capability are easily destroyed or at least degraded by the presence of random thermal turbulences. The major effect of the turbulences is to deflect the beam randomly and reduce its coherence. The deflection may be severe enough to make the beam miss entirely or partially the receiving aperture; the coherence degradation leads to beam broadening. In both instances, the resultant damage is a reduction of the useful signal intensity at the receiver coupled with undesirable amplitude and frequency modulation and polarization fluctuations. In addition, "quivering" or spot dancing caused by random beam deflection and blurring of the received image due to spatial coherence degradation impose serious limitations in direct optical display transmission. In this paper, we discuss the nature of turbulences, their effects on communication systems, and what meaningful measurements can or have been made.

## NATURE OF THERMAL TURBULENCES

Thermal turbulences affect primarily the refractive index of the medium. The refractive index change  $\Delta n$  and temperature change  $\Delta T$  are related by the ideal gas law in differential form:

$$\frac{\Delta V}{V} = - \frac{\Delta T}{T} \quad (1)$$

in which  $V$  is the gas volume and  $\Delta V$  the associated change in volume. The refractive index  $n$  for any gas is approximately (1):

$$n - 1 \simeq \frac{N}{V} \frac{e^2/2m}{\nu_0^2 - \nu^2} \quad (2)$$

$N$  is the number of atomic oscillators in the volume  $V$ ,  $e$  and  $m$  the electronic charge mass;  $\nu_0$  the transition frequency and  $\nu$  the signal frequency. The differential form of Eq. 2:

$$V \Delta n + (n - 1) \Delta V = 0 \quad (3)$$

combined with Eq. 1 gives the desired relation 2:

$$\Delta n = - \frac{n-1}{T} \Delta T \quad (4)$$

Taking the refractive air index as  $n = 1.0003$  and  $\Delta = 300^\circ\text{K}$ , we obtain the following useful order of magnitude change in  $n$  for a temperature increment of  $1^\circ\text{K}$ :

$$\Delta T \sim 1^\circ\text{K}, \quad \Delta n \sim 10^{-6} \quad (5)$$

We shall use this numerical result later on. The refractive index varies randomly as a function of space,  $r = \{x, y, z\}$  and time  $t$ . The relative index change,  $\Delta n(x, y, z, t)$  is a stochastic variable dependent on position and time. Such variables are more conveniently dealt with in terms of correlation functions and correlation parameters, in particular, the correlation distance  $L_c$  or "outer scale size" of the turbulence and the correlation time  $T_c$ . Both parameters are defined in terms of the rate of decay of the spatial and time correlation functions of  $\Delta n$ :

$$C_{12}(\rho) = \langle \Delta n(r) \Delta n(r + \rho) \rangle = \langle \Delta n_1 \Delta n_2 \rangle \quad (6a)$$

$$\Gamma_{12}(\tau) = \overline{\Delta n(t) \Delta n(t + \tau)} \quad (6b)$$

The angular bracket indicates ensemble average; the upper bar refers to a time average.

The spatial correlation function shown in Fig. 1 is taken from Tatarski via Fried *et. al.* (3) The distance where the function changes from square law to  $2/3$  power law decays is the inner scale turbulence  $l_c$ . The correlation distance  $L_c$  is the distance at which  $\langle \Delta n_1 \Delta n_2 \rangle$  falls to a predetermined value. The mean square refractive index variation  $C_{11}(0) = \langle \Delta n^2 \rangle \equiv \langle \Delta n(r) \Delta n(r) \rangle$ , decreases with altitude and is sketched in Fig. 2. The correlation distance  $L_c$ , on the other hand, increases with altitude as shown in Fig. 3. The respective dependence of  $\langle \Delta n^2 \rangle$  and  $L_c$  on  $h$  are:

$$\langle \Delta n^2 \rangle \sim 10^{-12} e^{-\frac{h}{1600}} \quad (7a) \quad (3)$$

$$L_c = \frac{.4h}{1 + 10^{-2}h} \quad (7b) \quad (4)$$

As we shall see later, the product  $L_c \langle \Delta n^2 \rangle$  determines in some cases the degree of beam scanning caused by turbulent atmosphere. This product is maximum between 300 m and 400 m; the corresponding correlation distance is about 30 m.

#### EFFECTS OF THERMAL TURBULENCES

We now proceed to obtain quantitative estimates of some of the most marked effects of thermal turbulence on the performance of laser communication systems. We follow Beckman's (5) approach in categorizing these effects, but derive the pertinent expressions somewhat more simply, although perhaps at the expense of some loss in accuracy. As mentioned earlier, thermal turbulences bring about random beam scanning and coherence reduction. The former effect is more likely to take place if turbulences occur

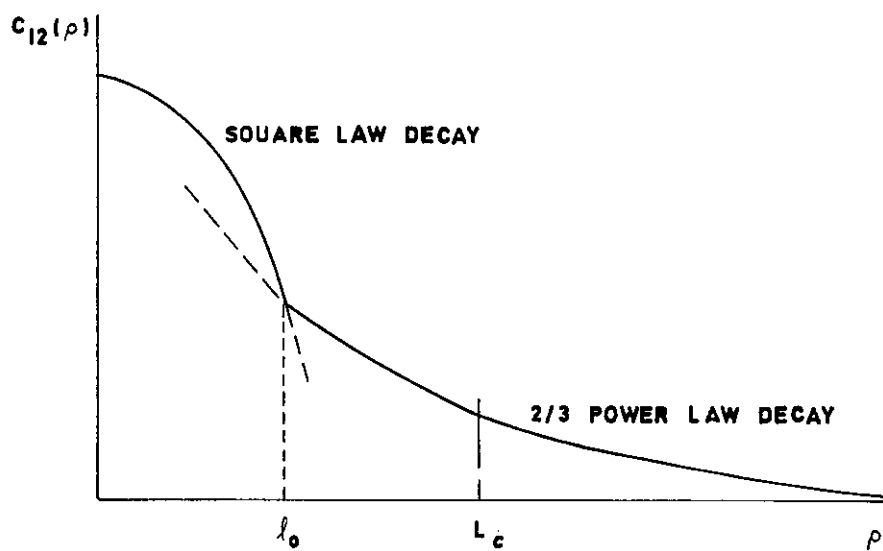


FIG. 1 Sketch of correlation function of variation in refractive index  $C_{12}(\rho) = \langle \Delta n(r) \Delta n(r + \rho) \rangle$

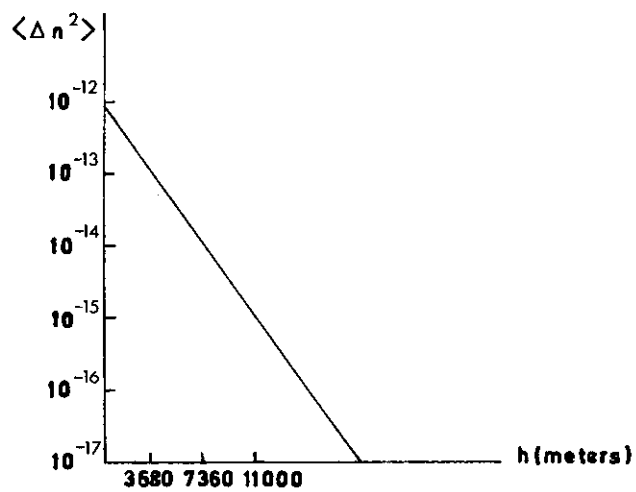


FIG. 2 Mean square variation  $\langle \Delta n^2 \rangle$  v. altitude  $h$

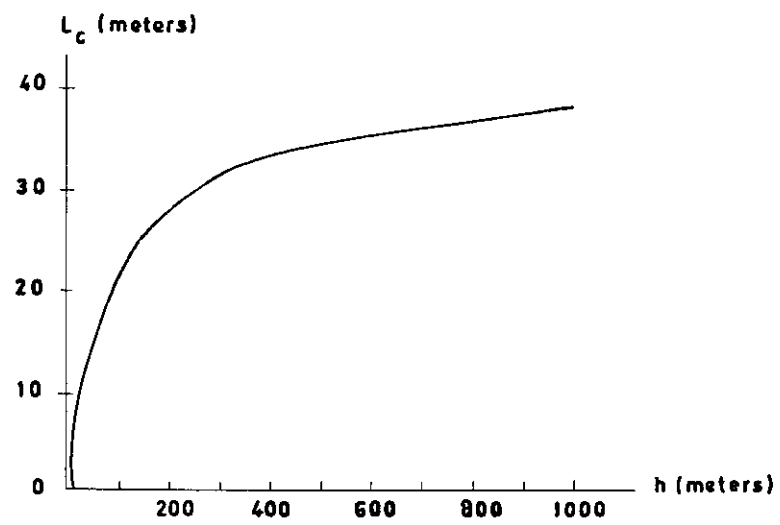


FIG. 3 Outer scale size  $L_c$ , v. altitude  $h$

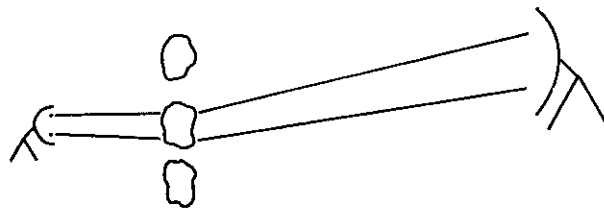


FIG. 4a Effect of turbulence near transmitter

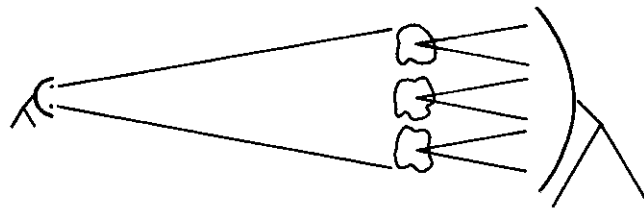


FIG. 4b Effect of turbulence near receiver

near the transmitter; the latter is more marked near the receiver as illustrated in Fig. 4. In addition to the known random amplitude and frequency modulation taking place, a development is given (possibly for the first time) of an estimate of the polarization fluctuation through the atmosphere. Let us proceed to obtain expressions for these effects.

**Random Beam Scanning (Quivering)** – Time variations of refractive index gradients bring about beam scanning. Expressions can be derived using geometric optics provided that the turbulence correlation distance  $L_c$  is much larger than the geometric mean distance between wavelength  $\lambda_0$  and path length  $L$  (6):

$$L_c \gg \sqrt{L\lambda_0} \quad (8)$$

This expression is obtained by requiring that the geometric shadow of the turbulence of width  $L_c$  be much larger than the width of its corresponding

diffraction pattern  $L\left(\frac{\lambda_0}{L_c}\right)$ .

Consider, then, a beam propagating along the  $z$ -direction and deviating little from it. In general, the medium is anisotropic; at any point we must take into account the correlation distances  $L_{cz}$  and  $L_{cT}$  respectively parallel and transverse to the direction of propagation. This simplification fits in two of the most common types of propagation: earth to earth and space to earth. Mark off as shown in Fig. 5a numerical distances  $L_{cz}$  and  $L_{cT}$  along two orthogonal axes; the line joining the end points of the two segments determines the loci of constant refractive index within a coherence interval. Within such interval the amount of beam deflection is given by Snell's law. Approximating the gradual index change by a discrete step from  $n + \Delta n$  to  $n$  (since  $n \sim 1$ ) and the corresponding refraction angles by  $\theta$  and  $\theta + \Delta\theta$ , we have for small increments:

$$\Delta\theta_c \sim \Delta n \tan \theta \quad (9)$$

$\Delta\theta_c$  is the beam deflection within one coherence interval. From the geometry of Fig. 5a we see that:

$$\tan \theta = \frac{L_{cz}}{L_{cT}} \quad (10)$$

yielding:

$$\Delta\theta_c \sim \Delta n \frac{L_{cz}}{L_{cT}} \quad (11)$$

The mean square temporal angular variation within a coherence interval is:

$$\overline{\Delta\theta_c^2} \sim \overline{\Delta n^2} \left( \frac{L_{cz}}{L_{cT}} \right)^2 \quad (12)$$

Over a path length  $L$ , the beam traverses  $\frac{L}{L_{cz}}$  coherence intervals as shown in Fig. 5b. Because the deflections are uncorrelated from one interval to the other, they add up on a mean square basis and the total mean square

deflection is:

$$\begin{aligned} \langle \Delta\theta^2 \rangle &= \frac{L}{L_{cz}} \overline{\Delta\theta_c^2} \\ &= \overline{\Delta n^2} \frac{L_{cz} L}{L_{cz}^2} \end{aligned} \quad (13a)$$

Thus, not only the refractive index gradient in the transverse direction is responsible for deflecting the beam, but also the gradient in the starting direction has an effect, since the beam eventually travels at non-zero angles with respect to both directions. For a given path length  $L$  and given a small deviation so that  $L_{cz}$  can be assumed constant throughout the path, the root mean square deflection  $\sqrt{\langle \Delta\theta^2 \rangle}$  depends on the product  $\sqrt{\overline{\Delta n^2} L_{cz}}$  ( $\overline{\Delta n^2} = \langle \Delta n^2 \rangle$ , the process is assumed ergodic.) As shown in the previous section, it is maximum between 300 and 400 m and yields  $L_{cz} \sim 30$  m. For earth-to-earth propagation at this altitude, with  $L_{cz} \sim 1$  m, a path length,  $L \sim 30$  km and  $\sqrt{\overline{\Delta n^2}} \sim 10^{-6}$ , the mean angular deflection  $\sqrt{\langle \Delta\theta^2 \rangle} \sim 1$  milliradian. The corresponding lineal deflection is 30 m. If, in order to increase its cross-section to say 10 cm, the beam is made to emerge from a recollimating telescope, it will miss entirely the receiver's collecting aperture.

If the two transverse directions are  $y$  and  $x$ , we have:

$$\langle \Delta\theta^2 \rangle = \langle \Delta\theta_y^2 \rangle + \langle \Delta\theta_x^2 \rangle = \overline{\Delta n^2} L_{cz} L \left[ \frac{1}{L_{cx}^2} + \frac{1}{L_{cy}^2} \right] \quad (13b)$$

For isotropic media:

$$L_{cz} = L_{cz} = L_{cx} = L_{cy} = L_c \text{ in (13b).}$$

$$\langle \Delta\theta^2 \rangle = \langle \Delta\theta_y^2 \rangle + \langle \Delta\theta_x^2 \rangle = 2 \overline{\Delta n^2} \frac{L}{L_c} \quad (14)$$

The preceding analysis points out that increasing the receiver's collecting aperture and the transmitted beam cross-section may minimize the deleterious effects brought about by random beam scanning. However, as illustrated in the numerical example, for a given angular deviation the beam may not be intercepted at all if the path is long enough. In practice, one increases the beam divergence in order to insure interception, but this is done at the expense of signal intensity reduction.

Random beam scanning also degrades the receiver performance in other ways for which collector-aperture increase is of no avail. This is the case in optical superheterodyning. Let the receiving aperture of diameter  $D$  be normal to the original direction of propagation  $z$ , but parallel to the  $y$ -direction and centered about  $y = 0$ . If the beam is deflected a mean angle  $\Delta\theta$  after traversing a distance  $L$  through a turbulent medium, the corresponding electric field at the aperture is proportional:

$$V \sim \cos(\omega_0 t - k_0 L \cos \Delta\theta - k_0 y \sin \Delta\theta) dy \Delta x \quad (15)$$

$\Delta x dy$  being an incremental area of the collecting aperture and  $k_0 = \frac{2\pi}{\lambda_0}$ . The received signal  $V$  is multiplied by a locally generated wave  $\cos \Omega t$ ; the

resultant beat:

$$V_{\text{beat}} \sim \int_{y=-D/2}^{y=D/2} \cos [(\omega_0 - \Omega)t - k_0 L \cos \Delta\theta - k_0 y \sin \Delta\theta] dy \quad (16)$$

is detected. Carrying out the integration over the aperture diameter and using  $\Delta\theta \ll 1$ :

$$V_{\text{beat}} \sim \cos \left[ (\omega_0 - \Omega)t - k_0 L + k_0 L \frac{\Delta\theta^2}{2} \right] \frac{\sin \left( \pi \frac{D}{\lambda_0} \Delta\theta \right)}{\pi \frac{D}{\lambda_0} \Delta\theta} \quad (17)$$

Two conclusions are immediate from the foregoing expression. In the case of amplitude demodulation, the signal intensity is reduced by the factor:

$$\left( \frac{\sin \pi \frac{D}{\lambda_0} \Delta\theta}{\pi \frac{D}{\lambda_0} \Delta\theta} \right)^2 \quad (18)$$

For practical purposes the signal is down into the noise if the angular deviation reaches the first zero of the function in Expression 18

$$\Delta\theta_0 \sim \frac{\lambda_0}{D} \quad (19)$$

For a collecting aperture as small as  $D \sim 10^{-2}$  m with  $\lambda_0 \sim 10^{-6}$  m, an angular deviation caused by thermal turbulence of not more than 0.10 milliradians is sufficient to obliterate the useful signal. There are, however, means to minimize this effect (7). In the case of frequency demodulation, it would seem from Expression 17 that a random frequency:

$$\Delta f_r = \frac{L}{2\lambda} \frac{d}{dt} (\Delta\theta)^2 \quad (20)$$

is introduced. The mean square frequency deviation is approximately:

$$\overline{\Delta f_r^2} = \frac{L^2}{4\lambda^2} \overline{\left[ \frac{d}{dt} (\Delta\theta)^2 \right]^2} \quad (21)$$

The foregoing expression is greatly simplified by means of the following relation which we assert to hold approximately true on intuitive grounds. Given a random function  $g(t)$ :

$$\overline{\left( \frac{d}{dt} g \right)^2} \leq \frac{\overline{g^2}}{T_c^2} \quad (22)$$

Hence,

$$\overline{\Delta f_r^2} \lesssim \frac{L^2}{4\lambda^2} \frac{\overline{\Delta\phi^4}}{T_c^2} \quad (23)$$

If  $\Delta\theta$  has Gaussian statistics, then its fourth moment  $\overline{\Delta\theta^4} = 0$  and  $\Delta f_r^2 = 0$ . No random frequency modulation is generated by random scanning, with this type of statistics.

**Random Phase Change** – Here we must distinguish whether the phase changes randomly in the direction of propagation or perpendicular to it. The first case corresponds to lack of time coherence, giving rise to random frequency modulation. In the second case, the spatial coherence is degraded.

We first take a look at the time-coherence degradation. It is due to random variation of the time of arrival of successive wave fronts brought about by refractive index changes along the path  $L$ . The phase of the wave front at any point  $z$  along the propagation path is:

$$\phi = \omega_0 t - k_0 z n \quad (24)$$

if there are no changes in  $n$ ; the phase  $\phi$  varies linearly with time. Instead, due to changing  $n$ , it departs from linearity by:

$$\psi = \phi - \omega_0 t \quad (25)$$

Over a coherence interval the change in  $\psi$  is:

$$\Delta\psi_c = -k_0 L_c \Delta n \quad (26)$$

Over the total path length  $L$ , there are  $\frac{L}{L_c}$  coherence intervals; we add up the foregoing changes on a mean square basis:

$$\langle \Delta\psi^2 \rangle = k_0^2 L L_c \overline{\Delta n^2} \quad (27)$$

The resultant frequency modulation comes about from the time rate of

change  $\left(\frac{d\Delta\psi}{dt}\right)^2$ . Again we avail ourselves of Eq. 22, which yields

$$\langle \Delta f_r^2 \rangle = \frac{L L_c}{\lambda_0^2} \frac{\overline{\Delta n^2}}{T_c^2} \quad (28)$$

There are two ways in which  $\langle \Delta f_r^2 \rangle$  arises. Either the medium changes temperature in time intervals of the order of the coherence time  $T_c$  or cross winds are responsible for moving in turbulences of different temperature at velocities  $v_T = \frac{L_c}{T_c}$ . Considering the first alternative and a correlation time  $T_c \sim 10^{-3}$  sec, the temperature change could not be expected to exceed  $1^\circ\text{K}$  or so. From Exp. 5, the corresponding change is  $\sqrt{\overline{\Delta n^2}} \sim 10^{-6}$ . For path length  $L \sim 10^5$  m, correlation distance  $L_c \sim 10$  m and  $\lambda_0 \sim 10^{-6}$  m we get:

$$\sqrt{\langle \Delta f_r^2 \rangle} \sim 10^6 \text{ sec}^{-1} \quad (29)$$

The second alternative yields:

$$\sqrt{\langle \Delta f_r^2 \rangle} = \frac{L}{L_c} \frac{v_T^2}{\lambda_0^2} \sqrt{\overline{\Delta n^2}} \quad (30)$$

which checks a result already obtained by Beckman (4). Assuming a cross-wind velocity  $v_T \sim 10$  m/sec and the same  $L_c$ , the corresponding equivalent correlation  $T_c \sim \frac{10}{10} = 1$  sec. Even with as high as  $\overline{\Delta n^2} \sim 10^{-10}$ :

$$\sqrt{\overline{\Delta f_r^2}} \sim 10^4 \text{ sec}^{-1} \quad (31)$$



Comparing Exp. 29 and Exp. 31 we see that an undesirable random frequency modulation as high as 1 Mc/s may be brought about by corresponding changes in the temperature of the medium. However, it is doubtful that even as little temperature change as 1°K takes place in 1 ms over the assumed path length of 100 km. The random temperature changes are more of the order of 0.1°K. One must expect the maximum random frequency modulation in the first alternative to be reduced by one or two orders of magnitude. It now falls between 100 kc/s and 10 kc/s and it is of the same magnitude as if it were caused by cross-wind. A frequency modulation of this magnitude may still pose some problems if one attempts to modulate the light signal rather than a lower frequency subcarrier. If optical mixing is used, this random frequency modulation forces the IF bandwidth to be opened up by an additional 10 kc/s to 100 kc/s with consequent signal-to-noise ratio decrease.

We now investigate space coherence degradation. Consider the phase variation over the detector aperture. We assume, as it is the case in practice, that the aperture is parallel to the average wave-front inclination. In the absence of turbulence, the aperture is an equiphase surface. Because the laser is quasi-monochromatic ( $\frac{\Delta f}{f} \ll c$ ) we are entitled to talk about phase. In general, given a polychromatic wave, for instance, a transient traveling wave pulse, coherence implies the existence of a surface which is equiphase for each frequency component in the wave. When local refractive index fluctuations take place within the path of the rays collected by the aperture, the wave front becomes distorted, twisting and bending as time goes on in a random fashion. The aperture is no longer an equiphase and its phase varies randomly in time over its surface. The phases at any two points in the aperture are:

$$\Phi^1 = \omega_0 t + \Delta\psi_1 \quad (32a)$$

$$\Phi^2 = \omega_0 t + \Delta\psi_2 \quad (32b)$$

$\Delta\psi_1$  is a random variable, such that  $\overline{\Delta\psi_1} = \overline{\Delta\psi_2} = 0$ ,  $\overline{\Delta\psi_1^2} = \overline{\Delta\psi_2^2} = \overline{\Delta\psi^2}$ . The resultant spatial coherence degradation is minimized by reducing the collecting aperture to the point where one of the following two criteria (9) is satisfied.

(a) The phases between the two extremes of the aperture exhibit strong correlation, i.e.:

$$0.9 \leq \gamma_{12} = \frac{\overline{\Delta\psi_1 \Delta\psi_2}}{\overline{\Delta\psi^2}} \leq 1 \quad (33a)$$

(b) The phase shift between the two extremes is much less than that corresponding to a path difference of half a wavelength, i.e.:

$$(\Delta\psi_1 - \Delta\psi_2)^2 \ll \pi^2 \quad (33b)$$

The first criterion is equivalent to:

$$(\overline{\Delta\psi_1 - \Delta\psi_2})^2 \leq 2 \times 10^{-1} \overline{\Delta\psi^2} \quad (33c)$$

indicating that for large fluctuations the second criterion is much more stringent. Which one applies depends upon the use the system is intended for.

As an example, if optical superheterodyne requires wave-front alignments between signal and local oscillator much smaller than  $\frac{\lambda_0}{D}$ ,  $D$  being the collector-aperture diameter, then the aperture must present nearly an equiphase surface, a phase shift much smaller than  $\pi$ ; Exp. 33b provides the proper criterion to use. On the other hand, direct photo-detection only requires as high signal-to-noise ratio as possible. This ratio increases directly with aperture as long as the signal is coherent over it. Further increase in aperture beyond this point does not improve the ratio. Coherence is maintained as long as the normalized spatial correlation  $\gamma_{12}$  of Eq. 33a is near unity. As we can judge from Eq. 33a, this criterion allows much larger aperture than what is dictated by Exp. 33b. The criterion choice depends on the system and its application. Following Beckmann (5) we investigate the restrictions brought about by the second criterion. Expanding Exp. 33b yields:

$$\overline{\Delta\psi_c^2} - \overline{\Delta\psi_{1c} \Delta\psi_{2c}} \ll \frac{\pi^2}{2} \quad (34)$$

The subscript  $c$  indicates phase shift caused by one coherence element over the transmission path. Over the total path length  $L$ , there are  $\frac{L}{L_c}$  coherence elements and the total phase shift must still satisfy the same criterion, namely:

$$\langle \Delta\psi^2 \rangle - \langle \Delta\psi_1 \Delta\psi_2 \rangle = \frac{L}{L_c} [\overline{(\Delta\psi_c^2)} - \overline{\Delta\psi_{1c} \Delta\psi_{2c}}] \ll \frac{\pi^2}{2} \quad (35)$$

But:

$$\overline{\Delta\psi_c^2} = k_0^2 L_c^2 \overline{\Delta n^2} \quad (36a)$$

and:

$$\overline{\Delta\psi_1 \Delta\psi_2} = k_0^2 L_c^2 \overline{\Delta n_1 \Delta n_2} \quad (36b)$$

We assume for simplicity an exponential decay of the correlation function  $\overline{\Delta n_1 \Delta n_2}$  over the aperture:

$$\overline{\Delta n_1 \Delta n_2} = \overline{\Delta n^2} e^{-D^2/L_c^2} \quad (37)$$

which after introducing the simplification:

$$\frac{D^2}{L_c^2} \ll 1$$

yields:

$$\frac{L}{L_c} k_0^2 \overline{\Delta n^2} D^2 \ll \frac{\pi^2}{2}$$

or:

$$D \ll \frac{\lambda_0}{2} \sqrt{\frac{L_c/L}{2 \overline{\Delta n^2}}} \quad (38)$$

For  $\sqrt{\overline{\Delta n^2}} = 10^{-6}$ ,  $\lambda_0 = 10^{-6}$  m,  $L_c = 10$  m,  $L = 10^5$  m, we find  $D \ll 3$  mm.

The phase variation over the collecting aperture also imposes limitations upon the maximum permissible amplitude modulation rate  $\omega_M$  (5). At this frequency the phase difference across the aperture corresponds to differences in transit times such that:

$$\langle (\Delta\psi_2^2 - \Delta\psi_1^2)^2 \rangle = \omega_M^2 \langle (\Delta t_2 - \Delta t_1)^2 \rangle \quad (39)$$

In order to avoid distortion of the amplitude modulation at this frequency, the transit time difference must be much smaller than the modulation period,

$$\frac{2\pi}{\omega} = \frac{1}{f_M}, \text{ or} \\ < (\Delta t_2 - \Delta t_1)^2 > \ll \frac{4\pi^2}{\omega^2_M} \quad (40)$$

This is the same criterion as Exp. 33b, except that now we are dealing with a phase difference at the modulation frequency. From Eq. 40 we have

$$f^2_M \ll \frac{1}{< (\Delta t_2 - \Delta t_1)^2 >} \quad (41)$$

Following the same line of reasoning as in Eqs. 35 to Eq. 37 and noting that the transit times across one coherence element and along the path length  $L$  are respectively

$$\overline{\Delta t^2_c} = \frac{L_c^2}{c^2} \overline{\Delta n^2} \quad (c = \text{speed of light}) \quad (42a)$$

$$< \Delta t^2 = \frac{L}{L_c} \overline{\Delta t^2_c} = \frac{L L_c}{c^2} \overline{\Delta n^2} \quad (42b)$$

we get

$$f_M \ll \frac{c}{\sqrt{2 L L_c \overline{\Delta n^2}} \sqrt{1 - e^{-D^2/L_c^2}}} \quad (43a)$$

or

$$f_M \sim \frac{10^{-1} c}{\sqrt{2 L L_c \overline{\Delta n^2}} \sqrt{1 - e^{-D^2/L_c^2}}} \quad (43b)$$

The most stringent limitation occurs with a collecting aperture much larger than the coherence interval

$$D \gg L_c \quad (44)$$

hence, the highest permissible amplitude modulation rate is

$$f_M \sim \frac{10^{-1} c}{\sqrt{2 L L_c \overline{\Delta n^2}}} \quad (45)$$

Using the same parameters as in the previous example

$$f_M \sim 10^9 - 10^{10} \text{ c/s}$$

At present, this is not a serious limitation.

**Random Cross-section Changes (Breathing)** – A more serious limitation is caused by random changes in beam cross-section,  $\delta S$ , known as “breathing”. Corresponding changes in intensity (scintillation)  $\delta I$ , follow which set a lower permissible limit to the modulation depth,  $m$ . Fractional intensity and cross-section changes are related by flux conservation

$$IS = I_0 S_0 \quad (46)$$

Here  $S_0$  and  $I_0$  are the initial undisturbed quantities, while  $S = S_0 + \delta S$ ,  $I = I_0 + \delta I$ . The increments  $\delta S$ ,  $\delta I$  are not necessarily small with respect to

$S_0$  and  $I_0$ . The relative changes in cross-section and intensity follow from Eq. 46:

$$1 + \frac{\delta S}{S_0} = \frac{1}{1 + \frac{\delta I}{I_0}} \quad (47)$$

Since  $\delta S$  is random, so is  $\delta I$  and  $\frac{\delta I}{I_0}$  is the relative noise power introduced by "breathing". For an amplitude modulated signal of the form  $(1 + m \cos \omega_m t) \cos \omega_0 t$ , the relative signal power is  $\frac{m^2}{2}$ . The signal-to-noise ratio is

$$\frac{S}{N} = \frac{m^2}{2 \left| \frac{\delta I}{I_0} \right|} \quad (48)$$

Given  $S/N$ , we now set out to determine the minimum tolerable  $m$  after calculating  $\frac{\delta I}{I_0}$  in terms of the statistics of the medium and path length. Refer to Fig. 6, where the increase,  $\delta S_c$  in the cross-section of a coherence area  $L_c^2$  is shown over a path length  $L$ . Assuming with no loss in generality the same mean square lineal deviation  $\langle \Delta y^2 \rangle$  in both directions normal to propagation, we have

$$\delta S_c = (\sqrt{\langle \Delta y^2 \rangle} + L_c)^2 - L_c^2 = \langle \Delta y^2 \rangle + 2 L_c \sqrt{\langle \Delta y^2 \rangle} \quad (49)$$

We now assert that the total cross-section change  $\delta S$  is the change in one coherence area  $\delta S_c$  times the number of coherence areas contained in the original cross-section  $S_0$ , namely  $\frac{S_0}{L_c^2}$ . It follows that

$$\frac{\delta S}{S} = \frac{\delta S_c}{L_c^2} = \frac{\langle \Delta y^2 \rangle}{L_c^2} + 2 \sqrt{\frac{\langle \Delta y^2 \rangle}{L_c^2}} \quad (50)$$

The mean square lineal deviation is related to the mean square angular deviation by

$$\langle \Delta y^2 \rangle = \langle \Delta \theta^2 y \rangle L^2 \quad (51)$$

which in conjunction with Eq. 14 yields

$$\langle \Delta y^2 \rangle = \overline{\Delta n^2} \frac{L^3}{L_c} \quad (52)$$

Substituting Eq. 52 into Eq. 50 yields

$$\frac{\delta S}{S} = \overline{\Delta n^2} \left( \frac{L}{L_c} \right)^3 + 2 \sqrt{\overline{\Delta n^2} \left( \frac{L}{L_c} \right)^3} \quad (53)$$

There are two cases of interest, (a)  $\frac{\delta S}{S} \ll 1$ , hence  $\frac{\delta S}{S_0} \sim -\frac{\delta I}{I_0}$  corresponding to relatively short path lengths such that  $2 \sqrt{\overline{\Delta n^2} \left( \frac{L}{L_c} \right)^3} \leq 10^{-1}$ , (b)  $\frac{\delta S}{S} \gg 1$ , hence  $\frac{\delta I}{I_0} \sim \frac{S_0}{\delta S}$  for long path lengths, so that  $\overline{\Delta n^2} \left( \frac{L}{L_c} \right)^3 \gg 1$ . As an example,



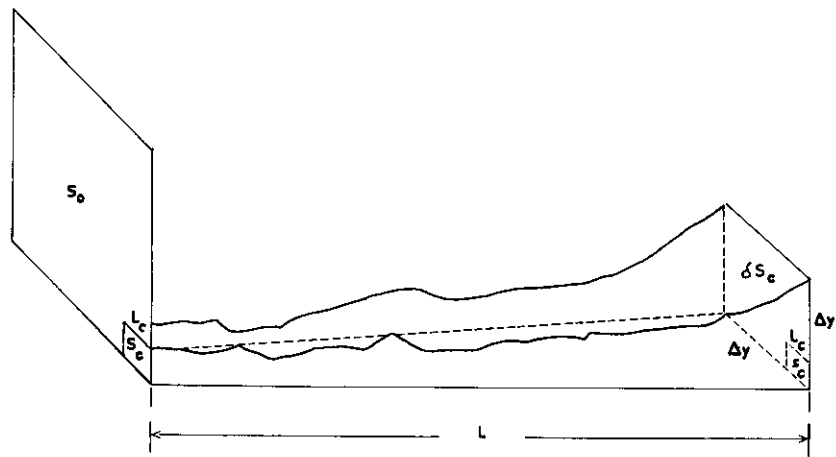


FIG. 6 Geometry of "breathing"

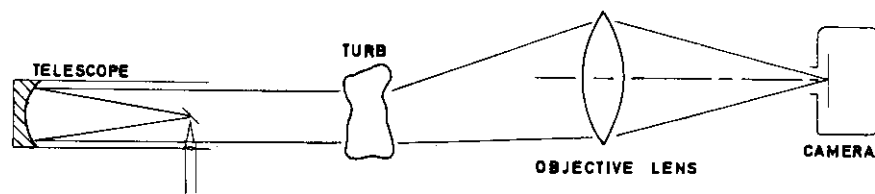


FIG. 7 Fraunhauffer pattern experiment

let us look at the second case; then

$$\frac{\delta^0}{I_0} = \frac{1}{\Delta n^2 \left(\frac{L}{L_c}\right)^3} \quad (54)$$

From Eq. 48 and Eq. 54 we see that  $m$  must satisfy the inequality

$$\sqrt{\frac{\frac{S}{N}}{\left(\frac{L}{L_c}\right)^3 \Delta n^2}} \leq m \leq 1 \quad \left(\frac{L}{L_c} \gg 5 \text{ km}\right) \quad (55)$$

in order to meet a minimum specified signal-to-noise ratio. For instance, taking  $S/N \sim 10$ ,  $L \sim 10^5 \text{ m}$ ,  $L_c \sim 1 \text{ m}$ ,  $\Delta n^2 \sim 10^{-12}$  we find that  $m \geq 15$  per cent in order to overcome the noise introduced by "breathing". For the first case we find

$$2 \sqrt{\frac{S}{N}} \sqrt{\left(\frac{L}{L_c}\right)^3 \Delta n^2} \leq m \leq 1 \quad \left(\frac{L}{L_c} \gg 5 \text{ km}\right) \quad (56)$$

Taking  $S/N \sim 10$ ,  $\Delta n^2 \sim 10^{-12}$ ,  $L \sim 200 \text{ m}$ ,  $L_c \sim 1 \text{ m}$ , we find  $m \geq 30$  per cent.  
**Random Polarization Fluctuation** – We now attempt an estimate of polarization fluctuations (refer to Fig. 5a). The initial polarization is broken up into components  $E_{1x}$  in the plane of incidence and  $E_{1y}$  parallel to the interface. The argument of

$$\tan \phi = \frac{E_{1y}}{E_{1x}} \quad (57)$$

gives the initial angular direction of polarization. After refraction through the interface, the transmitted components have different values,  $E_{2x}$ ,  $E_{2y}$  corresponding to a change in polarization given by

$$\tan (\phi + \Delta \phi_c) = \frac{E_{2y}}{E_{2x}} \quad (58)$$

The transmission coefficient according to transmission line theory is

$$\frac{E_2}{E_1} = \frac{2}{1 + \frac{\tilde{Z}_1}{\tilde{Z}_2}} \quad (59)$$

$\tilde{Z}_1$  and  $\tilde{Z}_2$  being the respective characteristic impedances of the first and second medium in the direction normal to the interface. They are defined as the ratio  $E_t/H_t$ , that is the ratio of components tangential to the interface. It is easily shown that for  $E_x$  polarization

$$\tilde{Z}_{1x} = \tilde{Z}_{01} \cos \theta \quad \tilde{Z}_{2x} = \tilde{Z}_{02} \cos (\theta + \Delta \theta) \quad (60)$$

since the electric field,  $E$ , tangent to the interface is  $E_{1x} \cos \theta$ . For  $E_y$  polarization

$$\tilde{Z}_{1y} = \frac{\tilde{Z}_{01}}{\cos \theta} \quad \tilde{Z}_{2y} = \frac{\tilde{Z}_{02}}{\cos (\theta + \Delta \theta)} \quad (61)$$

since the magnetic field  $H_t$  tangent to the interface is  $H_{1x} \cos \theta$ ;  $Z_{01}$  and  $Z_{02}$  are the unbounded characteristic of the media. It follows that

$$\frac{Z_{01}}{Z_{02}} = \sqrt{\frac{\epsilon_2}{\epsilon_1}} = \frac{1}{1 + \Delta n} \quad (62)$$

$\epsilon$ 's are the medium permittivities.

From Snell's law,

$$\cos(\theta + \Delta\theta_c) = \cos \theta \sqrt{1 - 2 \Delta n \tan^2 \theta} \quad (63)$$

The transmission coefficients follow,

$$\frac{E_{2x}}{E_{1x}} = \frac{2}{1 + \frac{1}{(1 + \Delta n) \sqrt{1 - 2 \Delta n \tan^2 \theta}}}; \frac{E_{2y}}{E_{1y}} = \frac{2}{1 + \frac{2}{\sqrt{1 - 2 \Delta n \tan^2 \theta} + \Delta n}} \quad (64)$$

Introducing the restriction (a valid one as long as  $\sqrt{\Delta n^2} \frac{L^2_{cz}}{L^2_{cT}} \ll 1$ ),

$$\Delta n \tan^2 \theta \ll 1 \quad (65)$$

yields

$$\frac{E_{2x}}{E_{1x}} = \frac{1 + \Delta n (1 - \tan^2 \theta)}{1 + \frac{\Delta n}{2} (1 - \tan^2 \theta)} = X; \frac{E_{2y}}{E_{1y}} = \frac{1 + \Delta n}{1 + \frac{\Delta n}{2} (1 - \tan^2 \theta)} = Y \quad (66)$$

The change in polarization through one coherent turbulent element

$$\Delta\phi_c = \tan^{-1} \frac{E_{2y}}{E_{2x}} - \tan^{-1} \frac{E_{1y}}{E_{1x}} \quad (67)$$

is in terms of Eqs. 66 and 9

$$\Delta\phi_c = \frac{\left(1 - \frac{X}{Y}\right) \tan \phi}{\tan^2 \phi + \frac{X}{Y}} \quad (68)$$

From Eq. 66

$$\frac{X}{Y} = 1 - \Delta n \tan^2 \theta \quad (69)$$

After using Eqs. 65, 69 and 10 in Eq. 68 we have

$$\Delta\phi_c \sim \frac{\Delta n}{2} \frac{L^2_{cz}}{L^2_{cT}} \sin 2\phi \quad (70)$$

The above confirms the intuitive fact that maximum polarization change occurs when both components  $E_{1x}$ ,  $E_{1y}$  are equal or  $\phi = 45$  deg. Dropping then the term  $\sin 2\phi$ , noting that over a path length  $L$ , there are  $\frac{L}{L_{cz}}$  coherence elements and that polarization changes add up on a mean square basis we have after taking time average



$$\sqrt{\langle \Delta \phi^2 \rangle} = \sqrt{\langle \Delta \phi_c^2 \rangle} = \frac{\sqrt{\Delta n^2}}{2} \frac{L^2_{cz}}{L^2_{cT}} \sqrt{\frac{L}{L_{cz}}} \quad (71)$$

Note that Eq. 71 is related to Eq. 14 as follows,  $\sqrt{\langle \Delta \phi^2 \rangle} \sim \frac{L^2_{cz}}{L^2_{cT}} \sqrt{\langle \Delta \phi^2 \rangle}$ .

As an example, if  $L_{cz} = 10 L_{cT} = 10$  m,  $L = 10^5$  m,  $\sqrt{\Delta n^2} = 10^{-6}$ , then  $\Delta \phi \sim 0.01$  radians; for  $\phi = 45$  deg.  $= \pi/4$

$$\frac{\Delta \phi}{\phi} \sim 1 \text{ per cent}$$

This seems to be consistent with the measurements of Goodwin and his group (10). On the other hand, Fried (11) and his group have measured  $\frac{\Delta \phi}{\phi} \sim 20$  per cent, which would seem to imply that the anisotropy in the propagation path was as high as  $\frac{L_{cz}}{L_{cT}} \sim 50$ . Note that if the medium is isotropic ( $L_{cz} = L_{cT}$ ),  $\Delta \phi \sim 10^{-4}$  radians.

The preceding analysis also shows that the mean square deviation in polarization angle are proportional to the mean square refractive index change. Since mean square intensity fluctuations are also proportional to it, we expect the spectral power density of both quantities to extend over approximately the same range of frequency. In concluding this section we remark that quivering and scintillation are reduced by increasing the collecting aperture while beam break-up is minimized by reducing it. The results are summarized in Table 1.

TABLE I

### Thermal Turbulence Effects on Laser Propagation

Random Angular Variation	Random Phase Variation	
↓	// Propagation	⊥ Propagation
Quivering	↓	↓
	Parasitic FM	Beam Break-up
$\langle \Delta \theta^2 \rangle = 2 \overline{\Delta n^2} \frac{L}{L_c}$	$\langle \Delta f_r^2 \rangle = \frac{LL_c}{\lambda_0^2} \frac{\overline{\Delta n^2}}{T_c^2}$	$D \ll \frac{\lambda_0}{2} \sqrt{\frac{L_c/L}{2 \overline{\Delta n^2}}}$
Random Intensity Variation	Random Polarization Variation	
↓		
Scintillation		
$\sqrt{\frac{2 S/N}{(L/L_c)^3 \overline{\Delta n^2}}} \leq m \leq 1$	$\langle \Delta \phi^2 \rangle = \frac{\overline{\Delta n^2}}{4} \left( \frac{L^2_{cz}}{L^2_{cT}} \right) \frac{L}{L_{cz}}$	

**Classification and Description of Measurements** – All measurements are broadly divided in two categories, Optical or Electronic, according to the way the measured data is processed. For ease of comparison, they are listed in Table 2, which is self-explanatory. In the first category, the measurements are made either visually or on film. In the second, the laser signals are first detected through photomultipliers and measurements are made on the

resulting electronic signals. In general, one can say that experiments in the optical class are easier to implement than those in the electronic category. The former, however, do not lend themselves as easily to real time processing, since measurements must be made on a dynamic basis due to fluctuation rates as high as several hundred cycles per second. These two broad categories are in turn subdivided according to whether one, two or multiple beams are used. Most experiments amount to a measurement of coherence of one form or another. Optical processing experiments involve measurement of amplitude correlation, that is, 2nd order coherence, while electronic processing measurements involve intensity correlation or higher-order coherence (4th and 6th). **Frauhaufer and Fresnel Pattern Experiments (Single Beam)** – This measurement has been reported in the literature (12). A Frauhaufer pattern of a laser beam transmitted through a turbulent atmosphere is photographed on a high-speed camera (500–800 fps) in which the lens has been removed. The removal is necessary because the beam, having been recollimated through a large aperture telescope operating in reverse (approximately 10 cm diameter), is too large to be intercepted by a conventional photographic lens. Instead, an objective lens as shown in Fig. 7, large enough to intercept the whole beam, is placed near the receiving end so that its focal plane coincides with the film in the camera. The area,  $A$ , of the Frauhaufer's pattern is related to the coherence area of the beam,  $A_c$ , by

$$A \sim \frac{(f\lambda)^2}{A_c} \quad (72)$$

where  $f$  is the objective lens focal distance. Angular beam shifts,  $\Delta\theta$ , due to turbulence are translated into lineal shifts of the Frauhaufer pattern,  $\Delta x$ , on the film according to the relation

$$\Delta x = f\Delta\theta \quad (73)$$

Large focal distances are then required to measure the coherence area and the beam shift independently. Since both phenomena take place simultaneously, it is difficult to measure  $\Delta\theta$  accurately if  $A$  is large; in such a case, it is difficult to locate the center of the pattern from which  $\Delta x$  is measured. Rapid cameras are needed, say 500 fps, if fluctuations as rapid as 1/500 fps = 2 ms are to be resolved.

If one lets the converging beam in Fig. 7 diverge further on to a sufficiently large observable area before it hits the photographic film, a Fresnel pattern is obtained. If the turbulences are close to the objective lens, the phase changes in the beam cause interference patterns in the film of an order of magnitude comparable with the Turb size. The number of interference patterns should also yield some gross idea of the number of Turbs.

**Laser Beam Illuminated Photographic Experiment (Single Beam)** – This technique, described in the literature (13) and verbally reported to us by Dr E. Bouche, is based on the fact that if the radiation is stationary in space, then the spatial coherence function,  $F_{12}(\rho, 0)$ , and the intensity over the beam,  $I(r)$ , are Fourier transforms of each other, according to the relation

$$I(\vec{r}) \sim \int_{-\infty}^{\infty} \int_{-\infty}^{\infty} F_{12}(\vec{\rho}) e^{i\frac{2\pi}{\lambda} \vec{\rho} \cdot \vec{r}} d\vec{\rho} \quad (74)$$

TABLE 2

**Classification of Optical Propagation Measurements**

## OPTICAL PROCESSING

**Single Beam**

<b>Physical Observables</b>	Franhauffer pattern		Fresnel pattern	
<b>Measurements</b>	Size of pattern	Shift in pattern	Size of spot	Distribution of spots
<b>Extracted data</b>	Coherence area, $A_c$ ↓ Turb size	Angular beam shift, $\theta$	Turb size	Number of turbs

**Double Beam**

<b>Physical Observables</b>	Photograph of laser beam illumination		Young fringes	
<b>Measurements</b>	Intensity distribution $I(x)$		Maxima and minima in fringe intensity	Shift in fringe maxima and minima
<b>Extracted data</b>	Magnitude of mutual coherence, $ \gamma $ Coherence area, $A_c$ ↓ Turb size		Relative phase change across wave front $\phi_{12}(\theta)$	

TABLE 2 (CONTINUED)

## ELECTRONIC PROCESSING

## DOUBLE BEAM (Optical Mixing)

	One Detector – One Laser		Two Detectors – Two Lasers	
	Intensity over two different paths	Intensity over two different portions of beam	Beats, Signal-to- noise ratio ( $S/N$ )	Beats, signal intensity, relative angle between beams
<b>Physical Observables</b>				
<b>Measurements</b>	Relative Phase shift between beam paths paths v. time	Relative phase shift between portions of beam v. time	$S/N$ v. Detector area, $A_c$	Maximum signal v. relative beam angle, $\theta$
<b>Extracted data</b>	Time fluctuation of optical path length	Time fluctuation of phase over beam cross-section, Coherence area, $A_c$ $\Downarrow$ Turb size	Coherence area, $A_c$ $\Downarrow$ Turb size	Angular beam shift $\theta$

## TRIPLE BEAM

Two Detectors		Three Detectors
Cross-correlation between detector outputs		Cross-correlation between detector outputs
Intensity cross-correlation (4th order coherence)	Intensity cross-correlation (6th order coherence)	Argument of complex coherence
Magnitude of mutual coherence, $ \gamma $ Coherence area, $A_c$ $\Downarrow$ Turb size		Relative phase change across wave front $\phi_{12}(\theta)$

Here  $I(\vec{r})$  is the intensity recorded on a photograph illuminated by a laser beam focused through a lens of focal distance,  $f$ , and  $\rho$  is the space interval between two points over the photograph. Formally, it is always possible by suitable optics, given  $I(\vec{r})$  as the object, to obtain an image which is its Fourier transform,  $I_{12}(\rho)$ . This last quantity yields both the magnitude and phase of the coherence function from which relative phase shifts across the beam and its coherence area could be extracted. This approach suffers serious drawbacks, the most important one being the restricted validity of the above expression to space stationary processes, that is statistical processes independent of the origin of the coordinates. This assumption never holds for finite wave fronts and is particularly inadequate in lasers, as compared to incoherent sources, because of their small beam diameter. Furthermore, the optical processing which yields the image as a Fourier transform of the object, although it is readily implemented if the amplitudes are Fourier mates (14), becomes quite intricate to construct and possibly impractical if the intensities are Fourier transforms of each other, as is the case with Eq. 74. As communicated verbally to us (15), it is not possible to obtain the phase of the coherence function through this method, but only the magnitude; the coherence interval is in turn determined by identifying the spacing between zeros of the intensity with the spacings between zeros of the coherence function. Finally, one of the big problems facing this technique at present is the limitations imposed by the nonlinearity in the photographic film (15).

**Young Fringes Experiment (Double Beam)** – This measurement, described by Long and Wortendyke (16), is similar in nature to the Fraunhofer pattern experiment, the only difference being that the observables are now interference fringes from two slits. In order to resolve fluctuations, a high-speed camera, of the order of 500 fps, is also used. From the interference patterns, the maximum and minimum intensity of the fringes can be measured after running the film through a densitometer and the magnitude of the normalized spatial coherence in the beam follows (17) from

$$\left| \gamma_{12}(0) \right| = \frac{I_{\max} - I_{\min}}{I_{\max} + I_{\min}} \quad (75)$$

where  $I$ , is the recorded intensity. This value of coherence corresponds to a specific spacing between the slits. For a complete plot of the coherence function from which the coherence interval is extracted, the experiment must be repeated for several slit spacings and different coordinates (since the coherence is not space stationary). The Fringe shift on the film,  $\Delta x$ , is related to the argument of the coherence function,  $\phi_{12} = \arg \gamma_{12}(t)$ , and the path difference between slits,  $\Delta s$ , as shown (17) in Fig. 8 by the equation,

$$\Delta x = \frac{\lambda}{2\pi} \frac{f}{d} \phi_{12}(t) + \Delta s \quad (76)$$

If  $\phi_{12}(0)$  is zero, the observed pattern at a point in the focal plane equidistant to the slits exhibits a maximum. At the same point, if  $\phi_{12}(0) \neq 0$ , the maximum is shifted by the amount

$$\Delta x = \frac{\lambda}{2\pi} \frac{f}{d} \phi_{12}(0) \quad (77)$$

Thus, the phase difference,  $\phi_{12}(o)$ , between two portions of the wave front intercepted by the respective slits can be determined according to Eq. 77 by measuring the shift in fringe maxima from the center of the focal plane.

**One-Laser Beat Experiment** – This method described by Read (18) measures the beats between a beam leaving the laser and the same beam returning from a turbulent region in order to determine the fluctuations in optical path. The beats between two portions of the same beam transmitted through turbulence are also measured in order to determine the relative phase fluctuations across the wave front. Both methods are described below.

The first experiment, described below, is sketched in Fig. 9, which is self-explanatory. The returned beam from the Turb is mixed with the beam at the laser and the resulting intensity fluctuations due to beats, are detected in a photomultiplier and recorded in a suitable device.

If the return signal is of the form  $\cos [\omega_0 t + \phi(t)]$  and the transmitted signal is  $\cos \omega_0 t$ , the beat signal fluctuation is

$$e_s \sim \cos [\phi(t)] \quad (78)$$

If the return and transmitted beams are in phase, the fluctuations are maximum,  $e_s \sim 1$  and if they are  $\lambda/2$  out of phase they are minimum,  $e_s \sim -1$ . If they are  $\lambda/4$  apart, they are zero,  $e_s \sim 0$ . If the fluctuations are displayed on a scope and photographed, in phase beats correspond to maximum up deflection,  $\lambda/2$  out of phase beats correspond to maximum down deflection and  $\lambda/4$  phase delay corresponds to no deflection on the scope screen. One of the difficulties with this method is to determine whether the phase difference is continually increasing or reverses as the path delay changes (see Fig. 10) since  $\phi(t)$  in Eq. 78 has the same value in both cases. The ambiguity is resolved as follows:  $\phi(t)$  being a dynamic variable of time, the slope of the fluctuation in Eq. 78 which is observable on a scope is given by

$$\frac{d e_s}{dt} \sim -\sin \phi(t) \dot{\phi}(t) \quad (79)$$

(The dot denotes time derivative.)

From Fig. 10a we see that, for phase reversal, the slope of  $\phi(t)$  is stationary when the path difference is near  $\lambda/2$ . The slope of the fluctuations as given by Eq. 79 is then flatter near the deflection peak ( $\lambda/2$ ) if phase reversal takes place Fig. 10a. Hence, observation of the relative sharpness of the peaks in the fluctuation records Fig. 10b resolve ambiguities concerning the absolute phase variation with time. An illustration of the resultant 4 ms. phase fluctuation v. path length taken from the same report (18) is shown in Fig. 11. To measure relative phase fluctuations across the beam, the wave front is split into two portions. Beats between these two portions are detected as shown in Fig. 12. In order to remove phase ambiguity, a piezoelectric transducer of displacement  $\lambda/4$  is inserted in one of the paths. The fluctuations in both positions of the beam are recorded; whenever the transducer displacement is  $\lambda/4$ , the wave reflected from it is recorded, thus insuring  $\lambda/4$  path difference between the two beam portions. It is now a simple matter to determine if phase reversal takes place across the beam by analyzing Fig. 13. If no phase reversal occurs, Fig. 13a, then one beam maintains the same slope sign while the other reverses sign. If phase reversal occurs, both beam slopes

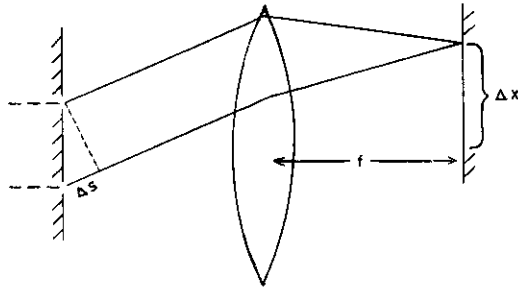


FIG. 8 Young fringes experiment

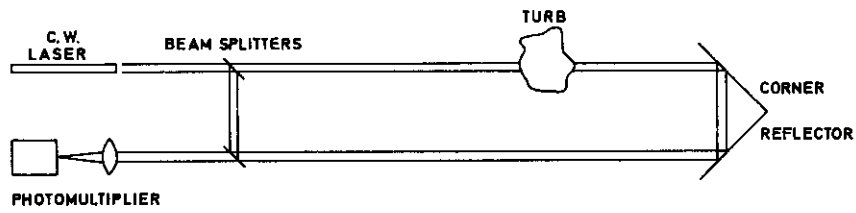


FIG. 9 One laser beat experiment

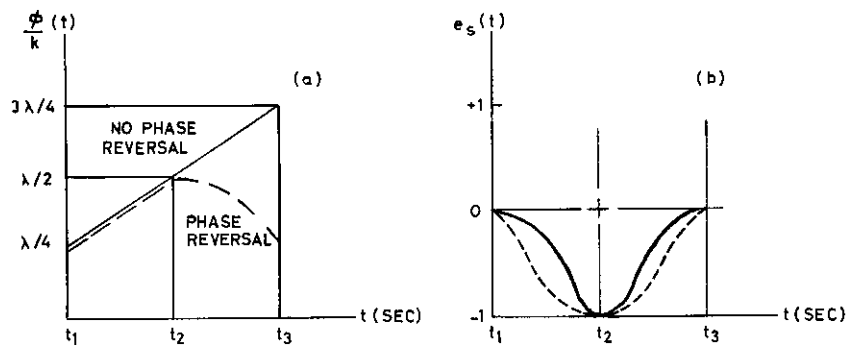


FIG. 10 Phase difference reversal

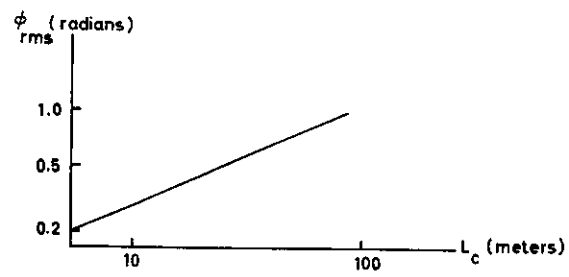


FIG. 11 R.M.S. phase fluctuation v. path length

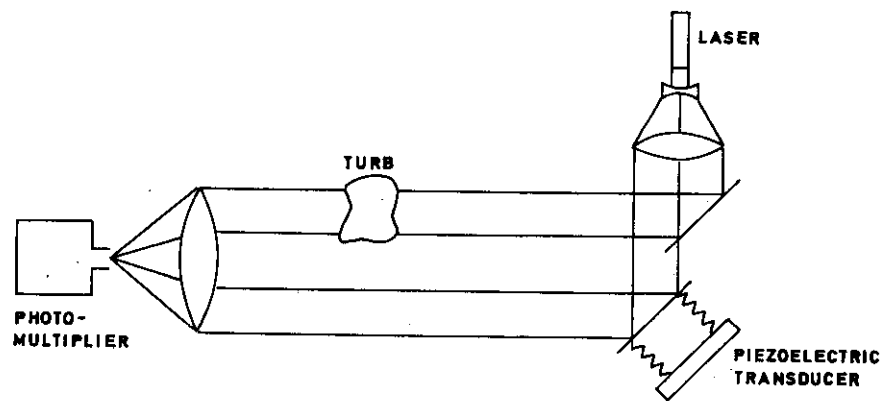


FIG. 12 Detection of beats

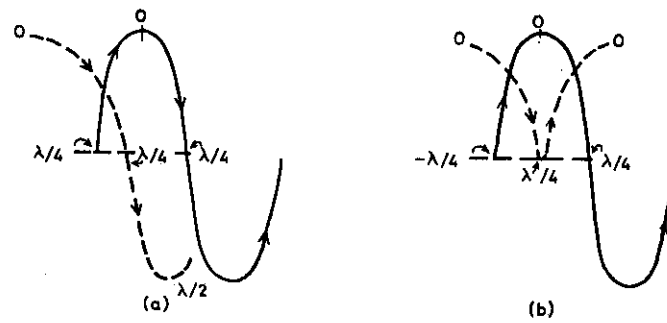


FIG. 13 Phase reversal analysis



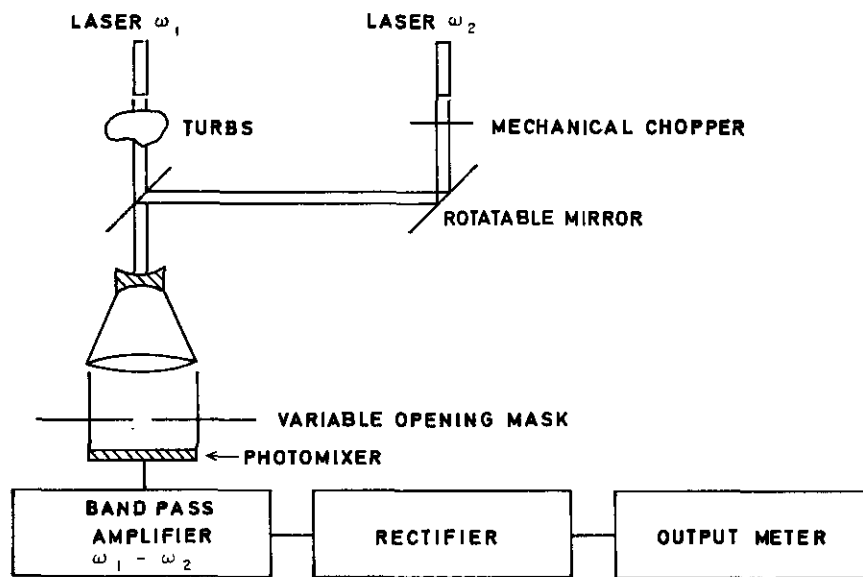


FIG. 14 Proposed system for measuring direction of wave-front arrival and coherence

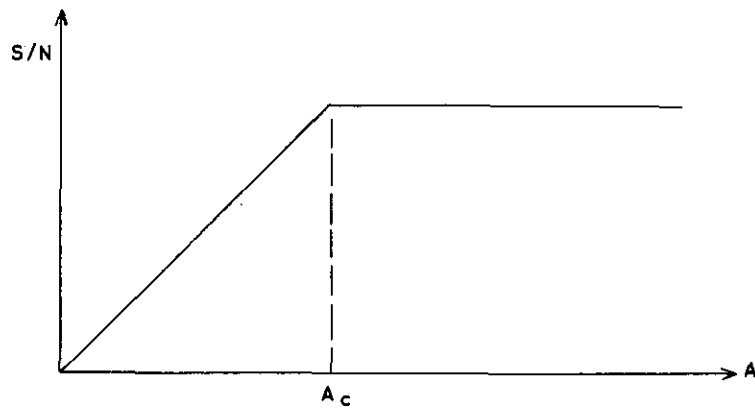


FIG. 15 Variation of signal-to-noise ratio with detecting area and coherence area

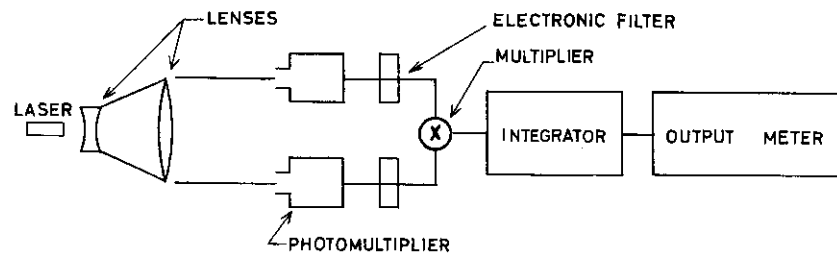


FIG. 16 Brown and Twiss experimental set-up (4th order coherence measurement)

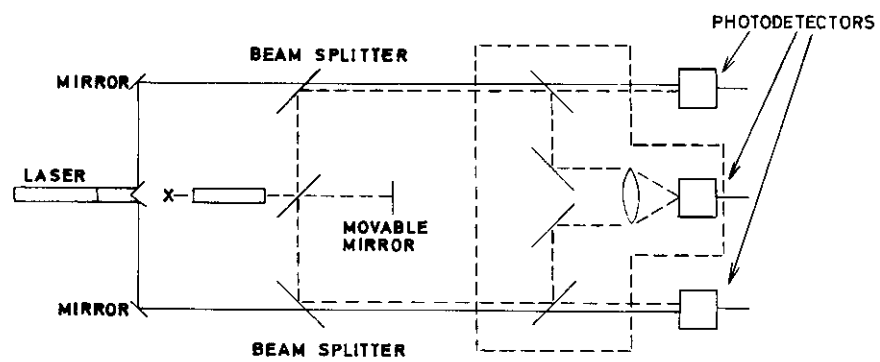


FIG. 17 Detector and phase modulator addition for 6th order coherence measurement

reverse sign at the same point (Fig. 13b). The major source of inaccuracy here is due to mechanical vibrations which in many cases swamp out completely the phase fluctuations across the beam unless extreme precautions are taken to stabilize the laser.

**Two-Laser Beat Experiment** – This method has been reported in an internal report (19). One method consists of measuring the wavefront inclination, in short, the amount of beam shift,  $\Delta\theta$ , created by thermal turbulence. The other method measures the coherence area,  $A_c$ , of the beam. Both methods are based on the properties of optical mixing, and the first method, in particular, is highly accurate and capable of measuring beam shifts of the order of microradians. A description of both methods follows.

**Measurement Wave-front Inclination** – Measurement of wave-front inclination is based on the well-known properties that the signal output from a photomixer is strongly dependent on the relative alignment between the local oscillator (frequency  $\omega_1$ ) and on the incoming signal (frequency  $\omega_2$ ). The photomixer output current at the intermediate frequency,  $\omega_1 - \omega_2$ , has an amplitude proportional to

$$\frac{\sin\left(\frac{\pi L}{\lambda} \sin \theta\right)}{\left(\frac{\pi L}{\lambda} \sin \theta\right)} \quad (80)$$

where  $L$  is the length of the photodetector, and  $\theta$  is the relative inclination between the local oscillator and signal wave fronts. It is thus seen that the output drops very rapidly with the angle of inclination. In fact, with a 10 mm long photocathode, the output drops down in the noise if misalignment between local oscillators and signal wave front is as little as 1 minute of arc.

In order to measure the direction of arrival of the wave front, a system based on Exp. 80 and shown in Fig. 14 is proposed. Two gas lasers of slightly different frequencies,  $\omega_1$  and  $\omega_2$ , are operated in unimode and selected so that  $\omega_1 - \omega_2$  falls within a convenient intermediate frequency of the order of a few megacycles. Both laser beams are initially aligned with parallel wave fronts normally incident on the photomixer, say at night. Thermal disturbances in the transmission path of one laser deflect the beam with respect to the other laser and the photomixer output drops sharply. The rotatable mirror is then rotated until the full output is restored, and the amount of rotation read-off is identical with the wave front inclination of the first laser. Actually, once the mirror is rotated to realign the wave fronts, since both wave fronts still make an angle with the photomixer, the output is theoretically reduced by the cosine of this angle. Since the angle is small the original full output is restored for all practical purposes. The experimental set-up described can be automated without too much difficulty in order to obtain a continuous plot of the temporal variations in wave-front inclination by using, for instance, electro-optic prisms to deflect the beam electrically in lieu of rotating mirrors.

**Measuring the Coherence Area** – Thermal turbulences in the transmission path lead to both changes in wave-front inclination and phase variation across the beam. Therefore, the measurement of the coherence area must

be conducted with the set-up used for the measurement of the wave-front inclination and both must be measured simultaneously. The measurement of optical phase variation across the wave front is not always revealing because of ambiguities that are usually associated with such a measurement and the difficulties in resolving them. Furthermore, from a detection standpoint the quantity of interest is the coherence function over the wave front. Although there are many methods available to measure the coherence function, the determining factor in detection performance is the number of coherence areas over the detecting surface. Over each coherence area the phase of the wave front can be taken as approximately spatially constant, although it varies randomly from one coherence area to another. The measurement of the number of coherence areas over the photomixer is based on the fact as illustrated in Fig. 15 that the signal-to-noise ratio,  $S/N$ , varies linearly with the detecting area,  $A$ , as long as it is smaller than the coherence area,  $A_c$ , ( $A < A_c$ ), but remains constant beyond this point ( $A > A_c$ ). The measurement is performed in the presence of background noise. The diverging converging lens system of Fig. 14 has the function of spreading the many coherence areas present in the beam over the photomixer surface. A variable opening over the photodetecting surface is provided by means of an electronically controlled shutter or mask. A mechanical chopper interrupts the second beam at regular intervals, so that when the beam is off the output of the rectifier measures the noise and when the beam is on the beat frequency output signal is obtained. As the shutter opens wider the  $S/N$  ratio increases until a point is reached beyond which no further increase is noted. At this point the opening of the shutter is measured and the ratio of the photomixer area to the area of the opening gives the number of coherence areas of the beam. In the actual experiment some threshold level electronic circuitry will be provided to carry out automatically a comparison of signal level and noise level; the ratio of the levels yields the signal-to-noise ratio.

**Two-Detector Intensity Correlation Experiment**—This method, based on the famous Brown and Twiss experiment (20), measures the cross-correlation between the current fluctuation,  $\Delta I_1(t)$  and  $\Delta I_2(t)$ , of two photodetectors illuminated by a source. Fig. 16 illustrates the method and is self-explanatory.

The expression relating the measured cross-correlation,  $\langle \Delta I_1(t) \Delta I_2(t) \rangle$ , to the spatial coherence of the wavefront  $\gamma_{12}(o)$  is:

$$\langle \Delta I_1(t) \Delta I_2(t) \rangle = I_1 I_2 \frac{B_1}{B_2} |\gamma_{12}(o)|^2 \quad (81)$$

where  $I_1$  and  $I_2$  are the d.c. currents of the two detectors and  $B_1$  and  $B_2$  are the optical and detector bandwidth respectively. This method, as seen from Eq. 81, does not give the argument of the coherence function, only its magnitude. However, the magnitude alone is sufficient to determine the coherence interval and the coherence area, provided that the experiment is repeated over a range of spacings between the two detectors. A more serious drawback is that the above expression is only valid for a light source with Gaussian statistics such as incoherent light; its validity for laser source is doubtful (12), since laser statistics are Poisson distributed and only in special cases approach a Gaussian distribution (22).

**Three-Detector Intensity Correlation Experiment** – This method devised by Gamo (23) is a refinement of the previously described method. The refined method extracts the argument as well as the magnitude of the coherence function. Whereas the previous method is a 4th order coherence measurement (intensity correlation), this method determines a 6th order coherence by means of an additional detector and a phase-modulated source as illustrated in Fig. 17. An additional source of known coherence,  $\gamma_{00}(t)$ , and yielding an average detected current,  $I_0$ , is superimposed on two coherent beams with a variable path difference,  $\theta$ , produced by the movable mirror. The expression relating the measured cross-correlation to the magnitude  $|\gamma_{12}(\theta)|$  and argument  $\phi_{12}$  of the desired coherence function is:

$$\langle \Delta I_1(t) \Delta I_2(t) \rangle = I_1 I_2 |\gamma_{12}|^2 + I_0^2 + 2\sqrt{I_0^2 I_1 I_2} \gamma_{12} \cos(\phi_{12} - \theta) \quad (82)$$

The third term represents a sinusoidal variation of the same frequency as the one introduced by the moving mirror. By proper filtering, this component can be measured and  $\phi_{12}$  determined separately from  $\gamma_{12}(\theta)$ . This method suffers the same serious drawback as the previous one, namely, that the above expression is only valid for light with Gaussian statistics such as incoherent light. However, Gamo has stated (24) that it may be possible to adapt the preceding equation to a laser source. If this is the case, the method deserves further study.

#### REFERENCES

1. FRANK, N. H., "Introduction to Electricity and Optics". McGraw-Hill, New York, 1940.
2. GOODWIN, F. E., "Laser Propagation in the Terrestrial Atmosphere". WESCON, 1964.
3. FRIED, D. L., and CLOUD, J. D., "Theoretical Examination of the Effect of Atmospheric Turbulence on Optical Propagation". Opt. Soc. of U.S.A., Spring Meeting, Washington, D.C., 1964.
4. BLACKADAR, A. K., "The Vertical Distribution of Wind and Turbulent Exchange in Neutral Atmosphere", J. Geophys. Res. 67, 8, 3095, 1962.
5. BECKMAN, P., "Signal Degeneration in Laser Beams Propagated Through a Turbulent Atmosphere", Radio Science J. Res., NBS/USNC-URSI 69D, 4, 1965.
6. TATARSKI, V. I., "Wave Propagation in Turbulent Medium". McGraw-Hill, New York, 1961.
7. READ, W. S., and FRIED, D. L., "Optical Heterodyning with Non-Critical Angular Alignment", Proc. IEEE, 1787, 1963.
8. STRANDS, H. W., "Coherence in Long-Range Laser Beams", Applied Optics, 4, 7, 875, 1965.
9. FORRESTER, A. T., "On Coherence Properties of Light Waves", Amer. J. Phys. 24, 192, 194, 1956.
10. GOODWIN, F. E., Private Communications. Hughes Research Labs.
11. FRIED and MEYER, "Atmospheric Optical Effects", Polarization Fluctuations, JDSA 55, 740, 1965.
12. GOODWIN, F. E., *ibid.*

13. BERAND, M. J., and PARRENT, G. B., Jr., "Theory of Partial Coherence". Prentice Hall, New York, 1964.
14. CUTRONA, L. J., *et. al.*, "Optical Data Processing and Filtering Systems", Trans. IRE Information Theory, 386, June, 1960.
15. BOUCHE, E., Private communication.
16. LONG, R. K., and WORTENDYKE, D. R., "Topics in the Propagation of Laser Radiation in the Atmosphere". Antenna Lab., Ohio State Univ., Columbus, Ohio, 1964.
17. BORN and WOLFE, "Principles of Optics". Pergamon, New York, 1959.
18. READ, W. S., "Phase Turbulence in Short Atmospheric Paths", North American Tech. Memo., 93, 1964.
19. NESCO Staff, "Degradation of Coherent Optical Signals Through the Atmosphere", Internal Report, August 1964.
20. BROWN and TWISS, "Interferometry of the Intensity Fluctuations in Light", Proc. Roy. Soc. 243, 291, 1957.
21. MANDEL, L., "Fluctuations of Light Beams", Progress In Optics, North Holland 2, 242, 1963.
22. HODARA, H., "Statistics of Laser and Thermal Radiation", Proc. IEEE, 53, 7, 1965.
23. GAMO, H., "On the Intensity Interferometer with Coherence Background", Advances in Quantum Electronics. Columbia Univ. Press, 1961.
24. GAMO, H., Private communication.

## CHAPTER 5-6

## PROPAGATION FACTORS AT 3.2 MILLIMETERS

L. A. HOFFMAN

Aerospace Corporation, El Segundo, California

## SUMMARY

Aerospace Corporation has been investigating millimeter wavelength systems for space applications for several years. The major instrument for these investigations is the 4.57-m (15-ft) precision paraboloidal antenna that was constructed for operation at millimeter wavelengths down to 1.0 mm. The full dish is effective at 1.46 mm (205 Gc/s), yielding a value of  $D/\lambda$  greater than 3000. The antenna characteristics have been measured by use of a transmitting facility located in the far-field of the antenna and, also, by drifting the antenna beam across the solar limbs. These measurements show that beam broadening of a high-resolution antenna is dependent on the elevation angle. This beam broadening correlates well with typical theoretical models of atmospheric turbulence.

Measurements indicate that the Van Vleck theory for collision-broadened lines satisfactorily accounts for the absorption through the clear atmosphere at 3.2 mm, if one uses the line-breadth constants for  $O_2$  and  $H_2O$  experimentally determined at other wavelengths. Thin layers of clouds and fog have a negligible effect on the propagation, whereas thick clouds and rain can cause appreciable attenuation.

In addition, a millimeter-wave system for the transmission and reception of an information-modulated carrier, including typical television material, has also been constructed. A baseband width of about 4 Mc/s is used to frequency modulate a 3.2-mm klystron to a modulation index of 2.5. The propagation path is 450 m above sea-level at the transmitter and traverses an 18.95-km path to the receiver, which is at an elevation of 39 m on top of a two-story building in El Segundo, California. The elevation angle is approximately  $1.17^\circ$  when corrected for curvature and refraction. Tropospheric attenuation ranged from about 13 dB on a typical day to approximately 36 dB when moderate rainfall ( $\sim 4$  mm/h) occurred over much of the 18.95-km path. Tropospheric turbulence effects were almost nonexistent on days of heavy fog or rainfall, but reached peak-to-peak magnitudes of 20 dB or more in received signal fluctuations on dry, windy days. High-quality television and voice reception were obtained over this link, even during light to moderate rainfall periods ( $\sim 3$  mm/h). A transmitter output of approximately 100 mW, 0.61-m (2-ft) parabolas at each end of the link, and a receiver noise figure of 25 dB were the main system characteristics.

This system has also been used to measure tropospheric attenuation at 3.2 mm over the nearly horizontal 18.95-km path. These measurements are in close agreement with values calculated from modified versions of the Van Vleck expressions for attenuation due to oxygen and water vapor. The average of measured tropospheric attenuation rates was approximately 0.7 dB/km for July 1965.

#### INTRODUCTION

Exploration of the millimeter-wave spectrum for possible Air Force systems applications is a major goal of the Electronics Research Laboratory of Aerospace Corporation. Propagation phenomena play a significant part in most of these applications. The objectives of the Aerospace research program are to investigate the feasibility and applicability of millimeter waves for solutions to the problems of communications in space and with re-entry vehicles, to evaluate the pointing and control requirements of future high precision antenna systems, and to enhance the understanding of the propagation characteristics of the earth's atmosphere at these wavelengths.

In addition to the potential of communication bandwidths exceeding the entire radio spectrum below 10000 Mc/s (30 mm), the use of millimeter wavelengths offers the opportunity to build space radar and long-range space communications systems that are lightweight and compact and that yield a high degree of directivity with small antennas. Also, ultrahigh resolution radar systems are possible with which radar photographs from moving vehicles or their appendages can be obtained. Further, by taking advantage of atmospheric absorption lines, it is possible to obtain privacy on millimeter wavelength communication links. The use of millimeter wavelengths also makes it possible to propagate through plasma sheaths that are opaque to the usual communication wavelengths.

To utilize the millimeter-wave region for the above applications, it is necessary, in addition to developing millimeter-wave components that have specifications comparable to those presently available at lower frequencies,

- (1) to construct very narrow beamwidth antennas that can be precisely controlled and pointed and
- (2) to determine the limitations imposed by the earth's atmosphere on propagation at these wavelengths.

In support of the stated objectives, Aerospace Corporation has engineered and established a Space Radio Systems Facility (SRSF) that consists of the five basic elements:

- (a) a 4.57-m (15-ft) diameter, equatorially mounted, precision-machined paraboloidal reflector with supporting structure,
- (b) a hydraulic servomechanism capable of positioning the 4.57-m antenna with high accuracy over a wide dynamic range of object-tracking rates,
- (c) a digital data-processing unit for performing the functions of ephemeris computations, servomechanism pointing control, and data reduction,
- (d) wide-band millimeter-wave receivers and associated calibration equipment, primarily for radiometric use,



- (e) a remote transmitting facility and a sensitive receiver of wide dynamic range for boresighting and pattern measurements.

In addition, a separate 3.2-mm (94-Gc/s) system for investigation of horizontal-path propagation factors was completed late in 1964. This system utilizes a low-level transmitting klystron, a 0.61-m (2-ft) diameter paraboloidal antenna at each end of the 18.95-km link, and a wide-band receiver.

All of the measurements to date have been taken at 3.2 mm at the "window" between the complex of absorption lines near 5 mm and the single oxygen absorption line near 2.5 mm. The attenuation is remarkably low in this region; values at zenith over Los Angeles, California, have been found by measurement to lie consistently between 0.4 and 0.8 dB.

The results described in this paper were obtained through the efforts of personnel of Aerospace Corporation's Electronics Research Laboratory. For additional information on the 4.57-m antenna, including historical data, see elsewhere (1-9).

#### THE 4.57-M MILLIMETER-WAVE ANTENNA

The original program of investigations, which included requirements for the 4.57-m antenna, was formulated by the Aerospace Electronics Research Laboratory. Reasoning leading to the selected approach was substantially as follows (6):

- (a) The possibilities for practical uses of the millimeter-wave spectrum, it appeared, could best be explored by using millimeter-wave components in an instrument that would have requirements on it similar to those placed on radar and communications equipment.
- (b) The practicality of millimeter-wave systems would depend to a large extent upon the ability to build relatively large antennas with extremely fine beamwidths and correspondingly fine tolerances on pointing control and boresight stability.
- (c) It also was evident that basic propagation data should be gathered.

It was therefore decided that the proper approach would be to build and operate a millimeter-wave antenna system that would have sufficient control and dynamic capability to permit subsequent tracking of near-earth satellites in communications and radar experiments. The completed instrument could then be used extensively for propagation, refraction, scattering, and emission measurements which would be valuable in studying millimeter wavelength systems.

The Cassegrainian antenna assembly consists of a 4.57-m diameter paraboloidal reflector with a hyperboloidal subreflector. The antenna mount is secured to the top of a stable 5-m tower. The tower is, in turn, secured to four building columns on the roof of a two-story laboratory building located in El Segundo, California, vicinity of Los Angeles, Fig. 1. The mount is equatorial (polar). Long-term building movements are corrected by the incorporation of tilt-angle transducers which generate a voltage proportional to tilt. These voltages are introduced into the servomechanism control loop as a continuous error function. Thermal gradients at the reflector surface and supporting tower are controlled by the use of a highly diffusing white paint.

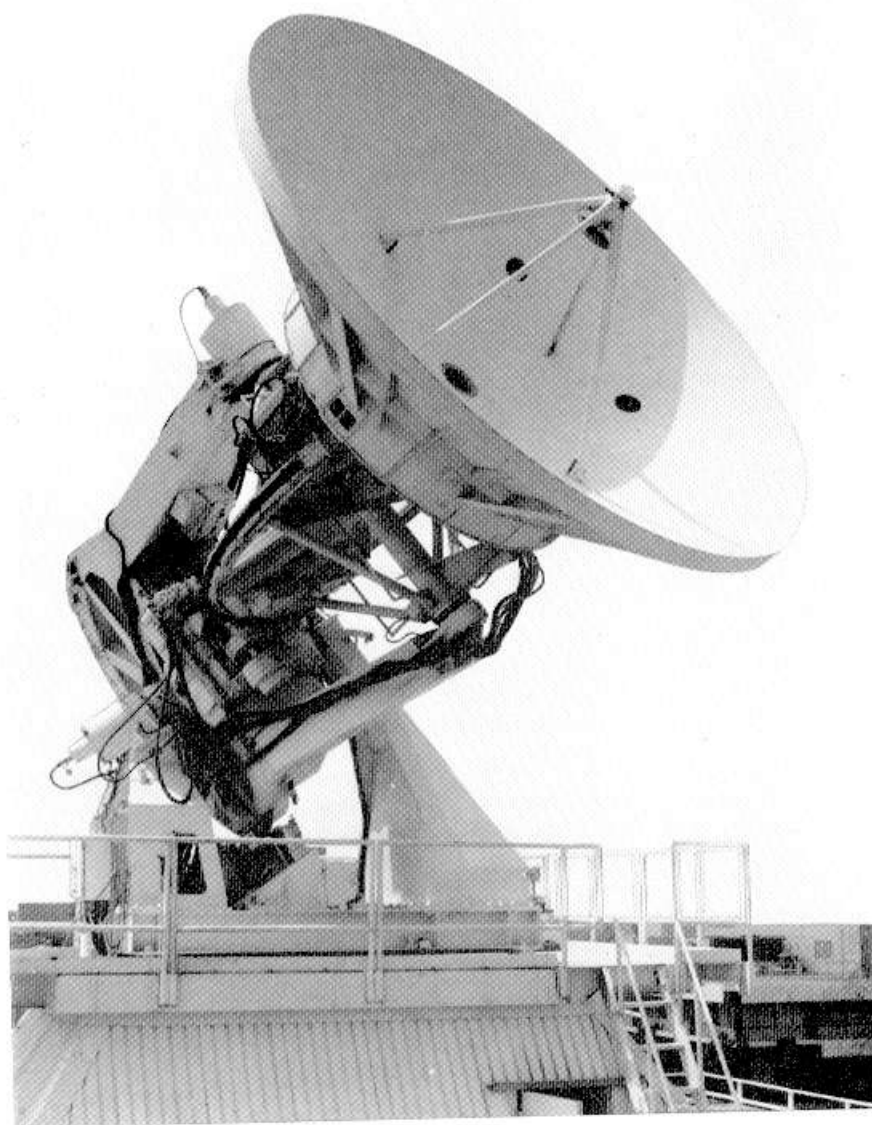


FIG. 1 The 4.57 m millimeter-wave antenna

**Antenna characteristics** – The antenna, as currently being used at 3.2 mm, has the characteristics given in Table 1. A diagonal horn (10) is used as the primary feed to obtain circular symmetry of the radiation pattern. The feed horn is approximately 46 cm long, this length serving two purposes: it minimizes the aperture phase deviation and it ensures a low-loss wave-guide section to the receiver input. Dry air is pumped continuously through the wave-guide feed lines and exits through the feed horn. Other advantages of the diagonal horn include good back-lobe suppression and ease of obtaining circular polarization.

The overall antenna pointing control system has a pointing accuracy of better than 20 seconds of arc, and possible tracking rates range from 0.001 to 3°/s. The pointing accuracy and dynamic tracking range, along with the in-line digital data-processing unit, make it possible to perform high-resolution measurements on objects ranging from celestial bodies to low-altitude earth-orbiting satellites.

TABLE 1

## MILLIMETER-WAVE ANTENNA CHARACTERISTICS

Reflector diameter	4.57 m (15 ft)
$f/D$	0.3
Magnification factor	14.74
Beamwidth, half-power:	
At 70° elevation angle	2.8'
At 15° elevation angle	3.1'

(Broadening at lower elevation angles caused by atmospheric turbulence.)

Gain:	
Computed	70.5 dB
Measured at 1.15° elevation angle	$70.3 \pm 0.4$ dB (1 $\sigma$ )
Aperture efficiency at 70.3 dB gain	53%
Solid angle main beam efficiency (computed)	76% (approx.)

The final measured reflector contour accuracy with respect to a true parabola, with the antenna directed at the zenith, is 0.046 mm r.m.s. (5). At horizon attitudes, the r.m.s. value degrades to 0.091 mm, i.e.,  $\lambda/16$  at 1.46 mm (205 Gc/s). Although the reflector is not unusually large physically, it is extremely large in terms of its electrical aperture, i.e.,  $D/\lambda = 3130$  at 1.46 mm. The inner 1.83 m (6 ft) diameter has a measured contour accuracy of 0.028 mm, which is better than  $\lambda/32$  at 1 mm (300 Gc/s). These contour accuracy measurements include the effects of solar heating and wind velocities up to 32 km/h.

**Gain and pattern measurements: remote facility** – A remote transmitting facility has been installed at a distance of 18.95 km ( $2D^2/\lambda = 13$  km at a wavelength of 3.2 mm) from the SRSF. The elevation is 450 m at the transmitter and 45 m at the vertex of the 4.57 m antenna. When corrected for

curvature and refraction, the calculated elevation angle becomes approximately  $1.15^\circ$ . The transmitting Cassegrainian-fed antenna (0.61 m or 2 ft diameter) has a gain of approximately 53 dB and a half-power beamwidth of 22 min. Its E-field polarization is continuously adjustable through  $360^\circ$ .

The radiometer used for making astronomical observations at the SRSF also served as a receiver for the antenna measurements. A block diagram of the system used for the measurements is given in Fig. 2. The reference antenna is a diagonal horn fabricated using the same mandrel as that used for the primary feed. The reference antenna has a measured gain of  $28.48 \pm 0.05$  dB peak at 3.2 mm and a half-power beamwidth of  $6.6^\circ$ . Figure 3 is a plot of the radiometer indicator relative response with a RC network response plotted for comparison. The integrated noise bandwidth of the radiometer output is approximately 1.5 c/s.

Large scintillations in received power made it impossible to take measurements on a point-to-point basis. Figures 4 and 5 are typical recordings of the power received with the antenna locked in position. The recorder scale is linear in power. The baseline (zero received signal condition) is nearly straight, which indicates a high level of receiver stability over the measurement interval and a low level of receiver noise. The power variations indicated for the strong signal condition therefore cannot be attributed to receiver instability or noise. The integrated noise bandwidth used in obtaining the plot of Fig. 4 is approximately 1.5 c/s. Figure 5 shows simultaneous recordings of the strong signal-received power for two output noise bandwidths (1.5 c/s for the top trace and 10 c/s for the lower trace). The frequency characteristics of the power fluctuations are essentially the same in both plots, indicating that the primary fluctuations are below 1.5 c/s. Therefore, the post-detection filter did not affect the observed fluctuations to any appreciable extent.

Possible sources for these variations in received power are transmitter instability, radiometer drifts, and atmospheric turbulence. However, frequent checks of the transmitter power level and frequency during measurement periods showed that the oil-bath-stabilized 3.2 mm klystron remained stable in both power output and frequency. Also, during the measurements, the radiometer was checked periodically, and its drift was found to be orders of magnitude less than the scintillations in received power. The transmitter frequency was chosen so as to be centered on a flat portion of the radiometer response, and measurements made over a short distance of the order of 0.3 km showed no scintillations in received power. Thus, the evidence clearly indicates that the scintillations were caused by atmospheric turbulence occurring along the 18.95 km path.

Because of these scintillations it was necessary to use statistical methods to interpret the antenna measurement data. The data processor/computer was so programmed that, after sampling the radiometer output, the data processor output indicated the number of samples, the mean and standard deviation of the sample distribution, and the time.

To take the measurements, the attenuator of the main-beam channel is set so that its output is near that of the reference-horn channel. The antenna is then locked in position, and alternate readings of 10 s duration are taken while sampling the reference antenna output and 20 s while sampling the

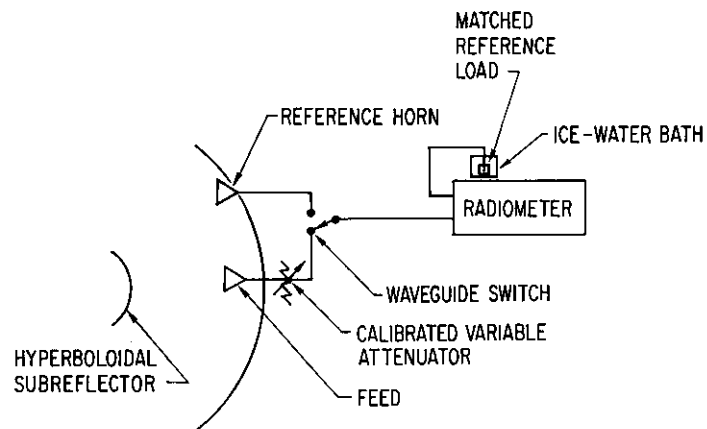


FIG. 2 Measuring circuit block diagram

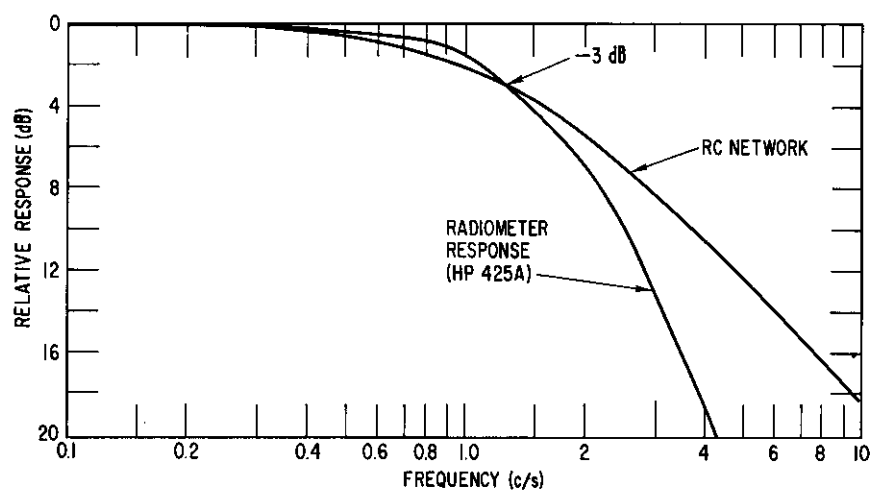


FIG. 3 Radiometer output relative response

AVERAGE POWER AT ANTENNA OUTPUT  
 TERMINAL  $\approx -57$  dBm,  $\beta \approx 1.5$  c/s

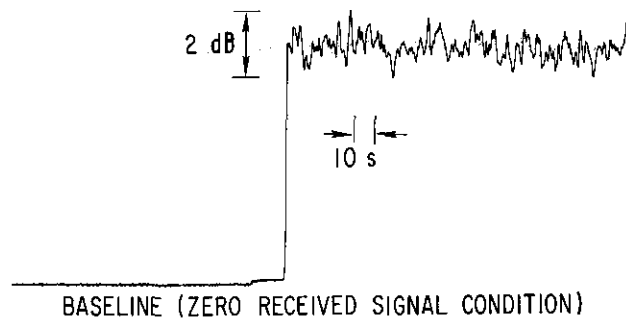
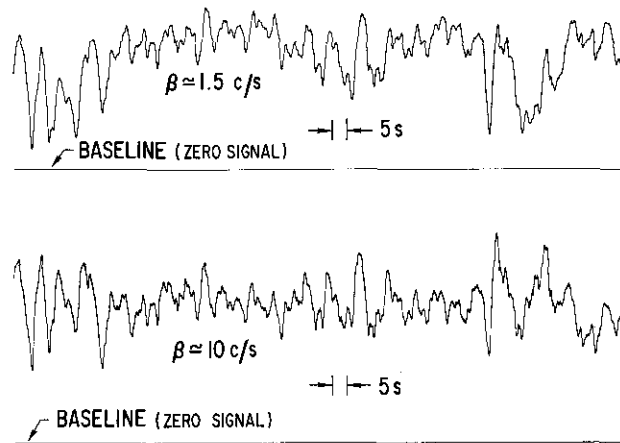


FIG. 4 Scintillation of main beam power



UPPER TRACE NOISE BANDWIDTH:  
 1.5 c/s; LOWER TRACE: 10 c/s.

FIG. 5 Scintillation of main beam power, simultaneous recordings

main antenna output. The mean outputs obtained just before and just after the main antenna measurement are then averaged. The average is taken as the value the reference antenna output would record if it could be measured simultaneously with the main antenna output. The validity of this technique is based on the assumption that the longer-term variations in received power in the reference antenna channel are linear and monotonic during a given measurement.

Groupings that quite obviously did not meet this requirement were rejected. Figures 6 and 7 are strip-chart recordings made during antenna gain measurements on a typical day and a quiet day, respectively. A value of gain is computed for each 40 s data interval. Because of variations in atmospheric refraction during gain measurements it was necessary to probe a solid angle in the vicinity of the expected maximum return position of the main antenna. Figure 8 is a plot of a typical probing. The value of gain shown for each point is the mean value for the sample; the peak deviations are shown alongside. This plot, and other similar ones, clearly indicate a shifting of the main beam antenna pattern during a measurement period (because of atmospheric refraction variations). Thus, one has the problem of making measurements wherein sufficient time must be spent sampling a point in order to obtain meaningful data and yet wherein the time spent must not be so long that the beam has shifted.

Measurements recorded over a period of 3 days yielded a mean value of antenna gain of  $70.3 \pm 0.4$  dB ( $1\sigma$ ). The uncertainty of the mean value includes a  $1\sigma$  value of 0.15 dB measurement error. This value of gain represents an aperture efficiency of approximately 53 per cent. All gain measurements were made at an elevation angle of  $1.15^\circ$ . Since the variations noted are due to atmospheric effects, it is expected that these variations will decrease in magnitude and frequency with an increase in elevation angle.

Pattern measurements are made in a manner similar to that used for the gain measurements. However, since pattern measurements are relative, the only critical component is a precision attenuator. Figure 9 is a plot of some typical measured patterns compared with a theoretical plot. The theoretical plot includes the effects of subreflector blockage, but not blockage due to the spars. Therefore, one would expect higher sidelobes in the measured data. There is a marked difference in the patterns taken on different days. This is to be expected because atmospheric conditions have considerable effect on the measured patterns and these conditions are continuously changing. In general, the measured half-power beamwidth and sidelobe level are higher than theoretical. On rare occasions there was only moderate beamwidth broadening in orthogonal patterns. However, on most occasions there was modest broadening in one plane and considerable broadening in the orthogonal plane. At other times this condition was reversed. On no occasion did this extensive broadening occur in both planes during one measurement period.

Unfortunately, with the point-by-point measurement technique it takes about one hour to make one pattern measurement. There is, most probably, a refraction change, or changes, during this period. Therefore the size of the half-power beamwidth indicated by the pattern measurement is probably a pessimistic one. The increase in sidelobe level, which is higher than can be

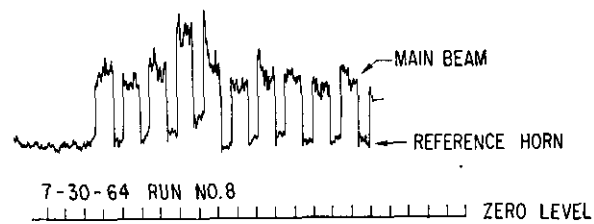


FIG. 6 Gain measurement, average atmosphere

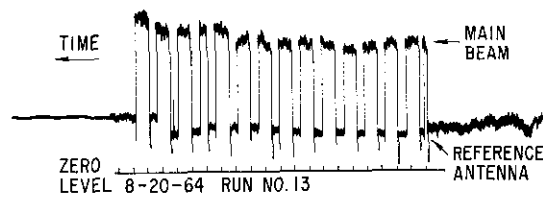


FIG. 7 Gain measurement, quiescent atmosphere

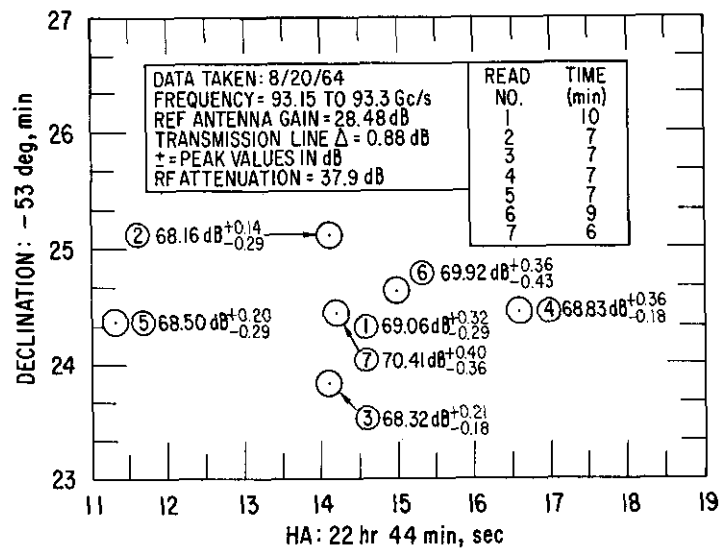


FIG. 8 Gain plot, 4.57 m antenna



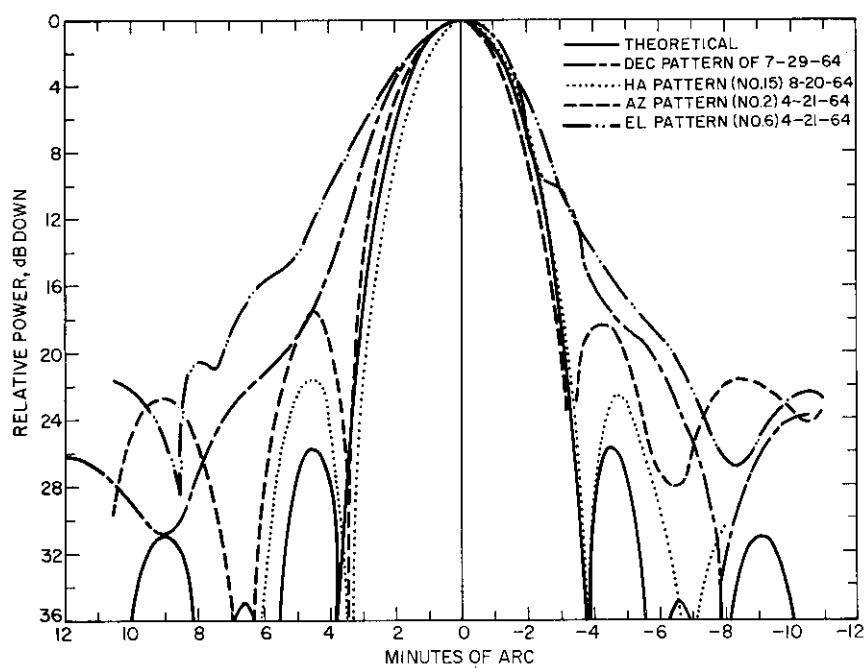


FIG. 9 Measured patterns of 4.57 m diameter antenna (3.2 mm transmitting source at elevation angle of  $1.15^\circ$  and located 18.95 km away)

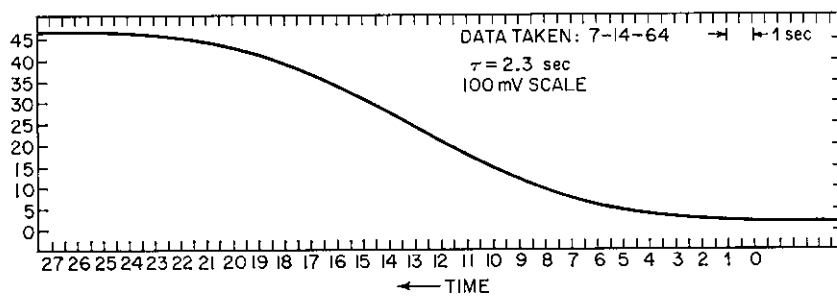


FIG. 10 Sun drift curve, forward slope

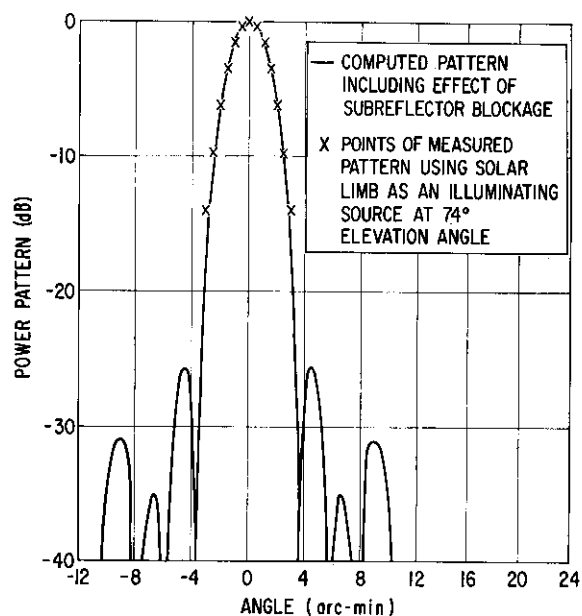


FIG. 11 Computed and measured radiation patterns

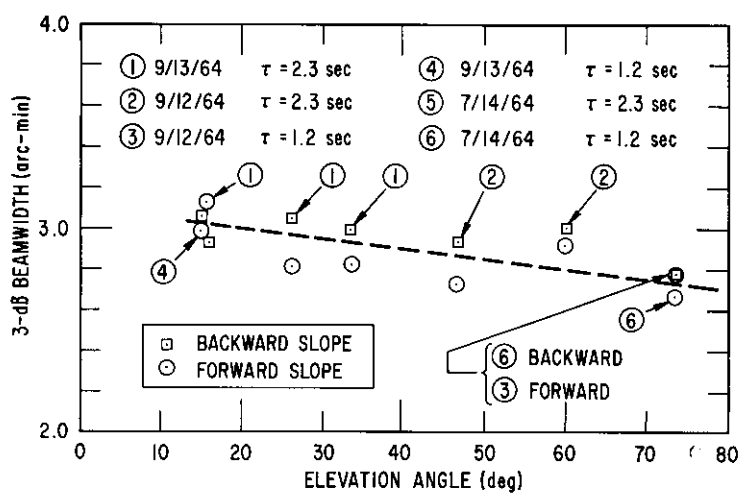


FIG. 12 Beamwidth (3 dB) versus elevation angle using solar limb as illuminating source

explained by spar blockage, can be attributed to the incoherence of the received wavefront caused by atmospheric variations. Due to the separation required for far-field conditions, the antenna looks through a greater amount of atmosphere than at the zenith position. The 18.95 km path used for these measurements is equivalent to approximately 3 atmospheric thicknesses from the standpoint of oxygen absorption and from 10 to 13 thicknesses for water vapor. Also, a propagation path close to the ground is subject to many temperature gradients and variations. For the case of radio-astronomy measurements, the antenna would normally be operated at relatively high elevation angles, and, therefore, the pattern characteristics should more nearly approach theoretical values.

**Sun measurement** – By locking the antenna in a position where it points at the declination of the sun and slightly ahead in hour angle, the normal rotation of the earth will cause the antenna beam to drift across the sun in hour angle. The measured output is referred to as a sun-drift curve. A portion of a drift curve is illustrated in Fig. 10. Figure 11 shows pattern data as determined from sun-drift data in comparison with the computed pattern. These data were taken at an elevation angle of  $74^\circ$ . Very good agreement with the theoretical pattern was achieved, but lack of sensitivity prevented obtaining sidelobe data.

Figure 12 is a plot of half-power beamwidth versus elevation angle as determined from sun-drift curves. On the basis of these preliminary data, the conclusion can be drawn that there is a general increase of beamwidth for this millimeter-wave antenna operating at 3.2 mm as the elevation angle is decreased. The beamwidth varies from about 2.8 min at a  $70^\circ$  elevation angle to 3.1 min or more at a  $15^\circ$  elevation angle.

#### PROPAGATION THROUGH THE ATMOSPHERE

The properties of the 3.2 mm atmosphere are principally determined by the atmospheric oxygen and water vapor, although some of the less-abundant gases, including those that are man-made, have lines in this wavelength region. The problem is in detecting these weak lines in the atmosphere, rather than in their effects on propagation over a broad wavelength interval such as the one used in this study. A Dicke-type radiometer was used in conjunction with the 4.57 m antenna for making the measurements. A block diagram of the system is shown in Fig. 13. The radio-frequency bandpass of the receiver is approximately 1.2 Gc/s. During the period in which the measurements were taken, the sensitivity at the antenna terminals,  $\Delta T_A$ , which is defined as the detected r.m.s. temperature differential that yields a receiver output signal-to-noise ratio of unity, was approximately 3°K for a 1 s integration time.

The results discussed in this section are essentially as reported by F. Shimabukuro (11).

**Absorption by oxygen and water vapor** – The expression used in this paper for the collision-broadened lines is the Van Vleck-Weisskopf equation (12–14) modified by the findings of subsequent experiments (15, 16). The oxygen absorption is:

$$k_0 = 6.67 \times 10^{-5} \frac{P}{T^2 \lambda^2}$$

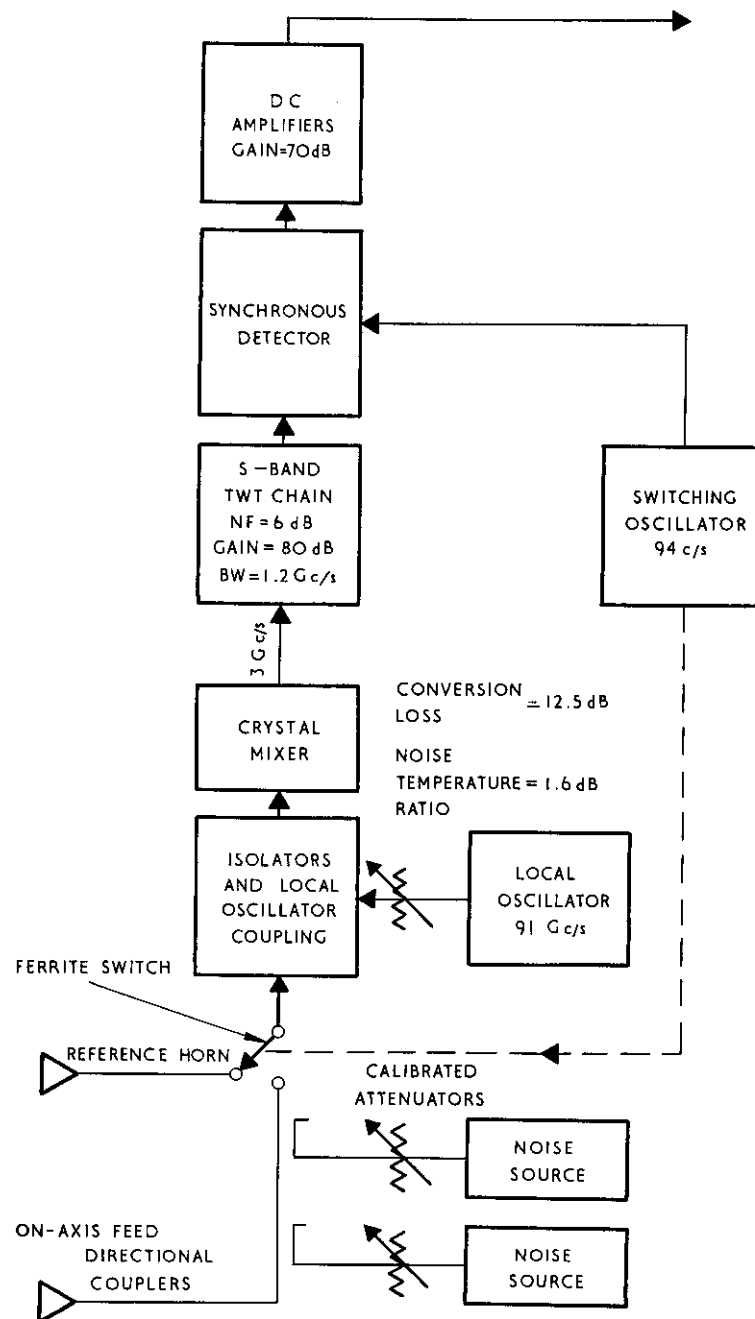


FIG. 13 Block diagram of the system

$$\left[ \frac{\frac{\Delta\nu}{c}}{\left(\frac{1}{\lambda} - \frac{1}{\lambda_0}\right)^2 + \left(\frac{\Delta\nu}{c}\right)^2} + \frac{\frac{\Delta\nu}{c}}{\left(\frac{1}{\lambda} + \frac{1}{\lambda_0}\right)^2 + \left(\frac{\Delta\nu}{c}\right)^2} + \frac{\frac{\Delta\nu}{c}}{\left(\frac{1}{\lambda^2}\right) + \left(\frac{\Delta\nu}{c}\right)^2} \right] \quad (1)$$

where  $k_0$  is in nepers (N)  $\text{cm}^{-1}$ ,  $T$  is the temperature in  $^{\circ}\text{K}$ ,  $P$  is the total pressure in millibars (mb),  $\lambda$  is the wavelength in cm,  $\lambda_0$  is 0.5 cm, and  $\Delta\nu/c$  is the line-width constant. The term  $\Delta\nu/c$  is:

$$\frac{\Delta\nu}{c} = 2.51 \times 10^{-3} P T^{-0.85} \quad (2)$$

and has a value of  $0.02 \text{ cm}^{-1}$  at  $P = 1013 \text{ mb}$  and  $T = 300^{\circ}\text{K}$ . This value is chosen to fit the high pressure data (15) and is consistent with measurements. The exponent of  $T$  is that determined from the results of Hill and Gordy (16), although the overall attenuation is not appreciably changed for exponent values between  $-0.5$  and  $-1.0$ . There is another oxygen line at 2.53 mm, but the absorption of this line at 3.2 mm is less by a factor of about 20 than that of the lines near 5 mm. The contribution of the 2.53 mm line was extrapolated from the data of Schulze and Tolbert (17).

The absorption for uncondensed water vapor is that determined by Schulkin (18) from the Becker and Autler data (19) and is given by:

$$k_w = \frac{e(C_1 \times 10^{-278/T})}{T^{7/2} \lambda^2} \left[ \frac{\frac{\Delta\nu}{c}}{\left(\frac{1}{\lambda} - \frac{1}{\lambda_w}\right)^2 + \left(\frac{\Delta\nu}{c}\right)^2} + \frac{\frac{\Delta\nu}{c}}{\left(\frac{1}{\lambda} + \frac{1}{\lambda_w}\right)^2 + \left(\frac{\Delta\nu}{c}\right)^2} \right] + C_2 \frac{e}{T^2 \lambda^2} \frac{\Delta\nu}{c} \quad (3)$$

where  $k_w$  is in  $\text{N cm}^{-1}$ ,  $C_1 = 23.7$ ,  $C_2 = (2.23 \times 10^{-2}) e/T + 7.18 \times 10^{-3}$ ,  $e$  is the vapor pressure in mb,  $\lambda_w = 1.349 \text{ cm}$ , and the line width is given by:

$$\frac{\Delta\nu}{c} = \frac{1.51 \times 10^{-3}}{T^{1/2}} (P + 3.7e) \quad (4)$$

The next strong water-vapor line occurs at 1.63 mm, and its absorption at 3.2 mm is negligible.

**Attenuation measurements** – The attenuation through the atmosphere was determined by measuring the intensity of an extraterrestrial source, the sun, through different zenith angles. The antenna can be pointed with an absolute accuracy of less than 30 seconds of arc; the sun could therefore be tracked even though it was optically not visible. The attenuation curve was obtained in the usual way. A reading was taken at the center of the sun; then a second reading was taken of the sky  $1^{\circ}$  away. The logarithm of the difference between the source and the sky background was plotted against the secant of the zenith angle. The slope of this plot is a measure of the zenith attenuation.

The attenuation measurements were usually made in the afternoon to utilize the data from the radiosonde that is released daily at 0000 UT (4 p.m.

PST on the previous day) at the Santa Monica Airport, which is located 13 km northwest of the antenna site. A data sheet obtained from the sounding is shown in Table 2. Plots of the theoretical attenuation coefficients computed from Eq. 1 and 3 for January 25, 1964, at 0000 UT are shown in Fig. 14. The attenuation is obtained by fitting a piecewise linear curve to the points.

TABLE 2

ATMOSPHERIC SOUNDING, 25 JANUARY 1964, 0000 UT

Pressure (mb)	Height (km)	Temperature (°K)	Dew-point temperature (°C)	Vapor pressure (mb)
1022	Surface	289.8	-1.2	5.70
1000	0.18	285.8	-7.8	3.40
880	1.24	278.0	-12.0	2.45
867	1.37	279.2	-9.5	3.00
850	1.53	278.2	-10.2	2.85
762	2.41	273.5	-13.2	2.20
726	2.79	275.8	-18.2	1.47
700	3.08	274.0	Missing	—
649	3.67	270.5	Missing	—
555	4.87	260.8	-28.8	0.57
506	5.56	255.5	-24.2	0.86
500	5.64	254.8	-25.2	0.80
400	7.26	243.8	-41.8	0.16
300	9.23	226.8	Missing	—
250	10.43	216.5	Missing	—
210	11.55	208.8	Missing	—
200	11.86	213.8	Missing	—
150	13.68	217.2	Missing	—
100	16.25	211.0	Missing	—

This corresponds to assuming that the attenuation can be approximated by a series of simple exponentials for different height intervals. The total attenuation can then be calculated by integrating the absorption through the atmosphere. The measured attenuation for January 25 (UT) is shown in Fig. 15. It is seen that the measured and calculated values are in fair agreement, i.e. 0.50 dB, measured, and 0.61 dB, calculated. This method of comparing the calculated and measured attenuation was used for the first 26 clear days of 1964, when both radiosonde and attenuation data were available. The results are shown in Table 3. If it is assumed that the calculated oxygen attenuation is accurate, then, from Table 3, one can get a statistically derived expression for the zenith attenuation, which is:

$$\alpha(\text{dB}) = 0.28 + 0.31w \quad (5)$$

where  $w$  is the precipitable water in cm (the height of water at the surface in that area if all the water vapor in the atmosphere is condensed out). Depend-

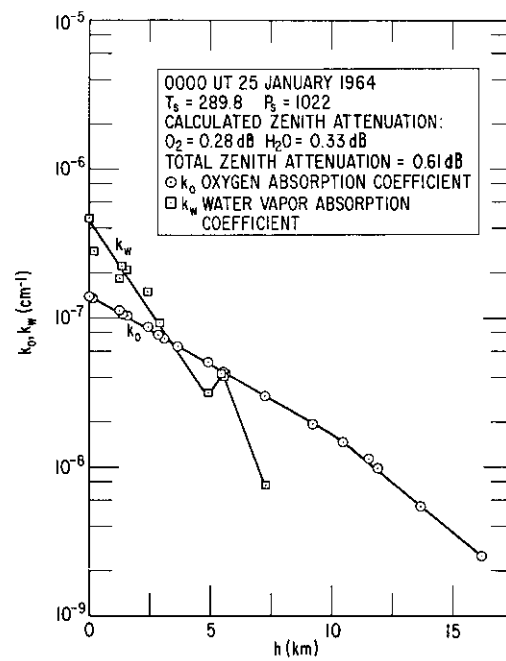


FIG. 14 Calculated absorption coefficients of oxygen and water vapor

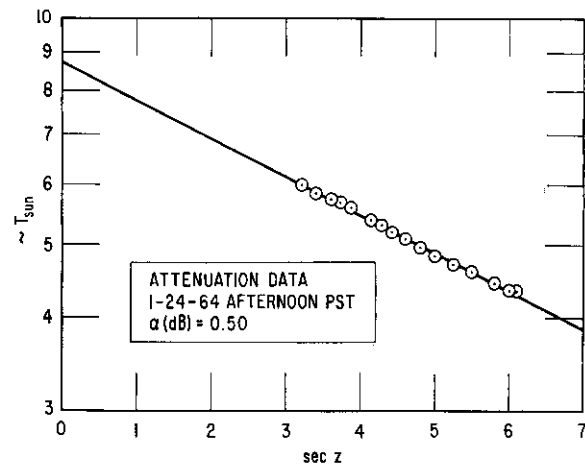


FIG. 15 Attenuation plot for the afternoon of January 24, 1964, PST



ing on the pressure and temperature distribution, the calculated oxygen attenuation varies between 0.26 and 0.30 dB, the attenuation being less on days with high temperature and low pressure. The U.S. Standard Atmosphere has a calculated oxygen attenuation of 0.28 dB (20).

The water-vapor distribution is a much more variable quantity, and the attenuation can be different from day to day, even though the precipitable water is the same. For example, in Table 4, the calculated water-vapor attenuation is given for the same amount of precipitable water, but with different density distributions and height intervals.

TABLE 3  
MEASURED AND CALCULATED ATTENUATIONS

Date (1964) 0000 UT		M Measured attenuation (dB)	C Calculated attenuation (dB)	Calculated O <sub>2</sub> attenuation (dB)	Calculated H <sub>2</sub> O attenuation (dB)
Jan.	3	0.58	0.54	0.27	0.27
	4	0.31	0.33	0.27	0.06
	8	0.67	0.56	0.27	0.29
	9	0.52	0.47	0.27	0.20
	10	0.44	0.45	0.27	0.18
	11	0.51	0.60	0.27	0.33
	15	0.52	0.66	0.28	0.38
	16	0.40	0.39	0.28	0.11
	17	0.59	0.68	0.29	0.39
	20	0.75	0.85	0.28	0.57
	23	0.65	0.65	0.30	0.35
	24	0.65	0.69	0.28	0.41
	25	0.50	0.61	0.28	0.33
	26	0.66	0.75	0.28	0.47
March	7	0.42	0.69	0.30	0.39
	10	0.64	0.73	0.30	0.43
	11	0.71	0.82	0.28	0.54
	12	0.79	0.75	0.28	0.47
	18	0.53	0.44	0.26	0.18
	24	0.85	0.91	0.30	0.61
April	4	0.62	0.93	0.29	0.64
	5	0.76	0.93	0.28	0.65
	7	0.52	0.69	0.30	0.39
	20	0.80	0.83	0.30	0.53
	25	0.70	0.84	0.30	0.54
	27	0.46	0.68	0.28	0.40

$$\sigma^2 = \frac{1}{26} \sum |M-C|^2 = 0.016$$

A plot of precipitable water versus zenith attenuation in 1964 is shown

in Fig. 16. An expression for the atmospheric attenuation can be obtained experimentally by plotting the measured attenuation versus precipitable water. The intercept is the oxygen attenuation. Measured attenuations on 93 clear afternoons in 1964 are plotted in Fig. 17 against the precipitable water obtained from the afternoon radio soundings. The scatter of the points is an indication of the variation in distribution of the water vapor and of temporal variations of attenuation. The least-squares-fit regression line yields excellent agreement with the statistically derived expression if we include only those more or less well-behaved points where the precipitable water was always less than about 2.5 cm. The agreement is not as good if those few widely scattered points above 2.5 cm of precipitable water are included. The least-squares fit for the regression line then gives, for 95 per cent confidence limits ( $2\sigma$ ):

$$\alpha(\text{dB}) = (0.18 \pm 0.08) + (0.40 \pm 0.06)w \quad (6)$$

Perhaps insufficient data have been gathered here. As more measurements are taken, it is believed that this difference will be resolved.

In the expressions for absorption, the important parameter is the line width, which is proportional to pressure. The oxygen distribution is fairly predictable, and it is expected that for a given area the day-to-day oxygen attenuation should not vary greatly. However, there may be seasonal differences if a region has wide temperature variations. In the case of the water vapor, the distribution is more variable, and changes from day to day can be expected. Generally, it can be stated that for the same amount of precipitable water the attenuation will be greater when the water vapor is concentrated lower in the atmosphere. Generally the water vapor is evenly enough distributed that on clear days Eq. 5 is a good indication of the attenuation. One should be careful in applying Eq. 5 or Eq. 6, especially the water-vapor contribution, to areas other than those that have weather conditions similar to the Los Angeles basin. Equations 1 and 3 show that the absorption is a function of both the pressure and the temperature.

TABLE 4  
WATER VAPOR ATTENUATION FOR DIFFERENT DENSITY  
DISTRIBUTIONS WITH THE SAME AMOUNT OF PRECIPITABLE  
WATER IN A STANDARD ATMOSPHERE

Density distribution (g/m <sup>3</sup> ) h in km	Distribution interval (km)	Calculated attenuation (dB)	Precipitable H <sub>2</sub> O (cm)
$5.1 \times 10^{-6}$	0 — 0.65	0.16	0.33
$(5.1 \times 10^{-6})e^{-1.55h}$	0 — 10	0.15	0.33
$(2.0 \times 10^{-6})e^{-0.37h}$	0 — 2.5	0.14	0.33
$(2.0 \times 10^{-6})e^{-0.6h}$	0 — 6.7	0.13	0.33

The theoretical expressions predict the actual physical situation well enough to warrant making some general observations about the absorption of

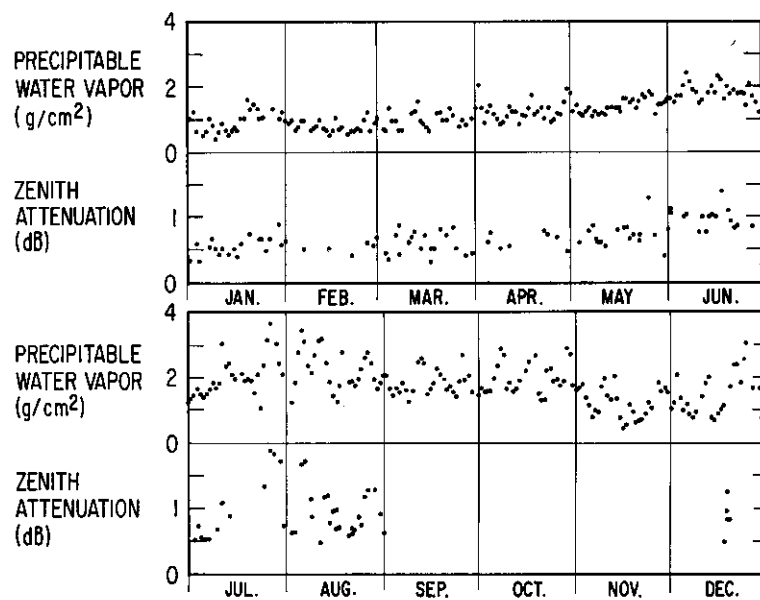


FIG. 16 Summary of zenith attenuation at 3.2 mm and precipitable water for the year 1964

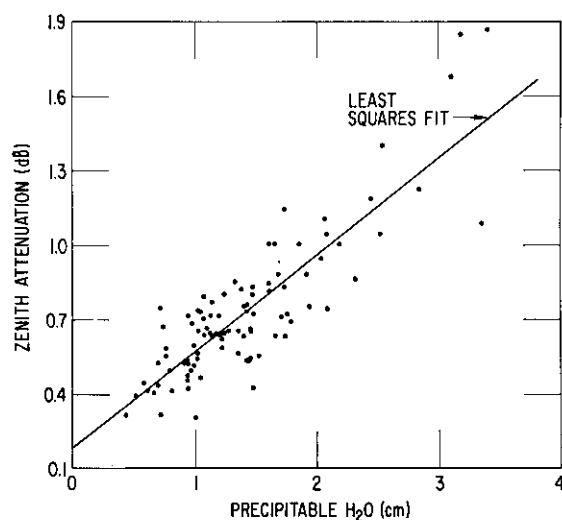


FIG. 17 Attenuation versus precipitable water - 1964

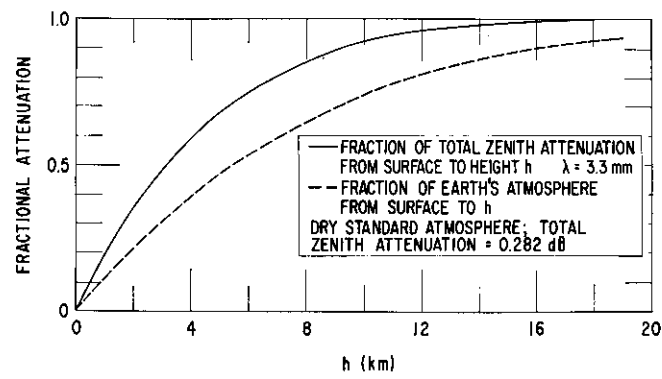


FIG. 19 Fraction of total attenuation from surface to height  $h$

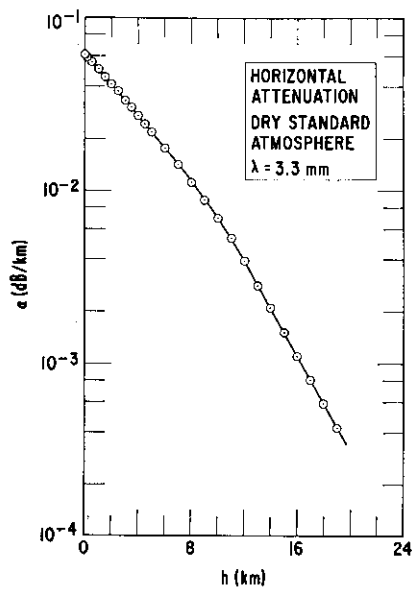


FIG. 18 Attenuation in dry standard atmosphere at different elevations

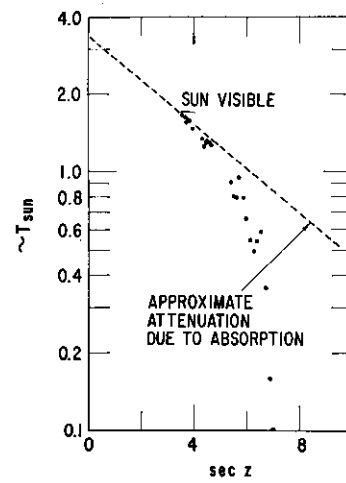


FIG. 20 Effect of thick clouds on attenuation

the dry atmosphere. The effect of water vapor will have to be analyzed for a specific distribution. The horizontal attenuation of dry air at different elevations is shown in Fig. 18, and the attenuation from the surface to some given elevation is shown in Fig. 19. The first 3.2 km, which comprises 32 per cent of the atmosphere, contributes half of the total attenuation. This is, of course, due to the pressure broadening of the complex of oxygen lines near 5 mm. Less than 1 per cent of the attenuation is due to the atmosphere above 17 km.

**Variations in precipitable water** – In Table 5 are listed the differences in the precipitable water in cm between the soundings at 4 a.m. and 4 p.m. PST. In the table,  $N$  is the number of days on which data were available,  $\Delta w$  is the average difference for the month, and  $\Delta w_m$  is the maximum difference for the month. If it is assumed that the change in attenuation is caused entirely by the change in the water-vapor content, then Eq. 5 can be used to estimate the change in attenuation over a 12 hour period. The maximum change in precipitable water between the morning and afternoon soundings occurred in July; this change of 1.4 cm corresponds to a change in attenuation of 0.44 dB. The average absolute difference in attenuation between the morning and afternoon for the year was approximately 0.08 dB.

TABLE 5  
DIFFERENCES IN PRECIPITABLE WATER BETWEEN  
4 A.M. AND 4 P.M. PST

1964 Month	N	$ \overline{\Delta w} $ (cm)	$ \Delta w_m $ (cm)
Jan.	28	0.24	0.56
Feb.	28	0.15	0.56
March	28	0.27	0.97
April	28	0.20	0.81
May	29	0.14	0.56
June	26	0.24	0.74
July	28	0.36	1.40
Aug.	27	0.29	0.84
Sept.	27	0.23	0.76
Oct.	30	0.27	0.92
Nov.	31	0.24	0.76
Dec.	29	0.35	0.86

$$\sum N = 339, \frac{1}{\sum N} \sum |\Delta w| = 0.25$$

From the previous discussion, it is apparent that one should be extremely careful in determining the brightness temperature of extraterrestrial sources in the millimeter wavelength region. The antenna temperature of an extraterrestrial source with a temperature of  $T_0$ , aside from a constant of proportionality, is:

$$T_A = T_0 e^{-\tau (\sec z)} \quad (7)$$

$$\ln T_A = \ln T_0 - \tau \sec z \quad (8)$$

where  $\tau$  is the attenuation constant at the zenith and  $z$  is the zenith angle. If  $\tau$  is constant with time, a plot of  $\ln T_A$  versus  $\sec z$  is a straight line and the slope is  $-\tau$ . The intercept at  $\sec z = 0$  is  $\ln T_0$ . If  $\tau$  is not constant with time, then the slope of a regression line fitting the points will be a false indication of the attenuation and the extrapolated intercept will no longer be the true temperature of the source. If the attenuation is changing linearly with time, an accurate determination of the source temperature can be made by averaging the pre- and post-transit values. In any case, many measurements should be made, both before and after transit, and more statistical weight should be given to those measurements during which the attenuation changes were small.

**Effects of rain, clouds, and fog** – The effects of thin clouds and thin layers of fog on propagation at 3.2 mm are quite small. In many cases they are undetectable in the sense that the measured attenuation as compared with that of clear days with a comparable amount of precipitable water is well within the scatter as depicted in Fig. 17. On the other hand, the effect of thick clouds and rain on propagation can be appreciable. The effect of thick cumulus clouds on the attenuation can be seen in Fig. 20, which indicates a rapidly increasing slope of the plotted points as the sun is occulted by the clouds. Measurements during rain are scarce, but on two occasions zenith attenuations of 3 dB and 4 dB were measured in drizzling rain. During the 4 dB measurement, 0.044 cm of rain fell in  $1\frac{1}{2}$  hours; it is not known whether the rainfall rate was uniform. It is difficult to compute the scattering loss due to the condensed water particles, because nothing is known about the drop-size distribution in the rain and the clouds on the particular days in question.

**Emission measurements** – Emission measurements made early in 1964 showed that the zenith emission temperature varied between 48 and 80°K. During the summer when the atmosphere is hotter and more humid, the emission temperatures are higher. The variation in emission is due not only to the attenuation but to the distribution of the absorbing particles and the temperature profile. The calculated emission temperature at zenith is:

$$T_e = \int_0^h \tau T \exp \left( - \int_0^h \tau dl \right) dl \quad (9)$$

where  $l$  is the length along the ray path and  $h$  is some convenient height where the attenuation is essentially zero.

The measured values are higher than the calculated values, but the difference can be attributed to the sidelobe contributions. The full main beam of the antenna is calculated to radiate 76 per cent of the total energy, and the rest of the sidelobes radiate the remaining 24 per cent (9). On a day when the measured zenith emission was 57°K, the calculated emission (from the radiosonde data) was 33°K. Then:

$$T_A = 0.76 T_m + 0.24 T_s \quad (10)$$

where  $T_m$  is the main lobe and  $T_s$  is the sidelobe contribution to antenna

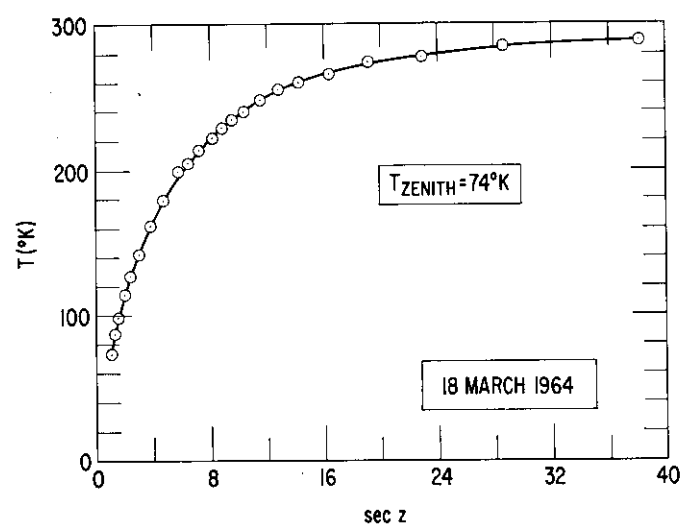


FIG. 21 Sky emission temperature on a clear day

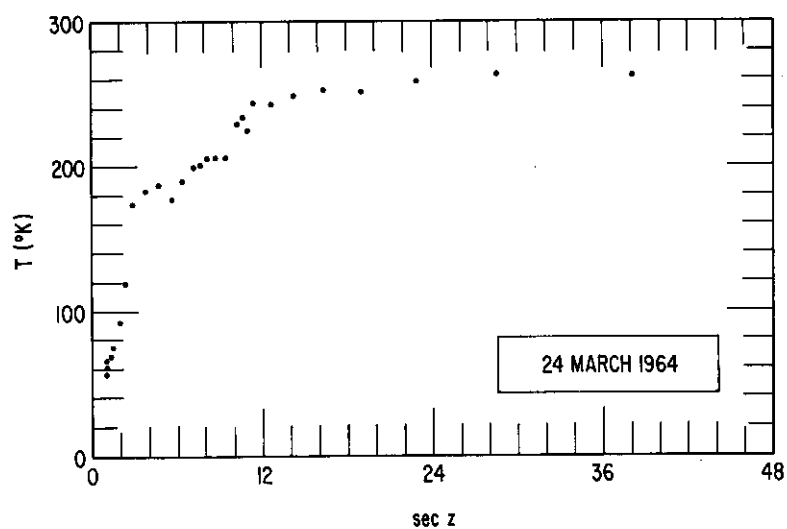


FIG. 22 Sky emission temperature on a day with scattered clouds

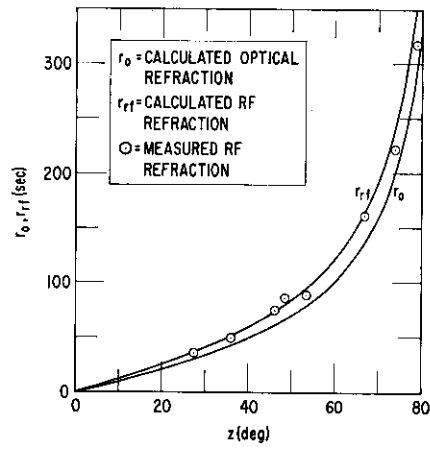


FIG. 23 Refraction measurements on September 1, 1964

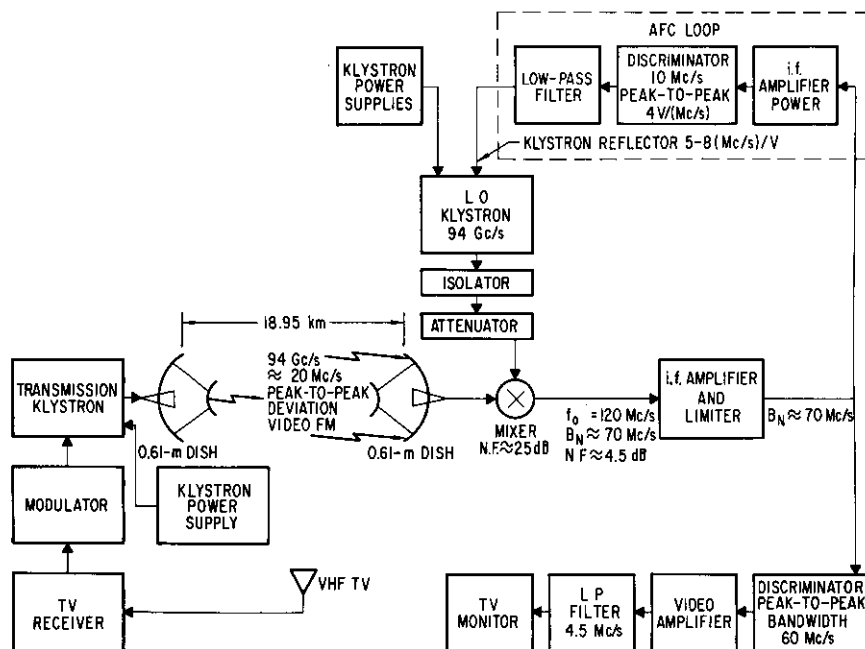


FIG. 24 Experimental millimeter-wave video transmission link



temperature. From the above, it is not unreasonable to assume that the average sidelobe level was looking at an average temperature of 133°K. Emission measurements on a clear day and on a day with scattered clouds are shown in Figs. 21 and 22.

**Refraction measurements** – The refraction measurements were made in the following manner. The sun was tracked at the solar rate across the sky. The optical and radio centers of the sun were determined by recording the optical and radio edges of the sun in right ascension and declination and taking the averages. What is measured is the offset between the optical and radio centers. With the tracking capability of the 4.57 m antenna, a single measurement is sufficient to determine the optical center within 10 seconds of arc and the r.f. center within 20 seconds of arc. Single measurement plots are, in general, similar to that of Fig. 23. The optical refraction is assumed to be accurate, and the measured difference is plotted from the optical refraction curve. The optical refraction is obtained from Van Vleck and Weisskopf (12):

$$r_0 = \frac{52.2}{613 + T} P \tan z \quad (11)$$

and the r.f. refraction is that determined by Smith and Weintraub (22) and is given by:

$$r_{rf} = \frac{16}{T} P + \frac{4810 e}{T} \tan z \quad (12)$$

where  $r_0$  and  $r_{rf}$  are measured in seconds of arc,  $P$  is the total surface pressure in mb,  $T$  is the surface temperature in °K, and  $e$  is the surface vapor pressure in mb.

If the radio refraction at 3.2 mm has to be known within 20 seconds of arc, Eq. 12 is adequate for zenith angles of less than 70°. From the refraction measurements, it appears that Eq. 12 applies too much correction for  $z > 70^\circ$ . It is not known whether the expression for the r.f. refraction is applicable for 3.2 mm waves only for  $z < 70^\circ$  or whether there were horizontal gradients in the water-vapor distribution when the measurements were taken. However, because of the attenuation of the atmosphere at short millimeter wavelengths, observations at large zenith angles will not be common. Information on refraction at other frequencies is given in Chapter 1-1. Figure 8 of Chapter 1-1 and Fig. C of the subsequent discussion can be compared with Fig. 23 of this chapter.

**Remarks** – The propagation characteristics, aside from turbulence effects, of 3.2 mm waves through the atmosphere have been determined. The Van Vleck expressions for the absorption by oxygen and water vapor are adequate for approximate values. Thin clouds and thin layers of fog have little effect on propagation, but the effects of thick clouds and rain can be appreciable. The emission temperature of the atmosphere is consistent with the absorption if one takes into account the contribution of the sidelobes. In determining the brightness temperature of an extraterrestrial source by the usual method of plotting the intensity as a function of  $\sec z$  and extrapolating to  $\sec z = 0$ , one should be aware of the possibility that the attenuation may be changing during the measurement. The best procedure is to take pre- and post-transit readings on the same day and use the average as the value for that day.

The usual expression used for radio refraction is accurate within 20 seconds of arc for 3.2 mm waves for  $z < 70^\circ$ .

#### PROPAGATION IN THE TROPOSPHERE

**General**—The preceding section has been concerned with zenith attenuation factors and emission and refraction measurements at relatively large elevation angles. For space applications of millimeter waves an understanding of these factors at low elevation angles is also required in order to more completely assess the limitations of systems such as those utilizing low-altitude satellites. Consequently, investigations of propagation in the troposphere at 3.2 mm have also been undertaken at Aerospace Corporation. The results discussed in this section are essentially those reported by Hoffman, Wintroub, and Garber (23).

These investigations began with qualitative evaluation of tropospheric effects on transmission of audio and video information over an 18.95 km path between the Aerospace facility in El Segundo and the remote laboratory facility described previously. The objectives were to determine, subjectively, whether tropospheric turbulence would result in phase dispersion (for a moderate bandwidth (30 Mc/s) FM signal) of sufficient magnitude to cause degradation of a high-quality (baseband approximately 4 Mc/s) television picture. In addition, the television picture would show results of multipath, if it were of significant magnitude, by "ghosts" in the received material. Quantitative investigations require considerably more sophisticated instrumentation and consequently were planned for later investigations. The experiments performed thus far have not indicated any subjective degradation of this type of signal from tropospheric turbulence over the 18.95 km path. However, moderate rainfall, as expected, did result in significant attenuation of the received signal.

**Audio and Video transmission**—High fidelity audio and "off-the-air" television video signals have been transmitted from the remote facility to the Aerospace building in El Segundo. A block diagram of the system is shown in Fig. 24. The equipment components and a received television picture are shown in Fig. 25. Initially, a high-fidelity tape supplied the modulation signal for the transmitter. The FM receiver discriminator output, after amplification, activated a conventional loudspeaker. In subsequent experiments on video transmission, modified television receivers were used. Television video was derived from a modified receiver whose composite video-audio signal was utilized to frequency-modulate a 3.2 mm klystron. The 100 mW transmitted signal, large-deviation FM ( $\sim 20$  Mc/s peak-to-peak), was received with a 3.2 mm FM receiver of relatively simple design. The receiver noise figure was approximately 25 dB. Amplitude limiting of the 120 Mc/s i.f. amplifier (20 dB under zero signal conditions) was used to eliminate effects of the anticipated signal amplitude scintillation resulting from tropospheric turbulence. Television-picture quality was not degraded under conditions of high turbulence as long as the minimum received signal was well above the video threshold of the receiver. In Table 6 system and weather characteristics are given for one day during which a good-quality television picture was received while light to moderate rainfall was occurring over much of the 18.95 km path. The i.f. bandwidth was narrowed to approximately 28 Mc/s

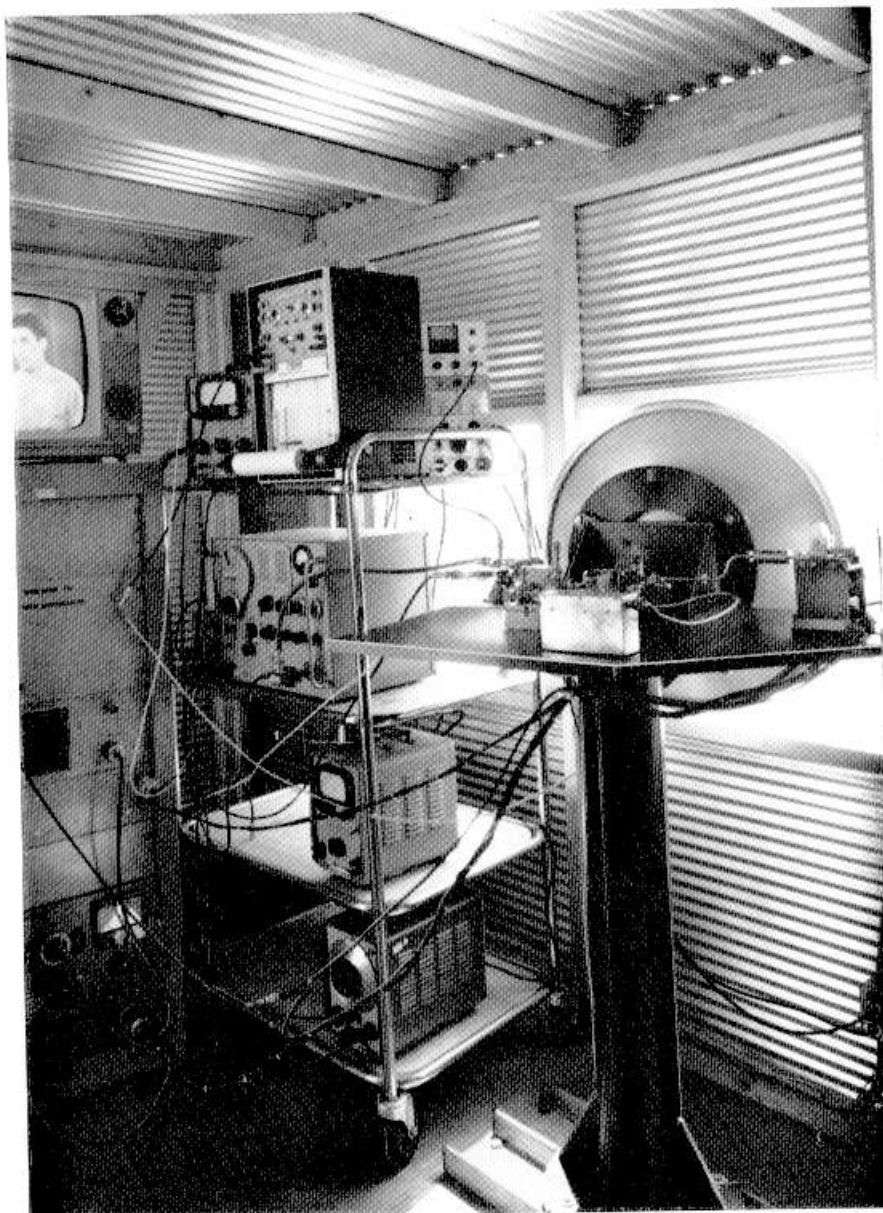


FIG. 25 The 3.2 mm television receiving system

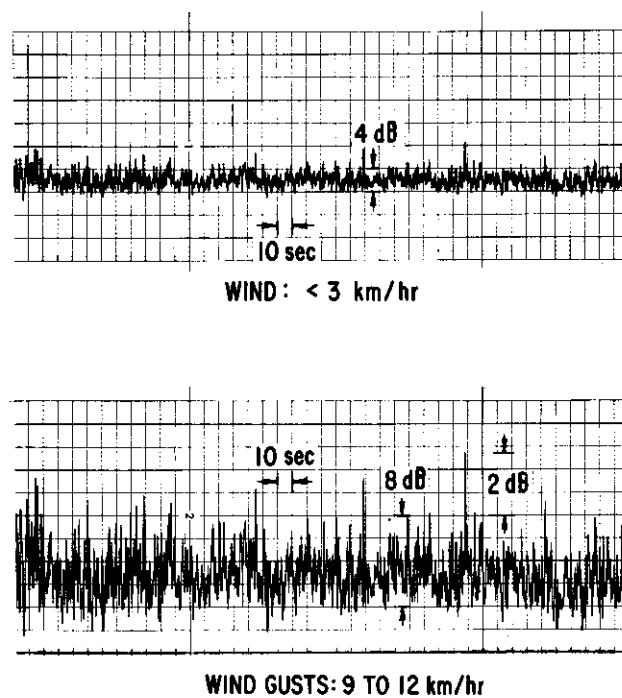


FIG. 26 Received signal amplitude scintillation resulting from tropospheric turbulence

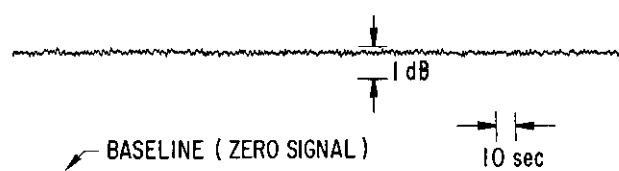


FIG. 27 Received signal amplitude scintillations on a foggy day

for this test. The received power level for no tropospheric attenuation, as listed in Table 6, is estimated to be accurate within  $\pm 1$  dB.

A received-signal power detector output test point, prior to limiting, provided a monitor point to indicate amplitude scintillation of the received signal. Two such recordings made on the same day are shown in Fig. 26. The upper recording was taken when the velocity of the wind was less than 3 km/h; the lower recording was taken during wind gusts of 9 to 12 km/h. Figure 27 is a recording of received signal power, before limiting, on a day when moderately heavy fog covered the entire path. The received-signal scintillation was extremely small. This lack of turbulence and refractive effects is due to the quiet, homogeneous properties of the lower troposphere such as is experienced on a calm but foggy day. However, the attenuation of the transmitted signal was larger than usual.

TABLE 6

## PERFORMANCE CHARACTERISTICS, PROPAGATION THROUGH RAIN

Thermal noise	-174.0 dBm/c/s
28-Mc/s i.f. bandwidth	+74.5 dB
Noise figure	+25.0 dB
<hr/>	
Receiver noise level	-74.5 dBm
S/N required if i.f.	+12.0 dB
<hr/>	
Receiver threshold	-62.5 dBm
Received power (no tropo. atten.)	-37.0 dBm
<hr/>	
Tropo. attenuation at threshold	25.5 dB
Average attenuation rate	1.35 dB/km
Estimated average rainfall rate	3 mm/h
<hr/>	
<b>Calculation of received power</b>	
Free space attenuation (18.95 km)	-157.4 dB
Calculated system gain ( $G_T + G_R$ - line losses)	+100.4 dB
Power transmitted (100 mW)	+20.0 dBm
<hr/>	
Received power (no tropo. atten.)	-37.0 dBm

Qualitative observations to this time indicate a somewhat equal tradeoff in the ability of a FM-limiting type of receiver to handle the two extremes of turbulence near threshold. The average received power is higher on dry days, but accompanying winds cause peak power excursions of 10 dB or more. Limiting must occur well below these peak excursions. On foggy days with little or no scintillation, the received power may be attenuated by 10 dB or more and no change in signal quality can be discerned, other conditions being equal.

## ATTENUATION IN THE TROPOSPHERE

The 18.95 km path used for the previously described experiments provided a means for measurement of the tropospheric attenuation over a nearly horizontal path. Calculations based on theoretical assumptions (12-19) indicate that the total attenuation on a reasonably dry day could be as low as 7 dB for the entire path (see Fig. 28 and 29). The equations used for plotting Fig. 28 and 29 are modified versions of the Van Vleck and Schulkin relationships for absorption by oxygen and water vapor, respectively. These equations were used in calculating the expected tropospheric attenuation. The expression used to calculate the values plotted in Fig. 28 is:

$$k_w = \frac{170}{T^{7/2}} e \left( e + \frac{P}{3.7} \right) \left( T + 3.11e + \frac{80.2}{T^{1/2}} \right)$$

in dB/km.

Since 7 dB is a relatively small value in comparison with the total possible for this path, the attenuation must be measured accurately. It is necessary to eliminate, as completely as possible, measurement errors that could accrue from the instrumentation. The most practical approach to remove instrumentation errors is to measure precisely the power transmitted and received over distances that are short enough to make the tropospheric attenuation negligible and yet still sufficiently distant that no appreciable Fresnel zone effects are present in the antenna systems. Distances of 139, 172, 218 and 314 m were used ( $2D^2/\lambda \simeq 230$  m).

The power applied to the antenna terminal from the transmitter and the power at the receiving antenna output terminal were accurately measured at each distance. The mean of these powers, extrapolated over the 18.95 km path, yielded the power expected at the receiving terminal, exclusive of tropospheric attenuation, to within 0.3 dB (90 per cent confidence). Subtracting the actual received power from the calculated received power then yields the total tropospheric attenuation for the weather conditions at the time of the measurement.

**Instrumentation** – A block diagram of the transmitter used for the attenuation measurements is shown in Fig. 30. A 3.2 mm klystron with a power output of 20 mW is used as the power source. The klystron output is coupled to the antenna feed through an E-band isolator, calibrated rotary-vane attenuator, 20 dB directional coupler, and rotary joint. A photograph of the E-band millimeter-wave components mounted on the transmitting antenna base is shown in Fig. 31.

Power radiated from the transmitter was monitored during propagation measurements by use of a calibrated E-band bolometer system. A portion of the radiated power was sampled through a 20 dB coupler (square-wave modulated at 1 kcs) with an E-band ferrite switch, and was detected with a calibrated E-band bolometer. The amplitude of the resulting 1 kcs square wave was then measured to determine the power applied to the antenna input terminal. Periodic calibration of the bolometer monitoring system was necessary to ensure that constant radiated power was maintained for all propagation measurements regardless of the time interval between measurements. For this purpose, a calorimeter and a precision rotary-vane attenuator were used as standards in power measurements of the transmitter and receiver.

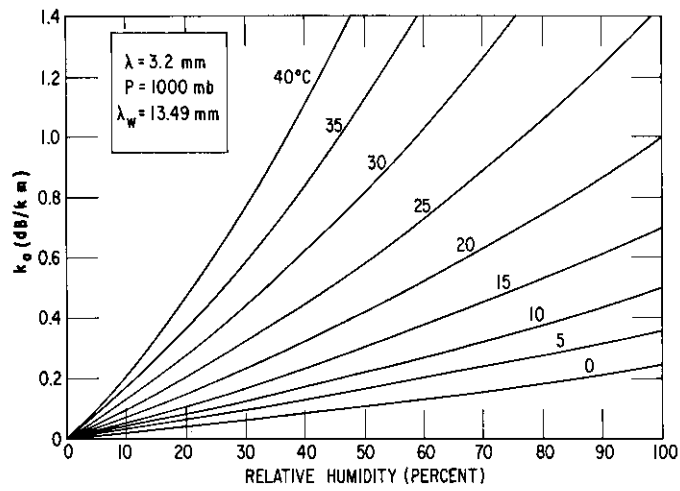


FIG. 28 Attenuation in the troposphere due to water vapor

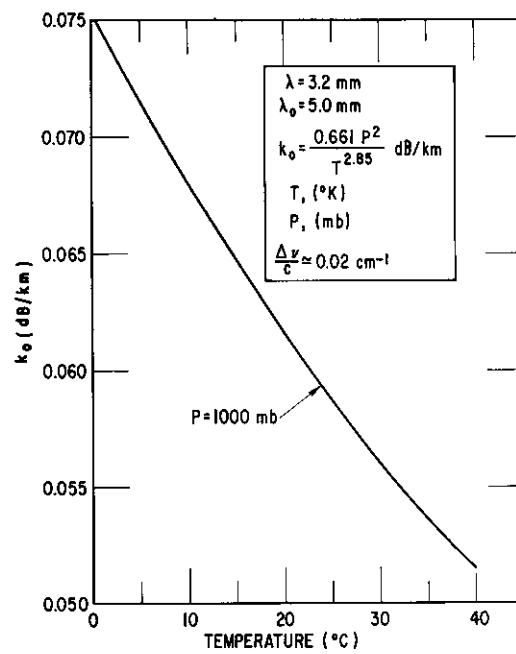


FIG. 29 Attenuation in the troposphere due to oxygen

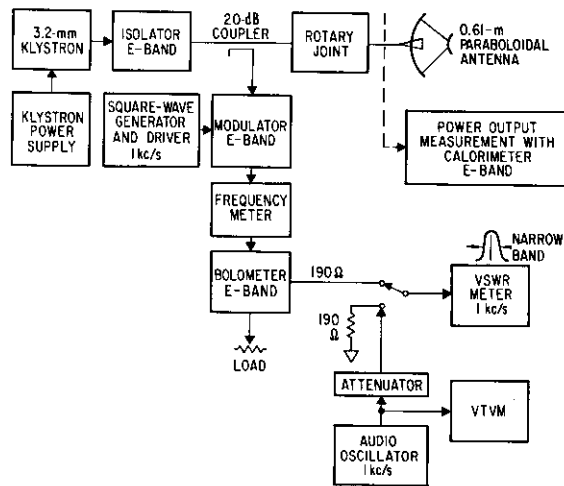


FIG. 30 Block diagram, 3.2 millimeter-wave transmitter and calibration equipment



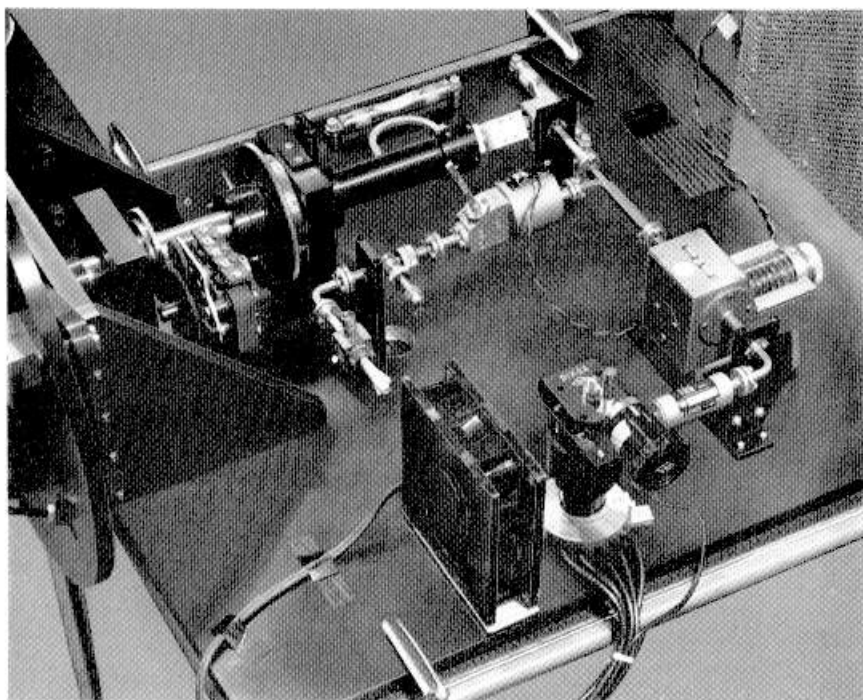


FIG. 31 Transmitter millimeter-wave components

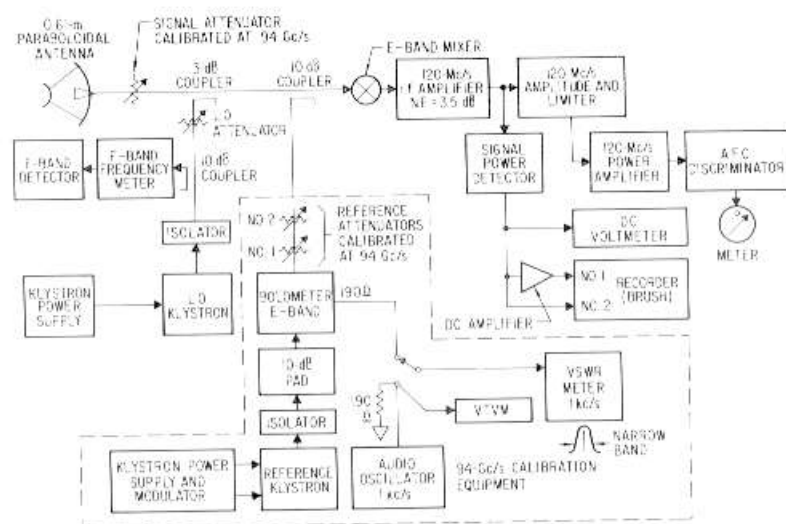


FIG. 32 Block diagram, 3.2 millimeter-wave receiver and calibration equipment

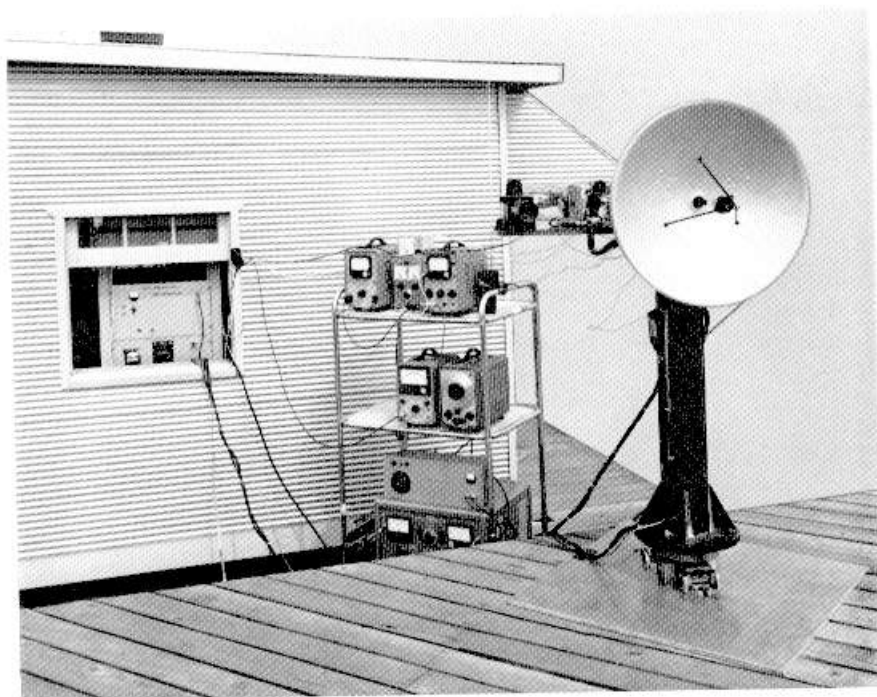


FIG. 33 Receiving system on top of laboratory building in El Segundo

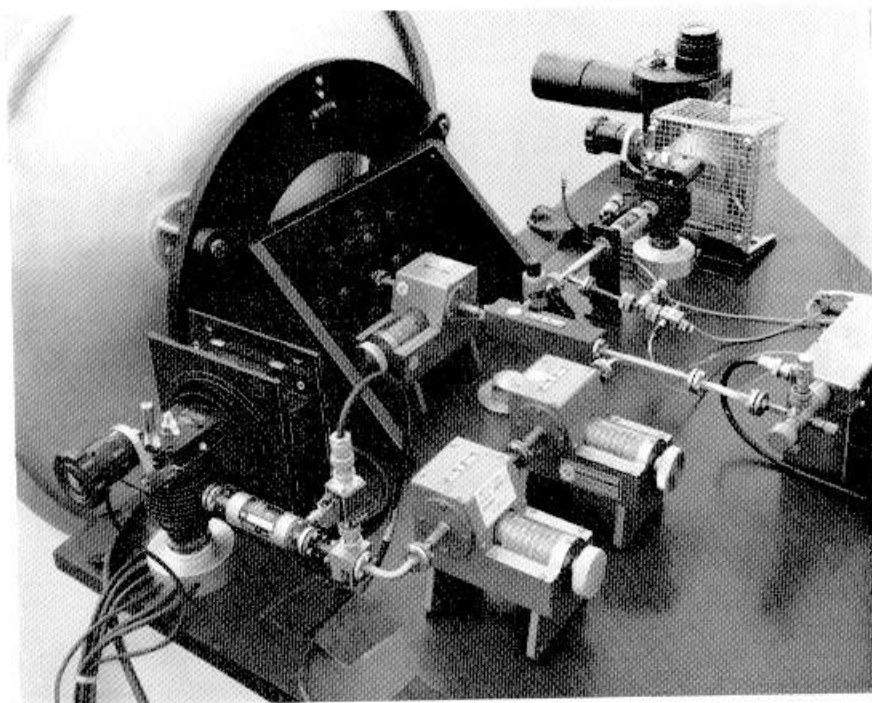


FIG. 34 Receiver millimeter-wave components

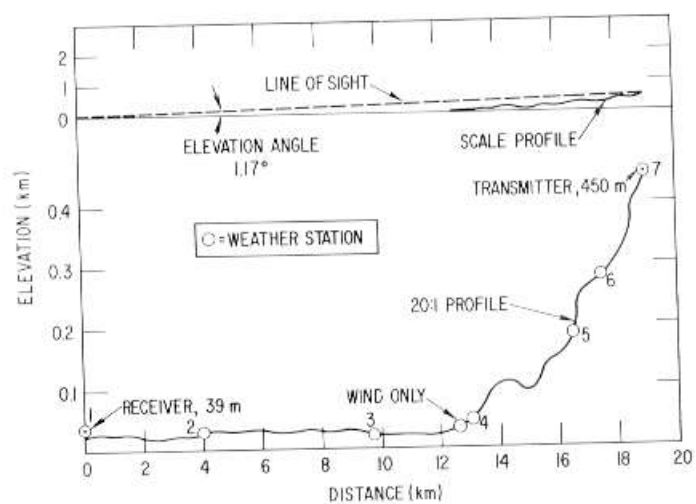


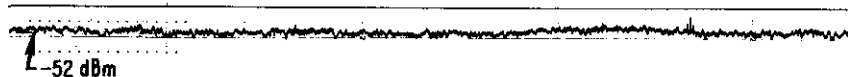
FIG. 35 Approximate profile, 18.95 km experimental link

$P_{trans} = 100 \text{ mW}$     $P_{recd} = -37 \text{ dBm} - \text{TROPO. ATTN}$

HAZY AND CALM

THURSDAY, 12-17-64

TIME: 11:45 a.m.

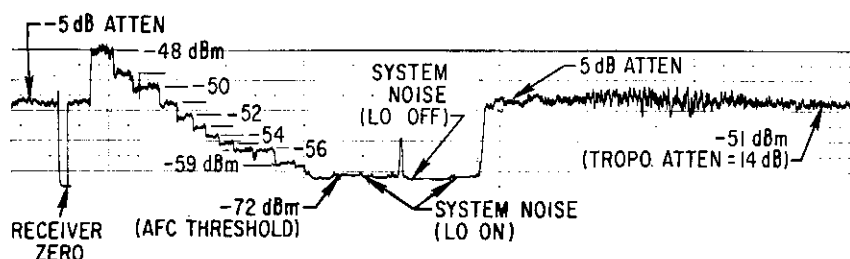


HAZY AND CALM

THURSDAY, 12-17-64

TIME: 12:10 p.m.

TYPICAL CALIBRATION PROCEDURE



RAINY AND CLEARING

FRIDAY, 12-18-64

TIME: 9:45 TO 11:05 a.m.

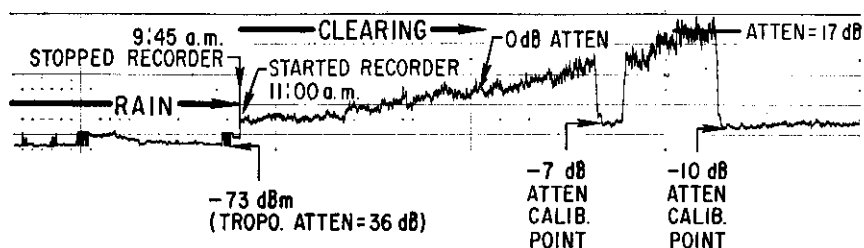


FIG. 36 Received signal power (at 3.2 mm)

Identical 0.61 m paraboloidal antennas are used for the transmitter and receiver. These antennas have a Cassegrainian feed system and exhibit a gain of approximately 53 dB at 3.2 mm. The 3 dB beamwidth is 22 min. The transmitting antenna has, as an additional feature, a continuously variable polarization feed system. A simple superheterodyne receiver with no preselection capability, other than that provided by the waveguide input, was used in the attenuation measurements. A block diagram of the receiver is given in Fig. 32. The millimeter-wave section of the receiver and an i.f. preamplifier are installed at the base of the antenna. Other portions of the receiver, i.f. amplifier, signal-power detector, calibration equipment, recorder, and system power supplies are rack mounted.

When used for the short-distance instrumentation calibration measurements, the receiving antenna was mounted on a lathe-bed assembly. This permitted introduction of small displacements for determination of whether any interference patterns were present that would affect the accuracy of the measurements. No interference patterns were observed. A photograph of the receiver, calibration equipment, and recording instruments on top of the roof of the laboratory building in El Segundo is shown in Fig. 33. This photograph was taken during instrumentation-calibration measurements; therefore the lathe-bed antenna mount is shown. Figure 34 is a photograph of the receiver millimeter-wave components.

Received signals are fed to the E-band mixer through a calibrated attenuator and two directional couplers. One coupler (3 dB) is used for local oscillator injection into the mixer; the other coupler (10 dB) is used for injection of the r.f. reference signal into the mixer.

The E-band mixer has a point-contact gallium arsenide diode mounted across an E-band waveguide with a coaxial output for the 120 Mc/s i.f. amplifier. The measured mixer noise figure at 3.2 mm was approximately 23 dB, including a 3.5 dB noise figure for the i.f. preamplifier. Total insertion loss of the millimeter-wave components between the antenna feed horn and the mixer input port was approximately 4 dB, yielding a total system noise figure of approximately 27 dB. A square-law diode amplitude detector was used to detect received signal power at the 120 Mc/s i.f. output terminal. The detector output was then amplified and recorded.

**Measurements** – A profile view through the line of sight of the 18.95 km path for the attenuation measurements is shown in Fig. 35. The upper profile is to scale. The circles on the profile indicate locations where weather data were recorded. Some early measurements were made with the system, using a 100 mW transmitting klystron, before complete weather data were gathered along the path and before an accurate determination was made of the expected free-space received-power level. Sample recordings are shown in Fig. 36 and 37. The accuracy of Fig. 36 is estimated to be  $\pm 1$  to 2 dB.

The center trace of Fig. 36 shows a calibration scale at the left (chart is linear in power) and a typical received power recording. For this hazy, calm day, the total tropospheric attenuation was 14 dB. A 5 dB attenuation step has been inserted in the signal line to enable recording of the  $-51$  dBm signal near the chart center. The lower trace dramatically indicates a 19 dB change in attenuation due to weather conditions over only a short period of time. The 5 dB attenuation step has been removed from the signal line. The

total chart time for the "clearing" period is 5 min. The amplitude scintillations are actually approximately equal over this 5 min period and are about 1 dB peak-to-peak. The linear power scale compresses variations in the lower received power levels. The lowest received signal level,  $-73$  dBm, is still of sufficient level to yield a 16 dB signal-to-noise ratio in a 1 Mc/s bandwidth system having a 25 dB noise figure.

The recordings shown in Fig. 37 again illustrate rather dramatically the variations in received-signal power that can be expected during only a few hours of a single day. Scintillations vary in amplitude from less than 1 dB to 20 dB or more peak-to-peak. The bottom recording clearly shows low-frequency cyclical variations of about 1 cycle-min superimposed on the higher frequency variations of somewhat greater than 1 c/s. The scintillations, or received signal strength fluctuations, are clearly a function of the turbulence of an inhomogeneous troposphere. This turbulence is the result of changing wind velocities and directions plus temperature variations along the propagation path, all of which, in conjunction with variable moisture content, cause time-dependent refraction and absorption variations in the medium.

TABLE 7  
OXYGEN AND WATER VAPOR ABSORPTION  
AT 3.2 MM ON 15 JULY 1965

Station	Data		Calculated		Measured	
	Temp. (°K)	Rel. hum.	Weighted H <sub>2</sub> O atten. (dB)	Weighted H <sub>2</sub> O (dB/km/g/m <sup>3</sup> )	Weighted O <sub>2</sub> atten. (dB/km)	Weighted H <sub>2</sub> O (dB/km/g/m <sup>3</sup> )
1	17.7	0.82				
			2.64	0.0111	0.0131	0.0112
2	20.9	0.68				
			3.77	0.0162	0.0190	0.0166
3	18.1	0.79				
			2.15	0.0092	0.0108	0.0093
4	20.1	0.71				
			2.34	0.0098	0.0115	0.0099
5	20.9	0.70				
			0.53	0.0022	0.0026	0.0022
6	19.3	0.75				
			0.97	0.0042	0.0049	0.0043
7	17.8	0.79				
Path totals			12.4	0.0527	0.0619	0.0535
Total measured attenuation				13.7 dB	H <sub>2</sub> O absorption (dB/km/g/m <sup>3</sup> ):	
— Calculated O <sub>2</sub> absorption				1.1 dB	Measured = 0.054	
					Calculated = 0.053	
Total measured H <sub>2</sub> O absorption				12.6 dB	O <sub>2</sub> Absorption: 0.06 dB/km	

Measurements were begun in July 1965 to determine accurately the attenuation experienced over the link. The measurements were then correlated with calculated values. Table 7 is a chart of data recorded for July 15, 1965. The temperature and relative humidity are determined at each of the station locations indicated in Fig. 35. These values are then averaged for each two contiguous stations, and the resultant is used in the attenuation calculations.

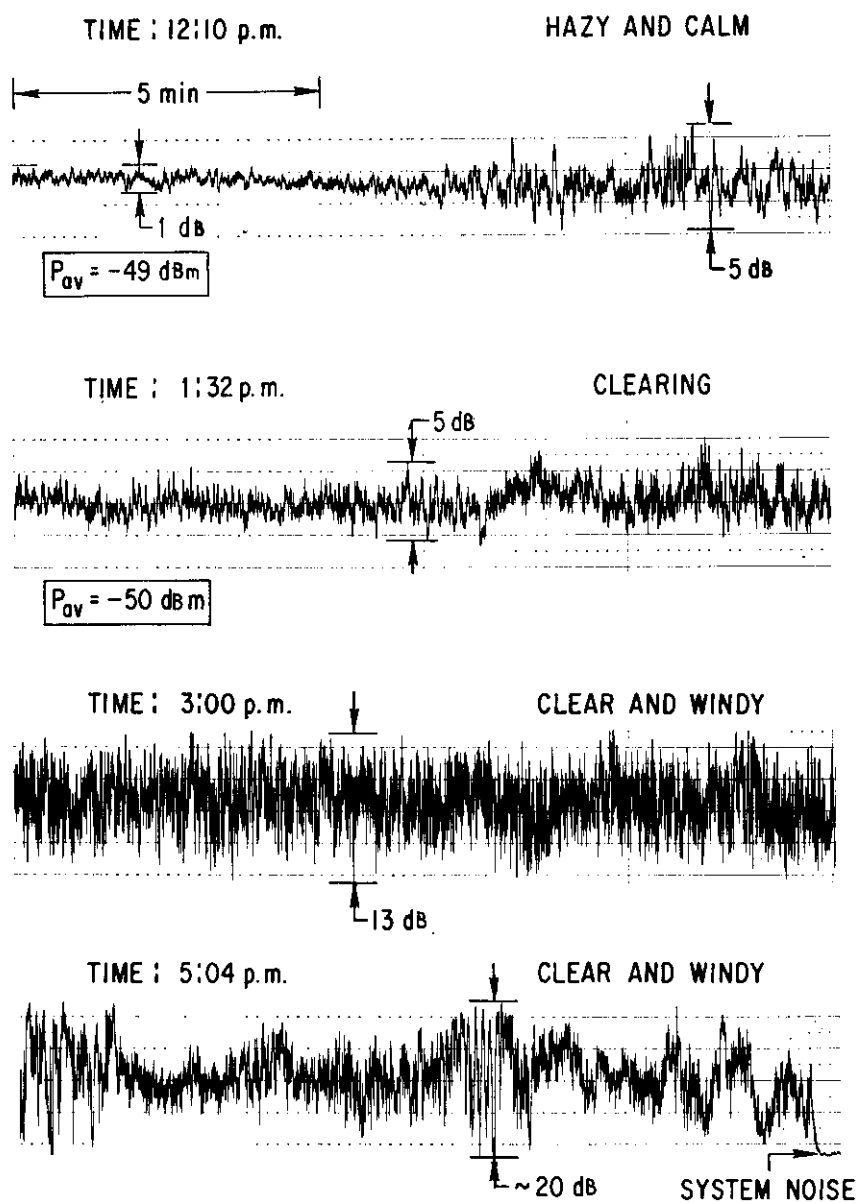


FIG. 37 Received signal power (at 3.2 mm); recorded on a single day

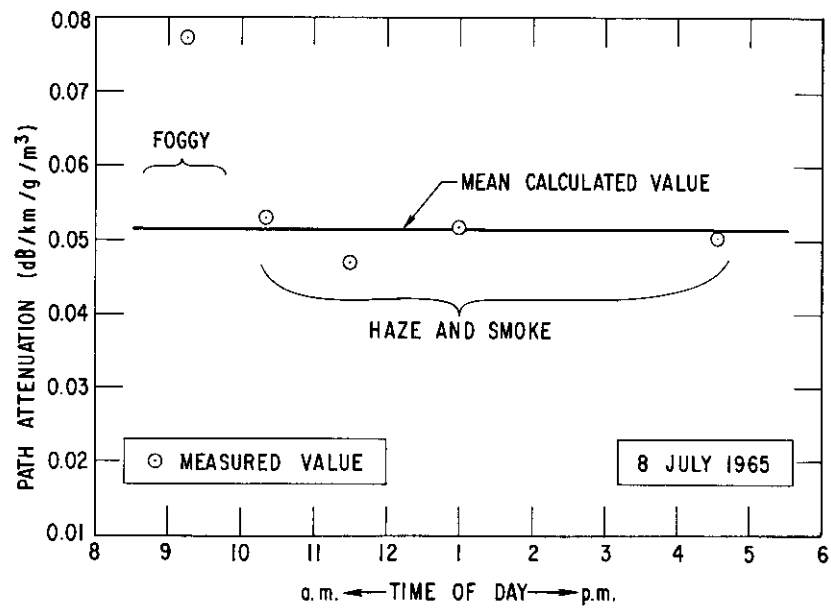


FIG. 38 Comparison of measured and calculated attenuation coefficients, 3.2 mm

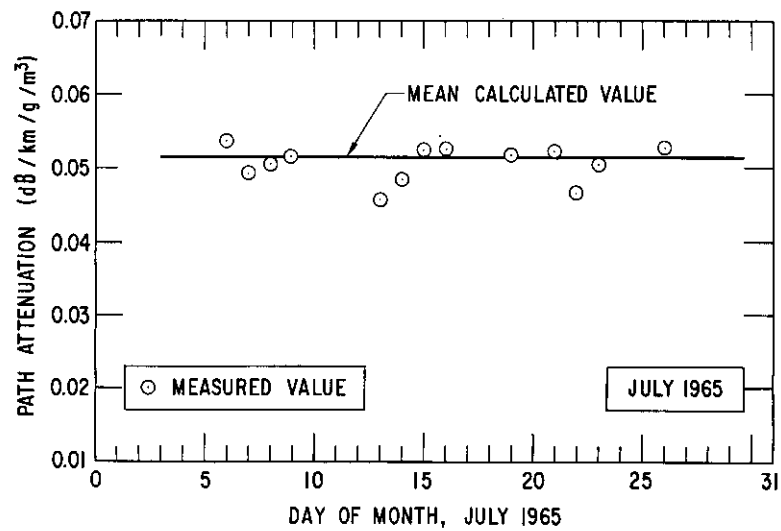


FIG. 39 Comparison of measured and calculated attenuation coefficients, 3.2 mm



The calculations are weighted in proportion to the distance between weather stations as compared with the length of the complete path. The calculated oxygen absorption is assumed to be correct and is subtracted from the measured total attenuation in order to derive a value of measured water-vapor absorption to compare with that calculated. A measurement of the total path attenuation is made with the calibrated transmitter and receiver at the same time that weather data are gathered. A value for atmospheric pressure ( $P$ ) of 1000 mb was used to calculate the oxygen and water-vapor coefficients. This value has been determined from radiosonde data to be a relatively constant mean value for the path during July 1965.

A comparison of measured and calculated water-vapor absorption for July 8, 1965, is shown in Fig. 38. The mean calculated value shown ( $0.0515 \text{ dB/km/g/m}^3$ ) is the average of the values calculated during the month of July using  $P$  equal to 1000 mb. (Deviations from this average were small enough to allow its use for clarity of comparison with negligible error.) Each measured value is equal to the total measured path attenuation in dB minus the calculated oxygen absorption, the difference then being divided by the product of the water-vapor density and the path length. The point of large deviation (Fig. 38, 9.15 a.m.) was measured while fog was obscuring much of the path. The large differential of attenuation above that calculated is attributed to scattering by precipitated water vapor. The Van Vleck equation is inadequate for total attenuation calculations during foggy weather as well as during rainy periods. As the fog lifted, leaving a typical hazy path, the differential in measured versus calculated values fell to the generally measured small values indicated in Fig. 38. The average of the measured values is approximately  $0.05 \text{ dB/km/g/m}^3$  (an attenuation of about  $0.6 \text{ dB/km}$  for this day). Oxygen absorption accounted for about  $0.06 \text{ dB/km}$ , thereby bringing the total attenuation to approximately  $0.7 \text{ dB/km}$  or about  $13 \text{ dB}$  for the path.

For the measurements taken during the month (Fig. 39), the average measured water-vapor coefficient was also  $0.05 \text{ dB/km/g/m}^3$ . Maximum deviations about the mean calculated value were  $+0.002$ ,  $-0.006$ . The absolute humidity for the month was relatively constant during each day at approximately  $12.5 \text{ g/m}^3$ . The differences in measured versus calculated values can be ascribed to a number of factors including:

- (1) the difficulty in obtaining accurately integrated weather information due to variable conditions over the long path,
- (2) approximations used in the expressions for calculating the water-vapor and oxygen coefficients,
- (3) instrumentation errors,
- (4) particulate scattering, which is some function of path visibility, and
- (5) atmospheric turbulence refraction effects.

Four charts found useful in this work are included in Fig. 40.

#### CONCLUSIONS AND IMPLICATIONS OF THE MEDIUM

Communications systems operating at  $3.2 \text{ mm}$  are feasible for short horizontal path lengths of the order of  $50 \text{ km}$  with only a minimum of required transmitting power ( $0.1$  to  $1 \text{ W}$ ). These systems can be small and rugged and will operate under most weather conditions, except perhaps for conditions

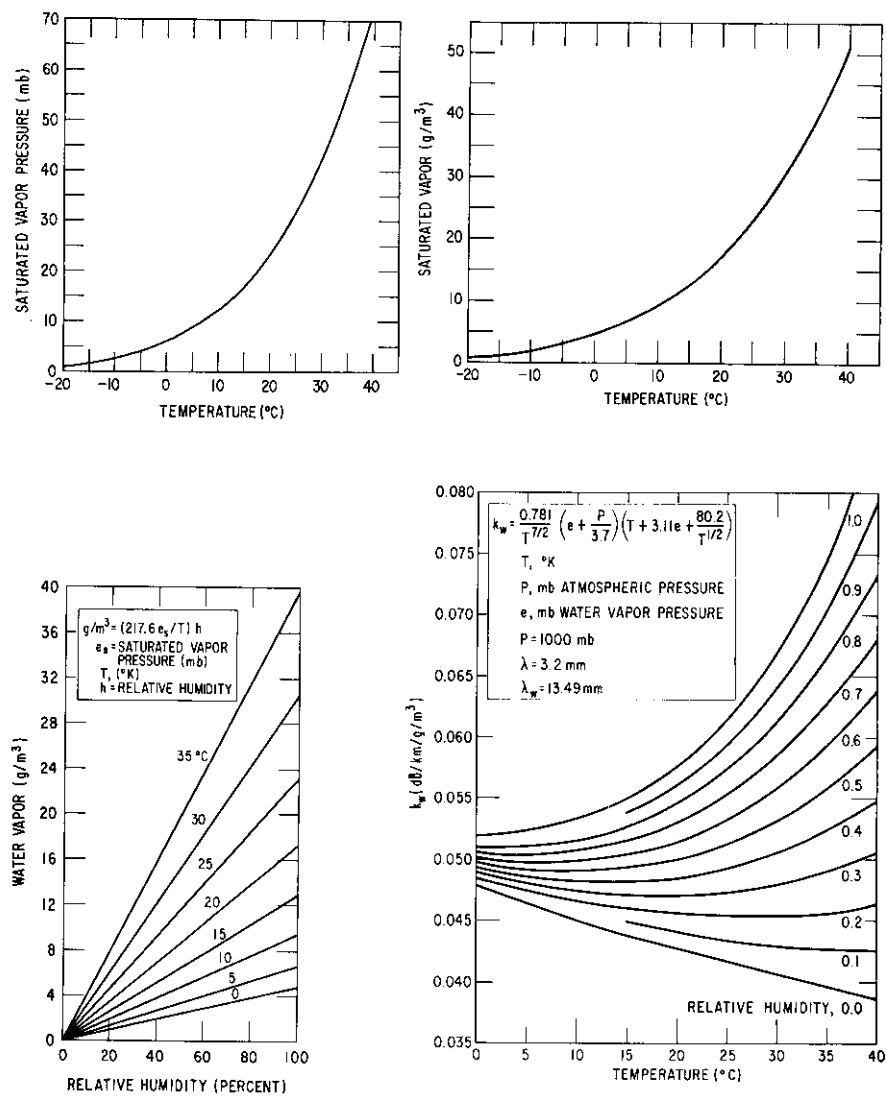


FIG. 40 Water vapor, pressure and attenuation versus temperature and relative humidity curves

of moderate to heavy rainfall and extremes of humidity. The bandwidth limitation of the medium has not yet been established, but it is known to be greater than 30 Mc/s. Further work is required to determine if there are limits imposed by phase dispersion. On the assumption that 90 per cent of the attenuation takes place in the first 10 km of the atmosphere, ground-space communications systems can be designed with components that will be useful at elevation angles as low as  $10^\circ$ .

The 3.2 mm wave window is useful for space communication (including such applications as radar and navigation) and astronomical observations for elevation angles exceeding about  $10^\circ$ . Thick clouds and rain adversely affect this capability, especially at the lower elevation angles.

Present technology is capable of providing millimeter-wave sources with significant power outputs (up to 100 W, average) such that the millimeter-wave region may assume an important role in space communications. This potential for the millimeter-wave region is due to the fact that the combination of a large bandwidth and a low inherent noise level is difficult to match at either the longer wavelengths or optical wavelengths.

Some further general observations that can be made are:

- (a) The feasibility of a precision, high gain ( $\sim 70$  dB), narrow beamwidth ( $\sim 3$  min) antenna capable of command pointing with 20 seconds of arc has been demonstrated.
- (b) Scintillation caused by turbulence in the atmosphere may have serious implications for antenna beamwidths much narrower than 3 min or for antennas significantly larger in diameter than about 5 m at the 3.2 mm wavelength.
- (c) At high altitudes, narrow absorption lines permit low-loss propagation between them that is undetectable at ground-levels due to pressure broadening of these lines.
- (d) Depending upon the type of application, one should be aware of the possibility that the attenuation of the atmosphere may be changing such as to significantly affect results.
- (e) Sky-emission temperatures vary between about  $35^\circ$  and  $290^\circ\text{K}$ , depending upon elevation angle and water-vapor distribution.
- (f) The Van Vleck and Schulkin expressions for the absorption by oxygen and water vapor through the atmosphere, respectively, are adequate for approximate values.
- (g) The Van Vleck and Schulkin expressions for the absorption by oxygen and water vapor, respectively, as modified herein for use in calculating attenuation in the troposphere, yield values in close agreement with measured values at 3.2 mm.
- (h) Because of extremely high losses caused by absorption and scattering from raindrops, water vapor, and thick clouds, long propagation paths at very low elevation angles cannot be utilized. For the month of July 1965 in the Los Angeles coastal area, the typical average tropospheric attenuation rate measured at 3.2 mm was approximately 0.7 dB/km ( $\text{H}_2\text{O}$  and  $\text{O}_2$ ).
- (i) The implications of large possible scintillations in received power level should be considered if amplitude modulation systems are contemplated.

- (j) Scintillation is not a problem for FM systems as long as sufficient margin is allowed for high-attenuation, low-scintillation weather.

## REFERENCES

1. STACEY, J. M., "General Research: Millimeter-Wave Radio Astronomy". Aerospace Corp., El Segundo, Calif., Report No. ATN-62(9223)-1, 1962.
2. STACEY, J. M., "Research and Experimentation on Space Applications of Millimeter Waves". Aerospace Corp., El Segundo, Calif., Report No. TDR-169(3250-41)TN-1, 1963.
3. STACEY, J. M., BOTTJER, M. F., EPSTEIN, E. E., GEDDES, R. N., JACOBS, E., KING, H. E., MORI, T. T., REBER, E. E., SHIMABUKURO, F. I., and WINTROUB, H. J., "Research and Experimentation on Space Applications of Millimeter Waves". Aerospace Corp., El Segundo, Calif., Report No. TDR-169(3250-41)TN-2, 1964.
4. REBER, E. E., and WILLIAMS, I. J., "Simulation of the Antenna Control System for the Space Radio Systems Facility". Aerospace Corp., El Segundo, Calif., Report No. TDR-269(4250-41)-1, 1963.
5. KING, H. E., EPSTEIN, E. E., GARBER, W. A., GEDDES, R. N., JACOBS, E., JOHNSON, W. A., MORI, T. T., REBER, E. E., SHIMABUKURO, F. I., STACEY, J. M., WINTROUB, H. J., and WONG, J. L., "Research and Experimentation on Space Applications of Millimeter Waves". Aerospace Corp., El Segundo, Calif., Report No. TDR-269(4250-41)-3, 1964.
6. DUWALDT, B. J., and HOFFMAN, L. A., "Research on the suitability of millimeter wavelength systems for space applications". Paper presented 1964 Western Electronic Show and Convention, Los Angeles, California, 1964.
7. EPSTEIN, E. E., JACOBS, E., KING, H. E., REBER, E. E., SHIMABUKURO, F. I., and STACEY, J. M., "The Total Lunar Eclipse of December 30, 1963; Observations at 3.2 Millimeters". Aerospace Corp., El Segundo, Calif., Report No. TDR-269(4250-41)-4, 1964.
8. JACOBS, E., and KING, H. E., "2.8-Minute Beamwidth, Millimeter-Wave Antenna—Measurement and Evaluation". Aerospace Corp., El Segundo, Calif., Report No. TDR-469(5230-41)-1, 1965; also 1965 IEEE Intern. Conv. Record 13, Pt. 5, 92-100, 1965.
9. KING, H. E., JACOBS, E., and STACEY, J. M., "A 2.8 Arc-Minute Beamwidth Antenna for Lunar Eclipse Observations at 3.2 mm." Aerospace Corp., El Segundo, Calif. (unpublished).
10. LOVE, A. W., "The diagonal horn antenna". Microwave J. 5, 117-22, 1962.
11. SHIMABUKURO, F. I., "Propagation through the Atmosphere at a Wavelength of 3.2 mm". Aerospace Corp., El Segundo, Calif., Report No. TDR-469(5230-41)-2, 1965.
12. VAN VLECK, J. H., and WEISSKOPF, V. F., "On the shape of collision-broadened lines". Rev. Mod. Phys. 17, 227-36, 1945.
13. VAN VLECK, J. H., "The absorption of microwaves by oxygen". Phys. Rev. 71, 7, 413-24, 1947.

14. VAN VLECK, J. H., "The absorption of microwaves by uncondensed water vapor". *Phys. Rev.* 71, 7, 425-33, 1947.
15. STRANDBERG, W. P., MENG, C. Y., and INGERSOLL, J. G., "The Microwave Absorption Spectrum of Oxygen". Res. Lab. for Electronics, Cambridge, Mass., Report No. 87, 1948.
16. HILL, R. M., and GORDY, W., "Zeeman effect and line breadth studies of the microwave lines of oxygen". *Phys. Rev.* 93, 1919-22, 1954.
17. SCHULZE, A. E., and TOLBERT, C. W., "Shape, intensity, and pressure broadening of the 2.53-millimeter wavelength oxygen absorption line". *Nature* 200, 4908, 747-50, 1963.
18. SCHULKIN, M., "Determination of Microwave Atmospheric Absorption Using Extraterrestrial Sources". Naval Res. Lab. Washington, D.C., Rep. No. 3843, 1951.
19. BECKER, G. E., and AUTLER, S. H., "Water vapor absorption of electromagnetic radiation in the centimeter wavelength range". *Phys. Rev.* 70, 300-7, 1946.
20. "U.S. Standard Atmosphere, 1962". Prepared under sponsorship of National Aeronautics and Space Administration, U.S. Air Force, and U.S. Weather Bureau.
21. BLANCO, V. M., and McCUSKEY, S. W., "Basic Physics of the Solar System", 92. Addison-Wesley Inc., Reading, Mass., 1961.
22. SMITH, E. K., and WEINTRAUB, S., "The constants in the equation for atmospheric refractive index at radio frequencies". *Proc. IRE* 41, 1035-37, 1953.
23. HOFFMAN, L. A., WINTROUB, H. J., and GARBER, W. A., "Propagation observations in the 3.2 mm wave window". Paper presented Boulder Millimeter Wave and Far Infrared Conf., Estes Park, Colorado, 1965.

## ACKNOWLEDGEMENT

U.S.A.F. for support under Contract No. AF 04(695)—269 and AF 04(695)—469.



## CHAPTER 5-7

SPACE COMMUNICATIONS PROPAGATION STUDIES  
AT LINCOLN LABORATORY

LEON J. RICARDI

Lincoln Laboratory, Massachusetts Institute of Technology, Lexington,  
Massachusetts 02173

## INTRODUCTION

The Massachusetts Institute of Technology Lincoln Laboratory of Lexington, Massachusetts, began devoting considerable effort toward the design, analysis, and development of active satellite communications systems during the latter part of 1962. Since that time the space communications division has designed, developed and constructed an active satellite, known as the Lincoln Experimental Satellite (LES), and a transportable terminal, called the Lincoln Experimental Terminal (LET). LES has been used with good success as a relay station between the terminals in Massachusetts (Westford), California (Camp Parks), and LET. Concurrently with these hardware-producing programs, considerable effort has been spent in studying various modulation and data-processing techniques, the design of solid-state components, special-purpose antennas, and investigating propagation effects. In connection with investigating propagation effects, a program was organized early in 1963 to study the propagation characteristics of the troposphere as they are affected by rain, clouds, etc. This chapter describes this program and presents some of the results obtained thus far.

Before proceeding with a detailed description of the propagation studies, it is important to present a more specific definition of the problem to which this chapter is addressed. Consider first the communication engineer: he must be able to calculate, or estimate, the path loss between the satellite and the ground station in order to specify satisfactorily the equipment that will be used at both the ground and satellite stations. He is well aware that rain and clouds are the predominant factors affecting the propagation of electromagnetic waves through the earth's atmosphere (over the frequency range 1-15 Gc/s), but he does not know, in general, what degree of deterioration must be accommodated. His next logical move is to ask the propagation specialist to supply him with the required information. The specialist can calculate the expected path loss for given meteorological conditions; however, he cannot estimate, with sufficient accuracy, the probable increase in antenna noise temperature, time-varying multipath, or Doppler spread. There have been several good theories developed that enable one to calculate these effects, but the meteorological data must be obtained first to establish the necessary connection with the communication engineer's problem. Hence, the problem can be considered as consisting of

- (1) the establishment of a clearer and more exact relationship between weather phenomena and propagation characteristics
- (2) the collection of meteorological data and putting them in an appropriate statistical form.

Since rainstorms generally produce the largest path loss, it was decided to study how they affect propagation characteristics. Keeping in mind that weather phenomena are most appropriately described by their statistical behaviour, it should be possible to tell the communication engineer the probability that the path loss for a given site location and satellite position will exceed a certain specific value. A good understanding of the weather data would help the propagation specialist to obtain this information. After a brief investigation, it became apparent that the weather data recorded by the many Weather Bureaus throughout the world during the past 50 to 100 years represent the only source of information from which a reasonably accurate probability distribution of rainfall can be obtained. It is desirable to obtain rainfall rates not only at the surface of the earth, but also at a sufficient number of altitudes above the surface of the earth to determine a profile of typical and extreme storm configurations. However, it is presently impossible to obtain this type of data at enough locations on the earth, because weather radars are rare meteorological instruments, and the extremely limited amount of data collected by them has not been "complete" and is not, in general, in a usable form. Consequently, one must resort to a system of analysis that will make the best use of the data presently available. As a result of this initial investigation, a three-phase program was organized to produce a method of converting "standard weather data" into the path loss distribution data required by the communication engineer.

#### THEORETICAL ANALYSIS

Phase one in converting the data is concerned with the calculation of the complex propagation constant associated with rain. By using the Mie scattering theory (1), a plane wave is assumed to be incident upon a volume of randomly located raindrops of various size distributions. Both single and multiple scattering are taken into account, and the phase and amplitude of the wave emerging from the volume are determined. By carrying out this calculation for three or more signal frequencies, it is possible to determine the attenuation and the dispersive characteristics of the medium. The analysis considers only the forward and back-scattered waves, and it is essentially a one-dimensional two-parameters analysis; i.e. only the size distribution and the index refraction of the raindrop affect the results. The calculated attenuation agrees with that obtained previously (2), but the effective "phase shift" through the medium represents a new contribution. These calculations were carried out at 1, 2, and 4 Gc/s intervals, with center frequencies of  $\approx 8$  Gc/s and  $\approx 16$  Gc/s. With a normal rain rate ( $\approx 50$  mm/hour), the results indicate that a Gaussian-shaped pulse will be expanded by a factor of two over distances greater than 1 000 km. It was also found that multiple scattering calculations do not produce results significantly different from those obtained by assuming single scattering. More details concerning these calculations and the results will be presented in a forthcoming paper (3) by Robert K. Crane of Lincoln Laboratory.



## SIMULATED RAIN EXPERIMENT

The second phase of the program consists of constructing water-showing equipment capable of producing a "simulated" rainstorm in a volume measuring 40 feet high, 40 feet wide, and 15 feet along the path of propagation. It is planned to transmit signals through this volume and to measure the attenuation, phase shift, and Doppler spread. The experimental configuration is shown in Fig. 1. The transmitting and receiving sites are separated by 1 000 feet, and the rain-simulating volume is located midway between them. A signal will be transmitted along two paths: one which includes the rain-simulating volume, and a second which consists of a standard rectangular waveguide buried below the surface of the earth. At the receiving site, an appropriate comparison between the two signals will be made to determine the change in amplitude, frequency and phase of the signals propagated along the free space path with and without the "simulated rain" falling across it. The equipment is designed to produce the equivalent rainfall rate of approximately 1 000 millimeters per hour. This rate will yield an attenuation on the order of 0.2 dB and a phase shift of approximately 2.5 deg. Initial equipment will be capable of measuring a 0.01 dB change in amplitude and a 0.1 deg. change in phase. In order to keep the rain-simulating equipment simple, no attempt was made to produce a drop-size distribution similar to that found in natural rain. It is planned to measure the actual drop-size distribution produced by the nozzles used and then to use this information to calculate the expected propagation characteristics and to compare them with the measurable results to establish an accurate connection between theory and experimental data. The experimental data will almost certainly be more accurate than any previously obtained data, because of the facility which the experiment can be repeated and the accuracy to which the various parameters can be controlled and measured. After obtaining the initial results, the length of the rain-simulating volume may be increased, and consideration will be given toward attempting to reproduce drop-size distribution normally found in natural rainfall. This introduces the additional problem of determining the latter. It is hoped that the results of this experimental work will increase the confidence in the method of theoretical analysis. This in turn will provide a better method for converting the available meteorological data into the desired propagation characteristics.

This range will also be used during natural rain to measure attenuation and phase shift for forward-scattered signals and "bistatically" for off-axis scattering characteristics.

## WEATHER-DATA ANALYSIS

The third phase of the program of data conversion consists of collecting weather radar data and comparing them with the standard synoptic data prepared by weather stations located on the surface of the earth. This unquestionably is the most difficult part of the program, and it is being carried out with the cooperation of the meteorological department at M.I.T., Cambridge. The goal of the program is to establish the correlation between rainstorms aloft and rain as it is recorded striking the earth. It is hoped that it will be possible to establish the confidence level with which the synoptic data

can be used to indicate the storm activity that occurs immediately above the data-gathering station.

As a parallel effort, the weather radar data were used to reconstruct a storm configuration in the memory bank of a computer. That is, the rainfall rate at all points in the storm is quantized in cubes  $\approx 8$  km on a side. The storm is allowed to drift over a ground station, and the path loss between an assumed satellite and the ground station is calculated for various configurations. These data provide a "feel" for the operational performance that might exist; and they may also be used to determine the resolution required to obtain rainfall data.

The weather radar group has also used several years of data obtained in the vicinity of Boston, Massachusetts, to calculate the path loss at various elevation angles and azimuth directions. The results of this effort have been reported elsewhere (4), but it is important to point out that path loss on the order of 10 dB has occurred as often as 0.4 per cent of the period of time investigated. The same weather data and additional results presently being obtained will be analyzed to obtain a path loss probability distribution. It should be realized, however, that these results will be based on only a few years of weather data and that more than a few storms would not be included in the results.

#### EFFECTIVE ANTENNA NOISE TEMPERATURE

The thermal radiation of raindrops is distributed over a broad frequency spectrum and causes an increase in the antenna noise temperature. The usual method for calculating this increase in antenna noise temperature neglects energy radiated from any source that is scattered into the antenna beam. The degree with which these two phenomena affect the performance of low-noise receivers attached to the antenna is not presently known with sufficient accuracy. Increasing the understanding of the phenomena involved may enable the appropriate processing of the meteorological data to obtain a probability distribution of the effective antenna noise temperature. This information, in addition to the path loss distribution, is valuable in determining the system parameters when a "low noise" receiver is employed. In an effort to determine a means of obtaining this information, the Lincoln Laboratory Haystack Antenna System will scan storms simultaneously with other meteorological measuring equipment.

#### CALIBRATION SPHERE

In order to provide a more general approach to the analysis of propagation effects produced by the earth's atmosphere, a rigid metal sphere approximately 44 inches in diameter was placed in a nearly circular orbit of an altitude of  $\approx 1500$  nautical miles. It is called a "Calibration Sphere" and its surface is spherical within 0.005 inches. The mean cross-section is nominally 1 square meter Fig. 2. The measured r.m.s. deviation of the cross-section is less than 0.25 dB over the frequency range 2–35 Gc/s, and it is considerably less at lower frequencies. Although the immediate use of the device is to examine refraction effects for making an accurate calibration of radar systems, it is also planned to evaluate the "channel" characteristics of the atmosphere by using multi-frequency correlation techniques (5) and this

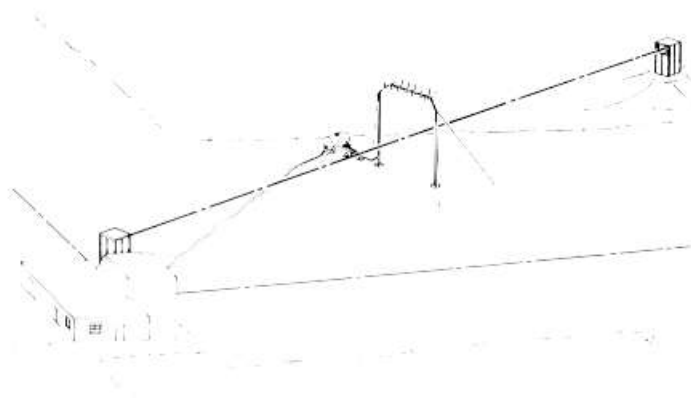


FIG. 1 Proposed rain range test facility

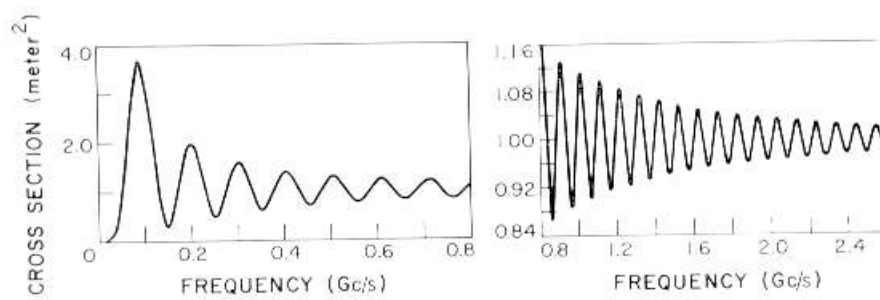


FIG. 2 Calculated cross-section of L.C.S.



FIG. 3 Lincoln Laboratory calibration sphere (L.C.S.)

calibration sphere as an inactive satellite relay terminal. A photograph of the satellite is shown in Fig. 3.

In summary, the space communications studies at Lincoln Laboratory include the investigation of the propagation characteristics of rainstorms and an attempt to establish a method of predicting the probable path loss due to their existence in a space-communications link. An experiment has been designed to increase the confidence in theoretical calculations and our understanding of the phenomena involved. A radar target with an accurately determined 1-square meter cross-section has been placed in a 1500 nautical mile circular orbit.

#### REFERENCES

1. MIE, G., *Ann. Physik* 25, 377, 1908.
2. RYDE, J. W., "The Attenuation and Radar Echoes Produced at Centimetre Wavelengths by Various Meteorological Phenomena", *Meteorological Factors in Radio Wave Propagation*, London Phys. Soc., 169-88, 1946.
3. CRANE, R. K., Calculations of scattering coefficients for measured rain-drop distributions for 8 and 16 GHz radiation (to be published).
4. AUSTIN, P. M., Observations of Attenuation of 3 cm Radiation by Precipitation, 1964 World Con. on Radio Meteorology, Boulder, Colorado, 166-170, 1964.
5. BURROWS, M. L., The Two-Frequency Measurement of Line-of-Sight Spread Channels, Tech. Note 1965-9, Lincoln Laboratory, M.I.T., 1965.

#### ACKNOWLEDGEMENT

The Lincoln Laboratory operated with support from the U.S. Air Force and the U.S. Advanced Research Projects Agency.

## CHAPTER 5-8

A REVIEW OF REFRACTION EFFECTS ON THE  
APPARENT ANGLE OF ARRIVAL OF RADIO SIGNALS

B. R. BEAN and R. E. MCGAVIN

Institute for Telecommunications Sciences and Aeronomy  
Environmental Science Services Administration Boulder, Colorado

## SUMMARY

Radio signals passing through the atmosphere are bent or refracted due to the changing structure of the radio refractive index. *Corrections can be made for errors in the angle of arrival (elevation angle errors).* These corrections are most useful if they are based on standard or mean models of the radio refractive index such that surface values can be used as a predictor. A successful method of deriving such a model is found in ray tracing through a representative sample of refractive index profiles and relating refraction variables to surface values using least square techniques. Ordinarily a linear relationship is sufficient with the coefficients being functions of the elevation angle and target height or range. Since the surface value of the refractive index is so central to refraction prediction a detailed examination of its behavior is essential.

An intensive study of the spectral behavior of the radio refractive index near the ground emphasizes the dependence of the spectral distribution upon the basic mechanisms involved in the production of atmospheric turbulence.

## INTRODUCTION

The first part of this chapter is a review of a technique for correction of the apparent radar elevation angles to a space vehicle. Most of this information has been published in the literature. For a more comprehensive treatment, the reader is referred to the paper by Bean and Thayer (1). The second part of the chapter is concerned with the time variability of the radio-refractive index and its influence on the determination of useable corrections to apparent radar elevation angles. The addendum to this chapter illustrates the relationship between the variability of the radio-refractive index and that of water vapor.

## CORRECTION TO APPARENT RADAR ELEVATION ANGLES

A radio signal leaving the earth's surface at a shallow elevation angle does not travel in a straight line, but in general is refracted or curved back towards the earth's surface due to the decreasing refractive index caused mainly by the decrease in air density. The geometry is as illustrated in Fig. 1, where the apparent elevation angle,  $\theta_0$ , is usually larger than the true elevation angle and where the apparent range is greater than the true range. To a

first approximation, it can be assumed that the atmosphere is horizontally homogeneous and that the refractive index is a monotonically decreasing function of altitude. Snell's law then applies:

$$n_1 r_1 \cos \theta_1 = n_2 r_2 \cos \theta_2, \quad (1)$$

where

$n_i$  = radio-refractive index at point  $i$   
 $r_i$  = distance from the center of the earth to the space target  
 $\theta_i$  = the elevation angles at the point under consideration.

In the present application Snell's law can be expressed in terms of the bending angle  $\tau$  which is the change of the apparent angle of elevation with altitude.

$$\tau = - \int_{n_1}^{n_2} \frac{dn}{n} \cot \theta \cong - \int_{N_1}^{N_2} \cot \theta dN \cdot 10^{-6} \quad (2)$$

where  $N = (n - 1)10^6$ .

Integration by parts yields

$$\tau_{1,2}(\theta) \cong -[N \cot \theta \cdot 10^{-6}]_{N_1}^{N_2} - \int_{\theta_1}^{\theta_2} \frac{N}{\sin^2 \theta} d\theta \cdot 10^{-6} \quad (3)$$

Since the last term yields no more than 3 per cent contribution, for  $\theta$  greater than  $10^\circ$  one can write

$$\tau_{1,2}(\theta_1) \cong \cot \theta_1 \cdot N_1 \cdot 10^{-6} - \cot \theta_2 \cdot N_2 \cdot 10^{-6} \quad (4)$$

and if transmission is through the entire atmosphere  $N_2 = 0$ ; hence,

$$\tau_{1,\infty}(\theta_1) \cong \cot \theta_1 \cdot N_1 \cdot 10^{-6} \quad (5)$$

Therefore it appears, Eq. 2 and 3, that the bending through the total atmosphere is a linear function only of the initial conditions  $N_s$ , the surface value of the refractivity, and the initial elevation angle  $\theta_0$  (2, 4).

$$\tau_{\infty}(\theta_0) = b N_s + a \quad (6)$$

where the term  $a$  absorbs the approximations in Eq. 2. The error,  $\epsilon$ , in the apparent angle of arrival from a point beyond the atmosphere is essentially equal to the bending  $\tau$ ; see Fig. 1. Hence to determine the total bending through the atmosphere it would appear that only the value of  $N_s$  is required, provided the intercept,  $a$ , and the slope,  $b$ , are known.

Bean and Cahoon (4) investigated the possibility of determining  $a$  and  $b$  as a function of the apparent elevation angle. Actual refractive index profiles were taken from thirteen radiosonde stations selected as representative of the full range of climatic conditions encountered in practice. This total sample was called the Central Radio Propagation Laboratory Standard Radio

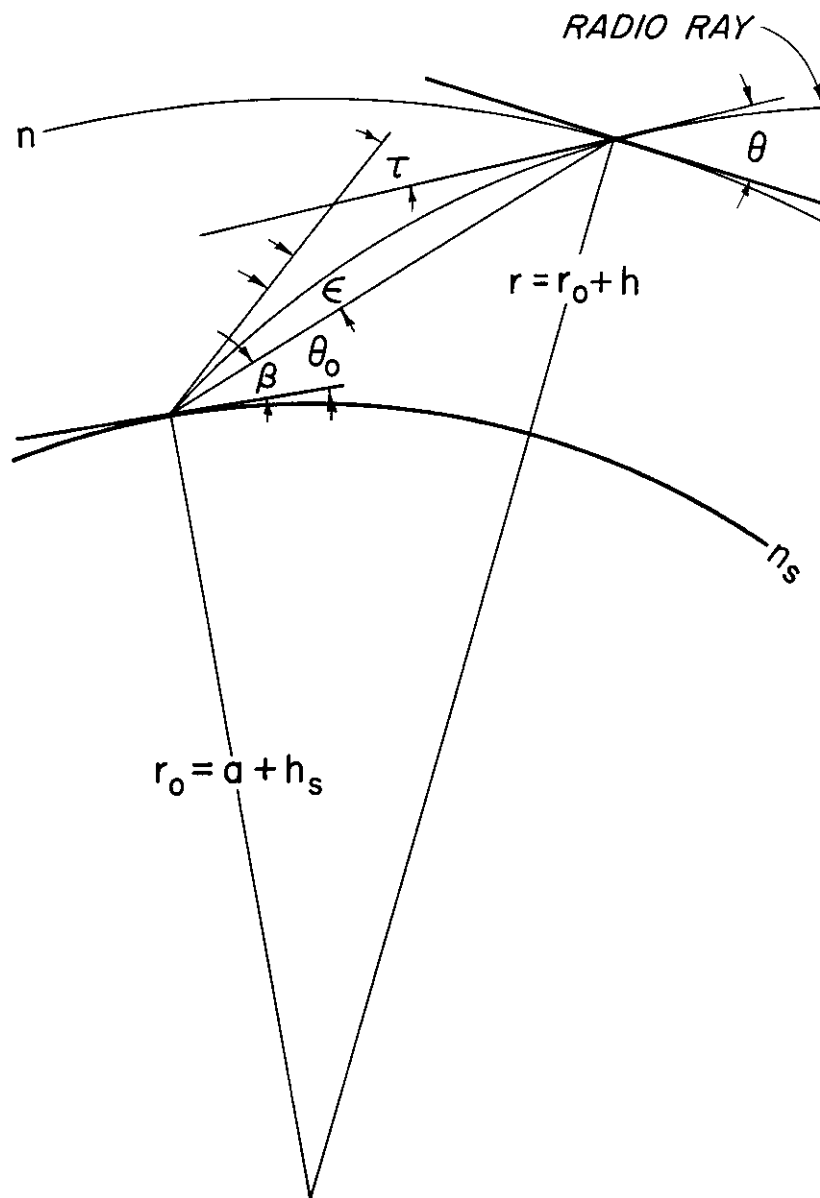


FIG. 1 Geometry of refraction

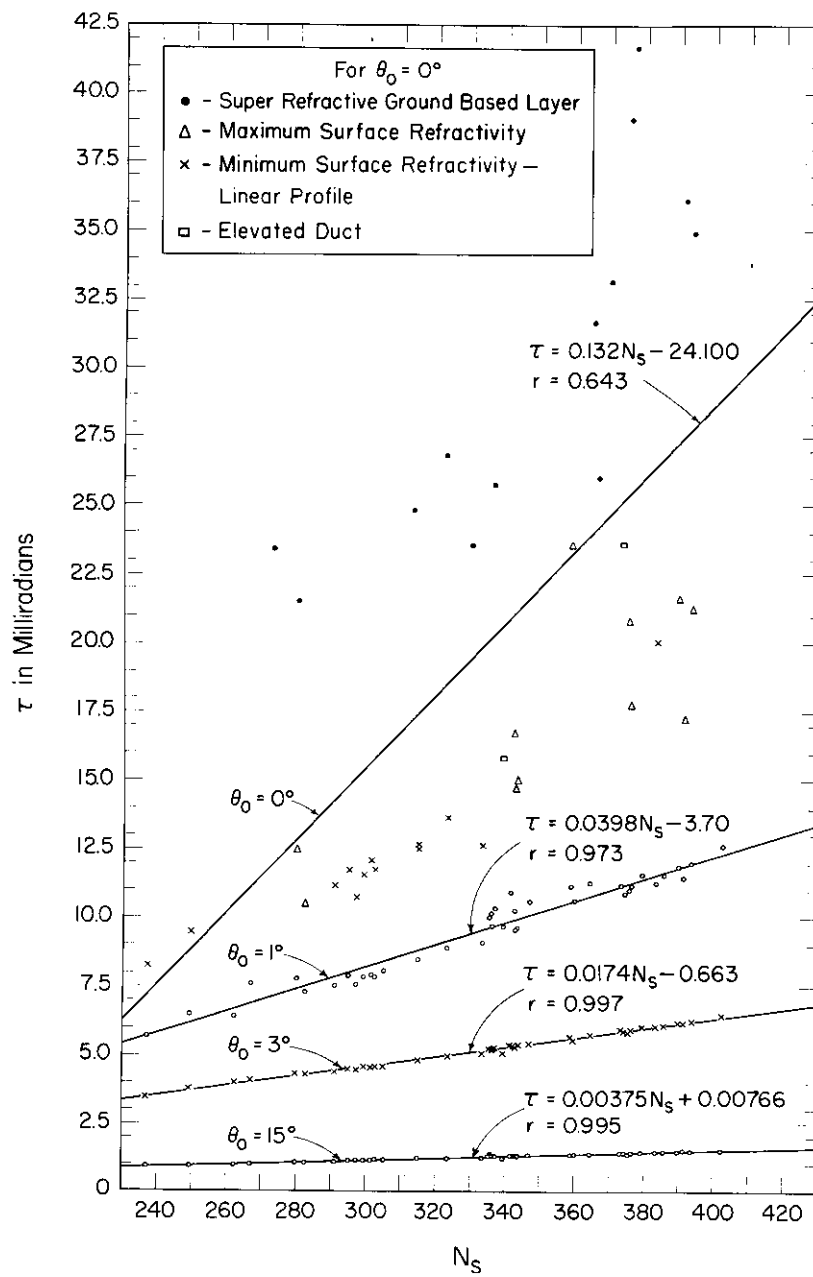


FIG. 2 Total atmospheric bending as a function of the surface value of refractivity for specified elevation angles



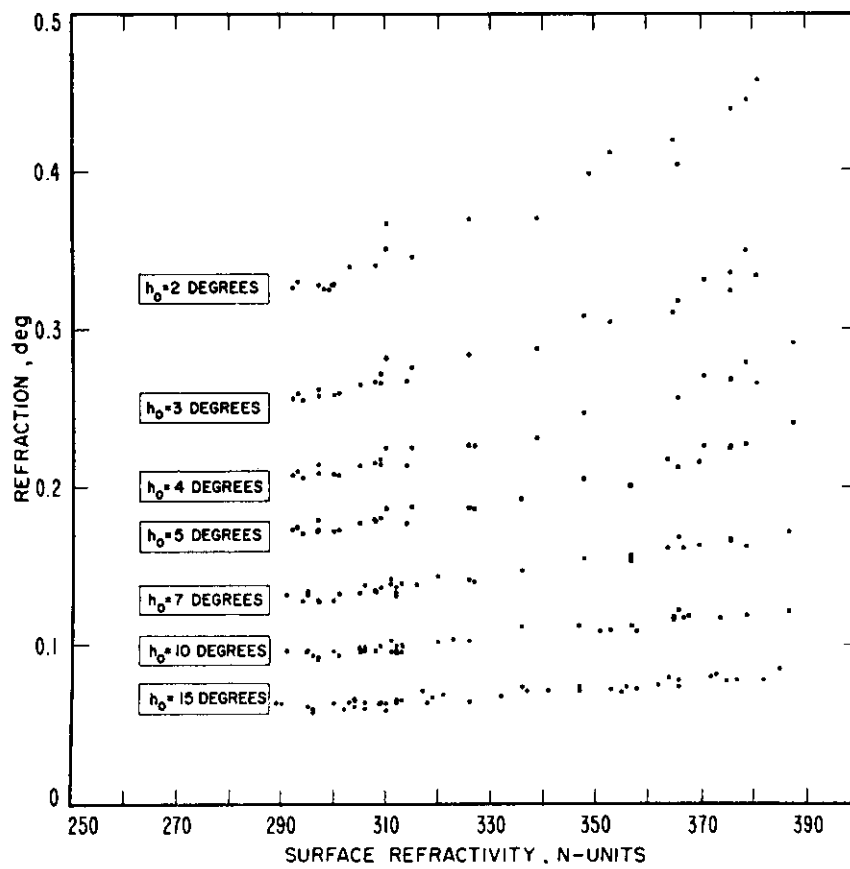


FIG. 3 Scatter diagram of measured refraction versus measured surface refractivity for selected observed altitude angles (Collins Radio)

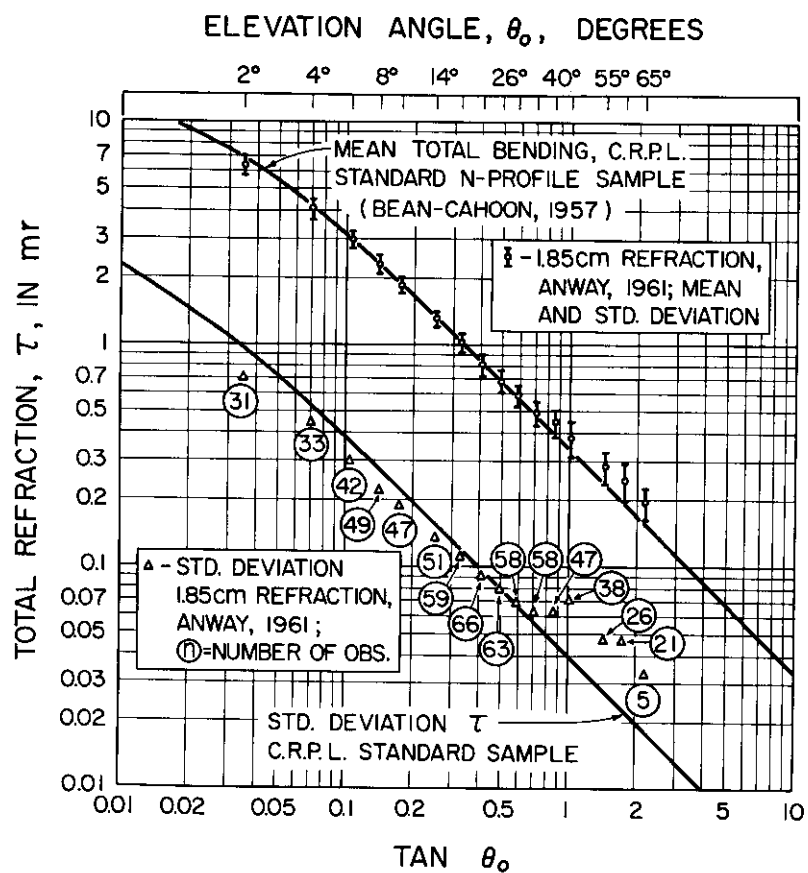


FIG. 4 Comparison of measured total atmospheric refraction of 1.85 cm radio waves at Cedar Rapids, Iowa, with values predicted from  $N_s$

Refractive Index Profile Sample, or the CRPL Standard Sample. Actual ray tracing to 70 km was performed on these samples and estimates of bending,  $\tau$ , were determined for each sample as a function of the initial elevation angle and the surface value of the refractivity. Regression lines were then drawn through the entire sample of 77 profiles, for each  $\theta_0$ , and values of  $a$  and  $b$  were determined as a function of the initial angle  $\theta_0$ .

Table 1 illustrates some of the values so determined. The standard deviation  $S_\tau$ , as well as the standard deviations from the regression line  $S.E.$ , is tabulated. The values in the last column  $P$  represent the decrease in the uncertainty of prediction from use of the regression line. Figure 2 illustrates graphically the results of this analysis for specified elevation angles. A more complete tabulation of values of the intercept and slope can be found in the National Bureau of Standards Technical Note 44 (3).

TABLE 1

$$h = 70.0 \text{ km (3)}$$

PARAMETERS IN THE DETERMINATION OF THE BENDING OF A  
RADIO RAY DUE TO TROPOSPHERIC REFRACTION, DERIVED  
FROM THE CRPL STANDARD SAMPLE

$\theta_0$	$\bar{N}_s$	$\bar{\tau}$	$r$	$b$	$a$	$S.E.$	$S_\tau$	$P$
0.0	334.0	21.1795	0.5174	0.1170	-17.9071	7.5113	8.7773	14.4236
1.0	334.0	18.1878	0.6391	0.0936	-13.0912	4.3738	5.6864	23.0831
2.0	334.0	16.4861	0.7361	0.0820	-10.8960	2.9251	4.3216	32.3144
5.0	334.0	13.9167	0.8837	0.6558	-7.9895	1.3481	2.8800	53.1910
10.0	334.6	11.9426	0.9051	0.0519	-5.4209	0.9539	2.2430	57.4721
20.0	334.6	9.1072	0.9797	0.0358	-2.8696	0.2862	1.4292	79.9748
52.4	334.6	5.1787	0.9979	0.0173	-0.6246	0.0445	0.6800	93.4559
100.0	334.6	3.0817	0.9997	0.0096	-0.1402	0.0095	0.3768	97.4788
200.0	334.6	1.6126	1.000	0.0048	-0.0212	0.0013	0.1910	99.3194
400.0	334.6	0.7862	1.000	0.0024	-0.0027	0.0002	0.0922	99.7831
900.0	334.6	0.2650	1.000	0.0008	-0.0002	0.0001	0.0310	99.6774

The use of the linear model based on the CRPL Standard Sample was tested experimentally by a group at Collins Radio Corporation at Cedar Rapids, Iowa, (5, 6). A precise radio sextant was used to observe the position of the sun. A circular scanning technique was used to accurately position the sun, assuming only that maximum signal intensity was at the center of the sun's surface. Sunspot and flare activity was observed and corrections made; instrument accuracy and stability were analyzed. Actual solar position was determined from an ephemeris specifically compiled for this purpose by the U.S. Naval Observatory. The experimentally determined correction to the elevation angle was then compared to that utilizing the surface value of the refractive index and the constants  $a$  and  $b$  determined from the CRPL Standard Sample. The Collins data are shown in Fig. 3, where the bending is shown as a function of  $N_s$  for several elevation angles. The Collins data were

compared with those predicted from the CRPL Standard Sample; this comparison is shown in Fig. 4. It should be noted that the mean of the experimental values of the elevation angle closely corresponds to that predicted from the CRPL Standard Sample. The standard deviation of the experimental data appears to be slightly smaller than that predicted from the standard sample for angles less than  $30^\circ$ . This presumably reflects the more extensive climatic conditions represented in the standard sample. The larger standard deviation exhibited in the experimental data for higher angles is probably due to the inaccuracies of the radio sextant. This departure can easily be explained by sextant inaccuracies of from 30 to 50 microradians.

Hence on the evidence to date it can be said that, in general, tropospheric refraction error in the angle of elevation to a space target can be adequately corrected utilizing the surface value of the refractivity and the CRPL Standard Sample. It appears at the present writing that very little increase in accuracy will result from the use of on-site radiosonde profiles as compared with that achieved using the CRPL Standard Sample. For elevation angles in excess of  $2^\circ$  the standard deviation will be less than 100 microradians; for elevation angles between  $2^\circ$  and  $1^\circ$  the standard deviation will be less than 200 microradians; and for an elevation angle of  $0.5^\circ$ , the standard deviation is 1 milliradian (7). This accuracy can be improved, especially at the lower angles, by use of the initial gradient of the refractivity through the region of the antenna beam. This method is discussed by Bean and Thayer (8). However, at these very low elevation angles it is difficult to determine whether the error in the elevation angle is due to atmospheric refraction or ground effects on the antenna beam.

It would appear that a similar method could be used to correct range errors. To date, this approach has not met with unqualified success. Although on paths in Colorado good agreement was found by Bean and Thayer (1), Thompson and Janes (9), using a phase-measuring system on various base-line tracking systems at Maui, have found poor correlation between  $N_s$  and range corrections, and also between  $N_s$  and elevation-angle corrections based on range measurements. It is yet to be determined whether these data indicate that this method fails for range measurements using base-line tracking systems or that Maui is an exceptional location.

The method of Eq. 6 does not apply for regions of climatic extremes, for angles less than  $3^\circ$  or  $4^\circ$ . For example, eastern regions of semi-permanent subtropical high pressure areas such as Dakar, Senegal, Southern California and the coast of South West Africa, the Arabian Gulf area and parts of the monsoon region in India and Pakistan, as well as arctic locations, can be cited as atypical areas.

#### TIME VARIABILITY OF $N_s$

The surface value of the refractivity changes as a function of time. Hence, the utility of using  $N_s$  and the CRPL Standard Sample is determined by this time variability. The Central Radio Propagation Laboratory (now Institute for Telecommunication Sciences and Aeronomy) has established a field site at Gunbarrel Hill, Colorado, near the Boulder Laboratories to investigate the variability of refractivity and its relationship to atmospheric parameters and processes. Figure 5 illustrates the measurements on a 45-meter tower used

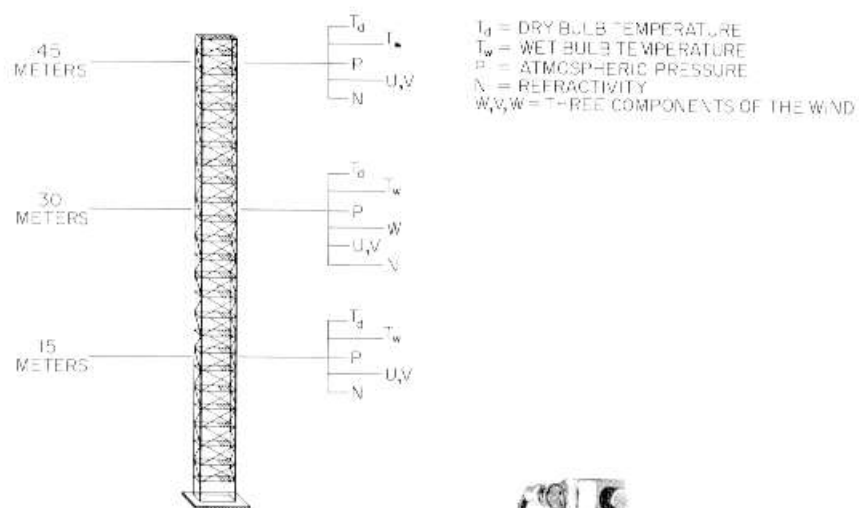


FIG. 5 45-m meteorological tower at Gunbarrel Hill, Colorado



FIG. 6 Sampling cavities for NBS microwave refractometer

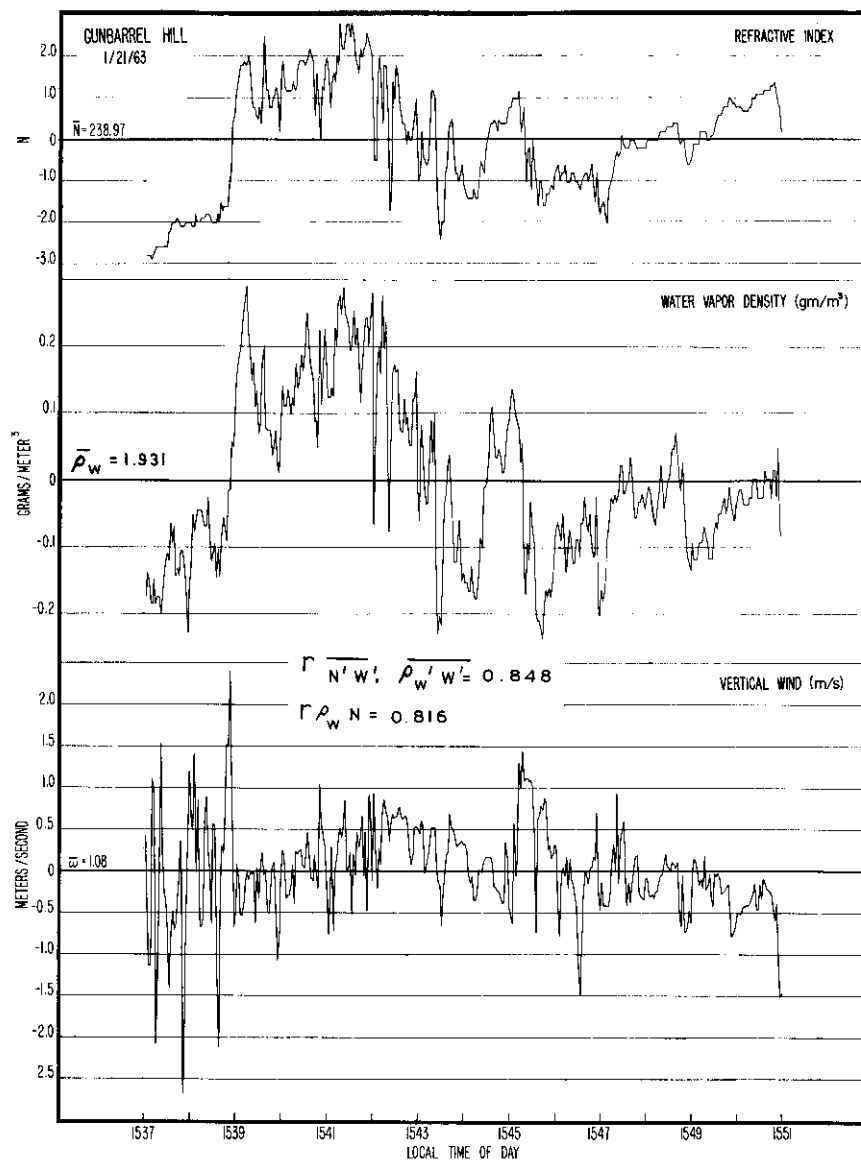


FIG. 7 Variability of the refractivity, water-vapor density and vertical wind in a 20-minute sample from an unstable atmosphere

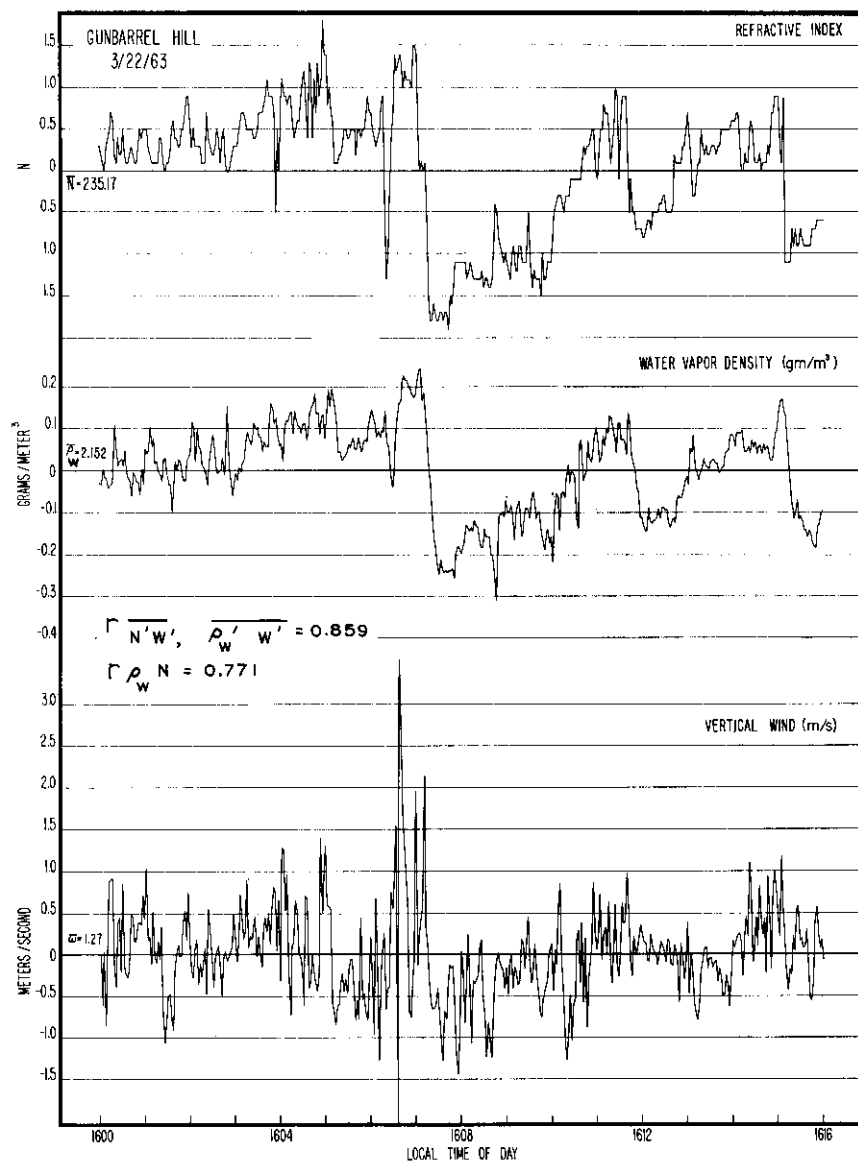


FIG. 8 Variability of the refractivity, water-vapor density and vertical wind in a 20-minute sample from a stable atmosphere

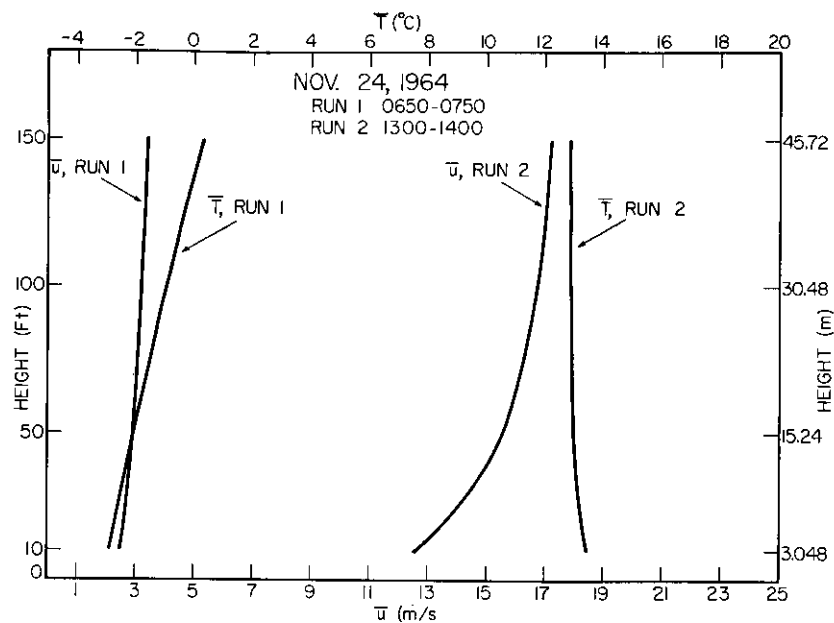


FIG. 9 Comparison between the vertical temperature and wind profiles for a stable sample (Run 1) and a neutral sample (Run 2)

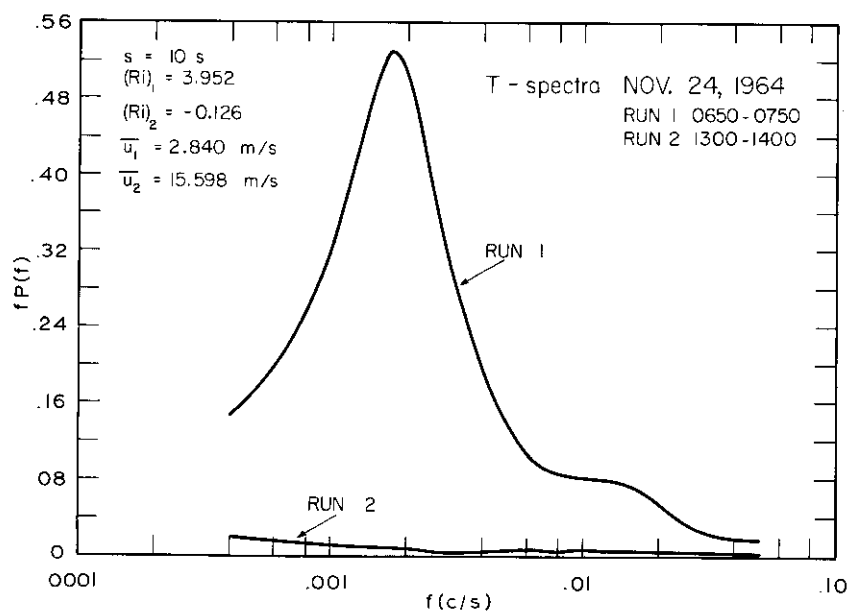


FIG. 10 The temperature spectra for a stable sample (Run 1) and a neutral sample (Run 2)



in these investigations. Temperature, pressure, humidity, three components of the wind, and refractivity are measured at various levels on the tower. The refractivity is measured using microwave refractometers. The types of sampling cavities used are shown in Fig. 6. Examples of the type of variability to be expected are illustrated in Fig. 7, where an unstable, turbulent atmosphere is present and Fig. 8, where a stable, stratified atmosphere is shown. The standard deviation for the unstable case is approximately 2  $N$  units, whereas the stable case yields a value of approximately 1  $N$  unit. Note that the second illustration on each of these figures is the water-vapor density ( $\rho_w$ ) measured at the same time. The correlation between  $N_s$  and  $\rho_w$  is of the order 0.8. The departure of the correlation coefficient from unity can be attributed largely to the errors in determining the water-vapor density (10).

Figure 9 shows the difference between a meteorologically stable sample (Run 1) and a neutral sample (Run 2). In the case of the stable sample the wind profile varies little with height and a temperature inversion is present. In Run 2 an almost classical example of a neutral or well-mixed atmosphere is shown, the lapse of temperature is adiabatic and the wind practically logarithmic. A comparison of the spectra of temperature (Fig. 10) shows the neutral case having very little variability for the hour sample, whereas the stable case indicates a large variability centered at a frequency of approximately .0015 c/s (a period in excess of 10 minutes). This characteristic of the temperature is reflected in the refractive index spectra, Fig. 11, where the stable cases indicate a power peak at .0015 c/s. Note the units of the ordinate are  $fP(f)$ . Since the total variance is equal to

$$\sigma^2 = \int_0^{\infty} P(f) df = \int_0^{\infty} fP(f) \frac{df}{f} = \int_0^{\infty} fP(f) d(\ln f)$$

the contribution to the variance for particular frequency bands can be determined by geometrically integrating the area under the curve. This has the advantage that the relative contribution to the variance for particular frequency bands can be estimated visually. For example Run 1 in Fig. 11, the contribution to the variance for all frequencies above .01 c/s (a period of 100 seconds) is approximately 0.085  $N^2$ , which is equivalent to a standard deviation of approximately 0.3  $N$  units.

Comparable estimates were determined by integration for contributions to the variability for both Runs 1 and 2 and for the samples in Fig. 7 and 8. The results are shown in Table 2. Cumulative contributions for all variations having periods less than 100 seconds, 5 minutes and 10 minutes are shown. In addition, the relative contribution to the total standard deviation is included. It can be seen that only for an unstable atmosphere is the contribution to the standard deviation in excess of 0.5  $N$  for variations having periods less than 5 minutes (.0033 c/s), even though this is better than half the contribution to the standard deviation. Hence, it would be expected that for stable or neutral conditions over a 5-minute period the value of  $N_s$  would remain within a range of less than  $\pm 0.5 N$  units from its mean value for at least 66 per cent of the time; unstable or turbulent conditions should produce a range half again as large.

TABLE 2

CONTRIBUTION TO THE STANDARD DEVIATION FOR ALL TURBULENT COMPONENTS HAVING PERIODS LESS THAN THAT INDICATED

Maximum period	100 sec.		5 min.		10 min.	
	<i>x</i>	<i>y</i>	<i>x</i>	<i>y</i>	<i>x</i>	<i>y</i>
Run 1 (stable)	.27 <i>N</i>	36%	.39 <i>N</i>	53%	.48 <i>N</i>	65%
Run 2 (neutral)	.32 <i>N</i>	49%	.43 <i>N</i>	66%	.50 <i>N</i>	77%
Figure 8 (unstable)	.45 <i>N</i>	27%	.70 <i>N</i>	42%	*	
Figure 9 (stable)	.30 <i>N</i>	43%	.40 <i>N</i>	57%	*	

*x* = the contribution to the total standard deviation from all components having periods less than that indicated.

*y* = the percentage of the total standard deviation of the sample.

\* Figures 8 and 9 are 20-minute samples; hence, no values are given for 10-minute periods.

These results can be used for the determination of the relative variability of the mean value of the bending, utilizing values from the CRPL Standard Sample (3). Assuming a surface value of the refractivity of 344 *N*, an elevation angle of 1°, and a target altitude of 70 km, it was found that a 0.5 *N* variation in *N* would produce an uncertainty in the mean value of  $\tau$  of no greater than 0.5 per cent. For the turbulent or unstable sample, the uncertainty is less than 1 per cent.

It would appear from this data that, at least in Colorado, the measured value of the surface-refractive index would be sufficiently stable over a 5-minute period to make its use practical. The use of microwave refractometers and relatively simple computers provide a realistic method for using the CRPL Standard Sample and the surface value of the refractivity for correcting observed elevation angles for atmospheric refraction.

#### ADDENDUM

**The correlation between the refractivity and water vapor** – It was noted in Fig. 7 and 8 that the refractivity as measured with a microwave refractometer is well correlated with water-vapor density as measured with wet- and dry-bulb thermocouples. In both the stable and unstable 20-minute samples the correlation was approximately 0.8. However, an error analysis indicates that this correlation could in reality be close to unity when the inherent accuracy of the thermocouple system is considered. A comparison between several 1-hour samples is shown in Fig. 12 and 13, the former a sample from a stable atmosphere, the latter one from an unstable atmosphere. It can be seen that the correlation is very good in the case of the unstable sample, whereas that for the stable sample is not as apparent. If a coherence spectrum is drawn for each of these samples (Fig. 14), then a different view of correlation can be seen. The coherence at frequency *f* is defined as (11)

$$\text{Coh}(f)_{xy} = \frac{Co(f)_{xy^2} + Q(f)_{xy^2}}{S(f)_x S(f)_y}$$

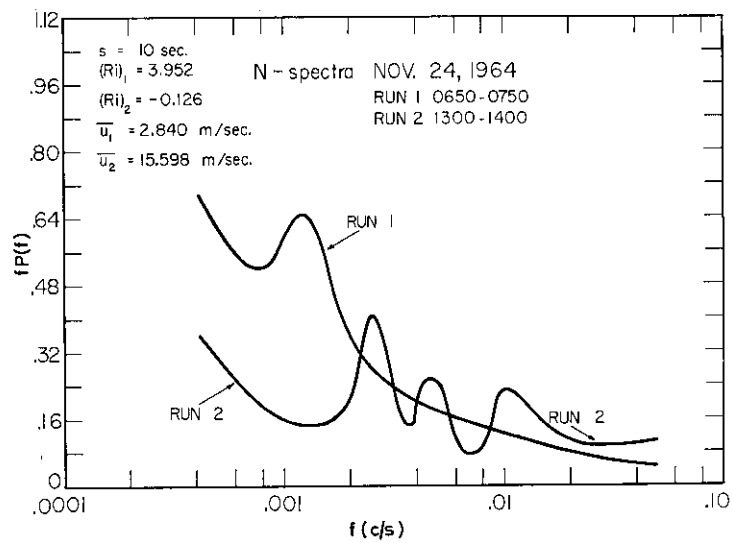


FIG. 11 Spectra of the refractivity for a stable (Run 1) and a neutral (Run 2) sample

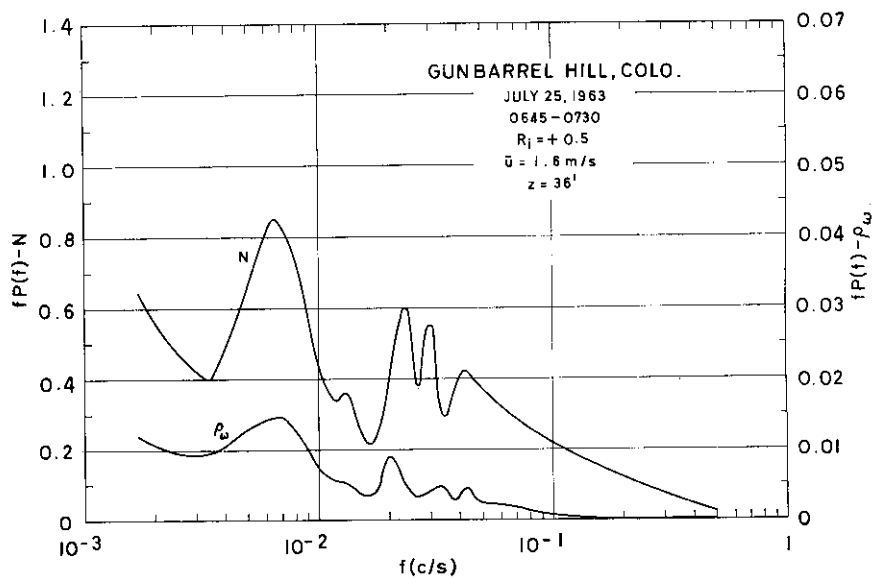


FIG. 12 Spectra of refractivity and water-vapor density for a stable sample

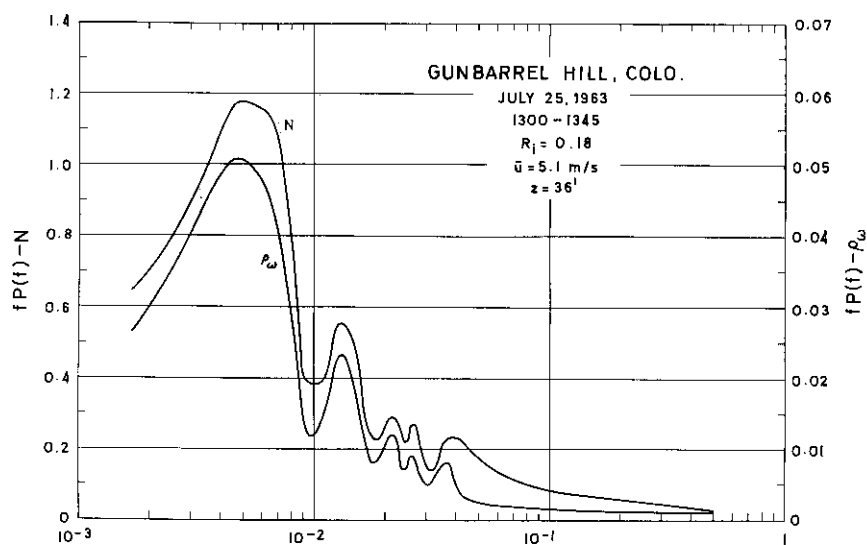


FIG. 13 Spectra of refractivity and water-vapor density for an unstable sample

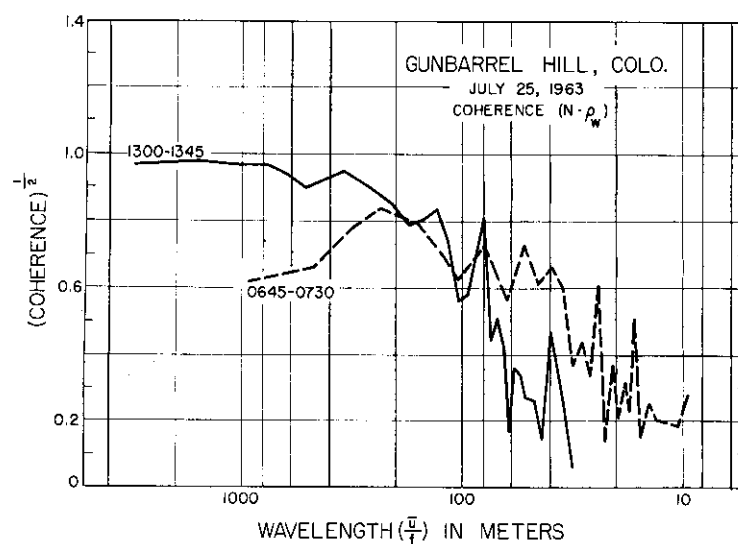


FIG. 14 Coherence spectra of the refractivity and water-vapor density under unstable and stable conditions

where

$$\begin{aligned} Co(f)_{xy} &= \text{Cospectral density of } x \text{ and } y \text{ at frequency } f \\ Q(f)_{xy} &= \text{Quadrature spectral density of } x \text{ and } y \text{ at frequency } f \\ S(f)_x &= \text{Spectral density of } x \text{ at frequency } f. \end{aligned}$$

The coherence is analogous to the square of the correlation coefficient at a particular frequency. It is always positive and normally no greater than unity. The advantage of the coherence spectrum is that the correlation is expressed as a function of discrete frequency bands. A high correlation coefficient may be reflecting the preponderance of low-frequency correlation and in actuality be a poor estimator for high-frequency correlation. This can be seen in Fig. 14, where frequency is converted to atmospheric scale lengths using the mean wind as a parameter. For the turbulent sample (1300–1345), the correlation or the square root of the coherence is above 0.9 for atmospheric scales in excess of 250 meters, but falls off drastically for scales smaller than this. The stable sample (0645–0730) exhibits the best correlation for scales larger than 200 meters, but falls off for scales greater or less than this value.

It is hoped that analyses of these kinds will lead to a better understanding of the physical processes involved in the production of the turbulence of the refractive index. These studies should produce optimum methods for measurement and evaluation, as well as provide the basis for development of techniques for correction.

#### REFERENCES

1. BEAN, B. R., and THAYER, G. D., "Comparison of observed atmospheric radio refraction effects with values predicted through the use of surface weather observations". J. Res. Nat. Bur. Stand. 67D, 273–85, 1963.
2. SCHULKIN, M., "Average radio ray refraction in the lower atmosphere". Proc. IRE 40, 554–61, 1952.
3. BEAN, B. R., CAHOON, B. A., and THAYER, G. D., "Tables for the statistical prediction of radio ray bending and elevation angle error using surface values of the refractive index". NBS Tech Note 44, March 16, 1960.
4. BEAN, B. R., and CAHOON, B. A., "The use of surface weather observations to predict the total atmospheric bending of radio waves at small angles". Proc. IRE 45, 1545–6, 1957.
5. ILIFF, W. R., and HOLT, J. M., "The use of surface refractivity in the empirical prediction of total atmospheric refraction". J. Res. Nat. Bur. Stand. 67D, 31–5, 1963.
6. ANWAY, A. C., Collins Res. Rep. No. CRR-2425, Collins Radio Co., Cedar Rapids, Iowa, 1961.
7. NORTON, K. A., "Effects of tropospheric refraction in earth-space links". Progress in Radio Science 1960–1963, Vol. II: Radio and Troposphere, Proceedings of Commission II on Radio and Troposphere during the XIVth General Assembly of URSI, Tokyo, 1963. Ed. F. Du Castel. Elsevier, New York, 192, 1965.

8. BEAN, B. R., and THAYER, G. D., "Models of the atmospheric radio refractive index". Proc. IRE 47, 740-55, 1959.
9. THOMPSON, M. C., and JANES, H. B., Private Communication.
10. BEAN, B. R., and MCGAVIN, R. E., "The use of the radio refractometer to measure water vapor turbulence, humidity and moisture, measurement and control in science and industry". Ed. Arnold Wexler. Reinhold, New York. 2, 581-568, 1965.
11. LUMLEY, J. L., and PANOFKY, H. A., "The structure of atmospheric turbulence". 19-23. Interscience, John Wiley, New York, 1964.

## CLOSING REMARKS

PROFESSOR M. ANASTASSIADES

Before closing the meeting I should like to make some comments on the way in which we have proceeded and to remind you that the 10th IRC Meeting was the first meeting to be held under our new Terms of Reference. This change has been justified by the success of this meeting. *It has enlarged our family by the introduction of specialists in tropospheric propagation, and shown that from our close collaboration new light can be thrown upon the work of the committee.*

*I am quite certain that the scientific community in the NATO nations, especially the Allied Command Europe, would be interested in our proceedings.*

Perhaps the most interesting feature of the symposium is the new light upon ionospheric irregularities thrown by the use of top-side sounders and other techniques. The top-side sounder has shown that these irregularities extend far above the F2 max. We are left wondering what can be the physical mechanism which can give use to such large effects – it may be that this would be a problem for Prof. V. Krzywoblocki. To the non-mathematician his optimal processes are difficult to understand, but clearly some method of this sort is necessary.

The papers on plasma sheaths have given a good survey of both theory and experiment in this modern and important field. In the past the great advance in this field by ionosphericists has provided *one more example of how tenuous is the boundary between pure and applied science.*

Tropospheric propagation has only recently come within the terms of reference of the IRC. The good crop of papers which we have had at this meeting has provided a thorough justification for the widening of our terms of reference.

But before closing I should like to express our gratitude to Prof. Ranzi for the excellent way in which he organized technical and social activities for this meeting.

I would also like, while speaking about the scientific programme to thank the Programme Committee Members, that is to say our Vice-Chairman, Dr Burgess of the United Kingdom, Dr Davies of the U.S. and Ing. en chef Voge of France, for having succeeded so well in their difficult task.

On behalf of all those present I would like to thank our colleagues and to ask Prof. Ranzi to convey our sincere thanks to the Institute Superiore of Posts and Telecommunications and the Italian authorities for their kind invitation and for this pleasant and useful time.

*I now declare the 10th Ionospheric Research Committee Meeting closed.*





# STUDY OF THE AMPLITUDE OF THE RADIO-ELECTRIC FIELD OF A SATELLITE AT THE HORIZON OF A RECEIVING STATION

J. F. AUREJAC and J. PAPET-LEPINE

Laboratoire de Physique de l'Atmosphere, Faculté des Sciences, Paris

## SUMMARY

Using a high-gain aerial at 40 Mc/s which can be pointed in any direction of azimuth, it is possible to receive the signals from the satellite *Explorer 22* at the Val-Joyeux Station, Paris, on all revolutions from  $330^\circ$  to  $206^\circ$  longitude of equatorial crossing. This represents in the extreme cases of the satellite observer distance sometimes reaching more than 5000 km.

From a very large survey of the ionosphere it is possible to demonstrate a considerable intensification of the effects due to the refraction and to the action of irregularities in the distribution of the electronic density of the medium traversed. In the same way a strong increase of the scintillations is noted when the angles of elevation are of the order of  $20^\circ$  and below. This intensification of the scintillations is particularly visible towards the north, but equally so towards the south. In the last case we have confirmed a certain correlation between the magnetic activity and of the scintillation index. A systematic comparison with the results obtained by other stations was afterwards made to determine the areas where these scintillations originate.

## INTRODUCTION

When the ionosphere shows irregularities in the spatial distribution of electron density, the refractive index varies a great deal from one point to another in the ionosphere and the receiving aerial collects many wave samples whose phase is determined by these surveys. Since the distribution of the phases is tied to the value of the local refractive index, an intensification or diminution of the received field according to the area of the irregularity by the incidental wave will have been verified, as well as a local modification which affects the frequency excursion due to the Doppler effect. The study of the sudden variations of amplitude which come from the phenomenon of scintillation must furnish information on the constitution of the areas where the irregularities originate. These variations of the emitted signal are amplified when the satellites appear on the horizon of the receivers. Important phenomena are produced from the effect of a very large sweep across the ionosphere which strikingly strengthens the effect of the refraction on the one hand, and on the other hand, the action of relatively weak heterogenities in the electron density.

Problems of refraction have already been gone into, but only in a theoretical manner, and it does not seem that up to now the observations undertaken with a dipole receiver can account for predicted phenomena, since the field diminishes rapidly with the departure of the satellite and the same applies to the scintillations. If an increase of scintillation when the angles of elevation decrease is verified, the nature and structure of the scintillations produced at angles of elevation less than or very much less than  $30^\circ$  is not known.

#### RECEIVING CHAIN

With the aim of studying the refraction and the action of the heterogeneities of the ionosphere when the satellite is low on the horizon, we first of all constructed a Yagi aerial of nine elements at 54 Mc/s to study signals of the satellite *Transit IV A* (61 omicron 1), then a Yagi aerial of eleven elements at 40 Mc/s for the study of the signals of the satellites *Explorer 22* and 27 (1964 – 64A and 1965 – 32A). The aerial is placed on a pivot driven by a servomotor in azimuth. It is fixed in elevation and its axis is placed at  $20^\circ$  above the horizon with its aperture angle a little greater than  $40^\circ$  at  $-6$  dB. The azimuth angle mechanical restoring unit is fairly delicate by reason of the aerodynamic problems caused by the large dimensions of this aerial. Sighting errors can arise from azimuth errors caused by the force of gusts of wind. Careful setting of the remote control unit would allow the exact azimuth position to be defined with precision, whatever fluctuating forces the aerial was subjected to.

The receiving chain consists of a primary frequency changer which also serves as a preamplifier and a superhet receiver. The local oscillators are controlled by high-stability quartz crystals ( $10^{-7}$  per hour). The signal amplitude is transmitted to a sensitive recorder with a low chart speed (60 mm per minute) in order to obtain the general character of the phenomena. Working in parallel a 100 c/s recorder with a chart speed of 75 cm per minute gives a fine analysis of the scintillations.

#### GENERAL RESULTS

From the recordings made on dipoles, we have always obtained important scintillations towards the north. However, when the satellite is low enough on the horizon, scintillations just as important can appear towards the south, generally when the emitted waves go through the dense layers of the ionosphere. These phenomena are particularly visible on the recordings of the 20 Mc/s of the Italian satellite *San Marco*, whose maximum point of ascent is at  $37^\circ$  latitude north, Fig. 1.

Although the frequencies used are different, these last findings are confirmed by observations made with a high-gain aerial. In fact, it is possible to receive the signals of the satellite *Explorer 22*, for example, for all revolutions from  $315^\circ$  to  $210^\circ$  longitude W. of equatorial crossing. This represents distances between satellite and observer of the order of 5000 km, the duration of the passage being thus increased from 5 to 6 minutes in comparison with the duration of a normal passage received on a dipole.

A strong increase of the scintillations is thus verified when the angles of elevation of the direction of propagation are less than  $20^\circ$ . This strengthening of the scintillations is in particular visible towards the north, and equally well

towards the south. In the last case, and more particularly in the south-east of the station, we have confirmed that the strengthening had not always taken place and that it was correlated with the index of magnetic activity. In general, we find many scintillations when the index of magnetic activity is weak. These large-amplitude scintillations completely mask the rotations due to the Faraday effect, whilst for a high value of this index the few scintillations of low amplitude superimpose themselves on the Faraday rotations, whose zeros then appear clearly. This is much more visible in this direction, because the product of the local magnetic field and the cosine of the angle between this field and the direction of propagation is important, hence because of this the period of the Faraday rotations is very short in that direction, Fig. 2 and 3.

However, a quick examination shows that the structure of the scintillations varies in terms of the angle of azimuth; in particular, the scintillations seen in the south are very different from those seen in the north. It even seems that this structural difference may be due to a difference in nature. The scintillations seen in the north are not only due to the dense layers of the ionosphere penetrated; they have rather more of a character which qualitative experience can distinguish from the others.

With the aim of investigating these structural differences, it was interesting to compare systematically the results of recordings from the station at Val-Joyeux with those obtained by European stations which received the same signal at higher angles of elevation. Since the areas in which we were interested were to the north and south-east of the station, we accordingly used 223 recordings obtained from each of the following stations: Kiruna, Sweden ( $20^{\circ} 26'$  long. E and  $67^{\circ} 50'$  lat. N), Kjeller, Oslo, Norway ( $10^{\circ} 46'$  long. E and  $60^{\circ} 13'$  N), and Athens, Greece ( $23^{\circ} 43'$  long. E and  $37^{\circ} 58'$  lat. N), with which the station of Val-Joyeux, Paris, France ( $2^{\circ} 1'$  long. E and  $48^{\circ} 49'$  lat. N) cross-checks, Fig. 4.

#### ABSTRACT FROM THE EXPERIMENTAL DATA

With regard to the study of refraction on the horizon, abstraction of the experimental data is made in the following manner. For each passage of the satellite *Explorer 22*, the exact times of the signals appearance and disappearance are measured. When this appearance or disappearance takes place slowly, the exact time corresponding to an amplitude of 20 per cent above background noise is measured. For the statistical study of the limiting angle of reception, an occasional distinction is made between the known times (clear variation of the signal above the background noise, a variation generally accompanied by rapid scintillations during a period of less than a minute) and doubtful times, given by a weak undulation of the background noise. (It is to be noted in passing that the difference between these times generally varies from 30 to 60 seconds.) Finally the times corresponding to the appearance and disappearance of the scintillations at the beginning and at the end of the passage are measured. As the aerial is fixed in elevation, the results for angles of elevation higher than  $40^{\circ}$  are not completely accurate, due to the radiation diagram of the aerial.

As can be seen from the recordings, the scintillations present an amplitude and shape which vary with time. In practice it is therefore necessary to make

a distinction between slow and rapid scintillations, the boundary being set at 1 c/s. This distinction also takes into account the fact that the slow scintillations are much more irregular, their false period can go down to 0.1 c/s. Detailed analysis shows that the frequency of the regular scintillations is of the order of 2 to 4 c/s; sometimes fairly irregular variations appear lasting some tens of seconds which have a false frequency of around 20 c/s. Moreover, these two scintillation types are separated into two categories; those with an amplitude of more than 25 per cent and those with an amplitude less than 25 per cent of the mean level of the received signal. Hence for each of the stations, four types of scintillation will be distinguished, numbered 2, 3, 4, 5:

$$\begin{aligned}\text{Type } S = 2 : A > 25\%, f_s > 1 \text{ c/s} \\ S = 3 : A > 25\%, f_s < 1 \text{ c/s} \\ S = 4 : A < 25\%, f_s > 1 \text{ c/s} \\ S = 5 : A < 25\%, f_s < 1 \text{ c/s}\end{aligned}$$

Figures 5 and 6 show examples of amplitude recordings of the signal given out by the satellite *Explorer 22*. In them can be seen the difference between the recording from a high-gain aerial and that from a dipole, as well as the different types of scintillation encountered.

The analysed passages of this satellite took place during the period from December 25, 1964, to March 31, 1965. Out of 228 revolutions considered as favourable, only 207 of them have been obtained for the Val-Joyeux station such that at least one foreign station was able to record one of the revolutions under good conditions. Val-Joyeux thus has 48 revolutions in common with Athens, 12 with Kjeller and 66 with Kiruna. There are also 60 rotations in common with three stations (Val-Joyeux, Athens, and Kiruna: 26; Val-Joyeux, Kiruna and Kjeller: 21; Val-Joyeux, Kjeller and Athens: 13). Finally 21 revolutions common to four stations were found. All these revolutions give 1068 cases of scintillations.

#### STATISTICAL DISTRIBUTION OF THE SCINTILLATIONS

Let us first introduce the degree of scintillations which we shall define as being the ratio of the number of cases of observed scintillations, to the number of revolutions recorded in one station. It is found that the degree of scintillations is 1.7 for Val-Joyeux, 1.9 for Athens, 2.2 for Kjeller and 2.8 for Kiruna. From this it can be broadly deduced that the probability of finding scintillations is nearly twice as great at the Kiruna station than at Val-Joyeux.

Tables 1, 2, 3 and 4 give the cases of scintillations for each station, in hourly periods, the type of scintillations and the value of K (index of diurnal magnetic activity). Percentages (marked on the table %T.G.) have been calculated from the number of cases observed in each of the stations. These tables have been compiled only from the cases of quasi-longitudinal propagation. In the 40 Mc/s band, the angle  $\theta$  between the direction of the magnetic field and the direction of propagation must satisfy the inequalities  $\theta > 91^\circ$  or  $\theta < 89^\circ$ . If  $89^\circ < \theta < 91^\circ$  we have cases of transverse propagation. The latter, observed here, are fairly rare; in percentages of the total they are as follows: Val-Joyeux < 1 per cent, Kjeller < 2.7 per cent, Athens < 0.5 per cent, Kiruna < 1.2 per cent.

From the preceding tables, a first series of histograms can be taken, giving

the number of cases of scintillations (total scale = 100 cases) in terms of the hourly period for  $K = 0$  and  $K = 1$  for each station. A second series gives the distribution of the four types of scintillations considered, Fig. 7. The following cases emerge successively in order of importance:

$$\left. \begin{array}{l} K = 1 \quad S = 3 \\ K = 1 \quad S = 5 \\ K = 1 \quad S = 2 \\ K = 1 \quad S = 4 \end{array} \right\} f_s \text{ 1 c/s}$$

$$\left. \begin{array}{l} K = 0 \quad S = 3 \text{ and } S = 5 \\ K = 0 \quad S = 4 \\ K = 0 \quad S = 2 \end{array} \right\}$$

From this it is to be noted that types 3 and 5 are preponderant in each one of the stations, which would tend to diminish the importance of the amplitude of the radio-electric signal perturbations. On the other hand, an inversion in the order of importance is verified for  $S = 2$  and  $S = 4$ , according to the value of the index of magnetic activity. Generally, for an index of diurnal magnetic activity of zero, there are far fewer scintillations than for  $K = 1$ .

Examination of Fig. 7 for hourly periods shows that the fewest observed for the hourly period 12–16 h is at Kjeller. This is verified at Athens, except for  $K = 0$  and  $S = 5$ , in the same way at Val-Joyeux, which is halved for the period 20–24 h and for  $K = 1$  and  $S = 3$  on the one hand and on the other hand for  $K = 1$  and  $S = 4$ . For Kiruna station, however, the fewest is shifted into the hourly period 4–8 h. Moreover, Val-Joyeux and Kiruna tend to observe one single maximum of scintillations (between 16 h and 24 h).

By scintillation type the following distribution is found:

$S = 3$ : This is the most frequent case for Val-Joyeux and Kiruna, with a very marked single maximum between 16 h and 20 h (Val-Joyeux) or 20 h and 24 h (Kiruna for  $K = 1$ ). A much greater distribution is observed during the day for Athens and Kjeller with the same maximum, but attenuated, and by contrast, with a strongly marked minimum between 12 h and 16 h.

$S = 5$ : This is the most frequent case at Athens and Kjeller. Note a maximum between 16 h and 20 h and a minimum between 4 h and 8 h for Val-Joyeux,  $K = 0$  and 1 and Kiruna  $K = 1$ .

$S = 2$ : Note the same tendency as for  $S = 3$ .

$S = 4$ : Note the same tendency as for  $S = 5$ ; except for Kiruna where the maximum of 16–20 h is replaced by a minimum.

#### GEOGRAPHICAL DISTRIBUTION OF THE SCINTILLATIONS AROUND EACH STATION

Table 5, where in each case the percentage of cases observed has been indicated, gives this geographical distribution.

The station at Athens always observes a maximum of scintillations towards the south, except for the scintillation type  $S = 5$ , where the maximum is towards the north.

Kiruna always observes a maximum towards the north (strongly marked maximum for  $S = 3$  and  $S = 2$ ) except for scintillation type  $S = 5$  and  $S = 4$ , where two maxima are found for  $K = 1$  at the north and at the south, a behaviour reverse to that of Athens. We would add that Kiruna always presents a secondary maximum towards the west.

In the case of Kjeller, the geographical distribution of the scintillations is fairly uniform with, however, a minimum in the east as for all the stations. Note also a marked maximum in the north for  $S = 3$  and  $K = 0$ , as well as for all types for  $K = 1$ .

Note a relatively uniform distribution at Val-Joyeux with, however, a maximum towards the north and a secondary maximum towards the south. The northern maximum is more accentuated for  $S = 3$ , as for Kjeller and Kiruna.

Rather more generally, the same tendency can be noted in all stations for cases  $S = 3$  and  $S = 5$ , whatever  $K$  may be

- a very marked tendency to a maximum towards the north of the stations for  $S = 3$ , except Athens, whose maximum is towards the south.
- a tendency to an important increase of the scintillation towards the south for  $S = 5$  in all station except for Athens, which presents a maximum towards the north for  $K = 0$ .

The scintillation types  $S = 2$  and  $S = 4$  appear much less frequently. For Val-Joyeux and Kjeller it is ascertained that they are equally distributed between the north and the south of the station. For Athens the maximum takes place towards the south for  $S = 2$  and  $S = 4$ . For Kiruna there is a maximum at the north and a secondary maximum towards the west.

#### GEOGRAPHICAL REPRESENTATION OF SCINTILLATION ZONES

Expressing latitude in ordinates, and longitude in abscissae, it is possible to obtain graphs showing the temporal limits of the sub-ionospheric trajectories in which scintillations of a given type took place. Then for each type, and for each value of the index of diurnal magnetic activity, from the graph it can be shown that there are chosen hourly periods.

By way of example we give the diagrams corresponding to the scintillations,  $S = 3$  and  $S = 5$  for the respective hourly periods: 20–24 h and 16–20 h, Fig. 8 and 9. Figure 8 shows a representation of the scintillation zones extending on all sides for the satellite projectories. Depending on whether the passages of this polar satellite ascend or descend, two beams can be distinguished which leave the south together, and end, one at the north-west, and the other at the north-east of Kiruna. In the case of Fig. 9, only a single one of these beams exists which converges towards the north-east of Kiruna. Note that this convergence at Kiruna is due to rotations of longitude west at the equator of the order of  $0^\circ$ , whilst Val-Joyeux, though also presenting rotations coming from some  $150^\circ$ , contributes, as well as the other stations, to the establishment of this convergence.

On the other hand, it is observed that the scintillations type  $S = 3$  tends to appear to the north-west of the stations (except for Athens), the arcs of the scintillation trajectory tending to form themselves into the shape of a V, the point of which takes the direction of the north-west of the station, into a region for which the angle  $\theta$  borders on  $90^\circ$ . This result shows that the farther away the observed scintillation is, then the more acute is the angular sector in which it appears in azimuth, the direction of this vector going towards the values of  $\theta$  which approach  $90^\circ$ . The scintillation type  $S = 3$  appears also in the west and the south-west of the stations, but this appearance is then a

function of time. Scintillations of type  $S = 5$  tend to appear from 4 h to 12 h in the north-west of the stations, as with type  $S = 3$ , but they tend to appear from 12 h to 24 h towards the south in an azimuth sector going from the south to the south-west for Kiruna and Kjeller; more open and going from the south-east to the south-west for Val-Joyeux. However, it must be noted that the intensity of apparition of these scintillations depends on the time. For example, from 12 h to 16 h type  $S = 3$  is more to the north than type  $S = 5$ ; from 16 h to 20 h it is type  $S = 5$  which is more to the north than type  $S = 3$ , whilst from 20 h to 24 h it is again type  $S = 3$ , which is more to the north than type  $S = 5$ . Note also for Val-Joyeux some scintillations in the west depend on the time.

On the other hand, geographical zones can be plotted in which scintillations of the same type, or of a different type, seen from two or three different stations are presented, but varying statistically within an hourly group. The principal zone is situated at the north of Val-Joyeux, between  $53^\circ$  and  $63^\circ$  of latitude north and between  $0^\circ$  and  $13^\circ$  longitude east. It affects the observations of Kiruna, Kjeller and of Val-Joyeux. The second zone is in the south-east of Paris, between  $40^\circ$  and  $44^\circ$  latitude north, between  $19^\circ$  and  $22^\circ$  longitude east.

Another way of illustrating a geographical representation of the scintillations consists of using a graph similar to those of Fig. 9 and 10, but limited to a single rotation of the satellite. Figures 10, 11 and 12 give three examples of such a representation. The three rotations used have almost the same longitude west to the equator, hence they have trajectories almost similar, but with intervals of time of several weeks. If these three figures are superimposed, then relatively narrow zones are found where the recorded scintillations repeat. Evidently these zones are compressed, since calculations have been made with a constant height of the ionosphere. Whatever it may be, the fact of using different heights would lead to an enlargement of the zone, but not to an extension along the sub-ionospheric trajectory.

#### STATISTICAL DISTRIBUTION IN TERMS OF THE ANGLE OF ELEVATION AND TYPE

For each value of  $K$  on the one hand and for each type of scintillation on the other hand, we have plotted a series of histograms for each of the stations, according to the value of the angle of elevation  $E$ , contained in the following series:

$$E\ 0^\circ, \quad 0\ E\ 8^\circ, \quad 8^\circ\ E\ 20^\circ, \quad E\ 20^\circ$$

The first series is made for  $K = 0$ , Fig. 13, the second is made for  $K = 1$ , Fig. 14, and the last is made on the total number of cases without taking into account the individual observation stations, Fig. 15.

From Fig. 13 and 14 we confirm that only Val-Joyeux has scintillation recordings when the angles of elevation are negative. The majority of the scintillation recordings take place in this station with angles of elevation much smaller than  $8^\circ$ , whatever the value of  $K$ .

The station at Athens has a distribution which is very little marked, except in the case of  $S = 4$ , which appears most often for very high angles of elevation whatever the value of  $K$ , but it must be noted that there is a tendency

for the more important scintillations to appear towards the low angles of elevation for  $K = 0$ . The station at Kjeller has few scintillations of the type  $S = 2$  and  $S = 4$ . For the other types, the occurrence is definitely stronger towards the low angles of elevation. For Kiruna, whatever the scintillation type of the value of  $K$ , the distribution is much more uniform than in the other stations. However, it is to be noted that there is a tendency towards more marked occurrence for  $S = 2$  and  $S = 4$  towards the higher values of elevation and for  $S = 3$  and  $S = 5$  towards the lower values of it.

Notice that on Fig. 15 there is a distribution almost identical of types  $S = 3$  and  $S = 5$ , whatever the value of  $K$ , with a maximum of occurrence in the zone between  $0$  and  $8^\circ$ . The zone for which the angle of elevation is negative appears under a low occurrence by reason of the fact that only Val-Joyeux has recordings under these angles. For type  $S = 2$ , there is a maximum between  $0$  and  $8^\circ$  and a secondary maximum for the angles greater than  $20^\circ$ , whilst a minimum for zone  $8-20^\circ$  is to be observed. For scintillations of type  $S = 4$  a tendency similar to the preceding one is noted, the maximum and the secondary maximum being inverted. But this only takes place for  $K = 0$ ; for  $K = 1$  there is a maximum for the high values of angle of elevation and a diminution of occurrence gradually with the decrease of the angle of elevation.

The distribution of the cases of scintillation being more important for  $K = 1$  than for  $K = 0$ , the total distribution is hence nearer to that of  $K = 1$  than that of  $K = 0$ .

#### CONCLUSION

In this report we have above all set forth the rough results which can be obtained when comparing the data from several stations in Europe whose listening areas are cross-checked by those of Val-Joyeux. It is very evident that a finer analysis should be undertaken in a greater number of cases, i.e. for a listening period of at least one year. Be that as it may, we have observed tendencies more or less marked which it would be interesting to report on in the future. In particular the strengthening of the scintillations when the index of the diurnal magnetic activity is important. This general tendency is not incompatible with the fact that for the index of magnetic activity we have made a survey by hourly periods. In effect we have pointed out that in a zone of azimuth situated between the south-east and the south of the station the scintillations disappear for low values of angles of elevation. Likewise regarding the difference in nature between the scintillations which appear to the north and to the south of the stations situated in southern Europe, and those observed by the stations situated in the north of Europe. In the same way the scintillations of type  $S = 2$  are more important at the south than at the north of the station of Val-Joyeux when the angles of elevation are low. This tendency is less clear for  $K = 1$  with an inversion of the north to the south. On the other hand, the other types of scintillations are predominantly seen in the north of the station. Finally it is strange to confirm the relative importance of types 3 and 5, whatever the value of the index of diurnal magnetic activity may be.

We are indebted to M. le Professeur Vassy, who allowed us to carry out this study, also to M. F. Bertin, for the help he gave us in the computer



calculations. We are also indebted to the organizations which furnished us with the means to carry out this study: AGARD and the Centre National d'Etudes Spatiales.

## DISCUSSION

M. ANASTASSIADES – From the point of view of the appearance of the scintillations the case of Athens is presented in a particular way. Have you any explanation to offer?

J. PAPET-LEPINE – We have not yet found a satisfactory explanation. The singularities noticed at Athens with respect to the other stations were particularly striking. It seemed interesting to us to introduce some of their main aspects from now on.

K. RAWER – I would very much like to know if the scintillation and its probability depends on occasions on the aspect, that is, on the angle between the terrestrial magnetic field and the direction of propagation. To find out the Faraday effect, the effect of scintillation compared to an effect depending on that angle is noted. In the case where this would have been studied, it would seem to indicate the re-study of the influence of the magnetic character, taking into account the distinction of the angles of aspect.

J. PAPET-LEPINE – Calculation of the angle  $\theta$  between the earth's magnetic field and the direction of propagation is automatically made by the computer programme used in particular in this report in order to know the cases of transverse propagation. A comparative study with this angle requires a certain number of precautions. Be that as it may, the present study now under way will not only take account of this angle but also of the product  $B \cos \theta$ , which interferes precisely in the Faraday effect.

E. VASSY – With regard to the investigations relating to the heterogeneities of the ionosphere, I should recall the interest which the Joint Satellite Studies Group showed. This group originated with the launching of the first Sputnik in October 1957, on the initiative of Dr Jules Aarons of the U.S. Air Force Research Lab., Cambridge, Mass. At the start, apart from Cambridge, it consisted of the teams of Breisach (Western Germany), Jodrell Bank (G.B.), Florence (Italy), Kjeller (Norway), Kiruna (Sweden), and Val-Joyeux (France). Also Japan was with us at the start. Our role then consisted of recording the Doppler effect, and notifying each day the U.S. Air Force Lab. of the approach moment at the minimal distance and the gradient of the Doppler curve, in order to reconstruct the trajectory. That was the project 'Spacetrack'. This work lasted almost a year until the installation of the Minitrack system enabled more efficient and quicker tracking to be done.

But the recordings of the Doppler curves had shown numerous irregularities due to heterogeneities of the ionosphere; also as the teams of the group were free from tracking duties they were able to concentrate on studying the ionosphere. In fact, it is extremely valuable to arrange recordings, with the aid of standardized apparatus, of the Doppler curve and the field of the satellites, showing the Faraday effect at points conveniently distributed, above all in Europe. It is then possible by triangulation to estimate the altitude and the extent of the heterogeneities.

The work of the group which had been governed initially by the U.S.A.F. was then taken over by the Bureau of Scientific Affairs of NATO, then by

AGARD. With time, their financial status became more and more assured with governmental grants. This effective patronage brought about a development in the work of the group and in the group itself. In this manner the Athens team was added some little time ago, and since last April we number fourteen, with a team in Denmark, a second in the U.K., another in Spain, in Israel and even in Africa.

The work of the teams is made easier by a liaison bulletin, edited by the Florentine team, in which is found recorded the data relative to the revolutions studied together, and also by an annual work meeting when each team brings kilograms of paper and compares recordings and prepares the work to be done in the following year.

Obviously each team keeps its individuality and concentrates on one speciality in agreement with the whole of the group. Above all, the recordings of each group are at the disposal of the other groups. From this arise frequent changes and transfers of team members. You have had an illustration of this by the work presented by Dr Papet-Lepine who went on site to study the recordings of Athens, Kjeller and Kiruna. It frequently happens that special recordings are called for by such-and-such a team. The geographical study of the ionosphere has been made easy, thanks to AGARD, and the aim of my intervention is to inform you of the existence of a considerable mass of data and to say that it can be placed at the disposal of the interested specialists. I will add that besides this the laboratories of the group prepare satellite equipment for special studies. This was the case for example for the *Orbis* satellite of the U.S.A.F. and the Italian satellite *San Marco*. Others are under way or projected.

There we have an example of co-operative study of the ionosphere, efficient because it is not weighed down by a large international association and also because working relations between its members are rapidly becoming friendly relations.

SUPPLEMENT—TRANSLATIONS



## SUBJECT INDEX

- Absorption events, 261-271  
 Anisotropic medium, 195-201, 297, 299-307  
 Antenna in plasma, 351-374, 376-382  
 Antenna loss of gain, 431, 433-440  
 Antenna noise (rain), 526  
*Alouette I*, 133-144, 147, 148, 151-153, 157-159, 203-207  
*Alouette II*, 133  
*Ariel*, 276, 280  
 Atmospheric, 398-401  
 Attenuation, deep space, 60, 65; ionospheric, 35, 39; tropospheric, 28, 31, 489, 490, 492-520; cloud, 34, 35, 420, 496, 498; fog, 34, 35, 420, 498; oxygen, 32, 385, 413, 415, 491-498, 514; rainfall, 33, 35, 386, 420, 507, 512, 525; water-vapour, 385, 413, 415, 417, 420, 491, 494, 507, 514, 518  
 Auroral zone, 209-223, 241-259  
  
 Camera, all sky, 227, 228, 231, 232, 236  
*Cassiopeia A*, 233, 234, 241-259  
 Cosmic noise, 44, 46  
 Critical frequency, 168-170  
*Cygnus A*, 241-259  
  
 D-region, 203, 275, 281  
 Delay, deep space, 68; ionospheric, 43  
 Deviation angle, 86, 93  
 Diffraction of random waves, 195-201  
 Dispersion, deep space, 68; ionospheric, 43  
 Doppler effects, 14; ionospheric, 19; tropospheric, 19  
  
 E-layer, 238  
*Earlybird*, 163, 167, 172  
*Explorer 20*, 141, 161, 204  
*Explorer 22*, 105, 109, 551, 552, 554  
  
 Faraday effect, 37, 40, 41, 50, 51, 164, 166, 169, 170, 172, 181, 200, 209-223, 307, 551-560  
  
 Gas spike, 332  
 Group delay effects, 44, 45, 46  
  
*Injun III*, 141  
 Industrial noise, 401-405  
 Integrated electron content, 221  
 Ionogram, topside, 135, 136, 139, 143  
 Ionospheric deviation angle, 86, 93  
 Ionospheric irregularity, diurnal variation, 185-189; E-layer, 238; general, 161, 181, 185-192, 204, 225-238  
 Ionospheric profile, Earth, 91, Mars, 78  
 Ionospheric resonance, 133-155; lower hybrid, 147, 153; upper hybrid, 137  
  
 Laser propagation, 445-472  
*LES*, 523  
 LF window, 393  
 Lincoln calibration sphere, 527, 528  
*Lofti I*, 171  
 Lyman- $\alpha$ , 275  
  
 Magnetic K index, 246-248  
*Mariner II*, 60, 72  
*Mariner IV*, 60, 72, 75  
 Mars, 73, 75-80  
 Martian atmosphere, 76; ionosphere, 78, 79  
 Mercury, radar cross-section, 62, 73  
 Millimeter propagation, 475-521  
 Moon, 73  
  
*Nimbus*, 226-233  
 Noise, antenna, 526; atmospheric, 398-401; cosmic, 44-46, 281; industrial, 401-405; terrestrial, 383  
  
*Orbis*, 131, 560  
 Optimal process, 309-325  
*OSO-D*, 280  
*OSO-I*, 283  
  
 Plasma measurements, 337-349  
 Plasma sheath, 287-307, 327-335, 351-374  
 Polarization rotation (see Faraday effect), deep space, 64; ionospheric, 37, 40, 41, 50, 51, 164  
 Proton whistlers, 143, 151, 152, 154

- Quivering, 449
- Radar coverage, 423-429
- Radio stars. *See Cassiopeia and Cygnus*
- Re-entry plasma, 287-307, 327-335
- Refraction, ionospheric, 7, 8, 9, 85-103;
  - total, 11, 50, 52, 529-545; tropo-
  - spheric, 4, 5, 6, 7, 423-429, 500, 501,
  - 535
- Refractivity and water vapour, 542-544
- Riometer, 263
- San Marco*, 107, 109-111, 131, 552, 560
- Satellites, *DE-C*, 181; *LES*, 523;
  - S-66*, 181, 187, 210, 216, 218, 223;
  - OSO-D*, 280; *OSO-1*, 283; *UK-2*, 150.
 (See also *Alouette I and II*, *Ariel*, *Early-*  
*bird*, *Explorer 20* and *22*, *Injun III*,  
*Lofti I*, *Mariner II* and *IV*, *Nimbus*,  
*Orbis*, *San Marco*, *Tiros 9*, *Topsi Transit*,  
 and *Vela*.)
- Scintillation effects, amplitude, iono-  
 spheric, 27, 105-131, 203, 207, 241-  
 259, 551-560; trophospheric, 504;  
 angle of arrival, ionospheric, 23, 244-  
 246, tropospheric, 20; phase change,  
 ionospheric, 24, 207; tropospheric, 24;  
 range fluctuations, ionospheric, 24;  
 tropospheric, 27
- Signal intensity, VLF, 175-178
- Sky emission, 498, 499
- Solar corona, 73
- Solar X-rays, 275-285
- Sudden cosmic noise enhancement, 281
- Sudden frequency deviation (SFD), 275,  
 284
- Terrestrial noise level, 383-408
- Thermal turbulence, 446, 461
- Time delay effects, ionospheric, 13;  
 tropospheric, 13
- Tiros 9*, 226, 235-239
- Topsi* (S48), 85-102, 161. (See also  
*Explorer 20*)
- Topside ionograms, 135, 136, 139, 143
- Topside spread-F, 203-207
- Transit*, 173
- Transit IVA*, 107, 552
- Tropospheric absorption, 411-421, 492-  
 520
- Tropospheric turbulence, 431, 445-473
- U.K. 2* (see *Ariel*), 150, 157
- Vela*, 276
- Venus, radar cross-section, 62; polariza-  
 tion, 64, 65; range, 69, 70, 71; refrac-  
 tion, 73; spectrogram, 66
- V.L.F. emissions, 144
- Water injection, 333
- Wavefront coherence, 433-444
- Whistlers, proton, 143, 151, 154; short  
 fractional hop, 141, 154

# NAMES INDEX

Entries in bold type indicate the authorship of a chapter

- Aarons, J., 13, 53, 130, 238  
 Adams, R. H., 261, 262, 264, 265, 268, 269, 270, 272, 335  
 Adgie, R. L., 242, 259  
 Aiken, A. C., 283  
 Albrecht, H. J., **175**, 179  
 Allis, W. P., 156, 320, 325, 335  
 Allison, W. D., 375  
 Al'pert, Ya. L., 90, 103  
 Altman, C., 175, 178  
 Anastassiades, M., 50, 102, 129, **181**, 547, 559  
 Anicin, B. A., 348  
 Anway, A. C., 545  
 Appleton, E. V., 90, 103, 429  
 Arendt, P. R., **209**, 223, 224  
 Arkin, H., 207  
 Arndt, D., 272  
 Atlas, D., 35, 54  
 Aurejac, J. F., **105**, **551**  
 Austin, P. M., 528  
 Autler, S. H., 489, 521
- Bachynski, M. P., **287**, 308, 335  
 Bailey, D. K., 261, 262, 264, 268, 272  
 Barrington, R. E., 144, 156, 157, 285  
 Barron, W. R., 53  
 Basler, R. P., 245, 259  
 Battesti, J., 431  
 Bauer, S. J., 224  
 Bean, B. R., 7, 13, 34, 53, 54, 529, 530, 536, 545, 546  
 Bearce, L. S., 178  
 Becker, G. E., 489, 521  
 Beckman, 446, 452  
 Beckman, P., 454, 473  
 Beers, N. R., 54  
 Belrose, N. M., 153, 156, 157  
 Bennett, S. M., 261, 270  
 Beran, M. J., 440  
 Bernstein, I. B., 150, 157  
 Berry, F. A., 54  
 Bers, A., 156, 325, 335  
 Bertin, F., 129, 558  
 Beynon, W. J. G., 90, 103  
 Biswas, S., 272  
 Blackadar, A. K., 473
- Blackband, W. T., xiv., 50, 130, 212, 213, 224  
 Blackman, R. B., 248, 259  
 Blanco, V. M., 521  
 Blumble, L. J., 224  
 Boithais, L., 431  
 Bollay, E., 54  
 Boltyanskikh, V. G., 325  
 Booker, M. G., 23, 27, 53, 201  
 Born, M., 440, 474  
 Bostrom, C. O., 272  
 Bottier, M. F., 520  
 Bouche, E., 462, 474  
 Bowen, 283  
 Bowhill, S. A., 224  
 Bowles, K., 90, 103  
 Boxhill, S. A., 43, 55  
 Boyd, G. D., 336  
 Bradley, P. A., 103  
 Breisach, 130, 559  
 Bremmer, H., 319, 321, 325  
 Brennan, P. M., 205  
 Brice, N. B. I., 140, 154, 156, 157  
 Briggs, B. H., 203, 206, 255, 256, 260  
 Bromley, E. N., 237, 239  
 Brown, 472, 474  
 Brown, R. R., 242, 259, 271, 272  
 Browne, I. C., 223  
 Buchsbaum, S. J., 156, 325, 335  
 Budden, K. G., 150, 156, 157, 158, 159, 178, 348  
 Burgess, B., 158, 282, 284, 547  
 Burrows, C. R., 421  
 Burrows, M. L., 528
- Cahoon, B. A., 7, 53, 530, 545  
 Cain, D. L., **75**, 80, 81  
 Calvert, W., 156, 157, **161**, 204, 206, 207  
 Calvin, T., 375  
 Campen, C. F., 4, 53  
 Carswell, A. J., 335  
 Castelli, J. P., 53  
 Chamberlain, J. W., 81  
 Checcacci, P. F., 130  
 Chivers, H. J. A., 30, 53, 206, 284  
 Chmela, A. C., 54  
 Chubb, T. A., 283

- Chvojikova, E., 85, 86, 103  
 Cloud, J. D., 473  
 Cloutier, G. G., 308, 335  
 Colavito, C., 433, 440  
 Cole, A. E., 4, 53  
 Colin, L., 8, 53  
 Colton, R. R., 207  
 Compton, R. T., 352, 375  
 Conner, J. P., 283  
 Cook, W., 260  
 Cory, H., 175, 178  
 Counter, V. A., 44, 55  
 Crane, R. K., 524, 528  
 Crawford, F. W., 157  
 Croghan, R. D., 177, 178  
 Culhane, J. L., 283  
 Cullen, A. L., 348  
 Cutrona, L. J., 474
- Daniell, G. J., 150, 157  
 Daniels, F. B., 224  
 D'auria, G., 440  
 Davies, K., 80, 102, 157, 158, 172, 207, 284, 336, 547  
 Davis, R. M., 45, 55  
 Deam, A. P., 24, 54  
 Deaton, T., 260  
 DeWitt, R. N., 245, 259  
 Dieminger, W., 50, 130, 285  
 Dimick, R. C., 335  
 Dingle, R. B., 265, 272  
 Dnestrovski, Yu. N., 336  
 Drake, F. D., 75, 80, 81  
 Du Castel, 421  
 Duncombe, 71  
 Du Waldt, B. J., 520
- East, T. W. R., 34, 54  
 Easterling, M., 59  
 Edwards, 413  
 Ehmert, A., 272  
 Elliott, R. S., 42, 44, 55  
 Epstein, E. E., 520  
 Eshleman, V. R., 73, 75, 80, 81  
 Evans, J. V., 43, 54, 103, 193, 223, 283
- Fannin, B. M., 24, 54  
 Fejer, J. A., 157  
 Fichtel, C. E., 272  
 Field, L. M., 336  
 Field, R. W., 336  
 Fischer, S. T., 308  
 Fischer, W. H., 209  
 Fjeldbo, G., 75, 81
- Flood, W. A., 233, 239  
 Fooks, 185  
 Forrester, A. T., 473  
 Forsyth, P. A., 226, 239  
 Frank, N. H., 325, 473  
 Freid, 473  
 Freier, P. S., 261, 271, 272  
 Fremouw, E. J., 225, 226, 233, 238, 239, 260  
 Freid, D. L., 473  
 Friedman, H., 283
- Gagnon, R. J., 252, 260  
 Galeys, J., 352, 375  
 Gamkrelidze, R. V., 325  
 Gamo, H., 473, 474  
 Garber, W. A., 502, 521  
 Garriott, O. K., 81, 224, 260  
 Geddes, R. N., 520  
 Gerson, N. C., 285  
 Ghosh, S. N., 413, 415, 417, 421  
 Gjessing, D. T., 411, 423, 429  
 Goe, G. B., 156  
 Goldstein, L., 348  
 Goldstein, R., 59  
 Gonzalez, V. H., 38, 54  
 Goodwin, F. E., 461, 473  
 Gordy, W., 421, 489, 521  
 Gould, R. W., 336  
 Graf, K. A., 306  
 Grau, J., 209  
 Gruber, S., 251  
 Gunn, K. L. S., 34, 54  
 Gurnett, D. A., 151, 156, 157  
 Guss, D. E., 272
- Hagg, E. L., 153, 156  
 Hall, S. C., 260  
 Hamilton, T. W., 80, 81  
 Hanbury, R., 242, 259  
 Hara, E. H., 265, 272  
 Hargreaves, J. K., 223  
 Harney, P., 325  
 Harnischmacher, E., 163, 172, 177, 179  
 Harris, J. H., 374  
 Hartsel, J. E., 335  
 Hartz, T. R., 156  
 Harvey, C. C., 157  
 Hayakawa, J., 260  
 Helm, R., 336  
 Hebstreit, J. W., 24, 53  
 Hernquist, K. G., 336  
 Herzberg, L., 157  
 Hessler, V., 260



# NAMES INDEX

- Hewish, A., 23, 27, 53, 54  
Hill, R. M., 489, 521  
Hodara, H., 294, 308, 351, 374, 445, 474  
Hoffman, J. W., 325  
Hoffman, L. A., 475, 502, 520, 521  
Hofmann, D. J., 265, 272  
Holt, J. M., 545  
Hook, J. L., 245, 259  
Hopkins, 34  
Hotston, E., 348  
Hultquist, B., 261, 272  
Hunsucker, R. D., 226, 239  
Hurlbut, 336  
Hurst, P., 375  
Hynek, D. P., 54
- Iliff, W. R., 545  
Ingersoll, J. G., 521  
Irgens, F., 429
- Jacobs, E., 520  
Jacob, K. G., 349  
Janes, H. B., 546  
Jespersen, J. L., 53, 203, 204, 207, 251, 259  
Johnson, E. O., 347, 348  
Johnson, W. A., 520  
Johnston, T. W., 156, 308  
Jones, T. B., 275, 284
- Kamas, G., 204, 207, 251, 259  
Kaplan, L. D., 81  
Katsujrakis, J., 156  
Keeley, D. A., 156  
Keppler, E., 265, 272  
Kerr, D. E., 33, 53  
Kharadley, M. M. Z., 348  
Khintchine, 199  
Kim, H. R., 325  
King, H. E., 520  
King, J. W., 224  
Kiruna, 187  
Kliore, A. J., 75, 80, 81  
Knecht, R. W., 156, 207  
Knop, C. M., 366, 374  
Kohl, H., 224  
Kostomarov, 336  
Kreplin, R. W., 283  
Krina, G. S., 157  
Krzywoblockiv, M. Z., 309, 321, 325  
Kuiper, G. P., 81
- Lamb, R. C., 53, 207, 259  
Landan, L. D., 201  
Lansinger, J. M., 207, 239, 241, 260
- Latimer, B. P., 375  
Lawrence, R. S., 13, 23, 27, 28, 30, 53, 193, 206, 207, 251, 259, 260, 281, 284  
Leinbach, H., 37, 54  
Leiphart, J. P., 175, 177, 178  
Lerjald, G. M., 270  
Levy, G. S., 75, 80, 81  
Lifshitz, E. M., 201  
Linder, E. G., 336  
Lindsay, J. C., 275, 283  
Liszka, L., 184, 187, 193, 245, 246, 251, 259, 260  
Little, C. G., 23, 27, 30, 37, 53, 54, 193, 206, 207, 233, 238, 239, 242, 246, 255, 256, 259, 270, 284  
Lockwood, G. E. K., 156  
Long, R. K., 465, 474  
Love, A. W., 520  
Lovell, A. C. B., 206  
Lumley, J. L., 546  
Lundberg, C., 325  
Lusignan, B., 37, 54, 72, 81
- McCready, L. L., 8, 53  
McCuskey, S. W., 521  
McEwen, D. J., 157  
McGavin, R. E., 529, 546  
Malaviya, V., 415, 417, 421  
Maliphand, R. G., 85, 86, 102, 103  
Malter, L., 347, 348  
Mandel, L., 474  
Mandelstam, S., 283  
Markevitch, 336  
Marner, G. R., 8, 13, 53  
Marshall, J. S., 54  
Masley, A. J., 261, 262, 264, 265, 268, 269, 270, 272  
Matsoukas, O., 181  
Maxwell, A., 27, 37, 54, 238, 318  
Meng, C. Y., 521  
Merrill, R. G., 187, 193, 252, 260  
Merritt, R. P., 53, 200, 239, 259  
Meyer, 473  
Middleton, D., 202  
Mie, G., 528  
Miller, J., 207  
Millman, G. H., 3, 43, 50, 53, 54, 55, 408  
Mischenko, E. F., 325  
Mitra, S. K., 335  
Moene, A., 429  
Moorcroft, 226, 233, 239  
Mori, T. T., 520  
Muchmore, R. B., 20, 23, 24, 53  
Muhleman, D. O., 73, 80, 408

- Muldrew, D. B., 103, 153, 156, 157  
Mullen, C. R., 306, 308  
Munch, G., 81  
Murray, W. A. S., 223
- Nelms, G. L., 156  
Nerem, R. M., 335  
Newcombe, 71  
Nichols, D. E. T., 55  
Nicolet, M., 283  
Nordberg, W., 269, 272  
Norton, K. A., 545  
Noyes, J. C., 260  
Nuttal, J., 156
- O'Brien, B. J., 272  
Oliner, A. A., 374  
Omura, M., 374  
Osborne, F. J. F., 308  
Owren, L., 226, 233, 238, 239, 245, 259, 260
- Paghis, I., 133, 158, 207, 349  
Palmer, H. P., 259  
Panofsky, H. A., 546  
Papet-Lepine, J., 105, 129, 130, 131, 551, 559, 560  
Parkin, I. A., 255, 260  
Parrent, G. B., 440, 474  
Parthasarathy, R., 260, 262, 263, 270  
Parzen, P., 335  
Paulsen, W. M., 54  
Payne-Scott, R., 53  
Pawsey, J. L., 45, 48, 53, 55  
Pearson, 205  
Petrie, L. E., 156  
Pfofzer, G., 272  
Piddington, J. H., 48, 55  
Pieper, G. E., 265, 272  
Pineo, V. C., 54  
Plank, V. G., 54  
Pontryagin, 313, 314, 325  
Posakany, D. J., 260  
Potts, B. C., 224  
Pounds, K. A., 283, 284  
Pryce, M. H. L., 325
- Ranzi, 547  
Ratcliff, J. A., 201, 335  
Rawer, K., 130, 158, 159, 172, 179, 270, 285, 348, 349, 375, 383, 408, 559  
Rawhouser, R., 327, 336  
Read, W. S., 473, 474  
Reber, E. E., 520
- Reichley, P., 73  
Reid, G. C., 53, 207, 239, 259, 261, 262, 270  
Reidel, 44  
Reppermond, H., 179  
Ricardi, L. J., 523  
Ringo, R. M., 8, 13, 53  
Roberts, J. A., 251, 259  
Robson, P. N., 337, 348, 349  
Roper, N. J., 193, 260  
Rosati, V. J., 224  
Rosen, G., 335  
Rossi, J. J., 335  
Rourke, G. F., 261  
Roy, S. K., 272  
Rusch, W. V. T., 373, 374  
Russell, S., 156  
Ryan, W. D., 246, 259  
Ryde, S. W., 33, 54, 418, 420, 421, 528  
Ryle, M., 259
- Samaras, D. G., 325  
Sanders, A. E., 54  
Sanford, P. W., 283  
Saxton, 34  
Schmid, C. W., 206  
Schulkin, M., 489, 506, 519, 545  
Schultze, A. E., 489  
Schwitters, R., 260  
Seidl, M., 348  
Sen, H. K., 265, 272  
Sengupta, D. L., 374  
Shapley, A. H., 45, 55  
Shawhan, S. D., 156, 157  
Sheriff, R. M., 103  
Shimabukuro, F. I., 520  
Shinn, D. H., 201  
Shkarofsky, I. P., 156, 308  
Shmoys, J. J., 348  
Shore, R. A., 440  
Shurygin, A., 283  
Simon, P. G. L., 50  
Sims, J. E., 335  
Singer, S. E., 283  
Slager, D. M. J., 348  
Slater, J. C., 325  
Smerd, S. F., 48, 55  
Smith, E. K., 4, 53, 521  
Smith, F. L., 81  
Smith, R. L., 141, 156, 157  
Soicher, H., 173, 209  
Soo, S. L., 335  
Spangenberg, K., 336

# NAMES INDEX

- Spencer, M., 207  
 Spinrad, H., 81  
 Spitzer, L., Jr., 325  
 St. Clair, C. R., Jr., 325  
 Stacey, J. M., 520  
 Steiger, W. R., 37, 54  
 Stewart, R. D., 337, 348  
 Stiltner, E., 53, 207, 239, 259  
 Stradberg, 416  
 Strandberg, W. P., 521  
 Strands, H. W., 473  
 Stratton, 421  
 Strimple, G., 224  
 Sughy, K., 158  
 Swenson, G. W., Jr., 224, 238  
 Swift, C. T., 348, 351, 375  
  
 Tamir, T., 309  
 Tatarski, V. I., 473  
 Tausworthe, R. C., 72  
 Taylor, G. N., 193  
 Thayer, G. D., 536, 545, 546  
 Thomas, J. O., 103  
 Thompson, A. R., 259  
 Thompson, M. C., 24, 53, 546  
 Thrane, E. V., 284, 285  
 Tindo, I., 283  
 Tinkham, 416  
 Titheridge, J. E., 187, 193  
 Tolbert, C. W., 489  
 Toth, E., 178  
 Turkey, J. W., 248, 259  
 Twiss, 472, 474  
  
 Van Vleck, J. H., 28, 31, 35, 53, 474, 475, 487, 501, 506, 519-521  
 Van Zandt, T. E., 156, 161, 207  
 Vasilyev, B., 283  
 Vassy, E., 129, 130, 172, 558, 559  
  
 Villeneuve, 352, 375  
 Voge, J., 547  
 Vogt, G., 209, 224  
 Voronko, Y., 283  
  
 Wait, J. R., 177, 178, 351, 362, 374  
 Warren, E. S., 157  
 Warwick, J. W., 37, 54, 251, 259  
 Watson, G. N., 177, 178  
 Watt, A. D., 177, 178  
 Webber, W. R., 261, 262, 264, 265, 268, 269, 271, 272  
 Weintraub, S., 4, 53, 521  
 Weir, R. A., 261, 262, 264, 268, 269, 271, 272  
 Weisbrod, S., 8, 53  
 Weiss, H. H., 175  
 Weisskopf, V. F., 487, 501, 520  
 Welcher, P., 325  
 Wharton, C. B., 348  
 Wheelon, A. D., 20, 23, 24, 53  
 Weiner, N., 199, 202  
 Wild, J. P., 251, 259  
 Williams, I. J., 520  
 Willmore, A. P., 283  
 Winckles, J. R., 265, 272  
 Wintroub, H. J., 502, 520, 521  
 Wolf, E., 440, 474  
 Wong, J. L., 520  
 Wortendyke, D. R., 465, 474  
 Wyller, A. A., 265, 272  
  
 Yaglom, A. M., 202  
 Yeh, K. C., 38, 54, 173, 195, 224, 238  
  
 Zeek, R. W., 178  
 Zernike, F., 440  
 Zmuda, A. J., 272  
 Zucker, F. J., 440

# INDEX OF PLACES AND INSTITUTIONS

- Accra, 284
- Aerospace Corps, 475-477, 502
- Africa, 560
- Airborne Instruments Laboratory, 103
- Air Force Avionics Laboratory Wright-Paterson, A.F.B., Ohio, U.S.A., 327, 330
- Air Force Research Laboratory, 559
- Air Force (U.S.), 476, 521, 528
- Alaska, 23, 226, 229
- Alexandropolis, 50, 182
- Arabian Gulf, 536
- Astronomical Unit, 71
- Athens, xiii, 50, 108, 109, 111, 113, 115, 118-130, 181, 182, 183, 186, 192, 285, 553-556, 559, 560
- Atlantic Ocean, 331
- Australia, 76
- Berne (Ionospheric station), 164, 168
- Boeing Scientific Research Laboratories, 237, 239, 241, 260
- Boston, Mass., 526
- Boulder, Colorado, 529
- Bundesministerium für Wissenschaftliche Forschung, 173, 408
- California, 76, 536
- California Institute of Technology, 75
- Cambridge, Mass., 525
- Camp Parks, Calif., 523
- Cedar Rapids, 533-553
- Central Radio Propagation Laboratory, Boulder, Colorado, U.S.A., 161, 203, 530, 536
- Centre National d'Etudes Spatiales, 559
- CNET, Issy-Les-Moulineaux, Seine, France, 431
- College Alaska, 138, 203, 204, 206, 225, 226, 229, 230, 233, 237, 238, 241, 243, 244, 245, 256, 248, 255, 256, 262, 263, 265
- Collins Radio (see Cedar Rapids), 533-535
- Colorado, 284, 536
- Cornel University, 75
- Crete, 50, 181, 182, 285
- Dakar, 536
- Defence Research Board, Ottawa, Canada, 103
- Defence Research Telecommunications Establishment, Ottawa, Ontario, Canada, 133, 134, 152
- Denmark, 560
- Earth, xiii
- El Campo, Texas, 102
- Electronics Research Laboratory (Aerospace Corp.), 476, 477
- El Segundo, 475, 477, 502, 510
- Environmental Science Services Administration, 529
- E.S.R.O., 226
- Europe, 172, 404, 558
- Fairbanks, 225
- Florence, 130, 131
- Forschungsinstitut für Hochfrequenzphysik 5321 Werthhoven, Federal Republic of Germany, 175
- France, 107, 431
- Freiburg (Ionospheric Station), 164, 168, 169
- Garchy (Ionospheric Station), 164, 168
- General Electric Company, Syracuse, New York, 3, 7, 27
- Genova (Ionospheric Station), 164, 168
- Geophysical Institute, University of Alaska, 225, 226, 229, 233, 260
- Ghana, 284
- Gilmore Creek, 225, 226, 229, 230, 233, 237, 238
- Goddard Space Flight Center, Washington, D.C., 152, 239
- Government Communications Headquarters, Cheltenham, England, 85, 103
- Greece, 50, 285
- Gunbarrel Hill, Calif., 536, 537
- Halley Bay, Antarctica, 205
- Hawaii, 284
- Honolulu, 284

- Illinois University, 193  
 India, 536  
 Instituto di Elettronica, Università di Roma, 433  
 Ionosphären-Institut Breisach, 163, 383  
 Ionospheric Institute of Athens, 285  
 Israel, 560  
  
 Japan, 130, 404, 559  
 Jet Propulsion Laboratory, Pasadena, 59, 60, 61, 80  
 Jodrell Bank, 130, 559  
  
 Kiruna, 108, 109, 111, 113, 117-127, 130, 131, 553-560  
 Kjeller, Oslo, 108, 109, 111, 113, 116, 118, 121, 122, 125, 126, 127, 130, 131, 553-560  
  
 Langley Research Center, 348, 351  
 Leicester University, 275  
 Lincoln Laboratory, M.I.T., 523, 524, 528  
 Los Angeles, 477, 519  
  
 Mare Acidalium, 7, 9  
 Mars, xiv  
 Martian Desert, 78  
 Massachusetts Institute of Technology, 523, 525  
 Mani, 536  
 Michigan State University, 309, 325  
  
 National Aeronautics and Space Administration, N.A.S.A., 103, 134, 221, 224, 226, 375  
 National Bureau of Standards, Boulder, Washington, 280, 281, 284  
 National Engineering, Science Company, Pasadena, Calif., U.S.A., 351, 445  
 Nato Advanced Study Institute, Finse, Norway, 161  
 Naval Observatory (U.S.), 535  
 Naval Research Laboratories, 276  
 New Zealand, 187  
 North America, 138, 140  
 North Atlantic, 138, 140  
  
 Norwegian Defence Research Establishment, 284, 411, 423  
  
 Oslo, 119, 120, 122, 123, 124  
 Ottawa, 151, 153  
  
 Pacific, 172  
 Pakistan, 536  
 Penteli Hill, 181, 184, 192  
  
 R.A.E., 55  
 Radio Physics Laboratory, Ottawa, 157  
 Radiophysics Laboratory, Dartmouth College, 239  
 Radio Research Station, Slough, 96, 103  
 R.C.A. Victor Research Laboratories, Montreal, Canada, 287  
 Resolute, 153  
 Resolute Bay, N.W.T., 138  
 Royal Norwegian Air Force, 429  
  
 Santa Monica Airport, 490  
 Saskatchewan, 226  
 Saskatoon, 226  
 Scaramaga Station, 192  
 Science Research Council, 348  
 Senegal, 536  
 Sheffield University, England, 337, 348  
 Slough (see Radio Research Station), 96  
 South Atlantic, 153  
 South West Africa, 536  
 Space Radio Systems Facility (SRSF), 476, 479  
 Stanford University, 75,  
  
 Trinidad, 27, 38, 43  
  
 United States, 331, 404  
 U.S.A.F., 521, 528, 560  
 U.S. Air Force Research Laboratory, Cambridge, Mass., 130  
 U.S. Army Electronics Command, Fort Monmouth, New Jersey, 209  
 U.S. Naval Observatory, 535  
  
 Val-Joyeux, 105, 109, 111, 113, 114, 118-130, 551, 553-559  
  
 Wallops Station, 331  
 Westford, Mass., 523